Accumulation and Clearing of Ions in Circular Electron Accelerators

Dissertation
zur
Erlangung des Doktorgrades (Dr. rer. nat.)
der
Mathematisch-Naturwissenschaftlichen Fakultät
der
Rheinischen Friedrich-Wilhelms-Universität Bonn

von
Dennis Sauerland
aus
Warburg

Bonn, Juni 2019

Angefertigt mit Genehmigung der Mathematisch-Naturwissenschaftlichen Fakultät der Rheinischen Friedrich-Wilhelms-Universität Bonn

1. Gutachter:	Prof. Dr. Wolfgang Hillert
2. Gutachter:	Prof. Dr. Klaus Desch
Tag der Promotion:	11.10.2019
Erscheinungsjahr:	2020

To everlasting Change
with enduring Friendships.

Abstract

Modern sychrotron light sources have to provide stable storage for electron beams with high charge densities to make brilliant synchrotron radiation available to users. Since requirements on the brilliance of the radiation are constantly rising, amongst others the stored beam current in these accelerators has to be increased further. The electron beam, however, interacts with residual gas within the vacuum chamber of the accelerator and thereby continuously produces positively charged ions. These are attracted by the electron beam and accumulate in its beam potential. Besides changing the focusing strength for the electron beam, the ions' space charge also cause beam instabilities. Both effects significantly reduce the lifetime of the beam and limit the storable beam current. Accumulated ions are therefore an obstacle to the provision of highly brilliant synchrotron radiation in future accelerators, which are even more susceptible to these effects. Consequently, efforts are being made to reduce accumulated ions to a minimum in electron accelerators. Here, for example, gaps in the beam's filling pattern are applied to remove ions from the beam. Since the use of filling gaps in recent accelerator developments is not feasible or desirable anymore, the use of local clearing electrodes, which systematically draw ions away from the beam, gains in importance. The correct positioning of these electrodes is essential for reducing the ion density to even lower levels than previously achieved. It is therefore indispensable to understand the ion dynamics and the longitudinal transport mechanisms towards clearing electrodes in all areas of the accelerator, especially within the fields of guiding magnets and rf cavities.

The thesis presented covers aspects of ion production and accumulation, their effects on the beam as well as their mitigation. These are studied by means of numerical simulations, modelling and deduced measurements at the ELSA storage ring, in which ion induced effects are observable with a large diagnostic variety.

The motion of ions in the accelerator is determined by their space charge interaction with each other and with the electron beam. A considerable part of ions are produced within dipole magnets via photo ionization of residual gas by synchrotron radiation, emitted from the electron beam. Here, their motion becomes more complex as additional cross-field drifts emerge. To identify clearing electrode positions for an effective removal of ions in these magnets, the ions have to be tracked by sophisticated numerical simulations. To provide reliable results, local ion production maps are required for these simulations, which are now provided by a tool developed within the course of this work.

The transversal ion production map is asymmetrical in the horizontal plane, as ions are also produced far outside the beam center by photo ionization. As the ions' spatial distribution determines their effect on the beam, this asymmetry also reflects in the ion induced change in focusing strength.

Additionally, the longitudinal ion transport through multi-cell rf cavities is studied in consideration of the cavities' electromagnetic rf fields. Here, emerging ponderomotive forces drive ions into field-free regions, trap them and thus prevent an transport towards clearing electrodes.

Furthermore, this work proposes measures to further reduce the ion density within the studied regions and provides an overview of ion phenomena and mitigation strategies at the ELSA storage ring.

Contents

CHAPTER 1

Introduction

1.1 Trapped Ions in Circular Electron Accelerators

Modern third-generation synchrotron radiation sources and future "Ultimate Storage Rings" (see e.g. [Bor+10]) have to store high-intensity electron beams with high charge density to provide high-brilliance synchrotron radiation light to their users. Ever-increasing requirements on the brilliance of synchrotron radiation light leads to the necessity to further increase the beam's charge density.

Stored electrons, however, interact with residual gas in the vacuum system of the accelerator and thus continuously produce positively charged ions. These ions are attracted by the electron beam, accumulate in its vicinity and interact with it by their space charge force. This interaction results in diverse effects on the beam. Especially ion induced beam instabilities are a limitation for acceleration and storage of high-intensity electron beams. The severity of these effects scales with the amount of accumulated ions in the accelerator. Therefore, countermeasures are deployed, aiming for a reduction of the ion population.

Since the 1980s, the subject of accumulated ions in circular electron accelerators has been studied. In theory, certain aspects of induced effects and their production by impact ionization have been described in an idealized form. Also the use of clearing electrodes and application of filling gaps for the mitigation of ion effects has already been discussed. These have been successfully used in older-model synchrotron radiation light sources, which have been constructed in the 1990s.

For new synchrotron radiation light sources, where current and charge density of the stored beam is increased further, these countermeasures are insufficient or not applicable anymore. As a consequence, high ion densities in combination with high beam currents intensify repercussions and therefore are a limiting factor for successful operation of these accelerators. While the planning of these new ambitious accelerator projects progresses, adequate ion mitigation strategies gain priority. To achieve this premise, profound knowledge about the ions' density distribution and their detailed dynamics in all sections of the accelerator, previously simplified or neglected, is mandatory.

A majority of produced ions propagates through regions of the accelerator where the magnetic guiding field inside dipole magnets affects their motion significantly. Additionally, ion production is augmented in these magnets due to photo ionization of residual gas by synchrotron radiation, emitted by the beam. This production mechanism has been predominantly neglected. The determination of the density distribution of these photo-produced ions is an essential ingredient for sophisticated numerical simulations. They are

used to track the ion motion in these fields and are mandatory for the formulation of an adequate local ion clearing strategy.

These simulations enable a precise tracking of trajectories of an ion population but their computations are time-consuming and are limited to very small sections of an accelerator. Therefore, it is also necessary to develop tools, giving a more coarse insight into certain aspects of ion motion or accumulation within a larger domain, to identify accelerator sections where e.g. an elevated ion accumulation is expected and subsequent investigations are required for the targeted use of local clearing measures.

The studies covered in this work represent a link between measurements and simulations regarding ion production, accumulation, their effects and mitigation or clearing in electron accelerators. This work has been funded by the Federal Ministry of Education and Research Germany in the course of a joint project[1] between associates of the University of Rostock, the Helmholtz Center Berlin and the University of Bonn.

The thesis includes the discussion of the ion production mechanism of photo ionization by synchrotron radiation in dipole magnets. Here, effective cross sections for this process are evaluated, enabling a determination of its contribution to the total ion production rate. Additionally, a calculation model for numerical determination of the transversal ion density distribution of impact- and photo ionization in dipole magnets has been developed. These so called ion production maps are essential for numerical simulations of ion dynamics in dipole magnets. In comparison to impact ionization, the map of photo ionization shows strong horizontal asymmetries. Using different numerical tracking tools, the equilibrium density distribution of ions in dipole magnets and adjacent sections has been obtained.

As these equilibrium ion distributions show significant deviations to expectations, the ions' space charge influence on the beam and the resulting tune shift has been investigated. Indeed, ions cause a spread and a shift of the horizontal and vertical tune which scales with the ions' abundance. However, this spread and shift is significantly reduced due to the photo ionization process and the related alteration of the ions' equilibrium density distribution.

Additionally, the accumulation of ions in several sections of an electron accelerator is investigated on basis of dedicated tracking simulations to identify locations where a high ion density is present. The ion accumulation characteristic within one complete FODO-cell[2] of the storage ring is studied where magnetic fields of dipole and quadrupole magnets influence the ions' trajectories. Here, the ion production mechanism by photo ionization is explicitly included in the simulation. In the rf section of the accelerator the electromagnetic field of rf cavities, oscillating with a frequency in the order of hundreds of MHz, also significantly influences ion trajectories. One basis of the results of these investigations, adequate ion clearing strategies are formulated for the corresponding sections.

In context of this work, also different numerical simulation tools, e.g. for the determination of the efficiency of customized filling patterns and the frequency spectrum of transversely oscillating ion populations, have been developed. Also an approximative method has been developed to estimate the minimal occurring local ion density in dependence of the shape of the attractive electric beam potential.

Although only indirect measurements on properties of the ion population can be conducted, developed models and simulation tools in this work are verified by dedicated and congruent measurements at the storage ring of the ELSA facility. All measurements and simulations therefore are conducted in context of the storage ring, about whose ion related subjects this work also tries to give a comprehensive overview.

[1] Under funding numbers 05K13PDA and 05K16PDA.

[2] In a FODO-cell a horizontally focusing quadrupole (F) is followed by a drift space or dipole (O), which is adjoint by a horizontally defocusing quadrupole (D) and a drift space or dipole (O).

1.2 Electron Stretcher Accelerator - ELSA

The following studies, models and measurements on production and accumulation of ions along with their influence on the beam and their removal from it are conducted exemplarily in context of the storage ring of the ELSA facility in the Physics Institute of the University of Bonn in Germany.

The **El**ectron **S**tretcher **A**ccelerator[3] is an accelerator complex with three cascaded accelerator stages which provides either a spin-polarized or an unpolarized thermionic electron beam for hadron physics experiments and tests of particle detectors. The facility is shown in figure 1.1. Electively, the two injectors LINAC 1 and LINAC 2 supply an electron beam for the booster-synchrotron. LINAC 1 provides an unpolarized beam from a thermionic electron source with a beam energy of 20 MeV whereas LINAC 2 accelerates either a thermionic beam or a spin-polarized beam, generated by the polarized source, to an energy of 26 MeV. Subsequently, the beam is injected into the booster-synchrotron which increases the beam's energy to typically 1.2 GeV during a 10 ms ramp with a cycle frequency of 50 Hz [Alt+68]. Several injections from the booster-synchrotron are accumulated in the storage ring[4] until a designated beam current is reached. Afterwards, the energy of the beam is increased with typically 6 GeV s^{-1} to up to 3.2 GeV. Depending on the operation mode of the storage ring, the beam is either stored for a certain time (storage mode) or subsequently is extracted to one of the experimental areas during a time period of several seconds (booster mode).

Since 2006, double-spin-polarization hadron physics experiments are conducted in form of nuclear spectroscopy measurements of baryon resonances and photo production of mesons. For the two experiments Crystal-Barrel/TAPS and BGO-OD, extracted electrons are converted by interaction with a radiator target into high energetic polarized Bremsstrahlung photons. The photon beam then interacts with polarized target material. For more information on the Crystal-Barrel/TAPS and BGO-OD experiment, see [Har17, section 3.2] and [Fre17, chapter 2], respectively.

Since 2017, the electron beam of the storage ring can be extracted to an additional experimental area. Here, primary electrons with an extraction rate ranging from 300 Hz to 400 MHz can be utilized to test new particle detector technologies and evaluate e.g. their temporal, spatial and energy resolution. See [Heu17] for more information.

In this work the subject of ion production, their accumulation and effects on the beam along with their clearing will be discussed in context of the storage ring exclusively. However, an adaptation of obtained knowledge along with developed models, tools and measurement techniques for other electron accelerators is possible and desirable. In table 1.1, a selection of the storage ring's typical operating parameters is given. For experimental investigations which have been carried out in the course of this work, the storage ring has always been operated in storage mode to guarantee stable conditions of relevant beam parameters like beam energy, pressure and current. To refer to sections of the storage ring which are discussed in the course of this work, the different segments, the RF and straight section as well as arc and missing magnet sections (MM sec.), are also displayed in figure 1.1.

[3] In german, the facility is named **El**ectron **S**tretcher **A**nlage.

[4] The storage ring of the ELSA facility is often denoted as stretcher ring.

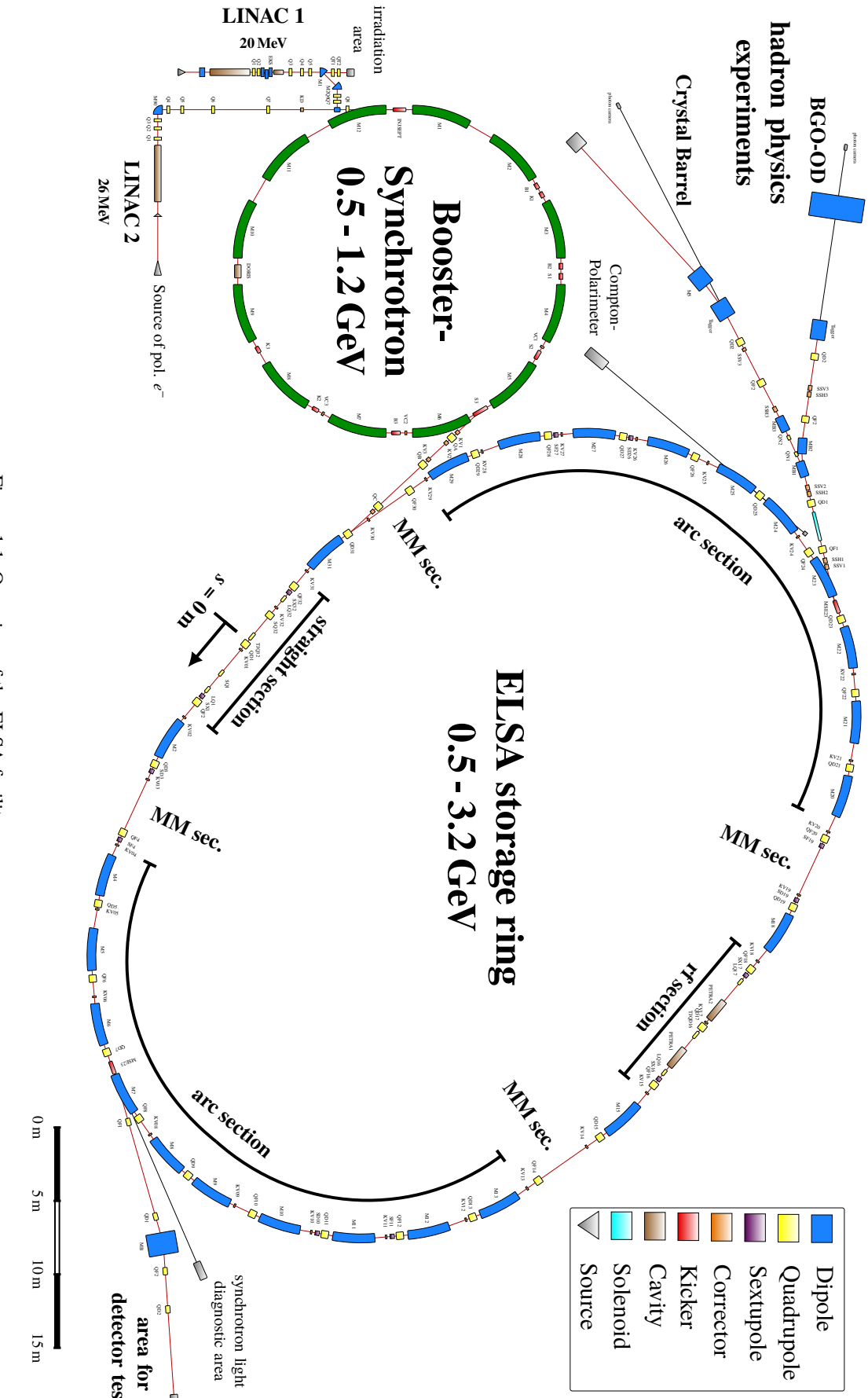

Figure 1.1: Overview of the ELSA facility.

Beam Energy	1.2 to 3.2 GeV
Beam Current	up to 200 mA
Harmonic Number	274
Revolution Frequency	1.824 MHz
Horizontal Tune (typ.)	4.612
Vertical Tune (typ.)	4.431
Horizontal Emittance	131 to 752 nm rad
Horizontal Betafunction	between 2.5 and 17.3 m
Betatron Coupling Coefficient	$\sim 7.2\,\%$
Vertical Emittance	9.4 to 54.1 nm rad
Vertical Betafunction	between 2.4 and 18.6 m
1σ Bunch Length	18.5 to 80 ps
Pressure (avg)	$< 5 \cdot 10^{-7}$ mbar

Table 1.1: Main operating parameters of the ELSA storage ring.

1.3 Investigation of Ion Induced Phenomena in the ELSA Storage Ring

In the course of the past few years, the storage ring has undergone several infrastructural upgrades to enable storage of an electron beam with a current of up to 200 mA for beam energies below 2.6 GeV[5]. These comprise the extension of corrective and diagnostic capabilities within the storage ring regarding occurring transversal and longitudinal beam instabilities.

To provide a stable electron beam, a bunch-by-bunch feedback system has been installed [Rot13; Sch15]. This feedback system detects the transversal and longitudinal oscillation amplitude of each bunch and damps occurring beam instabilities by application of individual correction kicks via a strip line kicker (transversal plane) or kicker cavities (longitudinal plane). Additionally, the position of each bunch can be recorded for a time span of several ms enabling analysis of the time-evolution of occurring beam instabilities in spatial and frequency domain. By excitation of individual bunches, their bunch current can be reduced enabling generation of almost arbitrary filling patterns.

In addition, a diagnostic photon beam line has been installed which enables the observation of the synchrotron radiation of the electron beam to, for example, obtain information about the size of the beam [Zan13]. When the optical image of the beam - the profile of the synchrotron radiation in the visible spectral range - is recorded by an installed streak camera, the length of individual bunches can be determined with a time resolution in the order of ps. This enables measurements of the filling pattern and time-evolution of emerging beam instabilities.

Especially at low beam energies of approximately 1.2 GeV and stored beam currents above 40 mA, transversal beam instabilities emerge in the storage ring. The occurrence of these instabilities can be influenced by variation of operation parameters of ion clearing electrodes, which are installed in every quadrupole of the storage ring. These electrodes remove accumulated ions from the beam and aim for the reduction of ion induced effects. The occurring instabilities' influenceability by operation of clearing electrodes indicates that they are driven by accumulated ions.

The existing extensive diagnostic capabilities in the storage ring motivate an in-depth analysis of emerging ion effects and their mitigation along with related topics such as their production and accumulation.

[5] For higher beam energies, the acceleration voltage provided by rf cavities is insufficient to maintain a beam lifetime which exceeds 60 s [Sch15, section 13.1].

This work will first introduce the theoretical basics of ion production and clearing before discussing the physics and characteristics of an electron storage ring followed by an idealized description of the ions' motion in vicinity of the beam in chapter 2. Before discussing the different ion production mechanisms of impact and photo ionization, their ion production maps and estimating their ion production rate in chapter 3, the residual gas composition and the average pressure within the storage ring has to be determined. In chapter 4, ion accumulation within one FODO-cell of the storage ring and in its rf section is discussed on basis of ion tracking simulations. Subsequently, the effect of these accumulated ions on the electron beam is studied in chapter 5. Here, this work emphasis on the influence of photo ionization on the ion induced tune shift and occurring beam instabilities in the storage ring. A suitable approach for mitigation of these effects in discussed in chapter 6 by using filling gaps and ion clearing electrodes.

CHAPTER 2

Basics of Ion Production, Motion and Clearing in Electron Accelerators

The following chapter will discuss the issue of accumulated parasitic ions in an electron synchrotron beginning with the ionization process, in which the ions are generated, followed by important concepts for the mathematical treatment of their production. The ions' accumulation and clearing will be discussed in section 2.2. The motion of ions in an electron accelerator is determined by the electromagnetic fields which the ions encounter during their lifetime in the accelerator. Besides the beam guiding dipole and focusing quadrupole magnets, the electric field of the electron beam is the main contribution to these fields. The field of the beam alters along the accelerator as the magnetic optics shape its charge density. Hence, fundamental concepts of circular electron accelerators will be discussed in section 2.3 before the resulting transversal and longitudinal motion of ions will be covered in section 2.4.

2.1 Ionization Process

Due to the processes of desorption, diffusion and permeation (see figure 2.1 (a), (b) and (c) respectively), electrically neutral residual gas continuously flow out of or through the vacuum chamber[1] into the vacuum system of an accelerator: The process of desorption denotes the detaching of residual gas from the surface of the vacuum chamber. Diffusion is the outgasing of molecules and atoms from within the vacuum chamber into the vacuum system. Small molecules and atoms, especially hydrogen, are capable of moving from the outside through the chamber walls into the system. This process is called permeation. More details regarding outgasing characteristics of the vacuum system are shown in appendix A.1.

Due to this continuous inflow, the lower pressure in the vacuum system is limited to typically 10^{-7} to 10^{-9} mbar. The residual gas molecules and atoms drift within the beam pipe with a Brownian movement with a mean free path length of 10^3 to 10^5 m at these pressures. For an accelerator with a beam pipe diameter in the order of centimeters and length of its straight sections in the order of several meters, the molecules and atoms mainly do not interact with each other but with the beam pipe. Thus, their motion inevitably crosses the region of the vacuum system, where the beam is guided through the accelerator.

Here, the residual gas can be ionized in two different processes: Impact ionization by the beam electrons, which collide with the residual gas, and photo ionization by synchrotron radiation photons, emitted by the beam electrons in the dipole magnets.

[1] The vacuum chamber in which the beam is guided through the accelerator is often also denoted as beam pipe.

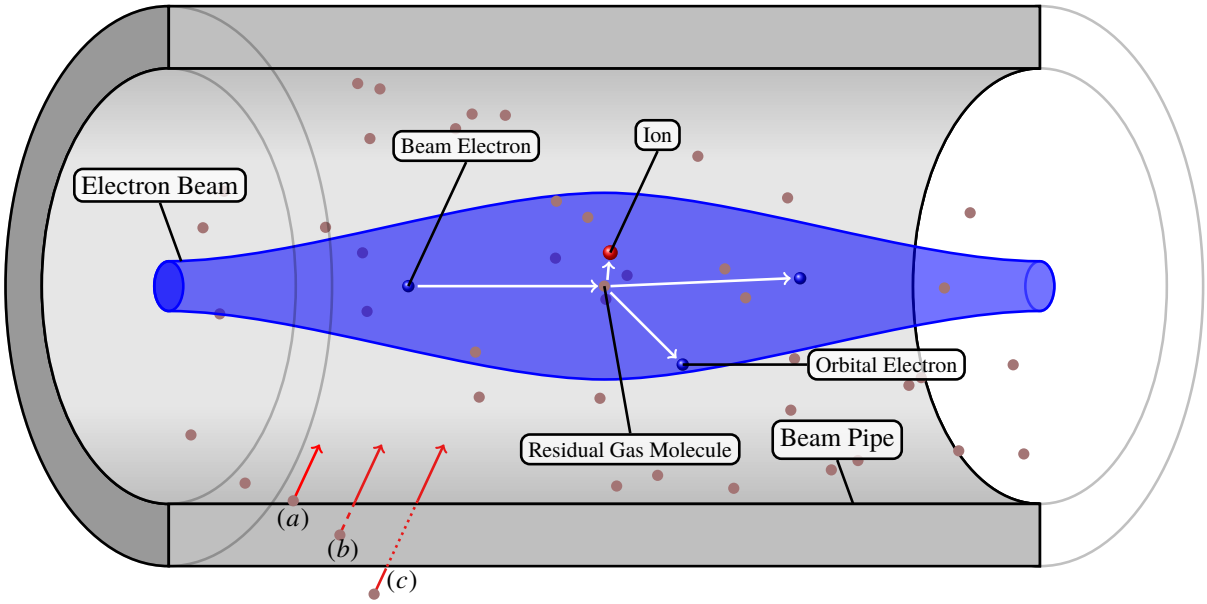

Figure 2.1: Illustration of the generation of an ion. Here, the electrons ionize the residual gas in the beam when colliding with them. New residual gas molecules and atoms are continuously entering the beam pipe by the processes of desorption (a), diffusion (b) and permeation (c).
Note that the illustration is not to scale.

In a circular accelerator with a circumference C and a beam current I, there is a number of

$$N_\mathrm{e} = \frac{I \cdot C}{\mathrm{e}\beta c} \tag{2.1}$$

electrons which travel with a velocity βc. Here, β is the fraction of the velocity to the speed of light c. e is the elementary charge. The electrons e^- of the beam have a kinetic energy E_kin and interact electromagnetically with the residual gas molecules and atoms $\mathcal{A}$, which have a thermal kinetic energy E_therm (see figure 2.1). During this interaction the residual gas is ionized. The interaction can be depicted[2] as

$$\mathrm{e}^-(E_\mathrm{kin}) \;+\; \mathcal{A}(E_\mathrm{therm}) \qquad \longrightarrow \qquad \mathrm{e}^-(E'_\mathrm{kin}) \;+\; \mathcal{A}^+(E_\mathrm{therm} + \Delta E_\mathrm{nucleus}) \;+\; \mathrm{e}^-(\Delta E_\mathrm{e})\,.$$

The beam electron's kinetic energy is reduced to E'_kin due to an energy transfer ΔE_e to an orbital electron and $\Delta E_\mathrm{nucleus}$ to the nucleus of the molecule as will be discussed in section 2.1.2. This process is called impact ionization and is discussed in detail in section 3.3.

When electrons are deflected in the dipole magnets, they emit synchrotron radiation (for details see section 2.3.2). The emitted synchrotron radiation photons γ_sr with energy E_γ can also ionize the residual gas. This represents another mechanism for ion production. The photo ionization process can be depicted as

$$\gamma_\mathrm{sr}(E_\gamma) \;+\; \mathcal{A}(E_\mathrm{therm}) \qquad \longrightarrow \qquad \mathcal{A}^+(E_\mathrm{therm} \;+\; \Delta E_\mathrm{nucleus}) + \mathrm{e}^-(\Delta E_\mathrm{e})$$

and will be discussed in section 3.4. During the interaction of the photon with the residual gas molecule,

[2] In this notation, the kinetic energy of the particle is given in brackets behind the particle's symbol.

a Compton-scattering of the synchrotron radiation photon with an orbital electron of the residual gas molecule is also probable for $E_\gamma > 100\,\mathrm{keV}$. However, this work emphasis on the photo ionization process.

In summary, only positively charged ions can be produced by the electron beam.

2.1.1 Initial Condition

Without beam, the neutral residual gas molecules and atoms are in a thermal equilibrium with their surrounding environment. In absence of cryo systems[3] in the accelerator, the ions are assumed to have a temperature T of approximately 300 K. The mean thermal kinetic energy is given by

$$\left\langle E_{\mathrm{kin}} \right\rangle = \frac{3}{2} k_{\mathrm{B}} T \,.$$

Here, k_{B} is the Boltzmann constant. Thus, the residual gas on average has a kinetic energy of 38.8 meV.

The corresponding average thermal velocity of a residual gas molecule j with mass m_j is given by

$$\left| v_{\mathrm{rms},j} \right| = \sqrt{\frac{3 k_{\mathrm{B}} T}{m_j}} \,. \tag{2.2}$$

In each direction, the residual gas molecule has an average velocity of

$$\left\langle |v_{x,j}| \right\rangle = \left\langle |v_{z,j}| \right\rangle = \left\langle |v_{s,j}| \right\rangle = \sqrt{\frac{2 k_{\mathrm{B}} T}{\pi m_j}} \tag{2.3}$$

in the horizontal, vertical or longitudinal plane[4].

2.1.2 Energy Transfer during the Ionization Process

To estimate the kinetic energy of an ion after the ionization process, one has to analyze the energy transfer from the incident beam electrons to the orbital electron, bound to the residual gas molecule.

The energy transfer to the orbital electron in dependence of the impact parameter b during the process of impact ionization is given by [Jac62, section 13.1, equation 13.2]

$$\Delta E_{\mathrm{e}}(b) = \frac{e^4}{8\pi^2 \varepsilon_0 m_{\mathrm{e}} \beta^2 c^2} \frac{1}{b^2} \,. \tag{2.4}$$

The incident electron has a velocity of βc. m_{e} is the electron mass and ε_0 is the electric field constant. The impact parameter b is unique to each interaction. The minimal impact parameter ($b \to 0$) resembles a head-on collision where the energy transfer is maximal, whereas long distant collisions ($b \to \infty$) show only a minimal energy transfer to the orbital electron.

If the energy transfer to an orbital electron is compared to the energy transfer to the nucleus with

[3] In some accelerators superconducting magnets or rf cavities are operated. In order to enable superconductivity, these elements have to be cooled down to temperatures of tens of K or below. Adjoining vacuum systems and their intrinsic residual gas molecules and atoms will therefore also have lower thermal velocities.

[4] The horizontal plane is denoted as x-plane, whereas the vertical plane is indexed with z. The longitudinal coordinate is s. See section 2.3.1 for more detailed information regarding the coordinate system in an accelerator.

identical impact parameters, it can be shown that [Pon94, section 2, equation 4]

$$\Delta E_{\text{nucleus}} = \frac{m_{\text{e}}}{2m_{\text{p}}} Z' \cdot \Delta E_{\text{e}} \,. \tag{2.5}$$

m_{p} is the mass of the proton, which is around 1 836 times larger than the electron mass. Z'[5] is the proton number of the nucleus. This implies that during the ionization process the main part of the beam electron's energy loss is transferred to the electron. Only a small fraction is transferred to the nucleus.

It has been calculated that the energy transfer ΔE_{e} to the orbital electrons is below 45 eV for 85 % of the occurring ionizations. The average energy transfer is around a few eV [LP80]. Thus, for atomic hydrogen H_1, the energy transfer $\Delta E_{\text{nucleus}}$ to the ion after the ionization process is approximately a factor of 4 000 lower and is in the order of a few meV. For carbon dioxide CO_2 the transferred energy is even lower with $6 \cdot 10^{-6} \Delta E_{\text{e}}$.

Consequently, it holds that $\Delta E_{\text{nucleus}} \ll \langle E_{\text{kin}} \rangle$ for the majority of the ionization processes. Therefore, one can assume that the energy transfer to the produced ions is approximately zero and their kinetic energy is the same as the neutral residual gas from which they originate.

Due to the opposite electric charge of the electron beam and the produced low-velocity ions, the emerging attractive Coulomb force prevents the ions' escape and transversely "traps" them close by the beam. The orbital electron leaves the interaction region with a velocity in the order of km s^{-1} and impinges on the beam pipe. The beam electron, in contrast, stays within the beam, if its energy loss does not exceed the accelerator's longitudinal acceptance.

2.2 Concepts of Production Rate, Clearing Rate and Neutralization

As singly or multiply charged particles, the ions will be accelerated and deflected by the electromagnetic fields in the accelerator after their generation and will move transversely and longitudinally along the accelerator. But before looking at the transversal and longitudinal motion of ions, which are described in section 2.4.1, it is necessary to look at the theoretical handling of production and clearing of ions.

Note that only a simple case with one ion species is considered here - the handling of production, clearing and accumulation of multiple ion species is discussed in section 2.2.4. Nonetheless, the discussed concept is valid for scenarios with single and multiple ion species alike.

2.2.1 Ion Production Rate

In a circular electron accelerator with circumference C in which a total number of N_{e} ultra relativistic electrons are stored, the number of recently produced ions $\mathrm{d}N_{\text{ion}}$ per time interval $\mathrm{d}t$ is given by [Hin11, section 5.3, equation (21)]

$$\frac{\mathrm{d}N_{\text{ion}}}{\mathrm{d}t} = \sigma_{\text{ion}} N_{\text{e}} \nu_0 n_{\text{rgm}} C \,. \tag{2.6}$$

[5] Contrary to the convention in physics, the ionization state of the residual gas molecule is referred to as Z in this work, whereas Z' denotes the atomic number.

Here, σ_{ion} is the total cross section for the ionization processes[6] and ν_0 is the revolution frequency of the electron beam in the accelerator. The number density of the residual gas n_{rgm} can be expressed as

$$n_{\text{rgm}} = \frac{N_{\text{rgm}}}{V} = \frac{\mathcal{P}}{k_{\text{B}}T} , \tag{2.7}$$

their total number N_{rgm} in a volume V or via the average (total) pressure $\mathcal{P}$ of the vacuum system inside the accelerator.

Using the relation between N_{e} and the beam current I from equation (2.1), one can obtain

$$\frac{\mathrm{d}N_{\text{ion}}}{\mathrm{d}t} = \frac{\sigma_{\text{ion}} \cdot I \cdot \mathcal{P}}{\mathrm{e}k_{\text{B}}T} ,$$

where measurable parameters of the accelerator, namely the beam current and pressure of the vacuum system, are introduced and are the only free parameters.

As can be seen in equation (2.6), the total number of produced ions is directly proportional to the number of electrons in the accelerator, therefore the *production rate* R_{p} *per electron* is defined as

$$\frac{\mathrm{d}N_{\text{ion}}}{\mathrm{d}t} = R_{\text{p}} \cdot N_{\text{e}} \qquad \text{and thus} \qquad R_{\text{p}} = \frac{\sigma_{\text{ion}} \cdot \beta c \cdot \mathcal{P}}{k_{\text{B}}T} , \tag{2.8}$$

where the relation $\nu_0 \cdot C = \beta c$ is used.

2.2.2 Clearing Time and Clearing Rate

When a singly charged ion i is generated out of a neutral residual gas molecule, it has a limited lifetime τ_i after which it recombines[7] with an electron and becomes an electric neutral particle again. The lifetime is different for every ion and is dependent of numerous factors such as the ion's mass and charge, as this defines the ion's motion, and its transversal and longitudinal position in the accelerator. The mean value of the lifetime of all ions is called $\langle\tau\rangle$.

To limit the number of ions in the accelerator, usually methods of *ion clearing* are applied. These methods aim for the reduction of $\langle\tau\rangle$. Concepts and methods of ion clearing will be discussed in chapter 6 in detail.

Since the mean ion lifetime $\langle\tau\rangle$ is directly related to the efficiency of the applied ion clearing methods, it is also called *clearing time* T_{c}. Its inverse is called the *clearing rate* R_{c}. So one obtains the relations

$$\frac{1}{\langle\tau\rangle} = \frac{1}{T_{\text{c}}} = R_{\text{c}} .$$

If multiple clearing processes with clearing rates $R_{\text{c},j}$ take place at once, the total clearing rate is given by

$$R_{\text{c}} = \sum_j R_{\text{c},j} = \sum_j \frac{1}{T_{\text{c},j}} .$$

For multiply charged ions, the clearing time is more precisely defined as the mean time in which one elementary charge e is removed. Consequently, for an ion i with charge Z_i the individual clearing time $T'_{\text{c},i}$ is $1/Z_i$th of its lifetime τ_i, if the ion is completely neutralized at once.

[6] σ_{ion} is the sum of all possible ionization cross sections. It includes the cross section for electron impact ionization and photo ionization and is dependent on the beam energy.

[7] This recombination predominately takes place, when the ion impinges on the beam pipe or on ion clearing electrodes.

2.2.3 Accumulation and Neutralization

As can be seen in equation (2.8), the production of singly charged ions is proportional to the number of electrons in the accelerator. The number of cleared ions per time interval $\mathrm{d}t$ is proportional to the actual number of ions in the beam. Thus, one obtains the differential equation for the evolution of the ion population in the accelerator with [Hin11, section 6.2, equation (36)]

$$\frac{\mathrm{d}N_{\mathrm{ion}}}{\mathrm{d}t} = R_{\mathrm{p}} \cdot N_{\mathrm{e}} - R_{\mathrm{c}} \cdot N_{\mathrm{ion}} \,. \tag{2.9}$$

Hence, the solution for the progress of the ion number $N_{\mathrm{ion}}(t)$ can be written as follows

$$N_{\mathrm{ion}}(t) = N_{\mathrm{ion}}(t_0) \cdot \exp\left(-R_{\mathrm{c}} \cdot t\right) + N_{\mathrm{e}} \frac{R_{\mathrm{p}}}{R_{\mathrm{c}}} \left(1 - \exp\left(-R_{\mathrm{c}} \cdot t\right)\right) \,, \tag{2.10}$$

where $N_{\mathrm{ion}}(t_0)$ is the initial number of ions. If one sets t_0 to a point in time where the beam is injected into the accelerator $t = 0$, it can safely be assumed that $N_{\mathrm{ion}}(t_0)$ equals zero.

When ions accumulate in the accelerator's electron beam, the so-generated ion cloud, consisting of positive charges, shields parts of the electron beam's attractive force from newly produced ions. Thus, the attractive force which traps the ions in the beam is reduced by every new ion in vicinity of the beam, eventually preventing the trapping of additional ions. This is the case when the number of ions is equal to the number of electrons. If this number is reached, ions will be repelled by the ion cloud and leave the vicinity of the beam. Since the production of ions never stops as long as the electron beam is stored in the accelerator, one expects a constant drift of ions away from the beam in that case.

Consequently, it is useful to parameterize the state of the accumulation for singly ionized residual gas with a parameter

$$\eta = \frac{N_{\mathrm{ion}}}{N_{\mathrm{e}}} \leq 1 \,, \tag{2.11}$$

which is called *neutralization*. When also considering multiply ionized residual gas molecules and atoms, N_{ion} is equal to the number of positive charges in the accelerator.

With the neutralization parameter, one can rewrite equation (2.10) to

$$\eta(t) = \frac{R_{\mathrm{p}}}{R_{\mathrm{c}}} \cdot \left(1 - \exp\left(-R_{\mathrm{c}} \cdot t\right)\right) \,, \tag{2.12}$$

if $\eta(t_0) = N_{\mathrm{ion}}(t_0)/N_{\mathrm{e}}$ is assumed to be zero.

Figure 2.2 shows different scenarios of $\eta(t)$ to visualize its behavior, if R_{p} and R_{c} are constant and do not change over time or with the neutralization itself. The blue curve shows a scenario where $R_{\mathrm{p}} = R_{\mathrm{c}} = R_0$. Consequently, the neutralization reaches a value of one in the equilibrium state at $t \to \infty$. If the clearing rate is a factor of three larger, as shown by the red curve, saturation occurs at a value of one third, while the initial slope of the curve resembles the blue one. This is due to the production rate R_{p}, which is equal in both cases. If the production rate decreases to half of R_0, the initial slope also decreases, resulting in an equilibrium level of one sixth, as displayed as the orange curve. If the initial neutralization is above the equilibrium state level, $\eta(t)$ decreases until this level is reached, as can be seen in the gray curve.

In equation (2.12), the equilibrium state of the neutralization is directly visible as

$$\eta\left(t \to \infty\right) = \frac{R_{\mathrm{p}}}{R_{\mathrm{c}}} \,, \tag{2.13}$$

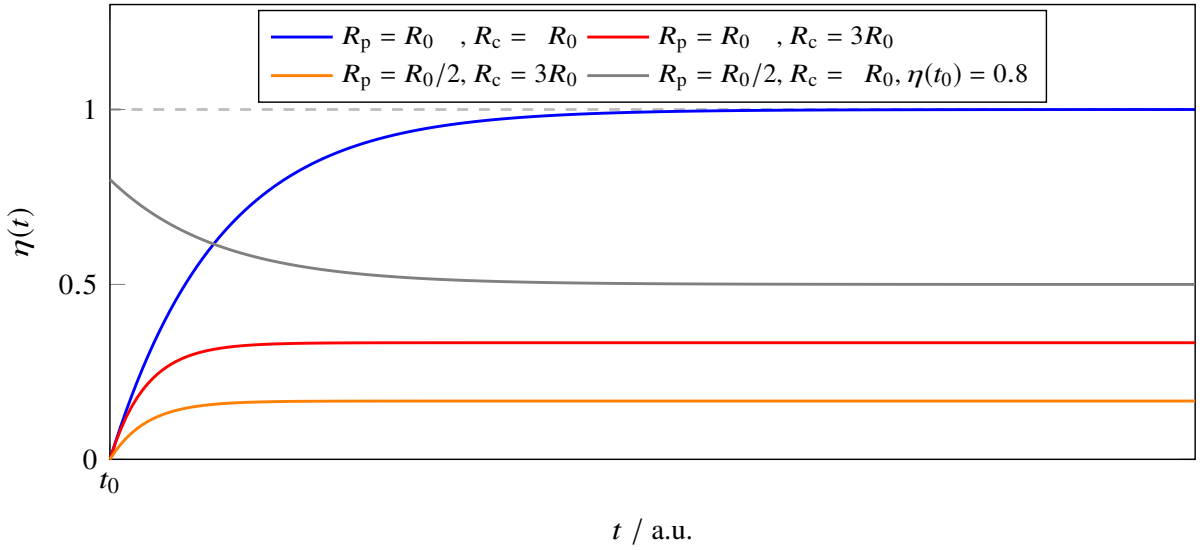

Figure 2.2: Time evolution of the neutralization $\eta(t)$ for different settings of clearing R_c and production rates R_p in reference to a rate R_0.

and in short is denoted as η. In most cases, the beam neutralization level η implicitly denotes the equilibrium state of the neutralization $\eta(t \to \infty)$. To fulfill the conditions at the space charge limit $\eta = 1$ for $t \to \infty$, it is implicitly postulated that at least at this limit the clearing rate R_c is dependent on the neutralization and that $R_c(\eta \to 1) = R_p$.

In order to compare the ability of an accelerator to produce ions with other machines, it is common to utilize the *neutralization time*. It is the time which is needed to reach full neutralization, or $\eta = 1$, in a hypothetical case where the total clearing rate R_c is zero. In this case, equation (2.9) can be modified to

$$\frac{\mathrm{d}}{\mathrm{d}t}\left(\frac{N_{\mathrm{ion}}}{N_e}\right) = \frac{\mathrm{d}\eta}{\mathrm{d}t} = R_p \,.$$

This simple differential equation can be solved by integration, since R_p is assumed to be constant over time. Thus, the solution reads

$$\eta(t) = R_p \cdot t \,, \tag{2.14}$$

with which the number of ions would linearly increase with time as expected. The neutralization time T_n is the time in which the number of ions equals the electron number in the accelerator, thus it requires

$$\eta(t = T_n) \stackrel{!}{=} 1 \,.$$

Using this relation with equation (2.14), one obtains

$$T_n = \frac{1}{R_p} \tag{2.15}$$

for the neutralization time. Since the residual gas constituents of the vacuum system of an accelerator usually consists of more species than one, R_p can be understood as a sum of the individual production rates of each species. This will be discussed in the following section.

2.2.4 Accumulation of Multiple Ion Species

In the vacuum system of an accelerator usually exists more than one species of residual gas molecules and atoms. Every species has its own probabilities to be ionized by the electron beam, which expresses in individual ionization cross sections $\sigma_{\mathrm{ion},i}$, as will be discussed e.g. in section 3.3 in detail. Each ion species has a specific contribution to the average total pressure $\mathcal{P}$ of the accelerator's vacuum system, which is called *partial pressure* p_i. The individual average partial pressures can be summed up as

$$\mathcal{P} = \sum_i p_i \ . \tag{2.16}$$

The difference of the partial pressure and ionization cross section of the ion species results in an individual production rate $r_{\mathrm{p},i}$. Hence, the total production rate can be obtained with

$$R_{\mathrm{p}} = \sum_i r_{\mathrm{p},i} \ . \tag{2.17}$$

The population of generated ions consists of singly or multiply ionized molecules and atoms which differ in their individual masses m_i. In this work the mass of an ion species will be approximated as

$$m_i \approx A_i \cdot m_{\mathrm{p}} \ , \tag{2.18}$$

where A_i is the mass number, the number of protons and neutrons in the molecule. The mass of an electron is negligibly small compared to the proton or neutron mass. Also the neutron and proton are approximated to have equal mass and the binding energies of the atom cores and molecules are omitted. In this work the relevant mass number regime is between two (molecular hydrogen H_2^+) and 44 (carbon dioxide CO_2^+). If this approximation is used for these molecules and atoms, the relative mass error is below 0.7 %. Thus, it is a suitable approximation.

Due to their different mass, the individual ion species will move with different velocities within the beam pipe when drifting with thermal energies or being accelerated by the attractive space charge force of the electron beam. Thus, each ion species has individual lifetimes and clearing rates $r_{\mathrm{c},i}$.

The different production rates $r_{\mathrm{p},i}$ and clearing rates $r_{\mathrm{c},i}$ influences the composition of the ion population which are trapped in the beam. If there are k different ion species within the beam pipe, where $N_{\mathrm{ion},i}$ is the number of a specific ion species i, equation (2.9) can be modified to

$$\frac{\mathrm{d}N_{\mathrm{ion}}}{\mathrm{d}t} = \sum_{i=1}^{k} \frac{\mathrm{d}N_{\mathrm{ion},i}}{\mathrm{d}t} = \sum_{i=1}^{k} \left(N_{\mathrm{e}} \cdot r_{\mathrm{p},i} - N_{\mathrm{ion},i} \cdot r_{\mathrm{c},i} \right) \ .$$

Since N_{ion} is the sum of all $N_{\mathrm{ion},i}$, the solution can be separated for each ion species by using the *partial neutralization* $\eta_i(t)$. Of course, this parameter has to fulfill the space charge limitation

$$\eta(t) = \sum_i^k \eta_i(t) = \sum_i^k \frac{N_{\mathrm{ion},i}(t)}{N_{\mathrm{e}}} \leq 1 \ . \tag{2.19}$$

Thus, the solution is similar to equation (2.12) and reads

$$\eta(t) = \sum_{i=1}^{k} \eta_i(t) = \sum_{i=1}^{k} \frac{r_{\mathrm{p},i}}{r_{\mathrm{c},i}} \cdot \left(1 - \exp\left(-r_{\mathrm{c},i} \cdot t\right)\right) \ . \tag{2.20}$$

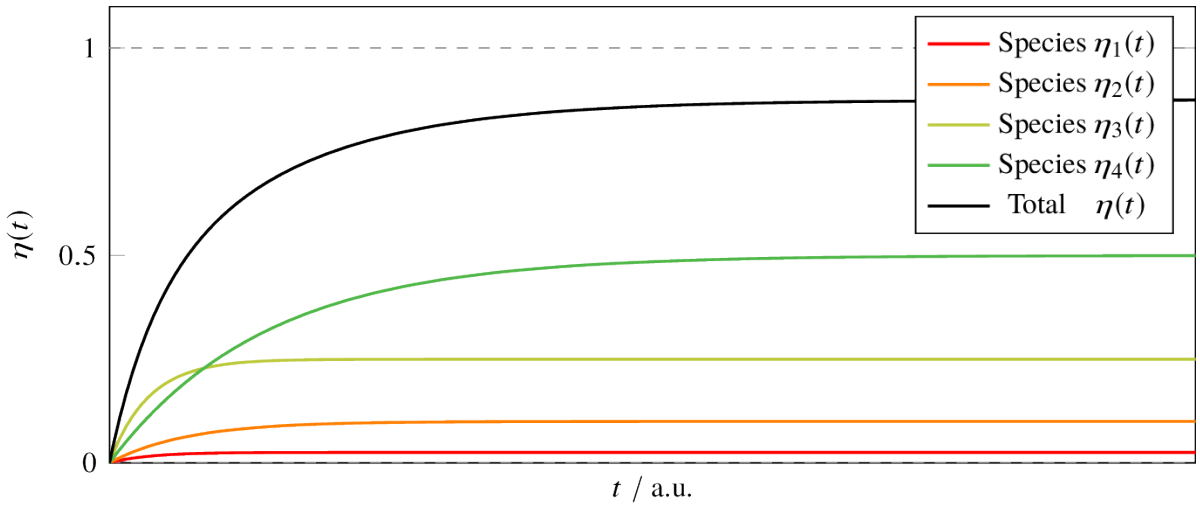

Figure 2.3: Time evolution of the partial neutralization $\eta_i(t)$ of four exemplary ion species. They have individual production $r_{\mathrm{p},i}$ and clearing rates $r_{\mathrm{c},i}$ which result in various η_i for $t \to \infty$. Exemplarily, a nominal rate r_0 is defined as reference. For the shown four species the production and clearing rates are modified as follows: Species 1 (green): $r_{\mathrm{p},1} = r_0/2$, $r_{\mathrm{c},1} = r_0$; Species 2 (yellow): $r_{\mathrm{p},2} = r_0$, $r_{\mathrm{c},2} = 4r_0$; Species 3 (orange): $r_{\mathrm{p},3} = r_0/5$, $r_{\mathrm{c},3} = 2r_0$ and Species 4 (red): $r_{\mathrm{p},4} = r_0/10$, $r_{\mathrm{c},4} = 4r_0$. Thus, their contribution to the ion population is different for each species. The total ion population is shown in the black curve.

In figure 2.3, the time evolution of the partial neutralizations of four ion species is shown, which have different configurations of production and clearing rate, thus reaching various levels of neutralization. It shows that the composition of the total ion population is strongly dependent on the production and clearing processes.

To determine the total clearing rate R_{c}, it is not possible to add up all individual clearing rates. The clearing rates have to be weighted by the individual contribution of the ion species to the population. Thus,

$$R_{\mathrm{c}} = \frac{1}{N_{\mathrm{ion}}} \sum_{i=1}^{k} N_{\mathrm{ion},i} \cdot r_{\mathrm{c},i} \ ,$$

as is shown in appendix A.2. Here, N_{ion} and $N_{\mathrm{ion},i}$ are the individual ion numbers in the equilibrium state for $t \to \infty$.

2.2.5 Local Ion Production and Clearing

Along the beam pipe of the accelerator, the conditions for ion production and clearing may vary strongly.

If one considers the ion production conditions, the variation occurs due to changes in the total pressure $\mathcal{P}$ along the accelerator which is expressed by $\mathcal{P}(s)$. Due to the varying vacuum characteristics of the beam pipe, the immission of individual residual gas molecules and atoms underlies changes along the accelerator. Thus, the partial pressure p_i of the individual species also changes, consequently resulting in a varying composition of the ion population along s. These effects condense in a (total) local production rate $\hat{R}_{\mathrm{p}}(s)$ changing along the accelerator. Additionally, the local clearing rate $\hat{R}_{\mathrm{c}}(s)$ is also not constant along the accelerator. This is due to variations of the lifetime of the ions along the storage ring.

The total production rate R_{p} can be expressed by the integral over all *specific* production rates $R_{\mathrm{p}}^{\dagger}(s)$

along s. The same relation applies to the *specific* clearing rates $R_{\mathrm{c}}^{\dagger}(s)$. Thus, it holds

$$R_{\mathrm{p}} = \oint_0^C R_{\mathrm{p}}^{\dagger}(s)\,\mathrm{d}s \qquad \text{and} \qquad R_{\mathrm{c}} = \oint_0^C R_{\mathrm{c}}^{\dagger}(s)\,\mathrm{d}s\ .$$

If one considers the local evolution of the ion population in the area of a length $\Delta s/2$ around a longitudinal position s in the accelerator, the local production rate in this area can be expressed as

$$\hat{R}_{\mathrm{p}} = \frac{R_{\mathrm{p}}}{C}\Delta s\ , \tag{2.21}$$

if one choses the production rate to be the average rate of the accelerator and thus $R_{\mathrm{p}}^{\dagger}(s) = R_{\mathrm{p}}/C$.

The local clearing rate due to applied clearing mechanisms in the same area is non-zero and is denoted as $\hat{R}_{\mathrm{c}}(s)$. Consequently, an ion population develops with a local equilibrium neutralization of

$$\hat{\eta}(s) = \frac{\hat{R}_{\mathrm{p}}(s)}{\hat{R}_{\mathrm{c}}(s)} = \frac{\hat{N}_{\mathrm{ion}}(s)}{\hat{N}_{\mathrm{e}}} \leq 1\ , \tag{2.22}$$

where $\hat{N}_{\mathrm{ion}}(s)$ is the number of ions in the described area. $\hat{N}_{\mathrm{e}}$ is the fraction

$$\hat{N}_{\mathrm{e}} = \frac{N_{\mathrm{e}}}{C}\Delta s$$

of the total electron number N_{e} in the accelerator.

The total neutralization η for the accelerator can be expressed as the average of all local neutralizations $\hat{\eta}(s)$. Thus, it holds

$$\eta = \frac{1}{C}\oint_0^C \hat{\eta}(s)\,\mathrm{d}s\ . \tag{2.23}$$

Note that the discussed calculus for the accumulation of an ion population, consisting of several ion species, can be applied in the formalism of the local ion production and clearing, too. In this work a convention is followed where the local quantities are denoted by a hat, e.g. $\hat{R}_{\mathrm{p}}$, $\hat{\eta}$ and quantities of one ion species are indexed and in lower case, e.g. $r_{\mathrm{p},i}$, η_i. Of course, it is possible to have a local quantity of a particular ion species, which will be denoted with a hat in addition to an index in lower case, e.g. $\hat{r}_{\mathrm{p},i}$, $\hat{\eta}_i$.

2.3 Beam Dynamics in an Electron Synchrotron

The understanding of the movement of ions in the accelerator is essential to formulate an adequate strategy for their clearing. Their motion is determined by the space charge forces the ions are exposed to. On one hand, this is the space charge of the ions' interaction with each other, which gets more dominant with rising neutralization. On the other hand, the space charge interaction with the electron beam, which is represented by an attractive electric potential which is called *beam potential*, is of importance. As will be shown in section 2.4.1, the transversal and longitudinal shape of this potential is determined by the dimensions of the electron beam and the vacuum chamber. Consequently, it is necessary to look at the dynamics of the electron beam.

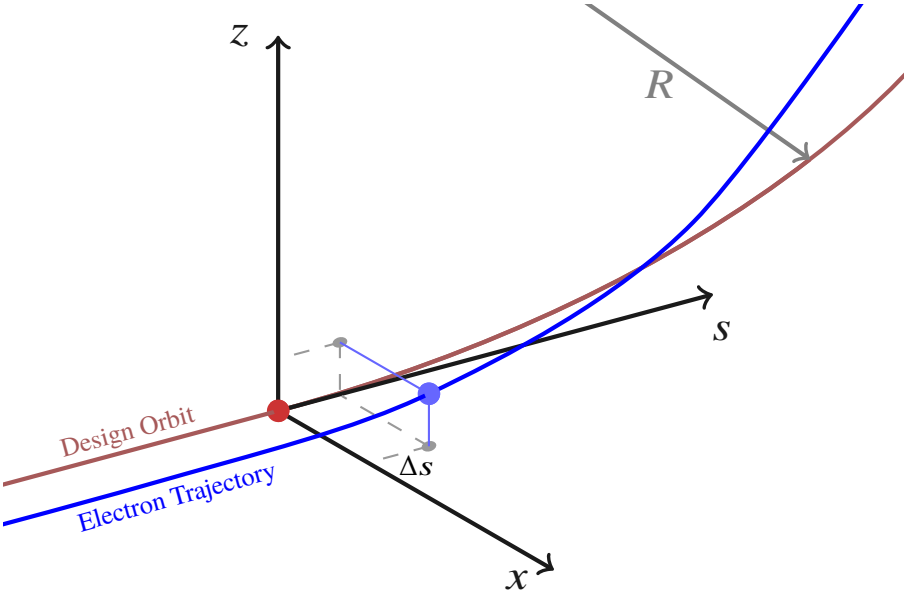

Figure 2.4: Curvilinear coordinate system in particle accelerators. The design orbit of an ideal electron trajectory, going through the center of every quadrupole magnet in the accelerator, is shown in red. In dipole magnets, the design orbit is bend by the LORENTZ force to a radius R. The individual electron trajectory, shown in blue, follows the design orbit but has a horizontal and vertical displacement x and z from it. Δs denotes its longitudinal deviation in reference to the ideal trajectory along the longitudinal s axis. This axis points in the direction of the momentum vector of the ideal trajectory on the design orbit.

2.3.1 Curvilinear Coordinate System

To describe the movement of electrons in the accelerator, a suitable coordinate system is used. The transversal beam size is typically in the order of a few millimeter or below whereas the dimension of the accelerator is in the order of tens or hundreds of meters. Therefore, all transversal coordinates of individual electrons are given in reference to the design orbit of the accelerator. It is the ideal trajectory of an electron going through the center of each quadrupole and it is fixed by the alignment of the optical elements during the construction of the accelerator[8]. Consequently, in dipole magnets, where the design orbit is deflected with a radius R, the coordinate system is rotated along with the electron trajectory.

As is illustrated in figure 2.4, the individual trajectory of an electron is described in the curvilinear co-moving coordinate system $K(x, z, s)$. The Δs-coordinate shows the longitudinal displacement of the individual electron in reference to a particle on the design orbit. The s-axis points in direction of the particle's momentum vector. The x-coordinate indents the horizontal displacement of the electron from the design orbit. This axis is aligned parallel to the radius R of the deflection in the dipole magnets and perpendicular to the s-axis. The z-axis denotes the vertical deviation from the design orbit and is aligned perpendicular to the x- and s-axis.

The individual electron trajectory follows the design orbit with a displacement x and z. This displacement does not stay constant along the accelerator. Thus, the variation of the transversal

[8] The rf frequency used in the rf cavities for the acceleration of the electron beam also defines the ideal trajectory. Here, a frequency shift varies the design energy of the beam which results in different deflection radii in the dipole magnets and consequently an altered ideal trajectory. For more information, see section 2.3.2.

coordinates along s are the derivative of x and z. They are denoted

$$x'(s) = \frac{\mathrm{d}}{\mathrm{d}s}x(s) \qquad \text{and} \qquad z'(s) = \frac{\mathrm{d}}{\mathrm{d}s}z(s)\,.$$

For an individual electron with a momentum deviation Δp from the momentum p_0 of the electron on the design orbit, one can construct a six-dimensional vector [Wil00, section 3.5, equation 3.107]

$$\mathbf{X} = \begin{pmatrix} x \\ x' \\ z \\ z' \\ \Delta s \\ \frac{\Delta p}{p_0} \end{pmatrix}\,.$$

With this vector an electron trajectory can be described suitably.

Due to magnetic field errors or misalignments of the magnets the real orbit is not necessarily equal to the design orbit. This orbit is called *closed orbit*. In this work, the deviation between design and closed orbit is assumed to be negligibly small. Under this assumption, a similar coordinate system can be used to describe the ion motion.

The beam, an ensemble of N_e individual electrons with slightly different trajectories, has its center of charge on the design orbit during the accelerator operation. Thus, the motion of the attracted ions is concentric around the center of charge, the design orbit, resulting in a mostly symmetric transverse ion distribution[9] around it. Therefore, it is useful to describe the horizontal and vertical displacement of the ions from the center of charge with x and z, too. For the longitudinal coordinate s, an absolute position is used in order to localize quantities, for example a local clearing rate $\hat{R}_\mathrm{c}(s)$, an electron beam size $\sigma_x(s)$ or the position of a clearing electrode $s_\mathrm{electrode}$, in the accelerator. The origin $s = 0\,\mathrm{m}$ of this absolute longitudinal coordinate system can be chosen arbitrarily along the ring and is typically defined during the accelerator's planning stage. The origin of the ELSA storage ring, to which absolute positions are referenced in the context of this work, is displayed in figure 1.1.

2.3.2 Longitudinal Dynamics of the Electron Beam

Dipole magnets are used to deflect the electron beam onto a circular trajectory. Quadrupole magnets, however, are utilized to focus the beam in the transversal plane. The reversing force of the focusing magnetic fields is proportional to electrons' displacement from the design orbit, resulting in a transversal incoherent[10] oscillation of the electrons around it, which is called *betatron oscillation*. In the longitudinal plane, the acceleration of the electrons is realized by alternating electric fields, applied on the beam by radio frequency cavities[11] operating with a frequency ν_rf. Thus, electrons with non-vanishing momentum

[9] Due to synchrotron radiation in the arc sections of the accelerator, ions can be produced by photo ionization there. The synchrotron radiation photons are emitted tangential to the electron trajectory into a cone with a mean angle of $1/\gamma$. Ions are produced in this irradiated area of the beam pipe. Thus, the local distribution of ions is not necessarily symmetric around the beam center. See section 3.4 for more details.

[10] An incoherent oscillation denotes an oscillation in which an ensemble of particles perform oscillations with a fixed frequency but arbitrary amplitude and phase relation to each other. In a coherent oscillation the particles have the same phase and frequency. See section 5.1.1 for more information.

[11] Radio frequency cavities are also denoted as rf cavities or simply cavities and their alternating electromagnetic fields are called rf fields.

deviation oscillate around a reference phase of the ideal electron trajectory. These incoherent oscillations are called *synchrotron oscillations*.

In a circular accelerator, electrons have a revolution frequency ν_0. In order to enable an acceleration in the cavities in every revolution, the cavity frequency ν_{rf} has to be chosen in reference to the accelerator's circumference C and revolution frequency the way that

$$\nu_{\mathrm{rf}} = h \cdot \nu_0 \qquad \text{and} \qquad C = h \cdot \lambda_{\mathrm{rf}} \,.$$

h is the harmonic number of the accelerator. h consecutive electron packets, called bunches, can circulate in the accelerator. In the ELSA storage ring, the cavities are operated with a frequency of 500 MHz, which corresponds to an rf wavelength λ_{rf} of 60 cm. h times this wavelength equals the storage ring's circumference of 164.4 m. Consequently, h is equal to 274. In "normal" operation, the storage ring has a almost homogeneous filling pattern. Here, all 274 bunches have approximately the same number of electrons per bunch, thus the so called *bunch current* is similar.

However, the longitudinal dynamics of the electrons in the bunches are mainly influenced by synchrotron radiation losses, which occur in the accelerator's arc sections, and the longitudinal acceleration in the cavities.

Synchrotron Radiation and Acceleration

In this section, the effects of synchrotron radiation losses in combination with the longitudinal acceleration in rf cavities will be discussed briefly. For a more detailed treatise regarding synchrotron radiation and its spatial and spectral distribution, see section 3.4.

Consider an electron with mass m_{e} and an energy E. Due to deflection of the electron by the Lorentz force of the magnetic fields in the dipoles to a trajectory with radius R, the electron experiences synchrotron radiation losses which amount to [Wil00, section 2, equation 2.18]

$$\Delta E_{\mathrm{rev}} = \frac{\mathrm{e}^2 \beta^3}{3\varepsilon_0 \left(m_{\mathrm{e}} c^2\right)^4} \frac{E^4}{R} \tag{2.24}$$

per revolution. In the energetic equilibrium state of the electron, the synchrotron radiation losses are exactly compensated by the cavity's accelerating rf fields. Thus, the electrons are accelerated with a total voltage of

$$U_{\mathrm{rev}} = \frac{\Delta E_{\mathrm{rev}}}{\mathrm{e}}$$

every turn, which is called *circumference voltage*. Since the rf fields in the cavities are sinusoidal with frequency ν_{rf} and amplitude U, the bunches only have an energy equilibrium at a specific reference phase φ_0. Thus, it holds

$$U_{\mathrm{rev}} = U \sin\left(\varphi_0\right) \,.$$

Synchrotron radiation losses occur due to stochastic emission of photons into a cone with a mean opening angle of $2/\gamma$ in flight direction. γ is the Lorentz factor[12]. Due to this angular distribution of the photon emission, the longitudinal and transversal momentum of the electron is altered with each emission. The longitudinal deficit in momentum is restored by the rf fields of the cavities, whereas the transversal

[12] γ is the Lorentz factor of the special theory of relativity. It is defined as $\gamma = \left(\sqrt{1-\beta^2}\right)^{-1}$.

loss results in a damping of transversal electron motions. For a synchrotron[13]-type accelerator as the storage ring, this natural damping has horizontal and vertical damping constants of [Wil00, section 6.3]

$$\frac{1}{\tau_x} = \frac{1}{2T_0}\frac{eU_{\mathrm{rev}}}{E}(1-\mathcal{D}) \qquad \text{and} \qquad \frac{1}{\tau_z} = \frac{1}{2T_0}\frac{eU_{\mathrm{rev}}}{E}\,. \tag{2.25}$$

The revolution time of the electrons is denoted as $T_0 = 1/\nu_0$. $\mathcal{D}$ is a quantity obtained from the optical configuration of the accelerator. For a separated function accelerator[14], usually $\mathcal{D} \ll 1$ holds. By emitting a synchrotron radiation photon, the energy of the electron is reduced and its current trajectory is not compatible to its energy anymore. As it shows a horizontal displacement from a compatible trajectory, it oscillates around it. This effect results in an excitation mechanism of electron oscillations in the horizontal plane in which the beam is deflected. Thus, the featured horizontal damping constant is reduced with a factor of $(1-\mathcal{D})$ in contrast to the vertical one.

The caused change of the ultra relativistic electron's dispersion trajectory also results in a change of the path length and thus a change of phase in reference to the rf fields of the cavities. In the context of phase focusing, which will be discussed in the next section, this leads to a damping of longitudinal motions, too. One obtains [Wil00, section 6.3]

$$\frac{1}{\tau_s} = \frac{1}{2T_0}\frac{eU_{\mathrm{rev}}}{E}(2+\mathcal{D}) \tag{2.26}$$

as the longitudinal damping constant. The damping constants for the ELSA storage ring are shown in figure C.1 in the appendix.

Phase Focusing

As stated above, the electrons move inside the accelerator in h consecutive bunches whose center of charge has a distance of $t_{\mathrm{rf}} = 1/\nu_{\mathrm{rf}}$ from each other. This bunching process is due to the phase focusing of electrons to the reference phase φ_0.

Figure 2.5 illustrates the principle of phase focusing. In an accelerator where ultra relativistic electrons circulate with a velocity of $\beta c \approx c$ and thus $\gamma \gg 1$, the path length L of an individual electron is dependent on its deflection radius and thus on its momentum p. The constant of proportionality between the relative change of momentum $\Delta p/p_0$ and the relative path length difference $\Delta L/L$ is the momentum compaction factor α_{c}. For ultra relativistic electrons, the relation [Wil00, section 3.6, equation 3.110]

$$\frac{\Delta L}{L} = \alpha_{\mathrm{c}}\frac{\Delta p}{p_0}$$

holds. An ideal electron without momentum deviation traverses the circular accelerator on the design orbit with a fixed phase φ_0 in reference to the cavity's rf voltage (green orbit and phase position). Electrons with a larger momentum than the design orbit's momentum p_0 ($\Delta p/p_0 > 0$) pass through the accelerator on a longer trajectory, a so called dispersion trajectory (blue orbit). Due to this elongation, the electron arrives at the accelerating cavities with a delay (b). Thus, its phase in reference to the rf fields lags behind, resulting in less accelerating voltage as the electron passes. For an electron with $\Delta p/p_0 < 0$, the behavior is complementary (red orbit and phase position). This mechanism forces the electrons to an incoherent

[13] A synchrotron, like the storage ring, is a circular particle accelerator in which the particles propagate on a closed loop trajectory with constant deflection radius. During the acceleration process, the beam energy increases synchronous with the increment of the magnetic fields of the dipoles.

[14] A separated function accelerator is an accelerator, which uses different magnet types for the function of beam focusing and deflection.

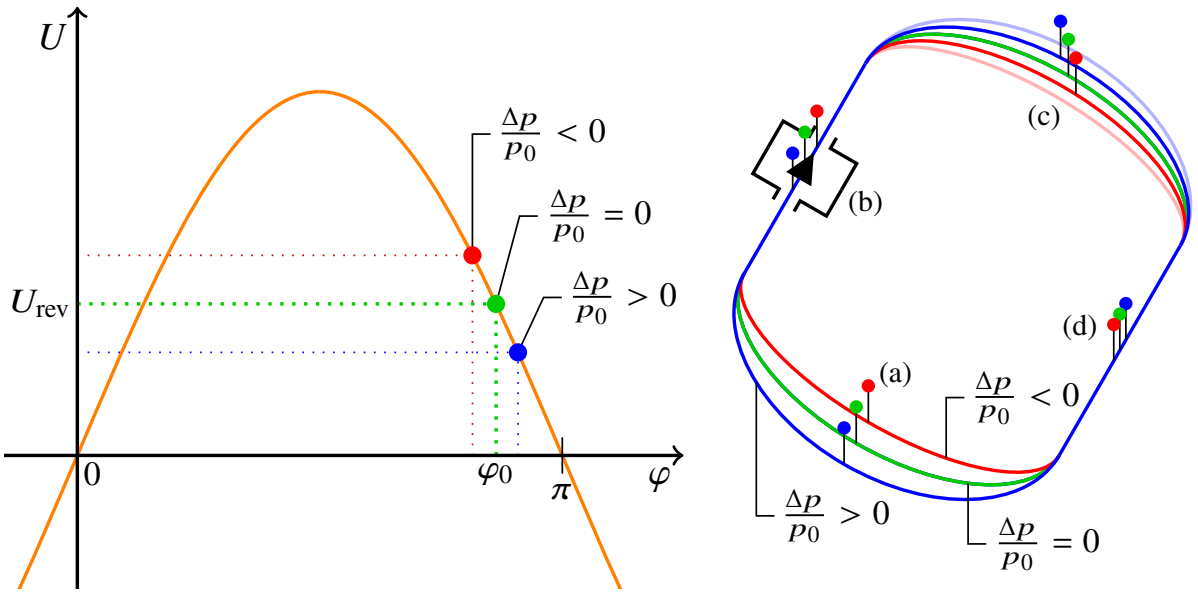

Figure 2.5: Illustration of the principle of longitudinal phase focusing in a circular accelerator for ultra relativistic electrons. On the right, the trajectories of particles with a momentum deviation $\Delta p/p_0$ equaling 0, > 0 and < 0 denoted in green, blue and red are shown. Due to the acceleration in the rf cavity, their trajectories changes from (a) to (d). The phase positions of the particles on the sinusoidal rf voltage when accelerated in the cavity (b) are shown on the left.

longitudinal synchrotron oscillation around the reference phase.

The equation of motion for this longitudinal oscillation can be written in terms of the energy difference ΔE between the individual electron and the reference beam energy E, as it is established by the configuration of the optics of the accelerator using a fixed ν_{rf}. For small ΔE, the equation reads [Wil00, section 5.6, equation 5.81]

$$\Delta\ddot{E} + 2\alpha_s \Delta\dot{E} + \left(2\pi\nu_s\right)^2 \Delta E = 0\,,$$

where $\alpha_s = \frac{1}{\tau_s}$ is the longitudinal damping constant. ν_s is the *synchrotron frequency*, which is given by

$$\nu_s = \nu_0 \sqrt{-\frac{\mathrm{e}Uh}{2\pi\beta^2 E} \cdot \left(\alpha_\mathrm{c} - \frac{1}{\gamma^2}\right) \cdot \cos\left(\varphi_0\right)}\,.$$

One defines a so called *synchrotron tune*, which is determined by the energy of the beam, the optics of the accelerator and the total voltage of the rf fields in the cavities, as

$$Q_s = \frac{\nu_s}{\nu_0}\,.$$

The tune describes the number of synchrotron oscillations per revolution.

In the ELSA storage ring, the synchrotron frequency is stabilized by a digital LLRF system[15], which

[15] A digital low-level-rf system is a system with monitoring and controlling capabilities. It controls and stabilizes the amplitude and phase of the rf fields in the cavities to compensate for various effects, such as *beam loading*, which occur during operation of the storage ring. Here, the electrons of the beam consume energy from the rf fields inside the cavities to compensate for synchrotron radiation losses. The resulting decrease of the cavities field strength is compensated by increasing the cavities input power. For more details, see [Sch15].

controls and stabilizes the cavity's voltage in reference to the beam energy, to a typical frequency of 89 kHz. Thus, the synchrotron tune is equal to 0.0488 which implies that the relative longitudinal motion is a slow oscillation in reference to the revolution frequency.

Natural Energy Width and Bunch Length

The stochastic process of synchrotron radiation leads to a variation of the individual electrons' energy and path length in the accelerator. On the one hand, this leads to damping of the longitudinal motion and thus an energy focusing towards the design beam energy E. On the other hand, the emission of a synchrotron radiation photon can excite longitudinal oscillations, if the individual energy is too close to the beam's energy. An equilibrium of damping and excitation of longitudinal oscillations establishes. Within time scales in the order of τ_s, an ensemble of electrons in a separated function accelerator establishes a *natural energy width* of [San70, section 5.2, equation 5.45]

$$\frac{\Delta E}{E} = \gamma \sqrt{\frac{C_\mathrm{q}}{(2+\mathcal{D})R}} \,, \tag{2.27}$$

with the quantum excitation constant $C_\mathrm{q} = 3.84 \cdot 10^{-13}$ m. ΔE denotes the r.m.s.[16] energy width. In the ELSA storage ring the natural energy width varies from 0.3 ‰ at 1.2 GeV to 0.8 ‰ at 3.2 GeV.

Utilizing the relationship between the energy amplitude ΔE of the electron and its r.m.s. phase displacement $\Delta\varphi_\mathrm{rms}$ for the reference phase,

$$\frac{l_\mathrm{bunch}}{2} = \lambda_\mathrm{rf} \cdot \Delta\varphi_\mathrm{rms} \,,$$

one is able to determine the natural length of the electron bunch l_bunch. Due to the stochastic nature of synchrotron radiation, the electrons' momentum distribution is Gauss-shaped. The longitudinal intensity profile of the beam has the same shape. Thus, the r.m.s. values are equal to the 1σ standard deviation. Consequently, $l_\mathrm{bunch}/2$ is equal to the 1σ bunch length σ_s of a longitudinally Gaussian shaped bunch. The bunch length can be determined as [San70, section 5.4, in accordance with equation 5.66]

$$\sigma_s = \frac{\alpha_\mathrm{c}\beta c}{2\pi\nu_s}\frac{\Delta E}{E} \,.$$

According to equation (2.27), $\Delta E/E$ increases linearly with γ, which is proportional to the beam energy E. This results in a linear bunch length dependency of the energy, if the synchrotron frequency ν_s is kept constant, as it is the case in the ELSA storage ring.

Figure 2.6 shows the energy dependence of the predicted and measured bunch length in the storage ring: Both, prediction and measurement have been carried out by M. Switka [Swi19, section 4.2.6]. In the storage ring operation, ν_s is fixed by the LLRF system. During the measurements, ν_s has been equal to (89.8 ± 0.8) kHz. The momentum compaction factor α_c is set to 0.0629 ± 0.0016[17]. Using the

[16] R.m.s. is the short form of Root Mean Square, the square root of the arithmetic mean of a distribution of squared values.

[17] This value is obtained from numerical simulations with ELEGANT. However, in the course of this work a momentum compaction factor of 0.0601 ± 0.0002 is assumed for the storage ring. This value for α_c has been obtained by measurements of [Sch+15].

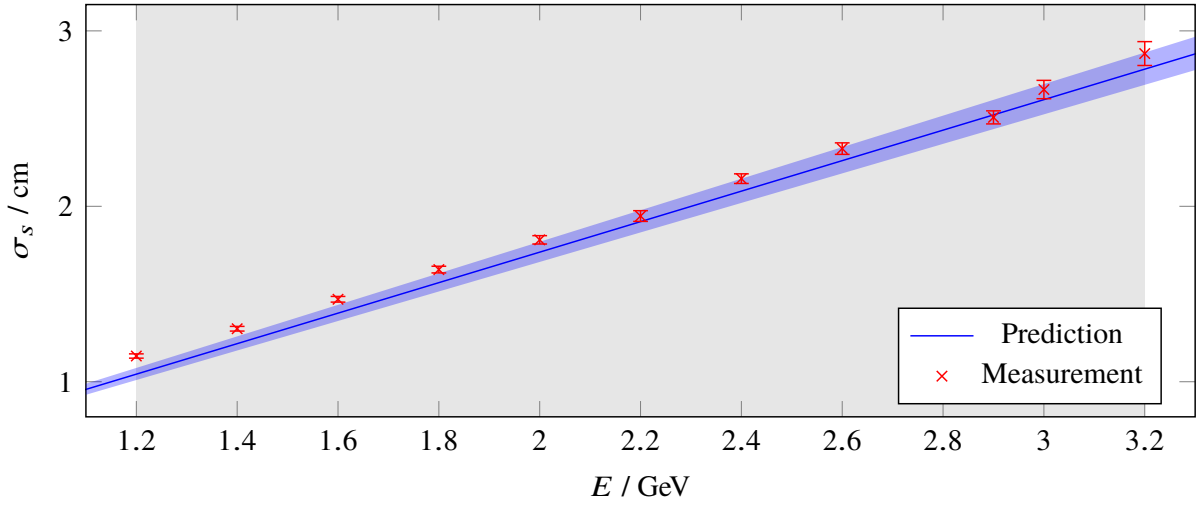

Figure 2.6: Predicted and measured bunch length of the electron beam in the ELSA storage ring for different energies. The typical beam energy range of the storage ring is highlighted in gray. The predicted bunch length assumes a momentum compaction factor of $(6.29 \pm 0.16)\,\%$ and a synchrotron frequency of $(89.76 \pm 0.78)\,\mathrm{kHz}$. Courtesy of M. Switka [Swi19, section 4.2.6].

parameter $\mathcal{D} = -0.005751$ and a deflection radius of 10.89 m from ELEGANT[18] simulations[19], one obtains a theoretical 1σ bunch length, rising linearly from approximately 1 cm at a beam energy of 1.2 GeV to approximately 2.75 cm at 3.2 GeV.

2.3.3 Transversal Dynamics of the Electron Beam

To determine the beam's transversal shape and how it alters along the storage ring, the transversal dynamics of the electron beam, as it is deflected in the dipole and focused in the quadrupole magnets, has to be studied.

Equation of Motion of the Electron in a Circular Accelerator

To describe the transversal trajectories of electrons along the circular accelerator, one uses the assumption of linear beam optics. In this treatment of the electron movement, the magnetic fields are constant along the dipole magnets. Also the quadrupole field strength increases linearly with the electrons' displacement from the magnets' center. To describe the horizontal component of the electron trajectory $x(s)$, a differential equation of the HILLian form can be found with [Wil00, section 3.2, equation 3.21]

$$x''(s) + \left(\frac{1}{R^2(s)} - k(s) \right) \cdot x(s) = \frac{1}{R(s)} \frac{\Delta p}{p_0} \,. \tag{2.28}$$

[18] ELEGANT is a versatile, numerical accelerator simulation program. Amongst others features, it enables the user to characterize lattices of circular and linear accelerators and determine machine parameters out of calculated twiss parameters and/or a 6D-tracking algorithm. For more information, see [Bor00].

[19] The ELEGANT simulations have been conducted on basis of the latest lattice of the storage ring (last update July 2014). Here, the quadrupole strength is set to $k_{\mathrm{QD}} = -0.579\,\mathrm{m}^{-2}$ and $k_{\mathrm{QF}} = 0.630\,\mathrm{m}^{-2}$, which results in a tune of $Q_x = 4.619$ and $Q_z = 4.431$. The sextupole strength is equal to $m_{\mathrm{SF}} = 3.5\,\mathrm{m}^{-3}$ and $m_{\mathrm{SD}} = 3.0\,\mathrm{m}^{-3}$. The optical functions (β_x, β_z, D_x) and parameters (e.g. $\mathcal{D}$ and $\mathcal{J}_5$) obtained from the simulations are used as the foundation of all calculations and simulations of this work.

Here, an electron with a relative momentum deviation of $\Delta p/p_0$ is horizontally deflected by the dipole magnets to a trajectory with radius $R(s)$. Quadrupole magnets introduce a local *quadrupole strength* of $k(s)$. Since one assumes a plane accelerator with solely horizontally deflecting dipoles, the equation of motion of the vertical component of the trajectory $z(s)$ is given by

$$z''(s) + k(s) \cdot z(s) = 0 \,. \tag{2.29}$$

The difference in the sign of $k(s)$ in the two equations of motion comes from the fact that a quadrupole magnet is focusing in one plane and defocusing in the other.

The solution to this equation of motion is a pseudo harmonic oscillation of the electrons around the closed orbit, the horizontal and vertical betatron oscillations. Equations (2.28) and (2.29) implicitly assume, that these transversal oscillations are decoupled from each other, which is not fully true in a real accelerator as will be discussed in section 2.3.3.

The beam consists of an ensemble of electrons, oscillating transversely in the accelerator. Each electron has its individual amplitude and phase. Due to the stochastic nature of synchrotron radiation and its influence on the transversal motion of the electrons, the horizontal and vertical charge distributions of the beam are of a Gaussian shape. Thus, the beam can be parameterized by its transversal width which is the r.m.s. or 1σ value of the charge distribution.

Consider a hypothetical electron which has an amplitude of exactly σ_z, the vertical 1σ beam width, in a quadrupole. Its oscillation in the vertical plane can be parameterized as

$$z(s) = \sqrt{\epsilon_z \beta_z(s)} \cos\left(\Psi_z(s) + \Psi_z^0\right) \,. \tag{2.30}$$

The trajectory of this hypothetical electron is used to represent or characterize the whole ensemble of electrons. The amplitude of $z(s)$ is determined by the *amplitude function* $\beta_z(s)$, also called the *beta function*, and the vertical *emittance* ϵ_z of the accelerator, which will be discussed in section 2.3.3. $\Psi_z(s)$ is the vertical *betatron phase* function and Ψ_z^0 denotes the electron's initial phase.

In the horizontal plane, the oscillation of this hypothetical electron is shifted by a dispersive contribution, resulting from the momentum dependence of the bent trajectories in the dipole magnets. Thus, it holds

$$x(s) = \sqrt{\epsilon_x \beta_x(s)} \cos\left(\Psi_x(s) + \Psi_x^0\right) + D_x(s)\frac{\Delta p}{p_0} \,, \tag{2.31}$$

where ϵ_x is the horizontal emittance. $D_x(s)$ is the horizontal *dispersion function* describing the dispersive contribution as a special orbit with $\Delta p/p_0 = 1$. The beta function $\beta_{x,z}(s)$ can be determined from the magnetic structure of the accelerator, enabling a calculation of its phase via

$$\Psi_{x,z}(s) = \int_0^s \frac{1}{\beta_{x,z}(\xi)} \,\mathrm{d}\xi \,.$$

The magnetic structure of the ELSA storage ring is a FODO lattice[20] with 32 equidistant quadrupoles. The lattice follows a periodicity where a horizontally focusing quadrupole, denoted as QF quadrupole, is adjoint by a drift or dipole magnet. This follows a horizontally defocusing quadrupole, called QD quadrupole, and another drift or dipole. This pattern repeats until the circle is closed in an oval shape with two opposing arc sections separated by the opposing straight and rf section (compare figure 1.1).

[20] In a separated function accelerator like the storage ring, which uses different magnet types for the function of beam focusing and deflection, quadrupole and dipole magnets are used in a *FODO lattice*. A lattice is the composition of the longitudinal positions of the magneto-optical elements of an accelerator along the path of the particle beam. Here, a horizontally focusing quadrupole (F) is followed by a drift space or dipole (O), which is adjoint by a horizontally defocusing quadrupole (D) and a

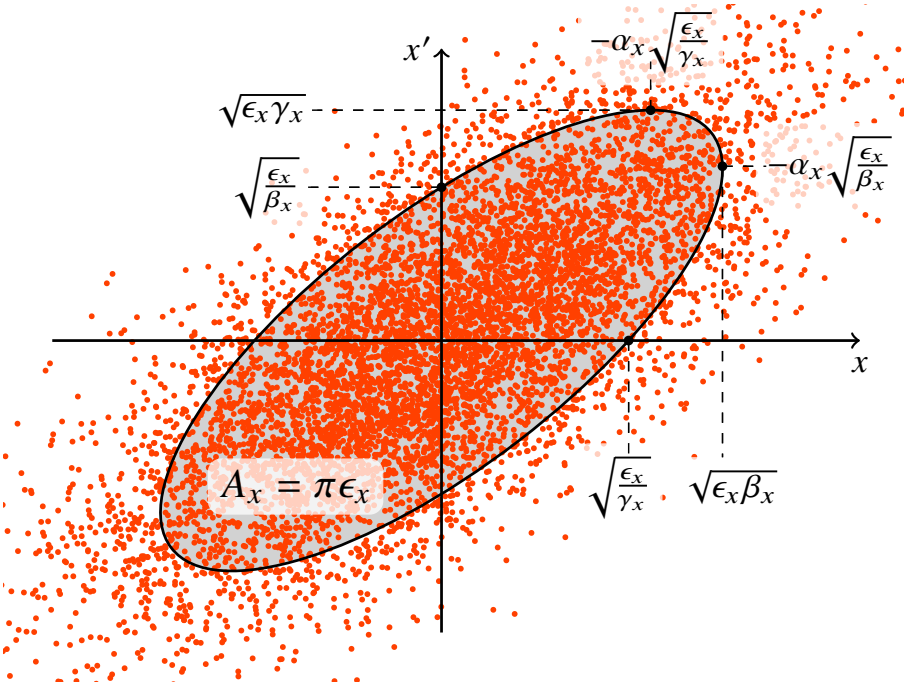

Figure 2.7: An ensemble of electrons in the horizontal phase space at a fixed time and position in the accelerator patterns a two-dimensional Gaussian distribution with an elliptical shape. Each dot corresponds to one electron in the phase space. An ellipse with semi minor and major axis of σ_x and $\sigma_{x'}$ of the distribution enclose an area A_x which is proportional to the horizontal emittance ϵ_x. From equation (2.32), the shown characteristic values for the x and x' components can be derived.

Emittance and Optical Functions

The constant contribution to the amplitude term $\sqrt{\epsilon_{x,z}\beta_{x,z}(s)}$ is the emittance $\epsilon_{x,z}$. Observing the electrons of the beam in the transversal phase space (x-x' or z-z' space) at a fixed time and position in the accelerator, one obtains something similar to figure 2.7 for the horizontal plane. A_x denotes the area in which 68.27 % of the ensemble's x-x' pairs are located. In a suitably rotated coordinate system, this area corresponds to an ellipse with a semi minor or major axis of σ_x or $\sigma_{x'}$ of the two-dimensional Gaussian distribution. The horizontal emittance is defined as

$$\epsilon_x = \frac{A_x}{\pi} \,.$$

For a given beam optic setup and energy of the accelerator, the ellipsoid area A_x is an invariant. Thus, the emittance is a constant of motion in accordance with the Liouville's theorem.

The rotated emittance ellipsoid changes its shape along the accelerator under conservation of its area A_x. The ellipse surrounding A_x can be parameterized as [Wil00, section 3.8, equation 3.135]

$$\epsilon_x = \gamma_x(s)\, x^2(s) + 2\alpha_x(s)\, x(s) \cdot x'(s) + \beta_x(s)\, x'^2(s) \,. \tag{2.32}$$

Here, $\alpha_x(s)$, $\beta_x(s)$ and $\gamma_x(s)$ are the optical functions of the accelerator, which are also called *twiss parameters*. For the vertical plane, the same parameterization holds true. As already stated, the beta function β_x can be derived out of the magnetic structure of the accelerator. The 1σ beam width σ_x is proportional to $\sqrt{\beta_x}$, whereas the angular displacement $\sigma_{x'}$ scales with γ_x. $\alpha_x(s)$ describes the coupling

drift space or dipole (O). This sequence of magnets is called FODO-cell.

of the x and x' plane and thus the rotation of the ellipsoid. Both functions, $\alpha_x(s)$ and $\gamma_x(s)$, can be determined by $\beta_x(s)$ and its derivative from

$$\alpha_x(s) = -\frac{\beta_x'(s)}{2} \qquad \text{and} \qquad \gamma_x(s) = \frac{1+\alpha_x^2(s)}{\beta_x(s)} \,.$$

Beam Width in the ELSA Storage Ring

For a dispersion free accelerator, the equation of motion for the horizontal and vertical trajectories resembles equation (2.30). Here, $\sqrt{\epsilon_x \beta_x(s)}$ equals the beam width $\sigma_x(s)$ of the beam. $\sqrt{\epsilon_x \beta_x(s)}$ is also called the *envelope* of the beam. In general, the horizontal beam width of a circular accelerator can be obtained using

$$\sigma_x(s) = \sqrt{\epsilon_x \cdot \beta_x(s) + \left(D_x(s) \cdot \frac{\Delta p}{p_0}\right)^2} \,. \tag{2.33}$$

$\beta_x(s)$ and $D_x(s)$ can be determined by the magnetic structure of the accelerator. Since it is assumed that the accelerator deflects the beam only horizontally onto a circular orbit, thus $D_z(s) \approx 0\,\mathrm{m}$ for all s[21], the vertical beam width can be determined by

$$\sigma_z(s) = \sqrt{\epsilon_z \cdot \beta_z(s)} \,. \tag{2.34}$$

As the beta and dispersion functions are defined as independent from the beam energy, the only energy dependencies are the emittance and the relative momentum deviation. For ultra relativistic electrons, as it is the case in the ELSA storage ring, the latter equals the natural energy width, which can be determined by equation (2.27).

As already mentioned in section 2.3.2, the synchrotron radiation leads to a damping of transversal electron oscillations. Additionally, the emission of a synchrotron radiation photon and the occurring energy loss modifies the electron's trajectory into a dispersion trajectory, resulting in an excitation of an oscillation around this trajectory[22]. For an ensemble of electrons, both effects eventually lead to an equilibrium beam width out of which an emittance can be extracted. This equilibrium state emittance is called the *natural beam emittance*. It is given by [San70, section 5.5, equation 5.83]

$$\epsilon_{x,0} = \frac{C_\mathrm{q}\gamma^2}{(1-\mathcal{D})} \frac{\left\langle \frac{1}{R^3(s)} \mathcal{H}(s) \right\rangle_s}{\left\langle \frac{1}{R^2(s)} \right\rangle_s} = \frac{C_\mathrm{q}\gamma^2}{(1-\mathcal{D})} \frac{\mathcal{J}_5}{\mathcal{J}_2} \,, \tag{2.35}$$

where $\langle \ldots \rangle_s$ denotes the mean value of the parameter along the accelerator. The averages are also labeled as $\mathcal{J}_2$ and $\mathcal{J}_5$ and denote the second and fifth *synchrotron* or *radiation integral*. From numeric ELEGANT calculations, one can obtain their values for the ELSA storage ring[19] as

$$\mathcal{J}_2 = 0.57215\,\mathrm{m}^{-1} \qquad \text{and} \qquad \mathcal{J}_5 = 2.76998 \cdot 10^{-2}\,\mathrm{m}^{-1} \,.$$

[21] Due to misalignments of the dipole magnets to each other and their fabrication tolerances, the horizontal plane is not perfectly even. Thus, minor vertical dispersive contributions may occur, which are typically negligible.

[22] As already mentioned, the synchrotron radiation photon is emitted into a cone, thus the emission also changes the direction of the electron due to additional transversal momentum loss. This effect is neglected here, since it is small compared to the change of the electron's dispersion trajectory.

For an isomagnetic accelerator like the ELSA storage ring, where the deflection radius is constant within each dipole magnet, the natural emittance can be suitably approximated as [San70, section 5.5, equation 5.89]

$$\epsilon_{x,0} \approx \frac{(2+\mathcal{D})}{(1-\mathcal{D})} \frac{\alpha_c R}{Q_x \nu_0} \left(\frac{\Delta E}{E}\right)^2 . \tag{2.36}$$

Q_x is the horizontal *betatron tune*, which will be discussed in the next section.

Although the accelerator is assumed to have a non-dispersive vertical plane, there exists a vertical natural beam emittance, too. It originates to a minor extend from the emission of synchrotron radiation into a cone with a mean opening angle $2/\gamma$ in flight direction. Consequently, this emission changes the vertical momentum and leads to a damping- and excitation mechanism, as it has been discussed in section 2.3.2. Both mechanisms result in an equilibrium emittance. Due to the fact that electrons in the storage ring are ultra relativistic, with a LORENTZ factor γ between 2 348 and 6 262 for beam energies of 1.2 and 3.2 GeV, this contribution to the vertical emittance can be neglected.

Due to construction imperfections[23], a vertical beam emittance is produced. Here, the dispersive excitation due to synchrotron radiation in the horizontal plane is partly transferred to the vertical plane leading to a vertical beam height. Hereby the horizontal natural emittance $\epsilon_{x,0}$ is reduced to [San70, section 5.6, equation 5.113]

$$\epsilon_x = \frac{1}{1+\kappa} \cdot \epsilon_{x,0} . \tag{2.37}$$

κ denotes the *betatron coupling coefficient* between the transversal planes and can attain values between zero and one. The vertical beam emittance consequently is increased to

$$\epsilon_z = \kappa \cdot \epsilon_x . \tag{2.38}$$

Since the coupling between the transversal planes is mostly[24] due to construction imperfections, the betatron coupling coefficient is assumed to be independent from beam parameters such as energy and beam current.

As can be seen in equations (2.35) and (2.36), the horizontal emittance increases quadratically with the beam energy. This is coupled to the vertical emittance, too. Consequently, the beam size increases horizontally and vertically according to equations (2.33) and (2.34) when the beam energy is increased.

In the ELSA storage ring, measurements of the beam profile by using synchrotron light monitors[25] can be utilized to obtain the beam emittance. In [Zan13], the horizontal emittance has been determined (see equations (2.33) and (2.34)) by measuring the horizontal 1σ beam width and using $\beta_x(s_0)$ and $D_x(s_0)$ values at the source point s_0. These twiss parameters, together with the natural relative momentum spread,

[23] Quadrupole, sextupole and dipole magnets may be tilted or twisted in reference to each other. Then e.g. a horizontal displacement results a vertical force and vice versa. Consequently, the planes are no longer decoupled from each other.

[24] A coupling can also be artificially generated by skew quadrupole magnets. These quadrupoles are tilted by 45° around the longitudinal plane in reference to a "normal" quadrupole magnet used to focus the beam [Wie95, section 3.3.2]. Also the non-linear magnetic field of a sextupole magnet leads to betatron coupling if the beam does not pass the magnet's center [Tsa+06]. As the sextupole field strength typically is well below the one for the dipole and quadrupole magnets, it is assumed to be negligible.

[25] A synchrotron light monitor is an optical device, which utilizes the synchrotron radiation for optical beam diagnostics. The visual synchrotron radiation of ultra relativistic electrons, coming from a quasi point-like source, is separated from the high energetic synchrotron radiation by a mirror and projected via a light-optical setup onto a CCD-Camera. Quantities such as beam shape and its dimensions can be obtained.

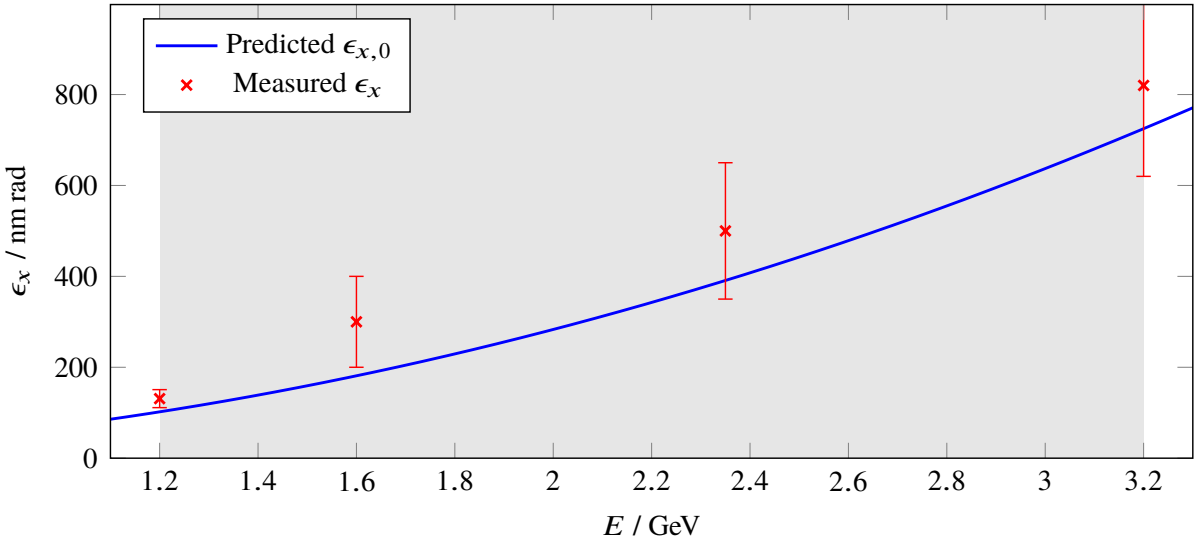

Figure 2.8: Energy dependence of the predicted horizontal natural emittance and the horizontal emittance, measured in [Zan13, section 6.3]. Between injection energy of 1.2 GeV and the storage ring's maximum energy of 3.2 GeV, denoted by the gray background color, the predicted natural emittance rises quadratically. It is calculated via equation (2.35) using parameters which have been obtained by ELEGANT for a typical optical configuration of the ELSA storage ring. The measured emittance follows this quadratic trend, with overall a higher emittance. The systematical errors are due to uncertainties in the measured optical functions. For more information, see [Zan13].

have been obtained by the SIMLIB tool[26]. Figure 2.8 shows the energy dependence of the horizontal emittance. The prediction shows a horizontal natural emittance of 98 nm rad at 1.2 GeV, quadratically rising with energy to 697 nm rad at 3.2 GeV. For this prediction, the optical functions obtained for the ELSA storage ring lattice[19] from ELEGANT have been used. The measurements of [Zan13] follow the quadratic correlation of the prediction but deviate from it by up to 100 nm rad. As can be seen in equation (2.36), the natural emittance is dependent on the horizontal betatron frequency and thus the beam optics. This can explain the deviation in parts, since different optical settings of the storage ring during the measurements and the ELEGANT lattice have been used. Thus, the predicted natural emittance does not necessarily represent the storage ring's emittance during these measurements. Additional systematic errors of 10 % emerge from the measurement setup and the analysis method (see [Zan13, section 5.6]).

During similar measurements, the vertical emittance has been determined using the vertical 1σ beam width. The betatron coupling coefficient has been determined using equation (2.38). The measurements reveal a betatron coupling coefficient of (7.2 ± 2.7) % at a beam energy of 1.2 GeV [Zan13, section 8.8, page 103].

Figure 2.9 shows the relevant optical functions of the ELSA storage ring and the resulting transversal 1σ envelope for an electron beam with an energy of 1.2 GeV and 3.2 GeV. The optical functions are obtained from ELEGANT simulations, on basis of the lattice of the storage ring[19]. These optical functions are used in every subsequent simulation or calculation of this work, when necessary.

In the storage ring, each quadrupole in the family of QD or QF type, is operated with the same quadrupole strength k_{QF} or k_{QD} in the FODO lattice. Consequently, $\beta_x(s)$ varies periodically between 2.45 m in QD and 17.28 m in QF quadrupoles. On average it is equal to 8.6 m. In a FODO structure,

[26] The SIMLIB is an simulation tool which derives beam parameters, such as the optical functions, for a desired configuration of the optical elements of the ELSA storage ring. It is integrated into the ELSA control system and uses the HAMILTON formalism to calculate these parameters [Wen94].

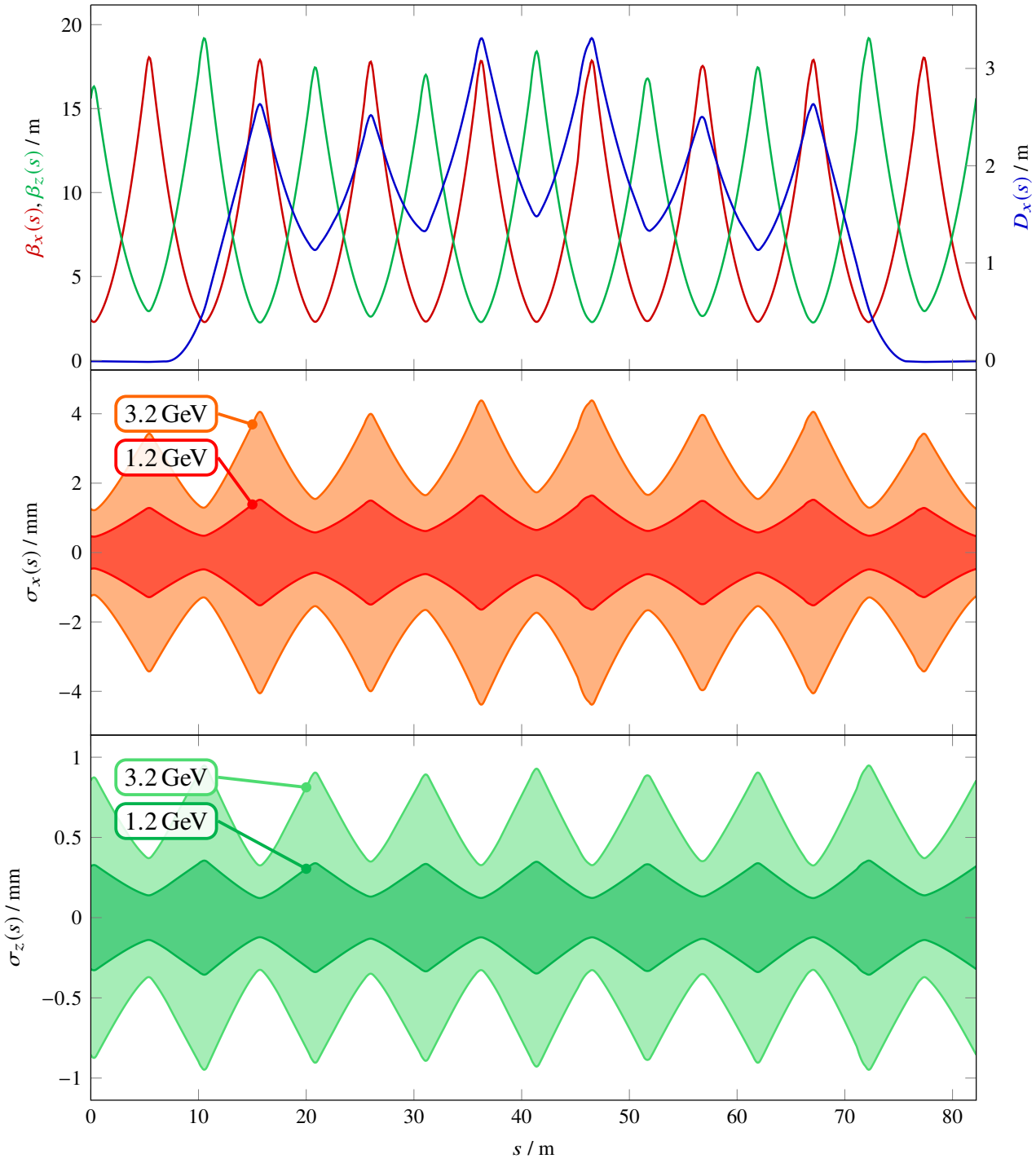

Figure 2.9: Twiss parameter of half of the ELSA storage ring. The graph on top shows the horizontal (red) and vertical (green) beta functions accompanied by the horizontal dispersion function (blue) along half the ELSA storage ring. Due to the symmetry of the storage ring, the other half is identical. In the middle and bottom graph the resulting horizontal (red) and vertical (green) 1σ envelope of the beam are shown for beam energies of 1.2 GeV and 3.2 GeV.

$\beta_z(s)$ also shows a periodic behavior shifted by one quadrupole in reference to $\beta_x(s)$ as the focusing strengths in a quadrupole show opposing signs for the horizontal and vertical plane. $\beta_z(s)$ periodically changes between 2.36 m in QF and 18.62 m in QD quadrupoles. The average vertical beta function is equal to 8.81 m. The horizontal dispersion $D_x(s)$ is maximal (3.28 m) in the arc sections and almost zero in the straight sections. Here, the dispersion is suppressed by omitting the installation of dipole magnets in certain sections of the lattice[27]. Since the deflection of the electrons onto a circular path is done horizontally, $D_z(s)$ is assumed to be negligibly small and is not shown in the figure.

On basis of $\beta_x(s)$, $D_x(s)$ and the horizontal emittance ϵ_x, the horizontal 1σ beam envelope can be determined. Note that the underlying natural emittance has been obtained from equation (2.35) and corrected by the measured betatron coupling coefficient of [Zan13] via equation (2.37). One obtains a horizontal 1σ beam width varying periodically between 0.5 mm and 1.6 mm at 1.2 GeV. As the emittance and natural energy width increase with energy, the beam width also increases. At 3.2 GeV the beam has a width ranging from 1.2 mm to 4.4 mm. At 1.2 GeV the vertical 1σ width varies between 120 µm and 350 µm. For a higher energy of 3.2 GeV, this width increases to values between 325 µm and approximately 1 mm.

Tune and Optical Resonances

The focusing elements of the accelerator's optic force the electron in the beam to undergo transversal betatron oscillations. One defines the horizontal and vertical *betatron tune* as [Wil00, section 3.14, equation 3.207]

$$Q_{x,z} = \frac{\Delta\Psi_{x,z}}{2\pi} = \frac{1}{2\pi}\oint \frac{1}{\beta_{x,z}(s)}\,\mathrm{d}s\ ,$$

which is the number of periods of the betatron oscillation per revolution. It is proportional to the betatron phase difference $\Delta\Psi_{x,z} = \Psi_{x,z}(s+C) - \Psi_{x,z}(s)$ after one revolution. The tune can be adjusted by the strength k_{QF} and k_{QD} of the QF and QD quadrupole magnets.

The phase difference or betatron tune is a crucial quantity, if one considers *optical resonances*. The electron beam in a circular accelerator repeatedly encounters the same magnetic structure every full revolution. For a specific betatron tune, unavoidable imperfections in the alignment of the magnets and magnetic field errors may force the beam to a resonant oscillation. This resonance increases the amplitude of the electrons' betatron oscillation. In dependence of the strength of this excitation it can lead to a blow up of the beam, decreased beam lifetime and eventually to a complete beam loss. Consequently, the accelerator's tune cannot be chosen arbitrarily. Optical resonances are characterized by their order. Its strength typically decreases with higher order. For example, dipole field errors correspond to a first order optical resonance. Due to their excitation strength, they lead to an instantaneous beam loss and thus forbid an accelerator operation at integer tunes. Quadrupole and sextupole field errors forbid an operation at half and third integer tunes. Due to coupling of resonances of different order, several other tune configuration are forbidden. In order to visualize the possible and forbidden combinations of Q_x and Q_z, one uses a so called *tune diagram* in which optical resonances of up to a specific order are drawn as stop bands.

The tune diagram for the ELSA storage ring is shown in figure 2.10. The magnified area shows the relevant horizontal and vertical tune range between four and five. The quadrupole strength are adjusted the way that typically $Q_x = 4.619$ and $Q_z = 4.431$.

[27] For a certain betatron phase advance $\Delta\Psi_x$ - proportional to Q_x - and magnetic field strength, the dispersion can be suppressed in certain extended regions of a FODO lattice accelerator by omitting pairs of dipoles in certain FODO cells. In the storage ring, the dispersion is suppressed in the rf section from QF16 to QF18 and in the straight section from QF32 to QF2. The dispersion suppressors, or missing magnet sections are located downstream of QF14, QD19, QF30 and QD3 and are denoted as MM sec. in figure 1.1. For more information on dispersion suppression, see e.g. [Aut79].

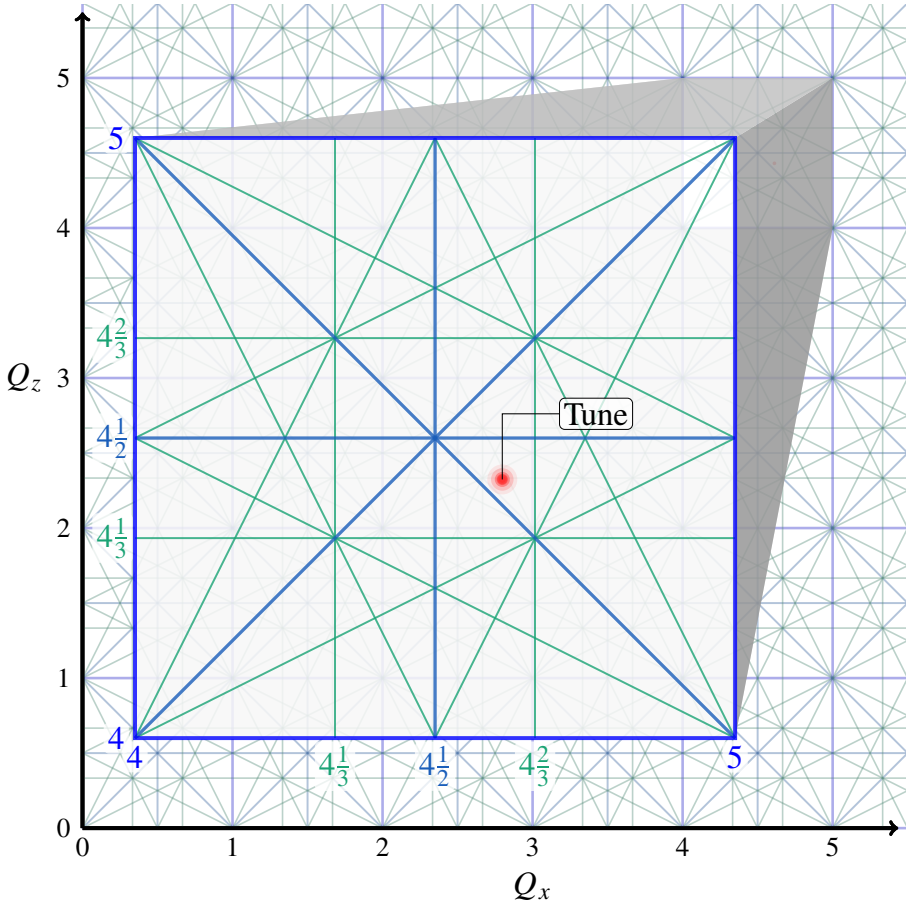

Figure 2.10: Tune diagram of the ELSA storage ring for optical resonances up to third order. The magnified area shows the relevant horizontal and vertical tune range between four and five with the tune at $Q_x = 4.619$ and $Q_z = 4.431$. Dark blue lines indicate the stop bands of the first order optical resonances caused by dipole field errors. Blue and cyan lines are the resonances of second and third order. They are produced by quadrupole and sextupole errors.

The tune pair (Q_x, Q_z) is not an infinitively sharp point in the tune diagram, but has a specific bandwidth or *tune spread*. For example, the finite chromaticity[28] of the accelerator leads to a certain tune spread resulting from the beam's energy spread.

Due to higher multi pole contributions to the magnetic fields in the accelerator, the assumption of linear beam optics does not hold true anymore. Due to octupole contributions, emerging from magnetic field errors for example, the reversing force in the quadrupoles increases non-linearly with the beam displacement from the quadrupole's center [Wie93, section 7.4.1]. Thus, the betatron frequency becomes dependent of the individual electrons' amplitude. Considering an ensemble of electrons with individual amplitudes, which change over time due to synchrotron radiation effects, one obtains a distribution of betatron frequencies. The modal value of this Gaussian distribution is the *coherent tune* Q_x or Q_z, whereas the distribution's standard deviation may be called *incoherent tune spread*.

[28] Electrons with a beam energy which deviate from the nominal energy experience a modified quadrupole strength. As the energy distribution of the beam has a finite width around the nominal beam energy, the tune also spreads. The chromaticity of the optics of an accelerator is this tune spread in relation to the relative characteristic energy deviation of the beam. For more information, see e.g. [Wil00, section 3.16].

If the distribution is shifted, while the shape of the tune distribution is unchanged, the tune shift is called *coherent tune shift*. Due to space charge effects of electron-electron or electron-ion interactions, this tune distribution is shifted and deformed asymmetrically by *incoherent tune shifts* as will be discussed in section 5.1.

2.4 Ion Motion in Electron Accelerators

As has been elaborated in section 2.3, the beam is a bunched ensemble of electrons which transversely and longitudinally has a Gaussian charge distribution. The transversal beam width changes along the accelerator due to its beam optics. With it changes the shape and depth of the beam potential, depending on the beam's charge density. This influences the transversal and longitudinal ion motion, as will be discussed in the next section.

When adding magnetic fields of the optical elements such as dipole and quadrupoles magnets into the consideration, new ion motions emerge. These *cross-field drifts* will be treated on an idealized level in section 2.4.2.

2.4.1 Ion Motion in the Beam Potential

The negatively charged electron beam attracts positive ions by its space charge, resulting from Coulomb forces. This space charge force acts as a reversing force towards the center of the beam which results in an oscillatory movement of the ions in the transversal plane.

The space charge force of the beam forms an attractive electric beam potential wherein the ions propagate. The beam's charge density varies along the accelerator in correlation with the transversal 1σ beam width $\sigma_x(s)$ and $\sigma_z(s)$. Since the shape and depth of the beam potential depends on the charge density of the electron beam, it is also a function of s. Consequently, a longitudinal force towards the minima of the beam potential arises which dominates the longitudinal ion motion in areas of the accelerator, where no additional electric or magnetic fields occur.

Transversal Beam Potential and Ion Motion

The beam is surrounded by a conducting vacuum chamber or beam pipe of a specific geometry, which is typically electrically neutral. This circumstance leads to a boundary condition for the beam potential $U(x, z, s)$. At the surface of the beam pipe, the potential vanishes. Therefore, the potential at the beam pipe's surface can be generally expressed as

$$U\left(x_{\mathrm{vc}}(s), z_{\mathrm{vc}}(s), s\right) \stackrel{!}{=} 0 \,.$$

Here, x_{vc} and z_{vc} are the transversal coordinates of the surface of the vacuum chamber.

For an understanding of the shape of the beam potential, one first can assume a simple radial symmetric case. A cw[29] beam with a radius a is transported centrically inside a circular beam pipe, which has a radius r_{vc}. The electron beam has a total charge of q and a homogeneous charge density. Its linear charge density $\lambda = \mathrm{d}q/\mathrm{d}s$ consequently increases quadratically[30] with the radius r until the edge of the beam is reached at a. For $r > a$, no new charges appear and it therefore stays constant. The result is a radial

[29] A cw beam is an unbunched beam with a homogeneous longitudinal distribution of electrons. It is denoted as a continuous wave beam, with its short form being cw beam.

[30] This quadratic increase comes from the fact that the number of charge carriers in a cylinder volume with fixed height ds and homogeneous charge density increases quadratically with the cylinder's radius.

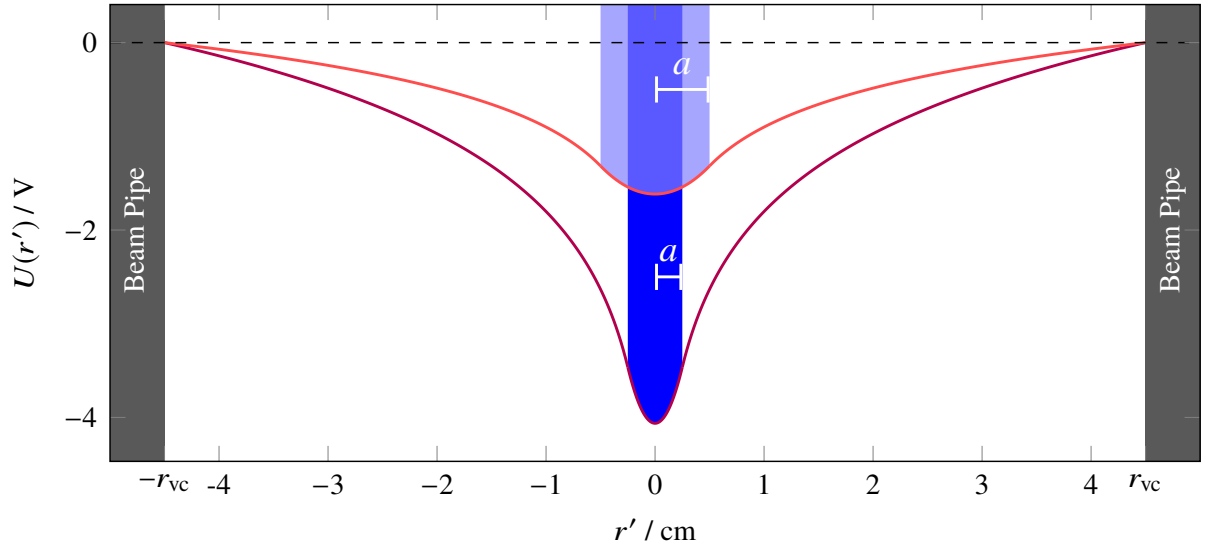

Figure 2.11: Cut through the transversal beam potential along the axis r' for two cases. For both cases the beam has a round shape with a homogeneous charge density. The beam pipe has a round geometry with radius r_{vc}. The transversal potential of a beam with a local radius of $a = 5\,\text{mm}$ and a beam current of 10 mA is shown in light red. The beam dimension is visualized as the light blue bar. If the beam current is twice as high and the width being half the size, the beam potential is deeper, as is shown in the dark red and the dark blue bar.

symmetric inner electric field $E(r)$ which increases linearly inside the beam towards its edge as [Hin12, section 3.1, equation (5)]

$$E(r) = \frac{\lambda}{2\pi\varepsilon_0}\frac{r}{a^2} \quad \text{for} \quad r \le a\,. \tag{2.39}$$

In direction of the beam pipe, the outer field strength decreases proportional to r^{-1}. For this idealized case, one obtains for the beam potential

$$U(r) = \begin{cases} \frac{\lambda}{2\pi\varepsilon_0}\ln\left(\frac{r}{r_{vc}}\right) & \text{for } r \ge a\,, \\ \frac{\lambda}{2\pi\varepsilon_0}\left(\frac{r^2}{2a^2} + \ln\left(\frac{a}{r_{vc}}\right) - \frac{1}{2}\right) & \text{for } r \le a\,. \end{cases} \tag{2.40}$$

For ions, the beam potential is attractive. Thus, $U(r) \le 0$ for all r. In appendix A.3, the complete deviation for this case is shown.

One can rewrite the linear charge density utilizing the beam current I. Thus,

$$\lambda = \frac{\mathrm{d}q}{\mathrm{d}s} = \frac{eN_e}{C} = \frac{I}{\beta c}\,, \tag{2.41}$$

by applying equation (2.1).

The beam potential for this simple model is illustrated for two cases in figure 2.11. Because the beam and the vacuum chamber have a round shape, this problem is radial symmetric. Therefore, one can cut through the transversal plane along an axis r', which goes through the beam's center of charge, which is positioned in the center of the beam pipe. For the two cases, the minimal value of the beam potential, the *potential depth*, is proportional to the beam current. Also the beam width and the geometry of the vacuum chamber are of great importance for the potential depth. For a smaller beam width, the charge density increases, resulting in a deeper potential. Also the potential is deeper for larger dimensions of the

beam pipe than for smaller ones.

As has been elaborated in section 2.3, the electron beam typically does not have a homogeneous transversal charge density. In the transversal plane, it rather resembles a two-dimensional Gaussian charge distribution, with its width being $\sigma_x(s) > \sigma_z(s)$ along the accelerator.

For the longitudinal plane, for now one can ignore the bunched structure of the beam and simply assume a cw beam. The calculated potential therefore only corresponds to its time average. In regard to the ion motion, this is a good approximation as will be discussed below. The expression of the transversal beam potential, on the other hand, is more complex. It has been developed on basis of Housais 1975 and Kheifets 1976 [Khe76] whereas Bassetti and Erskine developed an expression for the beam's transversal electric field for this scenario [BE80]. In the course of this development of the theory, one obtained the expression for the transversal and longitudinal beam potential of an electron beam with 1σ widths of σ_x and σ_z being [Alv87b, section 4, equation (24)]

$$\left\langle U_{\mathrm{bG}}(x,z,s)\right\rangle = \frac{I}{2\pi\varepsilon_0\beta c}\int_{r(s)}^{1}\frac{\exp\left[-\left(1-\xi^2\right)\cdot\left(A(x,s)+\frac{B(z,s)}{\xi^2}\right)\right]}{1-\xi^2}\,\mathrm{d}\xi\,. \tag{2.42}$$

Here, the distance of the beam to the beam pipe is assumed to be infinity. The variables $A(x,s)$ and $B(z,s)$ are given by

$$A(x,s) = \frac{\left(x-x_{\mathrm{C}}\right)^2}{2\left(\sigma_x^2(s)-\sigma_z^2(s)\right)} \qquad \text{and} \qquad B(z,s) = \frac{\left(z-z_{\mathrm{C}}\right)^2}{2\left(\sigma_x^2(s)-\sigma_z^2(s)\right)}\,.$$

x_{C} and z_{C} are the coordinates of the beam's center of charge in the transversal plane. Typically they are set to zero since the center of charge lies on the closed orbit. The start point for the integration $r(s)$ is

$$r(s) = \frac{\sigma_z(s)}{\sigma_x(s)}$$

and is only dependent on the beam dimensions. Despite its complexity, the potential for a Gaussian electron beam qualitatively shows the same behavior as the simple model, which has been discussed before and which is shown in figure 2.11. Equation (2.42) is assumed to have the boundary conditions $U_{\mathrm{bG}}(x_{\mathrm{vc}},z_{\mathrm{vc}},s)=0$ at x_{vc} and $z_{\mathrm{vc}}\to\infty$, but [Alv87b] also contains solutions for the beam potential for circular and rectangular vacuum chamber geometries. These solutions can be used to obtain approximations for the beam potential with the beam pipe geometries, which are encountered in the ELSA storage ring, as will be discussed in section 4.2.

Transversal Ion Motion As has been shown in equation (2.39) for an ion inside the beam, the electric field strength towards the center of the beam increases linearly with its displacement from this center. This still holds true for small displacements, if an electron beam with a Gaussian profile is assumed, as it is in [BE80]. For this scenario, the field strength can be approximated as [Hin11, section 3.2, equation (9)]

$$\vec{E}(x,z) = \begin{pmatrix}E_x(x)\\E_z(z)\end{pmatrix} = \frac{I}{2\pi\varepsilon_0\beta c}\,\frac{1}{\sigma_x+\sigma_z}\cdot\begin{pmatrix}\frac{x}{\sigma_x}\\\frac{z}{\sigma_z}\end{pmatrix}\,. \tag{2.43}$$

Since the beam width varies along the accelerator, $\vec{E}(x,z)$ is also a function of s. The linear field strength results in a reversing Coulomb force towards the center of the beam. Consequently, ions which are

produced with initial thermal velocities will oscillate around the center of charge of the beam.

For an ion i with a mass m_i which is singly ($Z_i = 1$) or multiply ($Z_i > 1$) ionized, the equation of motion in the horizontal plane at a specific longitudinal position in the accelerator can be written as [Hin12, section 14.1, equation (92)]

$$\frac{\mathrm{d}^2 x_i}{\mathrm{d}t^2} = -\frac{\mathrm{e}Z_i}{m_i} E_x(x_i) = -\frac{\mathrm{e}I}{2\pi\varepsilon_0\beta c}\frac{Z_i}{m_i}\frac{1-\hat{\eta}}{\sigma_x\left(\sigma_x+\sigma_z\right)} \cdot x_i \tag{2.44}$$

$$= -q_x^2\omega_0^2 \cdot x_i \tag{2.45}$$

using equation (2.43). This type of equation is well known and describes a harmonic oscillation around the beam center. $\hat{\eta}$ is the local neutralization at the specified position. Due to accumulation of ions to a level of $\hat{\eta}$, the space charge of the beam is shielded by ions. This results in the reduction of the reversing force by a factor of $1-\hat{\eta}$, if one uses a linear model to describe ion-ion space charge effects. The reversing force varies along the accelerator and therefore is a function of s. Due to the build-up of an ion population to a local neutralization level, one does not only obtain another s-dependency but also a dependency of time.

Consequently, the resulting frequency, called *bounce frequency*, with which the ions oscillate transversely inside the beam potential, is subject to variations. Using the angular revolution frequency ω_0, the oscillation frequency can be expressed in terms of a *bounce tune* q_x. Explicitly, the ions oscillate with a frequency of

$$\nu_{x,z}^{\mathrm{ion}} = \frac{1}{2\pi}\sqrt{\frac{\mathrm{e}I}{2\pi\varepsilon_0\beta c}\frac{Z_i}{m_i}\frac{1-\hat{\eta}}{\sigma_{x,z}\left(\sigma_x+\sigma_z\right)}} \overset{\text{def.}}{=} q_{x,z}\cdot\nu_0 \tag{2.46}$$

which varies with σ_x,σ_z and $\hat{\eta}$ along the accelerator. If one considers multiple ion species with different degrees of ionization at a specific position, one obtains several local oscillation frequencies of the ions scaling with $\sqrt{Z_i/m_i}$.

In the ELSA storage ring, the vertical bounce frequencies are in the order of hundreds of kHz, for heavy ions like CO_2^+, to up to several MHz, for light H_2^+ ions, at beam currents of 200 mA. Due to the emittance coupling κ of 7.2 %, the horizontal bounce frequencies are typically one order of magnitude lower than the vertical ones.

The distance of the electron bunches to each other is determined by ν_{rf}, which is equal to 500 MHz in the storage ring. Assuming a homogeneously filled accelerator, the beam potential shows periodic variations with this frequency. Because it holds

$$\nu_x^{\mathrm{ion}} < \nu_z^{\mathrm{ion}} \ll \nu_{\mathrm{rf}}$$

for the storage ring, even a light ion, which oscillates with a frequency of several MHz, moves too slow to react on the bunched structure of the beam. This justifies the made longitudinal approximations, since the ions only react on the temporal average of the beam potential.

Therefore, the average beam potential $\langle U\rangle$ is often denoted as U in the course of this work.

Longitudinal Potential and Ion Motion

As the shape and depth of the beam potential are determined by the vacuum chamber geometry and beam dimension, this results in a potential which is not constant along the longitudinal plane. Therefore, the ions experience a longitudinal Coulomb force towards the minima of the beam potential, resulting in an accelerated motion towards it. This motion superimposes with the transversal oscillations. For this

section, a scenario is assumed where no magnetic fields of the guiding magnets influence the longitudinal ion motion.

Most ions are produced in a production distribution which equals the Gaussian beam profile[31]. Consequently, the majority of the ions will be produced within the 1σ area of the beam. Thus, the initial potential energy of an ion, produced at coordinate $(x_{\mathrm{prod}}, z_{\mathrm{prod}}, s_{\mathrm{prod}})$ is proportional to

$$U\left(x_{\mathrm{prod}}, z_{\mathrm{prod}}, s_{\mathrm{prod}}\right) \approx U\left(x_{\mathrm{C}}, z_{\mathrm{C}}, s_{\mathrm{prod}}\right) \ll U\left(x_{\mathrm{vc}}, z_{\mathrm{vc}}, s_{\mathrm{prod}}\right) = 0\,.$$

Therefore, it is legitimate to only consider $U(x_{\mathrm{C}}, z_{\mathrm{C}}, s) = U(s)$ for the longitudinal ion dynamics. For a longitudinal field strength $E_s(x_{\mathrm{C}}, z_{\mathrm{C}}, s) = E_s(s)$, one obtains the following equation of motion for an ion i at position s with mass m_i and ionization state Z_i

$$\frac{\mathrm{d}^2 s}{\mathrm{d}t^2} = \frac{\mathrm{e}Z_i}{m_i} E_s(s) = -\frac{\mathrm{e}Z_i}{m_i}\frac{\mathrm{d}U(s)}{\mathrm{d}s}\,. \tag{2.47}$$

Figure 2.12 shows a segment of the storage ring's longitudinal beam potential near a local minimum. Consequently, ions, which are produced somewhere in this segment, are accelerated towards the minimum with field strengths of typically less than $1\,\mathrm{V\,m^{-1}}$. For ion clearing purposes, it is reasonable to place clearing electrodes in the vicinity of theses minima, which collect arriving ions and neutralize them (for more details, see section 6.1). Due to different geometries of the beam pipes, the potential shows various steps at the transition of one vacuum chamber geometry to another. So called *potential hollows* occur, in which produced ions cannot gain enough kinetic energy to leave the potential towards the minimum (and a clearing electrode). Thus, ions accumulate in these areas predominantly and increased neutralization levels are to be expected.

2.4.2 Ion Motion in Magnetic Guiding Fields

In an area with a pure vertical magnetic field B_z, for example in dipole magnets, the vertical ion motion is undisturbed. In contrast, longitudinal and horizontal components of the motion are affected by the occurring Lorentz force. An ion i with a mass m_i and an ionization state Z_i with a velocity component perpendicular to the magnetic field $v_{\perp,i}$ will perform a *cyclotron motion* around the magnetic field lines. The angular frequency of this motion, which is called *cyclotron frequency*, is

$$\omega_{\mathrm{cycl},i} = \mathrm{e}\,\frac{Z_i}{m_i}\cdot B_z\,. \tag{2.48}$$

For a H_2^+ ion in a dipole magnet of the storage ring, $\omega_{\mathrm{cycl},i}$ varies between 18 and 48 MHz at beam energies between 1.2 and 3.2 GeV. For CO_2^+, $\omega_{\mathrm{cycl},i}$ lies between 0.8 and 2.2 MHz for the same energy regime.

The ion's gyration around the magnetic field lines has a radius of

$$r_{\mathrm{cycl},i} = \frac{1}{\omega_{\mathrm{cycl},i}}\cdot v_{\perp,i}\,, \tag{2.49}$$

which scales with its velocity.

As shown in figure 2.13 for an idealized case, the interplay of electric and magnetic fields results in an additional ion motion. On the one hand, the electric field $\vec{E}$ pointing towards the beam center results in a

[31] If the production mechanism of photo ionization due to synchrotron radiation in the arc section of the accelerator is also taken into account, this production profile will be slightly asymmetric. For more details, see section 3.4.

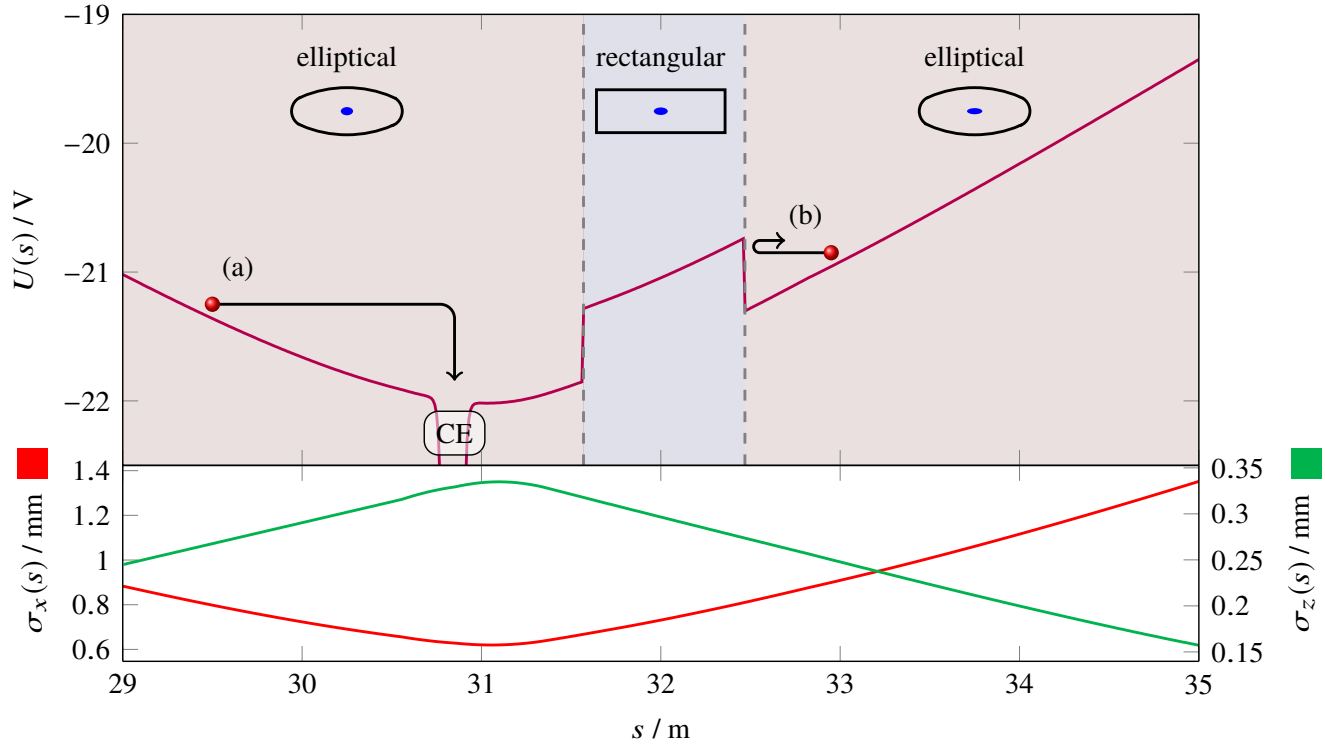

Figure 2.12: Segment of the ELSA storage ring's longitudinal beam potential at 1.2 GeV and 100 mA. Here, two segments with an elliptical beam pipe are separated by a rectangular one at the extraction septum MSE7. Due to variations of the horizontal (red) and vertical (green) beam width, the beam potential shows a minimum at 31 m. The utilization of different vacuum chamber geometries additionally elevates the beam potential by approximately 0.5 V inside the extraction septum. An ion produced at (a) follows the beam potential to its minimum. In the vicinity of the minimum, a clearing electrode, denoted as CE, is positioned which deforms the beam potential and catches arriving ions in its vicinity. An ion at (b), on the other hand, cannot reach the clearing electrode, since it cannot pass through the potential step at the transition from an elliptical to a rectangular beam pipe.

Coulomb force and accelerates produced ions towards it. On the other hand, the magnetic field $\vec{B}$ bends this straight trajectory into a gyration with an additional velocity component perpendicular to the ion motion. Since this motion is an accelerated one, $v_\perp$ is not constant and the gyro radius increases as the ion gets closer to the beam center. Eventually the ion motion towards the center stops and is reversed because the trajectory is bend fully perpendicular to the initial velocity. Once this point is reached, the electric field decelerates the ion's motion away from the beam center, resulting in a decreasing gyro radius.

This increasing and decreasing of the gyro radius along with the acceleration on one half and deceleration on the other half of the gyration cycle results in a *cross-field drift* perpendicular to the electric and magnetic field. One obtains the so called *cross-field drift velocity* as [Jac62, section 12.8]

$$\vec{v}_\mathrm{d} = \frac{\vec{E} \times \vec{B}}{\left(\vec{B}\right)^2} \,. \tag{2.50}$$

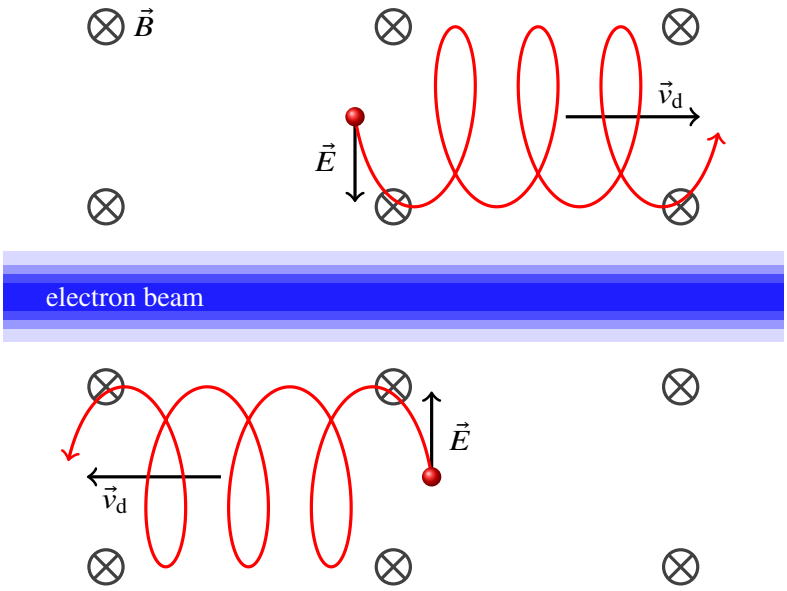

Figure 2.13: Illustration of the cross drift of ions in dipole magnets. In this idealized case, the electric force $\vec{E}$ and the magnetic field $\vec{B}$ are assumed to be constant in the relevant area of the ion motion. Also the bending radius of the electron beam is neglected. Produced ions, on the one hand, are attracted to the beam potential by the Coulomb force. On the other hand, the arising velocity towards the beam center leads to a Lorentz force perpendicular to the ions motion and the magnetic field. Eventually the momentum dependency of the gyro radius results in a longitudinal drift $\vec{v}_\mathrm{d}$. Its direction is dependent on the side of the beam where the ion is produced.

Cross-Field Drift in Dipole Magnets

For ions, which are produced in a dipole magnet, the vertical component of their motion remains unmodified due to the vertical magnetic field. Therefore, this component can be ignored for once. The electric and magnetic fields in this configuration are given by

$$\vec{E}(x,z,s) = \begin{pmatrix} E_x \\ 0 \\ 0 \end{pmatrix} \qquad \text{and} \qquad \vec{B}_\mathrm{dp}(x,z,s) = \begin{pmatrix} 0 \\ B_z \\ 0 \end{pmatrix} .$$

Here, E_x is the horizontal component of the electric field, pointing towards the center of the beam and B_z is the dipole field, which is assumed to be homogeneous and purely vertical. Using equation (2.50), one obtains

$$v_\mathrm{dp} = \frac{E_x}{B_z} \tag{2.51}$$

for the cross-field drift velocity. In this simple case the longitudinal ion motion is a steady motion with a velocity v_dp. The drift velocity is also independent of the ion mass. Thus, for example CO_2^+ and H_2^+ ions drift with the same velocity inside a dipole magnet. The direction of the drift changes sign from the one side of the beam to the other.

As the electric field strength E_x scales with the beam current, higher currents increase the drift velocity. On the contrary, an incrementation of the beam energy decreases the drift velocity because higher magnetic fields are used and E_x decreases due to an incrementation of the beam emittance and the resulting increase in beam size.

Since the lifetime of the ions indicates the neutralization level in the accelerator, a higher cross-field drift velocity is favorable. One can expect a neutralization sensitive to the beam current and energy. For a high beam energy with low current, a higher neutralization is expected than for a low energetic high current beam.

Additional Cross-Field Drifts and Magnetic Mirrors

The stated scenario can assumed to be an idealized case. The electric field E_x is assumed to be constant in the transversal plane in the relevant area of the ion motion. The longitudinal component of the field is omitted and the magnetic field is homogeneous.

In reality, there is a strong dependence of the electric field on the distance to the beam center, as is shown in equation (2.43). Ions gyrate with a non-zero radius, therefore the horizontal electric field varies during the gyration. Additionally, the longitudinal electric field is non-zero and is pointing towards the local minimum of the beam potential. Therefore, the electric field is not purely horizontal anymore. This results in a cross-field drift motion, which also has transversal components mixed to the longitudinal one.

Longitudinally, the magnetic field B_z has a finite length and thus is a function of s. On the edge of the magnets, fringe fields occur. Here, $B_z(s)$ rapidly rises from zero to the design magnetic field strength $B_{z,0}$. If one considers ions, which follow the longitudinal electric field and reaching the dipole fields, these fringe fields causes the ions to gyrate transversally. Due to the increment in $B_z(s)$, the gyro radius decreases, which may lead to reflexion of the ions away from the dipoles. The fringe field therefore can act as a *magnetic mirror*, which hinders longitudinal motion.

Additional cross-field drifts in other optical elements such as quadrupole and sextupole magnets also have to be taken into consideration. In Literature, estimated cross-field drift velocities are often in the order of several $\mathrm{km\,s^{-1}}$ [Hin11, section 8.5 and 8.6]. Here, the corresponding kinetic energies cannot be reached by thermal ions and the cross-field drift is therefore neglected in literature. However, these rough estimations do not take the transversal variation of the electrical field along the individual ion's trajectory with non-zero gyro radii into account.

In order to estimate the effects of quadrupole magnets and dipole fringe fields on the ion motion properly, tracking simulations are necessary. In section 4.3 these complex problems are mapped into a suitable simulation scenario.

CHAPTER 3

Residual Gas Constituents and Mechanisms of Ion Production

To formulate an adequate strategy for ion clearing, one first has to look at the production of ions. According to equation (2.8), the ion production rate has two major contributors. The local pressure $\hat{\mathcal{P}}(s)$ and the total ionization cross section σ_{ion}.

The total pressure $\mathcal{P}$ is a composition of the partial pressures p_i of individual residual gas molecules and atoms. The total pressure in the ELSA storage ring is in the order of 10^{-7} to 10^{-8} mbar, but along the storage ring it may be subject to variations: On the one hand, the total pressure varies due to conditions of the vacuum infrastructure. Here, the used vacuum pumps' type and the distance to them is important[1]. On the other hand, the fraction of individual molecules or atoms to the residual gas may change due to different desorption, diffusion and permeation characteristics of the beam pipe. To estimate a production rate, the first step therefore is to identify prominent constituents of the residual gas and their proportion, as will be discussed in section 3.1.

As all ion production rates scale linearly with the pressure within the vacuum system, in a second step a pressure model for the storage ring will be presented in section 3.2.

The next step is the evaluation of the ionization cross sections for each of these prominent residual gas species. They have individual ionization probabilities for different ionization mechanisms. One major contribution to the total ionization cross section is the impact ionization, which will be covered in section 3.3. Another contribution is the photo ionization of residual gas by synchrotron radiation photons, which is mostly neglected in literature. In section 3.4, its contribution to the production rate along with its spatial distribution will be estimated and simulated for the storage ring.

Note that in the course of this work only singly charged ions are considered. The ionization process in which a multiply ionized ion is produced is much less likely to occur than single ionization. Additionally, twofold ionization of an already ionized residual gas molecule or atom is also unlikely, as the ion density

[1] In a vacuum system with pressures below 10^{-2} mbar, molecular flow of the residual gas occurs. Here, more precisely the KNUDSEN number, the ratio of the mean free path to the minimal characteristic length of the vacuum system, is larger than one. Thus, pumping of residual gas in an accelerator with pressures of 10^{-7} mbar is not based on drag due to pressure differences along which the gas follows but on the statistical motion of the individual residual gas particles. Hence, the probability of a particle reaching a pump declines with increasing distance from the pump. A large distance from a pump results in reduced pumping speed as the conductance towards the pump is low. For more details, see [OHa03, section 3.4].

in the electron beam is significantly lower than the density of the residual gas in the vacuum system[2]. Also, a dissociation of the residual gas molecules into ionized atoms during the ionization process by impact and photo ionization is not considered because the corresponding cross sections are small compared to the ionization cross sections[3].

3.1 Residual Gas Composition

The residual gas composition in the accelerator's beam pipe is the main key to evaluate the production rate of ions inside it. First the vacuum infrastructure of the storage ring will be presented briefly which gives indications about possible residual gas constituents. Subsequently, mass spectrometric measurements and their analysis will be presented.

3.1.1 Vacuum Infrastructure in the Storage Ring

The ELSA storage ring is designed as an accelerator, in which electrons should be stored with lifetimes of 1 to 2 h[4] [Hil06, section 4]. Ideally, the beam lifetime should only be limited by the aperture of the accelerator[5]. The electron beam propagates within the storage ring with a velocity of βc, where $\beta \approx 1$ and thus has a revolution frequency of 1.824 MHz. If it is stored for 30 min, it circulates in the accelerator more than $3 \cdot 10^9$ times and thereby travels a distance of over $5 \cdot 10^{11}$ m. Thus, one factor limiting the beam lifetime is also the mean free path between collisions with the residual gas in the vacuum. The mean path scales inversely with the pressure in vicinity of the beam. Consequently, the beam travels inside an evacuated beam pipe in which an average pressure lower than 10^{-8} mbar ensures a mean free path of over 10 km, if possible. This reduces the probability of collisions with the residual gas to a minimum in which the energy loss of involved electrons exceeds the accelerator's energy acceptance and the electrons are lost.

Local Characteristics of the Storage Ring's Vacuum System

When pumping a vacuum chamber, the reachable minimal pressure is dependent on the pumping speed of the engaged vacuum pumps and the inflow rate of new residual gas molecules and atoms into the vacuum chamber. The inflow occurs through leaks, a back flow through the pump and due to the mechanisms of diffusion, desorption and permeation. For more information, see appendix A.1 and [OHa03, chapter 4].

[2] In the storage ring, the average electron density in the beam is equal to $9 \cdot 10^{11}$ m^{-3} for a beam current of 200 mA and an estimated volume of the beam of 0.76 m^3 (compare appendix A.9). For $\eta = 1$, the ion density is identical. In contrast, the number density n_{rgm} of the residual gas is equal to approximately $2.4 \cdot 10^{14}$ m^{-3} for a pressure of 10^{-8} mbar (compare equation (2.7)). Consequently, the probability of doubly ionizing an ion is a factor of 1 000 lower than ionizing a neutral residual gas molecule or atom.

[3] The cross sections for molecular dissociation by impact ionization exceeds the electrons' ionization cross section for low beam energies and shows its maximum in the energy region of approximately 100 eV. However, for higher beam energies in the order of GeV, this cross section is negligibly small (compare e.g. [Che+06]). The photofragmentation cross section for the dissociation of residual gas molecules by synchrotron radiation photons is a factor of 5 to 10 lower than the ionization cross section. For photo dissociation of H_2, this factor is approximately 75 (compare e.g. [Gal+88]).

[4] These values refer to an operation of the storage ring at a beam energy of 2.3 GeV with a current of 50 mA.

[5] Since the transversal and longitudinal distribution of individual bunches is Gaussian, the probability of high transversal or longitudinal amplitudes of single electrons in non-zero. These electrons collide with the beam pipe or leave the energy acceptance of the accelerator and are lost. The electrons' amplitude distribution is continuously mixed due to synchrotron radiation. Therefore, transport losses always occur and the beam lifetime is dependent of the minimal aperture in the accelerator.

Beam Pipe Type	Percentage	Shape	Properties
Quadrupole	31 %	elliptical	$a = 51.5\,\text{mm}$, $b = 22.0\,\text{mm}$
Dipole	44 %	elliptical	$a = 60.6\,\text{mm}$, $b = 20.7\,\text{mm}$
Other	25 %	round, rectangular	

Table 3.1: Overview of beam pipe geometries used in the storage ring. a and b denote the semi-major and minor axis of the beam pipes, when approximated as an ellipse.

Design Goals The storage ring is operated mostly in booster mode. Here, the accelerator operates with a repetitive cycle which has a length of approximately 5 s and only requires a storage duration slightly longer than that. As it has not been explicitly designed for a long-term storage of the beam, the emphasis during its design phase has not been mainly on the vacuum (or wake impedance[6]) finesse. Therefore, the storage ring can only reach an average pressure of 1 to $4 \cdot 10^{-7}$ mbar during operation, as will be discussed in section 3.2.

Vacuum Infrastructure The vacuum in the storage ring is sustained by ion getter and turbo molecular pumps. At 17 locations in the accelerator, separate sections[7] dedicated to this purpose are integrated into the beam pipe. In each section, an *ion getter pump* (IGP) of type *Leybold-Heraeus IZ 270 D* and a *Pfeiffer HiPace 300 turbo molecular pump* (TMP) with a *Pfeiffer MVP 015-4* diaphragm backing pump is operated. The setup is completed by a Pirani- and cold cathode vacuum gauge. Together with the pressure diagnostics of the IGP, using its ionization current, this provides the possibility to monitor the surrounding pressure in the vacuum system. These sections are positioned between each dipole-quadrupole pair in the arc sections of the storage ring.

On other locations in the storage ring, like the straight- and the rf section, in total 16 additional IGPs are installed. The vacuum system is separable by five sector valves, only open during operation, to enable a maintenance of vacuum components without breaking all of the storage ring's vacuum system.

The pumping speed of an IGP for reactive gas is higher than for noble gases [OHa03, section 14.2]. Additionally, their pumping speed also decreases significantly if hydrogen is continuously pumped [OHa03, section 14.2]. The TMP's pumping efficiency for light residual gas like H_2 is reduced compared to heavier gas species like CH_4 or CO_2. For more information regarding these pumps, their characteristics and other utilized vacuum technologies, see appendix A.4.

Beam Pipes In an accelerator a beam pipe with equal shape and size is desired to reduce the impact of wake impedances and to reduce the occurrence of potential hollows in which ions accumulate. Due to geometrical constraints of several components, this cannot be achieved and the stainless steel beam pipe therefore consists of several types with different dimensions. The major part of the beam pipe comprise an elliptically shaped pipe. In figure 3.1, three exemplaric types of beam pipes are shown which are used in the storage ring. The corresponding geometrical properties are given in table 3.1.

The curvature of the dipole beam pipe longitudinally follows the trajectory of the deflected beam and is bend with a radius of approximately 10.89 m. This pipe is less high than the quadrupole beam pipe to fit into the iron yokes of the dipole magnets and broader to compensate for the build-in radiation shielding.

[6] The wake impedance is a complex quantity which describes the strength of electromagnetic distortions acting on the beam due to e.g. changes in the beam pipe geometry. In section 5.2.1, this topic is discussed in more detail.

[7] These sections will be called pump sections in the course of this work.

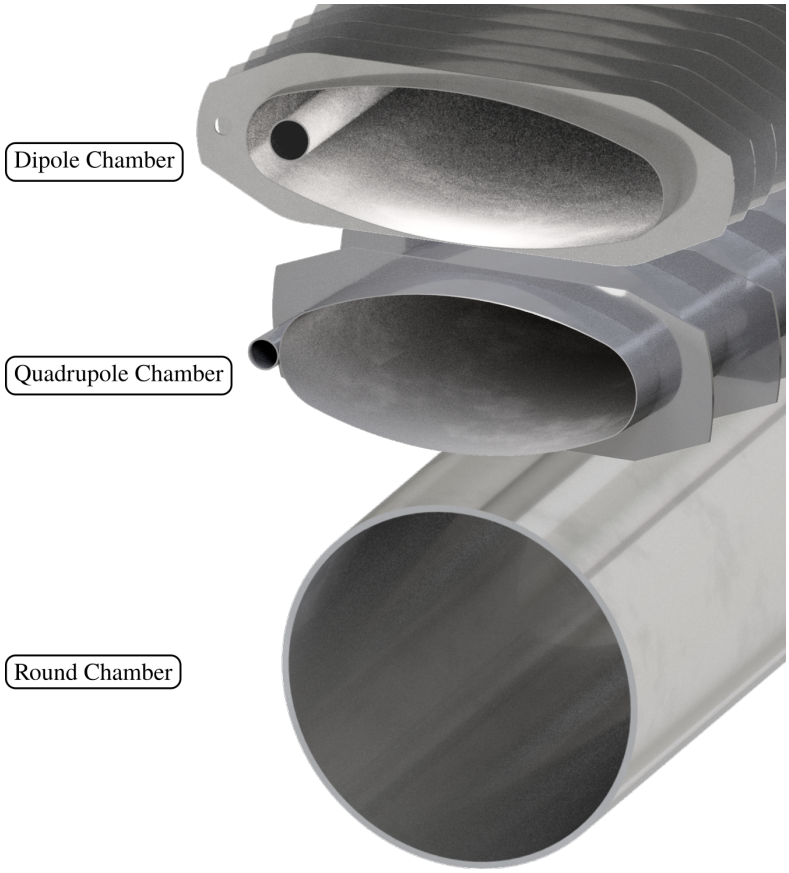

Figure 3.1: Sectional view of three different types of stainless steel beam pipes, used in the storage ring. On top, the dipole chamber with integrated radiation shielding is shown. The middle pipe is the quadrupole chamber used mainly in quadrupole magnets. A round beam pipe geometry is represented by the bottom pipe. This pipe has an inner diameter of 10 cm. Note that the dimensions of the pipes are to scale. Courtesy of P. Hänisch, ELSA.

The shielding is water-cooled to dissipate the radiative heating due to synchrotron radiation of a high intensity electron beam. More details regarding this beam pipe can be found in [HNH15].

Additional types of beam pipes, such as round or rectangular shapes, also are present in certain sections of the accelerator. Especially in the straight sections, beam pipes with a radial geometry of 50 mm and 25 mm radius are installed. In the rf section, the cavities' inner geometry themselves define the shape of the beam pipe (see section 4.4 for more details).

Unbaked stainless steel components desorb H_2, CH_4, H_2O, CO and CO_2 when evacuated [Mat94, section 7]. As the individual stainless steel components of the beam pipe have been annealed, the desorption rates of the different residual gas are unknown.

In the dipole chambers, an additional desorption process takes place during the accelerator's operation: Synchrotron radiation, emitted by the electron beam and irradiating the dipole chamber's shielding, leads to *photo stimulated desorption* (PSD). For irradiated stainless steel, this process increases the desorption rate of H_2, CH_4, CO and CO_2 into the vacuum system [OHa03, section 4.4.4].

Preparation of the Vacuum System As the accelerator is not designed for an ultra high vacuum with pressures below 10^{-9} mbar, the vacuum system is not intended to be baked out after a vacuum breach due to maintenance or repairs. An exception is the rf section, where the cavities have heating coils, designed to bake them out. In case the vacuum is broken intendedly, the concerned section of the accelerator is vented with dry, molecular nitrogen. This inert gas does not react or deposit on the surface of the vacuum chambers and extrudes atmospheric air, which consists of more reactive constituents or vapors, in order to avoid additional desorption processes when evacuating the section again.

When the storage ring's vacuum system or a section of it is evacuated, initially *rotary lobe pumps*[8], temporarily flanged to the system, are used to reduce the vacuum pressure to 10^{-1} mbar. Then backing pumps followed by TMPs reduce the pressure even further. When a pressure of 10^{-6} mbar is reached, the baken and conditioned IGPs are set into operation. They stay in operation all the time and reduce the system's pressure, measured at the IGPs, to below 10^{-8} mbar when the accelerator is not in operation. During storage ring operation, the TMPs are used to assist the IGPs.

The Vacuum System during Operation of the Storage Ring During operation of the storage ring, the electron beam emits synchrotron radiation photons in the dipole magnets, which mainly impinge on the radiative shielding and cause PSD. This process increases the emission rate of adsorbed gases. On one hand, desorption processes are conveniently sped up when surface contamination is present after the vacuum system has been vented. On the other hand, PSD permanently increases the emission rate of H_2, CH_4, CO and CO_2 out of stainless steel which increases the pressure in dependence of the synchrotron radiation intensity, and thus the beam current [OHa03, section 4.4.4][9]. This results in an increased local pressure in the arc sections. During operation, the measured average pressure, monitored by IGPs, varies between $5 \cdot 10^{-9}$ to $5 \cdot 10^{-8}$ mbar.

Indications on the Residual Gas Composition

From the described vacuum system and the utilized materials, finally possible candidates of the residual gas can be derived. The following residual gas molecules and atoms are expected to occur in the ELSA storage ring in descending order of abundance:

- Light residual gases, like H_2, may dominate the residual gas composition as these gases permeate the vacuum system from the outside all the time. Additionally, the utilized TMPs' pumping speed decreases with lower mass number due to an increased back streaming rate of these particles, which may result in a higher abundance. Also, the IGPs pumping speed decreases for hydrogen, if it is continuously pumped.
- CH_4, CO and CO_2 may appear commonly due to the usage of stainless steel beam pipes which desorb these gases. The desorption rate may rise with increasing beam energy and current since the beam pipes are subject to PSD due to irradiation with synchrotron radiation photons.
- N_2 may contribute sparsely as the vacuum system is exposed to dry nitrogen when it is vented. As it cannot permeate through the beam pipe and is not produced through desorption, its proportion can be assumed to be small.

[8] The rotary lobe pump is a positive displacement pump, which can generate a pressure of lower than 10^{-2} mbar. It operates oil-free and thus lacks the risk of contaminating the vacuum system with it. For more information, see e.g. [OHa03, section 10.3].

[9] The individual PSD desorption rates are also a function of beam energy, because the energy spectrum of the emitted synchrotron radiation photons varies with it. The individual desorption rates are also increased by *electron stimulated desorption* (ESD), when stray electrons impinge on the surface with high kinetic energy, producing a shower of secondary particles which contaminate the vacuum system. For more information regarding PSD and ESD, see section 3.2.

- Compositions of air including N_2, O_2 and H_2O may be present as it may flow into the vacuum system through leaks. Because the vacuum system is assumed to be leak free[10], the share of these gases should be low.
- Noble gases like He, Ne or Ar may contribute to a minor level because IGPs, the main vacuum pumps in the storage ring, show reduced pumping speeds for them.

3.1.2 Mass Spectroscopy

Individual characteristics of the used vacuum system components, such as surface treatment, contamination and irradiation intensity, lead to desorption rates of residual gas species which can vary strongly from component to component. Therefore, the used materials and their processing prior to the assembly only give indications about the composition of the residual gas in the vacuum system. Detailed residual gas analyses with a mass spectrometer, however, provides this information.

Residual Gas Analyzer

A residual gas analyzer is an instrument which measures the spectrum of the mass-to-charge ratio A/Z of a residual gas population in a vacuum system. It ionizes the residual gas, guides the particles through a mass bandpass filter and detects the filtered and amplified ion current. This current is proportional to the partial pressure of the individual ion species which passed through the filter.

In the following measurements, a quadrupole mass spectrometer of type *Balzers QMA 125* is used. For pressures below 10^{-6} mbar, this analyzer can detect residual gas constituents with an A/Z ratio of up to 100 [Bal91]. Thus, a singly ionized molecule or atom with a mass of 100 u is still detectable. For more information regarding the functional principle of the spectrometer, see appendix A.5.

Installation

To obtain the composition of residual gas in the storage ring, the mass spectroscopic measurements should be conducted in a representative vacuum section. Therefore, the quadrupole mass spectrometer has been installed in the pump section between dipole M12 and quadrupole QD13 (compare figure 1.1).

The chosen vacuum section is one of 17 identical sections installed in the two arc sections of the storage ring, which in total amount for more than 60 % of its circumference. The quadrupole mass spectrometer is installed at a distance of approximately 40 cm upstream to the adjacent dipole magnet. Thus, the influence of locally occurring synchrotron radiation on the residual gas composition due to PSD can be measured, as residual gas from the dipole chamber will pass the mass spectrometer on its way to the IGP or TMP in this section.

In close proximity to the spectrometer, an external electrometer *Balzers EP 112* and the mass filter support electronic *Balzers QME 125* are mounted. The electrometer amplifies the output signal and the *QME 125* controls the mass filter and the preamplifier's[11] high voltage. A computer on which the BALZERS QUADSTAR 6.03 software is installed, enabling the control of the quadrupole mass spectrometer via an RS-232 interface, is connected to the local ethernet. This allows for remote control of the computer, since it is located in a radiation protection area during storage ring operation.

Consequently, this setup enables a temporary monitoring of the residual gas composition in a representative section of the storage ring's vacuum system during its operation.

[10] The vacuum system is tested helium-tight down to a leak rate of $< 5 \cdot 10^{-12}$ mbar m^3 s^{-1} [Pfec, section 2.4]. However, the leak rate of the system may be subject to variations with time due to aging of components.

[11] The preamplifier of this mass spectrometer is a channeltron.

3.1.3 Vacuum Constituents in the Storage Ring

The quadrupole mass spectrometer has been used to analyze the composition of the residual gas molecules and atoms in the ELSA storage ring.

Measurements Procedures

Measurements have been conducted while the storage ring has not been operated and no beam propagated in the beam pipe. These ”background“ measurements have been accomplished shortly after each other to ensure the vacuum system to be in a comparable state. They are intended for an estimation of the measurement error.

Proper measurements with the spectrometer have then been carried out remotely at different beam energies. Besides at injection energy of 1.2 GeV, measurements have been conducted at beam energies of 1.7 GeV, 2.2 GeV, 2.4 GeV and 2.9 GeV. The beam current has been chosen to be approximately 35 mA for all of these measurements.

When the particular measurements are conducted, first the filament of the ion source is heated up and a high voltage of typically 1 300 V is applied to the preamplifying channeltron. This state is maintained for approximately 15 min to ensure a thermal stability of the apparatus and to allow degassing processes of the filament to subside, which otherwise would affect the measurement results.

During a measurement process, the mass filter sweeps the configured mass-to-charge ratio linearly from $A/Z = 1$ to 100 and detects and amplifies the collected ion current. As the measured peak current at $A/Z = 2$, denoted as $p_{\mathrm{meas}}(2)$, surmounts the other contributions by more than one order of magnitude during most measurements, different settings of the channeltron amplifier had to be used. Therefore, the sweep has been split up into two mass regions. In the first region, reaching from $A/Z = 1$ to 100, the amplification factor has been reduced by an order of magnitude, enabling the utilization of the complete dynamic range of the measurable current without saturation. Here, only the peaks at $A/Z = 1$ and 2 have been utilized in the subsequent analysis. In the second region, which comprises the mass region from $A/Z = 3$ to 100, the amplification factor has been increased to ensure enough sensitivity to measure also contributions with heights smaller than 1 % of $p_{\mathrm{meas}}(2)$. The `QUADSTAR` software stores the obtained mass spectrum. It is saved as an `ASCII`[12] format file for subsequent analysis.

Mass Spectrum Characteristics and Measurement Errors

As can be seen in figure 3.2 (top), the obtained mass spectrum shows the measured current I_{qma} in dependence of the mass-to-charge ratio A/Z, which is accepted by the mass filter. The peaks have a finite width because the mass-bandpass filter has a finite acceptance range.

As a first processing step the two measured mass spectra are merged into one. `QUADSTAR` already has subtracted the effect of different amplification factors in the measured current. Therefore, the data is only corrected by eventual offsets[13] appearing in measurements with low amplification. Then the maximum current of each peak $p_{\mathrm{meas}}(A/Z)$ is extracted out of the data. $p_{\mathrm{meas}}(A/Z)$ is marked as red hatched bar in figure 3.2 (middle). At $A/Z = 1$ and 2 the peaks appear not to be completely separated and the peak at $A/Z = 2$ can assumed to overlap with the one at $A/Z = 1$. Therefore, the $A/Z = 2$ peak has been

[12] ASCII - a short form of American Standard Code for Information Interchange - is a seven bit character encoding used for generating human-readable datasets in the Latin alphabet and Arabic numbers.

[13] These offsets emerge as the amplification subtraction of `QUADSTAR` is not perfectly adjusted to the real amplification of the channeltron. Here, the baseline of low amplification dataset has been offsetted slightly. The offset has been reversed using the overlap between the two mass regions and bring the base lines back into agreement by offsetting the low amplification measurement accordingly.

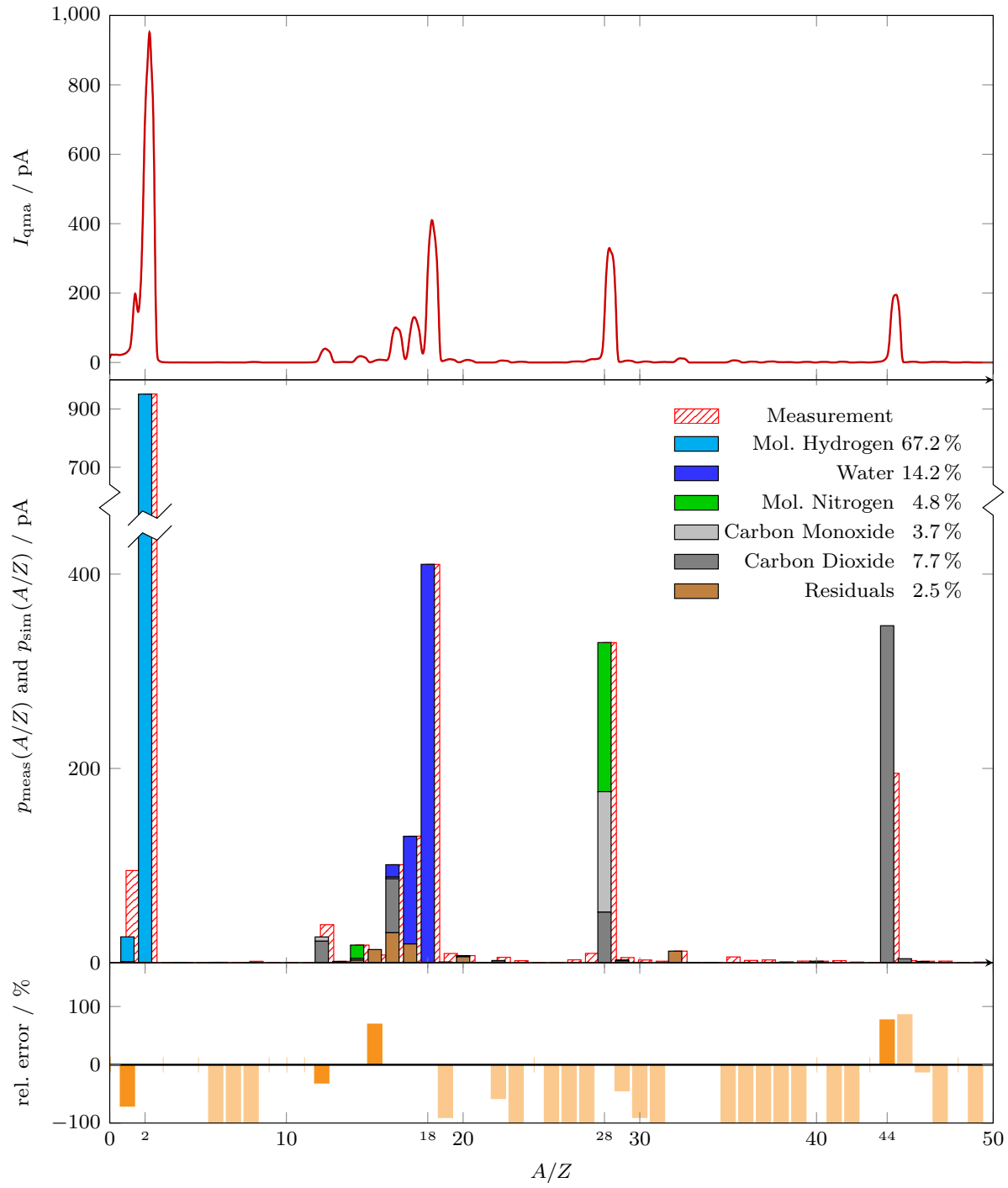

Figure 3.2: Residual gas analysis for a ”background“ measurement without beam. The upper graph shows the measured current of the quadrupole mass spectrometer I_{qma} for a relevant mass range from $A/Z = 0$ to 50. The red hashed bar plot in the middle graph is the extracted peak height $p_{\mathrm{meas}}(A/Z)$ for each A/Z. The software MSAUGA generates a simulated mass spectrum $p_{\mathrm{sim}}(A/Z)$, which consists of contributions of 11 different residual gas species. It is mapped on $p_{\mathrm{meas}}(A/Z)$ in the middle graph. The gas composition is listed in descending order of relevance. The bottom graph shows the relative deviation between measured and simulated mass spectrum.

A/Z	1	2	⋯	12	⋯	14	⋯	16	17	18	⋯	28	⋯	44
Rel. Error / %	20.0	9.6		16.5		9.0		2.5	3.6	2.8		2.2		12.2

Table 3.2: Relative errors of the mass spectroscopic measurements for different relevant A/Z. Here, only mass-to-charge ratios are shown which show a measured contribution of more than 2 %$p_{\mathrm{meas}}(2)$.

approximated as a Gaussian distribution and its overlap at position of the $A/Z = 1$ peak is subtracted. For the other peaks in the spectrum, the separations are clearer and only their maximum values are extracted. The spectrum is obtained as a datafile with discrete $p_{\mathrm{meas}}(A/Z)$ values for each A/Z from 1 to 100.

The first measurements have been the "background" measurements without beam. As can be seen in the top graph of figure 3.2 or the extracted $p_{\mathrm{meas}}(A/Z)$ in figure 3.2 (middle), labeled as "Measurement", a dominant contribution is present at $A/Z = 2$. Also strong contributions at $A/Z = 1$, 18, 28 and 44 are visible. Other proportions of the spectrum are located at $A/Z = 17$, 16 and 12. A minor amount comes from peaks at $A/Z = 14$, 20 and 32. All relevant contributions can be found in the A/Z-regime between 1 and 50. A small contribution to the mass spectrum can also be identified at $A/Z = 62$, 63 and 93 alongside 94. However, as their total proportion to the spectrum is well below 0.3 %[14], they are ignored in this analysis.

Utilizing the "background" measurements, the relative error for each A/Z-contribution has been obtained from their standard deviation. For the relevant contributions to the spectrum, table 3.2 shows the corresponding relative error $\Delta p_{\mathrm{meas}}(A/Z)/p_{\mathrm{meas}}(A/Z)$. As the peak at $A/Z = 1$ is not separated from the neighboring peak, its error is doubled to 20 % to explicitly overestimate its actual error. Additionally, the digitization of the measured current poses a minor error which is estimated as the discretization width of 0.03 pA[15] which is extracted from the measurements.

Analysis Procedure

To extract information about the storage ring's residual gas composition, the processed mass spectrum has to be analyzed regarding the individual contributions of the identified residual gas species. However, several processes obscure the measured mass spectrum and complicate the identification process.

Cracking Patterns In the ion source of the quadrupole mass spectrometer residual gas molecules and atoms are being ionized by bombardment with electrons, which have a kinetic energy of approximately 100 eV. Besides single ionization, additional processes occur. Multiple ionized particles can be generated in the ion source[16]. Also the electron bombardment can result in dissociation of molecules, where multiple fragments, which for themselves are electrically neutral or singly/multiply ionized, can be detected in multiple A/Z-regions[17]. Nearly all elements in the periodic table appear in an isotopic configuration, where different numbers of neutrons are arranged in the atom's nucleus. These isotopes have different

[14] Here, their relative sensitivity ς is assumed to be 1. For heavier residual gas species, where more orbital electrons and/or bound atoms are involved, ς trends towards higher values. Thus, higher ionization probabilities occur. This is a conservative estimate and therefore a contribution $\ll 0.3$ % is probable.

[15] The current, measured by the electrometer after the amplification, shows a larger absolute error. The stated error is that low because Quadstar scales down the obtained value by dividing by the constant amplification factor of the channeltron.

[16] For example, a nitrogen molecule can be ionized to N_2^+ and N_2^{2+}, resulting in a signal in the region $A/Z = 28$ and 14, respectively.

[17] An example is methane CH_4 which appears mostly as CH_4^+ in $A/Z = 16$, but also in 15 as CH_3^+, in 14 as CH_2^+, in 13 as CH^+ or in 12 as C^+. The split-off hydrogen atoms and molecules also contribute to A/Z of 1 and 2 as H^+ and H_2^+, respectively.

relative abundances[18]. All processes contribute with a certain probability to the mass spectrum of a particular residual gas species. Therefore, multiple A/Z contributions of one residual gas species appear in the mass spectrum. The peak heights of these contributions are proportional to the probability of the particular processes. These *cracking-* or *fragmentation patterns*[19] are individual for every species. In table C.2 in the appendix, a small collection of fragmentation patterns of molecules are shown which probably appear in the storage ring's vacuum system.

Relative Sensitivity The proportion of each contributing species is corrected by a factor, which is inverse to the so called *relative sensitivity* of these gases. This factor comes from the ionization process: Each individual species of the residual gas differs in its electron configuration, ionization energy and dimension. Also, molecules have different binding energies and additional excitatory degrees of freedom. Consequently, the cross section of the ionization process via electron bombardment - the impact ionization cross section - is individual for every residual gas species. Therefore, not all gas species have the same ionization probability in the ion source of the mass spectrometer and only a certain fraction of the actual population is ionized and detected after passing the mass filter. This fraction is smaller for species with lower cross section such as light noble gases like helium. It increases for heavier gases with large molecular structures such as methane (CH_4).

Therefore, each species' proportion has to be corrected by the relative sensitivity, mapping the cross section difference. Nitrogen (N_2) has a relative sensitivity ς of 1 per definition. Species with lower ionization cross sections have $\varsigma < 1$ and those with larger ones show $\varsigma > 1$.

Identification Approach The identification of the involved residual gas species from the mass spectrum is not trivial for a mixture of gases. For example, species like nitrogen (N_2) and carbon monoxide (CO) mainly contribute both to a peak at $A/Z = 28$ (N_2^+ and CO^+). To estimate their proportion to this peak, and thus to the gas composition, the analysis of side peaks has to be included. They contribute to these side peaks in accordance with their fragmentation patterns. Only CO contributes to the peaks at $A/Z = 12$ (C^+) and 16 (O^+), whereas N_2 mainly contributes to the $A/Z = 14$ peak (N^+). One approach to this problem is the creation and solving of a system of linear equations. Here, a numerical approach utilizing a genetic algorithm[20] is used. This algorithm is the core functional principle of the program `MSAUGA`[21] which has been developed in-house exclusively for this field of application (also see appendix B.1.1 for more information). It decodes the composition of a mixture of gases and vapors - each species contributing to an individual extend - into a genome. Using the fragmentation patterns of the individual species, the mixture can be transfered into a simulated mass spectrum $p_{\mathrm{sim}}(A/Z)$. The program uses a library of fragmentation patterns obtained from the software `QUADSTAR` and [OHa03, appendix E]. It consists of the patterns of 65 gases and vapors, which usually occur in an accelerator's vacuum system

[18] For example, 98.892 % of carbon exists in the form of ${}^{12}_{6}\mathrm{C}$, with six protons and neutrons and 1.108 % in the form of ${}^{13}_{6}\mathrm{C}$ with one additional neutron [OHa03, appendix D]. Consequently, singly charged carbon contribute to mostly to $A/Z = 12$ but also minorly to 13.

[19] The cracking patterns, also called fragmentation patterns, are obtained from spectroscopic measurements conducted with isolated probes of specific gases in a vacuum recipient. In literature, they are normalized to the peak with the largest magnitude, usually the signal of a singly ionized molecule of the particular species. Its amplitude is set to 100 %. For more details, see e.g. [OHa03, section 9.1 and appendix E].

[20] A genetic algorithm is a meta heuristic optimization algorithm. It optimizes a set of parameters, a genome, which evolves with every new generation via crossover, mutation and arbitrary replacement, by selecting the "fittest" genome. Here, an assessment function evaluates each genome regarding its adjustment to the stated problem. It is inspired by the natural selection process in a biological population, where only individuals survive which are best suited to live in a specific habitat.

[21] The program has been developed with major contributions from D. Proft, ELSA, who is greatly thanked by the author.

and includes all gases, expected in the storage ring's vacuum system. The program generates a population with a specific amount of individuals. Each having a genome which corresponds to an individual gas mixture. The first generation is a population whose individuals are randomly generated with a set of arbitrary genomes. To select the population's individual with the most appropriate genome, an assessment function rates every individual. Only the individuals which are rated best are able to reproduce and create a new generation. Additionally, mutation of arbitrary chosen genes occurs and periodically the individuals, which are rated lowest, are replaced by new ones. Thus, from generation to generation the population's genome alter towards the genome which is most suitable for the assessment function. The program uses

$$\mathcal{A} = \sum_{A/Z=1}^{100} \frac{\left| p_{\mathrm{meas}}(A/Z) - p_{\mathrm{sim}}(A/Z) \right|}{\Delta p_{\mathrm{meas}}(A/Z)} \tag{3.1}$$

as an assessment function which has to be minimized. $\Delta p_{\mathrm{meas}}(A/Z)$ is the measurement error of the particular A/Z. With this assessment function, solutions will be preferred which best reproduce the largest peaks. The inverse of the final value of the assessment function is denoted as *score*. After $2 \cdot 10^6$ generations, the best rated individual is selected. Its genome, encoding a gas mixture, produces a simulated spectrum which fits best to the measured one. In figure 3.2 (middle), such a simulated spectrum, broken down to the contribution of the individual residual gas species, is shown in comparison with the measured $p_{\mathrm{meas}}(A/Z)$. In figure 3.2 (bottom), the relative errors between the measured and simulated spectra are shown. Here, the error of A/Z contributions with a peak height of < 25 pA are faded because they are neglectable.

Eventually, MSAUGA outputs the simulated spectrum and the corresponding composition of the residual gas molecules and atoms along with their individual mass contribution. For a "background" measurement, this reproduced spectrum is shown in figure 3.2 (middle). For a reduced scope of the fragmentation pattern library, consisting of 11 possible residual gas species, the MSAUGA simulations with the best scores are shown in figure 3.3 and figures C.3, C.5, C.7 and C.9 in the appendix. This "complexity-reduced" analysis process is compared to the "default" process with 65 possible residual gas species in appendix A.6.

Results

Figure 3.4 shows the results for the "default" analysis procedure whereas figure 3.5 shows them for the "complexity-reduced" case. Both analysis processes produce a congruent residual gas composition within their simulation errors.

In case the accelerator is not operated and no beam is present the residual gas in the vacuum system in vicinity of the mass spectrometer consists of approximately 68 % hydrogen, 14 % water vapor and 8 % carbon dioxide. Carbon monoxide and molecular nitrogen approximately have the same share with approximately 3 to 5 %. Oxygen also exists in minor proportion (approximately 5 ‰). Ammonia NH_3 (5 ‰) and Methane (3 ‰) are also present. Also minor amounts of the noble gases helium (0.5 ‰), argon (0.3 to 0.4 ‰) and neon (8 ‰) can be identified.

This composition of the residual gas species results from permeation of hydrogen through the beam pipe. Water vapor is a remnant on the surface of the beam pipe, in case the vacuum system has not been properly vented with dry nitrogen. But pure desorption of water vapor into the vacuum system cannot explain the fact that water vapor is the second dominant species in the vacuum system. A probable explanation are small leaks of the water cooling of the radiative shielding in the dipole chambers towards the vacuum system. The explanation can be supplemented by the assumption of minor leakages of the vacuum system to the outside. This will not only top up the water contribution due to water vapor in

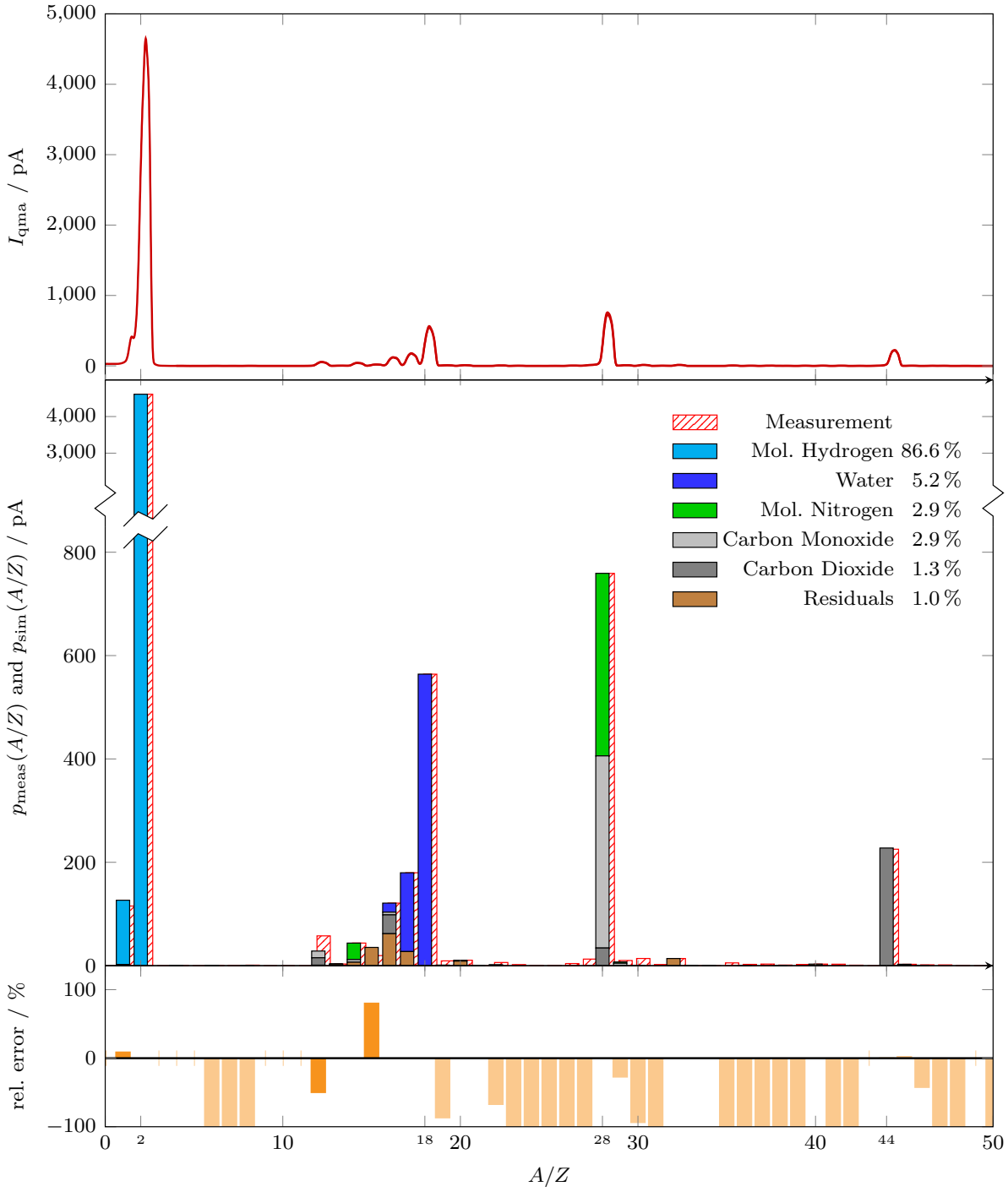

Figure 3.3: Residual gas analysis for a measurement at 2.2 GeV beam energy and 35 mA beam current. The upper graph shows the measured current of the quadrupole mass spectrometer I_{qma} for a relevant mass range from $A/Z = 0$ to 50. The red hashed bar plot in the middle graph is the extracted peak height $p_{\mathrm{meas}}(A/Z)$ for each A/Z. The software MSAUGA generates a simulated mass spectrum $p_{\mathrm{sim}}(A/Z)$, which consists of contributions of 11 different residual gas species. It is mapped on $p_{\mathrm{meas}}(A/Z)$ in the middle graph. The gas composition is listed in descending order of relevance. The bottom graph shows the relative deviation between measured and simulated mass spectrum.

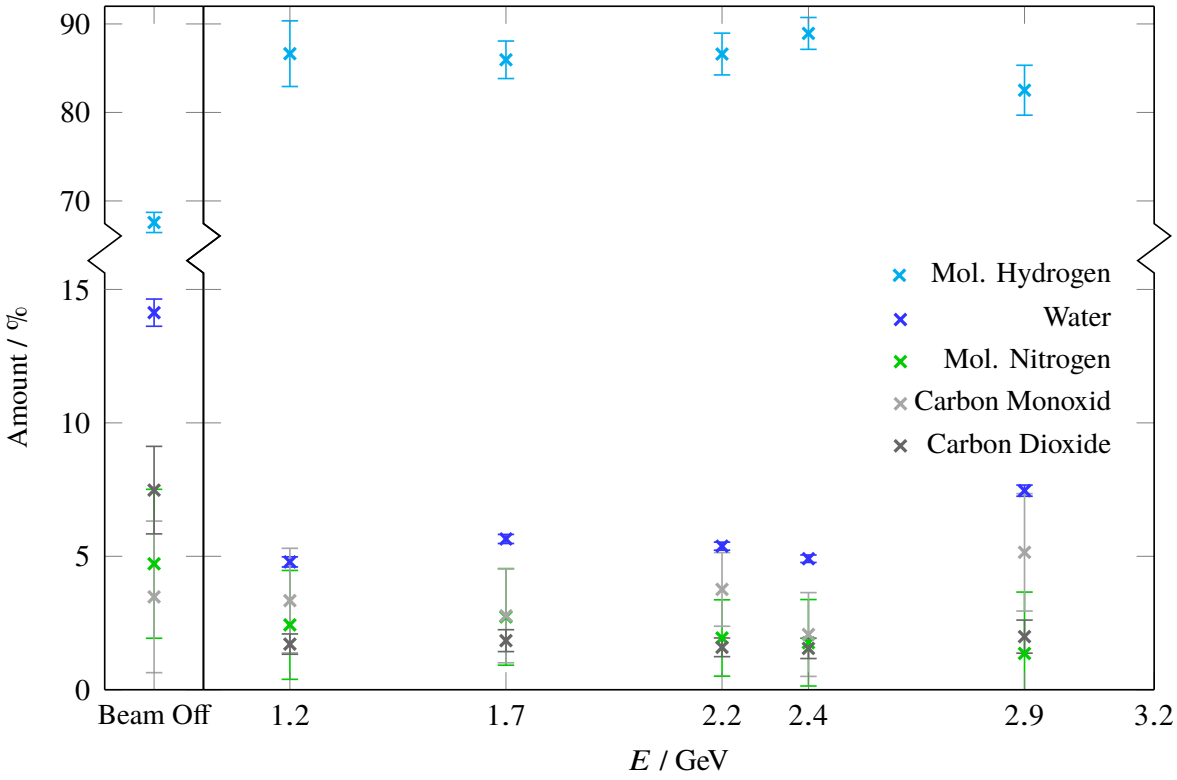

Figure 3.4: Results of the residual gas analysis via MSAUGA using a fragmentation pattern library of 65 residual gas species. Shown in the left part of the plot is the background measurement without beam. The composition of dominant residual gas species at certain beam energies at a beam current of approximately 35 mA are shown in the right plot. The data for this plot is shown in table C.1.

the air, but also explains the existence of oxygen and the noble gases. Additionally, noble gases cannot be pumped adequately by IGPs. The carbon monoxide, -dioxide and methane contributions probably will mainly not result from leaks but are typically desorbed molecules from the stainless steel beam pipe [Mat94, section 7].

When a beam current of approximately 35 mA is stored in the storage ring and the beam energy is increased to up to 2.9 GeV, the composition of the residual gas species changes. In general, there is no energy dependence visible in the composition. When the beam is stored in the accelerator, the absolute contribution of hydrogen has tripled in reference to measurements without beam, reaching a constant fraction of 85 to 90 % of the population. This tripling probably occurred due to PSD. Also, the absolute contributions of methane doubled due to the same effect. For carbon monoxide, on average a doubling of its absolute contribution occurred, but due to difficulties in distinguishing between carbon monoxide and molecular nitrogen in the mass spectra, this assertion is vague. However, the measured peak at $A/Z = 28$ more than doubled, implying an increase in the carbon monoxide contribution due to PSD. Oxygen and all noble gases retained their absolute values in the mass spectrum, as the inflow rate of contingent leaks is independent of PSD or *electron stimulated desorption* (ESD)[22]. The absolute amount of water vapor increases by 20 % indicating an increased desorption rate of bound vapor off the irradiated shielding[23].

[22] In case of ESD, stray electrons impinge on the surface with high kinetic energy and produce a shower of secondary particles which contaminate the vacuum system. For more information, see appendix A.7.1.

[23] Also a variation in the inflow rate of the contingent leak in the shielding's water cooling system is possible. The irradiation

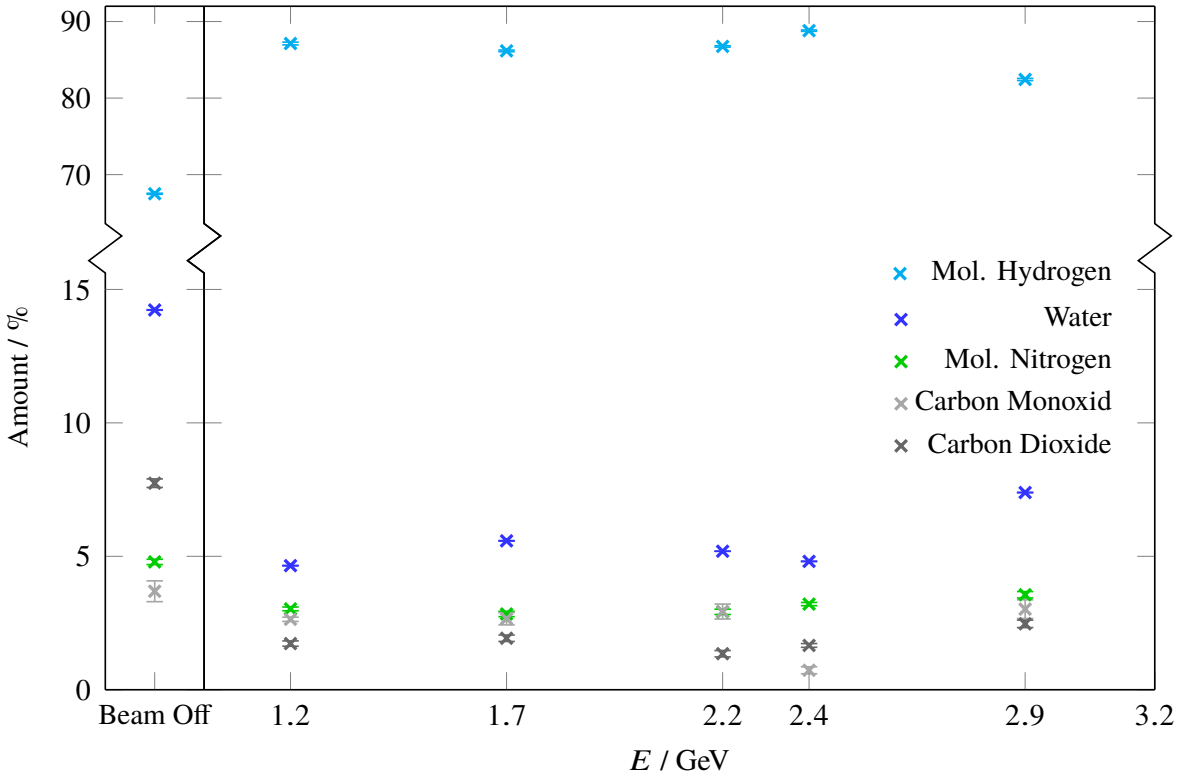

Figure 3.5: Results of the residual gas analysis via MSAUGA using a fragmentation pattern library of 11 residual gas species. Shown in the left part of the plot is the background measurement without beam. The composition of dominant residual gas species at certain beam energies at a beam current of approximately 35 mA are shown in the right plot. The data for this plot is shown in table C.1.

Water vapor shows a percentage of 5 to 7 %. In its absolute contribution carbon dioxide approximately stays constant when the beam is injected. Its percentage totals to 1.5 to 2.5 % of the residual gas.

For the "default" analysis process, the relative error of all N_2 and CO compositions are in the range of 100 % indicating a high uncertainty in distinguishing between the two species. For the "complexity-reduced" analyses, the simulation's error is a factor of ten smaller. But here various residual gas species, which may in fact are habituated in the storage ring's vacuum system, have not been considered. Therefore in both analysis processes the statistical error can only be exchanged for a systematic error and vice versa. Therefore, both analysis processes are combined by averaging with respect to their simulation errors. Since there is no significant energy dependence of the composition of the residual gas, these measurements can also be combined by weighted averaging.

The final composition of residual gas molecules in storage ring's vacuum system near the mass spectrometer are shown in table 3.3. It comprises approximately 86 % of molecular hydrogen and 6 % water vapor. Molecular nitrogen and carbon monoxide contribute approximately 5 %. Carbon dioxide also adds 2 %.

The question remains whether the measured residual gas composition is representative for the entire vacuum system. Since hydrogen, carbon monoxide and carbon dioxide are known to be desorbed from stainless steel vacuum chambers, it can be assumed that these contributions are characteristic for this

may induce additional thermal stress to the material, leading to changed leak rates.

	H_2	H_2O	N_2	CO	CO_2	Residuals
Fraction / %	85.9 ± 0.2	5.7 ± 2.6	2.1 ± 0.2	3.4 ± 0.3	1.8 ± 1.0	1.1 ± 2.8

Table 3.3: Composition of the residual gas molecules in the storage ring at a beam current of 35 mA and beam energies of 1.2 to 2.9 GeV. The values are the error-weighted average of the results of the "default" and "complexity-reduced" analyses.

vacuum system. For molecular nitrogen and water vapor contributions, the case is more difficult because they indicate leaks to the outside and to the radiative shielding's water cooling system. Because the influence of inflow from leaks onto the residual gas composition is localized in the vacuum system, these contribution may only appear there. On the contrary, the vacuum system, including the installed mass spectrometer, has been tested by a leak detector, ensuring its leakproofness to the outside. As no leak has been detected, the inflow must occur through leaks which are below the leak detector's threshold. Also it is possible that these gases desorb from the surface of parts of the vacuum system as its components are unbaked. In the past, mass spectrometric analyses at extraction septum MSE22 also revealed an increased water vapor proportion, which has also been attributed to the proximity of the spectrometer to the water cooling system of the septum [Ste95, section 2.1]. In addition, the identified dominant residual gas species coincide with those which have been found there. The questionable constituents, water vapor and nitrogen, also only contribute with approximately 8 % to the residual gas population. Thus, adding or ignoring these species does not drastically change the mass distribution of the residual gas and the ions, produced from it. Because this issue cannot be solved conclusively, the resulting composition from table 3.3 is assumed to be representative for the entire vacuum system of the storage ring.

The measured composition of the residual gas components in the storage ring should not be confused with the composition of the actual ion population. This population establishes itself as an equilibrium that results from the production and clearing rates of the individual ion species.

3.2 Pressure Evolution with Beam Energy and Current

To determine the correlations of the pressure in the storage ring with other beam parameters such as beam energy and current, the parameter archive database CSHISTORY[24] can be used. The measured values of both IGP and vacuum gauge pressures, beam current and energy along with the voltage, applied to the ion clearing electrodes, have been extracted for a time period ranging from November 2016 to November 2017. In this period, only intervals during operation of the storage ring are relevant. The number of fetched parameters amounts to 59 in total which have been sampled at two-minute intervals. A dataset of approximately 42 000 values per parameter is obtained which gives a statistical overview of occurring pressures within various operation scenarios of the storage ring.

In the following, a pressure model for the average pressure $\mathcal{P}_{\text{avg}}$ of the storage ring is developed on the basis of an analytical approach, which is substantiated by the obtained dataset.

[24] The CSHISTORY database is operational since May 2013 and stores every change of almost every parameter of the ELSA control system. The database is an archive engine with a noSQL database backend based on Hyptertable. It can be used to access values of measured quantities along with set-points and actual values of hardware components. For more information, see [PFH14].

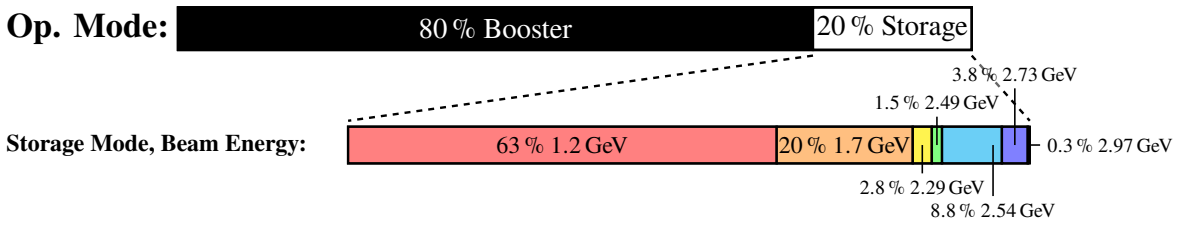

Figure 3.6: Composition of the CSHISTORY dataset regarding the two operation modes of the storage ring. The corresponding fraction of certain beam energies in the data set for storage mode operation is listed below.

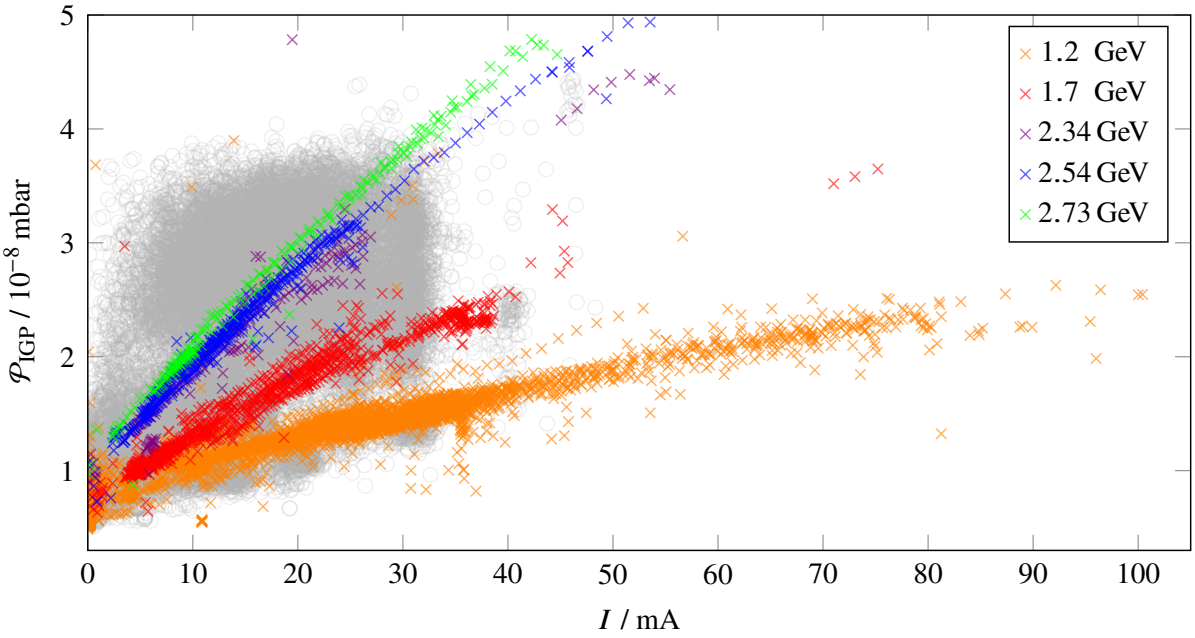

Figure 3.7: Evolution of the average IGP pressure within the storage ring with beam current for different energies. The gray dataset indicates IGP pressures during booster mode operation whereas colored datasets denote pressures, measured during operation in storage mode. The error on each pressure value, which is not shown here, is equal to $0.3 \cdot 10^{-9}$ mbar.

3.2.1 Pressure Statistics

In the obtained dataset, the storage ring is operated in two different modes, either the booster or the storage mode. The composition of the dataset regarding operation modes and beam energy is illustrated in figure 3.6.

The pressure $\mathcal{P}_{IGP}$ is the average of 33 individual pressures, monitored on basis of the IGP currents. $\mathcal{P}_{IGP}$ for the two operation modes is shown in figure 3.7 for different beam currents. The pressure during booster mode operation is shown in gray. Its data points are confined in a current region between 0 and 50 mA. The data point distribution forms a cloud with average IGP pressures between $0.5 \cdot 10^{-8}$ and $4 \cdot 10^{-8}$ mbar. As has already been described briefly in section 1.2, in booster mode operation a beam current of typically 25 mA is accumulated in the storage ring by consecutively injecting several fillings of the booster synchrotron. Then the beam energy is increased from injection to extraction energy with an energy ramp rate of typically 6 GeV s^{-1}. Afterwards, the energy is kept constant for several seconds while

the beam is extracted to the experiments. As a consequence, the energy and current within this dataset changes rapidly, altering the pressure simultaneously and resulting in the observed distribution.

In the storage mode, the beam energy is kept constant for a longer timescale. Since no beam extraction takes place, the current only decreases slowly in time due to a finite beam lifetime[25]. The storage mode datasets at different beam energies are shown colored. The data points in figure 3.7 show several correlations between current and pressure which manifest in different bands. In general, the average pressure increases with the beam current. Here, the increase is almost linear, although saturation is visible at higher currents as well. With increasing beam energy, the slope of the formed bands increases. The relative pressure difference for a fixed beam current is approximately 50 % between 1.2 and 1.7 GeV and reduces for higher beam energy. The bands for the 1.2 and 1.7 GeV datasets show a larger "thickness" than the other datasets. Each band is a superposition of several storage mode operation cycles in which a beam with a certain current is injected and stored at a certain beam energy for a time. Due to the finite lifetime of the beam, the stored current steadily decreases during each cycle. Each generates a sequence of pressures correlated with the beam current. At different storage mode operation cycles, the initial pressure at 0 mA beam current, the no-load pressure of the vacuum system, may be different. Assuming a constant slope of each pressure sequence, this leads to differently offset bands, which form a "thick" band. Since most data points are available for beam energies of 1.2 and 1.7 GeV, the dataset comprises various beam times with different no-load pressures. Apart from that, the slope approximately follows a similar behavior during each cycle. The no-load pressure varies by approximately $0.15 \cdot 10^{-8}$ mbar in the 1.2 GeV dataset, which is estimated from the "thickness" of the corresponding band at 25 mA. In the following analysis, this uncertainty is the underlying systematical error. For the statistical error, the average pressure has been monitored when the storage ring was not in operation. Here, the pressure can assumed to be constant for timescales in the order of minutes. The average as well as the individual IGP's statistical error have been estimated to be $0.3 \cdot 10^{-9}$ mbar.

3.2.2 Beam Current and Energy Dependence

In the vacuum system there is an equilibrium of desorbed residual gas and residual gas removed by IGPs and TMPs. The gas desorption is characterized by its desorption rate q whereas the gas removal rate of the pumps is quantified by their (effective[26]) pumping speed $S_{(\text{eff})}$. The ratio of q to $S_{(\text{eff})}$ defines the (local) pressure in the vacuum system [OHa03, section 7.1, equation (7.1)]. Residual gas desorbs from all surfaces into the vacuum system and the removal of the gas only takes place in local sections where pumps are installed. Thus, the pressure is a function of the distance from the pumps and the monitored IGP pressure is not identical to the average pressure in the storage ring.

As can be seen in figure 3.7, the average IGP pressure increases non-linear with the beam current. The curve follows a behavior proportional to $\sqrt{I}$. This saturation behavior, visible for every IGP in more or less same severity, implies that either the desorption rate decreases with beam current or the pumping speed of the pumps increased with the pressure. To resolve this issue, knowledge about the different desorption rates q and the pumping speed S in the storage ring is necessary.

The desorption rate is composed of the individual desorption rates of thermal desorption q_{therm}, photon stimulated desorption (PSD) q_{PSD} and electron stimulated desorption (ESD) q_{ESD}. Both PSD and ESD rates are dependent on the beam energy and current.

[25] Due to collisions with residual gas molecules and occasional large energy losses due to synchrotron radiation, individual beam electrons exceed the accelerator's transversal and longitudinal acceptance and are lost. Additionally, optical resonances and beam instabilities lead to a decrease of the beam's intensity. For more information, see e.g. [Wil00, section 10.2].

[26] The probability of a desorbed residual gas molecule at a certain longitudinal position s to reach a vacuum pump decreases with their distance. This reduces the pumping speed S of the pump to an effective pumping speed S_{eff} at position s.

q_{therm}: The thermal desorption rate comprises all "natural" desorption and diffusion processes, including permeation. It is the rate with which residual gas is released from the beam pipe at a specific temperature. In dependence of the temperature, the binding of residual gas to the surface is dissolved and gas is released into the vacuum system. For more information, see [OHa03, section 4.3]. For the storage ring, q_{therm} can assumed to vary with the accelerator's environmental temperature.

q_{ESD}: The electron stimulated desorption rate characterizes desorption which occurs due to bombardment of the beam pipe with electrons. Electrons have a finite lifetime τ_{e} in the accelerator due to the transversal beam pipe aperture and longitudinal dynamics as well as interaction with residual gas[27] [Wil00, section 10.2]. If the momentum loss of a beam electron after an interaction exceeds the accelerator's transversal and longitudinal acceptance, it is lost and impinges on the beam pipe. The successive electromagnetic shower heats up the impact area and increases thermal desorption rates. The desorption rate is equal to [Aic17, section 2.2]

$$q_{\text{ESD}} = \eta_{\text{e}} \frac{N_{\text{e}}}{\tau_{\text{e}}} ,$$

where η_{e} is the molecular desorption yield for electron bombardment. η_{e}, typically given as number of desorbed molecules per electron, is dependent on the bombarded material along with the energy distribution of the impinging electrons. τ_{e} and η_{e} are dependent on the beam energy.

q_{PSD}: Photo stimulated desorption occurs due to the irradiation of the beam pipe by synchrotron radiation photons. These photons locally heat up the irradiated area, produce photoelectrons and free adsorbed molecules. The desorption rate is linearly dependent on the synchrotron radiation photon flux Φ_γ and is given as [Grö99, section 1.1, equation (5)]

$$q_{\text{PSD}} = \eta_\gamma \Phi_\gamma .$$

The molecular desorption yield η_γ, defined as number of desorbed molecules per photon, is dependent on the irradiated material and the individual desorbed gas species. Also it is dependent on the energy spectrum of synchrotron radiation and thus, on the beam energy. Φ_γ scales linearly with beam energy and current.

The exact desorption rates of these processes are different for each material and also depend on the environmental exposure of each individual component of the vacuum system in the past. Consequently, the desorption rates have to be determined experimentally. q_{ESD} and q_{PSD} increase with the beam current whereas q_{therm} is assumed to be constant. Therefore, if S_{eff} is assumed to be constant, an opposite behavior of the pressure with the current would be expected than the saturation behavior which has actually been observed.

In the vacuum regime of the storage ring where molecular flow is present, the number of pumped residual gas molecules per time scales with the number of residual gas molecules N. Thus, it holds that (compare appendix A.7.2)

$$\frac{\mathrm{d}N}{\mathrm{d}t} = \upsilon \cdot N = \frac{\mathcal{P} \cdot S_{\text{eff}}}{k_{\text{B}} T} .$$

Here, υ is the rate with which residual gas is removed from the vacuum system by pumps. In the storage ring, the main vacuum pumps are IGPs, whose pumping speed depends on the pressure. For high pressures $> 10^{-5}$ mbar, the density of the electron and ionized gas clouds in the IGPs is high enough to start glow discharges between anode and cathodes. Here, the reduction of the mean free path length leads

[27] The Touschek effect, in which scattering processes of the electrons with each other within a beam of high charge density leads to particle losses, is neglected. For more information regarding this effect, see e.g. [Piw98].

to a reduced pumping speed. For low pressures $< 10^{-7}$ mbar, the pumping speed - being maximal at around 10^{-6} mbar - decreases. In this pressure region, the pumping speed results from an equilibrium between pumped and desorbed gas [Sch99, section 4]. Since the pressures considered are in the region of 10^{-9} to $5 \cdot 10^{-8}$ mbar, the increasing pumping speed with rising vacuum pressures can be approximated with the linear function

$$S(\mathcal{P}) = \varrho \cdot \mathcal{P} \ .$$

Because the pumping speed has this dependency, S increases with the pressure resulting in a visible saturation of the vacuum system's pressure. Because S_{eff} is proportional to S, the IGP's non-linear pumping rate can be expressed as

$$\frac{\mathrm{d}N}{\mathrm{d}t} \sim \frac{\varrho \mathcal{P}^2}{k_{\mathrm{B}} T} = \rho N^2$$

using the ideal gas equation.

3.2.3 Modeling and Parameterization of the Pressure Evolution

As the evolution of the pressure has been shown qualitatively, a model for the average pressure in the storage ring can be developed. To map the pressure evolution in the storage ring correctly, first its characteristic is derived analytically. For details regarding the deviation, see appendix A.7.

Because the pressure within a vacuum system with constant dimension and temperature is proportional to the number of particles N inside the system, one starts with the rate equation for N as

$$\frac{\mathrm{d}N}{\mathrm{d}t} = \underbrace{q_{\text{therm}} + q_{\text{PSD}} + q_{\text{ESD}}}_{= \frac{\mathrm{d}N_{\text{prod}}}{\mathrm{d}t}} - \underbrace{\upsilon N - \rho N^2}_{= \frac{\mathrm{d}N_{\text{pump}}}{\mathrm{d}t}} \ .$$

Here, residual gas is produced by thermal and photo/electron stimulated desorption with a rate $\mathrm{d}N_{\text{prod}}/\mathrm{d}t$. It is pumped away by IGPs which have a linear υ and non-linear pumping rate ρ which result in a total rate of $\mathrm{d}N_{\text{pump}}/\mathrm{d}t$ (compare appendices A.7.1 and A.7.2).

When solving this Riccati differential equation, an equilibrium number of residual gas molecules inside the vacuum system of

$$N(E, I) = \sqrt{\frac{\eta_\gamma(E)\, \delta \cdot E \cdot I + q_{\text{therm}}}{\rho} + \frac{\left(\eta_{\text{e}}(E)\, \chi_{\text{e}} \cdot I - \upsilon\right)^2}{2\rho^2}} \tag{3.2}$$

is obtained (compare appendix A.7.3). Here, $\delta = 8.08 \cdot 10^{17}\,\mathrm{GeV}^{-1}\,\mathrm{mA}^{-1}$ is the proportionality constant of the synchrotron radiation photon flux Φ_γ with beam energy and current [Grö+83, section 2.1]. χ_{e} is a constant characterizing the interaction probability of the electron beam with the residual gas which leads to beam loss and subsequent ESD. Note that the desorption yields for PSD and ESD, $\eta_\gamma(E)$ and $\eta_{\text{e}}(E)$, are dependent on the beam energy. $\eta_\gamma(E)$ and $\eta_{\text{e}}(E)$ characterize the exact mechanism of the desorption processes in the individual material. They are not known and must be obtained experimentally for the materials in the each vacuum system. $N(E, I)$ shows the observed saturation behavior with increasing beam current, visible in figure 3.7, and also comprises a "linear"[28] term proportional to the current. For a beam current of 0 mA, a no-load pressure is present in the vacuum system consisting of q_{therm}, υ and ρ.

[28] Note that the attribute "linear" denotes a functional behavior as $f(x) = \sqrt{x^2 + C'}$ with $C' > 0$ where $f(x)$ does not increase linear with x in a mathematical sense, obviously.

Energy / GeV	1.2	1.7	2.29	2.49	2.54	2.73	2.97
$\mathcal{P}_0$ / 10^{-9} mbar	7.1 ± 0.1	6.5 ± 0.2	4.9 ± 0.8	9.5 ± 0.9	8.4 ± 0.3	9.8 ± 0.3	9.3 ± 0.7

Table 3.4: No-load pressure $\mathcal{P}_0$ for different beam energies in the storage mode.

Model

This analytical approach with unknown parameters $\eta_\gamma(E)$, $\eta_e(E)$, q_{thermal}, υ and ρ, can be used as a reference for a pressure model. Since the pressure at a fixed volume and temperature is proportional to N, the model requires the same dependencies on beam energy and current as equation (3.2). The average pressure in the vicinity of the IGPs is modeled as

$$\mathcal{P}_{\text{IGP,model}}(E, I) = \sqrt{\mathcal{P}_0^2 + \Lambda(E) \cdot I + \Xi(E) \cdot I^2}\,, \tag{3.3}$$

with the parameters $\mathcal{P}_0$, $\Lambda(E)$ and $\Xi(E)$ (compare appendix A.7.3). Because the energy dependence of $\eta_\gamma(E)$ and $\eta_e(E)$ are unknown for the storage ring's vacuum system, it is completely transferred into $\Lambda(E)$ and $\Xi(E)$.

For the storage mode datasets with beam energies of 1.2, 1.7, 2.29, 2.49, 2.54, 2.73 and 2.97 GeV, equation (3.3) is fitted individually. One obtains $\mathcal{P}_0$, $\Lambda(E)$ and $\Xi(E)$ for different beam energies. In table 3.4, $\mathcal{P}_0$ is listed for every dataset. The no-load pressure $\mathcal{P}_0$ ranges from $0.5 \cdot 10^{-8}$ to $1 \cdot 10^{-8}$ mbar. Although $\mathcal{P}_0$ is not constant and gradually increases with the beam energy, it cannot be considered as a characteristic function of the storage ring. Instead, $\mathcal{P}_0$ depends on the temperature of the accelerator's vacuum system, which is influenced by the heat dissipation of its hardware components, their cooling, and the environmental temperature.

Since $\Lambda(E)$ and $\Xi(E)$ contain constants characterizing the processes of desorption and gas pumping, which are specific to the storage ring and are assumed to change little[29] with time, they can be utilized for the model of the average IGP pressure. Figure 3.8 shows $\Lambda(E)$ and $\Xi(E)$ with which the model is approximated to the measured pressure evolution at different beam energies. A large error emerges at 2.97 eV for $\Xi(E)$. Here, the dataset consists only of 29 data points within a current domain reaching from 3 to 10 mA. As data points for higher beam currents are not available, the "linear" current term, weighted by $\Xi(E)$, cannot be determined properly. However, within their errors all data points match a rise of $\Lambda(E)$ and $\Xi(E)$ with the beam energy. This increase is expected as $\Lambda(E)$ and $\Xi(E)$ contain the beam energy dependent molecular desorption yields for PSD and ESD.

To formulate a complete model of the pressure evolution, $\Lambda(E)$ and $\Xi(E)$ are parameterized by a second-order polynomial as

$$\Lambda(E) = \Lambda_1 \cdot E + \Lambda_2 \cdot E^2 \qquad \text{and} \qquad \Xi(E) = \Xi_1 \cdot E + \Xi_2 \cdot E^2\,.$$

The polynomials do not show an offset because it is expected that $\eta_\gamma(E)$ and $\eta_e(E)$ are zero for a beam energy of 0 eV. By including this parameterization into equation (3.3) a pressure function $\mathcal{P}_{\text{IGP,model}}(E, I)$ with free constants $\mathcal{P}_0$, Λ_1, Λ_2, Ξ_1 and Ξ_2 is obtained. While $\mathcal{P}_0$ is unique for every dataset, common values can be found for the other constants with which the average IGP pressure can be approximated.

[29] The characteristics of the storage ring's vacuum system may change, if modifications on the vacuum system are conducted. An example is the installation of new pumps, alterations on the existing pumps or the replacement of parts of the beam pipes. Also a process may change the desorption characteristics of the beam pipe material if, for example, the system is vented with air instead of dry nitrogen.

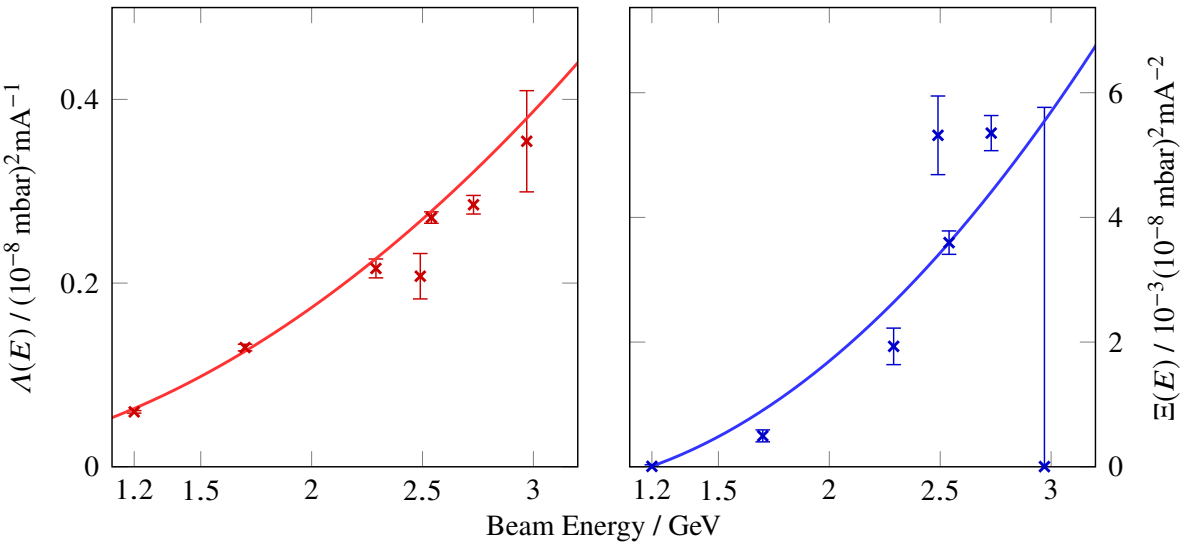

Figure 3.8: Parameter values of $\Lambda(E)$ and $\Xi(E)$ at different beam energies. The red and blue curve show the evolution of these parameters in case a second-order polynomial is fitted onto all datasets.

Results

Using the method of least squares[30], $\mathcal{P}_{\mathrm{IGP,model}}(E, I)$ is approximated on all storage mode datasets. Here, the total residuum R of the approximated function has to be minimized for all available beam energies. It is chosen to be

$$R = \sum_{i=1}^{7} \left(\sum_{j=1}^{N_i} \left(\frac{\mathcal{P}_{\mathrm{IGP}}(E_i, I_j) - \mathcal{P}_{\mathrm{IGP,model}}(E_i, I_j)}{\Delta\mathcal{P}_{ij}} \right)^2 \right) .$$

Here, i is the index of the datasets with seven different beam energies E_i. Each dataset has N_i number of measured data points $\mathcal{P}_{\mathrm{IGP}}(E_i, I_j)$ at different beam currents I_j. $\Delta\mathcal{P}_{ij}$ is the individual statistical error of the corresponding data point. It is equal to $0.3 \cdot 10^{-9}$ mbar.

The residuum is minimal for the following parameters

$$\Lambda_1 = (0.0053 \pm 0.0021)\,\mathrm{mA}^{-1}\,\mathrm{GeV}^{-1}(10^{-8}\,\mathrm{mbar})^2 ,$$
$$\Lambda_2 = (0.042 \pm 0.001)\,\mathrm{mA}^{-1}\,\mathrm{GeV}^{-2}(10^{-8}\,\mathrm{mbar})^2 ,$$

and

$$\Xi_1 = (-12.8 \pm 0.4) \cdot 10^{-4}\,\mathrm{mA}^{-2}\,\mathrm{GeV}^{-1}(10^{-8}\,\mathrm{mbar})^2 ,$$
$$\Xi_2 = (10.6 \pm 0.3) \cdot 10^{-4}\,\mathrm{mA}^{-2}\,\mathrm{GeV}^{-2}(10^{-8}\,\mathrm{mbar})^2 .$$

[30] The fitting of all datasets has been realized with great contributions of D. Proft, ELSA. Here, the Ceres-Solver [AM+], a free implementation of the least square method for non-linear problems in C++, has been used.

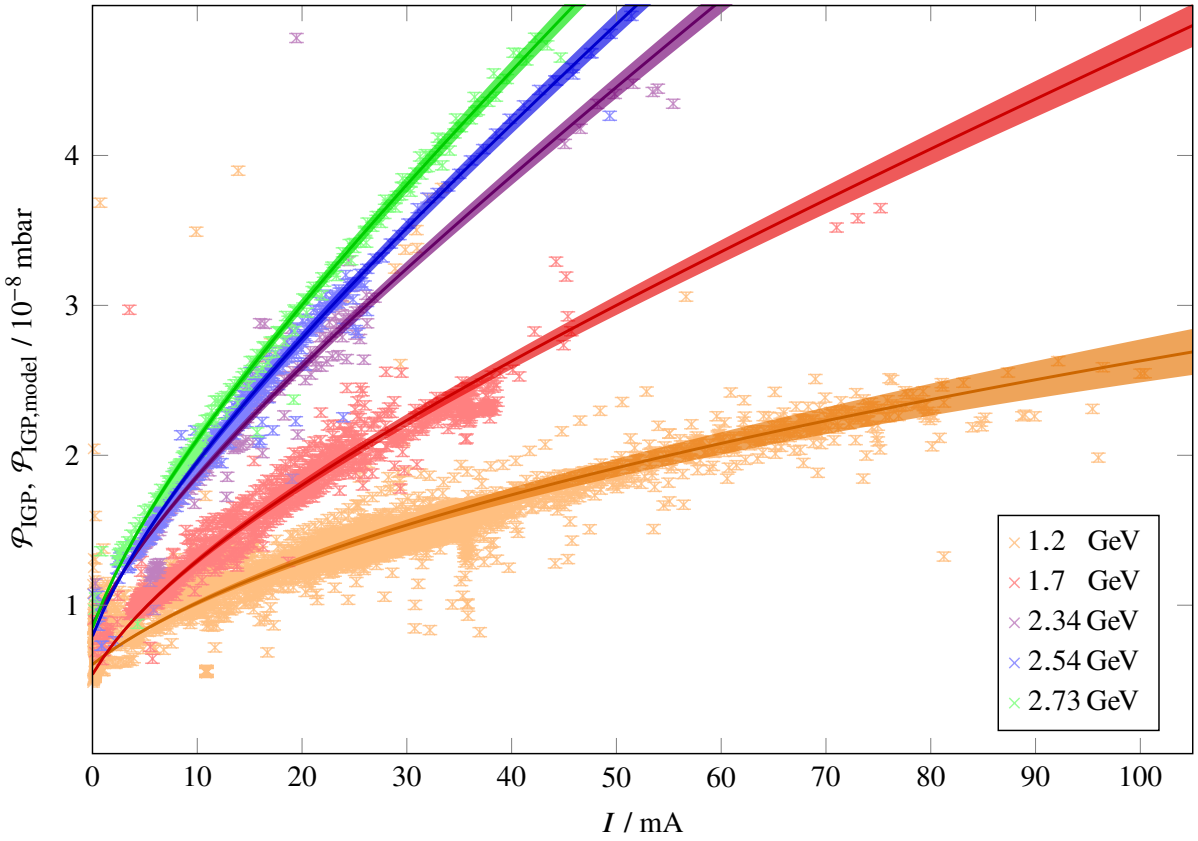

Figure 3.9: Comparison of the predicted evolution of the average IGP pressures with the measured ones at different beam energies. The predictions for the different beam energies are shown as lines with associated colors. The colored areas around the predictions denote its corresponding 1σ error region.

Figure 3.9 shows the average IGP pressure datasets for different beam energies as well as predictions from the deduced model. In general, $\mathcal{P}_{\mathrm{IGP,model}}$ agrees with the trend indicated by the measured pressures. For the 1.2 GeV dataset, the model follows the data well. Except for some outliers at beam currents between 30 and 40 mA along with an astray sequence of data points having an overall too high pressure, probably due to high $\mathcal{P}_0$, all measured pressures are in the 2σ error region. The same is true for 1.7 GeV. Here, even isolated measured pressures at 70 to 80 mA, are within the 2σ error region. For higher beam energies, the model matches the data points.

If the no-load pressure $\mathcal{P}_0$ is measured prior to the operation of the storage ring, the model is in principle able to predict the pressure evolution with the beam current for a given energy. However, the model only describes the evolution of the average pressure as it is monitored by the IGPs. The relevant pressure for the ion production is the average pressure $\mathcal{P}_{\mathrm{avg}}$ along the beam pipe to which the electron beam is exposed to. It diverts from $\mathcal{P}_{\mathrm{IGP}}$ by a factor, which is typically > 1. The factor can be determined from the geometry of the vacuum system, which will be discussed in the following section.

3.2.4 Average Pressure in the Storage Ring

The observed pressure $\mathcal{P}_{\mathrm{IGP}}$ only gives information about the pressure in close proximity to the IGPs. The pressure along the accelerator depends on the inner geometry of the vacuum chamber. In general, it is therefore not constant and e.g. increases with the distance to the pumps.

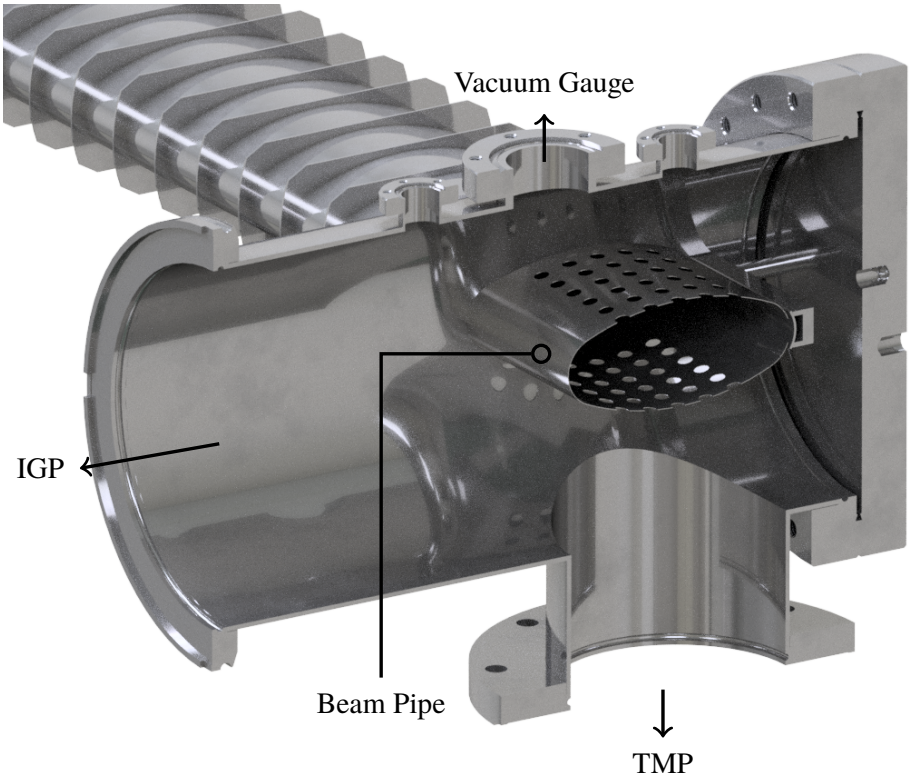

Figure 3.10: Sectional view of the vacuum chamber which conjunctions the beam pipe and the pump section. The junction is formed as a crosspiece, where the pump section antechamber is connected to the beam pipe via multiple orifices. In the antechamber an IGP, a TMP and a vacuum gauge are installed. Courtesy of P. Hänisch, ELSA.

Figure 3.10 shows a sectional view of the vacuum chamber which conjuncts the beam pipe with a pump section. The beam pipe has the shape of the quadrupole chamber design and passes through the cylindrical antechamber of the pump section. To allow for a gas transfer into the antechamber, the beam pipe is perforated where it is integrated into the antechamber. On the bottom of the antechamber, a TMP with a pumping speed of $300\,\mathrm{l\,s^{-1}}$ is installed. An IGP with equal pumping speed is installed at the face of the antechamber. On top of the antechamber, a flange for a vacuum gauge is provided.

In the arc sections of the storage ring, this segment of the beam pipe typically is connected to a dipole chamber which has a length of approximately 3.4 m. A quadrupole chamber is located adjacent to the dipole, followed again by another pump section.

To obtain the average pressure $\mathcal{P}_{\mathrm{avg}}$ along the electron beam's orbit in the beam pipe, first the local pressure $\hat{\mathcal{P}}(s)$ along the s-axis in between at least two pump sections has to be determined. Because the geometry of the discussed vacuum system is rather complex, an analytical estimation of the local pressure will not be carried out. Instead, $\hat{\mathcal{P}}(s)$ is obtained by using a numerical approach.

Determining the Local Pressure in a Vacuum System using MolFlow+

The program MolFlow+[31] is used to numerically determine the pressure in the vacuum system. The functional principle of MolFlow+ is introduced briefly in appendix A.8.

A simplified model[32] of the storage ring's vacuum system, reaching from one pump section to the other, is modeled in Autodesk Inventor[33] on basis of existing CAD models. The simplifications are necessary to reduce the required computational time and include mainly the modeling of only the essential parts of the vacuum system's inner geometry and keeping it as plain as possible by omitting flanges, mountings and seal faces. Additionally, the transversal profile of the two used beam pipe types of the dipole and quadrupole chambers is approximated as elliptical. The perforation of the beam pipe is simplified to multiple rectangular holes which in total shows the same transparency as the perforation.

The desorption rates and pumping speeds can be assigned to different sections of the inner surface of the vacuum system. In this model, only the desorption rate of ESD and PSD is considered. Thermal desorption and leaks are estimated as minor contributors to the total desorption rate because $\mathcal{P}_0 < \mathcal{P}_{\mathrm{IGP,model}}(E, I)$ for non-zero beam currents (compare figure 3.9). The inner surface of the dipole chamber and the adjacent quadrupole chambers are empirically assigned with a desorption rate of $5 \cdot 10^{-10}\,\mathrm{mbar\,l\,s^{-1}\,m^{-2}}$ to emulate ESD. The surface of the radiation shielding is assigned with a desorption rate of $5 \cdot 10^{-9}\,\mathrm{mbar\,l\,s^{-1}\,m^{-2}}$ to reproduce the increased desorption rate due to PSD. In contrast to the PSD surfaces, the ESD surfaces are homogeneously distributed along the beam pipe. In each pump section, the surfaces corresponding to the entries of the TMPs and IGPs are assigned a pumping speed of $300\,\mathrm{l\,s^{-1}}$ each.

Simulated Pressures in the Storage Ring's Vacuum System

To estimate the longitudinal pressure profile, first ESD and PSD desorption rates of the different surfaces have to be adjusted the way that a pressure of approximately[34] 10^{-8} mbar is present at the entrance of the IGP. The pressure profile along the antechamber of the pump section is shown in figure A.7 in the appendix.

The simulated longitudinal pressure profile $\hat{\mathcal{P}}(s_{\mathrm{bp}})$ is shown in figure 3.11. One pump section is positioned at approximately $s_{\mathrm{bp}} = 0.5\,\mathrm{m}$ and the other one at approximately 5 m. There, the pressure is equal to $1.7 \cdot 10^{-8}$ mbar. As the distance from the pump sections increases, a pressure elevation towards the midst of the dipole chamber is visible. Here, a maximum pressure of $1.8 \cdot 10^{-7}$ mbar is reached. The average pressure between the two pump sections is equal to $1.2 \cdot 10^{-7}$ mbar.

Thus, the maximum pressure in the vacuum system is a factor of approximately 19 higher than the average IGP pressure $\mathcal{P}_{\mathrm{IGP}}$. The average pressure along the s axis is a factor of approximately 12.5 higher than $\mathcal{P}_{\mathrm{IGP}}$.

[31] MolFlow+ (version 2.6.72) is a program developed at CERN which uses the *test particle Monte Carlo method* to numerically determine e.g. pressure profiles, effective pumping speeds, adsorption distributions and more in a complex vacuum system. See e.g. https://molflow.web.cern.ch and [KP09].

[32] The model which has been imported into MolFlow+ is shown in figure A.5 in the appendix.

[33] Autodesk Inventor is a CAD application for three-dimensional design, simulation, visualization and documentation of mechanical components. See e.g. https://www.autodesk.de/products/inventor/overview. CAD is the short form of Computer-Aided Design.

[34] The simulated pressure at the IGP's entrance is equal to $9.6 \cdot 10^{-9}$ mbar.

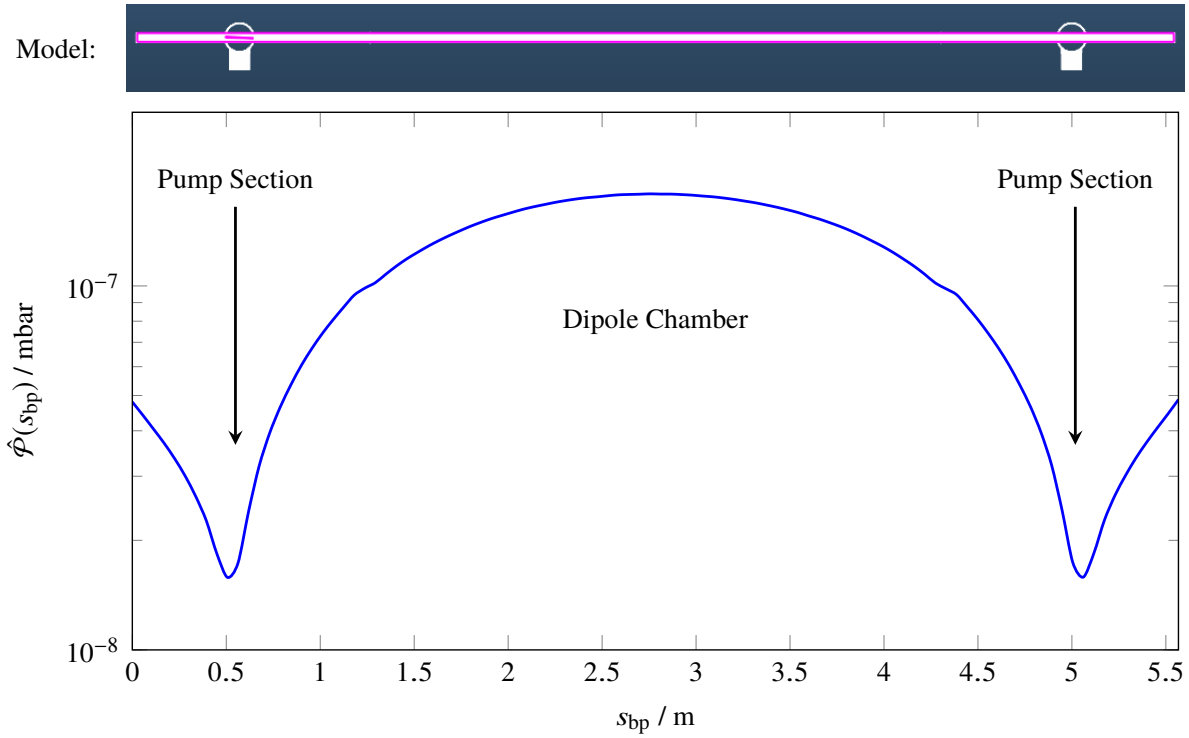

Figure 3.11: Simulated longitudinal pressure profile along the beam pipe from one pump section to the other. Here, the pressure at the entrance of the IGPs in the antechamber is equal to 10^{-8} mbar. The corresponding simulation model is shown in the top graph in the same orientation.

Completion of the Pressure Model

As a last step in the development of a model for the evolution of the average pressure, the pressure model $\mathcal{P}_{\mathrm{IGP,model}}(E, I)$ has to be scaled. Thus, the average pressure in the storage ring can be approximated by

$$\mathcal{P}_{\mathrm{avg}}(E, I) = 12.5 \cdot \mathcal{P}_{\mathrm{IGP,model}}(E, I) = 12.5\sqrt{\mathcal{P}_0^2 + \Lambda(E) \cdot I + \Xi(E) \cdot I^2}\,.$$

Here, E is the beam energy in GeV and I is the stored beam current in mA. The parameters $\Lambda(E)$ and $\Xi(E)$, each consisting of two sup-parameters, describe the desorption rate variation due to the processes of PSD and ESD. The values of these parameters can be found in section 3.2.3. $\mathcal{P}_0$ is the no-load pressure which is essentially defined by the thermal desorption rate of the vacuum system for given pumping speeds. It is subject to variations, as already outlined in section 3.2.3. Exemplaric values of $\mathcal{P}_0$ for different beam energies can be found in table 3.4.

By being able to estimate the average pressure in the storage ring for a given beam energy and current, the different pressure dependent ion production rates can be determined.

3.3 Impact Ionization

In general, the production rate of an ion, being produced by an electron with velocity βc in a beam potential of depth of U_0, can be expressed as [Pon94, section 2, equation (8) for electrons]

$$r_{\mathrm{p,ii},i} = \frac{\mathrm{e}^4 \left\langle p_i \right\rangle Z_i'}{8\pi^2 {\varepsilon_0}^2 \beta c m_\mathrm{e} k_\mathrm{B} T \tilde{E}_0} \ln\left(\frac{2\pi^2 \varepsilon_0 \hbar \gamma \beta^2 c^2}{\mathrm{e}^2 E_\mathrm{I} Z_i'} \cdot U_0\right)^{\frac{1}{2}} . \tag{3.4}$$

Here, the residual gas species has an average partial pressure of $\left\langle p_i \right\rangle$ in the vacuum system (compare equation (2.16)). Z_i' is the number of protons of the particular species. $\tilde{E}_0$ is the average energy for the formation of an ion-electron pair ($\approx 35\,\mathrm{eV}$). E_I is equal to $Z' \cdot 3.5\,\mathrm{eV}$. The production rate increases with the beam potential's depth since the probability of trapping the newly produced ion, showing sufficiently low kinetic energy, increases accordingly.

However, as already discussed in section 2.1.2, the energy transfer on the ion during the ionization process is similar to the thermal kinetic energy (on average 38.8 meV) of the residual gas or below. Thus, only for very low beam currents, the potential depth is insufficient to trap produced ions. Therefore, the production rate can be simplified by assuming that all produced ions are initially trapped within the beam potential.

The total production rate of impact ionization is given in its simplified form by [Pon94, section 2, conversion of equation (9)]

$$R_\mathrm{p,ii} = \sum_i r_{\mathrm{p,ii},i} = \sum_i \frac{\sigma_{\mathrm{ii},i} \cdot \beta c \cdot \left\langle p_i \right\rangle}{k_\mathrm{B} T} , \tag{3.5}$$

similar to equation (2.8). $\sigma_{\mathrm{ii},i}$ is the individual impact ionization cross section of ion species i whose characteristic will be discussed in the following section.

This definition of the production rate implies that the partial pressure p_i of neutral residual gases in the beam volume in which the ion production takes place is equal to the pressure of the residual vacuum system. In general, this is only an approximation, since the local partial pressure of the neutral residual gas is reduced by its conversion into ions during the ionization process. The ionized gas is replaced by a constant inflow of new neutral residual gas from outside the beam, resulting in an equilibrium partial pressure within the beam which is lower than in the rest of the vacuum system. However, as elaborated in appendix A.9, for the expected ion production rates within the storage ring, this approximation is still appropriate.

3.3.1 Cross Section

The theoretical quantum mechanical evaluation of the interaction of relativistic charged particles with (hydrogenic) matter has been carried out by Bethe [Bet30]. This theory has been expanded on gaseous atoms and molecules and parameterized to be experimentally accessible (see e.g. [Ino71]). The cross section for impact ionization of a residual gas species i by a relativistic electron with velocity βc is parameterized as [Ino71, section 4.3, equation 4.55]

$$\sigma_{\mathrm{ii},i} = 4\pi \left(\frac{\hbar}{m_\mathrm{e} c}\right)^2 \left\{ M_i^2 \left[\frac{1}{\beta^2} \ln\left(\frac{\beta^2}{1-\beta^2}\right) - 1\right] + \frac{C_i^2}{\beta^2} \right\} . \tag{3.6}$$

Here, the parameter M_i^2 is the *squared total dipole matrix element* for impact ionization. M_i^2 and C_i are different for each species of residual gas. They are determined experimentally for various gases in [RP72],

Molecule	Z_i'	A_i	M_i^2	C_i	$\sigma_{\mathrm{ii},i}$ / Mb
H_2	2	2	0.695	8.115	0.34 to 0.37
H_2O	10	18	3.24	32.26	1.49 to 1.61
CO	14	28	3.7	35.14	1.67 to 1.80
N_2	14	28	3.74	34.84	1.67 to 1.81
CO_2	22	44	5.75	55.92	2.61 to 2.82

Table 3.5: Cross section constants M_i^2 and C_i and the resulting impact ionization cross section at 1.2 GeV (first value) and 3.2 GeV (second value) for some residual gases, common in the storage ring's vacuum system. The neutral gases have a nucleon number of A_i and an atomic number of Z_i' [RP72, table II].

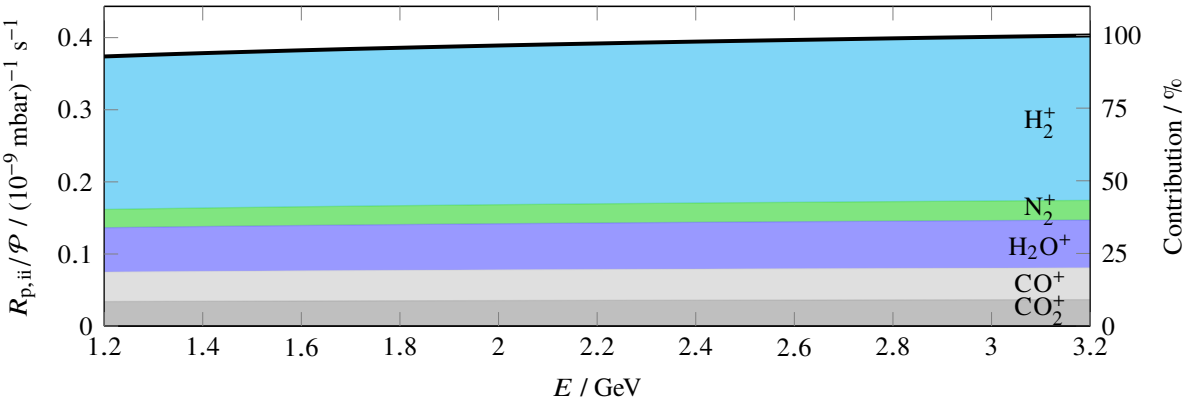

Figure 3.12: Beam energy dependence of the impact ionization production rate which is normalized to an average vacuum system pressure of 10^{-9} mbar. The production rates of the individual residual gas species add up to the black curve which is the total impact ionization production rate.

for example. Table 3.5 shows an excerpt of obtained constants for some residual gas species.

In general, the cross section increases for heavier molecules as the molecule's orbital dimension increases. The cross section for ionization of H_2 is 0.34 Mb at a beam energy of 1.2 GeV. For CO_2, it is 2.61 Mb. As the electrons in the storage ring are ultrarelativistic with $\beta \approx 1$ for all beam energies, the cross section only increases by less than 10 % for an energy increment from 1.2 GeV to 3.2 GeV.

3.3.2 Production Rate of Impact Ionization in the Storage Ring

With the impact ionization cross sections $\sigma_{\mathrm{ii},i}$ of the five main residual gas constituents, calculated via equation (3.6), and their individual proportion to the residual gas, estimated in section 3.1.3, the impact ionization production rate for a given average pressure $\mathcal{P}$ of the vacuum system can in principle be calculated. However, the pressure changes for different beam energies and currents, as has been shown in section 3.2. To have a general figure of the ion production in the storage ring and a quantity which is of technical relevance, the production rate is normalized to a pressure of 10^{-9} mbar.

Figure 3.12 shows the calculated impact ionization production rate normalized to an average pressure of 10^{-9} mbar (black curve). It increases from 0.375 $(10^{-9}\,\mathrm{mbar})^{-1}\mathrm{s}^{-1}$ at 1.2 GeV to 0.4 $(10^{-9}\,\mathrm{mbar})^{-1}\mathrm{s}^{-1}$ at 3.2 GeV. The ion population which is produced by impact ionization consists of approximately 57 % ionized molecular hydrogen (H_2^+) and 16 % ionized water molecules (H_2O^+). A share of 11 % and 9 % is contributed by ionized carbon mono (CO^+) and dioxide (CO_2^+). Ionized molecular nitrogen (N_2^+) amounts

to approximately 7 %. These partitions vary in the permille range for different beam energies and can be assumed to be constant.

For an average pressure of $5 \cdot 10^{-8}$ mbar, this production rate implies a neutralization time T_n ranging from 0.054 to 0.050 s for beam energies between 1.2 and 3.2 GeV. Within the timescale of T_n, the accelerator beam would be completely neutralized, if no ion clearing is applied (compare equation (2.15)). For higher average pressures, e.g. during storage ring operation, the neutralization time decreases since it is inversely proportional to the pressure. Additionally, a supplementary ion production process reduces T_n further, as will be discussed in the following section. Therefore, the process of ion accumulation takes place in the order of 10 ms or below.

3.4 Photo Ionization by Synchrotron Radiation

As already outlined in section 2.3.2, electrons emit synchrotron radiation when they experience a force. In the dipole magnets, the electron trajectory is bend by the vertical magnetic field which results in a horizontally deflecting Lorentz force. Thus, synchrotron radiation occurs in these magnets. Emitted synchrotron radiation photons are also capable of ionizing residual gas and thus contribute to the ion production rate. This section aims to determine whether photo ionization is another main process of ion production in the ELSA storage ring.

To start, the general form of a total ionization production rate of a particular residual gas species i with $N_{\mathrm{rgm},i}$ molecules can be formulated as

$$r_{\mathrm{p},i} = \sigma_{\mathrm{ion},i} \cdot \Phi \cdot \frac{1}{N_\mathrm{e}} \cdot \frac{N_{\mathrm{rgm},i}}{V_\mathrm{int}} \cdot l_\mathrm{int} \,. \tag{3.7}$$

Φ is the flux, the number of particles per second, of ionizing particles through an interaction volume V_int for a number N_e of stored electrons in the accelerator. Within this volume, ionizing particles propagate a length of l_int and ionize residual gas molecules according to the ionization cross section $\sigma_{\mathrm{ion},i}$. It can be shown that this formula can be converted into equation (3.5) for the process of impact ionization[35].

For the estimation of the photo ionization production rate $r_{\mathrm{p,pi},i}$, the cross section is equal to $\sigma_{\mathrm{pi},i}$ which is the photo ionization cross section. The corresponding particle flux is the synchrotron radiation photon flux Φ_γ.

For this ionization process, there are two issues to discuss:

- The production rate of this process will mainly depend on the photo ionization cross section, which is dependent on the energy E_γ of the incident synchrotron radiation photon. Synchrotron radiation photons have a broad energy and intensity distribution. Therefore, spectral properties of synchrotron radiation, more precisely the term $\sigma_{\mathrm{pi},i}(E_\gamma) \cdot \Phi_\gamma(E_\gamma)$, will have a major influence on this production rate.
- For the determination of the photo ionization production rate, also the interaction length $l_\mathrm{int}(s)$ of synchrotron radiation photons along the accelerator has to be estimated. This length is the distance of the emitted synchrotron radiation photon's source point, the electron beam, to the beam pipe.

Photo ionization occurs when synchrotron radiation photons are present in an interaction volume V_int with non-zero number density $n_{\mathrm{rgm},i}(s)$ of a particular residual gas species i. For a relativistic electron

[35] Here, $\sigma_{\mathrm{ion},i}$ is equal to the impact ionization cross section $\sigma_{\mathrm{ii},i}$. $N_{\mathrm{rgm},i}/V_\mathrm{int}$ is equal to the number density $n_{\mathrm{rgm},i}$ which can be expressed as $p_i/(k_\mathrm{B}T)$. Φ is the electron flux and can be expressed via the revolution frequency ν_0 as $N_\mathrm{e} \cdot \nu_0$. As the interaction volume of the electron beam with the residual gas molecules extends along the whole accelerator, the interaction length l_int is equal to the accelerator's circumference C. Using $C\nu_0 = \beta c$ equation (3.5) can be obtained.

beam with $\gamma \gg 1$, the photon's trajectory is assumed to propagate in forward direction of the beam along the path w until it impinges on the beam pipe after a distance $l_{\mathrm{int}}(s)$. The probability of emitting synchrotron radiation is constant along the dipole magnet when assuming a constant deflection radius. Thus, the number of emitted photons increases linearly along the dipole magnet. These photons pass through an interaction volume, being an extended transversal slice with longitudinal dimension ds, at position s within the dipole. Here, all photons which are emitted at positions w with $s - w > 0$ contribute to the ion production in the slice since they have not impinged on the beam pipe yet (propagation distance $< l_{\mathrm{int}}(s)$). This linear increment in the photon flux stops when the number of emitted photons equals the number of photons which impinge on the beam pipe. Downstream[36] of the dipole, where the emission rate of photons is equal to zero, the number of photons in the volume decreases with increasing distance from the magnet since their number reduces due to their absorption at the beam pipe.

As the photon flux at position s in the dipole (or downstream of it) is subject to variations which are mainly characterized by the interaction length $l_{\mathrm{int}}(s)$, the local production rate changes accordingly. Thus, this process shows a local specific production rate $r^{\dagger}_{\mathrm{p,pi},i}(s)$ (compare section 2.2.5) which is zero almost everywhere outside the dipole magnets and non-zero within them.

Including the dependence of $\sigma_{\mathrm{pi},i}(E_\gamma)$ and $\Phi_\gamma(E_\gamma)$ on the photon energy E_γ to the spatial variation of the flux, the total production rate of photo ionization can be expressed as

$$r_{\mathrm{p,pi},i} = \int_0^C \mathrm{d}s \underbrace{\left[\int_0^{l_{\mathrm{int}}(s)} \mathrm{d}w \left\{\int_0^\infty \mathrm{d}E_\gamma \left(\sigma_{\mathrm{pi},i}(E_\gamma) \cdot \mathcal{G}_\gamma(E_\gamma, s-w)\right)\right\} \cdot \frac{n_{\mathrm{rgm},i}(s)}{N_\mathrm{e}}\right]}_{=r^{\dagger}_{\mathrm{p,pi},i}(s)} . \tag{3.8}$$

Here, $\mathcal{G}_\gamma(E_\gamma, s-w)$ is the synchrotron radiation photon flux per photon energy expressed as longitudinal line density in units of $[\mathcal{G}_\gamma] = \mathrm{eV}^{-1}\,\mathrm{m}^{-1}\,\mathrm{s}^{-1}$.

The production of synchrotron radiation photons of different energies has statistically no preferential position in dipole magnets. Thus, $\mathcal{G}_\gamma(E_\gamma, s-w)$ is separable in E_γ and $s-w$ as $\mathcal{G}_\gamma(E_\gamma, s-w) = \mathcal{E}_\gamma(E_\gamma) \cdot \mathcal{S}_\gamma(s-w)$. $\mathcal{E}_\gamma(E_\gamma)$ is the synchrotron radiation flux per photon energy ($[\mathcal{E}_\gamma(E_\gamma)] = \mathrm{eV}^{-1}\,\mathrm{s}^{-1}$) and $\mathcal{S}_\gamma(s-w)$ is the photon emission probability line density ($[\mathcal{S}_\gamma(s-w)] = \mathrm{m}^{-1}$).

Thus, equation (3.8) separates into

$$r_{\mathrm{p,pi},i} = \underbrace{\int_0^\infty \frac{\sigma_{\mathrm{pi},i}(E_\gamma) \cdot \mathcal{E}_\gamma(E_\gamma)}{N_\mathrm{e}} \mathrm{d}E_\gamma}_{\text{energy dependent part } =:A(E_\gamma)} \cdot \underbrace{\int_0^C n_{\mathrm{rgm},i}(s) \left[\int_0^{l_{\mathrm{int}}(s)} \mathcal{S}_\gamma(s-w)\,\mathrm{d}w\right] \mathrm{d}s}_{\text{spatial dependent part } =:B(s)} . \tag{3.9}$$

The energy dependent term of this equation will be discussed in the following section. In section 3.4.2, the spatial component of the production rate will be investigated and suitably approximated.

3.4.1 Energy Dependence

The term $\sigma_{\mathrm{pi},i}(E_\gamma) \cdot \mathcal{E}_\gamma(E_\gamma)$ is essential for the numerical computation of the photo ionization production rate. The synchrotron radiation flux is given by

$$\Phi_\gamma = \int_0^\infty \mathcal{E}_\gamma(E_\gamma)\,\mathrm{d}E_\gamma . \tag{3.10}$$

[36] "Downstream" indicates a longitudinal orientation which points into the same direction as the electron beam's velocity vector. In an "upstream" orientation, the direction is antiparallel to the beam's velocity.

Therefore, the energy dependency of the synchrotron radiation flux and the ionization cross section is of importance for the determination of the energy dependent part of equation (3.9).

Synchrotron Radiation Flux The following section will only comprise a rough excerpt of the topic of synchrotron radiation of electron beams. For a more detailed treatise of this topic, consult e.g. [Lee04]. The synchrotron radiation emitted by the electrons in the dipole magnets has a broad spectrum. The energy flux as a function of emitted photon energy per electron, integrated over all emission angles, can be derived as [Lee04, chapter 4, section I.3, E, equation 4.67]

$$I(E_\gamma) = \frac{\sqrt{3}e^2}{4\pi\varepsilon_0\hbar c}\gamma\frac{E_\gamma}{\omega_c}\int_{\frac{E_\gamma}{\hbar\omega_c}}^{\infty} K_{\frac{5}{3}}(y)\,\mathrm{d}y \;=\; \hbar\omega\cdot\underbrace{\frac{\mathcal{E}_\gamma(E_\gamma)\,\mathrm{d}E_\gamma}{N_e}}_{:=\dot{n}_\gamma(E_\gamma)/N_e}\,. \tag{3.11}$$

$K_{\frac{5}{3}}(y)$ is the modified Bessel function of second kind. ω_c is the *critical frequency* which divides the energy spectrum of synchrotron radiation into two parts of equal integrated photon energy. This frequency is given as [Lee04, chapter 4, section I.3, A, equation 4.55]

$$\omega_c = \frac{3\gamma^3 c}{2R} \tag{3.12}$$

where R is the radius of the deflected electron beam trajectory in the dipole magnets. $\dot{n}_\gamma(E_\gamma)$ is the energy dependent number of synchrotron radiation photons per second which are emitted by a beam of N_e electrons. $\dot{n}_\gamma(E_\gamma)$ may be called the flux spectrum *per bandwidth*.

Figure 3.13 shows the evaluated flux spectrum for the storage ring at beam energies of 1.2 GeV and 3.2 GeV with a beam current of 50 mA. It is numerically evaluated by the program `XOP 2.4`[37]. The synchrotron radiation flux per bandwidth is continuously increasing from infrared to visible and UV eventually reaching X-ray spectral range. Here, the low energetic contribution is almost independent of the electrons' kinetic energy. Because of this invariance in the low energy range, the flux per bandwidth of high energetic photons has to increase for higher beam energies in order to ensure an energy loss which is proportional to E^4 (compare equation (2.24)). Thus, when comparing the flux spectrum for 1.2 GeV and 3.2 GeV it can be observed that it is almost congruent for E_γ below 100 eV. The beam energy dependency becomes visible at large photon energies > 100 eV. With increasing beam energy, the spectrum gets broader and shifts its flux maximum towards higher E_γ.

Note that the bandwidth is also a function of E_γ and increases towards higher photon energies. Thus, the number of synchrotron radiation photons with a specific energy is proportional to $\dot{n}_\gamma(E_\gamma)/E_\gamma$, resulting in an increasing photon flux at lower beam energies.

Photo Ionization Cross Section The photo ionization cross section is a part of the photo absorption cross section, which also includes molecular absorption processes - e.g. excitation of vibrational states of molecules - which not necessarily result in ionization of affected molecules but deexcite through emission of (several) photons. For energies in the eV- or meV region, the excitation of vibrational excitation dominates the photo absorption processes. Here, the photo ionization cross section is zero, as E_γ deceeds

[37] The program XOP, a short form of X-ray Oriented Programs, is a program that is used as a common front-end interface for computer codes of interest to the synchrotron radiation community. Amongst others it enables to model X-ray sources, such as synchrotron radiation sources along with undulators and wigglers, and compute and extract energy spectra and other characteristics of these sources [RD; RD11].

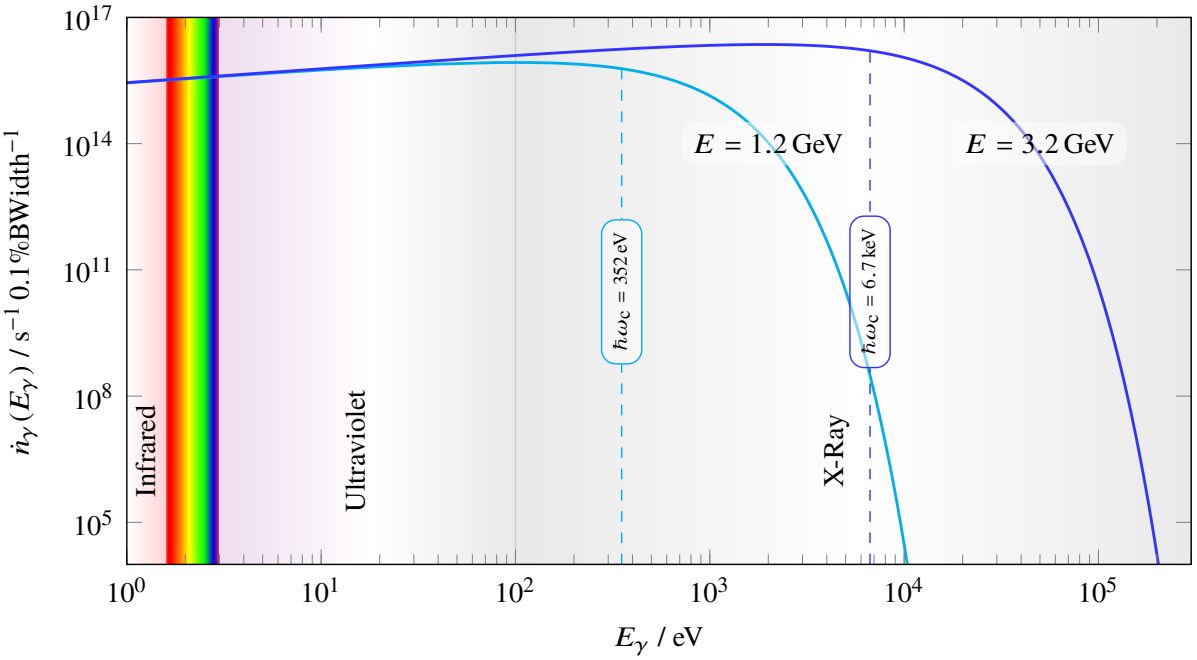

Figure 3.13: Synchrotron radiation flux spectrum $\dot{n}_\gamma(E_\gamma)$ per 0.1 % bandwidth (0.1%BWidth) of the storage ring at 1.2 GeV and 3.2 GeV with a stored beam current of 50 mA. The spectrum reaches from far infrared to X-ray range. For 3.2 GeV, even hard X-rays are emitted. The spectrum has been calculated via `XOP 2.4`. The dashed lines show the energy corresponding to the critical frequency ω_c.

the lowest binding energy[38] E_b of the orbital electrons to the molecule. Typical ionization energies of molecules are between 10 and 20 eV. For higher photon energies above 100 keV, the Compton effect exceeds the photo ionization cross section. For energies higher than $2m_e = 1.022$ MeV, this effect again is superseded by pair production.

Figure 3.14 shows the photo ionization cross section of several molecules which appear dominant in the residual gas of the storage ring's vacuum system within the relevant energy range between 10 and $2 \cdot 10^5$ eV. The shown cross section is obtained by two online databases and measurement data of [Gal+88]. For $E_\gamma > 10^3$ eV, the molecular cross sections are obtained from calculations by the `NIST XCOM` database [Ber+08]. For 20 eV $< E_\gamma \leq 10^3$ eV, calculated atomic cross sections from the `WebCrossSection` database [Ele] are used. The atomic cross sections are used to approximate the molecular ones as no database is available for this photon energy range. In this process, the cross sections of H, C, N and O are combined and scaled according to the composition of the molecules H_2, N_2, H_2O, CO and CO_2[39]. Here, the shift of binding energies of the orbitals of the molecule is ignored. Also the change in the entire electron configuration with the build-up of molecular orbitals is omitted. As can be seen at the transition energy at 10^3 eV where the approximation encounters the `XCOM` data, both models seem to comply. For H_2, a relative deviation of −1.6 % of `XCOM` data to the approximation can be found. For the other molecules, the relative deviation is in the order of −0.5 ‰ or closer. In the energy region between 10 and 20 eV, the photo ionization cross section dataset is completed by measured molecular cross sections of [Gal+88]. Here, the approximated low energy cross sections of `WebCrossSection` are

[38] In literature, the lowest binding energy is also called the first ionization energy of a particular molecule or atom.

[39] For example, the cross section of CO_2 is approximated as $\sigma_{\mathrm{pi},CO_2}(E_\gamma) \approx 1 \times \sigma_{\mathrm{pi,C}}(E_\gamma) + 2 \times \sigma_{\mathrm{pi,O}}(E_\gamma)$.

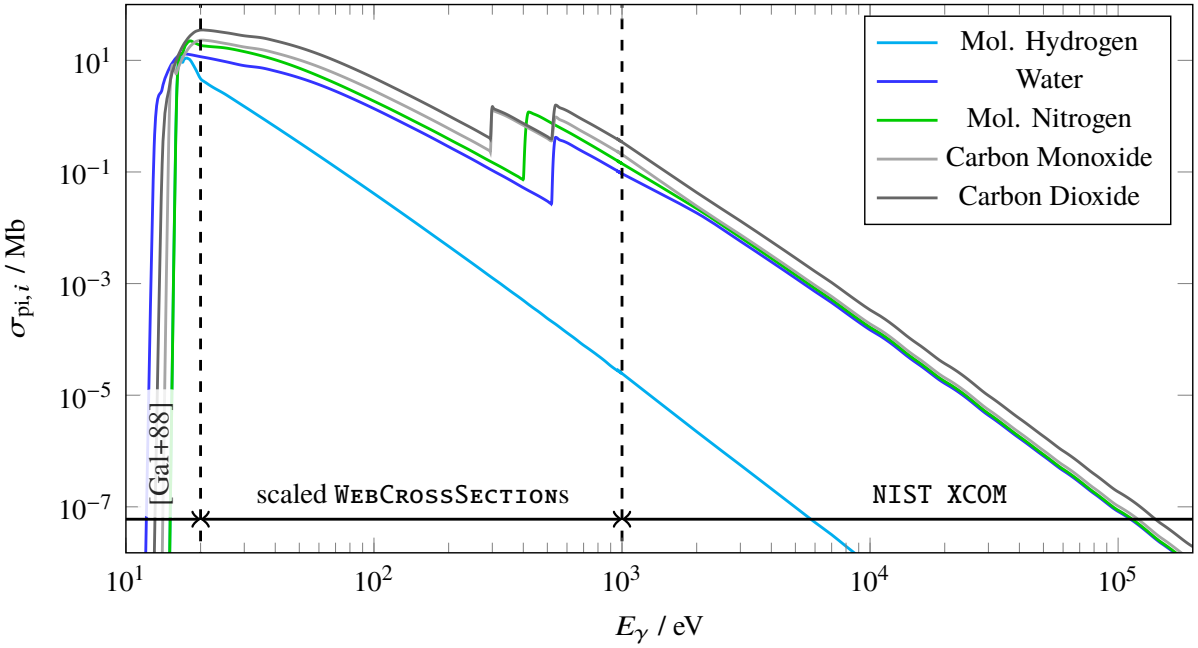

Figure 3.14: Photo ionization cross sections of several molecules in dependence of the synchrotron radiation photon energy E_γ. For $E_\gamma > 10^3$ eV, the molecular cross sections are calculated by NIST XCOM [Ber+08]. For $20\,\mathrm{eV} < E_\gamma \leq 10^3$ eV, the molecular cross sections are approximatively scaled by combining the atomic cross sections obtained from WebCrossSection [Ele] according the molecular composition. Measurements from [Gal+88] are included for the energy domain reaching from 10 to 20 eV.

scaled globally using the measured cross sections at 20 eV as reference. Additionally, the measured peak cross sections with their corresponding photon energies are added. Finally, $\sigma_{\mathrm{pi},i}$ is set to zero for energies below E_b (compare table 3.6).

To account for this "modeling" of $\sigma_{\mathrm{pi},i}$ for photon energies below 1 keV, a relative error of 25 % is assumed for all cross sections in this low energy region. To the other region with a photon energy ≥ 1 keV, a relative error of 5 % is assigned. These relative errors will be considered in the error estimation for the production rate.

For photon energies $> 10^3$ eV, the cross section decreases like $E_\gamma^{7/2}$ as predicted by the Born approximation[40]. The volatile rise in the cross sections results from the ionization of the closer-bound $1s$ electron orbital by photons with energies higher than 200 eV. Since these electrons add up to the ones from the $2s$ and $2p$ orbitals, the number of potential targets increases and thus the cross section rises.

Weighting As both, cross section and photon flux, show a broad spectrum, the weighted average of the cross section is used which is given by

$$\langle \sigma_{\mathrm{pi},i} \rangle = \frac{\int_0^\infty \sigma_{\mathrm{pi},i}(E_\gamma) \cdot \mathcal{E}_\gamma(E_\gamma)\,\mathrm{d}E_\gamma}{\int_0^\infty \mathcal{E}_\gamma(E_\gamma)\,\mathrm{d}E_\gamma}\,. \tag{3.13}$$

[40] In scattering theory, the Born approximation is the lowest order term of the perturbation series for the scattering of electromagnetic waves off atoms. It can be used if the potential of the atom is small in comparison to the energy of the incident photon. The Born approximation is valid between photon energies $\hbar\omega$ between $\gg W_\mathrm{I}$ and $\ll m_\mathrm{e}c^2$ [HS15, section 5.5.2]. $W_\mathrm{I} = 13.6$ eV is the hydrogen ionization energy.

	H_2	N_2	H_2O	CO	CO_2
E_b / eV	15.43	15.58	12.61	14.01	13.77

Table 3.6: Lowest ionization energy of orbital electrons of residual gas molecules [Nat18].

Here, $\mathcal{E}_\gamma$ is used as a weight, because it is proportional to the flux spectrum $\dot{n}_\gamma(E_\gamma)$ and an additional dependence on E_γ cancels out.

According to equation (3.10), the divisor of equation (3.13) is equal to the total flux Φ_γ. Thus, the equation can be stated as

$$\langle \sigma_{\mathrm{pi},i} \rangle \cdot \Phi_\gamma = \int_0^\infty \sigma_{\mathrm{pi},i}(E_\gamma) \cdot \mathcal{E}_\gamma(E_\gamma)\, \mathrm{d}E_\gamma \,. \tag{3.14}$$

The right-hand side of this equation is identical to the energy dependent part $A(E_\gamma)$ of equation (3.9). Thus, the energy dependence of the photo ionization process via synchrotron radiation can be mapped into the quantity $\langle \sigma_{\mathrm{pi},i} \rangle \cdot \Phi_\gamma$. As both energy dependent quantities, $\sigma_{\mathrm{pi},i}$ and Φ_γ, are available via approximations based on online databases or via a numerical calculation tool such as `XOP 2.4`, this quantity can be determined for the storage ring.

Table 3.7 shows the average cross section for relevant residual gas species at three different beam energies. For higher beam energies, the average cross section decrease since the barycenter of the synchrotron radiation spectrum shifts towards higher photon energies where the photo ionization cross section declines.

3.4.2 Spatial Dependence

The energy dependent part $A(E_\gamma)$ of equation (3.9) is constant for one beam energy and does not change along the accelerator. The spatial dependent part is more complex. However, a suitable approximation can be found if only the total production rate of this process is of interest.

Since emitted synchrotron radiation photons are not deflected by magnetic fields and therefore propagate approximately tangential[41] to the electron beam's propagation direction, the geometric modeling of the photo ionization process differs strongly from the impact ionization process. Therefore, it cannot be

[41] In general, synchrotron radiation is emitted in a cone of an opening angle, which is proportional to $2/\gamma$. For a beam energy of 1.2 GeV, γ is equal to 2 348, which results in a mean opening angle of 0.86 mrad. For higher beam energies, the opening angle is smaller because γ increases. This opening angle, on the one hand, will decrease the photon flux density on its way along the direction of the tangential propagation. On the other hand, this divergence also increases the target volume accordingly. In total, this effect cancels out as long as the photon flux density is not significantly reduced through absorption, which can be safely assumed at XHV vacuum conditions with pressures around 10^{-7} mbar.

Energy	$\langle \sigma_{\mathrm{pi},i} \rangle$ / Mb				
/ GeV	H_2	N_2	H_2O	CO	CO_2
1.2	0.81 ± 0.06	5.19 ± 0.20	3.41 ± 0.13	6.44 ± 0.23	10.36 ± 0.37
2.2	0.38 ± 0.03	2.60 ± 0.09	1.72 ± 0.06	3.31 ± 0.11	5.30 ± 0.17
3.2	0.24 ± 0.02	1.70 ± 0.06	1.13 ± 0.04	2.18 ± 0.07	3.50 ± 0.11

Table 3.7: The average photo ionization cross section due to synchrotron radiation of residual gases at different beam energies. The values are obtained by weighting the photo ionization cross section with the synchrotron radiation flux spectrum in accordance with equation (3.13).

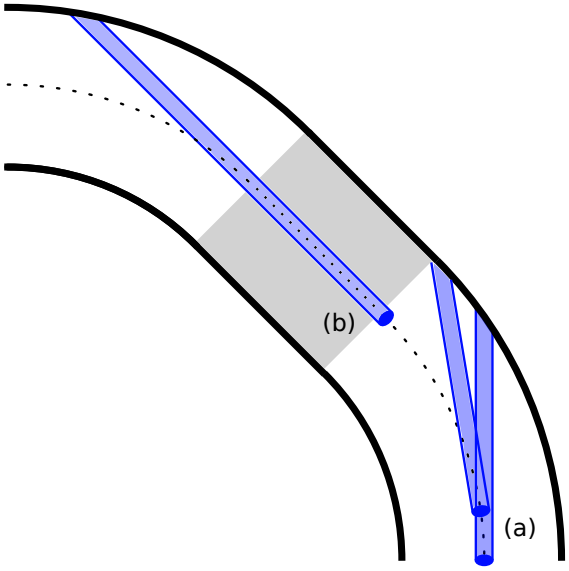

Figure 3.15: A schematic drawing of the horizontal vacuum chamber geometry (thick line) for an exemplaric section consisting of two dipole magnets connected via a straight section (gray background). The beam is guided centrically in the vacuum chamber of this section (dotted line). The beam emits synchrotron radiation in forward direction when it is deflected within dipole magnets. The synchrotron radiation's interaction regions are illustrated as blue areas. The distance between the source of the synchrotron radiation and its impinge position is the interaction length.

assumed that the interaction length is equal to the circumference of the accelerator.

Figure 3.15 illustrates the geometric circumstances of the trajectories of the electron beam and the synchrotron radiation photons within a dipole magnet in the horizontal plane. A dipole magnet bends the electron beam with an angle α_{dipole} on a trajectory with radius R, which is indicated as dashed line. In the storage ring, each of the 24 dipole magnets deflects the electron beam by 15° followed by straight sections of different lengths. Also the beam is assumed to propagate centric in a beam pipe. The beam pipe's boundaries are denoted as thick lines. Inside the magnet, the electrons emit synchrotron radiation photons whose irradiated volume at the specific positions is visualized by blue areas.

The spatial dependent part $B(s)$ of equation (3.9), being proportional to the integrated photon flux at position s, is strongly dependent on the interaction length $l_{\text{int}}(s)$ along the dipole magnet and downstream of it. If the photon is emitted in the first 63.7 % of the storage ring's dipole magnet, the photon hits the vacuum chamber after 1.06 m (see figure 3.15 (a)). If it is emitted in the second half of the magnet, the interaction length increases to up to 8.46 m (see figure 3.15 (b)). This length is dependent on the dimension of the adjoining straight section after the dipole magnet.

The value of the term $\int_0^{l_{\text{int}}(s)} \mathcal{S}_\gamma(s-w)\,\mathrm{d}w$ of $B(s)$ is dependent on $l_{\text{int}}(s)$. If more photons are emitted upstream of position s than impinge on the beam pipe, $\mathcal{S}_\gamma(s-w)$ is positive. $\mathcal{S}_\gamma(s-w)$ is equal to zero in regions of the magnet where the number of emitted photons equals the number of impinging photons and negative when more photons impinge than are emitted.

For the determination of the total production rate, it is sufficient to determine the average interaction length $\langle l_{\text{int}} \rangle$ in the storage ring. From geometric considerations using the known horizontal beam pipe dimensions in the storage ring, a worst-case estimation of the interaction length within dipole magnets can be given by

$$\left\langle l_{\text{int}} \right\rangle \leq 2.3\,\text{m}\,. \tag{3.15}$$

Details on its evaluation can be found in appendix A.10.1.

Using $\langle l_{\mathrm{int}} \rangle$, the spatial dependent part of equation (3.9) can be approximated as

$$B(s) \approx \int_0^C n_{\mathrm{rgm},i}(s) \cdot \frac{\langle l_{\mathrm{int}} \rangle \, \eth_{\mathrm{dipole}}}{C} \, \mathrm{d}s \; .$$

Here, every position within a dipole magnet contributes equally to $B(s)$. $\eth_{\mathrm{dipole}}$ is equal to one within dipole magnets and zero outside of them.

3.4.3 Photo Ionization Contribution

Assuming a constant number density of the residual gas $n_{\mathrm{rgm},i}$ along the storage ring, which can be expressed as partial pressure p_i of residual gas species i via the ideal gas equation, the total production rate for the photo ionization process can be determined as

$$r_{\mathrm{p,pi},i} \leq \frac{2\pi R}{C} \cdot \frac{\langle \sigma_{\mathrm{pi},i} \rangle \cdot \Phi_\gamma}{N_{\mathrm{e}}} \cdot \frac{p_i}{k_{\mathrm{B}} T} \cdot \langle l_{\mathrm{int}} \rangle \tag{3.16}$$

by integrating the approximations for $A(E_\gamma)$ and $B(s)$ into equation (3.9). This expression is congruent to a derivation prior to this work by [Miy87, section §2, equation (7)].

Figure 3.16 (top) shows the total photo ionization production rate normalized to a pressure of 10^{-9} mbar. At 1.2 GeV, the process of photo ionization represents 59 % of the total ion production. This increases to 62 % at 3.2 GeV, as shown in figure 3.16 (middle). The sum of the individual residual gas species' production rates is shown as the black curve in figure 3.16 (top). Congruent to the process of impact ionization, their individual production rate contribution changes only slightly with beam energy.

Figure 3.16 (bottom) shows the relative error in the evaluation of the photo ionization production rate. It mainly results from the uncertainty in the low-E_γ region of the photo ionization cross sections. Another contribution is the uncertainty in the exact average residual gas composition, shown in table 3.3 in section 3.1.3.

Conclusively, the process of photo ionization due to synchrotron radiation is an important ion production process which contributes strongly to the total production rate. Therefore, it is essential when estimating the ion production characteristics of the storage ring. A junction of impact and photo ionization will be conducted in section 3.5.

3.4.4 Simulating the Spatial Distribution of the Photo Ionization Process

For the study of the transversal and longitudinal ion movement, sophisticated tracking simulations like MOEVE PIC TRACKING[42] have been developed. These programs track the movement of several thousands to 10^7 macro-ions[43] as they interact with the electron beam and with each other. For these simulations,

[42] MOEVE Pic Tracking is a 3D particle-in-cell tracking program to simulate the interaction of a relativistic beam with initially static charged particles. Since it has been first designed to simulate electron cloud instabilities of proton accelerators, it also enables the simulation of the mutual space charge effects of an electron beam with an ion population. For more information, see [Mar13] or publications regarding MOEVE Pic Tracking such as [MPR11; MPR12; MR12; Pöp+12; Zhe+14; Mar+14].

[43] The number of involved electron and ion particles in these scenarios in reality is in the order of 10^{10} to 10^{12}. As the computation of the space-charge forces acting on the particles scales with the squared number of involved particles, the simulation of these scenarios with the realistic number of particles is not achievable within a suitable amount of time. Therefore, the number of involved particles in reduced by using macro-particles. Each macro-particle represents hundreds or thousands of particles and incorporate their accumulated charge and mass. Since the macro-particle's mass-to-charge ratio is not altered by this incorporation, the dynamic behavior in electromagnetic fields is equal to the particles it represents.

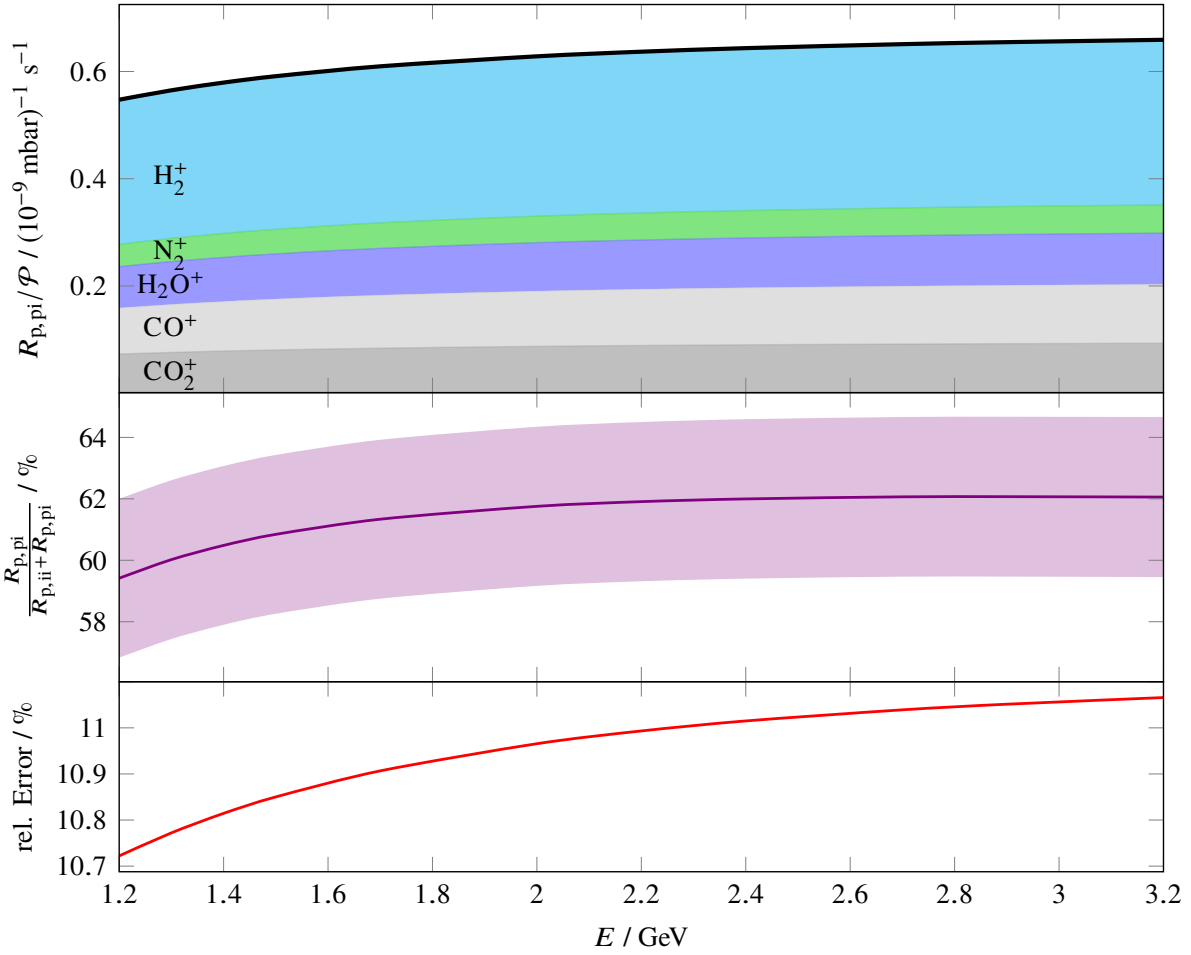

Figure 3.16: Energy dependence of the photo ionization production rate, normalized to an average pressure of 10^{-9} mbar. It is shown as the black curve in the upper graph. This curve is a sum of the contributions of the individual residual gas species' production rates. The middle graph shows the photo ionization contribution to the total ion production rate. The colored area denotes the error of this contribution. The bottom graph shows the production rate's relative error.

the initial transversal distribution of the ion population within a transversely extended slice with small longitudinal thickness ds has to be known. Thus, the local transversal distribution of the ion production within this slice, which may be called *ion production map* $\breve{R}_{\mathrm{p}}(x, z, s)$, has to be evaluated.

For the process of impact ionization of an electron beam, this map is trivial. As stated earlier in section 2.3.3, the electron beam resembles a Gaussian density distribution. Thus, the transversal ionization probability scales with the electron density and the beam's density distribution is transferred to the ion production map. Thus, the impact ionization production map $\breve{R}_{\mathrm{p,ii}}(x, z, s)$ shows a Gaussian profile with horizontal and vertical widths $\sigma_x(s)$ and $\sigma_z(s)$. Its amplitude has to be chosen in such a way that the relation

$$\hat{R}_{\mathrm{p,ii}}(s) = \iint_{-\infty}^{\infty} \breve{R}_{\mathrm{p,ii}}(x, z, s)\,\mathrm{d}x\,\mathrm{d}z$$

applies. Thus, the local production rate is used to normalize the ion production map.

For the photo ionization process due to synchrotron radiation, the evaluation of $\breve{R}_{\mathrm{p,pi}}(x, z, s)$ is more

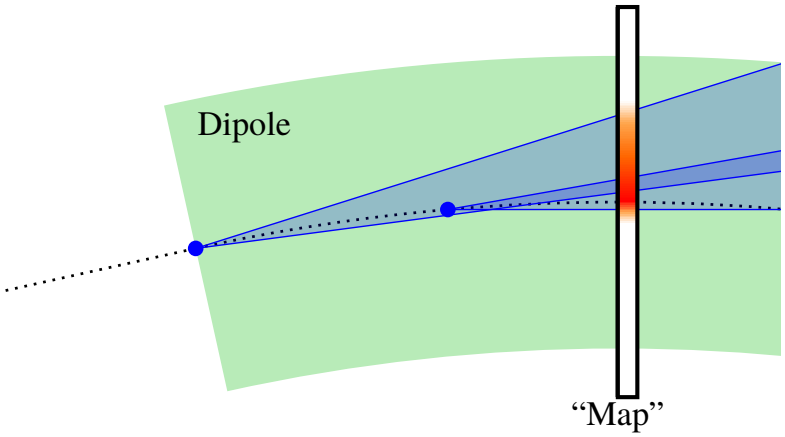

Figure 3.17: Schematic of the ion production distribution due to photo ionization by synchrotron radiation. The electron beam propagates on its trajectory (dotted line) and is deflected within a dipole magnet. The electron beam is the source of synchrotron radiation (blue dot). The radiation is emitted into a cone with an average opening angle of $2/\gamma$ (blue). The horizontal ion production map is shown exemplarily in the middle of the dipole magnet.

complex. Figure 3.17 illustrates the geometrical considerations. As the transversal ion production map at a specific position in the dipole is of interest, a volume ”map“ with longitudinal thickness ds is defined which covers all relevant horizontal and vertical dimensions. When an electron enters a dipole magnet, it starts to emit synchrotron radiation. The angular distribution of the emitted synchrotron radiation is energy dependent. High energetic synchrotron radiation photons with an energy $> \hbar\omega_c$ are emitted in forward direction into a narrow cone with an opening angle $< 2/\gamma$. The low energetic part with an energy $< \hbar\omega_c$ is emitted into a wider cone with opening angle $> 2/\gamma$. The average opening angle is equal to $2/\gamma$. In reference to the electron beam's trajectory (dotted line), the emitted synchrotron radiation photons permeate the ”map“ eccentrically. While the electron moves closer to the ”map“, the irradiated area shrinks and thus the photon flux density increases. Also the irradiated area shifts closer toward the beam axis. Thus, a horizontally asymmetric ion production map is expected whose maximum is not necessarily located on the beam axis.

PhotoIonProd

To perform this non-trivial evaluation of $\breve{R}_{\mathrm{p,pi}}(x, z, s)$, the MATLAB script PhotoIonProd has been developed. In PhotoIonProd, the intensity of synchrotron radiation emitted from a position within the dipole magnet into a certain solid angle is projected onto the ion production map, located at position s. The projected intensity is weighted by $\sigma_{\mathrm{pi},i}(E_\gamma)$. While the source of the radiation - an electron bunch with a Gaussian intensity distribution - approaches the position s, the different contributions accumulate on the map and eventually generate $\breve{R}_{\mathrm{p,pi}}(x, z, s)$.

In a post-processing phase, all entries on the ion production map are summed up. This is used for the normalization of the production map as

$$\hat{R}_{\mathrm{p,pi}}(s) = \iint_{\mathrm{map}} \breve{R}_{\mathrm{p,pi}}(x, z, s)\,\mathrm{d}x\,\mathrm{d}z$$

with $\hat{R}_{\mathrm{p,pi}}(s)$ being the local photo ionization production map in the dipole at position s. Along dipole magnets $\hat{R}_{\mathrm{p,pi}}(s)$ increases linearly with s since the average number of emitted synchrotron radiation

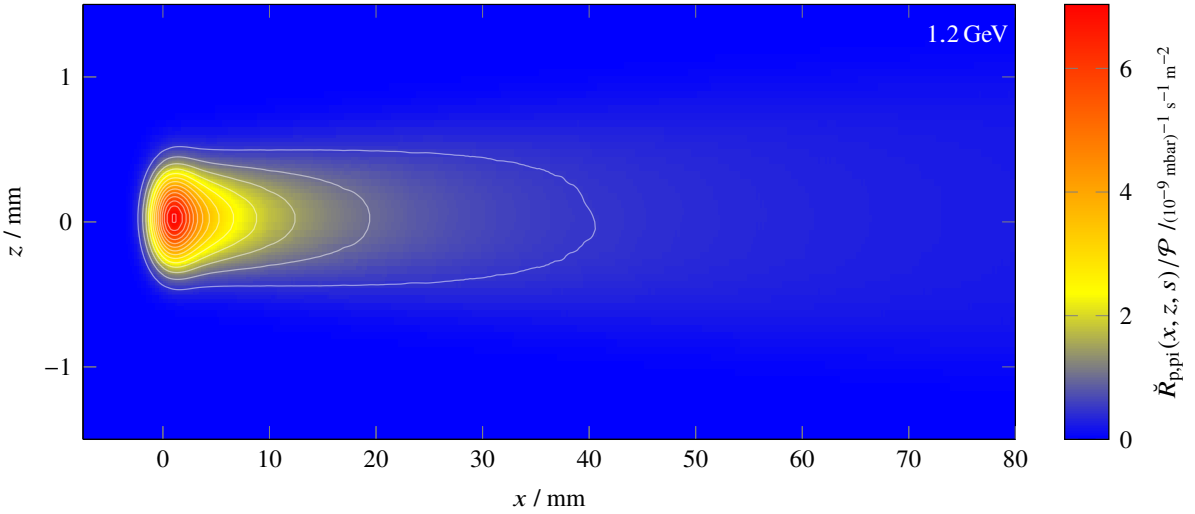

Figure 3.18: Transversal ion production map for the process of photo ionization due to synchrotron radiation in the ELSA storage ring at 1.2 GeV. The map shows a thickness ds of 1 cm and is positioned halfway through dipole magnet M26.

photons and thus produced ions increases accordingly. For details, see appendix A.10.3. In appendix B.2.1, PhotoIonProd is presented in more detail. An overview of its basic physical functional principles is given in appendix A.10.2.

Using PhotoIonProd, several ion production maps have been simulated for the storage ring.

Simulated Photo Ionization Production Map

In this work several simulations have been conducted to generate transversal ion production maps of photo ionization. The simulated maps are located midway through dipole magnet M26 of the storage ring (s = 130 m) and show a thickness of 1 cm. The presented simulated scenarios comprise beam energies of 1.2, 2.2 and 3.2 GeV, covering the typical energy range of the storage ring. In dipole M26, the optical functions are assumed to be

$$\beta_{x,\mathrm{M26}} = 9.21\,\mathrm{m} \qquad \beta_{z,\mathrm{M26}} = 5.49\,\mathrm{m} \qquad \text{and} \qquad D_{x,\mathrm{M26}} = 2.38\,\mathrm{m}\,.$$

With a betatron coupling coefficient of 7.2 %, the beam width ranges from 1.3 to 3.4 mm in the horizontal and from 0.2 to 0.6 mm in the vertical plane within the simulated energy range.

Figures 3.18 and 3.19 show the simulated ion production maps for 1.2 GeV and 3.2 GeV. The horizontal and vertical position of 0 mm represent the center of the beam at the longitudinal position of the map. The production map is shown from the perspective of the incoming beam, thus a positive horizontal coordinate indicates a position radially ”outside“ of the accelerator whereas a negative coordinate denotes a position radially ”inside“ of it. The ion production map is similar for both beam energies. The distributions are both vertically mirror-symmetric along the x axis whereas an asymmetry is visible in the horizontal plane. Almost all contributions to ion production accumulates on the right side of the beam axis. The asymmetry can be explained by the geometrical circumstances which are visualized in figure 3.17. At 1.2 GeV the beam width is smaller than at 3.2 GeV. Hence, the ion production map at 3.2 GeV displays a broader distribution in the vertical plane than at 1.2 GeV.

The photo ionization process via synchrotron radiation shows a clear difference in the ion production

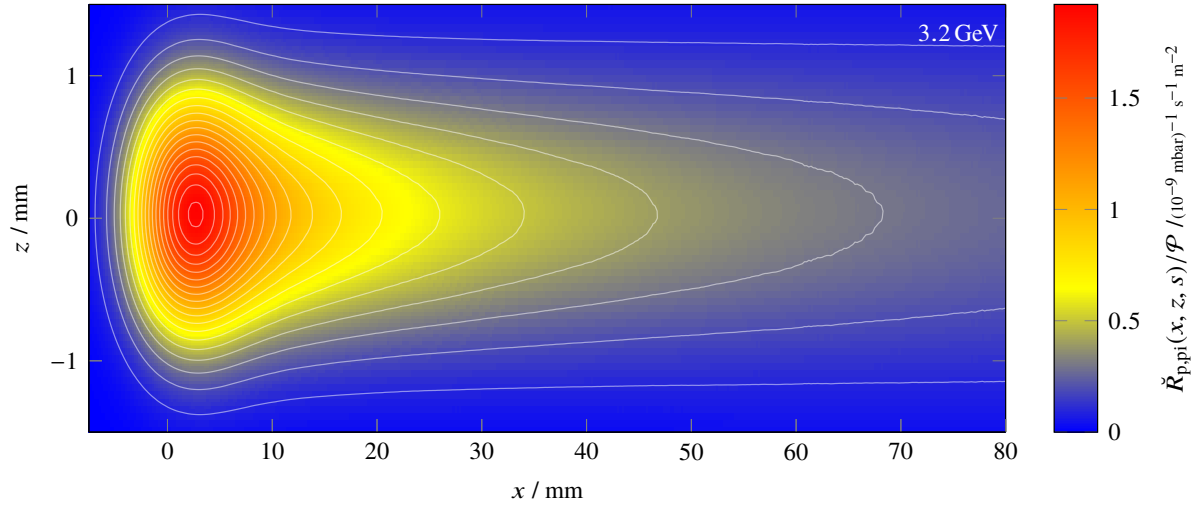

Figure 3.19: Transversal ion production map for the process of photo ionization due to synchrotron radiation in the ELSA storage ring at 3.2 GeV. The map shows a thickness of 1 cm and is positioned halfway through dipole magnet M26.

map when compared to the process of impact ionization by the electron beam. In figure 3.20, both mechanisms of ion production are compared exemplarily. A horizontal slice of the photo ionization production map at the vertical center of the beam at 0 mm is shown as the red curve. The impact ionization production map resembles the density distribution of the electron beam and is shown as the blue curve. The impact ionization map is symmetric around the beam trajectory showing its maximum of the ion production rate at the beam axis at $x = 0$ mm. In contrast, the photo ionization production map shows significant contributions on the right side of the beam trajectory. The maximum of the photo ionization production rate is shifted slightly towards the right to approximately $x = (1.8 \pm 0.1)$ mm.

Horizontal Barycenter of the Total Ion Production

Table 3.8 shows the horizontal shift of the barycenter x_{cm} of the total ion production with beam energy within the center of dipole magnet M26 at $z = 0$ mm. Since the production map is confined to regions within the beam pipe, excess contributions that would lie outside the pipe are truncated. At a beam energy of 1.2 GeV the photo ionization process shifts the barycenter to (8.0 ± 0.1) mm. For higher beam energies, the barycenter is shifted to (11.6 ± 0.1) mm at 3.2 GeV. The error is due to the resolution of the ion production map in PhotoIonProd simulations which is equal to approximately 0.1 mm.

For a beam energy of 1.2 GeV, the total ion production map is simulated by PhotoIonProd at different positions in the dipole magnet. The barycenter at each position is extracted from the truncated ion production maps. Figure 3.21 shows the results for this simulation series. Between an angle of beam

Energy / GeV	1.2	1.7	2.2	2.7	3.2
x_{cm} / mm	8.0 ± 0.1	9.7 ± 0.1	10.7 ± 0.1	11.4 ± 0.1	11.6 ± 0.1

Table 3.8: Horizontal barycenter x_{cm} of the total ion production map, including impact- and photo ionization, at $z = 0$ mm in dependence of the beam energy. The map is truncated to the size of the beam pipe. The production map is positioned in the center of dipole magnet M26.

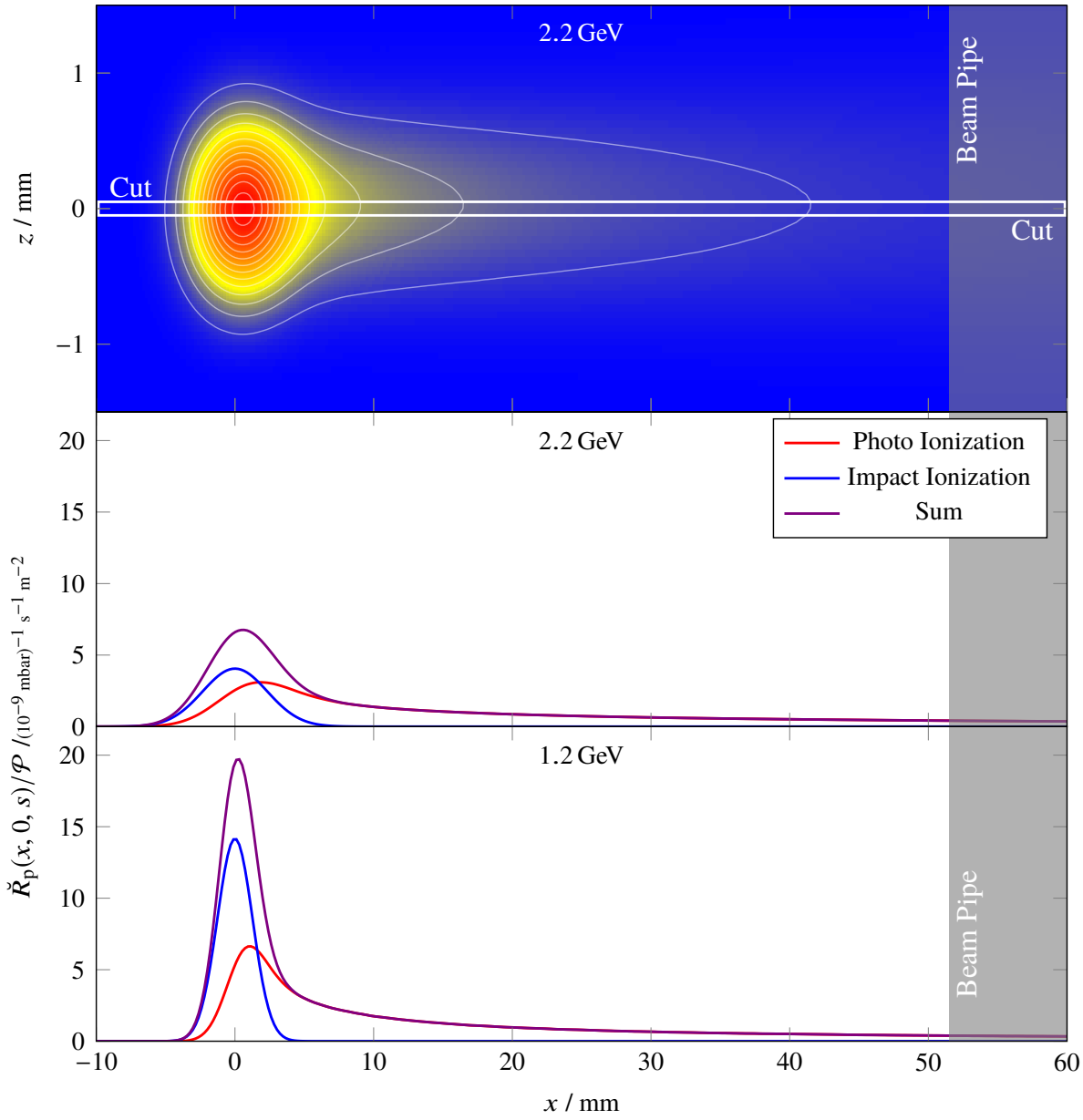

Figure 3.20: Comparison of the impact and photo ionization production map. The upper graph shows a photo ionization production map. The map is positioned midway through dipole magnet M26 of the storage ring at 2.2 GeV. The beam pipe has a horizontal half-diameter of 51.5 mm which confines the production map (thickness of 1 cm). A cut through this production map along the horizontal plane at vertical position $z = 0$ mm, illustrated as the white rectangle, results in the red curve in the middle figure. Here, the impact ionization production map along the horizontal plane at $z = 0$ mm is shown in blue. The sum of both production mechanisms is shown in violet. In the bottom graph, these cuts through the production map are shown for a beam energy of 1.2 GeV.

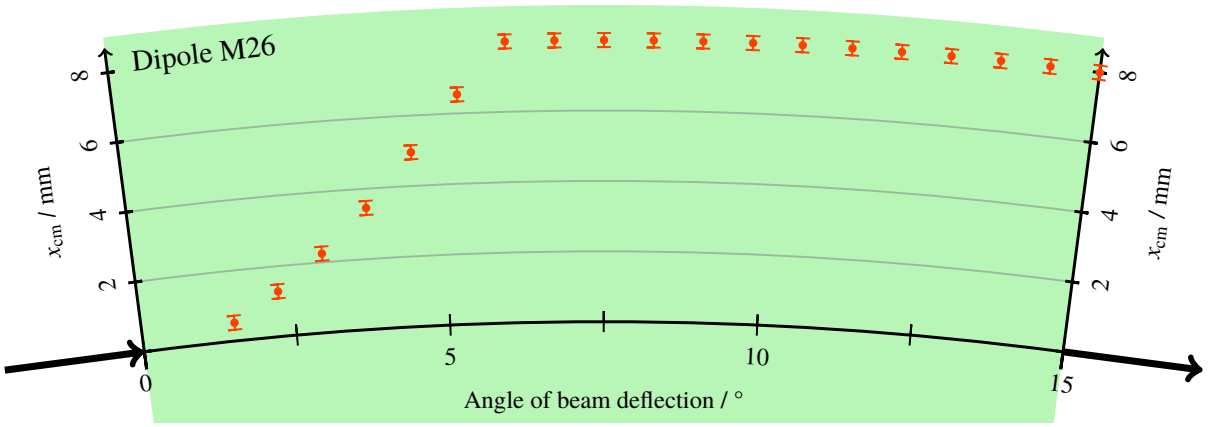

Figure 3.21: Barycenter x_{cm} of the total ion production, including impact- and photo ionization, along dipole magnet M26 at 1.2 GeV. x_{cm} is obtained from PhotoIonProd where the production map has been numerically simulated at different positions in the dipole. The black arrows indicate the propagation direction of the electron beam.

deflection[44] α of 0° and approximately 6°, x_{cm} increases from 0 to 8.0 mm. After reaching this value, x_{cm} stays constant within the simulation error. This behavior can be explained on one hand by the form of the production map at the beginning of the dipole and on the other hand by the limitation of the map by the beam pipe dimension at the end of the dipole. At the beginning, the synchrotron radiation "searchlight" of the beam only crosses a small area of the production map as the start point of synchrotron radiation emission and the map itself are positioned in close proximity. Additionally, the number of emitted synchrotron radiation photons increases linearly with the beam's propagation path within the dipole, rendering the effect of photo ionization to the total ion production comparably small. With increasing path length of the beam and thus increasing ion production by photons, x_{cm} increases. At approximately 6° beam deflection, the irradiated area on the production map reaches the beam pipe dimension. Due to the map's limitation to this dimension, the barycenter henceforth stays constant and the truncated production map does not change anymore.

During the passage of the electron beam through the dipole magnet, the optical functions are subject to variations. $\beta_x(s)$ changes from 15.5 to 4.8 m whereas $\beta_z(s)$ from 2.7 to 10.0 m. $D_x(s)$ changes from 3.1 to 1.8 m. This of course results in a variation of the transversal beam width in the horizontal plane from 1.5 to 0.9 mm and vertical from 134 to 256 µm which is not yet mapped by PhotoIonProd. Instead, it uses the optical function in-between the beginning of the dipole magnet and the position of the production map. Therefore, these results may be subject to minor quantitative changes.

Simulated Local Production Rate of Photo Ionization

The simulation of the photo ionization maps allows for a derivation of the local production rate within the dipole magnets. To do so, the truncated production maps at different positions within the dipole are individually integrated. Figure 3.22 shows the resulting local production rate $\hat{R}_{p,pi}(s)$. Due to absorption of synchrotron radiation photons at the dipole magnet's beam pipe, the simulated local production rate deviates from the theoretically predicted linear rise at an angle α_{break}.

If emitted synchrotron radiation photons are absorbed at the beam pipe along the dipole magnet, the

[44] Note that the angle of beam deflection is not to be confused with the fixed deflection angle of the electron beam when passing one dipole magnet. Whereas the angle of beam deflection increases from 0 to 15° while the beam propagates further into the dipole, the deflection angle is constant at 15° for each dipole magnet in the storage ring.

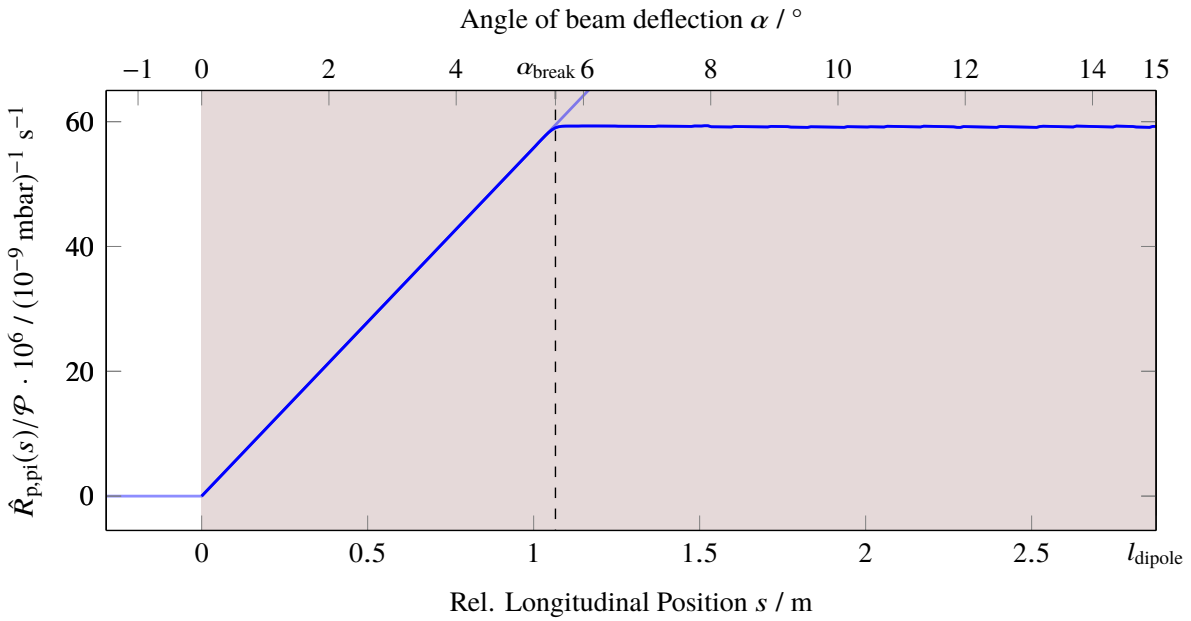

Figure 3.22: Local photo ionization production rate in a dipole magnet of the storage ring at a beam energy of 1.2 GeV, simulated by PhotoIonProd. The position is given in deflection angle and its corresponding relative longitudinal position within the dipole magnet. The storage ring's dipole magnets have an effective length of $l_{\text{dipole}} = 2.875$ m and deflect the beam by 15°. Note that the shown local production rate is normalized to an average pressure of 10^{-9} mbar and refers to a slice thickness Δs of 1 cm. Additionally, it is magnified by a factor of 10^6.

linear rise of $\hat{R}_{\text{p,pi}}(s)$ with s stops at a specific position, which corresponds to α_{break} and transfers into a constant production rate for $\alpha > \alpha_{\text{break}}$, if the beam pipe's dimensions do not change along the dipole magnet. Here, the number of absorbed and newly emitted synchrotron radiation photons passing through the map's interaction volume is constant.

From simple geometric considerations α_{break} can be determined as

$$\alpha_{\text{break}} = \arccos\left(\frac{R}{R + \frac{d}{2}}\right)$$

for a given bending radius R and horizontal beam pipe diameter d (see appendix A.10.1). For the storage ring's dipole chambers where $d/2$ is assumed to be approximately 51.5 mm, α_{break} of 5.56° is obtained. This agrees well with the simulation.

Further Investigation Strategy

Due to the contribution of photo ionization, the transversal ion production map is not a horizontally symmetric Gaussian distribution in vicinity of dipole magnets. Instead, ions are also produced far off on one side of the beam due to photo ionization. Thus, also an alteration of the ions' equilibrium density is expected:

- In dipoles, the vertical magnetic field modifies the horizontal motion of ions by emerging $\vec{E} \times \vec{B}$ forces, rendering ions less mobile in that plane. Thus, this initial asymmetry may persist and also reflect in the ions' equilibrium density distribution. In section 4.3.6, this equilibrium

density distribution is evaluated.
- In magnet field-free regions downstream of dipole magnets, the production map is still asymmetric due to a non-zero synchrotron radiation photon flux. Here, also a different equilibrium density distribution is expected.

As will be discussed in section 5.1, the transversal ion density distribution has a significant effect on the coherent and incoherent part of the ion induced tune shift.

3.5 Summary: Total Production Rate in the Storage Ring

In the course of this chapter, the residual gas composition of the storage ring has been determined by using a quadrupole mass spectrometer. Approximately 86 % of residual gas molecules are H_2, whereas 6 % are H_2O and 2 % are CO_2 (compare table 3.3). A distinction between N_2 and CO is possible only to a limited extend due to their identical mass-to-charge ratio. However, it is estimated that CO contributes to 3 % whereas the fraction of N_2 to the residual gas is 2 %.

For the determination of the total ion production rate, a realistic estimate on the average pressure in the storage ring is essential. Therefore, an analytical model for the average pressure has been developed and its beam energy and current dependency has been suitably parameterized on basis of recorded pressure values of the IGPs within the storage ring during storage mode operation. However, the measured IGP pressure in the pump section is not identical to the pressure within the beam pipe and differs by a certain proportionality factor due to the vacuum system's finite conductance. Using MolFlow+, the geometry of relevant parts of the storage ring's beam pipe and pump section has been modeled, enabling a determination of this factor to be approximately 12.5. Thus, the average pressure in the storage ring ranges between approximately $6 \cdot 10^{-8}$ and $6 \cdot 10^{-7}$ mbar and increases with beam energy *and* current.

Using the abundance of the individual residual gas species and thereof derived partial pressures, the total production rate can be determined, which comprises the ion production processes of impact and photo ionization. In figure 3.23, the total production rate in the storage ring is shown for combinations of beam energy and current. The production rate varies from approximately $100\,\mathrm{s}^{-1}$ at a beam energy of 1.2 GeV and a current of 5 mA to over $480\,\mathrm{s}^{-1}$ at 3.2 GeV and 200 mA[45].

The predominant part of the variation in R_p results from the pressure increment with beam energy and current as the pressure-normalized production rate, visible in figure 3.24, only increases by approximately 15 % from 1.2 to 3.2 GeV. The fractions of the produced ion species approximately stays constant for different beam energies.

The developed tool PhotoIonProd enables the determination of the transversal ion production maps of impact and photo ionization in dipole magnets. Since photo ionization contributes to approximately 2/3 of the ion production in the storage ring, the total production map is asymmetric in the horizontal plane within dipole magnets. The barycenter x_cm of ion production, characterizing this asymmetry, shifts away from the beam center with increasing angle of beam deflection, eventually staying constant for angles $> \alpha_\mathrm{break}$. It is expected that this asymmetry also affects the equilibrium ion density distribution in dipole magnets and adjacent sections and eventually also influences the ions' space charge interaction with the beam.

As the ions' initial position is important for the determination of their motion within a dipole magnet, the developed tool PhotoIonProd and thereof derived ion production maps are an essential ingredient for sophisticated numerical simulations of ion dynamics in these accelerator sections.

[45] An operation of the storage ring with this combination of beam energy and current is not feasible due to a low quantum lifetime of the beam of below 60 s at a synchrotron frequency of 95 kHz. For more information, see [Sch15, section 13.1, figure 13.2].

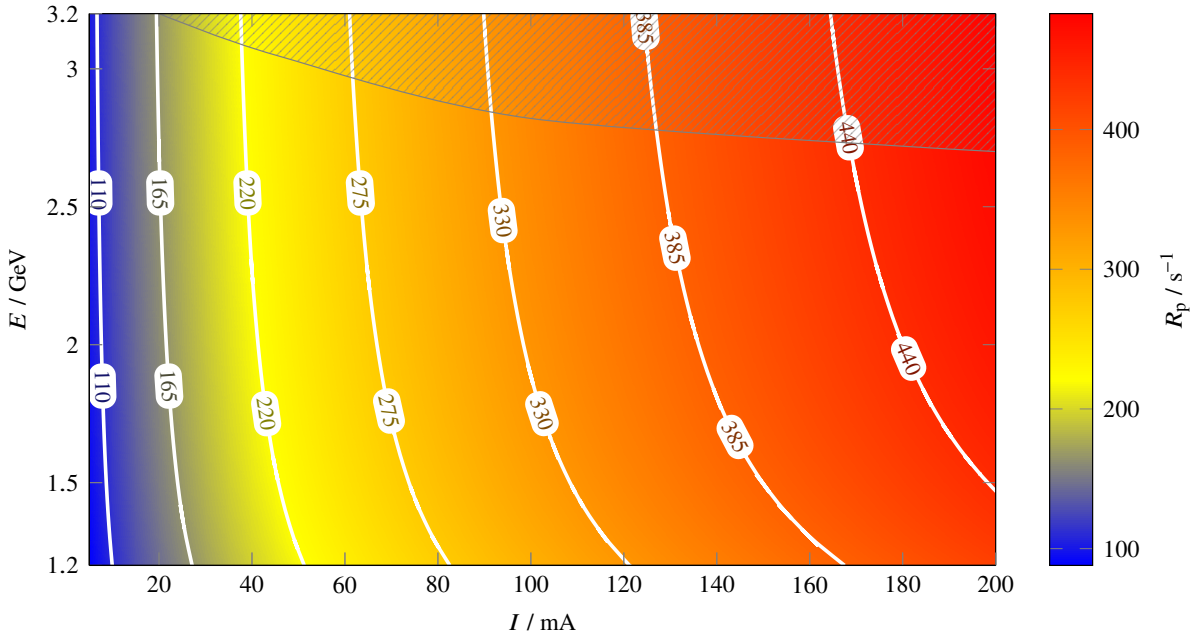

Figure 3.23: Total ion production rate in the storage ring due to the processes of impact and photo ionization. The white lines indicate the contour-lines of constant production rate. The hatched area indicate combinations of beam energy and current, where an operation of the storage ring is only possible to a limited extend due to a beam lifetime below 60 s [Sch15, section 13.1, figure 13.2].

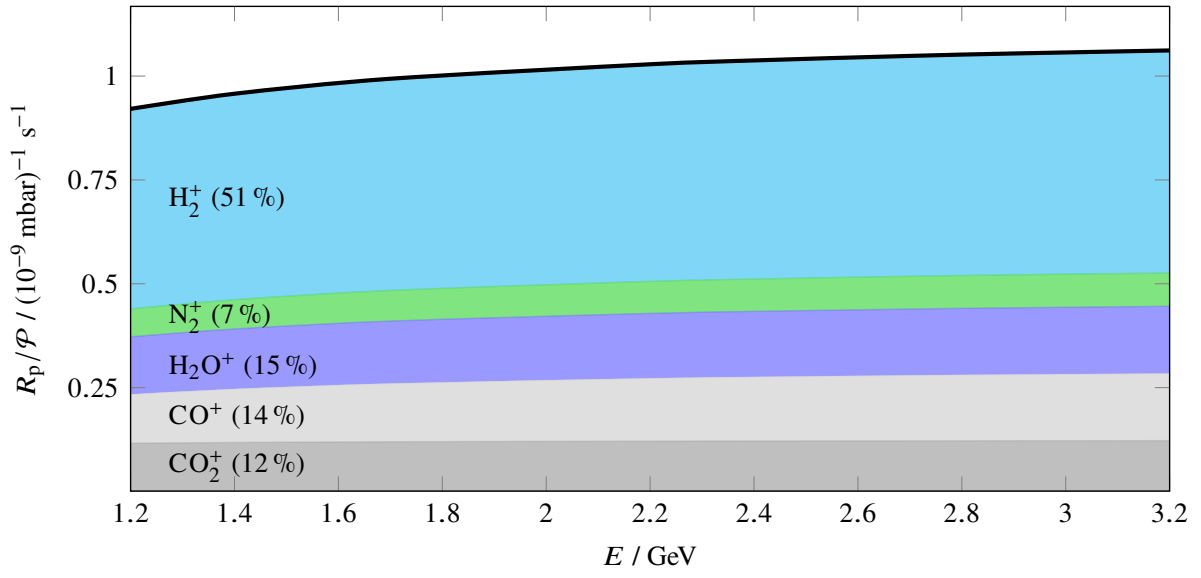

Figure 3.24: Total production rate of ions per electron due to impact and photo ionization in the storage ring, normalized to an average total pressure of 10^{-9} mbar. It is shown as the black curve, which is the sum of the contributions of the individual residual gas species' production rates.

CHAPTER 4

Accumulation of Ions

In the prior chapter the relevant ion production mechanisms in the storage ring have been elaborated. The production rates of specific ion species at different beam energies and currents are known in principle. Nonetheless, these quantities reveal little about the actual (local) neutralization in the accelerator and the composition of the ion population. If a particular ion species shows instable trajectories in a circular electron accelerator in some circumstances, this species cannot accumulate to a relevant level. The stability of the individual ion species in the storage ring will be discussed in the following section.

In section 4.2, the average beam potential within the accelerator will be used to locate potential hollows. In them, stable ion species are trapped longitudinally and cannot reach positions where they could be neutralized, by clearing electrodes for example. Consequently, an elevated local neutralization level is expected in potential hollows. This level can be estimated utilizing the concept of *static neutralization*.

The locations of ion accumulations in the storage ring are also influenced by the presence of magnetic fields. These fields alter ion trajectories, hinder their clearing under certain conditions and thus lead to an elevated local neutralization. In section 4.3, a two-dimensional particle tracking approach is utilized to determine regions of increased ion accumulation outside potential hollows.

In the rf section of the storage ring, the longitudinal transport of ions may be altered by the electromagnetic rf fields, present in the cavities. The effect of these time dependent fields on ion motion and the resulting ion accumulation behavior will be discussed in section 4.4.

4.1 Criteria for Stable Ion Trajectories

In the following, the stability of the relevant ion species in the storage ring is evaluated. In this consideration, no other[1] clearing mechanisms than ion clearing electrodes (compare section 6.1) are applied. Counter-intuitively, particular ion species may not accumulate as the bunched structure of the beam forces them on instable trajectories.

4.1.1 Critical Mass of Ions

As stated earlier in this work, the electron beam has a bunched time structure. Thus, the linear charge density $\lambda(t)$ of the bunches changes with time, when observed from a fixed position in the accelerator. If the storage ring shows a homogeneous filling pattern, 274 bunches with the same charge per bunch propagate in it. The distance between the center of charge of two neighboring bunches is equal to $\beta c/\nu_{\mathrm{rf}}$

[1] The electron beam shows a homogeneous filling pattern without any filling gaps (compare section 6.2). Also the ions are not shaken off the beam (compare appendix A.20).

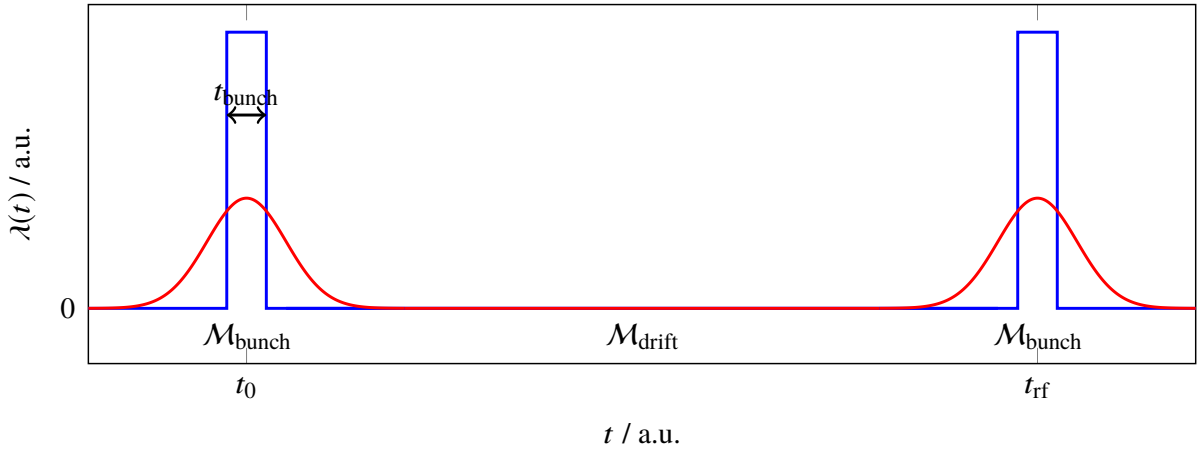

Figure 4.1: Linear charge density $\lambda(t)$ at a fixed position in the accelerator for one rf period going from t_0 to t_{rf} and comprising two bunches. The realistic charge variation is shown in red, whereas the approximated form, used in the transfer matrix formalism, is show in blue. The corresponding transfer matrices are shown below. Note that the width of the bunches is exaggerated.

which equals the rf wavelength λ_{rf} of approximately 60 cm for an rf frequency $\nu_{\text{rf}} = 1/t_{\text{rf}}$ of 500 MHz. Longitudinally, each bunch has a GAUSSian density distribution with a width of σ_s, as visualized in figure 4.1. As stated in section 2.3.2, this width varies approximately from 1 cm at 1.2 GeV to 2.7 cm at 3.2 GeV, if the synchrotron frequency is kept constant at 89 kHz (compare figure 2.6). The fact that σ_s is small compared to λ_{rf} implies that the longitudinal charge density varies between a maximum at the center of charge to approximately zero after a few σ_s distance from it.

In the perspective of ions, which are attracted by the electron beam, this variation in the linear charge density results in a time dependent transversal reversing force towards the beam center. Its magnitude is maximal if the ions face the bunches' center of charge and it is approximately zero between the bunches. Thus, the transversal ion motion can be described as a combination of an oscillation, when facing the charge of the bunch, interrupted by a drift, when being between the bunches.

For a certain time structure of the reversing force, dependent on the charge density of the individual bunches (compare equation (2.43)) and the filling pattern[2], the trajectory of a specific ion species may become instable. The stability of the ions' trajectorie depends on their mass-to-charge ratio.

The lower boundary for the mass-to-charge ratio of a stable ion species in a bunched beam is called *critical mass*. All ion species which have a mass-to-charge ratio above [BB80, section 4, conversion of equation (12)]

$$\left(\frac{A_i}{Z_i}\right)_{\text{crit},x,z} = \frac{\mathrm{e}}{8\pi\varepsilon_0(\beta c)^3 m_{\text{p}}} \cdot \frac{I}{h^2} \cdot \frac{C^2}{\sigma_{x,z}(s)\left(\sigma_x(s)+\sigma_z(s)\right)} \tag{4.1}$$

are in principle able to accumulate in the accelerator in the considered plane. Ions with a mass-to-charge ratio below show instable transversal trajectories, cannot accumulate and will eventually leave the beam potential. In the following, this mass-to-charge ratio will be denoted as $A_{\text{crit},x,z}$, assuming singly charged ions with $Z_i = 1$. The derivation of $A_{\text{crit},x,z}$ using the transfer matrix formalism can be found in appendix A.11.

[2] The filling pattern of a circular accelerator denotes the repetitive longitudinal sequence of appearance of bunches, each showing an individual bunch current.

The critical mass increases for higher beam currents and smaller beam size. Therefore, the critical mass is higher in the vertical plane than in the horizontal one because in most storage rings the vertical beam size $\sigma_z(s)$ is small compared to the horizontal size. This implies that ions tend to show instability in the vertical plane first. Due to the ions' mutual space charge interaction, their motion in one plane is not decoupled from the other. Consequently, a horizontally oscillating ion will also show vertical movements after a certain time. Thus, if this ion is horizontally stable and vertically instable, it will will not accumulate. Therefore, it is sufficient to evaluate only the vertical critical mass to estimate which species can accumulate. Of course, the critical mass also varies along the accelerator in accordance with the beam dimension $\sigma_{x,z}(s)$, rendering it a local quantity.

Note that the evaluated critical mass is only an approximation. A reversing force of the electron beam is assumed which rises linearly with the ions' amplitude x_i or z_i. Non-linearities for amplitudes larger than σ_x or σ_z are omitted. Also short bunches $l_{\text{bunch}} \ll \lambda_{\text{rf}}$ have been assumed[3]. In this derivation, also the neutralization is assumed to be zero. In reality, the reversing force would be decreased due to the shielding of the electron beam by the ion population. Thus, for a certain neutralization level, a previously instable ion species may accumulate. This effect is called *ion ladder* where the accumulation of a heavier ion species enables the accumulation of lighter ions which have been instable beforehand. Amongst others, it is discussed briefly in appendix A.12.

4.1.2 Stable Ion Species in the Storage Ring

To study which ion species can accumulate in the storage ring with a homogeneous filling pattern, the critical mass has to be evaluated. To do so, the twiss parameters of the storage ring have been extracted out of ELEGANT calculations and the beam dimensions have been calculated. The critical mass in the transversal planes is calculated using equation (4.1) for different beam energies and currents of the storage ring.

Figure 4.2 (top) shows the critical mass for one half of the storage ring at a beam energy of 1.2 GeV and 50 mA beam current. Due to the symmetry of the storage ring, the other half is identical and is therefore omitted. As the local minima of the vertical beam size concur with the local maxima in size in the horizontal plane (compare figure 2.9), the critical mass in the horizontal and vertical plane are antagonistic. Because $\sigma_x > \sigma_z$ the vertical critical mass is always above the horizontal one and approximately a factor of 2 higher. The horizontal critical mass varies between $0.1 \cdot 10^{-3}$ and $0.6 \cdot 10^{-3}$ u along the storage ring whereas the vertical critical mass shows values between $0.6 \cdot 10^{-3}$ and $1.2 \cdot 10^{-3}$ u. As the mass of the lightest possible ion (H_1^+) is 1 u, all ion species can accumulate in this scenario. It is shown in figure 4.2 (bottom), that the vertical critical mass only rises to values of $1.7 \cdot 10^{-3}$ to $2.2 \cdot 10^{-3}$ u and $3 \cdot 10^{-3}$ to $4.4 \cdot 10^{-3}$ u for higher beam currents of 100 and 200 mA, respectively. Even at these currents, the critical mass does not exceed 1 u. Thus, all ion species can accumulate at a beam energy of 1.2 GeV in case all buckets are homogeneously filled.

With higher beam energy, the beam dimension broadens. The critical mass consequently decreases with increasing beam energy. Thus, even at low beam energies the bunched structure of the beam does not destabilize the ion population.

There exists no realistic operation scenario for the storage ring in which the critical mass exceeds 1 u. Thus, the accumulation of all ion species is not hindered if a homogeneous filling pattern is present.

[3] This formalism is also valid for ion accumulation in anti-proton storage rings. Here, the bunch length can be drastically increased by switching off rf cavities or the use of barrier-bucket rf cavities which are able to manipulate the longitudinal proton density distribution [Gar10, section 5].

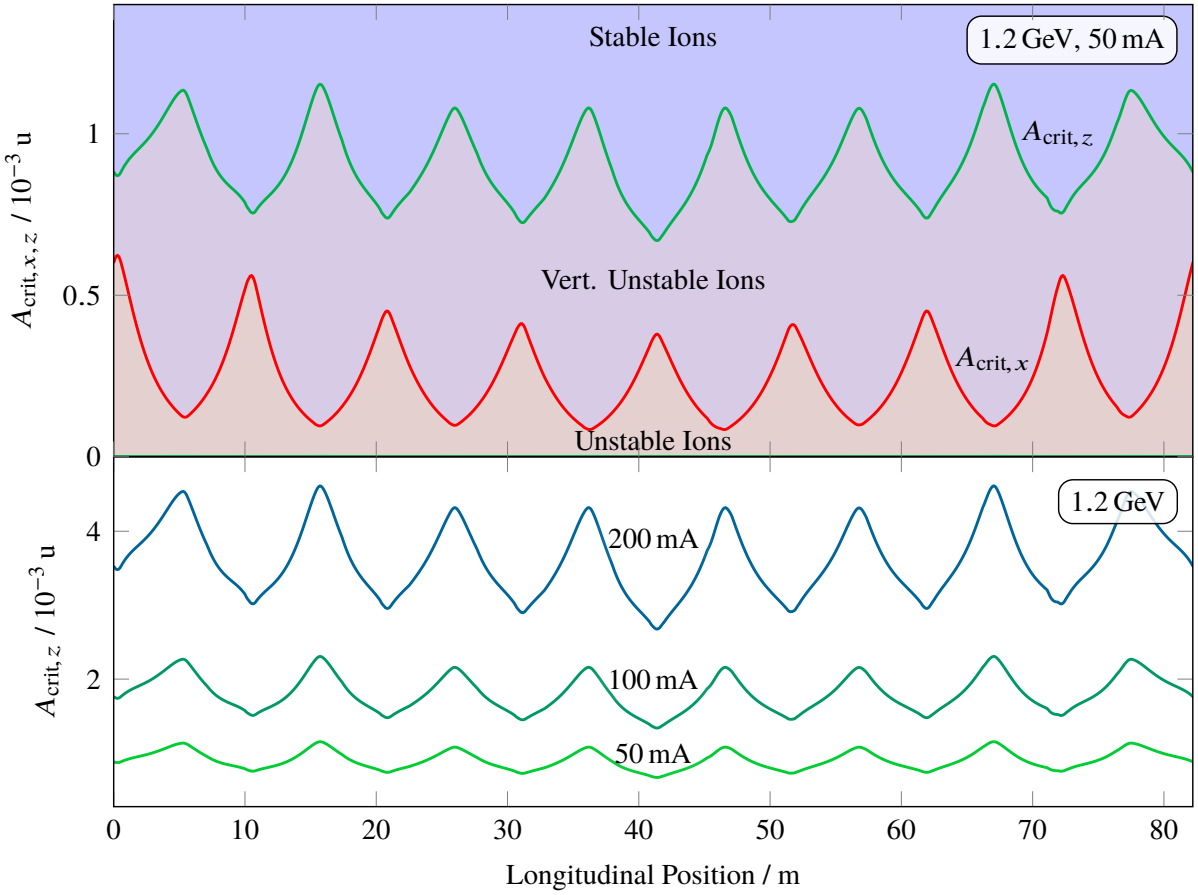

Figure 4.2: Horizontal and vertical critical mass $A_{\mathrm{crit},x,z}$ along one half of the storage ring at a beam energy of 1.2 GeV. Due to the symmetry of the storage ring, the other half is identical. The top graph visualize the difference between horizontal and vertical critical mass at 50 mA beam current. Ions which only show vertical instable trajectories are also considered unstable. The bottom graph shows the vertical critical mass for different beam currents.

4.2 Ion Accumulation in Potential Hollows

Since ions oscillate stably in the transversal plane, they also propagate longitudinally and follow the beam potential to its minimum. This longitudinal motion may eventually lead them into the vicinity of clearing electrodes, which neutralize them. Other ions may not be cleared by clearing electrodes as the shape of the beam potential traps them in potential hollows. Thus, it is essential to evaluate the beam potential for the entire accelerator and identify potential hollows. With a linear space-charge theory, it is also possible to evaluate the accumulated neutralization in these potential hollows (see section 2.2.3).

Note that the discussed beam potential in the following sections is the time averaged beam potential at the beam center at $x = 0$ mm and $z = 0$ mm.

4.2.1 Beam Potential in the Storage Ring

To calculate the beam potential $\langle U(s) \rangle$, on one hand, the dimension of the electron beam along the storage ring is needed. It is calculated using the optical functions $\beta_x(s)$, $\beta_z(s)$ and $D_x(s)$, calculated from the lattice of the storage ring via ELEGANT, along with the measured horizontal and vertical beam emittance

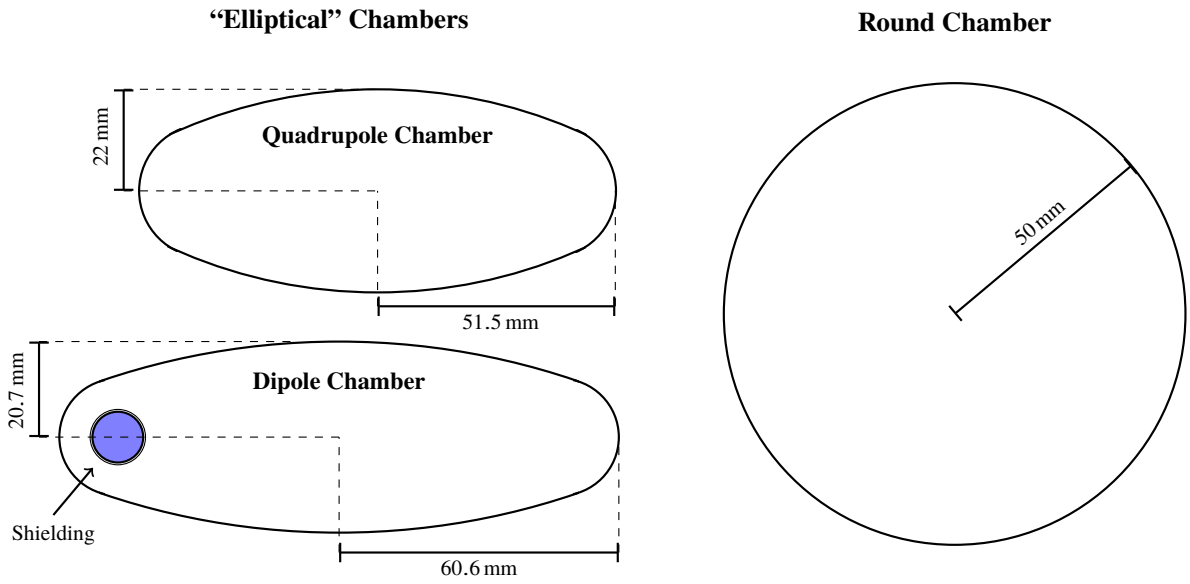

Figure 4.3: Transversal cut through the beam pipes which are most commonly used in the storage ring. The round chamber on the right side and the "elliptical" chambers on the left. The round chamber is a cylinder with an inner diameter of 10 cm and a wall thickness of 2 mm. The quadrupole chamber (top, left) has a wall thickness of 0.3 mm. The dipole chamber (bottom, left) is equipped with a water-cooled radiative shielding to protect the beam pipe from thermal stress induced by synchrotron radiation. It has a wall thickness of 0.3 mm. See [HNH15] for more details.

(see section 2.3.3). On the other hand, the beam pipe geometries have to be known. Thus, a map of these geometries, which are used in the storage ring, has been created. Out of this map, the horizontal and vertical half-diameters of the vacuum chambers and elements along the accelerator, $x_{\mathrm{vc}}(s)$ and $z_{\mathrm{vc}}(s)$, have been extracted with a resolution of 1 cm[4].

In the storage ring, several types of beam pipes are installed commonly:

- Inside quadrupole and sextupole magnets, vacuum chambers with a virtually "elliptical" profile are installed. In the course of this work, this type of beam pipe is called quadrupole chamber. Although the chamber's profile is not perfectly elliptic due to manufacturing constrains, it's profile can be approximated as an ellipse with semi-major axis of 51.5 mm and semi-minor axis of 22 mm (see figure 4.3 (top, left)).
- In all dipole magnets, so called dipole chambers are installed [HNH15]. This type of chamber is equipped with an integrated shielding to protect the beam pipe from thermal stress induced by synchrotron radiation. The chamber can be approximated by an ellipse with semi-major axis of 60.6 mm and semi-minor axis of 20.7 mm. It is broader than the quadrupole chamber to house the radiative shielding (see figure 4.3 (bottom, left)). Subtracting the space for the shielding, the quadrupole and dipole chambers show almost identical dimensions.
- In several sections of the storage ring, especially in parts of the straight and missing magnet sections, round beam pipes are installed. These pipes have an inner radius of mostly 5 cm (see figure 4.3 (right)). In certain places, the radius is decreased to 2.5 cm.

[4] The longitudinal position error can assumed to be approximately 3 cm.

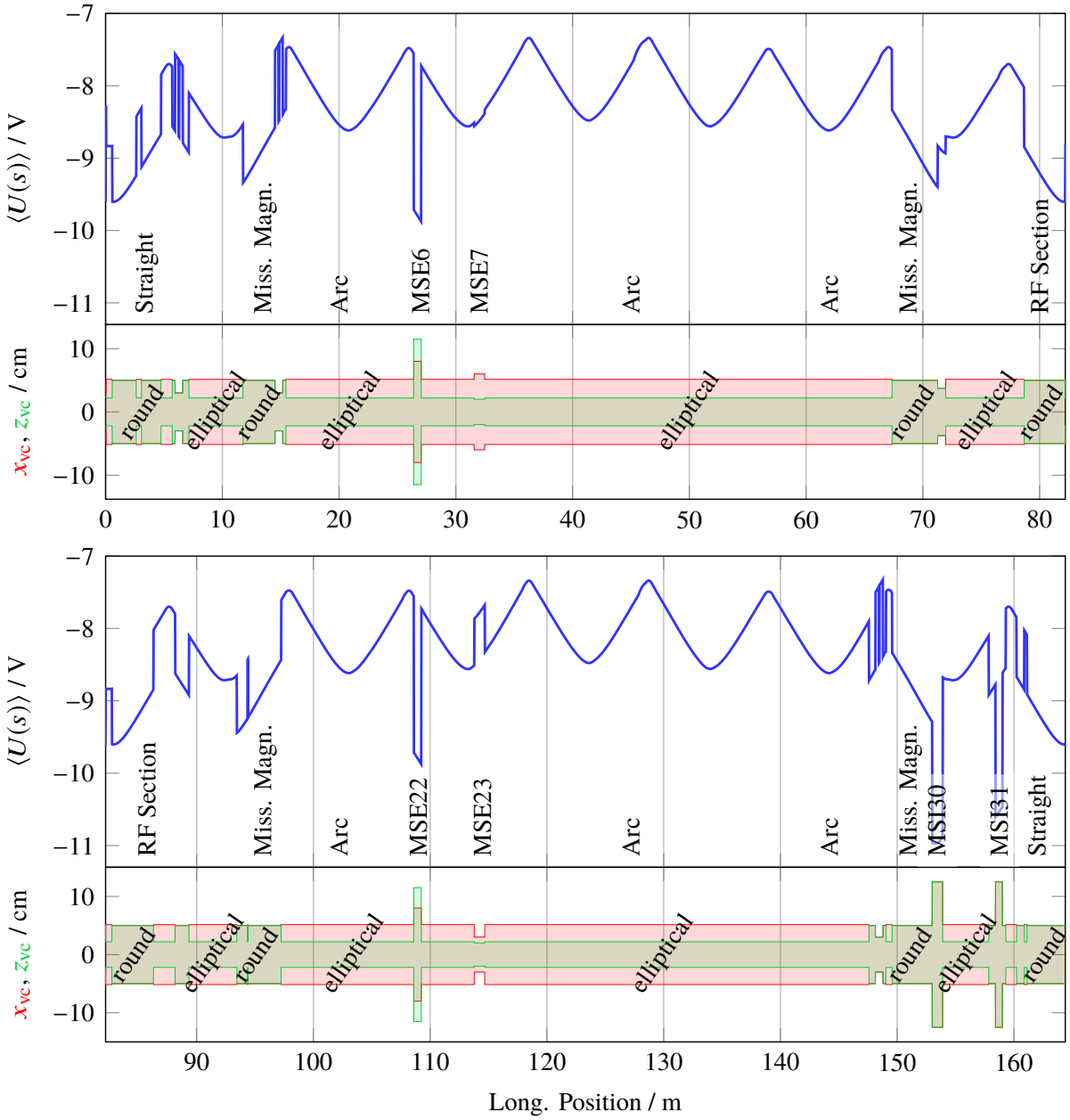

Figure 4.4: Average beam potential of the storage ring in the beam center at an energy of 1.2 GeV and current of 35 mA. The first half of the storage ring is displayed in the upper half of the figure whereas the second half is shown below. For each half of the accelerator, the beam potential is shown as blue curve. Below it is the corresponding horizontal (red) and vertical (green) beam pipe geometry. Additionally, the longitudinal position of the extraction (MSE) and injection septa (MSI) are shown in the lattice as their vacuum chamber geometry also results in volatile rises of the potential. Also the positions of the straight, rf and missing magnet section along with the arcs are labeled. Note that the geometry of the rf cavities in the middle of the accelerator at 79 m and 83 m are not included.

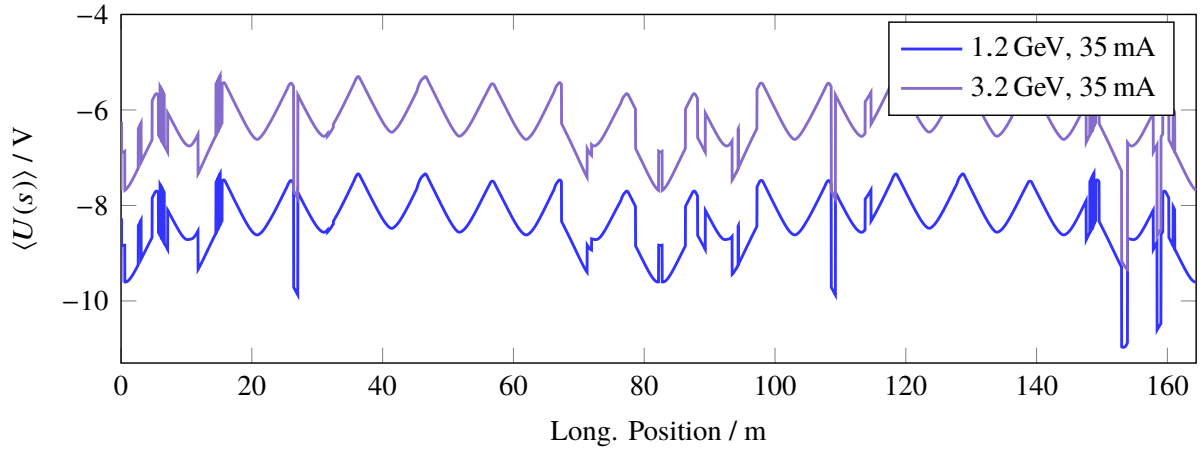

Figure 4.5: Average beam potential of the storage ring for beam energies of 1.2 and 3.2 GeV at a beam current of 35 mA.

Beam Potential

The resulting time averaged potential at the beam center is shown in figure 4.4. Here, the beam potential is required to be equal to zero at the surface of the vacuum chambers. It has been calculated by utilizing the developed MATLAB script 1DBEAMPOT (see appendix B.2.2 for more information). Here, a beam energy of 1.2 GeV and current of 35 mA is used. The figure is split up into two parts. The upper graph shows the beam potential and the corresponding transversal beam pipe geometry for the first half of the storage ring. The bottom graph shows the second half.

Summarily, the average beam potential $\langle U(s) \rangle$ shows an oscillating behavior due to beam dimension variations with an amplitude of approximately 10 % in reference to its longitudinal average. This behavior is superimposed by the volatile potential change due to utilization of beam pipes of different geometries.

The emphasis on the relative amplitude variations is made, as the depth of the potential scales linearly with the beam current in the accelerator, leading to an increment of the beam's charge density. Of course, this scales the longitudinal gradient accordingly, leading to a change in the longitudinal movement of ions (compare equation (2.47)). Figure 4.5 shows the storage ring's beam potential for a current of 35 mA for 1.2 and 3.2 GeV. As the beam width increases with energy, the absolute depth of the potential increases by approximately 30 % from 1.2 to 3.2 GeV.

Error Estimation

The calculated beam potential of the storage ring is an approximation as an analytical expression of the potential cannot be derived for the existing complex geometries of the beam pipe in the storage ring.

Instead, the beam potential has been determined separately for the horizontal and vertical boundary conditions which are given by the corresponding beam pipe diameters. By averaging the values of both potentials, the beam potential has been estimated. Here, the standard deviation of both potentials to their average can be used as an error estimation. It results in a relative average uncertainty of approximately 10 %.

Additionally, the dimension of the beam is derived on basis of the optical functions with a fixed horizontal and vertical tune ($Q_x = 4.619$ and $Q_z = 4.431$). The optical functions, however, are changing with tune, resulting in variations of the beam width, which affects the beam potential depth. Thus, all

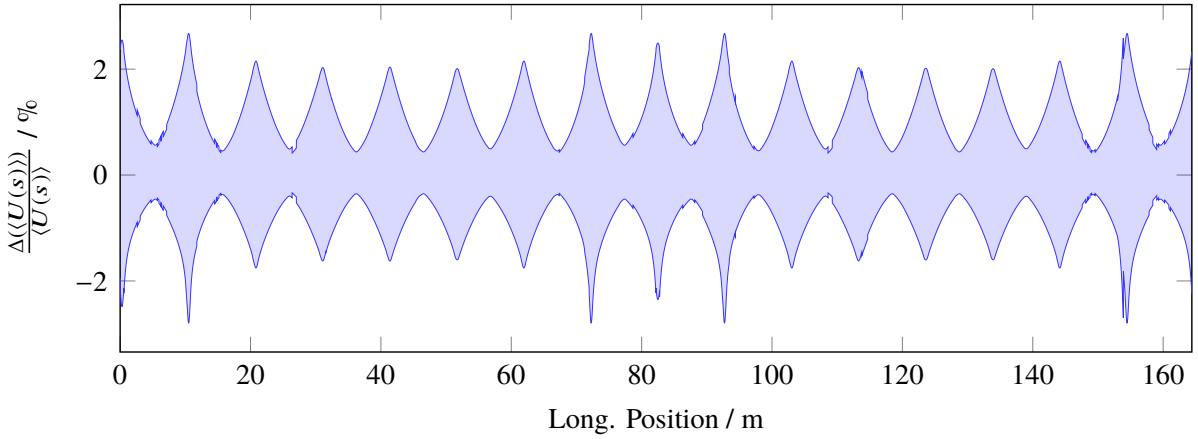

Figure 4.6: Relative error of the beam potential at 1.2 GeV due to the coupling between horizontal and vertical plane ((7.2 ± 2.7) %, compare section 2.3.3).

shown beam potential's are valid only for the configured tune. However, for small variations of the tune in the order of 0.1, the alteration of the beam potential, its shape, depth and location of potential hollows, is negligibly small.

Besides the optical functions, the beam width is dependent on the emittance and the betatron coupling coefficient κ. Whereas the natural emittance of equation (2.35) can in principle be used for the horizontal emittance, the vertical emittance is dependent on κ (measured by [Zan13] to be (7.2 ± 2.7) %). The error imposes an uncertainty in the beam potential which is visualized in figure 4.6. Here, the relative error on the beam potential amounts to maximal 2.5 %.

4.2.2 Estimating the Static Neutralization in Potential Hollows

The ions' confinement in potential hollows can be explained by energy considerations. Ions are produced by the electron beam all along the accelerator. Here, an ion, produced at s_{prod}, has an initial potential energy of $eU(s_{\text{prod}})$. Ions have an average kinetic energy of 38.8 meV at the moment of their generation (compare section 2.1.1). Obviously, they can only pass a potential barrier which is lower than the sum of their kinetic and potential energy. If the potential barrier is higher, they are trapped. Here, only additional kinetic energy, transferred by collision with other trapped ions or the electron beam, may enable a passage through the barrier. If the confining electric potential is deformed, the variation in the ion's potential energy may enable an escape from the potential hollow. This deformation results from the repulsive ions' space charge while more and more ions accumulate in the potential hollow.

The energy considerations, on one hand, can be used to identify potential hollows. The concept of deformation of the beam potential by the ions' space charge, on the other hand, is used to estimate a quantity which one may call *static neutralization*. It is the unpreventable[5] local neutralization level of ions in these potential hollows.

[5] Ion accumulation in potential hollows is unpreventable in case of inherently stable transversal ion trajectories of at least one ion species. The accumulation can be slowed down or hindered by applying supplementary clearing mechanisms such as beam shaking or filling gaps (see chapter 6).

Identification of Potential Hollows

To identify the potential hollows, a map of the positions of every functional ion clearing electrode in the storage ring's lattice is generated. At the storage ring, nearly all clearing electrodes are positioned in the vicinity of the quadrupole magnets. As will be discussed in section 6.1 in more detail, these clearing electrodes are an integral part of the quadrupole chambers. With the known geometrical alignment of the clearing electrodes to other elements in the accelerator, their positions have been added to the storage ring's lattice definition.

The clearing electrodes are biased with a high voltage of typically −3 kV. They are positioned above or below the beam at the edge of the quadrupole chamber and thus have a distance of 22 mm to the beam center. Due to the electrode's position and the geometry of the beam pipe, its electric potential drops to −118 V at the beam center, as will be discussed in section 6.1. Also the electrode's potential decreases longitudinally with increasing distance to it. The electric potential is superimposed with the beam potential to obtain a realistic $\langle U(s) \rangle$ for a clearing electrode voltage of −3 kV.

The tool 1DStatNeut, implemented in MATLAB, identifies potential hollows and estimates the static neutralization on basis of the shape of the beam potential (see appendix B.2.3 for more details). The algorithm identifies them by tracking ions along the accelerator utilizing the Euler-Newton method[6]. The algorithm consecutively generates test ions every 1 cm along the accelerator and tracks their longitudinal movement in $\langle U(s) \rangle$. If a test ion, generated at position s_0, reaches the position of a clearing electrode, the algorithm concludes that a potential hollow is not existent at s_0. If the tracking time exceeds a specific threshold time in which the test ion has not reached an electrode, the algorithm marks this position as a potential hollow.

Concept of Static Neutralization

In case produced ions with stable trajectories are not removed from potential hollows by supplementary clearing measures, which will be discussed in chapter 6, they accumulate there. Here, only natural clearing processes by e.g. beam heating, which is discussed briefly in appendix A.13, reduce the number of trapped ions. These processes typically occur on a longer timescale than the neutralization time and only reduce the growth rate of the trapped ion population insignificantly.

During the process of accumulation, every newly produced ion in the potential hollow is a new positive charge carrier, repelling other positively charged ions. Hence, the accumulation stops when the beam potential is neutralized by the ions' space charge. Subsequently, excess ions are ejected from the ion accumulation in the potential. The dynamic of this ejection process at the (local) space charge limit is complex as the interaction of the trapped ion population with different masses with each other is a non-linear and time dependent[7] problem. No analytical model is capable of mapping the problem adequately.

The developed concept of static neutralization is a drastic simplification of this accumulation process on basis of a linear space charge model. Also only the longitudinal ion motion along the accelerator's beam potential is considered as the transversal oscillation amplitudes are small compared to the longitudinal dimension of the accelerator. In this model, the local neutralization is interpreted as cause of a local

[6] The Euler-Newton method is one of many tracking methods which can be used to numerically determine the trajectory of a particle which is exposed to a force field. For more information, see e.g. [Joy07].

[7] The ions move under the influence of the electrical field of the beam and their neighboring ions. While the electrical field of the electron beam, also varying with time due to the bunched structure of the beam, can be described suitably, the electrical field generated by numerous moving ions is a chaotic system. Sophisticated numerical tracking simulations like MOEVE Pic Tracking (see [Mar13]) are capable of mapping such problems and simulate the dynamic processes within the ion population.

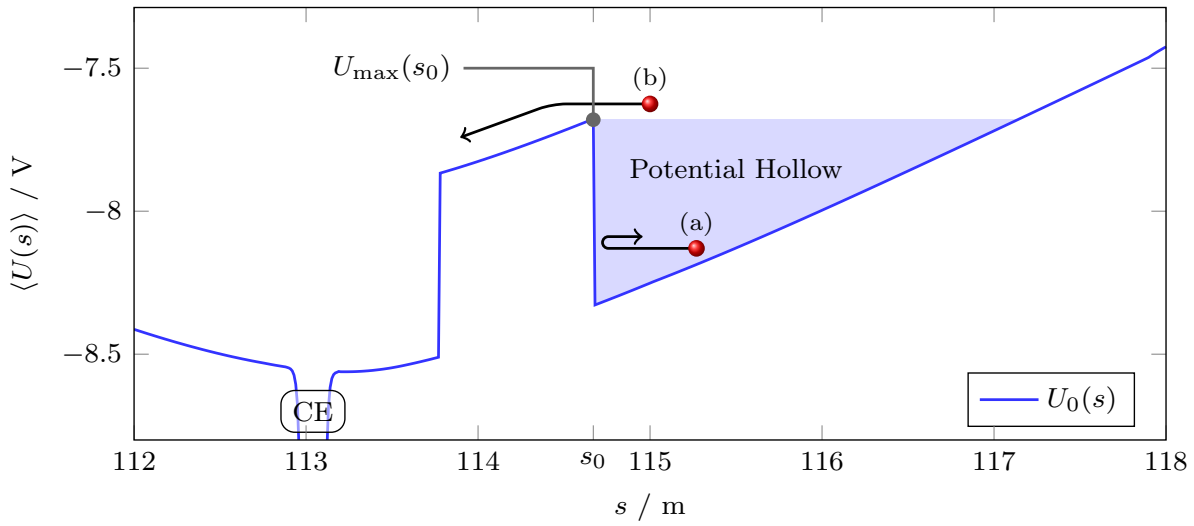

Figure 4.7: Exemplaric section of the beam potential of the storage ring around a potential hollow. Initially, an ion (a), produced within the unfilled potential hollow, has not enough kinetic energy to overcome the potential barrier which hinders its propagation towards a clearing electrode (CE). As additional ions accumulate the potential $U_0(s)$ is deformed the way that is on the same potential level as $U_{\max}(s_0)$. Thus, ions like (b) in the potential hollow can pass the barrier and reach the clearing electrode.

deformation of the beam potential by the ions' space charge. The local neutralization at longitudinal position s is defined as

$$\hat{\eta}(s) = \hat{\eta}_{\text{dyn}}(s) + \hat{\eta}_{\text{stat}}(s) \,.$$

Here, the local neutralization is caused, on one hand, by ions on their way towards clearing electrodes, which one may call *dynamic neutralization* $\hat{\eta}_{\text{dyn}}(s)$. On the other hand, by ions which accumulate in potential hollows and form a static neutralization $\hat{\eta}_{\text{stat}}(s)$ there. This part of the neutralization is attributed to be "static" as it is the local neutralization level in the potential hollow of a trapped ion population in its equilibrium for $t \to \infty$.

The linear space charge model works as follows: Each ion, produced at position s, slightly deforms the beam potential at its position. When it follows the field gradient towards the potential minimum, it deforms the local beam potential for other ions. An ensemble of ions does the same on every ion position. The ions interact with each other due to their local potential deformation. If the ions of the ensemble are spatially separated from each other by a longitudinal distance of centimeters, their mutual repulsive space charge force is negligibly small. If the separation distance is decreased below centimeters, the strength of this force increases. Consequently, the mutual repulsion of the ensemble leads to a longitudinal dispersal of this accumulation. If the ensemble is longitudinally confined to a potential hollow, as shown in figure 4.7 between 114.7 and 117.1 m, it cannot disperse. As more ions accumulate in this potential hollow, the neutralization rises and deforms the local beam potential $U_0(s) < 0$ according to the linear space charge model as

$$U_{\max}(s_0) = \left(1 - \hat{\eta}_{\text{stat}}(s)\right) \cdot U_0(s) \,. \tag{4.2}$$

Thus, by increasing the neutralization, the local beam potential is elevated as the beam's attracting force is diminished for the ions. Here, it is implicitly assumed that the transversal density distribution of the ion population, generating the repulsive ion potential which superimposes the beam potential, is equal to the electron beam's distribution.

Rearranging the previous formula, an expression for the static neutralization in potential hollows is received as

$$\hat{\eta}_{\mathrm{stat}}(s) = 1 - \frac{U_{\mathrm{max}}(s_0)}{U_0(s)} \,. \tag{4.3}$$

$U_{\mathrm{max}}(s_0)$ is the potential at position $s_0 \neq s$, the highest point in the potential barrier, which hinders ions in the potential hollow to move towards a clearing electrode. For the exemplaric potential hollow in figure 4.7, $U_{\mathrm{max}}(s_0)$ is labeled. When the neutralization reaches a level of $\hat{\eta}_{\mathrm{stat}}$, the local potential is elevated the way that it is equal to $U_{\mathrm{max}}(s_0)$. The potential hollow is "filled up". Here, the ion accumulation in the potential hollow stops, as excess ions are longitudinally ejected through the potential barrier and are removed by a clearing electrode.

Note that the static neutralization is independent of the (local) pressure of the vacuum system. The pressure only determines the time scale after which the potential hollow is filled up[8].

Prevention of Static Neutralization

To prevent static neutralization, the installation of clearing electrodes at least in the local minima of the beam potential is advised. These minima are located in every horizontally defocussing quadrupole magnet. To additionally avoid a high static neutralization level in the accelerator, the usage of beam pipes of equal geometry is recommended to prevent volatile rises in the beam potential, which may act as a potential barrier. If the beam pipe geometry cannot be modified sufficiently, the installation of additional clearing electrodes at the minima of these potential hollows is advised [Alv87a, section 3].

Beam Current and Energy Dependence

The depth of the beam potential scales linearly with beam current. This implies that $U_{\mathrm{max}}(s_0)$ of individual potential hollows scales accordingly. Thus, in accordance to equation (4.3), the static neutralization is invariant for different beam currents.

For a variation of the beam energy, the static neutralization changes. As the beam energy rises, the transversal beam width increases which results in a decreased depth of the beam potential. This beam width increment also changes the transversal shape of the beam potential, additionally shifting the beam potential's depth as the potential still has to fulfill the boundary conditions. Because the boundary condition of different beam pipe geometries have to be valid at different distances from the beam center, this shifting is different for each geometry. Consequently, $U_{\mathrm{max}}(s_0)$ and $U_0(s)$ change differently with beam energy, resulting in an energy dependence of the static neutralization.

Corrections to the Static Neutralization in Potential Hollows

The ions' initial kinetic energy is neglected in the general definition of the static neutralization, given in equation (4.3). Thus, $U_{\mathrm{max}}(s_0)$ should be more precisely be rephrased as $U'_{\mathrm{max}}(s_0) = U_{\mathrm{max}}(s_0) - E_{\mathrm{therm}}/\mathrm{e}$, where E_{therm} is the initial kinetic energy of a trapped ion. As $E_{\mathrm{therm}} \gtrsim 0$, $\hat{\eta}_{\mathrm{stat}}$ is only an upper approximation. Because ions initially are produced with thermal velocities, the average of E_{therm} is equal to 38.8 meV (compare section 2.1.1). Thus, for a beam potential depth in the order of −10 V, the relative alteration of the static neutralization due to this correction is half a percent. However, in dependence of

[8] If there are no clearing mechanisms present in the potential hollow, the number of ions in the potential hollow increases linear with time. The time it takes until the potential hollow is filled up can be estimated out of the neutralization time T_n, which is dependent from the local pressure. After a time $T_n \cdot \langle \hat{\eta}_{\mathrm{stat}}(s_{\mathrm{hollow}}) \rangle$ the potential hollow is "filled up". $\langle \hat{\eta}_{\mathrm{stat}}(s_{\mathrm{hollow}}) \rangle$ is the average static neutralization in the potential hollow.

Energy / GeV	1.2	1.7	2.3	3.2
η_{stat} / %	1.57	1.71	1.85	2.03

Table 4.1: Static neutralization of the storage ring for different beam energies. The values for η_{stat} are obtained by calculating the beam potential at different beam energies using 1DBeamPot. The generated potential has been analyzed by 1DStatNeut which identifies potential hollows and determines their local static neutralization.

the kinetic energy distribution of the ion ensemble in the potential hollow, an escape of ions for $\hat{\eta} < \hat{\eta}_{\mathrm{stat}}$ is possible. The ions' escape rate is difficult to estimate as the ions' mutual space charge interactions alter their kinetic energy distribution in the potential hollow.

4.2.3 The Storage Ring's Static Neutralization

The beam potential of the storage ring for a beam energy of 1.2 GeV and a current of 200 mA, which has been calculated by 1DBeamPot, is used to estimate the static neutralization. Here, 1DStatNeut identifies the longitudinal position and scale of potential hollows, identifies $U_{\mathrm{max}}(s_0)$ for each and eventually calculates $\hat{\eta}_{\mathrm{stat}}(s)$ within them using equation (4.3).

Figure 4.8 shows the beam potential in its native (blue) and space-charge deformed state (violet) along the storage ring. The corresponding local static neutralization in the potential hollows, causing the space charge deformation of the potential, is shown as red curve below. 11 significant potential hollows with $1\,\% \leq \hat{\eta}_{\mathrm{stat}} \leq 10\,\%$ can be found. For five potential hollows, the local static neutralization reaches values above 10 % up to 21.5 %.

At approximately $s = 40\,\mathrm{m}$, $\hat{\eta}_{\mathrm{stat}}(s)$ rises to 12.9 % for a length of 9.4 m. This is due to a missing clearing electrode in the vacuum chamber of quadrupole QD9. Here, an older type of quadrupole chamber is installed at which no clearing electrode is provided.

It amounts to a total[9] static neutralization η_{stat} of 1.57 % in the shown scenario. The static neutralization is independent on the beam current, as mentioned in section 4.2.2. As already discussed, the static neutralization changes with energy of the electron beam as its beam size changes. Table 4.1 shows η_{stat} for the storage ring for different beam energies. In the typical energy regime of the storage ring between 1.2 and 3.2 GeV, the total static neutralization increases to over 2 %.

Reduction of Static Neutralization in the Storage Ring

On basis of the previous analysis, the possibility of a reduction of the static neutralization for the storage ring is discussed. To reduce η_{stat} there are two possibilities. The installation of equal beam pipe geometries in the storage ring is advised as potential hollows are prevented. The complete revision of the storage ring's vacuum chambers to one single elliptical beam pipe geometry is not possible because the inner geometry of several functional elements of the storage ring cannot be altered without replacing the component. Instead of pursuing this expensive and labor-intensive endeavor, the focus should be on the installation of additional clearing electrodes at crucial positions, in case these sections will be modernized in future. Clearing electrodes should be positioned in the minimum of the particular potential hollows in order to clear it completely.

In the following list, ideal clearing electrode positions will be given. The list is sorted by the impact on η_{stat} in descending order. The relative positions "upstream" and "downstream" of a particular element in

[9] The total neutralization is determined from the average of the local neutralizations $\hat{\eta}_{\mathrm{stat}}(s)$ (see equation (2.23) in section 2.2.5).

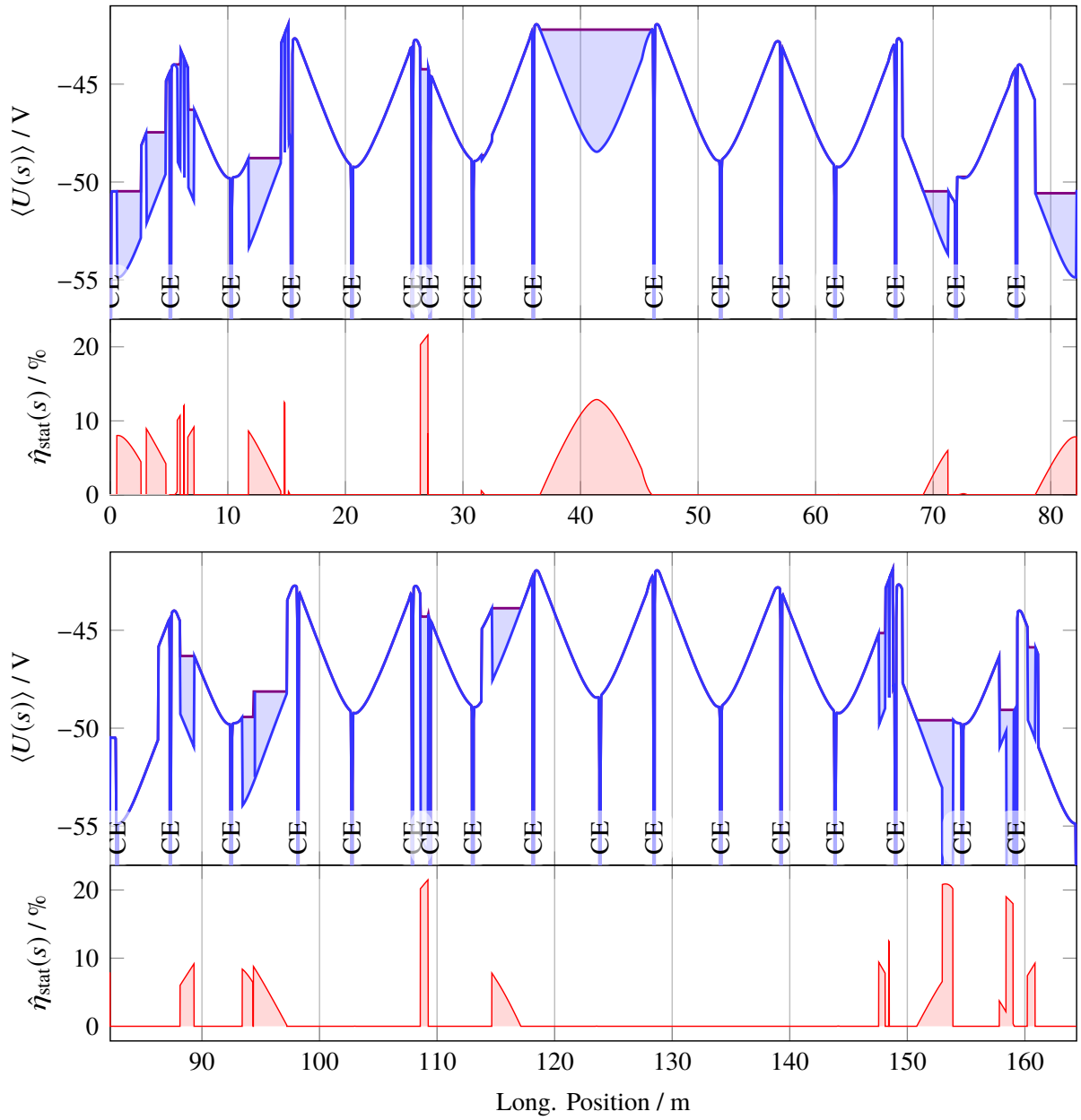

Figure 4.8: Average beam potential of the storage ring at the beam center at 1.2 GeV and 200 mA. The deformation of the beam potential due to local accumulation of ions which form a static neutralization is shown. The upper part of the figure shows the first half of the storage ring whereas the bottom part shows the second half. For each half the average beam potential (blue) and its deformed state (violet) due to static neutralization is shown. Also the corresponding local static neutralization $\hat{\eta}_{\mathrm{stat}}(s)$ is shown for each half in the lower graph. The beam potential is also deformed by the potential of clearing electrodes, whose longitudinal position in the lattice is denoted by CE.

the lattice are given in reference to the propagation direction of the electron beam. Since η_{stat} is stated in units of ‰, its reduction is given as an absolute relation.

- At $s = 41.37\,\mathrm{m}$, at quadrupole QD9, a new beam pipe should be installed with an integrated clearing electrode. This would reduce the static neutralization by approximately 4.4 ‰.
- At $s = 152.97\,\mathrm{m}$, a clearing electrode should be integrated into the vacuum chamber in vicinity to injection septa MSI30. If it is positioned as close as possible upstream of the septa, the electrode's field should attract all ions, accumulating in the septa's potential hollow. The termination of this potential hollow would reduce the static neutralization by approximately 1.5 ‰.
- A clearing electrode, installed at $s = 93.43\,\mathrm{m}$, would clear the potential hollow which reaches from $s = 93.4$ to $97.2\,\mathrm{m}$, if the potential barrier at $s = 94.36\,\mathrm{m}$ is terminated by removing an extant beam position monitor and replacing it with a round beam pipe with an inner radius of 5 cm. A decrease of the static neutralization of 1.2 ‰ would be the result.
- A clearing electrode positioned at $s = 82.18\,\mathrm{m}$, upstream of quadrupole QD17, would reduce the static neutralization by 1 ‰. Downstream of this quadrupole, a clearing electrode is already installed. Yet, due to the elliptical beam pipe of QD17 surrounded by round beam pipe geometries in the rf section, two clearing electrodes are essential to clear both potential hollows upstream and downstream of it. The same is true for the opposing straight section. Here, an additional clearing electrode, installed at $s = 0.56\,\mathrm{m}$, would have the same effect. It would decrease the static neutralization by 0.8 ‰.
- To clear the potential hollows at extraction septa MSE6 and MSE22, a repositioning of the already installed clearing electrodes is advised. If the distance between septa and electrodes can be reduced to at least 3 cm, each electrode's electric potential at −3 kV bias voltage is attractive enough and ions are drawn out of the potential hollows[10]. This would reduce the static neutralization by 0.8 ‰ each.
- Additional clearing electrodes at $s = 3.07$, 11.76, 71.25, 89.32 and 114.66 m would clear potential hollows at transitions between round and elliptical beam pipe geometries. An installation would reduce η_{stat} by 0.6, 0.8, 0.4, 0.5 and 0.6 ‰.

If all suggested changes would be followed, the total static neutralization for a beam energy of 1.2 GeV would be reduced by 1.3 % to a value of 0.21 %. In figure C.11 in the appendix, the corresponding beam potential and static neutralization are shown.

4.3 Ion Accumulation in Vicinity of Dipole and Quadrupole Magnets

In this section the influence of the accelerator's magnetic fields on the trajectories of ions will be discussed. As the fields' influence cannot be neglected in most cases, they alter the ions' accumulation behavior. To study the ion accumulation in presence of these fields, a 2D tracking tool has been developed.

In the following section a detailed motivation for this investigation is given. In section 4.3.2 the 2D tracking tool TracTIon is presented. Here, the tool's features will be elucidated by reference to the simulated scenario in the storage ring. On one hand, in section 4.3.3 the tool is used to simulate trajectories of individual ions to analyze the effect of magnetic fields on them. In sections 4.3.4 and 4.3.5, on the other hand, TracTIon is utilized to track a continuously increasing population of ions until a

[10] Here, the maximal depth of the MSE's potential hollow has to be compared with the clearing electrode's potential. The depth is maximal with 13 V if the accelerator is operated at a beam energy of 1.2 GeV and a current of 200 mA. The electrode's longitudinal electric potential on the beam axis shows a value of −13 V at a distance of 3.5 cm from the electrode. Thus, it must be positioned closer to the potential hollow than 3.5 cm to distort the potential enough to draw trapped ions away.

dynamic equilibrium of ion generation and clearing emerges. The resulting local neutralization is used to identify additional potential hollows and discuss possible extended ion clearing measures. Since the production process of photo ionization due to synchrotron radiation in dipole magnets is implemented in TracTion, the local equilibrium ion density distribution can be determined and will be discussed in section 4.3.6.

4.3.1 Motivation for an Investigation

As already discussed in theory in section 2.4.1, the longitudinal motion of ions is a key component of the ion clearing mechanism by clearing electrodes. Here, the longitudinal electric gradient, generated by charge density variations of the beam along the accelerator, transports ions towards the electrodes. This transport is mandatory for ion clearing as the electrodes only affect the ions' motion in their close vicinity and thus can only neutralize nearby ions. If this transport is hindered by potential hollows, as has been discussed in section 4.2, an ion population accumulates inside them, increasing the neutralization in the accelerator.

An additional impediment for the longitudinal ion transport are magnetic fields in the accelerator. Here, cross-field drifts of ions occur due to the interplay between the attractive Coulomb force of the electron beam and the Lorentz force due to the magnetic field of the dipoles (compare section 2.4.2). In literature, these cross-field drifts are often discussed in an idealized[11] form, yet their assumptions usually are not applicable in a real accelerator.

In the following sections, ion trajectories and their accumulation in presence of magnetic fields are studied using the tracking tool TracTion. Prior to a brief description of its functional principle, characteristics of quadrupole and dipole magnetic fields are outlined. These magnet types which occur prominently in the storage ring and are implemented in TracTion.

Dipole Magnets The dipole magnets show the highest magnetic field strength in the accelerator. To bend the electron beam on a circular orbit, 24 dipoles are installed in the storage ring, each deflecting the beam by 15°. Because the bending radius of the dipoles is fixed at 10.89 m, the field strength typically ranges from 0.37 to 0.98 T to achieve beam energies of 1.2 to 3.2 GeV. Each dipole has an effective length[12] of 2.88 m [Hän19]. In 42 % of the storage ring's circumference, the magnetic field of dipole magnets is present.

As ion production is additionally increased by the process of photo ionization due to synchrotron radiation in these magnets (compare section 3.4), at a beam energy of 1.2 GeV more than 59 % of the ions (62 % at 3.2 GeV) are produced there. If additionally a longitudinal ion transport is considered, the percentage of ions whose trajectories are affected by these dipole fields is even higher.

Dipole magnets can be assumed to have a purely vertical magnetic field. For an ion with a vertical velocity component, the Lorentz force vanishes. Consequently, the vertical ion motions are not affected by dipole magnets. Inside it, ions perform vertical oscillations within the beam potential. Their dynamics can be described by the theory in section 2.4.1. As already discussed in section 2.4.2, the vertical magnetic field in combination with the horizontal electric field forces ions to longitudinal cross-field drifts. The resulting drift velocity is independent from the ions' mass and thus changes the longitudinal dynamics of the ion population within magnets.

[11] The electric field is assumed to be purely transversal. Additionally, electric and magnetic fields within the magnet are assumed to be constant.

[12] The effective length of a magnet is its length, if the magnetic field is assumed to be constant in longitudinal direction. The integral along s over the real magnetic field, including its fringe fields, is equal to the peak value of the magnetic field times the effective length.

Since most ions interact with dipole fields and their influence on ion trajectories is obvious due to their high field strength, these fields have to be implemented in TracTIon.

Quadrupole Magnets In the storage ring 32 quadrupole magnets are installed, each quadrupole having an effective length of 44.97 cm [Hän19]. Consequently, quadrupole fields are present in approximately 10 % of accelerator. Here, ions are only produced by impact ionization. Thus, the percentage of ions which are produced within quadrupole magnets at a beam energy of 1.2 GeV is only approximately 7 % (approximately 6 % at 3.2 GeV). To adjust the optics of the storage ring for a typical tune of $Q_x = 4.612$ and $Q_z = 4.431$, a quadrupole strength pair of $k_{\mathrm{QF}} = 0.63\,\mathrm{m}^{-2}$ and $k_{\mathrm{QD}} = -0.583\,\mathrm{m}^{-2}$ is needed according to the SimLib. QF quadrupoles are supplied with an adequate current to provide a quadrupole strength of k_{QF}. QD quadrupoles provide k_{QD}. Their magnetic gradient amounts to $g_{\mathrm{QF}} = (\mathrm{d}B_z/\mathrm{d}x)_{\mathrm{QF}} = 2.5\,\mathrm{T\,m}^{-1}$ and $g_{\mathrm{QD}} = (\mathrm{d}B_z/\mathrm{d}x)_{\mathrm{QD}} = -2.3\,\mathrm{T\,m}^{-1}$ at a beam energy of 1.2 GeV. For 3.2 GeV, $g_{\mathrm{QF}} = 6.67\,\mathrm{T\,m}^{-1}$ and $g_{\mathrm{QD}} = -6.13\,\mathrm{T\,m}^{-1}$ are achieved.

When ions are produced in quadrupole magnets or being longitudinally transported to quadrupole fields, their trajectories are perturbed by the Lorentz force induced by quadrupole fields. Theoretically, also a longitudinal cross-field drift velocity emerges, similiar to the case within dipole magnets. In literature, the trajectory perturbations and cross-field drifts in quadrupole magnets are often neglected (compare e.g. [MTH88, section 2.4] and [Hin11, section 8.5]). However, in these studies only ion amplitudes in the order of the beam width have been considered. Ions, which are produced by synchrotron radiation photons in dipoles, potentially may show amplitudes comparable to the beam pipe's half diameter. At these amplitudes, the local magnetic field strength is higher than the field strength in vicinity of the beam which results in an increased influence of quadrupole fields on the ions' trajectories. Therefore, fields of quadrupole magnets are implemented in TracTIon, too.

Implementing Realistic Conditions To study the motion of ions in vicinity of dipole and quadrupole magnets in a realistic simulation scenario and thus non-idealized way, the following circumstances have to be considered properly:

- **Thermal Initial Velocity of Ions:** In an environment with complex configurations of electric and magnetic fields, the ions' initial condition may alter their trajectories significantly. Therefore, the thermal velocity of generated ions has to be considered. Their average initial velocity scales with $m_i^{-1/2}$ (compare equation (2.3)).
- **Realistic Beam Potential:** The electric field is caused by an electron beam with Gaussian charge density distribution. The resulting transversal electrical field $\vec{E}(x, z)$ approximately increases linearly within the beam (compare equation (2.43)) but decreases to zero if the distance to the beam center is increased further. The resulting beam potential, computed in [Alv87b], is based on this charge distribution and thus is a realistic approach for the beam potential.
- **Longitudinal Electric Field:** The longitudinal electric field due to longitudinal variation of the electron beam's charge density acts as longitudinal force on ions. The emerging longitudinal transport carries ions into quadrupole and dipole magnets. In them, the additional longitudinal field may alter the ions' cross-field drift trajectories.
- **Quadrupole and Dipole Magnets with Fringe Fields:** The field of an accelerator's dipole magnet with field strength $B_{z,\mathrm{dp}}$ has a relative field error of below $2 \cdot 10^{-4}$ inside its iron yoke to enable a stable orbit of the beam in the accelerator [Wil00, section 3.3.2]. Therefore, the field can assumed to be homogeneous. Also the magnetic field of the quadrupole magnets can assumed to be longitudinally constant within their yokes. However, this is not true for adjoining regions outside the yokes. Here, the dipoles' and quadrupoles' magnetic field steadily decreases to zero

with increasing distance from the yokes. Thus, the magnetic field is inhomogeneous there. These fringe fields lead to variations of the ions' gyro radii in these regions, locally influencing the ions' trajectories.

- **Ion Production due to Photo Ionization:** In dipole magnets the production of ions is augmented due to the process of photo ionization by synchrotron radiation photos emitted by the electron beam. As a result, the transversal ion production map in dipole magnets shows an asymmetry in the horizontal plane which increases along the magnet. Local production rates $\hat{R}_{\mathrm{p,pi}}(s)$ and local production maps $\check{R}_{\mathrm{p,pi}}(x, z, s)$ within dipole magnets are known and have been discussed in detail in section 3.4.

Simplifications The magnetic field of a dipole is orientated vertically. Thus, the vertical motion of ions proceeds unhindered by dipole fields as the emerging LORENTZ force vanishes. Also the average vertical amplitude of ions is small compared to the horizontal one, as the ion production map resembles the dimension and shape of the electron beam in most parts of the accelerator. Due to this small vertical amplitude, the horizontal magnetic field, which is experienced by ions in a quadrupole field, is negligible small. Thus, the resulting alteration of their trajectory due to the LORENTZ force can be ignored.

In contrast, the horizontal component of ion trajectories within dipole magnets is influenced by the LORENTZ force. In them, ions may be generated with a horizontal amplitude in the order of the beam pipe's half diameter due to photo ionization by synchrotron radiation photons. When these ions are being produced in or being transported through quadrupole magnets, they experience a higher vertical magnetic field than ions which have an amplitude in the order of the beam size. Therefore, also the field of quadrupole magnets is expected to alter the horizontal trajectories of these ions.

It is therefore justified to restrict the tracking simulation TRACTION onto the horizontal and longitudinal plane. This simplifies the implementation of the tracking algorithm and additionally reduces computational time.

TRACTION is used to simulate ion trajectories and/or identify areas with increased dynamic neutralization. Consequently, the effect of the ion population *on the electron beam* is not relevant here. Thus, TRACTION uses a so called weak-strong[13] simulation model in which the influence of the electron beam on ions is simulated and the reversed case is omitted. Accordingly, computations of individual electron trajectories and their effect on the ion population is replaced by determination of the electric potential of a rigid electron beam with known dimensions.

Another necessary simplification is the neglect of mutual space charge interactions within the ion population. An implementation of these interactions would increase computational time for a simulation with N_{ion} ions by a factor of $N_{\mathrm{ion}} \cdot (N_{\mathrm{ion}} - 1)$ [14].

[13] In the field of numerical simulations of two-stream scenarios, this terminology is used often [Ohm00, section 1]. A numerical simulation of ions within an electron beam is a two-stream scenario in which one stream, the ion population, influences the other stream, the electron beam, and vice versa. Another two-stream scenario is the simulation of the reciprocal interference of two electron beams within an electron collider. The two streams are given the attributes "weak" and "strong" describing the degree of their effect on the other beam. A "strong" stream affects the second stream by its space charge and alters e.g. its width or its optical functions. A "weak" stream does not affect characteristics of the other stream. For example, a weak-weak or rigid bunch/beam simulation model is used to compute the electromagnetic forces of the two streams, represented by e.g. two equilibrium charge distributions, on each other. Here, the alteration of the streams due to these forces is omitted, as both already are in equilibrium. In a strong-strong model it is necessary to simulate the dynamics of the two streams and include their effect on each other. Because this model is the most realistic, it also is in need of far higher computational capacities as a weak-strong or rigid bunch/beam model.

[14] For a computation of the electric field strength acting on one ion, its distance to all other $N_{\mathrm{ion}} - 1$ ions has to be evaluated. This computation has to be repeated for all ions.

4.3.2 The 2D Tracking Simulation TracIon

The developed tool TracIon is a two-dimensional simulation tool using a Kunge-Kutta tracking algorithm to compute trajectories of individual ions or a complete ion population within electric and magnetic fields of a confined section of an accelerator. All aspects for a simplified but realistic simulation scenario, as discussed in section 4.3.1, are implemented. In appendix B.2.4, TracIon is described in full detail.

Different aspects of TracIon, its functional principle and the simulation process will be explained in the following based on the chosen simulated scenario of the storage ring.

Simulation Scenario

To obtain informative and useful results from the TracIon simulation, the chosen simulation scenario must be located in a representative region of the storage ring. The storage ring's lattice consist of 16 FODO cells, in which separations between QF and QD quadrupole magnets are either drift sections or are accompanied by dipole magnets. From one QF to the next QF quadrupole, the beam potential $U(s)$ goes from one local maximum to the next. In the QD quadrupole between them the potential is minimal (compare figure 4.4 in section 4.2.1). Thus, ions, starting from both QF quadrupoles and following the longitudinal gradient, will eventually arrive at the QD quadrupole. As the absolute value of the longitudinal gradient, experienced by these ions, is similar, $U(s)$ can be approximated as being symmetric around the minima of the beam potential. Consequently, the smallest representative region of the storage ring is one half-cell of the FODO lattice. This half-cell should include one dipole and at least one quadrupole to assess their influence on the accumulation of ions. In close vicinity to almost every quadrupole, an ion clearing electrode is installed. Since ion accumulation is always an interplay between ion generation and clearing, these have to be included in the scenario, too.

To simplify the computation of the beam potential is it also useful to avoid regions in which the beam pipe geometry changes. On one hand, this would complicate the definition of the area of valid ion propagation in the simulation. This area may be called ion propagation environment (IPE). If ions exceed this environment, they are cleared from the ion population as they are neutralized when interacting with the beam pipe. On the other hand, the calculated beam potential $U(x, s)$ only takes into account the beam pipe diameter at s. For $|x| \gg \sigma_x(s)$, the potential may be altered due to the different beam pipe geometry at an adjacent s-position. Also in regions with various beam pipe geometries, potential hollows may be present where the number of ions is elevated ($\hat{\eta}_{\mathrm{stat}}(s) > 0$). There, the ions' mutual space charge force has a dominant influence on the their motion. Consequently, simulations with TracIon would lead to wrong results as these forces are not considered.

Considering these constrains, an area of the storage ring, shown in figure 4.9, has been chosen as the TracIon simulation scenario. It is located in the storage ring lattice between $s = 46.5\,\mathrm{m}$ and $s = 56.8\,\mathrm{m}$ in an arc section. It starts in the center of quadrupole QF10 and ends in the center of QF12. At the start and endpoints of this scenario, the beam potential shows a local maximum. QD11 and its local clearing electrode is located in the minimum of the beam potential. Consequently, two half cells of the FODO lattice are included in the scenario. Between QF10 and QD11 dipole magnet M10 is located and M11 in-between QD11 and QF12. Along this region within the storage ring an "elliptical" beam pipe geometry is used with a half diameter of approximately 51.5 mm. Consequently, no potential hollows are present in this region and all ions are in principle able to reach the ion clearing electrode near QD11.

Close to QF10 and QF12 ion clearing electrodes are installed. Since these electrodes lie outside the simulated region, for simplification they are shifted to the center of each quadrupole, hindering ions from leaving the IPE. The beam pipe confines the IPE horizontally.

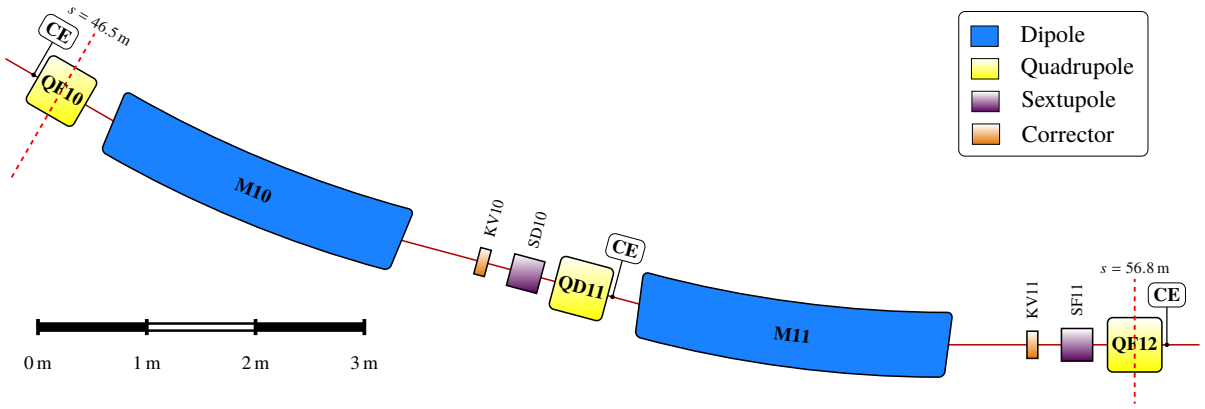

Figure 4.9: Lattice of the parts of the storage ring, which is used in TRACTION simulations. The dashed lines indicate beginning and end of the simulation scenario. The lattice elements denoted in bold lettering are implemented in TRACTION, whereas corrector and sextupole magnets are neglected. CE denotes the position of clearing electrodes.

The comparably weak magnetic fields of sextupole (SD10, SF11) and corrector magnets (KV10, KV11) are omitted[15].

The beam energy is set to 1.2 GeV. A beam current of 35 mA is set to be stored as it is a current which is often used as typical maximal current in booster and storage mode operation. All ions are assumed to be singly ionized only. The pressure is set to be constant along the IPE at 10^{-8} mbar.

Beam Potential and Magnetic Fields

The beam potential and the magnetic fields within the ion propagation environment are precomputed prior to the execution of the actual ion tracking procedure. They are calculated at grid points on a two-dimensional map. The map size is equal to the IPE. Although the dipole magnets deflect the beam by a total angle of 30°, this deflection is not reproduced on the maps. Instead, the coordinate system of the maps and the IPE follows the convention of the curvilinear co-moving coordinate system (compare section 2.3.1). As changes in the beam potential along the longitudinal axis s is more gradual than along the horizontal axis x, the map has different resolutions in s and x directions. For this scenario, the s-resolution is equal to $\Delta s_{\text{res}} = 1$ cm whereas the x-resolution is $\Delta x_{\text{res}} = 250\,\mu$m.

Beam Potential The beam potential $U(x, s)$ is precomputed according to equation (2.42) as the time average beam potential generated by the electron beam with known beam width $\sigma_x(s)$ and $\sigma_z(s)$. The beam width modifies the shape of the beam potential and varies along s.

The known electric potential of the clearing electrodes with bias voltage of −3 000 V, which will be presented in section 6.1.2 and is shown in figure 6.5, is also implemented in this scenario. The electrodes' potential superimposes the beam potential $U(x, s)$.

[15] The vertical corrector magnets have a negligible horizontal field strength of (39.9 ± 0.8) mT at maximum current of 8 A [Mal13, field strength calc. using section 4.2 and table 3]. The horizontal corrector magnets show a field strength of 4.4 mT at a maximal current of 16 A which is 1 % or below of the dipoles' total field strength [Pro18, calc. from integrated field strength of section B4]. If sextupole magnets are operated with a maximal current of 200 A, a vertical magnetic field strength in the horizontal plane of 140 µT is present at a distance of $x = 3$ mm from the beam center [Zim86, field strength calc. from section 5.1 b)].

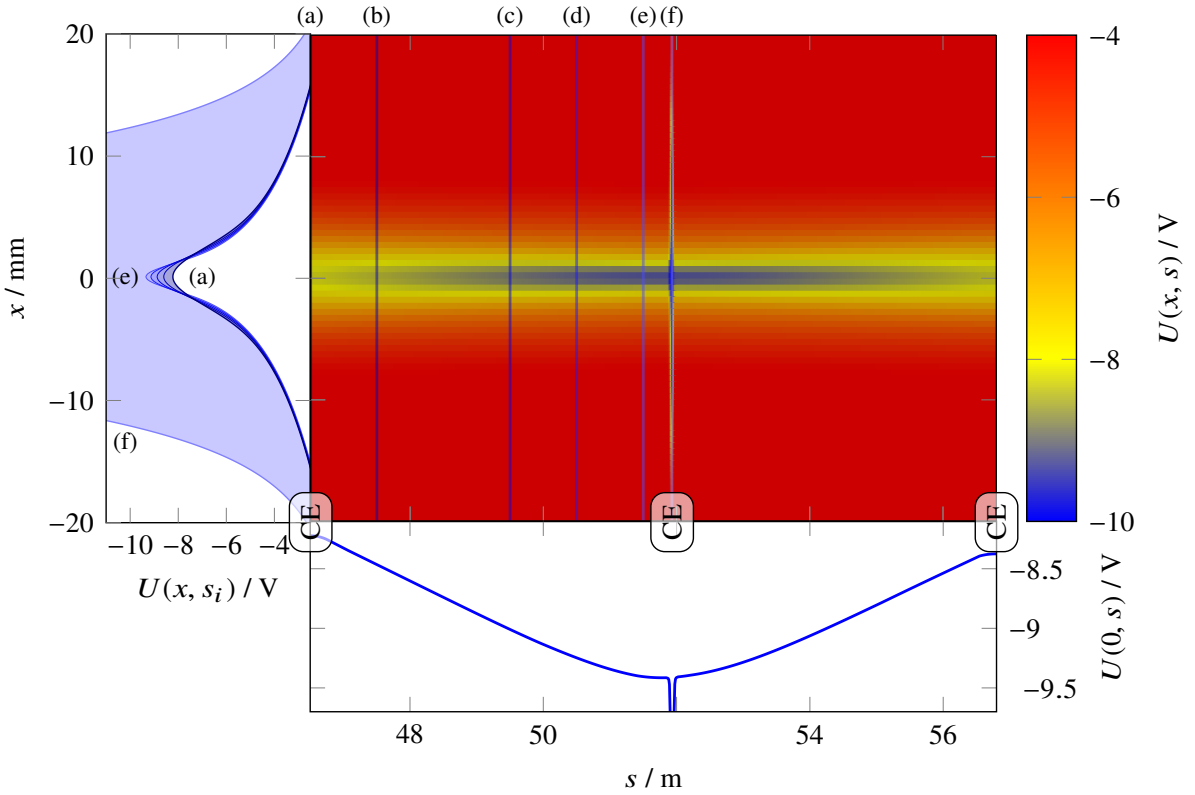

Figure 4.10: Horizontal and longitudinal shape of the beam potential of a part of the storage ring at a beam energy of 1.2 GeV and current of 35 mA. The surface plot shows the beam potential which is deformed by the clearing electrode (CE) at approximately $s = 52$ m. The same deformation is visible in a longitudinal cut through this potential at $x = 0$ mm, which is shown in the graph below. The graph on the left shows horizontal cuts through the beam potential at different longitudinal positions s_i. s_i corresponds to 46.5, 47.5, 49.5, 50.5, 51.5 and 51.93 m.

The resulting beam potential for this scenario is shown in figure 4.10. The surface map shows an excerpt of the potential in-between $x = \pm 20$ mm. The longitudinal shape of the potential in the beam center at $x = 0$ mm along the entire region is shown in the bottom plot. At the longitudinal borders of the IPE, clearing electrodes (CE) are positioned[16]. In-between them the potential $U(0, s)$ steadily decreases from −8.1 V to −9.3 V at around $s = 52$ m. Then it rises again to −8.3 V. Produced ions are consequently expected to follow the longitudinal field gradient to the local potential minimum, where a clearing electrode is positioned at $s = 51.93$ m. Its field deforms the beam potential locally and neutralizes every ion which propagates into its reach. The horizontal shape of the potential $U(x, s_i)$ at different s_i is shown in the left graph. The first five s_i are 46.5, 47.5, 49.5, 50.5 and 51.5 m and visualize the variation of the beam potential's shape as the horizontal beam dimension decreases with increasing s_i. The sixth s_i at 51.93 m shows the local potential deformation by the clearing electrode.

Magnetic Fields The vertical magnetic fields of the dipole and quadrupole magnets are precomputed on a map with the same size and resolution as the beam potential map. The dipole magnets' field strength $B_{z,\mathrm{dp}}$ is adjusted in accordance with the beam energy E to deflect the electron beam onto its designated

[16] Here, no deformation of the beam potential by these clearing electrodes takes place, as they are only "virtually" positioned there. Their position is shifted from the scenario-averted sides of the quadrupole magnets QF10 and QF12 to the center of the corresponding quadrupoles where they limit the IPE in the longitudinal direction.

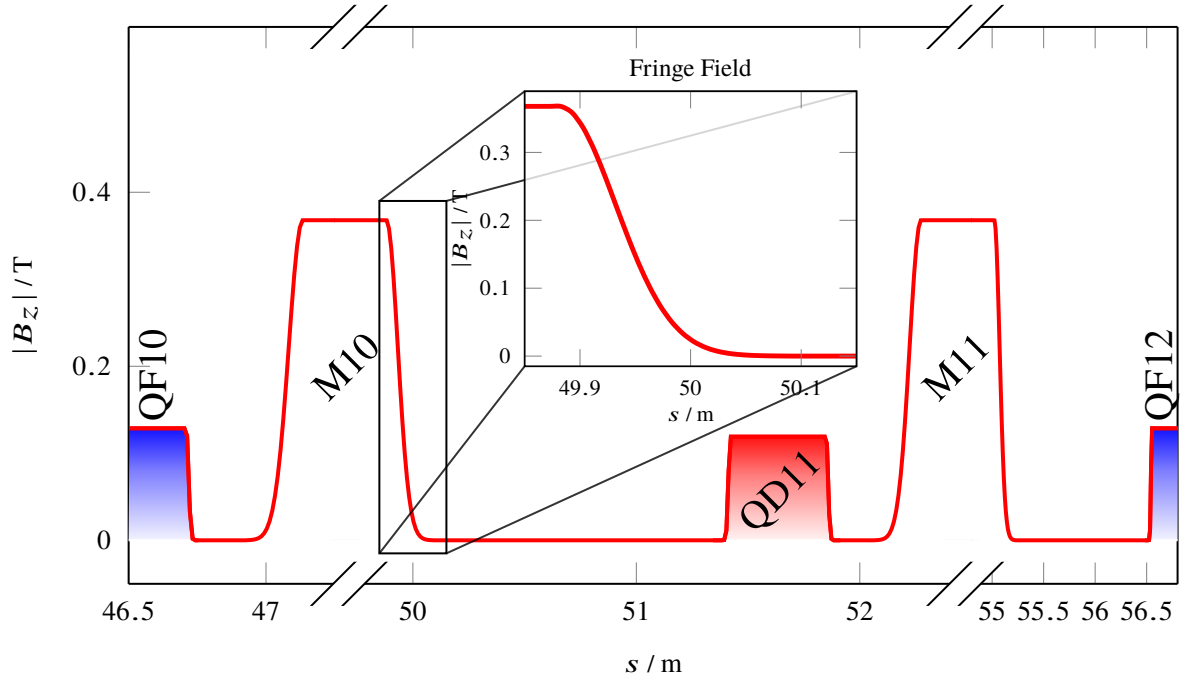

Figure 4.11: Magnetic field configuration of an excerpt of the storage ring at 1.2 GeV which is used in TracTion. It includes two dipole magnets, M10 and M11, and the quadrupoles QF10, QD11 and QF12. QF10 and QF12 are denoted in blue, as their field gradient shows the opposite sign of QD11, which is marked in red. The quadrupoles magnetic fields increase linear with horizontal distance from the beam axis. They also feature adequate fringe fields. Note that the longitudinal scale changes along the s axis.

trajectory with a radius of 10.89 m. Along the x axis, $B_{z,\mathrm{dp}}$ is constant. The vertical field of the quadrupole magnets, in contrast, is not. It rises linearly with increasing distance x from the beam center with spatial gradient g_{QF} or g_{QD} in the respective quadrupoles. The gradients are adjusted in accordance to beam energy and desired tune of $Q_x = 4.612$ and $Q_z = 4.431$.

Both magnet types feature longitudinal fringe fields. Here, the transitional field between the magnets' field to adjacent field-free regions is decreasing like a Gaussian bell curve with distance from the magnets' iron yokes. The decrementation rate of the field strength is determined from the difference between the magnets' geometric and effective field length.

Figure 4.11 shows the absolute value of B_z along the ion propagation environment for a beam energy of 1.2 GeV. All transitions from magnetic fields to field-free regions are realized with adequate fringe fields. In case of the quadrupoles, the shown field strength is the maximum value of the quadrupole field at the horizontal edge of the IPE. Table 4.2 shows parameters used for the dipole and quadrupole magnets in this TracTion simulation scenario.

For more information regarding the beam potential and magnetic fields, see appendix B.2.4 on page 281.

Tracking Algorithm

To compute trajectories of ions within the IPE, TracTion uses a 4th order Runge-Kutta method in combination with a momentum correction scheme based on the ions' individual potential and kinetic energy. This algorithm determines the spatial increment of the ion in the longitudinal and horizontal plane (Δs and Δx) for a fixed time increment Δt when exposed to local electric and magnetic fields.

For more information, see appendix B.2.4 on page 282.

Dipole	R	10.89	m
	l_{eff}	2.875	m
	l_{geom}	2.747	m
Quadrupole	k_{QF}	0.630	m^{-2}
	k_{QD}	–0.583	m^{-2}
	l_{eff}	44.97	cm
	l_{geom}	43.00	cm

Table 4.2: Parameters of dipole and quadrupole magnets used in the TracTion simulation scenario of the storage ring. The magnets' geometrical lengths have been obtained from [Hän19].

Ion Generation and Clearing

For a beam current of 35 mA, the storage ring is filled with approximately 10^{11} electrons in total (compare equation (2.1)). Assuming a moderate neutralization of 5 %, an amount of more than 10^8 ions are present in a segment of the storage ring with length of the scenario shown in figure 4.9. The computation of the motion of all those ions for a simulation timespan of a few 10 ms is practically not feasible within a suitable amount of time when using the presently available computing power of a desktop computer. Initial conditions like start position and velocity, ionization status and mass of generated ions follows different probability distributions. Therefore, each ion shows an individual trajectory in the simulation scenario. Several ions share similar initial conditions and thus follow a similar trajectory. Therefore, the simulation is speed up by replacing μ_{ion}[17] ions of the same species by one macro-ion (see e.g. [Mar13, section 3.1]). In electromagnetic fields, macro-ions behave like "normal" ions with ionization status Z and mass $m_i \approx A \cdot m_{\text{p}}$. Only in cases where the absolute number of ions is relevant, the ion number is scaled by μ_{ion}. For example, in case η, $\hat{\eta}(s)$ or a simulated clearing electrode current is calculated.

The ion population is simulated from $t_0 = 0\,\text{s}$ to a configured end at t_{end}, where an ion population is in equilibrium, for example. For a given Δt, which is the order of several ns, ions are tracked for typically more than 10^6 iteration steps. Each iteration, the time index $\iota = t/\Delta t + 1$ is incremented. Initially, the ion propagation environment is empty. In TracTion, macro-ions are not produced statistically in time. Instead, ion generation subroutines are executed at specific ι. The specific time indices depend on the production rate of the process, the beam current and μ_{ion} and are elaborated in appendix B.2.4 on page 286 in more detail.

Impact Ionization The ion generation subroutine of impact ionization generates a macro-ion of a specific species at every longitudinal grid point s_{gen} of the precomputed maps. To which species each of the generated macro-ion belongs, is assigned randomly on basis of their production probability (compare section 3.3.2). The horizontal start position is chosen randomly using a Gaussian probability distribution with a standard deviation which resembles $\sigma_x(s_{\text{gen}})$. Consequently, the production map of these ions resembles the dimension of the electron beam. The horizontal and longitudinal initial velocities are also assigned randomly, using the one-dimensional mean thermal velocity (compare equation (2.3)) as the standard deviation of a Gaussian probability distribution.

[17] In general, μ_{ion} is much greater than one and in the order of 1 000. Its value depends on the scale of the simulated scenario. For a given time frame the ion motion is simulated in, the computation time for the scenario depends on the available computing power and scales with the number of simulated macro-ions. For a larger simulation scenario, μ_{ion} must be chosen bigger than for a smaller scenario to actually compute the motion of approximately the same number of macro-ions within the same time. If μ_{ion} is choosen too large, the statistical significance decreases.

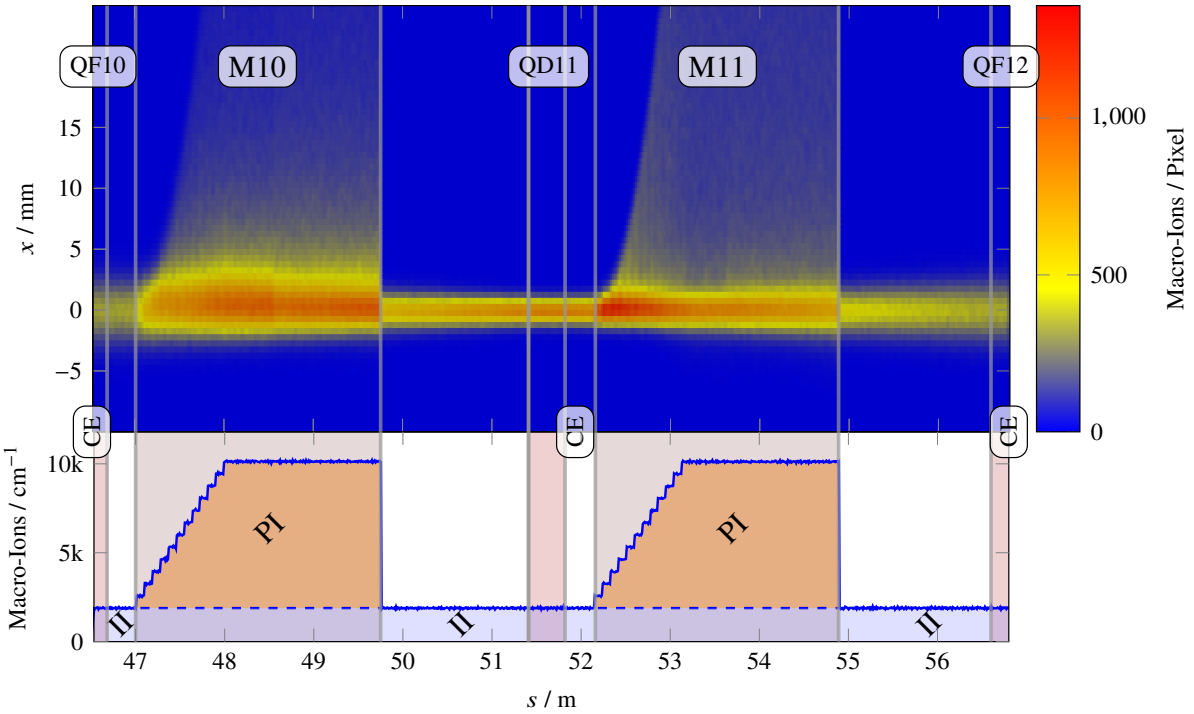

Figure 4.12: Ion production map in the horizontal and longitudinal plane for an excerpt of the simulated part of the storage ring at a beam energy of 1.2 GeV and 35 mA. The surface plot shows initial horizontal and longitudinal positions of approximately six million macro-ions being produced by TracTIon. The bottom plot shows the longitudinal macro-ion line density in this scenario. Here, II denotes the contribution of impact ionization, whereas PI denotes the part of photoionization. CE mark the longitudinal positions of ion clearing electrodes.

Photo Ionization In dipole magnets M10 and M11, additionally photo ionization by synchrotron radiation photons occurs. The transversal ion production map of this process is asymmetric in the horizontal plane (compare figures 3.18 to 3.20 in section 3.4.4). The transversal ion production map at every grid point within the dipole magnets has been simulated by PhotoIonProd and is used in TracTIon as a local probability distribution to randomly assign the horizontal starting position of generated macro-ions. In contrast to impact ionization, the local photo ionization production rate is not constant along s within the dipole magnet (compare figure 3.22 in section 3.4.4). It first rises linearly in s along the dipole until a position is reached which corresponds to an angle of beam deflection α of α_{break}. For $\alpha > \alpha_{\text{break}}$, it then stays constant within the rest of the dipole. Therefore, the number of produced ions at each s_{gen} is defined by a function. This function is piecewise constant for s_{gen} which corresponds to $\alpha \leq \alpha_{\text{break}}$ to approximate the linear rise of the local production rate. For $\alpha > \alpha_{\text{break}}$, it is constant.

Figure 4.12 shows distribution of the horizontal and longitudinal starting positions of approximately six million generated macro-ions in the IPE. The impact ionization process, denoted as II, produces a longitudinally constant line density of macro-ions. It resembles the electron beam in dimension and thus shows the highest number of macro-ions per pixel in quadrupole QD11 where the horizontal diameter is smallest. Towards the QF quadrupoles where the beam widens, the horizontal ion distribution broadens, too. Outside dipole magnets M10 and M11, the distribution is symmetric around the x axis. Inside, macro-ions are additionally generated by photo ionization, denoted as PI in the figure, deforming the distribution asymmetrically. The linear rise of the longitudinal macro-ion linear density in the first part of a dipole is approximated by 10 steps.

Ion Clearing Ions are cleared or removed from the simulation, when they reach specific positions in the ion propagation environment.

The macro-ions are cleared when

- they reach the clearing electrodes in the center of quadrupoles QF10 and QF12 at the longitudinal borders of the IPE. The charge of removed macro-ion is transformed into a current, detected at each clearing electrode.
- they show a horizontal amplitude of $\pm x_{\mathrm{vc}}$. Here, the ion impacts on the surface of the beam pipe and is neutralized.
- they are neutralized by the clearing electrode in vicinity of quadrupole QD11.

4.3.3 Realistic Ion Trajectories Inside and Outside of Magnetic Fields

TracTIon can operate in two different modes. One mode is used to simulate the ion accumulation process for a defined time, typically until the population is in dynamic equilibrium of ion production and clearing. It can be used to quantitatively determine $\hat{\eta}(s)$ or η for example. The other mode enables the simulation of trajectories of individual ions. This makes a qualitative investigation of individual trajectories of ions possible which are exposed to a particular configuration of electric and magnetic fields.

In the following sections, the single-ion tracking mode is used to visualize ion trajectories at different positions in the IPE. The gained knowledge is essential to understand the form of the local neutralization distribution which results from simulation of the accumulation of ions which will be discussed in section 4.3.5 Additionally, resulting trajectories are compared with theoretically predicted ones.

Ion Motion without Magnetic Fields

The transversal and longitudinal motion in absence of magnetic fields has been discussed in section 2.4.1 on a theoretical level already.

The top graph of Figure 4.13 shows exemplary trajectories of H_2^+, H_2O^+ and CO_2^+ ions starting from position ($x = -2.9\,\mathrm{mm}$, $s \approx 46.74\,\mathrm{m}$) in the magnetic field-free region between quadrupole QF10 and dipole M10. The beam width is equal to 1.74 mm at this position, thus the ions start with an amplitude of $1.66\sigma_x$.

Horizontal Oscillations In the horizontal plane, the ions oscillate around the beam center, as expected from theory. In the shown graph approximately 13 periods of these oscillations are visible for each ion species. Each ion has a different oscillation frequency. H_2^+ completes 13 periods within 20 µs which corresponds to a frequency of 650 kHz. H_2O^+ oscillates with 220 kHz and CO_2^+ with 137 kHz. As theoretical values, 882 kHz for H_2^+, 294 kHz for H_2O^+ and 188 kHz for CO_2^+ are obtained which are conclusively 35 % higher than the simulated frequencies. This discrepancy can be explained by the high amplitude of the ions' oscillation. Theoretical predictions on basis of equation (2.46) assume a horizontal electric field which increases linearly with ion amplitude, resulting in an oscillation frequency which is independent of the ions' amplitude. In reality, the electric fields starts to decrease for amplitudes $> \sigma_x$ due to the inverse square law of the Coulomb force as the distance from the center of charge increases. This results in a lower oscillation frequency with increasing amplitude. However, the simulated oscillation frequencies follow the relation $\nu_{x,i}^{\mathrm{ion}} / \nu_{x,j}^{\mathrm{ion}} = \sqrt{m_j / m_i}$ and thus scale correctly.

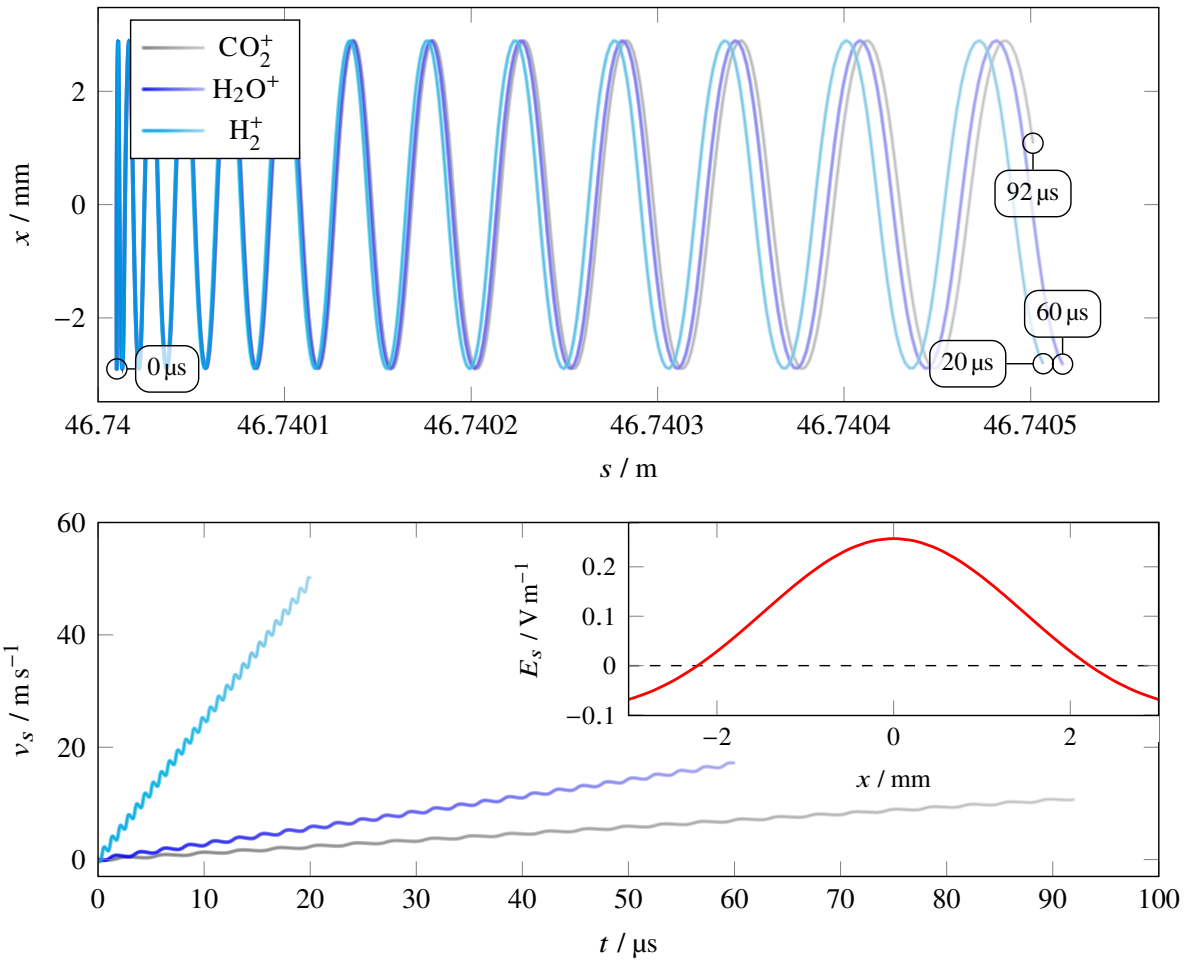

Figure 4.13: Simulated ion trajectories within the beam potential without the influence of magnetic fields at a beam energy of 1.2 GeV and a current of 35 mA ($\sigma_x \approx 1.6$ mm). The top graph shows the evolution of trajectories of H_2^+, H_2O^+ and CO_2^+ ions in the IPE with time. The bottom graph shows the longitudinal velocity v_s of each ion. Note that the average velocity increases linear in time because the longitudinal gradient field E_s of the beam potential can assumed to be constant within this s-range. The red curve visualizes the variation of E_s along the horizontal plane.

Longitudinal Acceleration In the longitudinal plane, an accelerated motion towards the minimum of the beam potential is visible. The evolution of the longitudinal velocity v_s with time is shown in the bottom graph of figure 4.13. As considered longitudinal dimensions are small, a constant longitudinal gradient can be assumed. $v_s(t)$ of each ion increases almost linearly with time. When approximating a linear function on each $v_s(t)$ an acceleration of $(2\,484.9 \pm 2.8) \cdot 10^3$ m s^{-2} for H_2^+, $(282.5 \pm 0.3) \cdot 10^3$ m s^{-2} for H_2O^+ and $(116.6 \pm 0.1) \cdot 10^3$ m s^{-2} for CO_2^+ can be determined. With this values the experienced gradient field E_s can be calculated using equation (2.47). H_2^+ experienced a field strength of 0.052 V m^{-1}, whereas H_2O^+ and CO_2^+ have been accelerated with a field of 0.053 and 0.054 V m^{-1}, respectively. The error on the field is omitted as it is below 1 ‰ for each species. According to TRACTION, the average gradient field is equal to 0.052 V m^{-1} for H_2^+ and H_2O^+ and 0.051 V m^{-1} for CO_2^+, which each ion has experienced in this simulation. Consequently, the longitudinal tracking algorithm behaves correctly within an error of below 4 %.

Coupled Longitudinal Oscillations A closer look to each $v_s(t)$ shows an additional oscillatory behavior. Within the simulated time, approximately twice as many longitudinal oscillations are visible than horizontal oscillations. Thus, $v_s(t)$ is modulated longitudinally with a frequency of $2\nu_{x,i}^{\text{ion}}$. This modulation results from the variation of E_s along x. As can be seen in the red curve of figure 4.13 (bottom), $E_s(x)$ is not always positive. For high amplitudes, it changes sign. This is due to the shape of the beam potential (compare figure 4.10 (top, left)): If the beam width decreases along s, the potential in the beam center is deeper than the adjacent potential which leads to a positive E_s there. The increasing depth, however, leads to a steeper potential outside the beam. Outside, the potential is shallower resulting in a negative E_s there. Ions oscillating horizontally with large amplitudes thus experience a longitudinal deceleration for a finite period of time. This longitudinal velocity modulation results in an incoherent quadrupole oscillation which, however, has an amplitude which is small compared to transversal oscillation amplitudes. Therefore, this effect is not expected to have an impact on the electron beam.

Ion Motion in Vicinity of Magnetic Fringe Fields

In regions where fringe fields are present, the vertical magnetic field strength B_z is also dependent on s. Ions, drifting in from field-free regions, experience a LORENTZ force, which compels them onto gyro trajectories in the horizontal plane. $B_z(s)$ deflects ions horizontally and thus gradually transfers their longitudinal velocity into the horizontal plane. This transfer is completed within a quarter of a gyration period. The gyro radius shrinks with increasing $B_z(s)$, while the ions penetrates deeper into the fringe field. The radius is also dependent on the ions' velocity and mass (compare equation (2.49)). If the ion's average gyro radius is smaller than the longitudinal dimension of the fringe field, the longitudinal velocity is transferred to the horizontal plane and is subsequently reversed when it is coupled back to the longitudinal plane.

Thus, an ion can be reflected by fringe fields. If its velocity is high enough, however, the ion is transmitted through the fringe field and propagates within the constant magnetic field of the dipole magnet.

Magnetic Mirror Figure 4.14 shows the two discussed cases. The trajectory of a H_2O^+ ion with an initial velocity of 400 m s^{-1} is shown in the top graph. It is reflected by the fringe field whose field strength is shown in the bottom graph. In the middle graph, the ion's velocity is increased by a factor of ten. The deformation of the horizontal oscillation into a spiral trajectory indicates the gradiual decrement of the ion's longitudinal velocity component while it penetrates the fringe field. When reaching $s = 47.02$ m with an amplitude $x < 0$ mm, it is transported further downstream by the cross-field drift with an average longitudinal velocity of approximately 1 000 m s^{-1}. If it would have reached the dipole magnet's field with $x > 0$ mm, the emerging cross-field drift velocity would have transported the ion back towards the fringe field region. Thus, one may expect a maximal transmission of 50 %.

The minimum longitudinal velocity for transmission of an ion i into a dipole magnet is approximated as [MTH88, section 2.3, equation (31)]

$$v_{s,\mathrm{T}} \cong \left| \frac{\omega_{\mathrm{cycle},i,x}(B_{z,\mathrm{dp}}) \cdot x_{0,i}}{\sqrt{2}} \right| . \tag{4.4}$$

Here, $x_{0,i}$ is the ion's initial horizontal amplitude and $\omega_{\mathrm{cycle},i,x}(B_{z,\mathrm{dp}})$ is the cyclotron frequency of the ion within the dipole magnet (compare equation (2.48)). If a H_2O^+ ion is produced with a horizontal amplitude of $\sigma_x \approx 1.7$ mm, an initial longitudinal velocity of approximately 2 400 m s^{-1} is required for transmission into a magnetic field of 0.37 T (corresponds to a beam energy of 1.2 GeV). A H_2^+ ion

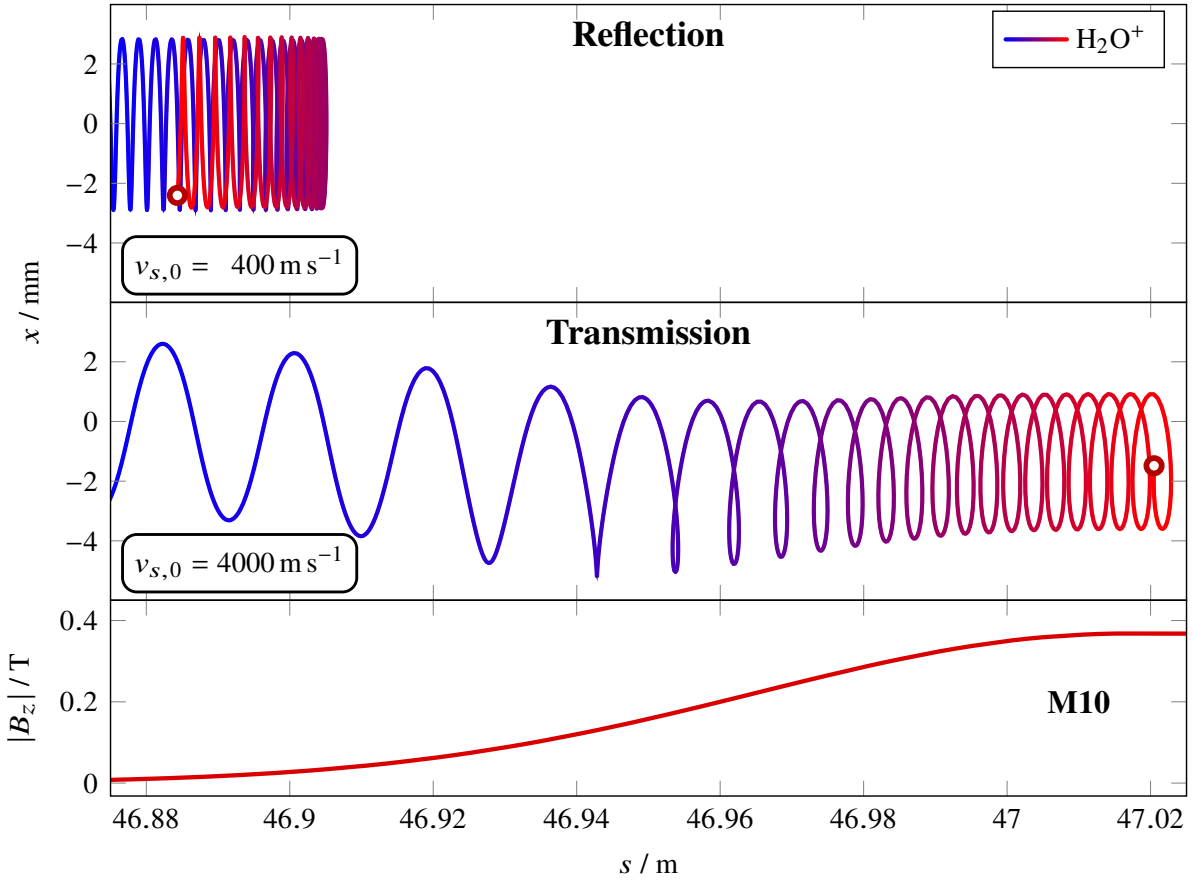

Figure 4.14: Simulated trajectories of a H_2O^+ ion entering the magnetic fringe field of dipole M10 from the left. The top graph shows the trajectory of an ion which has been generated with an initial longitudinal velocity $v_{s,0}$ of 400 m s^{-1} while it is reflected at the fringe fields. The middle graph visualize the trajectory of a transmitted ion which has been generated with a ten times larger velocity. The bottom graph shows the longitudinal variation of the vertical magnetic field in this scenario.

requires approximately 21 800 m s^{-1}, whereas a CO_2^+ ion needs 1 000 m s^{-1}. For a field strength of 0.98 T (3.2 GeV), the required velocities increase by a factor of 2.6.

The average thermal velocity $|v_{\mathrm{rms}}|$ of CO_2^+ is 411 m s^{-1}. For H_2^+, it is 1 927 m s^{-1}. As these thermal velocities are smaller than the corresponding $v_{s,\mathrm{T}}$, almost no transmission of these ions is expected if they are produced in close proximity to the dipole fringe fields. The additional longitudinal velocity obtained from the ions' acceleration by E_s may enable the transmission of ions which are produced away from the fringe fields. For the same amplitude a CO_2^+ ion would need to gain an energy of 0.22 eV to enter a 0.37 T dipole field and 1.5 eV at 0.98 T. For H_2^+, a gain of 4.8 eV and 32.6 eV is required.

Transmission Probability Since the initial amplitude and velocity of the different ion species are assigned randomly on basis of the corresponding probability distributions, a statistical analysis of the ions' transmission is possible. To do so, for each relevant species (H_2^+, H_2O^+, N_2^+,CO^+ and CO_2^+) 200 individual ions have been generated at s = 46.73 m. E_s accelerates them towards the fringe field of dipole magnet M10. Their encounter with the fringe field at s_{b} = 46.79 m is detected. If they subsequently reach the marker at s_{c} = 47.04 m inside the dipole, they are counted as transmitted. In contrast, a subsequent

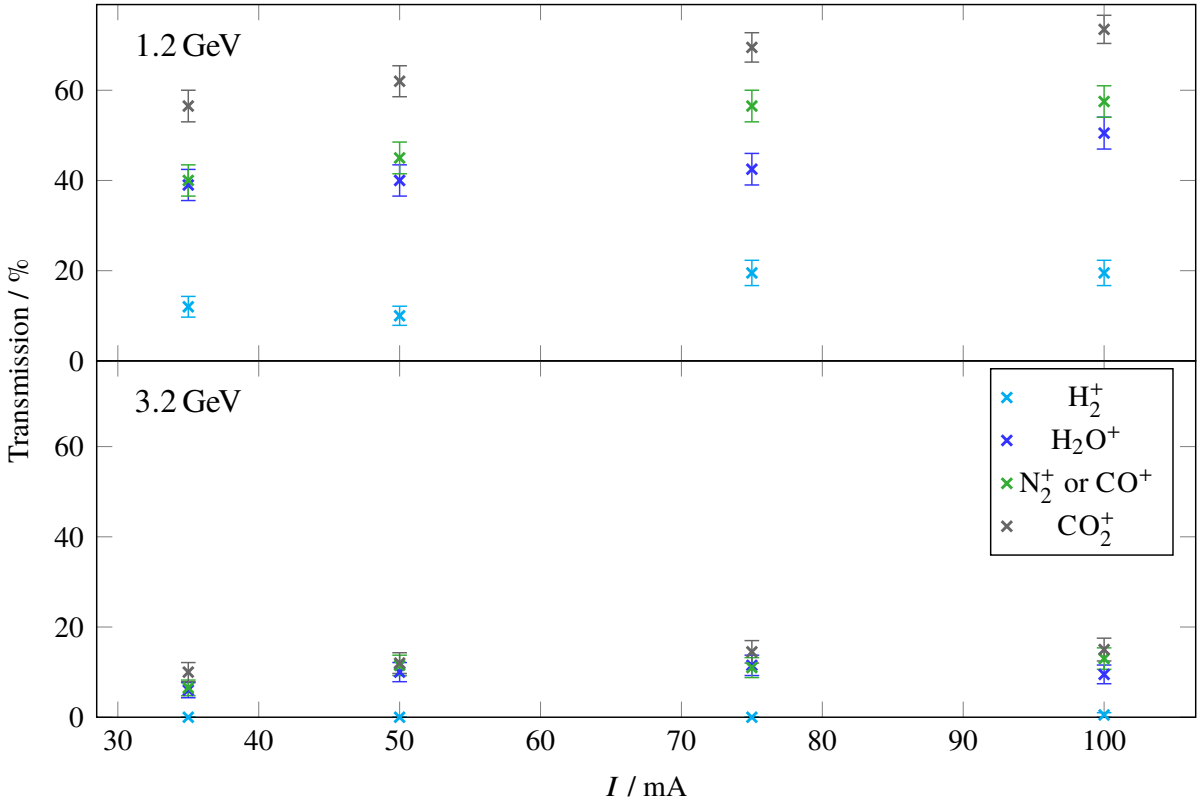

Figure 4.15: Simulated transmission probability of different ion species through the fringe field of dipole magnet M10 at different beam energies and currents.

passage of a position $s_a = 46.77\,\text{m}$ outside the fringe fields indicates that they have been reflected by the fringe field.

Figure 4.15 shows the results of this study. The top graph shows the transmission probability at a beam energy of 1.2 GeV. In general, the transmission probability increases with stored beam current, as ions reach higher velocities due to acceleration by E_s prior to their encounter with the fringe field. For 100 mA beam current, $(74 \pm 5)\,\%$ of the CO_2^+ ions are transmitted. This transmission exceeds the expected maximum of 50 %. The statistical error when simulating only 200 ions is relatively large. However, the transmission probability lies 5σ above the 50 % margin. The excess may results from the marker position for determination of the transmission. It may be positioned too close to the entrance of dipole magnet M10. Thus, ions which eventually will be transported out again by the longitudinal cross-field drift, may have already passed the marker and are counted as transmitted. It is also possible that E_s increases the overall transmission margin as it also transports ions into the dipole magnet.

For lighter ions, the transmission decreases, as the cyclotron frequency scales with their mass, resulting in an increased $\nu_{s,T}$. Only a maximum of $(20 \pm 1)\,\%$ of H_2^+ ions are transmitted, the rest is reflected back. For a beam energy of 3.2 GeV, the transmission probability for all ions decreases to below 20 %. Here, on the one hand, the field strength of the magnets is increased, which causes an increment in $\nu_{s,T}$. On the other hand, the beam dimension is larger in comparison to 1.2 GeV, resulting in decreased depth of the beam potential. Thus, the acceleration of ions by E_s is smaller, preventing access into the fringe fields for most ions due to an insufficient longitudinal velocity. Consequently, H_2^+ ions are not transmitted and CO_2^+ ions only show a transmission probability of $(15 \pm 1)\,\%$ at 100 mA.

As a result, an increased accumulation of trapped[18] ions, which are accelerated by the longitudinal gradient to the minimum of the beam potential, is expected in front of dipole magnets. Also higher dynamic neutralization levels are expected when the beam energy, and thus the magnetic field strength, is increased.

Cross-Field Drifts in Dipole Magnets

The discussion of cross-field drifts in dipole magnets in section 2.4.2 has only been conducted in an idealized way. The horizontal electric field E_x has been assumed to be constant along the ion trajectory. Additionally, the longitudinal gradient field E_s has implicitly been set to zero. In general, these assumptions are not true: E_s is always non-zero except within the center of quadrupole magnets, where the beam dimensions are extremal and the potential shows its local maximum or minimum. Also, E_x is a function of the ions' horizontal position x. Thus, only for a gyro radius close to zero, thus high magnetic field strength B_z, the drift velocity can be approximated as $v_{\mathrm{dp}} = E_x/B_z$ (compare equation (2.51)).

To study the influence of these unconsidered effects, TracIon is used to simulate trajectories of different ion species within dipole magnets where the magnetic field B_z is constant. At a fixed position in the middle of either dipole M10 or M11, ions are generated at various horizontal start positions $x(t_0)$. For each species and $x(t_0)$, 20 ions are generated with thermal velocities. After each single-ion simulation, the average longitudinal velocity $\langle v_s \rangle$ within the dipole magnets is extracted.

The results of this study are shown in figure 4.16. In the following, first the results are described qualitatively and short explanations to observed phenomena are given if possible. Phenomena, whose explanation requires a more detailed discussion, are handled in the sections below.

The top and bottom graphs shows the velocity distribution in dipole M10 and M11 with $B_z = -B_{z,\mathrm{dp}}$, respectively. For both, $\langle v_s \rangle$ decreases to zero for large values of $|x(t_0)|$. Also both show the expected dipole characteristic of the cross-field drift velocity when going from $x(t_0)$ to $-x(t_0)$. Here, $\langle v_s \rangle$ changes sign in case the electric field reverses from $-E_x$ to E_x. Outside the blue area, all ion species show a mass independent drift velocity as expected from theory. Within the area, $\langle v_s \rangle$ increases to its extremal values and decreases to zero as $x(t_0) = \pm 2\,\mathrm{mm}$ is approached. Here in general, $\langle v_s \rangle$ follows the shape of $E_x(x)$, which is proportional to v_{dp}, but $\langle v_s \rangle$ also becomes dependent on the ions' mass.

Within dipole M10, the maximum $\langle v_s \rangle$ of H_2^+ is approximately $3\,300\,\mathrm{m\,s^{-1}}$ whereas the minimum value is approximately $-2\,700\,\mathrm{m\,s^{-1}}$. Consequently, E_s increases $\langle v_s \rangle$ for positive velocities and decreases it for negative ones. Because dipole M11 is positioned on the other side of the beam potential valley, $\vec{E}_s$ points into opposite direction and increases negative $\langle v_s \rangle$ while decreasing positive ones.

Inside the blue area, $\langle v_s \rangle$ of the individual ion species is sorted by mass. Light H_2^+ ions with $A/Z = 2$ reach the highest possible velocities. The heavier the ion, the lower its $\langle v_s \rangle$. In close vicinity to $x(t_0) = 0\,\mathrm{mm}$, on one hand $\langle v_s \rangle$ decreases linearly from left to right for both M10 and M11. This linear decrement does not cross the point $(x(t_0) = 0\,\mathrm{mm}\,,\ \langle v_s \rangle = 0\,\mathrm{m\,s^{-1}})$, as expected for E_x being equal to $0\,\mathrm{V\,m^{-1}}$ in the beam center, but is shifted upward for M10 and downward for M11.

The mass dependent cross-field drift velocities, the linear decrement in $\langle v_s \rangle$ and its upward or downward shift will be explained in the following sections utilizing trajectories of individual ions as visualizations.

[18] The vertical magnetic field of fringe fields also couples the transversal velocity into the longitudinal plane by the Lorentz force. Although reflected by the fringe field, an ion may be able to leave this region if a suitable amount of the horizontal velocity component is coupled into the longitudinal plane. Than it may enter the dipole field or is neutralized by a clearing electrode in the opposite direction.

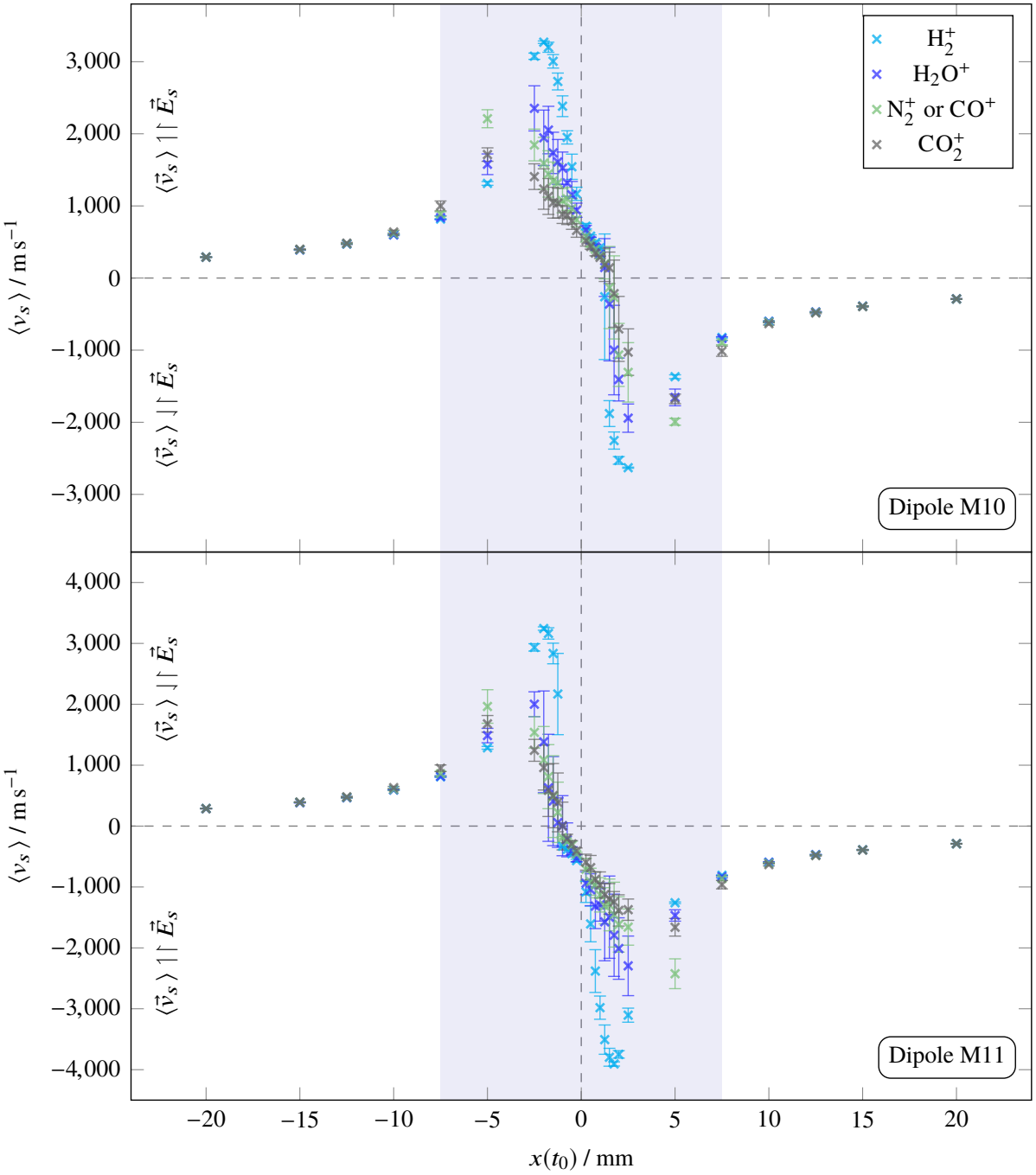

Figure 4.16: Simulated longitudinal cross-field drift velocities for different ion species at a beam energy of 1.2 GeV and a beam current of 35 mA. Here, TRACTION is used as a single-ion tracking-simulation in which the ion's trajectory is recorded. 20 ions of each species are consecutively generated at different horizontal starting positions $x(t_0)$ with randomly assigned thermal velocities. The top graph shows the resulting average longitudinal velocity $\langle v_s \rangle$ of ions which have all being generated in the middle of dipole magnet M10. $\vec{E}_s$ denotes the direction of the longitudinal gradient field at the beam center. Ions with positive $\langle v_s \rangle$ propagate in direction of E_s. Ions with negative $\langle v_s \rangle$ propagate anti-parallel to E_s. For ions which are generated in dipole magnet M11 in the bottom graph, it is the opposite.

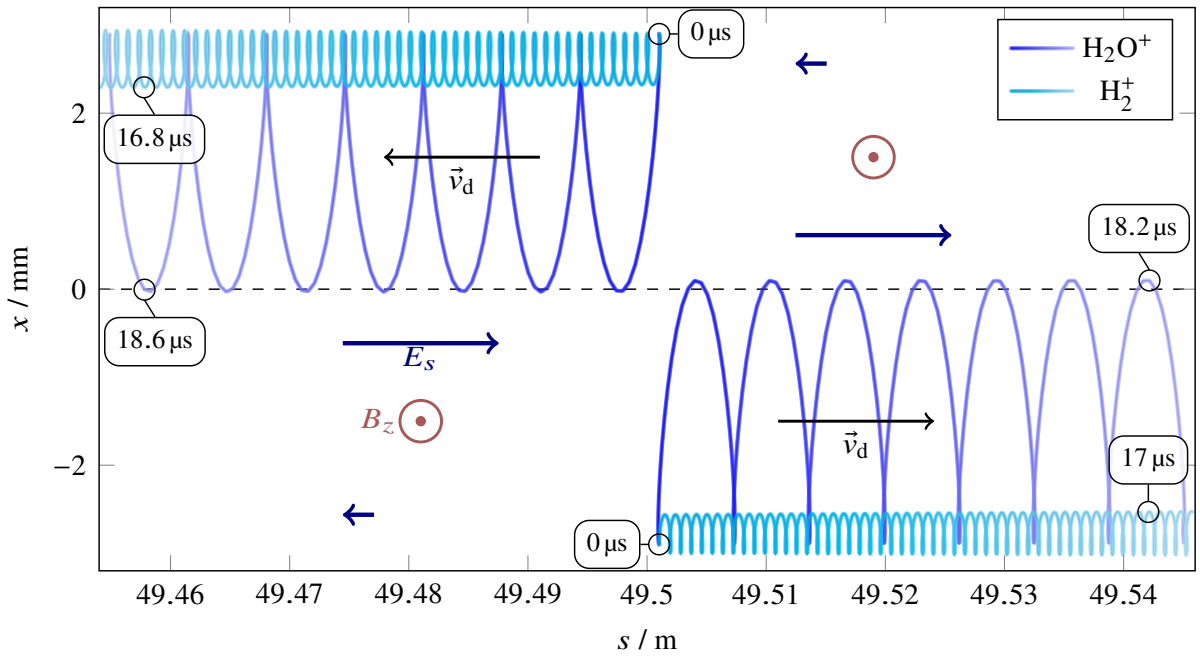

Figure 4.17: Simulated cross-field drift trajectories of H_2^+ and H_2O^+ ions within the constant magnetic field of dipole M10. The beam energy is 1.2 GeV and the stored beam current 35 mA. The ions are generated at the same s coordinate but on opposite sides of the beam. The average horizontal electric field strength for H_2O^+ is approximately $\pm 840\,\mathrm{V\,m^{-1}}$. For H_2^+, it is $\pm 920\,\mathrm{V\,m^{-1}}$. Note that an additional longitudinal gradient field E_s superpose this field configuration and inflict an additional electric force on the ions.

High-Amplitude Cross-Field Drift To visualize the mass dependent cross-field drift velocity exemplarily, the trajectories of H_2^+ and H_2O^+ ions in the center of dipole magnet M10 are shown in figure 4.17. A H_2^+ and a H_2O^+ ion is generated with negligible initial velocity with an amplitude of $x(t_0) = 2.9\,\mathrm{mm}$ and another pair of H_2^+ and H_2O^+ ions with $x(t_0) = -2.9\,\mathrm{mm}$, respectively. This corresponds to an amplitude of approximately $\pm 3\sigma_x(s)$.

As expected, the cross-field drift velocities v_d point into opposite directions when going from $x(t_0)$ to $-x(t_0)$. The light H_2^+ ion ($A/Z = 2$) has a lower mass than the H_2O^+ ion ($A/Z = 18$). Thus, its gyro radius is smaller than the radius of H_2O^+ which results in a less extended horizontal motion. E_x changes along x and showing a value of $0\,\mathrm{V\,m^{-1}}$ in the beam center. The average electric field $\langle E_x \rangle$, which an ion experiences, is therefore dependent on the scale of its the horizontal motion. Due to its large gyro radius, H_2O^+ crosses the zero point for a short time period during its propagation. During this period, v_d is reversed. Thus, $\langle E_x \rangle$ and subsequently $\langle v_s \rangle$ is reduced. In this scenario, $\langle E_x \rangle$ is approximately $\pm 840\,\mathrm{V\,m^{-1}}$ for H_2O^+. For H_2^+, it is approximately $\pm 920\,\mathrm{V\,m^{-1}}$. Consequently, $\langle v_s \rangle$ for the H_2^+ ion is larger than for the H_2O^+ ion.

The variation of E_s along x (compare figure 4.13 (bottom)) also results in different $\langle v_s \rangle$ of the ions. Here, the longitudinal velocity is increased or decreased in dependence of the x range the ions are moving in.

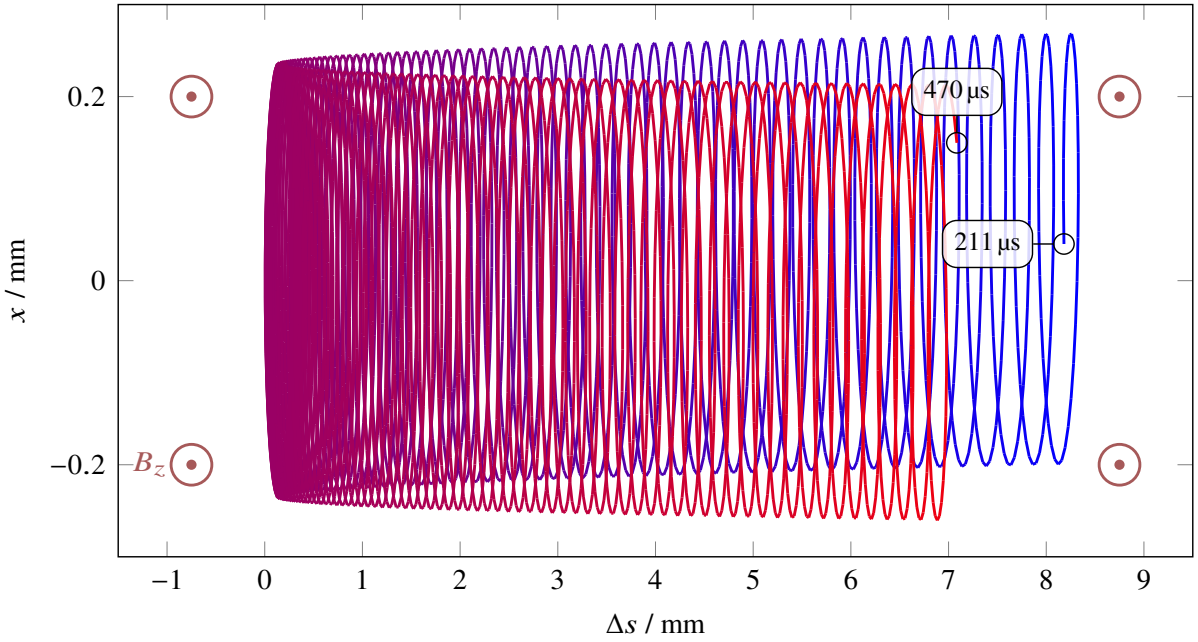

Figure 4.18: Exemplaric trajectory of an H_2O^+ ion with low amplitude within the field of dipole magnet M10. The longitudinal position is given in reference to $s = 49.435\,\text{m}$. The color change denotes the time evolution of the ion trajectory. Note that a longitudinal electric gradient field E_s additionally accelerates the ion downstream.

Low-Amplitude Cross-Field Drift Figure 4.18 shows an excerpt of the trajectory of an H_2O^+ ion with a low initial amplitude of $0.29\,\text{mm} \approx 0.26\sigma_x$. During its upstream cross-field drift v_d, it crosses the zero point of $E_x(x)$ at $x = 0\,\text{mm}$ for an extended time span. In this time span the cross-field drift is reversed, reducing its overall upstream drift velocity.

Additionally, E_s acts on the ion. In this scenario, E_s points into opposite direction of the cross-field drift velocity for low amplitudes. As a consequence, the electric field vector $\vec{E}$, consisting of horizontal E_x and longitudinal components E_s, is not perpendicular to the x axis. Thus, v_d shows an additional component in x direction pointing towards the beam center. Hence, the ion is forced "downward" and spends more time in the negative x regime. This gradually reduces its cross-field drift velocity to zero, eventually reversing it downstream. On the other side of the beam, E_x is reversed to $-E_x$ under conservation of the direction of E_s. Due to change in $\vec{E}$, v_d obtains a new direction while its "downward" component is conserved. Consequently, the H_2O^+ ion drifts away from the beam center, simultaneously increasing the downstream cross-field drift velocity.

The non-point symmetric characteristic of $\langle v_s \rangle$ around the origin in figure 4.16 is caused by this mechanism. For a given $x(t_0)$, $\langle E_x \rangle$ of a heavy ion with large gyro radius is lower than for a light ion. Consequently, $\vec{E}$ is influenced by E_s more strongly resulting in a less parallel orientation of v_d in reference to the s axis. This eventually leads to reversal of longitudinal drift velocity for higher $x(t_0)$. Thus, the definition of a "low" amplitude is dependent on the ion species' gyro radii and thus their mass.

An alternative consideration of these trajectories comes from the conservation of energy. As ions do not gain additional energy within the beam potential, only a transfer between kinetic and potential energy occurs during their cross-field drift. Consequently, they longitudinally drift along the equipotential line of the beam potential. In case E_s is non-zero and the potential is not constant along s, the equipotential line crosses the beam center at a certain position. Thus, an ion, whose trajectory follows this line, will eventually cross the beam center resulting in a reversal of direction of its longitudinal drift.

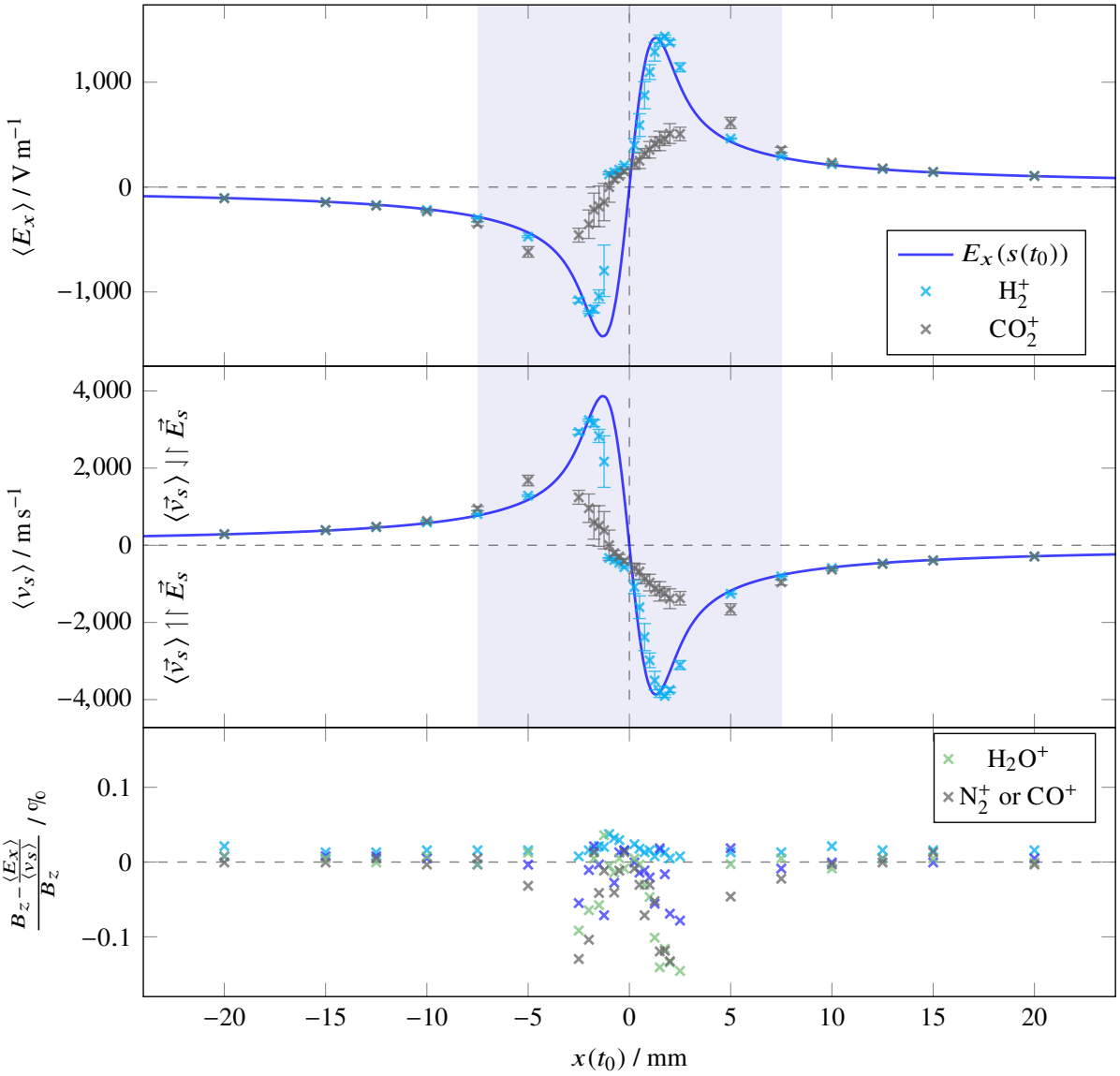

Figure 4.19: Comparison of theoretical and simulated longitudinal cross-field drift velocities in dipole magnet M11 at a beam energy of 1.2 GeV and a current of 35 mA. The top graph shows the average horizontal electric field strength experienced by H_2^+ and CO_2^+ ions and the corresponding field strength $E_x(s(t_0))$ at their longitudinal starting position $s(t_0)$. Resulting cross-field drift velocities $\langle v_s \rangle$ in presence of a magnetic field $-B_{z,\mathrm{dp}}$ are shown in the middle graph with identical color scheme. For positive velocities, $\langle v_s \rangle$ is orientated anti-parallel to the direction of the longitudinal gradient E_s, whereas negative velocities are oriented parallel to it. The bottom graph shows the relative deviation between $B_{z,\mathrm{dp}}$ and a magnetic field, which is reconstructed from $\langle v_s \rangle$ and $\langle E_x \rangle$ of different ion species using equation (2.51).

As can be seen in the top graph of figure 4.19, $\langle E_x \rangle$ within dipole magnet M11, experienced by H_2^+ or CO_2^+ ions, follows the form of $\langle v_s \rangle$ in figure 4.16. $E_x(s(t_0))$ visualizes the theoretical horizontal profile of the electric field at the ions' longitudinal start position $s(t_0)$. Only the light H_2^+ ion with its small gyro radius follows this curve to an extend. Consequently, the theoretical cross-field drift velocities, equal to equation (2.51) with $B_z = -B_{z,\mathrm{dp}}$, diverge from ones for CO_2^+ ions most, as visible in the middle graph. $E_x(s(t_0))$ and the resulting $\langle v_s \rangle$ are only valid for a gyro radius of zero and at position $s(t_0)$. Since very ion longitudinally propagates away from $s(t_0)$ and shows a finite gyro radius, the observed deviations are expected.

To verify if the relation for the cross-drift velocity of equation (2.51) is still valid, the experienced $\langle E_x \rangle$ and $\langle v_s \rangle$ are used to calculate $B_{z,\mathrm{dp}}$. Relative deviations to the designated value show only an error in the order of maximal 0.15 % in the low amplitude region. In this region, E_s has a more dominant effect because $\langle E_x \rangle$ is comparably low. The negligence of E_s presumably leads to an asymmetric increment in the relative deviation. For higher $x(t_0)$, the relative deviations are below 0.02 %, which verifies equation (2.51).

Ion Trajectories inside Quadrupole Magnets

In contrast to the magnetic field of dipoles, quadrupole fields B_z are not constant along the horizontal plane but increase linear with x and do not show a field strength in the beam center.

The top graph in figure 4.20 visualize the trajectory of a CO_2^+ ion close to the center of quadrupole magnet QD11. It is generated with an amplitude of −2.9 mm, which is equal to $4.3\sigma_x$. Its initial velocity v_0 is set to approximately 24 m s^{-1} ($v_{s,0} = 6\,\mathrm{m\,s^{-1}}$) and is low compared to the mean thermal velocity $v_{\mathrm{rms}} = 411\,\mathrm{m\,s^{-1}}$. In this rare case, where the ion's initial amplitude is high and its velocity low, the ion experiences a cross-field drift v_d. Because the electric and magnetic field both change sign when going from x to $-x$, v_d always points upstream. In a QF quadrupole, v_d points into opposite direction.

As is shown in the bottom graph, $\langle v_s \rangle$ initially is in the order of $-4\,\mathrm{m\,s^{-1}}$. In the course of this simulation, it increases to approximately $-3\,\mathrm{m\,s^{-1}}$ due to E_s, accelerating the ion downstream. Eventually, this acceleration diminish v_d within approximately 180 µs, assuming a constant decrease by $1\,\mathrm{m\,s^{-1}}$ within every 30 µs. Subsequently, the ion will propagate downstream, following the electric field gradient of the beam potential towards its local minimum. Although the considered ion initially experience a cross-field drift in the quadrupole magnet, for larger time scales the acceleration by E_s is dominant.

For lower initial amplitudes in which the experienced $\langle |E_x| \rangle$ and the average absolute value of the magnetic field is also smaller, the cross-field drift velocity within quadrupoles is also decreased simultaneously. For larger amplitudes, the opposite behavior becomes visible[19].

For moderate amplitudes between $\pm 3\sigma_x$, v_d is at least one order of magnitude lower than average thermal velocities. Therefore, it is expected that the influence of quadrupole fields on ions is negligibly small and no effect of the quadrupole fields on the local spatial distribution of ions is anticipated.

Summary of the Ion Trajectory Characteristics

Using TracIon in single-ion tracking operation mode, it has been possible to simulate trajectories of relevant ion species in several scenarios. Here, the following issues have been discussed:

- **Drift Sections:** In absence of magnetic fields, ions behave as predicted by theory. They show an oscillatory behavior in the horizontal plane and are accelerated due to the longitudinal electric

[19] In figure C.12 in the appendix, simulated initial cross-field drift velocities for different ions with an initial velocity of $0\,\mathrm{m\,s^{-1}}$ are shown for larger amplitudes.

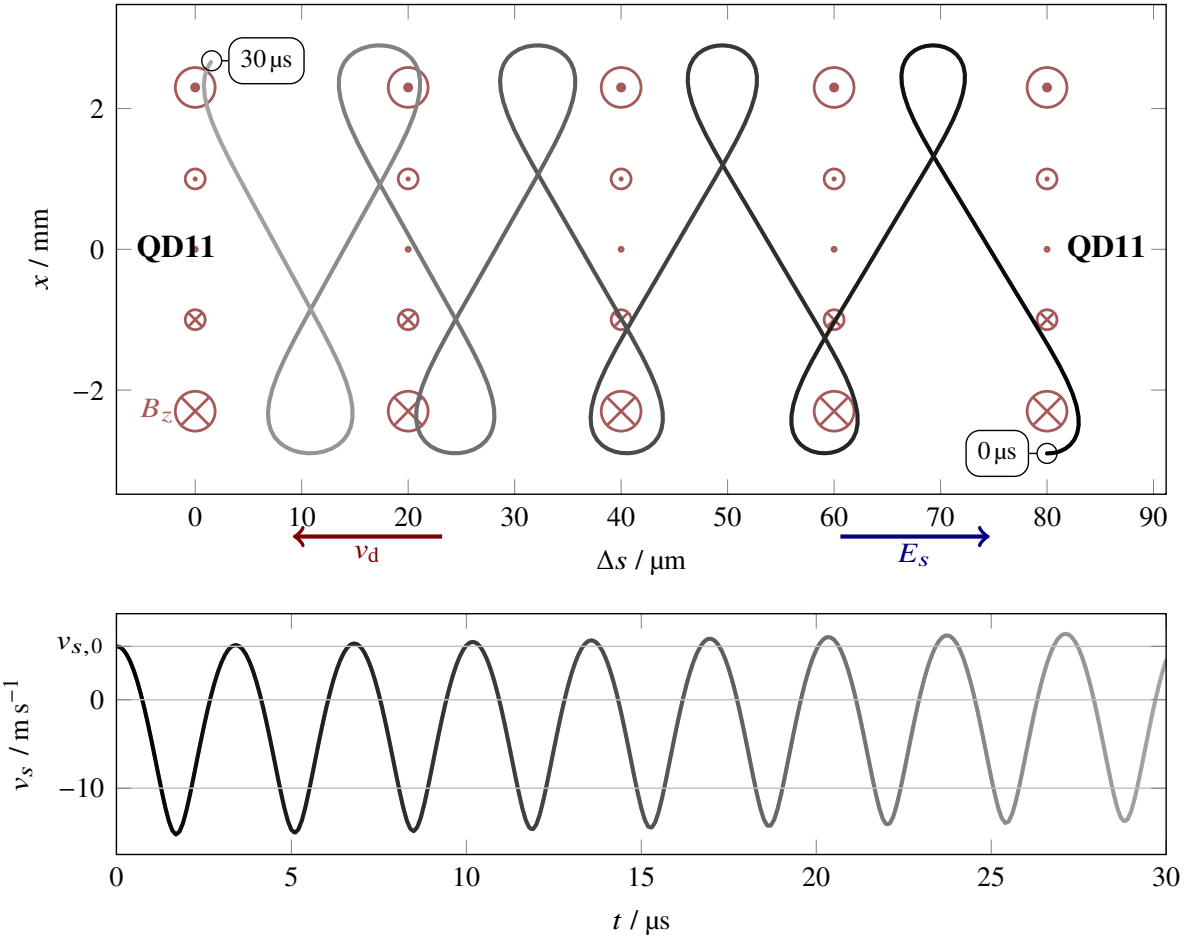

Figure 4.20: Exemplaric trajectory of a CO_2^+ ion within quadrupole magnet QD11 as it has been simulated in TRACTION. The top graph visualizes the ion trajectory in the horizontal and longitudinal dimension for a time of 30 µs. The direction of the vertical magnetic field of the quadrupole changes sign, when going from x to $-x$. The electric and magnetic field configuration results in an upstream cross-field drift velocity $\vec{v}_d$, whereas the longitudinal gradient field $\vec{E}_s$ accelerates ions downstream ($\langle E_s \rangle = 0.024\,\mathrm{V\,m^{-1}}$). The bottom graph shows the evolution of the longitudinal velocity with time. Positive velocities refer to a downstream propagation in the top graph, whereas negative ones to an upstream movement.

gradient field E_s. Since the gradient field strength is dependent on the horizontal position x, the experienced average acceleration by E_s is dependent on the ions' amplitude. For a certain $|x|$ position, E_s even changes its direction resulting in a reversed longitudinal acceleration. For oscillation amplitudes $> \sigma_x$, this leads to a modulation of v_s with $2\nu_x^{\mathrm{ion}}$. For even higher amplitudes, an acceleration of ions away from the minimum of the beam potential may occur.

- **Dipole Fringe Fields:** Here, the local field strength of B_z increases as ions enter the fringe field region. This leads to a gradual transfer of the longitudinal velocity component into the horizontal plane, slowing down the ions. If the velocity of entering ions is below $v_{s,\mathrm{T}}$, they is reflected back. In the storage ring the transmission shows a maximum of $(74 \pm 5)\,\%$ for CO_2^+ ions at a beam energy of 1.2 GeV and 100 mA of stored beam current. The transmission probability scales with beam current as the entry velocity into the fringe fields is higher due to acceleration by E_s. With decreasing mass, the transmission probability decreases. It also decreases with increased beam

energy as the magnetic field strength is higher.

- **Cross-Field Drift in Dipoles:** For the relevant ion amplitudes between $\pm 2\sigma_x$, the simulated cross-field drift velocity v_d is predominantly lower than theoretically predicted and, in contrast to previous assumptions, depends on the mass of the ions. Simulated cross-field drift velocities of light H_2^+ ions with small gyro radii, however, approximately follow theoretical predictions. The deviations are more significant for heavier ions with large gyro radii. In general, v_d is lower for larger gyro radius in vicinity of the beam center. Additionally, E_s deforms cross-field drift trajectories of ions and may lead to a reversal of their longitudinal propagation in case ions show a low initial amplitude $x(t_0)$. These influences have to be considered for the theoretically prediction of v_d. As a result, particularly heavy ions are expected to accumulate in dipole magnets to a higher level than would have been expected in theory.
- **Cross-Field Drift in Quadrupoles:** v_d in quadrupole magnets is small compared to cross-field drift velocities in dipole magnets. For the relevant amplitude regime of $\pm 2\sigma_x$, it is negligible. Instead, their motion is dominated by the ions' thermal velocities and E_s.

Overall, individual ion trajectories within this simulation scenario with dipole, quadrupole magnets and clearing electrodes show a large complexity. The variation of the beam potential depth along the x and s plane in combination with a vertical magnetic field with the same dependencies leads to various trajectories which strongly depend on initial starting positions and velocities. The study and evaluation of a relevant number of trajectories is not possible within a reasonable timescale. Additionally, assertions about individual trajectories are of low practical use, if quantities such as the local dynamic neutralization are of interest. Consequently, TracTion is used to simulate the evolution of an ion population, where ions are continuously generated and cleared, towards a steady-state. Results of this simulation will be discussed in the following sections.

4.3.4 The Ion Population in Its Equilibrium State

In this and the following sections, the results of a TracTion simulation will be discussed. Here, an ion population is continuously produced within the simulation scenario (compare section 4.3.2) by impact and photo ionization. Generated ions propagate within the electric and magnetic fields of the defined IPE and eventually are neutralized by clearing electrodes or collisions with the beam pipe. If the simulation time t_{end} is chosen long enough, a dynamic equilibrium of ion production and clearing emerges.

The beam energy is set to 1.2 GeV and the stored beam current is 35 mA. The vacuum pressure is set to 10^{-8} mbar. t_{end} is equal to 35 ms. This time is chosen empirically resulting from gained experience in TracTion's single-ion simulations within the IPE. Consequently, the ion population is expected to reach its equilibrium state until t_{end}. The generated ions are the relevant species H_2^+ ($A/Z = 2$), H_2O^+ ($A/Z = 18$), CO^+ or N_2^+ (both $A/Z = 28$) and CO_2^+ ($A/Z = 44$). They are represented by macro-ions, each being equivalent to $\mu_{ion} = 20\,000$ ions. Their individual production probabilities during impact and photo ionization are assigned according to results from studies in sections 3.3.2 and 3.4.3, respectively.

Accumulation of the Ion Population in the IPE

Figure 4.21 shows the accumulation process of the macro-ion population in the ion propagation environment. In gray, the actual number of macro-ions is shown. Its volatile rises results from periodic execution of ion generation subroutines of impact and photo ionization. The green line denotes the moving average of the population with a window size which equals the average periodicity of the subroutines' executions. At the end of the simulation at 35 ms, the population is in a dynamic equilibrium where the

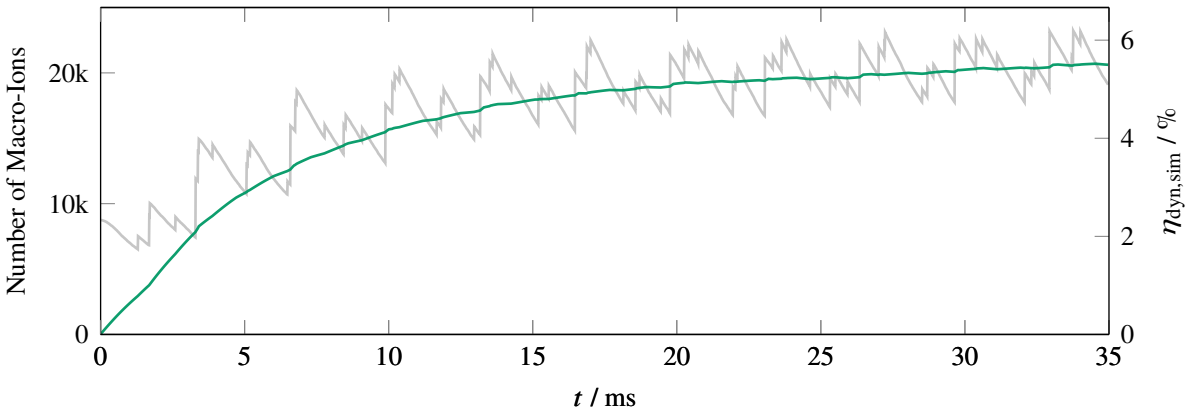

Figure 4.21: Evolution of the macro-ion number within the IPE with time at an average pressure of 10^{-8} mbar. In gray, the actual number of macro-ions is shown, whereas the green line denotes the moving average. This evolution has been simulated by TRACTION. The beam energy is set to 1.2 GeV and the stored current is equal to 35 mA.

number of macro-ions has settled at approximately 20 600. This corresponds to a simulated dynamic neutralization $\eta_{\mathrm{dyn,sim}}$ of approximately 5.5 % in the IPE. Note that in reality the neutralization is higher because the production rate exceeds the configured rate due to higher average pressure. Also, $\eta_{\mathrm{dyn,sim}}$ includes ions which propagate close to the beam center and distant ions which are generated by photo ionization.

The evolution of neutralization with time $\eta(t)$ has been derived in section 2.2.3 and is given by equation (2.12). For a known production rate of 7.4 s^{-1} at a pressure of 10^{-8} mbar, equation (2.12) can be approximated onto the moving average and the clearing rate can be determined. The ion population on average shows a clearing rate of

$$R_{\mathrm{c}} = (134.8 \pm 0.1)\,\mathrm{s}^{-1}$$

implying an average lifetime of approximately 7.4 ms in the IPE. Since this cell is representative for the storage ring, the total clearing rate of ions in the storage ring can assumed to be identical. Beam energy and current dependency of the clearing rate is discussed in appendix A.14.

Ion Composition and Individual Clearing Rates

Also, the equilibrium composition of the ion population within the IPE is simulated. Here, 48.9 % of the ions are H_2^+. H_2O^+ contributes to 16.7 %. A fraction of 22.1 % of the population shows a mass-to-charge ratio of 28 and consequently consists of N_2^+ or CO^+ ions. 12.4 % are CO_2^+ ions.

Using the definition of partial neutralization η_i in its equilibrium state (compare equation (2.20)) with known production rates $r_{\mathrm{p},i}$ of different ion species, individual clearing rates can be determined. They are shown in table 4.3. In general, light H_2^+ ions show a higher clearing rate than heavier ion species. This is expected as ions with lower mass are accelerated to higher velocities and consequently reach clearing electrodes within a shorter time period than heavier ions. Nonetheless, the clearing rate of H_2^+

	H_2^+	H_2O^+	N_2^+/CO^+	CO_2^+
$r_{\mathrm{c},i}$ / s^{-1}	144.1 ± 3.5	121.2 ± 2.9	128.2 ± 3.2	126.3 ± 3.1

Table 4.3: Clearing rates of different ion species in the IPE at a beam energy of 1.2 GeV and a current of 35 mA.

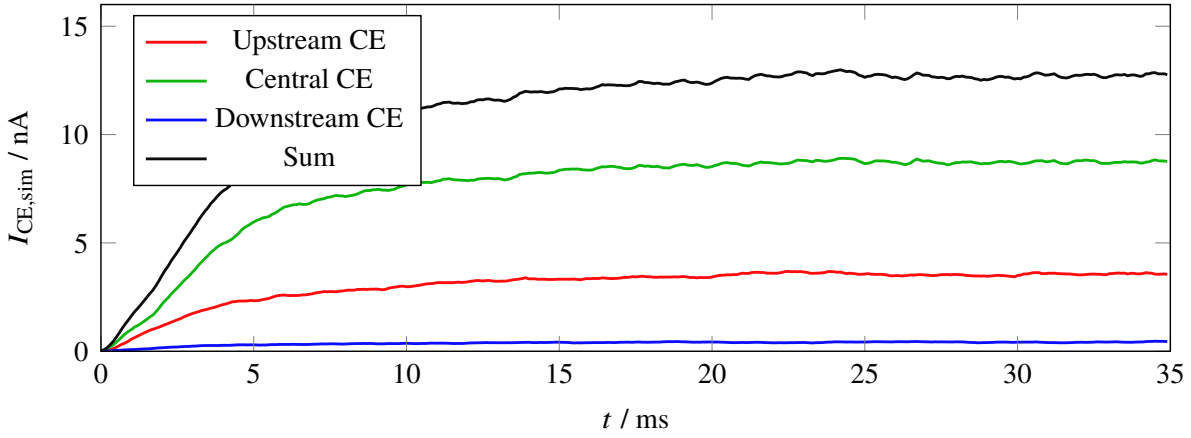

Figure 4.22: Build-up of the ion current at different clearing electrodes (CE) with time at an average pressure of 10^{-8} mbar. It results from a post-processing step of the TracTion simulation. The beam energy is 1.2 GeV and the stored current is 35 mA.

is comparably low. Due to longitudinal acceleration by E_s, a mass dependence of the clearing rate as $1/\sqrt{m_i}$ is expected. Thus, the clearing rate of H_2^+ should be in the order of 300 to 600 s^{-1} in dependence of which of the other residual species are used for extrapolation. As already discussed in section 4.3.3 and shown in figure 4.15, the transmission probability of H_2^+ through fringe fields of dipole magnets is the lowest of the entire ion population. The field's influence on H_2^+ ions' motion seems to decrease their clearing rate by a factor of approximately 2 to 4.

Simulated Ion Current and Comparison with Measurements

To verify if the estimated ion production rates are congruent with reality in the storage ring, also the hypothetically measured ion current at the clearing electrodes is simulated with TracTion.

Simulated Ion Current Figure 4.22 shows the growth of the ion current with time while the ion population reaches its dynamic equilibrium. Shown in red, green and blue is the running average of the simulated ion current at the upstream (s = 46.5 m), central (s = 51.93 m) and downstream (s = 56.8 m) clearing electrode, respectively. In the equilibrium state after 35 ms, the central electrode near the minimum of the beam potential shows the highest ion current. It is equal to 8.74 nA and exceeds the combined ion current at upstream (3.57 nA) and downstream (0.45 nA) clearing electrodes by a factor of two.

The central clearing electrode collects the highest percentage of ions because it is located near the beam potential's minimum. Most of the ions, which are produced close to the beam, are accelerated towards this electrode by E_s. Up and downstream electrodes show a lower current because they are positioned at the local maximum of the beam potential. Here, only ions which are produced in close proximity to these electrodes can be cleared. Other ions propagate towards the potential's minimum. Another current source for these electrodes is the fraction of ions, which are reflected by the dipoles' fringe field. Ions whose transversal momentum is coupled into the longitudinal plane by the magnetic field may escape from the magnetic mirror, reach these clearing electrodes and are removed. Of course, the amplitude of the transversal oscillation determines the available transferable momentum. The ion current at the upstream

electrode is a factor of approximately 8 higher than the downstream one. This is due to difference in electric potential between the clearing electrode and the nearest fringe field. The upstream electrode is positioned 0.5 m from dipole M10's fringe field whereas the downstream electrode shows a distance of approximately 1.9 m from M11. Therefore, the potential difference between the upstream electrode to the fringe field is smaller than in case of the downstream electrode. As a consequence, a lower momentum transfer from transversal to longitudinal is necessary for a reflected ion to reach the upstream electrode. This results in a higher current at the upstream electrode than in the downstream electrode.

Comparison with Measurements The simulated ion current is directly proportional to the ion production rate of impact and photo ionization. The former ionization process is established well, whereas the second process has often been neglected in literature. For photo ionization, a model congruent to [Miy87], has been developed in the course of this work in section 3.4. Additionally, the production rate directly scales with the average pressure within the vacuum system. For the storage ring, a model for the evolution of the average pressure with beam energy and current has been developed in section 3.2. To verify these two models, a comparison of simulated and measured ion current is conducted.

In total, a simulated ion current of approximately 12.8 nA is hypothetically detectable within the IPE at a set average pressure of 10^{-8} mbar. If the IPE, consisting of one complete FODO cell, is assumed to be representative for the storage ring with its 16 FODO cells, the total measured ion current would correspond to 204.8 nA. For a beam energy of 1.2 GeV and a current of 35 mA, identical to the simulation scenario, the pressure model estimates an average pressure $\mathcal{P}_{\mathrm{avg}}$ of $(20.9 \pm 0.5) \cdot 10^{-8}$ mbar for a no-load IGP pressure $\mathcal{P}_0$ of $(0.71 \pm 0.01) \cdot 10^{-9}$ mbar. Scaling the simulated current according to the actual pressure in the storage ring yields a hypothetical ion current of $(4.3 \pm 0.1)\,\mu$A.

Using the dataset introduced in section 3.2.1, which contains the measured ion current with the applied high voltage as well as corresponding beam energy and current, the average measured ion current can be determined. The dataset is filtered for ion currents which have been measured at a high voltage of $(-1\,400 \pm 150)$ V at a beam current of (35 ± 5) mA and energy of 1.2 GeV. The average measured ion current is equal to $(3.5 \pm 0.3)\,\mu$A.

Simulated and measured ion currents show the same order of magnitude and are congruent within a 3σ error region. The simulated current is approximately 20 % higher than the measured current. This is expected because the simulation does not involve any clearing or loss mechanism except for clearing electrodes and collisions with the beam pipe. The longitudinal distribution of these collisions along the IPE is shown in figure C.13 in the appendix. A current of 126 pA cannot be detected by clearing electrodes, as corresponding ions have collided with the beam pipe instead. Thus, approximately 1 % of the ions are removed due to collisions in the simulation. In reality, other natural clearing mechanism exist which are discussed in appendix A.13. Ions may be removed due to beam heating during their propagation in the beam pipe. Since the mutual space charge interaction of the ion population is not implemented in TracTIon, any clearing mechanisms which may result from these many-body dynamics is not included. In future, more sophisticated simulation programs may solve this issue.

However, when considering these moderate losses of the ion population, the simulated ion production processes seem to be consistent with the measurements. Thus, the made comparison confirms the two models for photo ionization and pressure.

4.3.5 Local Dynamic Neutralization

To determine the local dynamic neutralization $\hat{\eta}_{\mathrm{dyn,sim}}$ in this representative section of the storage ring, the ion population's spatial distribution is analyzed at the end of the simulation. The results of this analysis is shown in figure 4.23.

Ion Density within the IPE

The top graph of figure 4.23 shows the longitudinal and horizontal distribution of macro-ions in the ion propagation environment in its equilibrium state. Along the beam axis at $x = 0\,\mathrm{mm}$, the overall macro-ion number per pixel[20] is highest. Although the areal density along this axis is approximately $\lessapprox 5$ macro-ions per pixel for most of the IPE, three regions of increased ion density > 10 macro-ions per pixel are visible at approximately $s = 46.75\,\mathrm{m}$, 52.5 m and 55.25 m.

Accumulation region ① and ③ are positioned at the entrance of dipole magnets M10 and M11. Here, the fringe field of the magnets hinders the propagation of macro-ions, which are accelerated by E_s towards the minimum of the beam potential. In dependence of the ions' momentum, they are either transmitted into the dipole or are reflected back, as has already been discussed in section 4.3.3. Due to the low momentum of H_2^+ ions, their transmission is low compared to other ion species (compare figure 4.15). Consequently, the fraction of this species to the total ion population is increased in these two regions, as visible in the bottom graph of figure 4.12. The fraction of H_2^+, having a share of approximately 50 % of produced ions, increases to 80 % there. Of course, the lifetime of reflected ions is increased significantly, resulting in a locally increased ion density.

The occurrence of accumulation region ② can be explained by considering the ion production map of the IPE in figure 4.12. In this region, the ion production per pixel due to impact and photo ionization is highest. Additionally, the local E_s, which accelerates ions towards the central clearing electrode, is the lowest within all dipole magnets.

Due to photo ionization, macro-ions are also generated at positions far off the beam axis at $x > 5\,\mathrm{mm}$. These macro-ions are visible as diffuse clouds with a low macro-ion areal density which extend from approximately $x = 10\,\mathrm{mm}$ to the horizontal edge of the IPE. The density of these clouds increases towards the upstream end of the two dipole magnets. Additionally, the density is higher in dipole M10 than in M11. This can be explained by the interplay of the cross-field drift and E_s. The cross-field drift velocity in both magnets transports ions upstream (compare figure 4.16). In contrast, E_s accelerates ions either upstream or downstream in dependence of their position in the beam potential. Since the direction of E_s reverses for large distances from the beam center (compare figure 4.13 (bottom)), these macro-ions are accelerated parallel to the cross-field drift velocity in dipole M10 and antiparallel in M11. Consequently, their lifetime is higher, resulting in a higher macro-ion density of the cloud in M11 than in M10.

An effect of the magnetic fields of quadrupole QD11 on ion density is not visible. As already conjectured in section 4.3.3, the emerging cross-field drift is not high enough to alter ion trajectories significantly and their motion is dominated by E_s instead.

Longitudinal Ion Density

The discussed regions of ion accumulation are also visible in the longitudinal line density of the macro-ions, shown in the middle graph of figure 4.12. To obtain the longitudinal line density, the ion distribution of figure 4.12 (top) is integrated either entirely along the horizontal plane of the IPE (blue curve) or horizontally ±5 cm around the beam center (orange curve).

A maximal line density of approximately 75 macro-ions per cm is reached at $s = 52.3\,\mathrm{m}$ in dipole M11, if all ions are considered (blue curve). In the magnetic field-free region, reaching from $s = 49.75\,\mathrm{m}$

[20] A pixel has the size of $\Delta s_{\mathrm{res}} = 1\,\mathrm{cm}$ in the longitudinal and $\Delta x_{\mathrm{res}} = 250\,\mu\mathrm{m}$ in the horizontal plane.

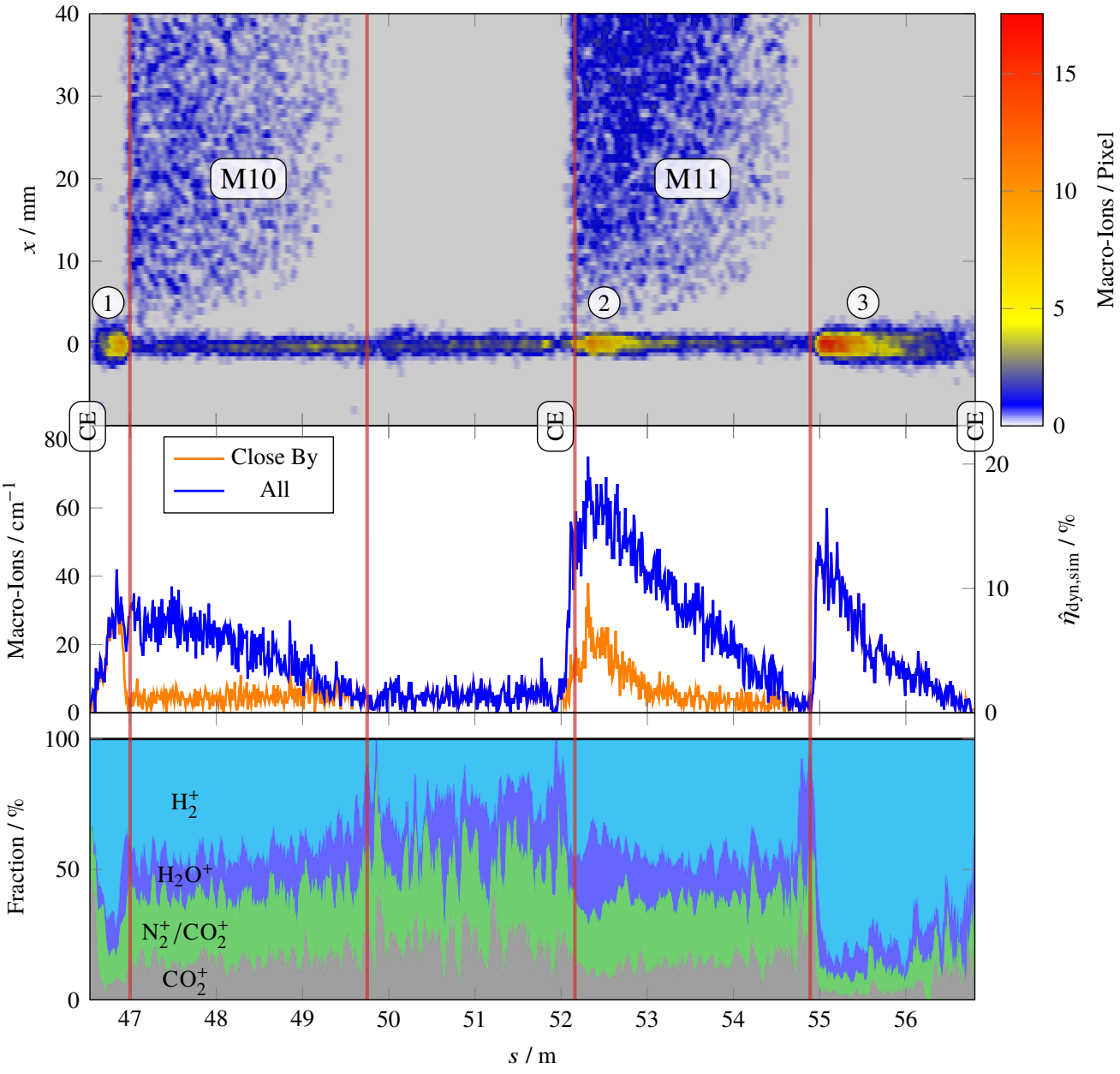

Figure 4.23: Distribution of the macro-ion population in its equilibrium state as it has been simulated by TRACTION at a beam energy of 1.2 GeV, a current of 35 mA and a pressure of 10^{-8} mbar. The top graph shows the two-dimensional macro-ion distribution of the horizontal and longitudinal plane within the IPE.
The longitudinal macro-ion line density is visualized in the middle graph. Here, the horizontally integrated ion line density "close by" the beam (integrated ±5 cm around the beam center) is colored in orange, whereas the integrated line density of all ions within the IPE is shown in blue. The ion density is also converted into a local dynamic neutralization.
The local composition of the ion population is shown in the bottom graph. Beginning and end of dipole magnets M10 and M11 are marked as red lines. CE denotes the longitudinal position of clearing electrodes.

to approximately 52 m, the average line density is approximately 5 macro-ions per cm.

Both macro-ion line densities can be transferred into a local dynamic neutralization $\hat{\eta}_{\mathrm{dyn,sim}}$ for the scenario using equation (2.22). The local neutralization is used to characterize the influence of the ions' space charge on the beam. Usually, the ions' transversal density distribution is not taken into account when determining $\hat{\eta}_{\mathrm{dyn,sim}}$, as ions are considered to be trapped in close vicinity to the beam. In case of an off-axis ion cloud, generated by photo ionization, this usual approach is in question.

For the usual approach on basis of the line density in blue, a maximal local "neutralization" $\hat{\eta}_{\mathrm{dyn,sim}}$ of 20 % is reached in dipole M11 due to the enhanced ion production by photo ionization. In M10 the maximal "neutralization" is equal to 8 %. However, $\hat{\eta}_{\mathrm{dyn,sim}}$ is only valid for the set average pressure of 10^{-8} mbar.

The term neutralization is set in quotation marks due to the following reason: As has been discussed in the previous section, a large fraction of photo-produced ions shows a large distance from the beam center in dipole magnets. The inverse square law of the electromagnetic force predicts that the space charge force of these ions do not affect the electron beam as severe as ions which are situated closer to it. The space charge force between cloud and close-by ions is reduced due to the same effect. Additionally, the ion cloud's own space charge may leads to its dispersal. Instead of utilizing the usual approach, each ion's distance from the beam should to be considered individually when calculating the neutralization of the electron beam and the space charge limit. In the following, the neutralization is only calculated under inclusion of ions which are positioned "close by" the electron beam (orange curve). The "close by" neutralization mostly follows the blue curve. Only in dipole magnets a strong deviation is visible, resulting from the photo-produced ion cloud.

Due to photo ionization, on average 65 % of the ions are positioned far off the beam and affect it only marginally. Only approximately 35 % are positioned "close by" the beam and directly influence the beam. To stay with the formalism presented in section 2.2, only the "close by" ions are considered for $\hat{\eta}_{\mathrm{dyn,sim}}$ which implies a reduction of the effective production rate to 35 %. The effective production rate in the storage ring has to be corrected down by the same factor. Only "close by" ions will be considered in the following.

Scaling the Simulated Neutralization To obtain the local dynamic neutralization $\hat{\eta}_{\mathrm{dyn}}$ of the storage ring in this simulation scenario, $\hat{\eta}_{\mathrm{dyn,sim}}$ must be scaled according to the actual pressure in the vacuum system. For this beam energy and current, the pressure model predicts an average pressure of $(20.9 \pm 0.5) \cdot 10^{-8}$ mbar (compare section 3.2). Thus, the production rate has to be scaled by a factor f of 20.9 ± 0.5, resulting in a local neutralization of

$$\hat{\eta}_{\mathrm{dyn}} = f \cdot \hat{\eta}_{\mathrm{dyn,sim}} \,.$$

Especially in region ③ this scaling would result in $\hat{\eta}_{\mathrm{dyn}} > 1$. In this case, excess ions would disperse transversely and $\hat{\eta}_{\mathrm{dyn}}$ is subsequently reduced to one. Using this space charge limit of $\hat{\eta}_{\mathrm{dyn}} \leq 1$, the average dynamic neutralization η_{dyn} within the IPE, or sections of it, can be deduced from $\hat{\eta}_{\mathrm{dyn}}$ by using equation (2.23).

The accumulation region ① shows an average neutralization of (63 ± 1) %. In region ③ an average dynamic neutralization of (68 ± 2) % is present. Within dipole magnets M10 and M11, an average neutralization of (27 ± 1) % and (39 ± 1) % is present. In the magnet field-free region between M10 and M11, the average neutralization is equal to (28 ± 1) %. Since the simulated section can assumed to be representative for the storage ring, the average neutralization η_{dyn} at a beam energy of 1.2 GeV and a current of 35 mA can be estimated as (40 ± 1) %.

Systematical Errors There are two main sources of systematical errors, which have to be taken into account when interpreting this result.

As the influence of the ions' mutual space charge interaction is not implemented in TRACTION, the simulated motion of ions, when propagating through regions with high local neutralization or when being trapped within a certain area, is not accurate. For example, ions may be longitudinally repelled from fringe fields of dipole magnets due to a locally fully neutralized beam ($\hat{\eta}_{\mathrm{dyn}} \approx 1$). Consequently, ions may be accelerated away from these entrances towards up and downstream electrodes. In this case, the neutralization in the IPE would be lower than expected from simulation.

When assuming that the transmission probability of an ion species through the dipoles' fringe fields at region ① and ③ is equal to zero, the static neutralization approach (compare section 4.2.2) can be used to estimate whether the local neutralization is high enough for a longitudinal repulsion towards the electrodes to take effect. In this case, the local neutralization $\hat{\eta}_{\mathrm{dyn}}$ in regions ① and ③ has to be higher than $\hat{\eta}_{\mathrm{stat}}$. The accumulation region ① shows a maximal $\hat{\eta}_{\mathrm{stat}}$ of approximately 1 % (see figure C.14 in the appendix). In region ③ it is equal to 4.2 %. Since $\hat{\eta}_{\mathrm{dyn}}$ exceeds 50 % in the relevant region and even is equal to one for regions which extends up to 30 cm, the ions' space charge indeed repels excess ions towards up and downstream clearing electrodes.

However, the magnitude of this systematical error cannot be estimated precisely. As $\hat{\eta}_{\mathrm{dyn}}$ is highest at regions ① and ③, the relative error of these $\hat{\eta}_{\mathrm{dyn}}$ values is locally set to 100 %. This results in a systematical overestimation of the *average* neutralization within the IPE by approximately 9 %.

The other source is the non-constant longitudinal pressure profile $\hat{\mathcal{P}}(s)$ along the beam axis. In TRACTION, $\hat{\mathcal{P}}(s)$ is assumed to be constant at $\mathcal{P}_{\mathrm{c}}$, which results, for example, in a constant production rate of impact ionization along the IPE. In reality, $\hat{\mathcal{P}}(s)$ is not constant. With increasing distance from the pump sections, the pressure increases as visible in figure 3.11 in section 3.2.4. Thus, the production rate varies along the IPE and consequently also influences $\hat{\eta}_{\mathrm{dyn}}$. Resizing each simulated local $\hat{\eta}_{\mathrm{dyn,sim}}(s)$ with an individual factor $\hat{\mathcal{P}}(s)/\mathcal{P}_{\mathrm{c}}$ instead of globally scaling it according to the average pressure, leads to a different average neutralization[21]. In this case, the dynamic neutralization is equal to (24 ± 1) %. Using the standard deviation of the two neutralization results as an error estimate, the systematical overestimation is supplemented by additionally 11 %.

Finally, the absolute systematical error can be estimated to overrate the average neutralization by 14 %.

4.3.6 Horizontal Equilibrium Ion Density Distribution within Dipole Magnets

As has been already stated in section 3.4.4, the asymmetric ion production map of the process of photo ionization, which contributes predominantly to ion production, may result in an asymmetric equilibrium ion density distribution in the horizontal plane. Therefore, the horizontal ion distribution in dipole magnets is analyzed.

The bottom graph of figure 4.24 shows the average ion production probability along the horizontal plane within dipole magnets M10 (red) and M11 (blue). The shape of the two distributions is similar, both having their maximum near the beam axis at $x = 0$ mm and showing an asymmetric contribution for $x > 0$ mm. Due to different dimensions of the electron beam, the distributions show differences. In dipole M10, the peak of the distribution is broader, substitutional for a lower probability for ions to be produced at $x > 10$ mm. In contrast, the peak of the distribution in dipole M11 is narrower with a higher probability for ions to be produced at $x > 10$ mm.

[21] Of course this scaling of $\hat{\eta}_{\mathrm{dyn}}$ instead of the local production rates within the IPE does not produce correct $\hat{\eta}_{\mathrm{dyn}}$ values. Yet, it gives an estimate of the influence of $\hat{\mathcal{P}}(s)$ on the simulation.

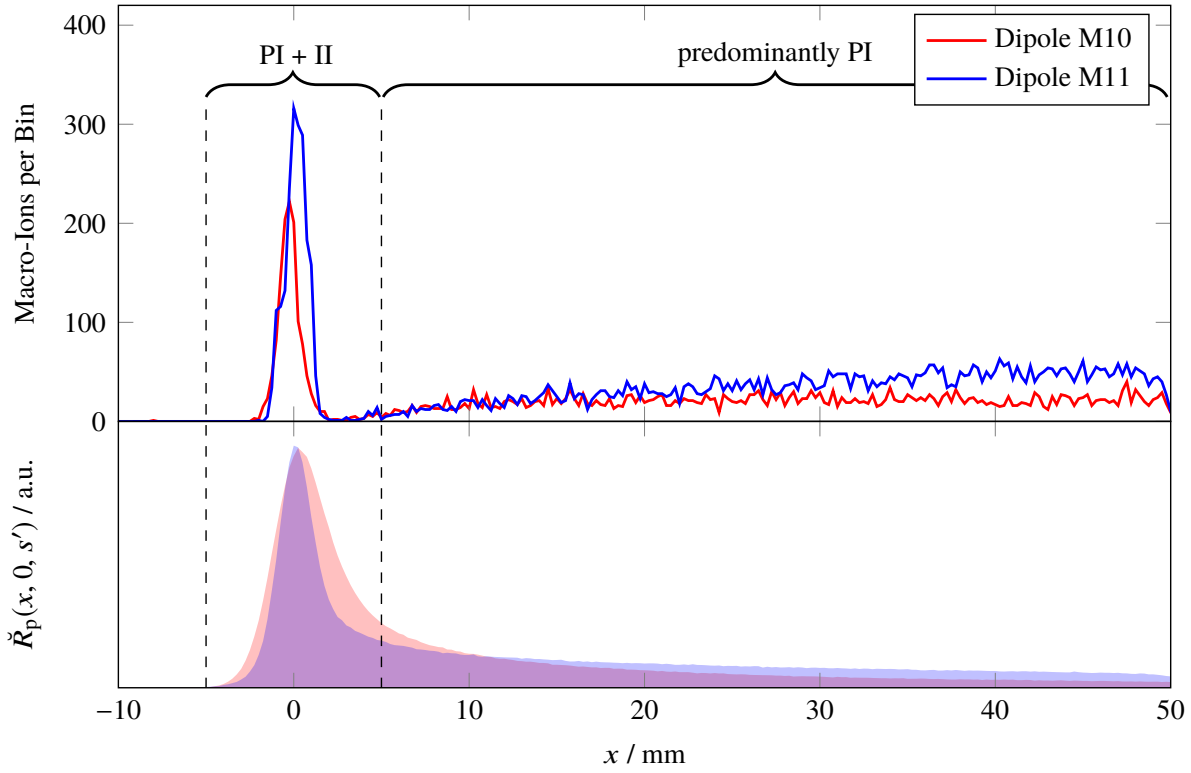

Figure 4.24: The horizontal equilibrium ion density distribution in dipole magnets M10 and M11 as it has been simulated by TRACTION (top). The beam energy is equal to 1.2 GeV and the current is 35 mA. The width of the bin is equal to $\Delta x_{\text{res}} = 250\,\mu\text{m}$. In the bottom graph, the ion production map, longitudinally integrated within the corresponding dipole magnet, is shown in corresponding color. In regions around the beam, ions are produced by impact ionization (II) and photo ionization (PI) whereas for $x > 5$ mm, photo ionization is dominant.

The top graph of figure 4.24 shows the integrated horizontal distribution of the macro-ion population within the two dipole magnets. Here, the two equilibrium distributions are similar to each other. Within a region of ±5 mm around the beam center, where ions are produced by impact *and* photo ionization, the distributions show their maximum on the beam axis. The density decreases to 1 macro-ion per bin for M10 and M11 at $x = 2.5$ mm and than increases again for $x > 2.5$ mm. In this adjoining region, ion production is dominated by photo ionization. Within M10, the density increases to approximately 20 macro-ions per bin and stays constant. In dipole M11, the density increases with distance from the beam center to up to 61 macro-ions per bin. This density behavior can be explained under consideration of the longitudinal cross-field drift in the dipoles. Since the cross-field drift velocity decreases with increasing distance from the beam center (compare figure 4.16), the lifetime of macro-ions rises accordingly. This results in an increasing macro-ion density along x in case of an almost constant production map, for ions in dipole M11, and an almost constant density for a decreasing production map, for ions in M10.

Thus, the macro-ion distribution consists of a core region of high density ±2.5 cm around the beam center and a cloud of macro-ions which horizontally extends from the region adjacent to the beam towards the surface of the beam pipe. As previously conjectured, the magnetic field prevents a horizontal drifting of most macro-ions within the cloud towards the beam center. The asymmetry due to the ion production map persists.

4.3.7 Conclusions for the Storage Ring

In short, results of TracTIon simulations presented in sections 4.3.4 to 4.3.6 are the following:

- The conjectured horizontal asymmetry of the equilibrium ion density in dipole magnets could be verified. Investigations regarding the effect of this asymmetry on the electron beam will follow in section 5.1.4.
- The simulated ion current is congruent with measurements conducted at the storage ring. This substantiates the developed pressure model and the contribution of the photo ionization process to the total ion production.
- The average dynamic neutralization within the IPE at a beam energy of 1.2 GeV and stored current of 35 mA can be determined as

$$\eta_{\mathrm{dyn}} = (40 \pm 1(\mathrm{stat}) - 14(\mathrm{sys}))\,\%$$

  with corresponding statistical (stat) and systematical (sys) errors.

Scaling of the Clearing Rate and Neutralization with Beam Energy and Current

Along with the production rate, the extracted clearing rate varies with beam energy and current, rendering the neutralization also dependent on these parameters.

The production rate directly scales with pressure $\mathcal{P}$ and ionization probability $R_{\mathrm{p}}/\mathcal{P}$ of the ion production processes. $R_{\mathrm{p}}/\mathcal{P}$ changes only moderately[22] within the energy range of the storage ring while $\mathcal{P}$ increases with beam energy and current. Thus, when comparing a low energetic beam with low stored current to a high-energy beam with an increased current, the total production rate may change by more than a factor of four (compare figure 3.23).

For a worst case estimation on the evolution of the neutralization with beam energy E and current I, it is assumed that the pressure, and thus the production rate, increases linear with E and with I. The clearing rate scales differently with beam energy and current in dependence on the region the ions propagate in.

In appendix A.14, useful scaling laws for the clearing rate, production rate and the resulting neutralization are given for the different regions. According to these scaling laws, the neutralization is estimated to scale as proportional to $\sqrt{I} \cdot E^2$ in magnetic field-free regions, where ion dynamics are dominated by E_s. In regions where the magnetic field influences the ions' motion and how they are cleared, e.g. in dipole magnets and their fringe fields, the neutralization is proportional to E^4.

Thus, the neutralization is estimated to increase slightly for different beam currents in the storage ring. The enlargement of the beam's dimension with beam energy reduces its attractive electric field. This slows down all ion dynamics accordingly and consequently prolongs the ions' lifetime within the storage ring. Additionally, the increased magnetic field strength decreases the ions' cross-field drift velocity in dipoles and their transmission probability into or through the magnets. Therefore, the increment of neutralization with beam energy is expected to scale as E^2 to E^4.

Consequences for the Storage Ring

The highest local dynamic neutralization in the IPE can be found at the fringe fields of dipole magnets M10 and M11. Here, an ion accumulation region estabishes at the entrance of each dipole magnet. However, in the four FODO cells of the storage ring's missing magnet sections, only one dipole magnet

[22] For impact ionization, $R_{\mathrm{p}}/\mathcal{P}$ increases by 8 % within the storage ring's energy region (compare figure 3.12). Within the same energy range, $R_{\mathrm{p}}/\mathcal{P}$ of photo ionization increases by approximately 20 % (compare figure 3.16).

is installed (compare MM sec. in figure 1.1). Additionally, in two FODO cells, in the rf and in the opposing straight section, no dipole magnets are installed. Therefore, the simulated neutralization can be interpreted as an upper limit for the total neutralization of the storage ring at this beam energy and current.

Nonetheless, a reduction of the neutralization may be desired to avoid effects on the beam, resulting from accumulated ions (compare chapter 5). Except for fringe-field regions of dipole magnets, the average dynamic neutralization is approximately 30 %. In fringe fields, the neutralization exceeded 60 %. The installation[23] of additional clearing electrodes at the entrance of each dipole magnet is advised to reduce the local neutralization in these regions significantly. If these regions would show the same neutralization as the magnetic field-free regions of 20 % due to installed clearing electrodes, an average neutralization of approximately 29 % could be reached in the entire IPE. This implies an absolute neutralization reduction by 11 % which is equal to a relative reduction by 1/4th.

4.4 Ion Accumulation in Vicinity of RF Cavities

In rf cavities, accelerating voltages in the order of MV[24] are generated for beam acceleration using resonant field exaltation. They are installed in the rf section of the storage ring.

On one hand, the motion of ions in the longitudinal plane may be altered by the large amplitudes of the cavities' electromagnetic fields. On the other hand, these fields oscillate with a high frequency ν_{rf}, altering the direction of its longitudinal component every 1 ns. Previous theoretical studies on this topic have concluded, that the influence of the cavities' field on ion motion is negligibly small [MTH88, appendix]. ν_{rf} is believed to be too high to show an influence on ion motion on a noticable level.

Therefore, the implications of this argumentation are tested by simulating the accumulation of ions within the rf section of the storage ring, using a one-dimensional tracking tool developed for this purpose. This tool utilizes the electromagnetic field distribution of the deployed five-cell PETRA cavities on the beam axis, simulated by CST Microwave Studios[25].

But first, a very brief introduction into rf cavities is given. For a detailed introduction into this topic, see e.g. [Wil00, chapter 5, esp. section 5.2].

4.4.1 RF Cavities

A cavity is a conducting, hollow body in which a standing electromagnetic wave with a certain eigenfrequency can be excited. This eigenfrequency is only dependent on the geometry of the cavity and results from solutions of the Maxwell equations with certain boundary conditions: In order to enable a build-up of a standing electromagnetic wave, its magnetic field perpendicular and its electric field parallel to the cavity's inner surface has to vanish ibidem. Otherwise electric currents, induced by the magnetic fields or generated by the electric fields, would prevent a propagation of the wave due to Ohmic losses on the surface of the cavity.

In case of a cavity which is rotationally symmetric around the longitudinal beam axis, the solution to

[23] The electrodes should be positioned at the entrance of the magnet which is facing away from the minimum of the beam potential.

[24] In comparison, the longitudinal gradient field E_s is in the order of several $\mathrm{V\,m^{-1}}$. Thus, the cavities' field exceeds E_s by several orders of magnitude.

[25] CST Microwave Studios is a program for simulation of three-dimensional electromagnetic high frequency components such as rf cavities. It is one component of CST Studio Suite, a program suite which offers computational solutions for electromagnetic design and analysis, developed by Computer Simulation Technology (CST). For more information, see https://www.cst.com.

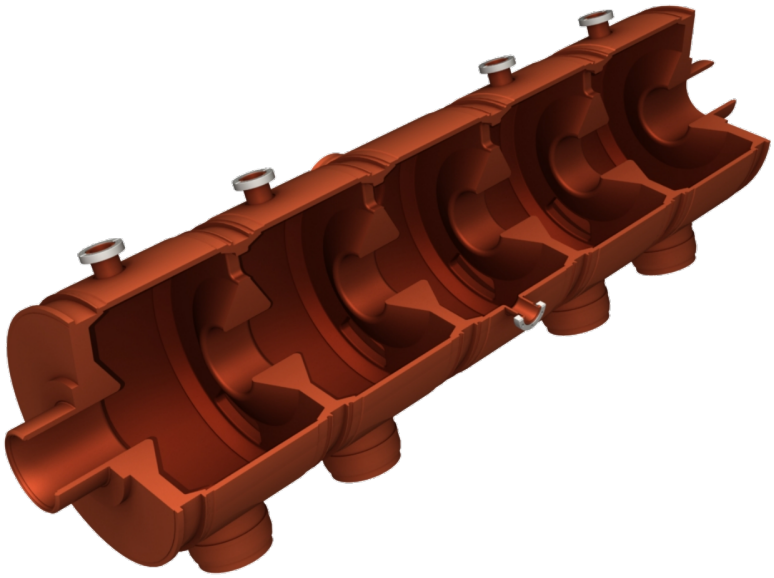

Figure 4.25: Sectional view of a five-cell PETRA cavity [Sch15, section 5.1, figure 5.2].

the MAXWELL equations are TM or TE[26] modes. For given boundary conditions, multiple of these modes exist in the cavity, each having an individual eigenfrequency with which it can be excited externally.

For particle acceleration, typically the TM_{010}[27] mode is used. The utilized cavities are designed the way that its fundamental mode shows the lowest eigenfrequency and that the longitudinal electric field of that mode has its highest field strength on the beam axis. In longitudinal direction, the cavity is open and integrated into the vacuum system of the accelerator to allow the entrance of the electron beam for acceleration.

Cavities, used for particle acceleration, are designed to have the highest acceleration voltage U_{acc} feasible. In analogy to the OHMIC law, the so called shunt impedance R_{S} determines the acceleration voltage within the cavity in dependence of the injected rf power P_{rf} as [Wil00, section 5.2.2, conversion of equation (5.43)]

$$P_{\mathrm{rf}} = \frac{U_{\mathrm{acc}}^2}{2R_{\mathrm{S}}} \,.$$

Consequently, the shunt impedance has to be maximized to obtain a high acceleration voltage for a given P_{rf}. For normal conducting cavities manufactured from copper or aluminum, R_{S} is in the order of MΩ.

To additionally reduce the required space for the cavities, the shunt impedance per unit length is optimized. Due to this constrain, typically multi-cell cavities are utilized which consume less space than single-cell cavities to achieve the same acceleration voltage. Here, the direction of the longitudinal electric field changes its direction when going from one cell to another (π mode). Thus, when a particle traverses one cell within the accelerating half of the rf period, it is also accelerated in the adjoining cell.

In the storage ring, two rf cavities of the PETRA type are used. The PETRA cavity is a five-cell cavity,

[26] In short for transversal magnetic or transversal electric modes. Since the electric and magnetic field in an electromagnetic wave are orthogonal to each other, this implies a longitudinal electric field for TM and a longitudinal magnetic field for TE modes.

[27] The three indexes denote the number of maximum points of the electric field along the azimuthal, radial and longitudinal direction. A TM_{010} mode consequently has a constant field along the azimuthal and longitudinal plane, but has one radial maximum at the center of the cavity where the beam passes.

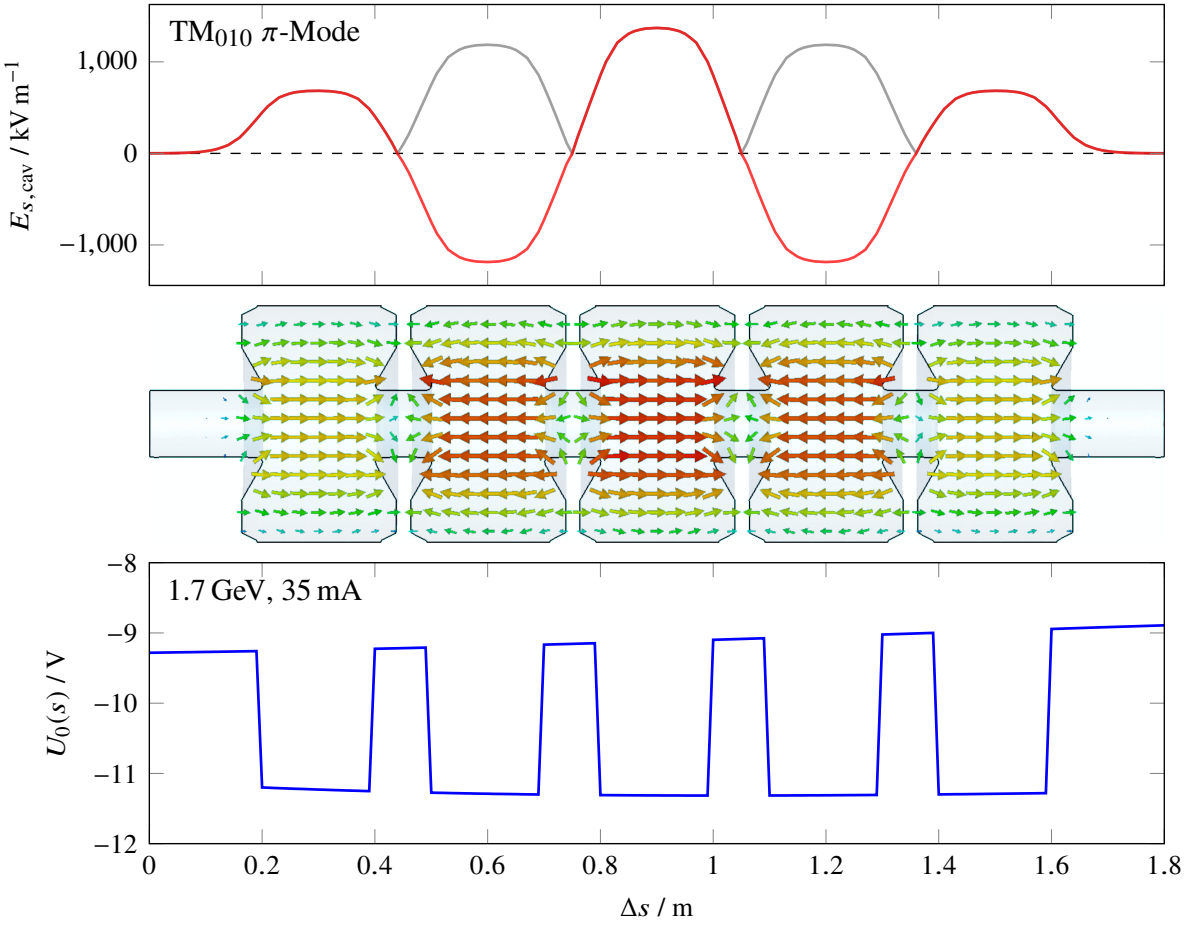

Figure 4.26: The top graph shows the electric field strength at the beam center at $x, z = 0$ mm of the TM_{010} π mode with a total acceleration voltage of 1.1 MV in red. In gray, the absolute value of $E_{s,\mathrm{cav}}$ is shown. The middle graph shows the configuration of the electric field within the cavity's cell as it is simulated with CST MICROWAVE STUDIOS (courtesy of M. Schedler [Sch15, section 5.1, figure 5.3]). The beam potential, which results from the inner geometry of the PETRA Cavity, is shown in the bottom graph in blue. The potential depth corresponds to a beam energy of 1.7 GeV and 35 mA current in the storage ring. Note that the longitudinal coordinate Δs is given in reference to the upstream start position of PETRA Cavity 2 at $s = 83$ m in the storage ring.

made out of copper, which is optimized for an rf frequency of 499.667 MHz of the TM_{010} π mode. It has a shunt impedance per unit length of 12.3 MΩ m^{-1} [Ger+77, section Elektrische Daten]. A sectional view of the cavity can be seen in figure 4.25.

The two cavities are positioned in a dispersion-free straight section of the storage ring. One between quadrupole QF16 and QD17 and the other between QD17 and QF18. They are operated with an rf frequency of typically 499.669 MHz and can be supplied with an rf power of up to 100 kW each. For this rf power, the sum of both cavities acceleration voltage is 3.5 MV [Sch15, section 13.2, figure 13.3].

In figure 4.25, the inner geometry of the PETRA cavity is shown. Here, the individual cells have an inner diameter between 423.5 to 419.3 mm. They are separated from each other by thin copper walls with coupling slits for transmission of the rf wave between the cells.

In the top graph of figure 4.26, the amplitude of the longitudinal electric field at the beam center for the TM_{010} π mode is shown in red. It is denoted as $E_{s,\mathrm{cav}}$. The field, oscillating with ν_{rf}, has its maximum amplitude in the center cell, where the rf power is coupled in. Towards the outer cells, the field strength

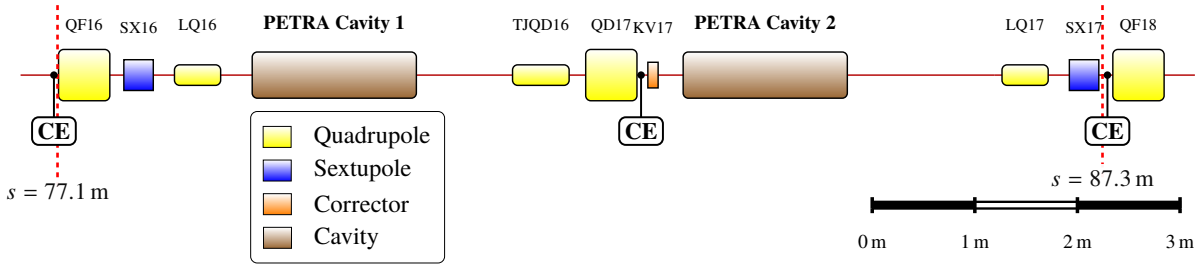

Figure 4.27: Lattice of the rf section of the storage ring. The IPE is denoted by the dashed red lines starting from $s = 77.1$ m and ending at 87.3 m. The position of the clearing electrodes are denoted with CE.

decreases[28].

In the middle graph of figure 4.26, the electric fields of the TM_{010} π mode is shown as it is simulated with CST MICROWAVE STUDIOS. The simulation has been conducted using CST's EIGENMODE SOLVER on basis of a CST PETRA cavity model[29].

The inner geometry of course also changes the beam potential $U_0(s)$ in the beam center. The resulting potential is shown in the bottom graph. Here, $U_0(s)$ is calculated using equation (2.42) and an inner radius of 230 mm for every cell. Due to the geometry of the cavities, there is a potential hollow in each cell.

4.4.2 Simulation Tool

The developed MATLAB tool, simulates the motion of an ensemble of macro-ions of different species in the rf section of the storage ring using a 4th order RUNGE-KUTTA method. Here, the ions are generated[30] in the vicinity of the rf cavities and are influenced by their electric rf fields. A weak-strong simulation model is used. For more information regarding this tool, see appendix B.2.5.

Under the assumption, that ions in this scenario show a low transversal amplitude of $\lesssim \sigma_{x,z}$ in comparison to the transversal dimension of the beam pipes or the cavity, the ion motion is reduced to its longitudinal component. Here, only the longitudinal gradient field E_s and additionally the time dependent $E_{s,\mathrm{cav}}$ within the cavities affects them.

Simulation Scenario As can be seen in figure 4.27, the ion propagation environment (IPE) reaches from $s = 77.1$ to 87.3 m and comprises quadrupole magnets QF16, QD17 and QF18 in addition to tune jump quadrupole TJQD16[31] and the two air core quadrupoles[32] LQ16 and LQ17. None of the magnetic fields of these elements are implemented in the simulation, as quadrupole fields vanish at the beam center.

[28] The field strength within the individual cells can in principle be altered by tuning plungers, installed in the two adjacent cells to the middle one, which deliberately change the geometry of the cells. This results in a different coupling of the injected rf power into the individual cells and modifies the field strength within them. For more information, see e.g. [Yu+13, section Accessories Setup].

[29] The CST model has been created on the basis of technical drawings from DESY Hamburg as part of the work of M. Schedler [Sch15].

[30] At every ι_{ii}th iteration step of the simulation, the ion generation subroutine is executed, producing one macro-ion every centimeter within the IPE.

[31] Tune jump quadrupoles are used for a fast change of the tune during the energy ramp when the storage ring is operated with a spin-polarized electron beam. These tune changes are necessary to increase the crossing velocity of intrinsic resonances during the ramp which depolarize the beam. For more information regarding the spin dynamic of the electron beam in the storage ring, see e.g. [Sch17].

[32] Air core quadrupoles are used to for the fine adjustment of the horizontal tune of the accelerator during extraction of the stored beam to the experiments. For more information, see e.g. [Gen99, section 3.2.6].

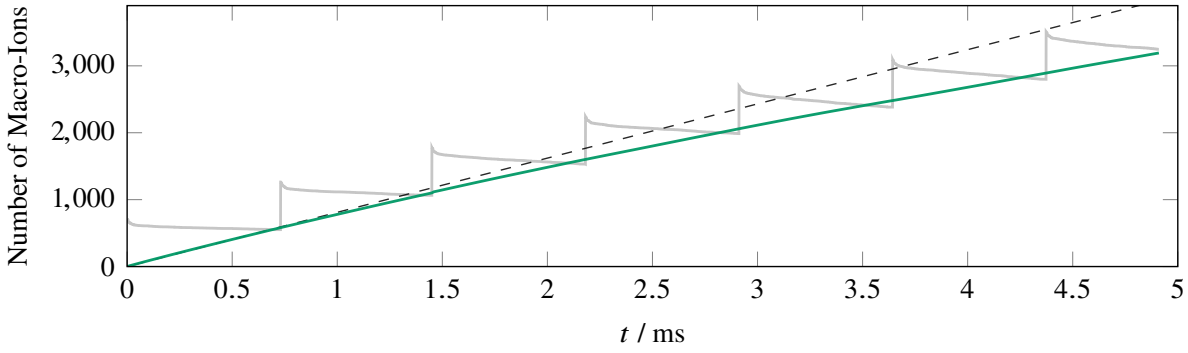

Figure 4.28: Simulated time evolution of the macro-ion population in the rf section. The gray curve indicates the actual macro-ion number whereas the green curve denotes its moving average with a window size of ι_{ii} samples. The dashed line indicates a linear growth of the averaged macro-ion population.

The beam potential $U_0(s)$ at the beam center is precomputed using equation (2.42) and known geometries of the storage ring's beam pipe segments. In the computation, also the inner geometry of the PETRA cavity is included. In vicinity of clearing electrodes, the beam potential is superimposed by their electric potential. Additionally, $E_{s,\text{cav}}(s,t)$ within the cavities is precomputed for a given time increment Δt of the tracking algorithm. $U_0(s)$ and $E_{s,\text{cav}}(s,t)$ are precomputed on a grid with a spatial resolution of $\Delta s_{\text{res}} = 1\,\text{cm}$.

4.4.3 Simulated Longitudinal Ion Density Distribution

In this simulation, the beam energy is chosen to be 1.7 GeV. The stored beam current is equal to 35 mA.

The simulation is configured as follows:

- The acceleration voltage of each of the two cavities is set to 1.1 MV in the simulation. This value is in the order of the cavities' acceleration voltage at this beam energy.
- Δt is set to 50 ps. Here, the movement of the ions, exposed to the rf fields of the cavities, is determined within an rf period of $1/\nu_{\text{rf}} = 2\,\text{ns}$ in 40 iteration steps.

Growth of the Ion Population

The accumulation of the ion population is simulated within a time frame of 4.9 ms. Figure 4.28 shows the time evolution of the macro-ion population. During this time frame, the ion generation subroutine has been executed seven times as visualized by the steps in the macro-ion population (gray). The averaged population (green) shows an almost linear growth with a noticeable flattening when compared to a hypothetical linear population growth (dashed line).

If all ions would be cleared at the potential's minimum by a clearing electrode, the sojourn time of the heaviest, thus slowest, ion denotes the maximum clearing time in this scenario. A heavy CO_2^+ ion, which is produced at the local maximum of the beam potential, reaches the local minimum and would be cleared after a time of 4.5 ms in this scenario. If the entire ion population could be cleared by clearing electrodes, it is expected to reach its equilibrium state during this time frame. In this scenario, the simulation's time frame is similar to the sojourn time of the CO_2^+ ions. However, the population has not reached its equilibrium state yet. Thus, potential barriers exist in the IPE, which prevent the removal of ions by clearing electrodes.

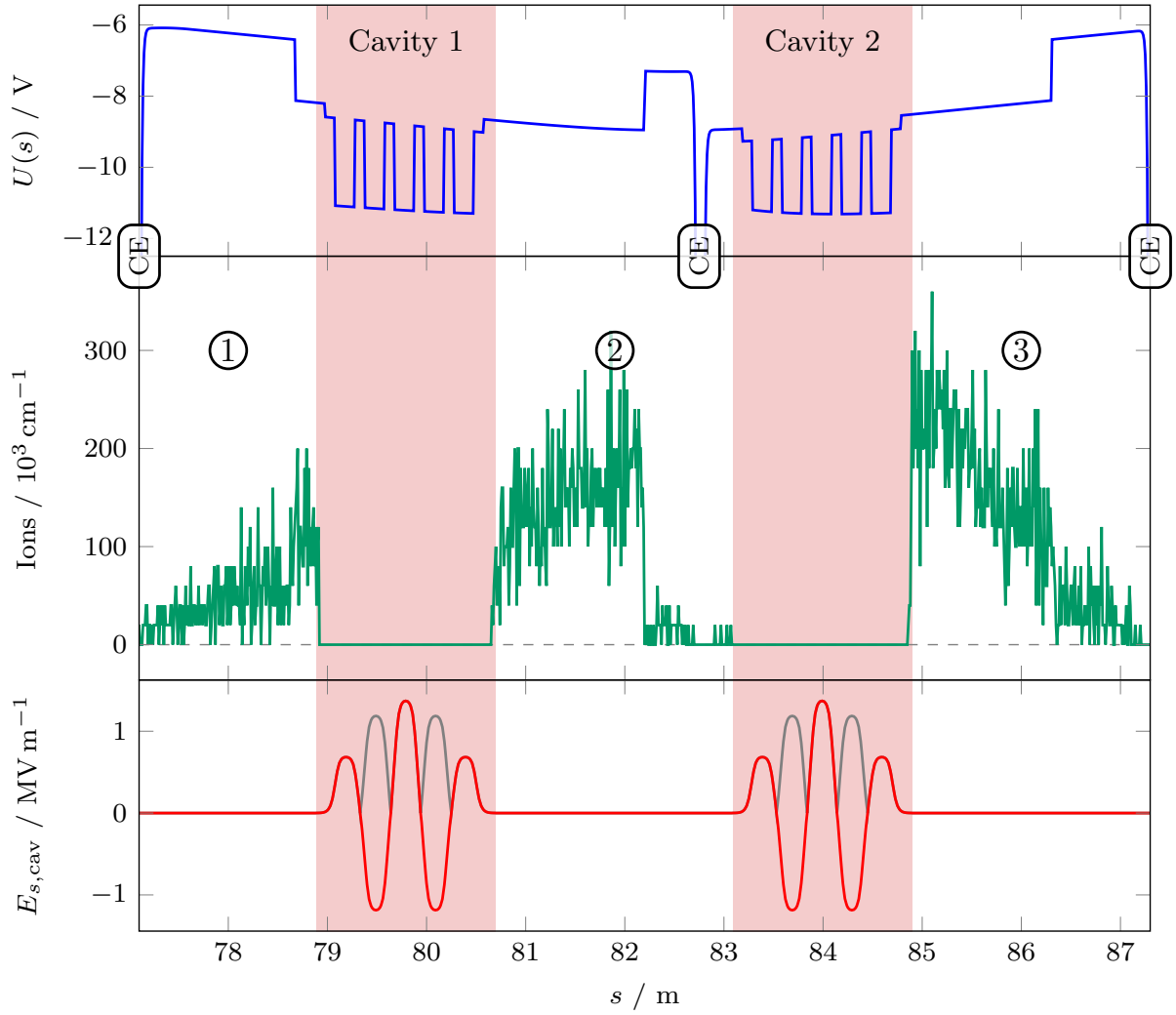

Figure 4.29: Beam potential, rf fields within the cavities and longitudinal ion distribution in the rf section of the storage ring. The top graph shows the potential in the beam center at a beam energy of 1.7 GeV and current of 35 mA. CE denotes the position of clearing electrodes. The middle graph shows the distribution of the ion population at the end of the simulation. Note that no ions are generated within the cavities. The bottom graph shows the amplitude of the electric field strength of the TM_{010} mode within the PETRA cavities in red. The absolute value of the amplitude is shown in gray. The red area denotes positions at which $E_{s,\mathrm{cav}} \neq 0$.

Accumulation Regions

The beam pipes in this section of the storage ring are mainly either round or "elliptical" quadrupole chambers (compare figure 4.3 in section 4.2.1). The resulting beam potential is shown in the top graph of figure 4.29. The red areas indicate regions where $E_{s,\mathrm{cav}}$ is present (bottom graph). Here, also the beam potential is modified in accordance with the cavities' inner geometry.

Due to the shape of the beam potential, a potential hollow can be identified for ions which are produced within $s = 78.7\,\mathrm{m}$ and $82.2\,\mathrm{m}$. Here, potential hollows in the cavities are not considered, as ions are not generated within them in this simulation. All other ions can in principle reach a clearing electrode, some by passing through a cavity.

In the middle graph of figure 4.29, the resulting longitudinal ion distribution is shown. It shows three

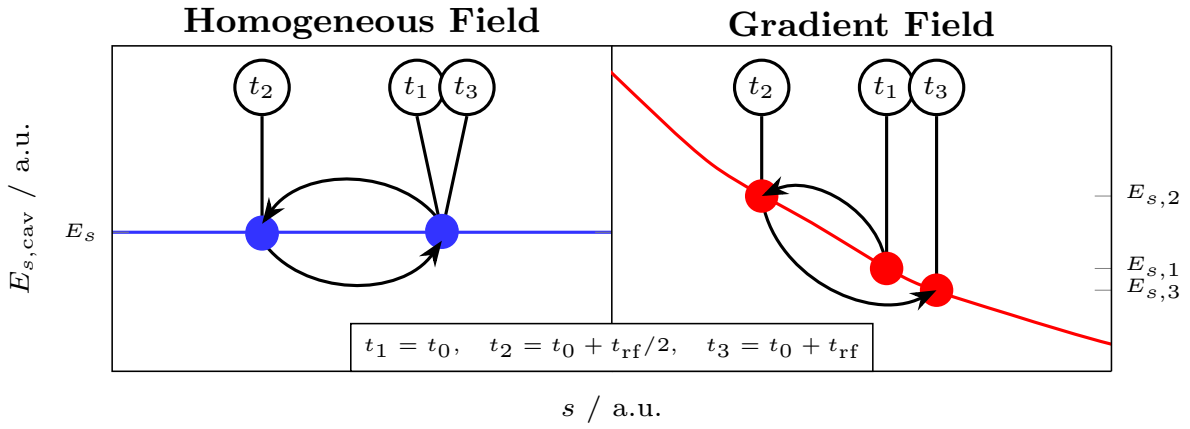

Figure 4.30: Illustration of the longitudinal ion movement in a homogeneous and gradient electric rf field. Here, the ion position at times corresponding to three consecutive zero crossing of the rf field is shown for a case with no spatial dependency of the amplitude of the rf field (left) and with non-linear spatial amplitude (right).

separated main accumulation regions. From the upstream border of the IPE to the edge of the rf fields of cavity 1 on average $5 \cdot 10^4$ ions per cm accumulated. The second accumulation region is positioned between the downstream entrance of cavity 1 and the volatile beam potential rise at 82.2 m. Here, on average $15 \cdot 10^4$ ions per cm accumulated within the simulated time frame. The third region extends from the downstream entrance of cavity 2 to the downstream edge of the IPE where on average $11.4 \cdot 10^4$ ions per cm accumulated.

Ion Transmission Characteristics of RF Cavities

The transmission characteristics of the cavities determine the shape of the longitudinal ion distribution in vicinity of the cavities.

Ions, produced in region ① between $s = 77.2$ m and 78.7 m, are accelerated downstream by the longitudinal gradient field E_s. To be neutralized by the clearing electrode in the center of the IPE, these ions would have to be transmitted through cavity 1. Ions, which are generated in region ③ between $s = 84.9$ m and 87.2 m, are accelerated upstream and would have to pass cavity 2 to be cleared. The ion density in both regions is highest at the entrance to the rf cavities. Here, ions only enter a few centimeters into the cavities.

Region ② shows the highest average ion density in the entire IPE. Here, the ions' mutual space charge interaction, implemented as a linear model, would lead to a longitudinal dispersal of the ion accumulation, if no potential barriers would be present. Because the ion population is trapped between two barriers, it keeps assembled. Downstream, it is obviously confined by the potential barrier at $s = 82.2$ m whereas the upstream side seems to be blocked by cavity 1.

Hence, at all three accumulation regions, the rf fields within the cavities prohibit the propagation of ions through them. In figure A.19 in appendix A.15 trajectories of different ion species are shown when entering an rf cavity.

When exposed to the rf fields of the cavities the ions are accelerated by emerging poderomotive forces towards field-free regions. The ponderomotive force emerges because of the spatial gradient of the longitudinal field strength amplitude $E_{s,\mathrm{cav}}(s)$ of the rf field. In figure 4.30, the exemplaric movement of an ion when exposed to an rf field is shown for a case of a homogeneous $E_{s,\mathrm{cav}}$ (left) and an inhomogeneous

$E_{s,\mathrm{cav}}$ with a spatial gradient (right). The ion's position is marked at three different times corresponding to zero crossings of the rf field. In case of a homogeneous amplitude of the rf field, the ion is first accelerated upstream within the positive half period with an average force of $\left\langle F_{\mathrm{rf}}\right\rangle_{t_1}^{t_2}$. In the negative half period, it is decelerated with an average force of $\left\langle F_{\mathrm{rf}}\right\rangle_{t_2}^{t_3}$. Because $E_{s,\mathrm{cav}}$ is constant, both average forces are equal and no ponderomotive force emerges. Hence, the ion motion is not influence by the rf field, as already stated by [MTH88, appendix].

In case of an inhomogeneous $E_{s,\mathrm{cav}}$, which is present within an rf cavity, the ion is accelerated upstream in the positive half period of the rf field. In the negative half period, the ion is decelerated within a region where the field strength is higher than in the previous half period. Consequently, $\left\langle F_{\mathrm{rf}}\right\rangle_{t_1}^{t_2} > \left\langle F_{\mathrm{rf}}\right\rangle_{t_2}^{t_3}$ in this case and the resulting ponderomotive force accelerates the ion towards regions with lower field strength.

Ion Motion within RF Cavities

The ponderomotive force of inhomogeneous electric rf fields is used e.g. in Paul ion traps (see e.g. [PS53; Pau90]). Here, trapped ions are stored in a field-free central region and the amplitude of the rf fields rise with increasing distance from the center. In this field configuration, the ponderomotive force acts as a reversing force and prevents an escape of the ions. The same field configuration appears in the longitudinal plane in between the cavity cells in the transversal beam center where the magnetic field is zero. Thus, ions are be trapped between two cells.

For an assessment of the ion motion in the transversal plane due to the electromagnetic fields of the TM_{010} mode, only its magnetic fields have to be taken into account. Except for the electron beam's attractive Coulomb force, the transversal electric rf field of the mode is zero. The magnetic field distribution $B_{x,z,\mathrm{cav}}$ shows a field strength of zero at the beam center. It increases with distance from the beam center and reaches its maximum at the inner surface of the cavity, as visualized in figure 4.31 (bottom). As shown in figure 4.31 (top), the magnetic field lines of $B_{x,z,\mathrm{cav}}$ are orientated circularly around the beam center and its field strength oscillate with a phase difference of $\pi/2$ in reference to the electric field [Wil00, section 5.1.2]. As a consequence, the motion of an ion, which drifts away from the beam center in the transversal plane, is deflected into the longitudinal plane by the Lorentz force caused by $B_{x,z,\mathrm{cav}}$ (see figure 4.31 (middle)). Since $B_{x,z,\mathrm{cav}}$ oscillats with ν_{rf}, the deflection is directed upstream within one half period of t_{rf} and downstream during the other half period. If the amplitude of the magnetic field would be constant along x or z, the ion would undulate longitudinally and the average direction of the drift would be unchanged, enabling a transversal escape. Yet, the magnetic field increases with the distance from the beam center (see figure 4.31 (bottom)). The illustrated trajectory of an out-drifting ion for a time of $9t_{\mathrm{rf}}$ is shown in the middle graph. Due to the increment in the magnetic field strength, the ion's gyro radius decreases in transversal direction (x or z). The deflection angle per half period increases accordingly, because the ion's transversal velocity is not altered. Consequently, the ion trajectory winds up as $B_{x,z,\mathrm{cav}}$ increases, reducing the effective transversal drift velocity significantly. In consequence, this mechanism may prevent a transversal escape of ions.

To estimate the dimension of the region around the beam center in which ions are trapped transversely, the maximal strength of the magnetic field is estimated. It can be evaluated[33] by [Wil00, section 5.1.2, conversion of equation 5.27]

$$\left|B_{x,z,\mathrm{cav}}^{\mathrm{max}}\right| = -\varepsilon_0 c J_0'\left(\frac{2\pi\nu_{\mathrm{rf}}}{c}\cdot r\right)\cdot\left|E_{s,\mathrm{cav}}^{\mathrm{max}}\right| \ .$$

[33] Here, a simple inner geometry of a pillbox cavity is assumed. This single-cell cavity has a cylindrical inner geometry and its field distribution is therefore analytically describable.

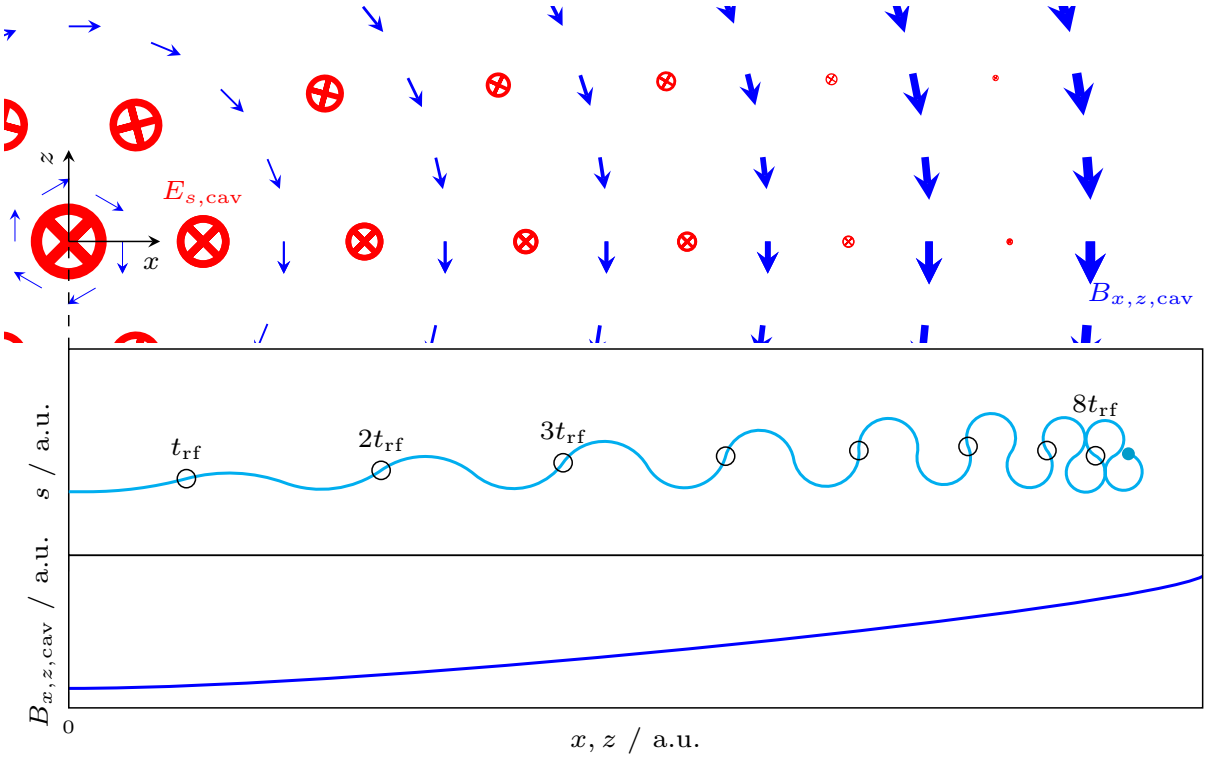

Figure 4.31: Illustration of the influence of the circular magnetic rf field of the TM_{010} mode on the motion of an ion. The top graph illustrates an excerpt of the field strength distribution of the longitudinal electric ($E_{s,\mathrm{cav}}$) and transversal magnetic fields ($B_{x,z,\mathrm{cav}}$) of the TM_{010} mode around the beam center. The beam center is located in the origin of the transversal coordinate system. For this field configuration, the trajectory of an ion which propagates away from the beam center is illustrated in the middle graph. The variation of $B_{x,z,\mathrm{cav}}$ with increasing distance from the beam center is shown in the bottom graph.

$B_{x,z,\mathrm{cav}}$ is maximal at the inner surface of the cavity cell at a radial distance which equals the inner diameter. At this location, $J'_\nu(y)$, the derivative of the Bessel function of the first kind, has its first local maximum which is equal to approximately 0.582. With a maximal electric field $E^{\max}_{s,\mathrm{cav}}$ within the cavity of $1.37 \cdot 10^6\,\mathrm{V\,m^{-1}}$, $|B^{\max}_{x,z,\mathrm{cav}}|$ is equal to approximately 2 100 T. By linear interpolation of the mode's magnetic field between zero and $|B^{\max}_{x,z,\mathrm{cav}}|$, a field strength of 5 T is determined at a distance of $\sigma_x \approx 1$ mm from the beam center. Here, a CO_2^+ ion, drifting away from the beam center perpendicular to the magnetic field with the average thermal velocity of $189\,\mathrm{m\,s^{-1}}$, shows a gyro radius of 1.7 pm. The shown trajectory in figure 4.31 (middle) consequently takes place in distances of micro meters from the beam center, where the magnetic field is much lower than 5 T and the gyro radius is larger.

However, the strong magnetic component of the TM_{010} mode's rf field in principle hinders a transversal drifting of ions. Of course, this component also influences all longitudinal ion motions which have an offset from the beam center. A detailed treatment by dedicated numerical simulations is desirable in future to specify the effect of these electromagnetic rf fields on ion motion on a scope which exceeds these rough assertions.

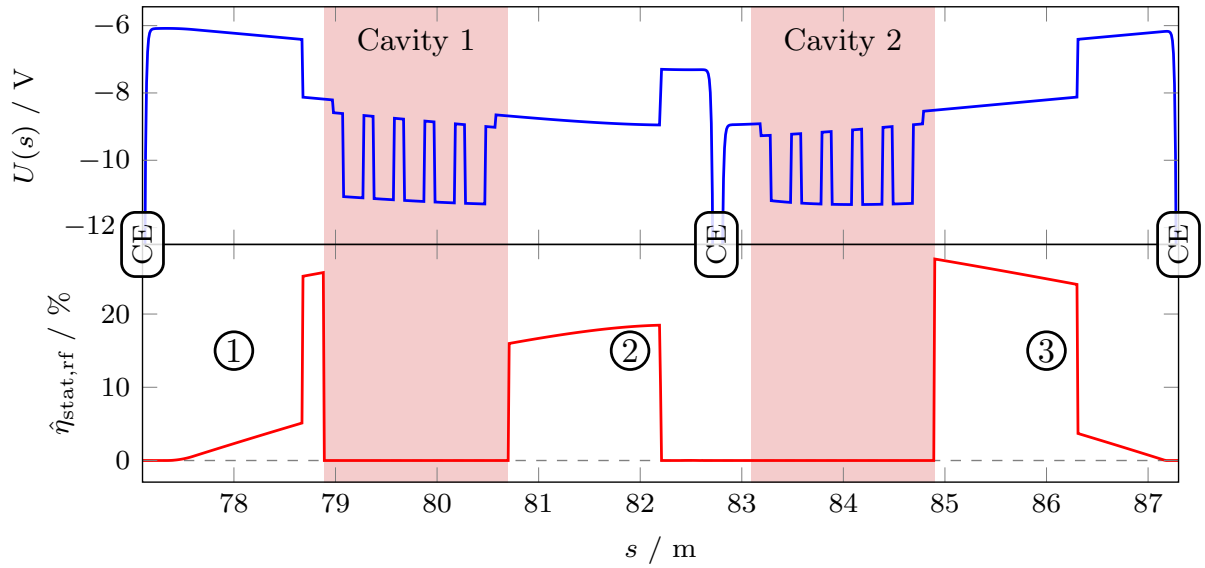

Figure 4.32: Local static neutralization in the rf section of the storage ring (bottom). It is determined on basis of the beam potential (top) and the assumption, that the ion transmission through the rf cavities is zero.

4.4.4 Implications for the Ion Clearing in RF Sections

The simulation of the ions' dynamics adjacent to rf cavities and their motion within them, lead to implications regarding ion accumulation in rf sections of electron accelerators.

Additional Potential Hollows The transmission of ions through the rf cavities of the storage ring can assumed to be zero. Consequently, they should be interpreted as potential barriers for ions and thus additional potential hollows emerge in the storage ring. Using the static neutralization approach, presented in section 4.2.2, the additional amount of accumulated ions can be estimated on basis of the shape of the beam potential. The bottom graph of figure 4.32 shows the local static neutralization $\hat{\eta}_{\mathrm{stat,rf}}$ in the rf section, under the assumption that no ion transport takes place through the cavities. Consequently, ions in region ① have to accumulate locally up to 26 % to drive excess ions towards the upstream clearing electrode. In region ② $\hat{\eta}_{\mathrm{stat,rf}}$ has to be equal to approximately 18 % to enable ion clearing at the central electrode. In region ③ is positioned, the static neutralization locally reaches values of up to 28 %. If this neutralization is reached, excess ions propagate downstream and are cleared. Due to these additional potential hollows, the average static neutralization in the storage ring increases from 1.71 % (compare table 4.1) to 1.86 %.

To prevent the formation of these potential hollows, the installation of additional clearing electrodes near the rf cavities' entrance is advised. Here, a clearing electrode at the upstream entrance of cavity 1 at approximately $s = 78.8$ m would eliminate the region ①. A clearing electrode near the downstream entrance of cavity 2 at $s = 85$ m would remove region ③. Region ② emerges due to the shape of the beam potential and is not caused by cavity 1. Here, a clearing electrode which is positioned at the "bottom" of this potential hollow ($s \approx 82$ m) would prevent its formation.

Ion Accumulation Limits within RF Cavities The longitudinal electric component of the rf field and its spatial distribution prevents the escape of most ions in longitudinal direction by emerging ponderomotive forces. However, the ion trajectories are additionally altered by the transversal magnetic component of

the field. The effect of this alteration is difficult to estimate. Consequently, a transversal confinement[34] of ions at the beam center cannot be confirmed with certainty[35].

However, if the lifetime T_c of ions in vicinity of the beam is prolonged significantly by these electromagnetic rf fields, large ion accumulations may be present there. Then the attractive space charge force of the electron beam is not necessary to generate an ion confinement and an accumulation of ions to a level of $\eta > 1$ is possible[36].

To clear these ions, the use of clearing electrodes may be suitable for new cavity designs. The installation of electrodes in field-free regions in-between the cells may reduce the local ion population significantly.

4.5 Summary: Ion Accumulation in the Storage Ring

The bunched structure of the electron beam does not destabilize any ion species when the storage ring is homogeneously filled. Consequently, all ion species show stable trajectories, transversely oscillating and longitudinally propagating within the beam potential.

Due to longitudinal shape of the beam potential, potential hollows emerge in the storage ring in which ions are longitudinally trapped. Thus, a static neutralization emerges which can be estimated by using the developed static neutralization approach. It is approximately 1.6 to 2 % in the storage ring for beam energies between 1.2 and 3.2 GeV, respectively. This neutralization could be reduced to 1/8th if additional ion clearing electrodes would be installed at several locations in the storage ring.

However, in the static neutralization approach, ion trapping within magnetic mirrors, which are present in form of the dipole magnets' fringe fields, is not considered. The tracking tool TracTIon has been developed to simulate the horizontal and longitudinal propagation of ions within a representative FODO cell of the storage ring. Indeed, the dipoles' fringe fields create magnetic mirrors for ions, which are accelerated towards them by the longitudinal gradient of the beam potential. These mirrors reflect ions with low momentum, especially light ions, and significantly hinder an ion transport towards clearing electrodes. According to the simulation, the local dynamic neutralization can reach values of approximately one at the location of these fringe fields, resulting in an average neutralization of approximately up to 40 % at 1.2 GeV and 35 mA. However, this value may be overestimated due to systematical errors. Additional clearing electrodes, installed in vicinity of these fringe fields, would reduce the dynamic neutralization in the storage ring by approximately 1/4th.

The simulated composition of the ion population in its equilibrium state is similar to the individual species' production probability as their clearing rates are almost identical. Although the composition varies along the accelerator, on average H_2^+ ions represent approximately 49 % of the population, H_2O^+ 17 %, N_2^+/CO^+ 22 % and CO_2^+ 12 %.

In the TracTIon simulation, the clearing electrodes' current, resulting from removed ions and being dependent on the total ion production rate, is congruent with ion current measurements during operation of the storage ring with identical beam energy and current. With this agreement, the made assumptions

[34] Indeed, rf cavities can in principle be used to confine charged particles. See e.g. [Min05]. Here, the rf field within a spherical cavity, operating with a so called H_{120} mode, is used.

[35] Dedicated numerical simulations are required to determine the lifetime of ions which are produced in rf cavities and verify their confinement. Subsequently, a proper positioning of clearing electrodes can be planned on basis of the simulated ion movement within the rf field of the cavities.

[36] To accumulate to this neutralization level, the average lifetime of the ion population must exceed the neutralization time T_n. For the storage ring, T_n ranges from 2.1 to 11.4 ms in dependence of the beam energy and current (see figure 3.23 with $T_n = 1/R_p$).

for the ion production, namely the pressure model (compare section 3.2) and the production rate for photo ionization (compare section 3.4), could be verified.

Moreover, a dedicated simulation with TracIon has shown that the cross-field drift velocity within dipole magnets is *mass* dependent for horizontal ion amplitudes between $\pm 2\sigma_x$, in contrast to theoretical expectations. Here, the different non-zero gyro radii of the ion species result in deviations in their experienced average electric field $\langle E_x \rangle$ which determines the effective drift velocity. Heavy ions with larger gyro radii show a lower drift velocity than light ones with small radii. As a consequence, it is expected that especially heavy ions accumulate in dipole magnets to a higher level as would have been expected from theory.

Ion accumulation in the rf section of the storage ring has been considered, too. Due to emerging ponderomotive forces, resulting from the longitudinal gradient of the electric rf field, ions cannot propagate through rf cavities. Thus, the cavities represent potential barriers for the ions' longitudinal propagation towards clearing electrodes. This results in additional potential hollows and an increased static neutralization. Ions, which are produced within a cavity, are longitudinally trapped and oscillate between the cavity's cells. It is expected that ions are also confined transversely to some extend due to the influence of the transversal magnetic rf field on the ions' motion. Since this confinement is not caused by the beam, an occurrence of a local neutralization above one is possible. Future sophisticated numerical simulations on the ion dynamics within the cavity's rf field should verify these findings and clarify if additional ion clearing electrodes within the cavity or in its vicinity have to be installed to reduce the neutralization there.

CHAPTER 5

Ion Induced Effects in an Electron Accelerator

In chapters 3 and 4, the ion production mechanisms along with their accumulation in the storage ring have been studied. Numerical simulations on ion accumulation obtained a neutralization in the order of tens of percent with a local neutralization which, in principle, is close to one in certain regions of the accelerator (compare section 4.3.5).

A variety of effects emerge due to the ions' COULOMB interaction with the beam via their space charge. One effect is a transversal tune shift. This tune shift can result in a significant reduction of the beam's lifetime due to resonant excitation of parts of the beam electrons in optical resonances. The shift and especially its coherent and incoherent components will be discussed in the following section.

Every ion oscillates around the beam's center of charge while it is trapped in the beam potential. Depending on its mass, the ionization status and the spatial shape of the electrical reversing force of the beam, each ion oscillates with a specific frequency (compare section 2.4.1). If the transversal oscillation frequency of an ensemble of ions is congruent to the frequency of an oscillation mode of the beam, a resonant excitation of both electrons and ions may occur. For sufficiently large growth rates, the amplitude of the beam oscillation may exceed the accelerator's transversal acceptance and significant beam losses occur. This so called beam-ion instability (BII) will be discussed in section 5.2.

In appendix A.16, two additional effects are discussed briefly: A pressure increment in the vicinity of the beam due to accumulated ions and an increased betatron coupling. Both effects, however, show a negligible impact in the storage ring.

5.1 Ion Induced Coherent and Incoherent Tune Shifts

During accumulation of ions within the electron beam, the beam's own electromagnetic space charge field is superimposed by the ions' electric field. Their field perturbs the *relativistic cancellation* of the electric and magnetic field of the beam and results in an additional focusing force. In the following section, the electron beam's electromagnetic field resulting in this cancellation along with the ions' field and the emerging tune shift will be discussed in an analytical approach.

In section 5.1.2, the MATLAB tool DQTOOL is presented, enabling the determination of the tune shift distribution of the beam due to the space charge of the electrons and ions.

Subsequently, this tool is used to determine modified tune distributions for different charge distributions of the ion population in sections 5.1.3 and 5.1.4.

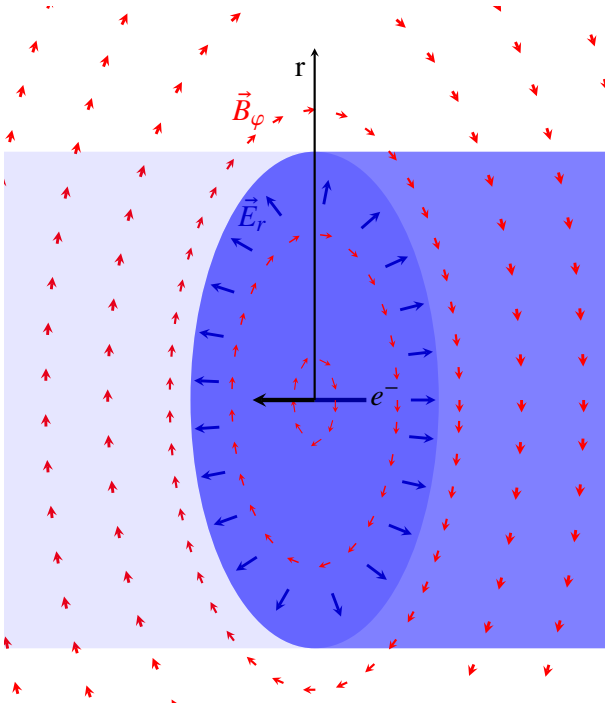

Figure 5.1: Illustration of the electric and magnetic field of the electron beam. Here, the electrons propagate from right to left and generate a circular magnetic field $\vec{B}_\varphi$ and a radial electric field $\vec{E}_r$.

5.1.1 Analytical Approach for the Determination of the Tune Shift

To model the mutual space charge interaction of electrons within the beam and the effect of accumulated ions on them, first an analytical approach is discussed. In this approach an unbunched electron beam with a round transversal profile with homogeneous charge density is considered without ions first, before the ion induced tune shift is determined. A more detailed derivation of the tune shift can be found in appendix A.17.

Space Charge Induced Tune Shift

In figure 5.1, the electric and magnetic fields generated by the relativistic electrons of the beam are illustrated. On one hand, the electrons generate a radial electric field $E_r(r)$ with a radial profile which is dependent on their transversal charge distribution. Due to their equal electric charge, they experience a radial repulsive Coulomb force. On the other hand, the electrons propagate with a velocity of $v_s = \beta c$ with $\beta \approx 1$ and consequently generate a circular magnetic field $B_\varphi(r)$ around the beam. For an ultra relativistic electron which propagates longitudinally, the Lorentz force, emerging from the magnetic field, counteracts the Coulomb repulsion. The resulting radial force $F_e(r)$ approaches zero for an ultra relativistic beam with $\beta \to 1$. Here, the repellent electric component of the Lorentz force is compensated by its attractive magnetic component in a so called *relativistic cancellation*.

Effect of Accumulated Ions The accumulation of ions perturbs this equity of forces. The ion population generates a radial electric field and the resulting force $F_{\text{ion}}(r)$ attracts the electrons towards the beam center. Since ions propagate with non-relativistic velocities, they do not generate a magnetic field which would counteract the electron-ion attraction. In dependence of the local neutralization $\hat{\eta}$, ions reduce the

repellent force of the electrons' space charge as

$$F(r) = \mathcal{B} \cdot F_{\mathrm{e}}(r) - F_{\mathrm{ion}}(r, \hat{\eta}) \, .$$

and consequently lead to a dominance of the attractive force.

$\mathcal{B} > 1$ is the bunching factor which emerges due to the bunched structure of the beam. The ions' longitudinal charge distribution along the accelerator is constant, assuming a constant production and clearing rate. In contrast, the electrons in the beam are compressed into bunches resulting in an elevated local charge density when compared to the ion density. This compression is taken into account by scaling their charge density, and thus $F_{\mathrm{e}}(r)$, by $\mathcal{B}$, which is the ratio of the longitudinal charge density in the center of the bunch to its time average. For the derivation of $\mathcal{B}$, see appendix A.18.

Quadrupole Kick and Resulting Tune Shift The attractive space charge force acts as an additional focusing strength on the beam and can be expressed as a radial quadrupole kick δk_r, assuming that $F(r)$ is linear proportional to r. If the ions' transversal charge distribution is assumed to be equal to the distribution of the beam, the kick is given by (compare equation (A.30) in appendix A.17)

$$\delta k_r = -\frac{F(r)}{m_{\mathrm{e}}(\beta c)^2 \gamma} \frac{1}{r} = -\frac{eI}{2\pi\varepsilon_0 m_{\mathrm{e}}(\beta c)^3 \gamma} \frac{1}{a^2} \left(\frac{\mathcal{B}}{\gamma^2} - \hat{\eta}(s) \right) \, . \tag{5.1}$$

For an elliptical beam, a^2 can be replaced by $\sigma_{x,z}(\sigma_x + \sigma_z)$ and δk_r decomposes into individual horizontal and vertical kicks $\delta k_{x,z}$.

A quadrupole kick results in a tune shift $\Delta Q_{x,z}$ which can be determined by [Wil00, section 3.15.2, equation 3.274]

$$\Delta Q_{x,z} = \frac{1}{4\pi} \oint \delta k_{x,z} \cdot \beta_{x,z}(s) \, \mathrm{d}s$$

assuming that $\delta k_{x,z}$ is small compared to the quadrupole strength of the accelerator and does not alter the optical functions $\beta_{x,z}(s)$ significantly.

The space charge interaction of accumulated ions with the beam and its own space charge leads to a tune shift of [Hin11, section 17.1, equation (148)]

$$\Delta Q_{x,z}^{\mathrm{sc}} = -\frac{\mathrm{e}I}{8\pi^2 \varepsilon_0 m_{\mathrm{e}}(\beta c)^3 \gamma} \int_0^C \frac{\beta_{x,z}(s)}{\sigma_{x,z}(s) \left(\sigma_x(s) + \sigma_z(s)\right)} \left(\frac{\mathcal{B}}{\gamma^2} - \hat{\eta}(s) \right) \mathrm{d}s \, . \tag{5.2}$$

An approximation for $\Delta Q_{x,z}^{\mathrm{sc}}$ in case of a constant neutralization along the accelerator is given by equation (A.31) in the appendix.

Characteristics of the Tune Shift Note that the tune shift due to electrons' mutual repulsion is negative and proportional to $1/\gamma^3$. Due to the relativistic cancellation, it can be neglected for electron accelerators with $\gamma \gg 1$. The mutual attraction of electrons and ions in contrast only decreases as $1/\gamma$ and thus has a more dominant effect on the beam. Its positive tune shift increases linear with neutralization and beam current, and thus, with the total number of ions in the accelerator[1]. For increasing beam energy E, however, $\Delta Q_{x,z}^{\mathrm{sc}}$ decreases approximately as $1/E^3$ since not only γ increases but the beam dimensions

[1] At a beam energy of 1.2 GeV and a current of 200 mA, ΔQ_x^{sc} is equal to 0.89 and ΔQ_z^{sc} to 3.73 for a fully neutralized storage ring with $\eta = 1$ in a worst case scenario.

$\sigma_{x,z}$ enlarge with E, too[2]. Due to the different beam dimension in the horizontal and vertical plane with $\sigma_x > \sigma_z$, the vertical tune shift is larger than the horizontal one in a plane circular accelerator[3].

A typical tune in the storage ring is $Q_{x,0} = 4.619$ and $Q_{z,0} = 4.431$. In the vertical plane, the distance to the nearest major[4] optical resonance in positive direction - a half integer resonance at $Q_{z,\mathrm{res}} = 4\frac{1}{2}$ - is equal to approximately 0.07 (compare figure 2.10). The distance to the nearest horizontal third integer resonance at $Q_{x,\mathrm{res}} = 4\frac{2}{3}$ is equal to approximately 0.05.

At a beam energy of 1.2 GeV, the neutralization is equal to approximately 40 % at a current of 35 mA according to simulations with TracTIon (compare section 4.3.5). For these parameters, tune shifts of $\Delta Q_x^{\mathrm{sc}} = 0.062$ and $\Delta Q_z^{\mathrm{sc}} = 0.261$ are obtained which exceed the distances to these resonances significantly. Yet the expected reduction of the beam life time due to excitation of beam electrons in the resonance does not occur in reality. This results from the mostly incoherent nature of the ion induced tune shift.

Coherent and Incoherent Tune Shift

Each electron in a bunch experiences different electric and magnetic fields in dependence of its position in the bunch. The electron beam has a Gaussian transversal charge distribution. Thus, the assumption that the space charge force $F(r)$ increases approximately linear with the electrons' displacement from the beam center is only valid for a small region with $|x| < \sigma_x$ and $|z| < \sigma_z$.

Additionally, the ratio of the electrons' to the ions' charge density alters in the bunch along the longitudinal axis. In the head and tail of the bunch, the electron density is below the ion density. Here, $F_{\mathrm{ion}}(r)$ exceeds $F_{\mathrm{e}}(r)$ and the resulting force $F(r)$ is clearly attractive. In the beam center, the electron density exceeds the ion density resulting in a still attractive, but reduced, force $F(r)$. Consequently, $\delta k_{x,z}$ is not identical for all electrons in each bunch. In fact, each electron experiences a different $\delta k_{x,z}$ which additionally changes in time in dependence of its transversal and longitudinal position while it oscillates within the bunch. Additionally, the amplitude and phase of these transversal and longitudinal oscillations is continuously changed by emission of synchrotron radiation. Instead of a collective $\Delta Q_{x,z}^{\mathrm{sc}}$, the electrons' tunes are represented in a tune distribution with finite width. Therefore, $\Delta Q_{x,z}^{\mathrm{sc}}$ in general is called an incoherent tune shift.

The difference between coherent and incoherent tune shift is visualized in figure 5.2 (a). Consider a beam with an initially sharp transversal tune distribution at its initial tune Q_0. When the electrons are influenced coherently where all electrons experience the same quadrupole kick due to e.g. a change in the accelerator's quadrupole strength, a coherent tune shift ΔQ_{coh} changes the tune of the beam without altering its distribution.

In case of an incoherent effect, such as ion accumulation, an incoherent tune shift $\Delta Q_{\mathrm{incoh}}$ emerges, altering the shape of the tune distribution. The majority of the electrons still shows a tune at approximately Q_0 for most of their lifetime within the bunch but some electrons experience larger quadrupole kicks for short time periods, extending the tune distribution asymmetrically.

Coherent Tune The peak of a tune distribution defines the *coherent tune*. This is the tune with which the majority of electrons oscillates in time average. If the electron beam is excited by a narrow band

[2] In comparison, $\Delta Q_{x,z}^{\mathrm{sc}}$ at a beam energy of 2.2 GeV decreases to 16.2 % of its value at 1.2 GeV. At 3.2 GeV, it is reduced to 4.2 %.

[3] In the storage ring with a betatron coupling of approximately 7.2 %, the ratio $\Delta Q_z^{\mathrm{sc}} / \Delta Q_x^{\mathrm{sc}}$ is approximately 4.2.

[4] Here, only up to third order resonances are considered. Higher order resonances in general show reduced resonance strength. However, several higher order resonances - located closer to $Q_{x,0}$ and $Q_{z,0}$ than the one mentioned - have been detected and measured which significantly reduce the lifetime of the electron beam in the storage ring. For more information see [Pro18, chapter 8].

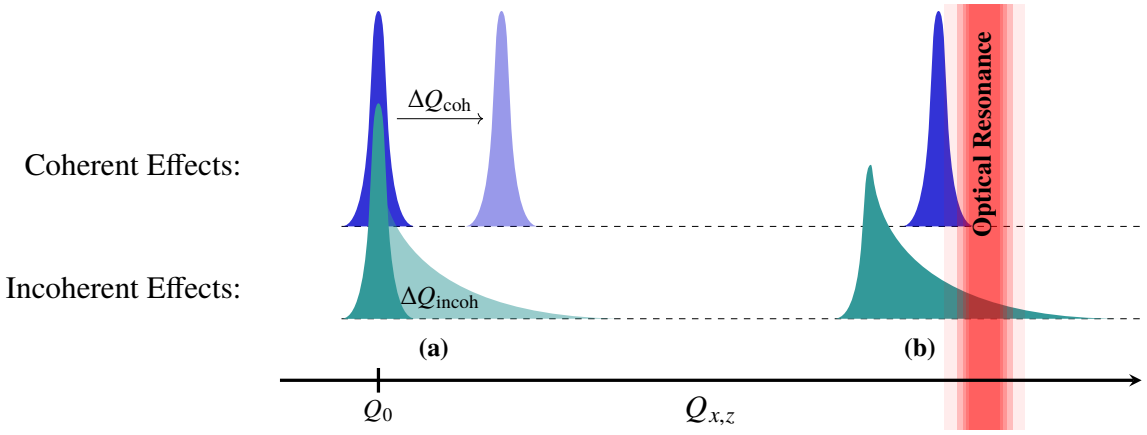

Figure 5.2: The effect of a coherent and incoherent tune shift (ΔQ_{coh} and ΔQ_{incoh}) on the tune distribution of the beam with initial tune Q_0 is shown in (a). In (b) these tune distributions are shown in close proximity of an optical resonance.

sinusoidal electric field, all electrons within a bunch will start to oscillate coherently with the same amplitude and phase when the excitation frequency equals the coherent tune [Ng06, section 3.2.3]. The coherence of the electrons' motion results in a corresponding oscillation of the beam's center of charge. This oscillation can be detected by the pick-up electrodes of beam position monitors in which each bunch of the beam influences a position dependent voltage signal[5]. By analyzing the frequency composition of this signal, the frequency spectrum of the beam can be obtained for the transversal and longitudinal planes. Here, transversal coherent beam oscillations are represented by contributions in certain frequency domains of the spectrum, enabling the determination of the fractional component of the coherent tune. In section 5.2.1, this beam spectrum will be discussed in more detail.

Incoherent Tune In contrast to the coherent tune, the incoherent tune cannot be measured in electron accelerators the same way[6]. Since a small minority of the electrons oscillate with a multitude of frequencies deviating from Q_0 for a short period of time, the beam does not show any other dominant frequency component than Q_0 to a significant extent. Consequently, the beam will not respond to an excitation with a coherent oscillation, if the excitation frequency is congruent with a component of its incoherent tune which is too far away from Q_0.

Tune Distributions Near Optical Resonances In figure 5.2 (b), a tune distribution with negligible incoherent tune shift (blue) and one with larger incoherent tune shift (cyan) due to ΔQ_{incoh} is shown close to a destructive optical resonance. If the tune approaches a resonance with finite bandwidth, electrons which oscillate with an individual betatron tune close to the resonance are excited by magnetic field errors in the accelerator (compare section 2.3.3 on page 30). With increasing oscillation amplitude of the

[5] The electron bunch only generates a significant signal when it is close to the pick-up electrodes. Consequently, the signal shows a time structure equal to the beam's bunch structure. For the storage ring, the signal shows a base frequency of $\nu_{\text{rf}} = 500\,\text{MHz}$ frequency-modulated by transversal and longitudinal beam oscillations. The beam position monitor consists of four pick-up electrodes, two pairs of electrodes above and below the beam. Each pair is located left and right of the beam. The horizontal and vertical bunch position can be obtained by comparing the voltage signal of the left with the right electrodes and the upper electrodes' signal with the lower ones, respectively. The longitudinal position can be determined by sampling the sum signal of all electrodes with ν_{rf} at a fixed phase. For more information, see e.g. [Sch15, section 6.1.1].

[6] Here, the diagnostic capabilities by using the Schottky noise of the beam, induced onto pick-up electrodes, is omitted as this method is mostly used in proton accelerators. For more information, see e.g.[Wie95, section 10.1.1].

individual electrons, the quadrupole's magnetic field strength gets more non-linear with increasing x and z which results in a change of their betatron tunes. Therefore, the tune of an excited electron shifts in and out of the resonance's stopband in correlation to its amplitude (compare e.g. [Wil94, section 3, figure 5]). If the electron's tune stays within the stopband for most of the time, its trajectory is mostly in phase with the field error's excitation which resonantly increases its amplitude until the electron is lost. In dependence of the strength of the resonance and distance of the beam's tune to it, the beam's life time will decrease.

One might argue that the beam showing the cyan tune distribution already experience beam losses for a larger distance to the resonance than the blue one because electrons show individual tunes already within the stopband, consequently are excited, destabilized and lost. However, this is not true as the space charge force's strength, causing $\Delta Q_{\mathrm{incoh}}$, alters when the tune of individual electrons coincide with an optical resonance [Ng06, sections 4.1 and 4.2]. Here, the previously described amplitude-correlated variation of an electron's betatron tune in proximity to a resonance is superimposed by $\Delta Q_{\mathrm{incoh}}$ which is also bunch-position and therefore time dependent. Thus, the variation range of the electron's tune alteration close to a resonance increases with $\Delta Q_{\mathrm{incoh}}$. It depends on the excitation strength of the resonance along with the tune's variation range and alteration rate[7], if an electron is lost when encountering an optical resonance. Therefore, $\Delta Q_{\mathrm{incoh}}$ cannot be used as a similar criterion for beam stability as ΔQ_{coh}. $\Delta Q_{\mathrm{incoh}}$ may can be larger than the distance of Q_0 to a destructive optical resonance without significant beam losses, whereas ΔQ_{coh} must be smaller to ensure beam stability.

5.1.2 Numerical Evaluation of the Tune Shift by Using dQTool

The previous analytical approach for the determination of $\Delta Q^{\mathrm{sc}}_{x,z}$ included several simplifications:

- The bunched structure of the beam has been taken into account by using the bunching factor. Here, the bunch is implicitly approximated as having a longitudinal rectangular intensity profile and not a Gaussian charge distribution.
- The ions' transversal charge distribution has been assumed to be equal to the electron beam. As will be discussed in section 5.1.3, the electrons' and ions' distributions deviate from each other significantly.
- A linear dependency of $\delta k_{x,z}$ with x and z has been assumed. For $|x| > \sigma_x$ and $|z| > \sigma_z$, this is not valid.

Thus, $\Delta Q^{\mathrm{sc}}_{x,z}$ only gives indications about its dependencies on the beam energy and current as well as the accelerator's optical functions (beam dimension) and the (local) neutralization.

The developed MATLAB tool dQTool, in contrast, is capable of determining the tune distribution for arbitrary transversal ion density distributions and extracts the measureable coherent tune shift due to space charge effects.

Functional Principle of dQTool

dQTool is a numerical tool, which uses a rigid beam[8] simulation model of the interaction of the electron beam and the ion population.

[7] If, for example, an electron shows an integer individual tune for a duration of half a revolution in the accelerator, it presumably will not be lost as the rise of its amplitude typically occurs during several revolutions.

[8] In a rigid beam/bunch simulation, the distributions of the electron beam and the ion population are not altered by their mutual space charge interaction (compare [Ohm00, section 1]). Here, the equilibrium distributions of the beam and the ions are used.

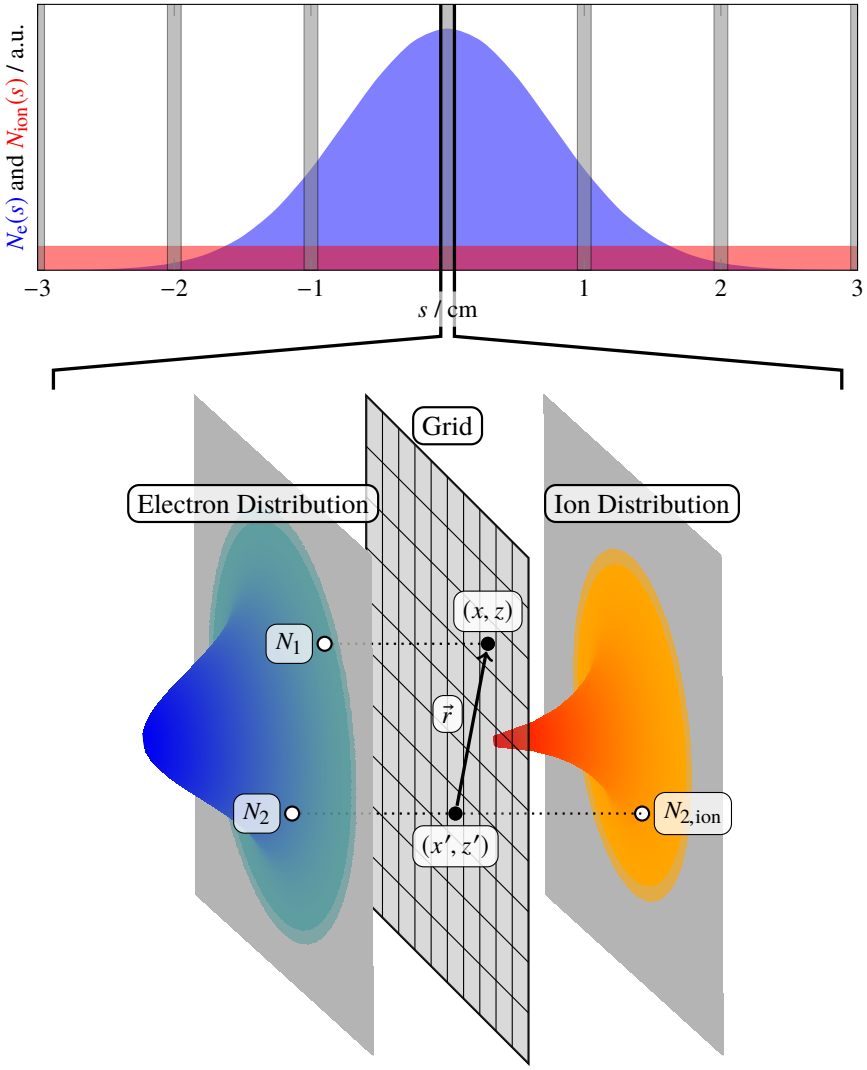

Figure 5.3: Illustration of the functional principle of DQTOOL. In the top graph, the longitudinal charge density of electrons (blue) and ions (red) in a bunch at time t_0 is shown exemplarily. The bunch is separated into several slices which are denoted as gray areas. As visualized below, in each bunchslice the transversal space charge force on an electron at (x, z) due to N_2 electrons and $N_{2,\text{ion}}$ ions at (x', z') is calculated for each position of the grid.

Bunch Slices and Voxel Grid In figure 5.3, DQTOOL's functional principle is visualized. As can be seen in the top graph, ions have a constant charge density in the longitudinal plane whereas the electron beam is bunched. Consequently, the ratio of electrons to ions depends on the longitudinal position s in the bunch, resulting in different forces acting on the electrons. Therefore, the bunch is separated into several thin longitudinal slices (typically 25 equidistant slices reaching from $-4\sigma_s$ to $+4\sigma_s$) and the emerging transversal space charge forces on each electron in the slice is determined. Here, the electrons' and ions' transversal positions are discretized on a two-dimensional voxel-grid reaching from $-4\sigma_{x,z}$ to $+4\sigma_{x,z}$ with typically 200 bins with equal width. On this grid, the number of electrons $N_1(x, z)$ and ions $N_{2,\text{ion}}(x, z)$ in each voxel is determined on basis of the transversal electrons' and ions' charge density distribution. The ion distribution can in principle be chosen arbitrarily to study its effects on the beam.

Quadrupole Kick on Individual Electrons The determination of the horizontal and vertical quadrupole kick shows similarities with the derivation of $\Delta Q^{\mathrm{sc}}_{x,z}$ from section 5.1.1 which is discussed in detail in appendix A.17.

However, here only the transversal space charge force acting on an individual electron is of importance. Consider an electron at position (x, z) on the grid, as visualized in figure 5.3 (bottom). The total number of electrons in this voxel is equal to N_1. In another pixel at position (x', z') with a distance of $|\vec{r}|$, a number of N_2 electrons are positioned. $\vec{r}$ is the difference vector between (x, z) and (x', z') in the transversal plane. It can be expressed as

$$\vec{r} = \begin{pmatrix} x - x' \\ z - z' \end{pmatrix} = \begin{pmatrix} \Delta x \\ \Delta z \end{pmatrix} .$$

The force due to the Coulomb repulsion $\vec{F}_{\mathrm{el}}(\vec{r})$ and the magnetic attraction $\vec{F}_{\mathrm{mag}}(\vec{r})$ of two parallel currents can be expressed as

$$\vec{F}_{\mathrm{el}}(\vec{r}) = \frac{N_1 N_2 \mathrm{e}^2}{4\pi\varepsilon_0} \frac{\vec{r}}{|\vec{r}|^3} \qquad \text{and} \qquad \vec{F}_{\mathrm{mag}}(\vec{r}) = -\frac{N_1 N_2 \mathrm{e}^2 \mu_0 \beta^2 c^2}{4\pi} \frac{\vec{r}}{|\vec{r}|^3} .$$

At position (x, z) a charge of $-N_1 \cdot \mathrm{e}$ is present, whereas a charge of $-N_2 \cdot \mathrm{e}$ is located at (x', z'). Consequently, the space charge force $\vec{F}_{\mathrm{e,e}}(\vec{r})$ on the electron at (x, z) can be expressed as

$$\vec{F}_{\mathrm{e,e}}(\vec{r}) = \frac{N_1 N_2 \mathrm{e}^2}{4\pi\gamma^2\varepsilon_0} \frac{\vec{r}}{|\vec{r}|^3}$$

by using the relation $\mu_0 c^2 = 1/\varepsilon_0$ and $(1 - \beta^2) = 1/\gamma^2$.

Alongside electrons, also $N_{2,\mathrm{ion}}$ ions with a total charge of $+N_{2,\mathrm{ion}} \cdot \mathrm{e}$ are located at position (x', z'). Their space charge attracts the electron at (x, z) with a force $\vec{F}_{\mathrm{e,ion}}(\vec{r})$ which can be expressed as

$$\vec{F}_{\mathrm{e,ion}}(\vec{r}) = \vec{F}'_{\mathrm{el}}(\vec{r}) + \underbrace{\vec{F}'_{\mathrm{mag}}(\vec{r})}_{=0} = -\frac{N_1 N_{2,\mathrm{ion}} \mathrm{e}^2}{4\pi\varepsilon_0} \frac{\vec{r}}{|\vec{r}|^3} .$$

Here, the magnetic contribution vanishes due to the low velocity of the ions.

The total space charge force of electrons and ions positioned at (x, z) and (x', z') adds up to

$$\vec{F}(\vec{r}) = \vec{F}_{\mathrm{e,e}}(\vec{r}) + \vec{F}_{\mathrm{e,ion}}(\vec{r}) = \frac{N_1 \mathrm{e}^2}{4\pi\varepsilon_0} \left(\frac{N_2}{\gamma^2} - N_{2,\mathrm{ion}} \right) \frac{\vec{r}}{|\vec{r}|^3} .$$

Under the assumption that the number of electrons inside one voxel is large, thus their mutual space charge force on average cancels out and the additional $N_1 - 1$ electrons do not contribute to $\vec{F}(\vec{r})$ of a single electron, the electrons in one voxel are independent from each other. Consequently, it holds $N_1 = 1$ and only the electrons and ions in the surrounding voxels are relevant for the determination of $\vec{F}(\vec{r})$ for the single electron. However, all N_1 electrons in the voxel at (x, z) experience the same force.

Using the definition of $\vec{r}$, $\vec{F}(\vec{r})$ can be decomposed into its horizontal and vertical component. The transformation into corresponding quadrupole kicks $\delta\mathcal{K}_{x,z}(x, x', z, z')$ can finally be expressed as (compare equation (5.1))

$$\delta\vec{\mathcal{K}}(x, x', z, z') = \begin{pmatrix} \delta\mathcal{K}_x \\ \delta\mathcal{K}_z \end{pmatrix} = -\frac{\mathrm{e}^2}{4\pi\varepsilon_0 m_{\mathrm{e}} \beta^2 c^2 \gamma} \left(\frac{N_2(x', z')}{\gamma^2} - N_{2,\mathrm{ion}}(x', z') \right) \frac{1}{\left(\Delta x^2 + \Delta z^2\right)^{\frac{3}{2}}} \begin{pmatrix} \frac{\Delta x}{x} \\ \frac{\Delta z}{z} \end{pmatrix} .$$

The actual transversal quadrupole kick $\delta k_{x,z}(x, z)$, acting on electrons at position (x, z), is a superposition of $\delta\mathcal{K}_{x,z}$ from all other positions (x', z') in the bunch slice as

$$\delta k_{x,z}(x, z) = \sum_{\substack{x' \neq x \\ z' \neq z}} \delta\mathcal{K}_{x,z}(x, x', z, z') \, .$$

Note that the number of electrons N_2 and ions $N_{2,\mathrm{ion}}$ in each voxel is dependent on the resolution of the transversal voxel grid and the longitudinal thickness Δs of the considered bunch slices. Whereas a variation of the grid resolution only changes the precision of the simulation and the number of calculation steps, Δs has a significant influence on the obtained values of $\delta k_{x,z}$. Therefore, in `dQTool` $\delta k_{x,z}$ is normalized to reproduce the theoretical ion induced tune shift, derived in section 5.1.1, in a simple and predictable scenario, as will be discussed below.

Transformation into the Tune Distribution To obtain the tune distribution, $\delta k_{x,z}(x, z)$ is determined for every position in each bunch slice. All quadrupole kicks are recorded together with the corresponding number of electrons $N_1(x, z)$ which experience these kicks. Using these numbers as weights for the abundance of these kicks in the distribution, the horizontal and vertical kick distribution is determined with a binning width of typically $4 \cdot 10^{-6}\,\mathrm{m}^{-2}$.

Assuming a constant neutralization in the accelerator, this distribution can be transformed into the tune distribution by scaling the binning width according to

$$\Delta Q_{x,z} = \frac{\langle \beta_{x,z} \rangle \cdot C}{4\pi} \cdot \delta k_{x,z} \, , \tag{5.3}$$

if the average beam dimensions are used when calculating the tune distribution. Here, $\langle \beta_{x,z} \rangle$ is the average horizontal or vertical beta function of an accelerator with circumference C.

Supplementary to the distribution, the peak, representing the coherent tune, and the centroid of the tune distribution, representing the beam's average tune, are extracted along with the maximal incoherent tune shift. Also a transversal map of $\delta k_{x,z}(x, z)$ is generated to enable an identification of regions inside the bunch where certain quadrupole kicks are experienced.

Exemplaric Tune Distribution and Calibration

To demonstrate the capabilities of `dQTool` the tune distribution is simulated which results from the space charge of an ion population with a round shape and constant charge density onto a beam with equal charge distribution. This example is the identical scenario to the derivation of $\Delta Q^{\mathrm{sc}}_{x,z}$ in section 5.1.1 and can be used for calibration of the bunch slice thickness Δs. Here, the beam energy is set to 1.2 GeV with a stored beam current of 100 mA and a neutralization of 50 %. The horizontal and vertical beam width is set to $\sigma_x = \sigma_z = a = 0.66\,\mathrm{mm}$[9]

[9] This hypothetical value emerges in case the betatron coupling is equal to one and the optical functions are set to $\beta_{x,z} = 8.6\,\mathrm{m}$ without dispersion.

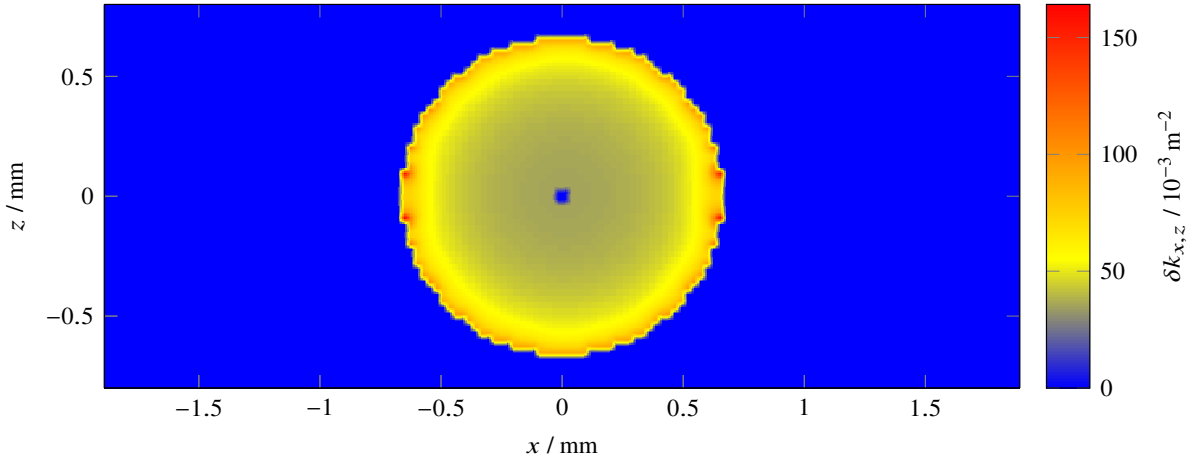

Figure 5.4: Transversal distribution of the horizontal (top) and vertical (bottom) quadrupole kicks $\delta k_{x,z}$ simulated by DQTOOL. The beam energy is 1.2 GeV and the current is 100 mA with a neutralization of 50 %. In the blue regions with $\delta k_{x,z} = 0\,\mathrm{m}^{-2}$, except in the beam center, no electrons are present.

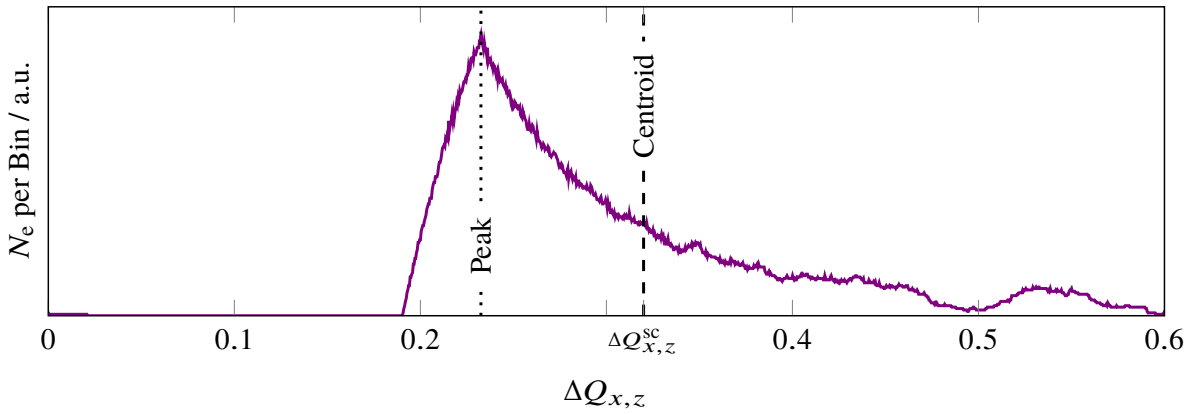

Figure 5.5: Exemplaric horizontal and vertical tune distribution of a round beam with an energy of 1.2 GeV and current of 100 mA at a neutralization of 50 %. Here, the beam and ion population show an identical round transversal shape with constant charge density.

In figure 5.4, the transversal distribution of the horizontal and vertical quadrupole kicks $\delta k_{x,z}$ is shown which the electrons experience at corresponding positions in the bunch slice.

The quadrupole kick $\delta k_x = \delta k_z = \delta k_r$ is proportional to $F_r(r)/r$. Since both charge distributions are constant within the beam, the sum of the space charge forces decreases for $x, z \to 0$ mm as the increased isotropy of the ion density results in a cancellation of forces. In the center, $\delta k_{x,z}$ is set to zero since $F_r(r)$ and r are zero. Towards the edges of the beam, the isotropy is reduced and results in an increment of $\delta k_{x,z}$.

Figure 5.5 exemplarily shows the tune distribution of the electrons in this scenario. As predicted by theory in section 5.1.1, the tune shift is positive. Since the beam shows identical dimensions in the horizontal and vertical plane, both tune distributions look the same.

For this scenario, theory predicts an equal tune shift in the horizontal and vertical plane of $\Delta Q_x^{sc} = \Delta Q_z^{sc} = 0.32$. For an appropriately chosen Δs in DQTOOL the centroid of the tune distribution, being identical to the average tune of the beam, is normalized to be equal to $\Delta Q_{x,z}^{sc}$. The peak of the distribution

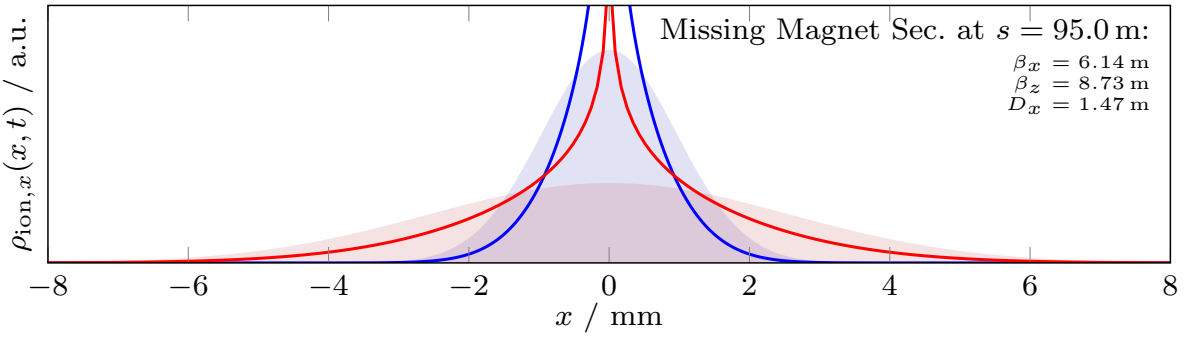

Figure 5.6: Theoretical horizontal ion density distribution for two beam energies in the missing magnet section of the storage ring at $s = 95.0\,\mathrm{m}$. Thus, the horizontal beam width is equal to 0.96 mm for 1.2 GeV and 2.6 mm for 3.2 GeV. The corresponding average electron density distribution is a Gaussian distribution shown in light blue and light red for 1.2 and 3.2 GeV. The accumulated ion density distribution is shown for $t = T_\mathrm{n}$ in corresponding colors.

$\Delta Q_{x,\mathrm{coh}} = \Delta Q_{z,\mathrm{coh}}$ is equal to 0.23 ± 0.01. The maximal detected tune shift of electrons in the beam is equal to 0.89 in the horizontal and vertical plane.

However, the transversal charge distribution of the ion population is not Gaussian. Thus, before numerically determining a realistic tune distribution in section 5.1.4 by using dQTool, the ions' realistic charge distribution and its perturbations will be discussed in the following section.

5.1.3 Simulation of the Transversal Ion Density Distribution Using TransversIon

Equilibrium Charge Distribution for Ions Produced by Impact Ionization

Ions which are produced by the electron beam by impact ionization show an initial transversal density distribution which resembles the beam. After ionization, they show kinetic energies in the order of meV. Attracted by the space charge force of the electrons, ions oscillate around the beam's center of charge in the transversal plane with bounce frequency $\nu_{x,z}^{\mathrm{ion}}$ (compare equation (2.46)). New ions are continuously produced at different positions of the beam and at different times with isotropic initial propagation directions. Each ion oscillates with an individual amplitude and phase.

The local ion population forms a transversal density distribution in the horizontal plane which can be expressed[10] as [Tav92b, section 3, equation 17]

$$\rho_{\mathrm{ion},x}(x,t) = \frac{1}{\sqrt{2\pi}\pi\sigma_x} \cdot \frac{t}{T_\mathrm{n}} \cdot \exp\left(-\frac{x^2}{4\sigma_x^2}\right) \cdot K_0\left(\frac{x^2}{4\sigma_x^2}\right) . \tag{5.4}$$

σ_x is the horizontal beam width. K_0 is the modified Bessel function of the second kind K_ν with argument $\nu = 0$. The vertical distribution $\rho_{\mathrm{ion},z}(x,t)$ is obtained by replacing x with z.

Figure 5.6 shows the ion density distribution $\rho_{\mathrm{ion},x}(x,t)$ for two beam energies at $t = T_\mathrm{n}$. T_n is the neutralization time where the neutralization reaches a value of one (compare equation (2.15) in section 2.2.3). In comparison to the Gaussian density distribution, the ion distribution shows a higher density in the beam center and lower density at larger amplitudes.

[10] Here, it is assumed that ions are produced at rest with zero initial kinetic energy. Along with additional assumptions, the repelling space charge force between ions is neglected, too. Additionally, the beam potential is assumed to be a harmonic potential where $\nu_{x,z}^{\mathrm{ion}}$ is constant for all amplitudes. The ion density increases linearly with time t as newly produced ions increase the local population. The clearing rate is assumed to be zero.

Equation (5.4) becomes infinity for $x = 0\,\text{mm}$. Therefore, the used simple form is only valid in the tails of the distribution, where the ratio of the ion's initial kinetic energy to its potential energy is negligible. A more realistic expression of equation (5.4) which includes a non-zero initial kinetic energy of the ions can be found in [Tav92b, section 4].

The MATLAB tool TRANSVERSION, which has been developed in the course of this work for the determination of the frequency spectrum of transversal ion oscillations, can be used to simulate the transversal equilibrium ion density distribution for arbitrary production maps. Using it, the ion density distribution downstream of dipole magnets can be determined. Subsequently, DQTOOL can be utilized to determine if this altered charge distribution locally modifies the tune distribution.

TRANSVERSION

TRANSVERSION is a one-dimensional tracking algorithm with which the motion of multiple ions within the beam potential is consecutively tracked. In the following, its functional principle is stated in a short form. For more details, see appendix B.2.6.

TRANSVERSION simulates the horizontal or vertical propagation of typically several ten thousand ions within a precomputed time averaged beam potential using an EULER-NEWTON tracking algorithm. Here, the beam potential is either static or oscillates in time with a certain frequency and amplitude[11]. The simulated time is typically much larger than the ion oscillation period within the potential. The species to which the ion belongs as well as its initial velocity is assigned according to corresponding probability distributions[12]. For the ions' initial horizontal or vertical position within the potential, arbitrary probability distributions on basis of ion production maps can be defined.

After each tracking, a frequency analysis of the simulated trajectory is conducted. This allows the frequency spectrum of the entire ion ensemble to be determined. In addition to each ion's initial position, its amplitude at a random[13] time during the simulation is extracted. Thus, the initial and equilibrium ion density distribution in the horizontal or vertical plane are obtained.

In figure 5.7, a simulated equilibrium ion density distribution is shown for two beam energies of 1.2 GeV (dark red) and 3.2 GeV (dark blue). In the respective colors of red and blue, the two corresponding theoretical predictions by equation (5.4) are shown for comparison. Note that the binning width differs for both beam energies (9.6 µm at 1.2 GeV and 26 µm at 3.2 GeV) and thus magnitudes are not directly comparable.

5.1.4 Influence of Photo Ionization on the Tune Distribution

In the storage ring, the transversal equilibrium density distribution of an accumulated ion population shows several shapes in dependence of its position within the accelerator, as has been elaborated in the course of this work. The distributions' shape, on one hand, results from the form of the beam potential. On the other hand, the transversal ion production map, composed of the individual contributions of different

[11] By exciting the beam to coherent betatron oscillations it is possible to reduce the number of accumulated ions. To determine the clearing rate of this so called beam shaking counter measure, the ion ensemble is tracked within the time dependent beam potential. If an ion crosses certain transversal boundaries, it is assumed to be cleared. By recording this crossing time for each ion, the time evolution of the ion population can be determined and the clearing rate can be determined. For more information, see appendix B.2.6.

[12] The probability for the production of a certain ion species can be determined using the total production rate of the individual species. The initial velocity distribution has been discussed in section 2.1.1.

[13] A random time is used for selection of the amplitude of a single ion to emulate the different lifetimes of individual ions in the beam. In an ion ensemble, all lifetimes are equally represented and consequently all ions show different phases of their transversal oscillating motion. Consequently, this ensemble represents a population in its equilibrium state.

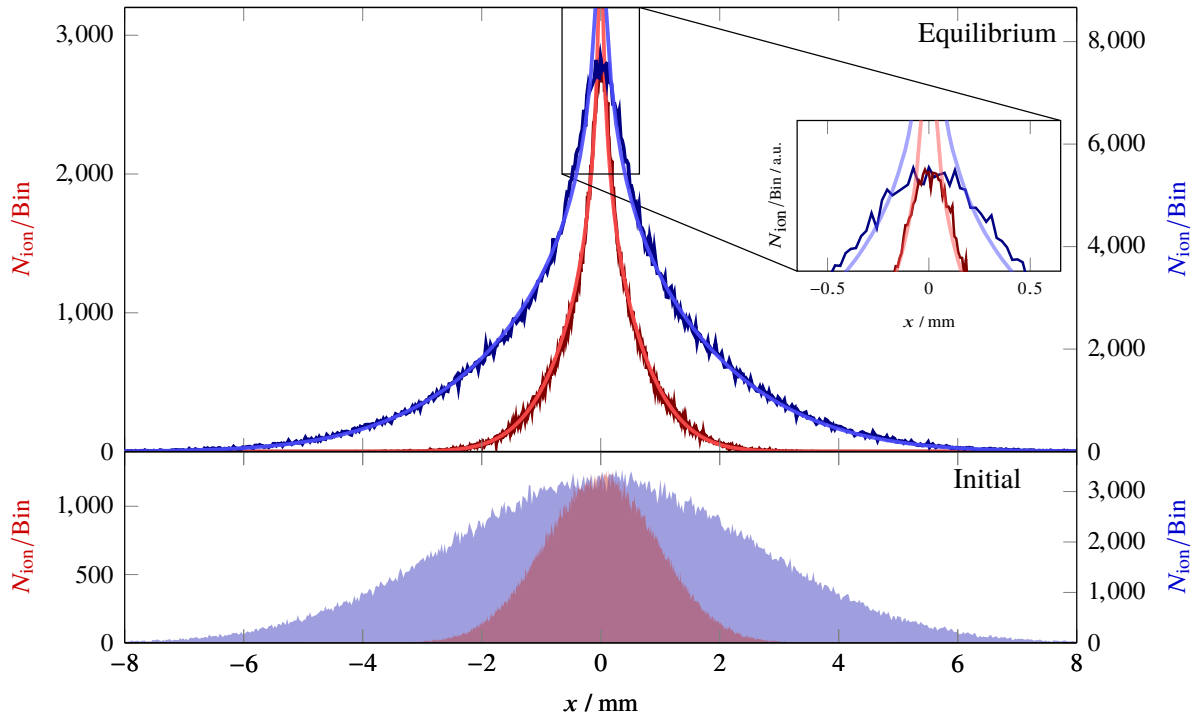

Figure 5.7: Regular ion distribution in the horizontal plane in the missing magnet section at $s = 95\,\text{m}$, simulated by TRANSVERSION. The top graph shows the equilibrium ion distribution. The dark red and dark blue curves denote the simulated distribution at 1.2 and 3.2 GeV, respectively. In the respective colors of red and blue, the corresponding theoretical predictions proportional to equation (5.4) are shown for comparison. The initial positions of the population, thus the ion production map, is shown in the bottom graph. Note that the binning width differs for both energies (9.6 µm at 1.2 GeV and 26 µm at 3.2 GeV) and magnitudes are not directly comparable.

ion production mechanisms like impact and photo ionization, influences the ions' charge distribution severely.

In the storage ring, the following shapes of the ion charge distribution exist:

- In sections of the accelerator, in which ions are *only* produced by impact ionization, the regular ion density distribution in accordance to equation (5.4) of [Tav92b, section 3, equation 17] is present. Since sections without dipole magnets are present in approximately 58 % of the storage ring, this distribution can assumed to be the predominant one.
- Within dipole magnets, the asymmetric ion production map due to photo ionization results in a horizontally asymmetric equilibrium density distribution of ions, as has already been discussed in section 4.3.6. Here, the asymmetry is reflected in the ions' equilibrium distribution since horizontal ion oscillations are hindered by the dipole's vertical magnetic field.
- Downstream of each dipole magnet, the ion production map is still asymmetric. Yet, the resulting equilibrium ion density distribution is horizontally symmetric because magnetic fields are not present, as will be discussed in the following section on page 161. However, significant deviations to the regular ion distribution are visible.

Subsequently, the influence of these charge distributions on the $\delta k_{x,z}$ distribution will be determined using DQTOOL.

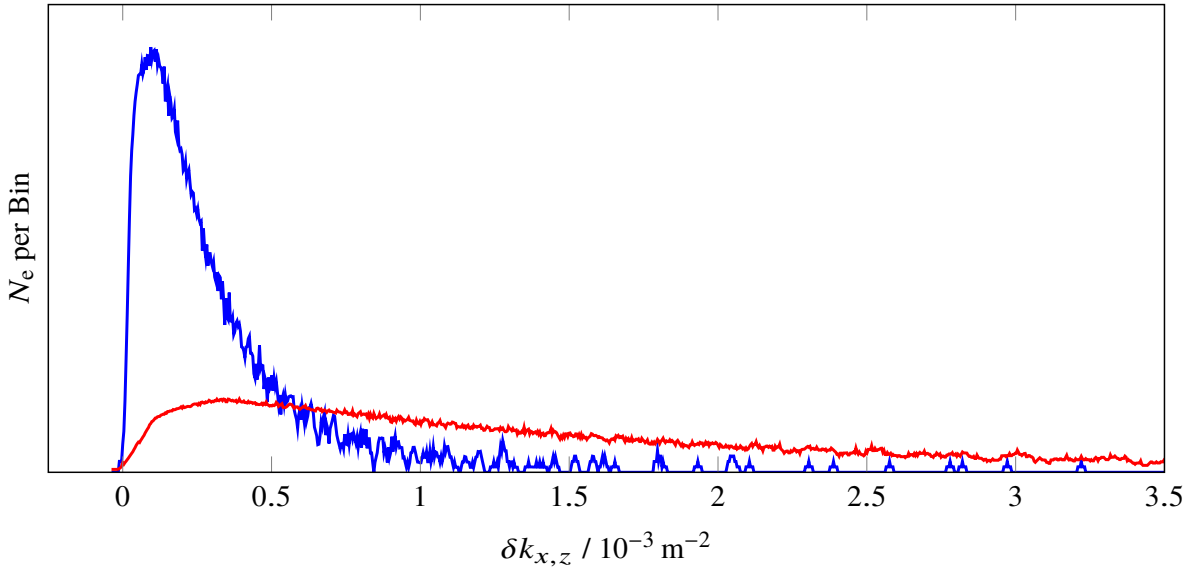

Figure 5.8: Horizontal (blue) and vertical (red) distribution of quadrupole kicks acting of the electron beam when experiencing the space charge forces of accumulated ions whose transversal charge distribution has a regular shape. The beam energy is equal to 1.2 GeV and the stored current is 30 mA with a neutralization of 40 %.

Regular Tune Distribution

The $\delta k_{x,z}$ distribution resulting from the regular transversal charge distribution of ions is simulated by DQTOOL using the average optical functions of the storage ring.

Figure 5.8 shows the distribution of transversal quadrupole kicks $\delta k_{x,z}$ acting on the beam when experiencing the space charge force of an ion population with a regular charge distribution. Here, the beam energy is 1.2 GeV and the stored beam current is 30 mA. The neutralization is chosen to be 40 %. As the beam is vertically more compact than horizontally and consequently the distance between electrons and ions is reduced, vertical space charge forces are larger. As a result, the δk_z distribution extends to larger kicks in comparison to δk_x. The number of electrons showing a kick of $0\,\mathrm{m}^{-2}$, is minimal. The amount of electrons which experience a kick $> 0\,\mathrm{m}^{-2}$ rises to a maximum at approximately $1 \cdot 10^{-4}\,\mathrm{m}^{-2}$ in the horizontal and $3 \cdot 10^{-4}\,\mathrm{m}^{-2}$ in the vertical plane and than decreases for higher kicks in a tail.

In DQTOOL, the peak of the individual distributions ($\delta k_{x,z,\mathrm{max}}$ or the coherent tune shift $\Delta Q_{x,z,\mathrm{coh}}$) and the distribution's centroid $\langle \delta k_{x,z} \rangle$ or $\langle \Delta Q_{x,z} \rangle$ is extracted to characterize the $\delta k_{x,z}$ or $\Delta Q_{x,z}$ distributions[14].

Effect of the Ions' Space Charge Due to the ions' space charge, the $\delta k_{x,z}$ distribution changes with the number of accumulated ions in the accelerator. For an increased neutralization and higher beam currents, the ions' space charge force results in larger quadrupole kicks. Figure 5.9 shows the vertical quadrupole kick distribution of a beam with an energy of 1.2 GeV and a current of 200 mA for different neutralizations. For $\eta = 0$ %, the distribution shows a peak at $0\,\mathrm{m}^{-2}$ with a width which is lower than the resolution of the binning[15]. With increasing neutralization, more electrons experience larger δk_z and

[14] The shown $\delta k_{x,z}$ or $\Delta Q_{x,z}$ distributions are generated by filtering the simulated distributions with a running average. Since the running average in principle shifts the peak of a distribution, an error on the peak and centroid values is estimated using the variance between the unfiltered and filtered distributions.

[15] To visualize the δk_z distribution resulting from the beam electrons' mutual space charge interaction, the distribution is shown in figure C.15 in the appendix with a binning width of $4 \cdot 10^{-10}\,\mathrm{m}^{-2}$.

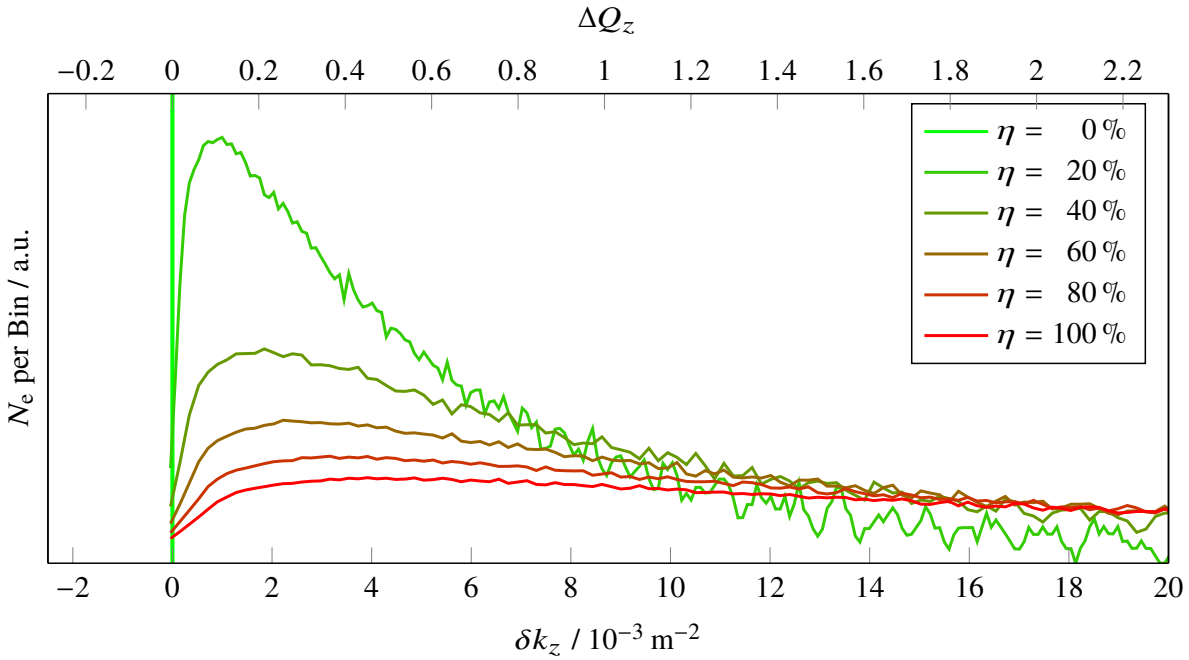

Figure 5.9: Distribution of the beam's vertical quadrupole kicks at an energy of 1.2 GeV and a current of 200 mA for different neutralizations. For this scenario, the theory predicts a tune shift ΔQ_z^{sc} of 0, 0.75, 1.49, 2.24, 2.98 and 3.73 for the shown neutralization of 0, 20, 40, 60, 80 and 100 %, respectively.

form an asymmetric tail which consequently shifts the centroid $\langle \delta k_z \rangle$ of the distribution to higher kick strengths. Additionally, the peak of the distribution $\delta k_{z,\mathrm{max}}$, which is related to the coherent tune ΔQ_z, is shifted towards larger δk_z. The exact values of the peak and centroid shift of the δk_z distribution in reference to theoretical predictions are shown in figure C.16 in the appendix.

Beam Energy and Current Dependence Using DQTOOL, the transversal tune distribution is simulated with a fixed neutralization for different beam energies and currents.

In figure 5.10, the centroid and coherent tune shift of the distributions are shown at different beam energies for fixed current (30 mA) and neutralization (40 %). Their values are shown for the horizontal (blue) and vertical plane (red). Theoretical predictions by equation (5.2) are shown as dashed lines in respective colors.

In general, the obtained values $\langle \Delta Q_{x,z} \rangle$ and $\Delta Q_{x,z,\mathrm{coh}}$ follow the expected $1/E^3$ energy dependence of $\Delta Q_{x,z}^{\mathrm{sc}}$ of equation (5.2). However, the shape of the tune distribution, its peak and centroid, does not agree with these predictions.

In the horizontal plane, the coherent tune is (85 ± 5) % smaller than predicted. The centroid of the horizontal tune distribution also deceeds ΔQ_x^{sc} by a factor of 0.83 ± 0.01. In the vertical plane, the tune distribution is more extensive with a longer tail in direction of positive tune shifts. This results in the distribution's centroid to be larger than ΔQ_z^{sc} by a factor of 1.25 ± 0.01. In contrast, $\Delta Q_{z,\mathrm{coh}}$ is only (18 ± 1) % of ΔQ_z^{sc}. For the relation between the centroid of the tune distribution to the coherent tune shift holds

$$\langle \Delta Q_x \rangle = (3.4 \pm 0.6) \cdot \Delta Q_{x,\mathrm{coh}} \qquad \text{and} \qquad \langle \Delta Q_z \rangle = (6.9 \pm 0.4) \cdot \Delta Q_{z,\mathrm{coh}} \,. \tag{5.5}$$

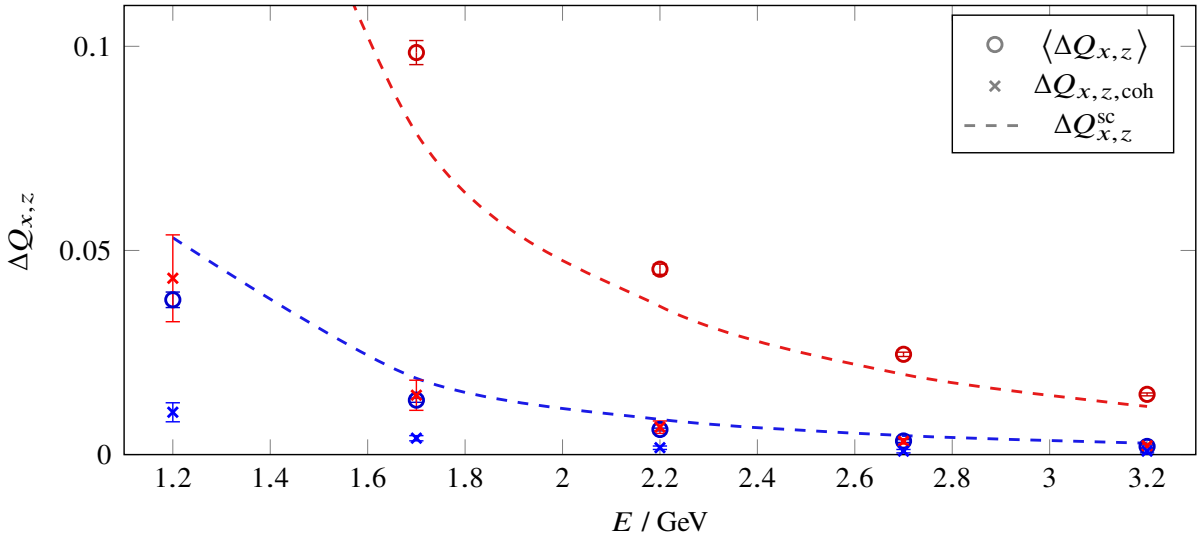

Figure 5.10: Energy dependence of the ion induced tune shift. The dashed lines indicate the theoretical tune shifts $\Delta Q^{\mathrm{sc}}_{x,z}$ for a simplified model in the horizontal (blue) and vertical plane (red). $\langle \Delta Q_{x,z} \rangle$ denotes the shift of the distribution's centroid. $\Delta Q_{x,z,\mathrm{coh}}$ is equal to the coherent tune shift. In this scenario, the beam current is equal to 30 mA with a neutralization of 40 %.

Observed deviations from theory are expected because only a simple model of the space charge forces of electrons and ions is used in the predictions. Consequently, deviations to theoretical predictions persist when studying the current dependency of the tune distribution. Its current dependency at a fixed energy of 1.2 GeV with an average neutralization of 40 % is shown in figure 5.11. The simulated values for $\langle \Delta Q_{x,z} \rangle$ and $\Delta Q_{x,z,\mathrm{coh}}$ deviate from $\Delta Q^{\mathrm{sc}}_{x,z}$ by factors, which are consistent to the ones, stated above.

Using linear regression the slope of the centroid-shift with the beam current can be obtained for the horizontal and vertical plane. The increment of the coherent tune with the stored beam current can be determined by using equation (5.5). An additional normalization on the neutralization results in

$$m_{x,\mathrm{coh}} = (9.39 \pm 1.66) \cdot 10^{-6}\,\mathrm{mA}^{-1}\,\%^{-1} \tag{5.6}$$

in the horizontal plane and

$$m_{z,\mathrm{coh}} = (33.32 \pm 1.96) \cdot 10^{-6}\,\mathrm{mA}^{-1}\,\%^{-1}$$

in the vertical plane for a beam energy of 1.2 GeV. These slopes scale in beam energy with $1/E^3$, in accordance with $\Delta Q^{\mathrm{sc}}_{x,z}$ (compare figure 5.10).

Measurement of a Coherent Ion Induced Tune Shift The majority of electrons which experience the space charge of an ion population shows a tune different from the initial tune $Q_{0,x,z}$ in case of $\eta > 0$.

A coherent tune shift is measurable in an accelerator, as has already been discussed in section 5.1.1. In the storage ring, the bunch-by-bunch feedback system can be utilized to measure the transversal and longitudinal tunes by excitation of the beam to coherent oscillations. Here, a frequency analysis of the beam's response to this excitation reveals its fractional tune. For more information regarding tune measurement techniques in the storage ring, see [Pro18, chapter 7].

As will be discussed in section 6.1 in more detail, the bias voltage of ion clearing electrodes affects the

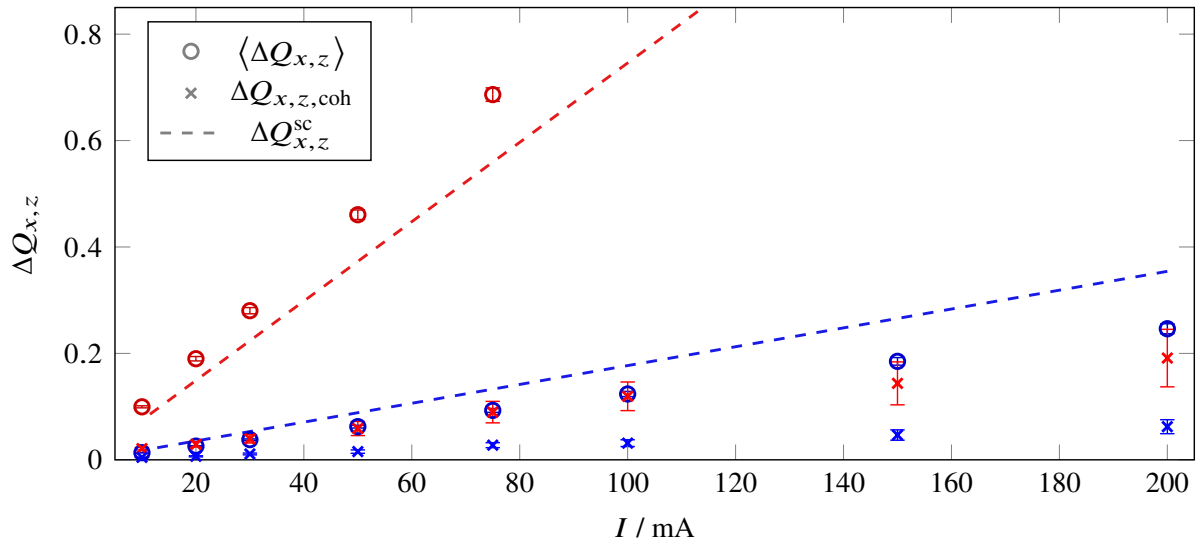

Figure 5.11: Dependence of the ion induced tune shift on the beam current. The dashed lines indicate the theoretical tune shifts $\Delta Q^{\mathrm{sc}}_{x,z}$ for a simplified model in the horizontal (blue) and vertical plane (red). $\langle \Delta Q_{x,z} \rangle$ denotes the shift of the distribution's centroid. $\Delta Q_{x,z,\mathrm{coh}}$ is equal to the coherent tune shift. In this scenario, the beam energy is 1.2 GeV with a neutralization of 40 %.

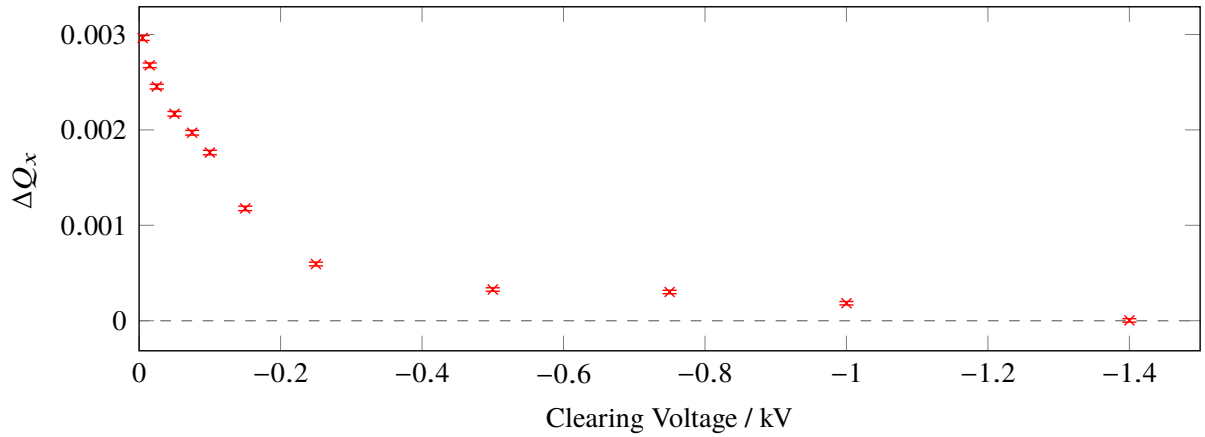

Figure 5.12: Coherent horizontal tune shift ΔQ_x due to variations of the bias voltage of clearing electrodes in the storage ring at a beam energy of 1.2 GeV and current of approximately 28 mA.

neutralization significantly. In figure 5.12, the measured horizontal tune shift ΔQ_x for different clearing electrode voltages is shown at a beam energy of 1.2 GeV and a current of approximately 28 mA. The tune shift refers to the initial tune at a bias voltage of −1.4 kV where the neutralization of the beam is comparably low. As expected, the coherent tune is shifted towards higher tunes when the absolute clearing voltage is reduced and results in $\Delta Q_x \approx 0.003$ for a voltage of 0 V[16].

Using equation (5.6) with known beam energy and current, an increment of the neutralization by (11.3 ± 2.0) % can be estimated. Under the assumption that the storage ring is fully neutralized ($\eta = 1$) in case all clearing electrodes are switched off (0 V), this would imply a neutralization of approximately

[16] In shape, the measured tune shift curve resembles the theoretical variation of $\hat{\eta}_{\mathrm{stat}}$ with clearing voltage (compare figure 6.7) and the measured ion current variation (compare figure 6.9) which will be discussed in section 6.1.

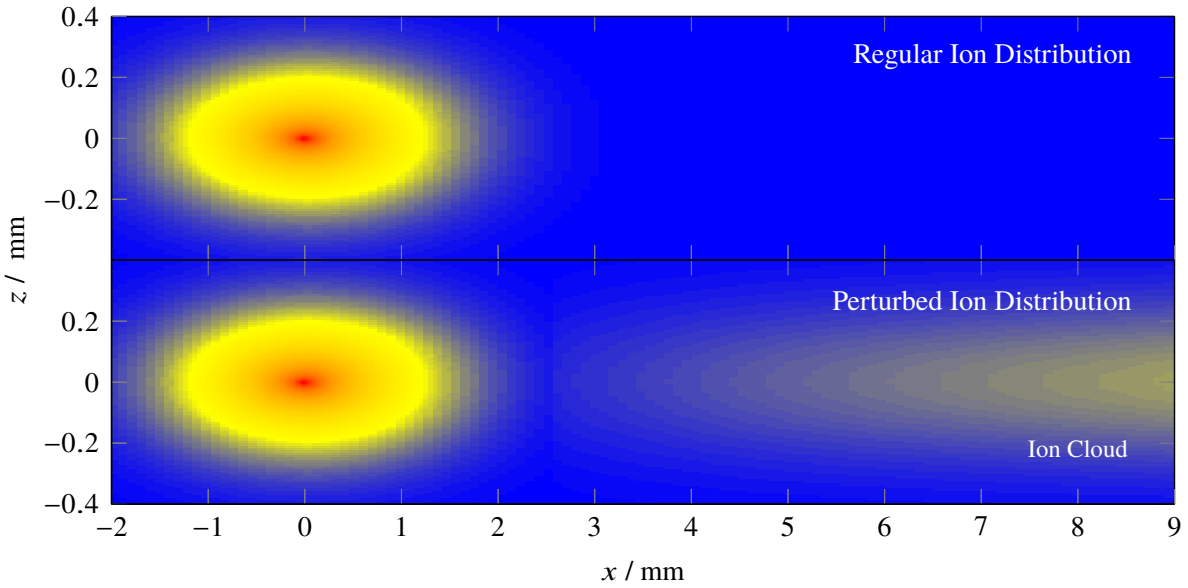

Figure 5.13: Regular (top) and perturbed transversal ion density distribution (bottom) within dipole magnet M10. The ion density increases from blue to red. The perturbation results from ion production due to photo ionization and manifests in an additional ion cloud around $x \geq 2.5\,\text{mm}$ (compare figure 4.24 in section 4.3.6). The beam energy is equal to 1.2 GeV.

90 % during storage ring operation where −1.4 kV is applied as a typical clearing voltage. This result is contradicting to the TracTIon simulations in section 4.3 in which an average neutralization of approximately 40 % (at 1.2 GeV, 35 mA; compare section 4.3.5) has been estimated in case of clearing electrodes operating with sufficiently high clearing voltage. Here, a neutralization increment from approximately 40 % to 100 % would be expected when the electrodes are switched off, manifesting in a horizontal tune shift which is approximately six times larger than the measured one.

However, the locally perturbed transversal ion density distribution due to photo ionization alters the horizontal and vertical $\delta k_{x,z}$ distributions and in consequence also the coherent tune shift. These alterations explain deviations between the predicted and measured coherent tune shift qualitatively, as will be discussed in the following section.

Perturbation of the Tune Distribution within Dipole Magnets

Horizontal Ion Charge Distribution In figure 5.13, the regular (top) and perturbed transversal ion density distribution (bottom) in the center of dipole M10 is shown for a beam with an energy of 1.2 GeV. The peak ion density in the beam center is equal in both cases. Due to photo ionization an additional ion cloud is present in the perturbed case, reaching from approximately $x = 3\,\text{mm}$ up to the edge of the beam pipe. The maximal density of this cloud is approximately 1/10th of the density at the peak. The shape of this distribution has been determined from simulations with TracTIon in section 4.3.6.

Altered $\delta k_{x,z}$ Distribution The modified ion density distribution results in different space charge forces which act on the electrons in the beam and alters the horizontal and vertical quadrupole kick distribution.

In figure 5.14, the influence of the additional ion cloud on the $\delta k_{x,z}$ distribution is shown for the horizontal (top) and vertical plane (bottom). The light colored distributions are associated with the

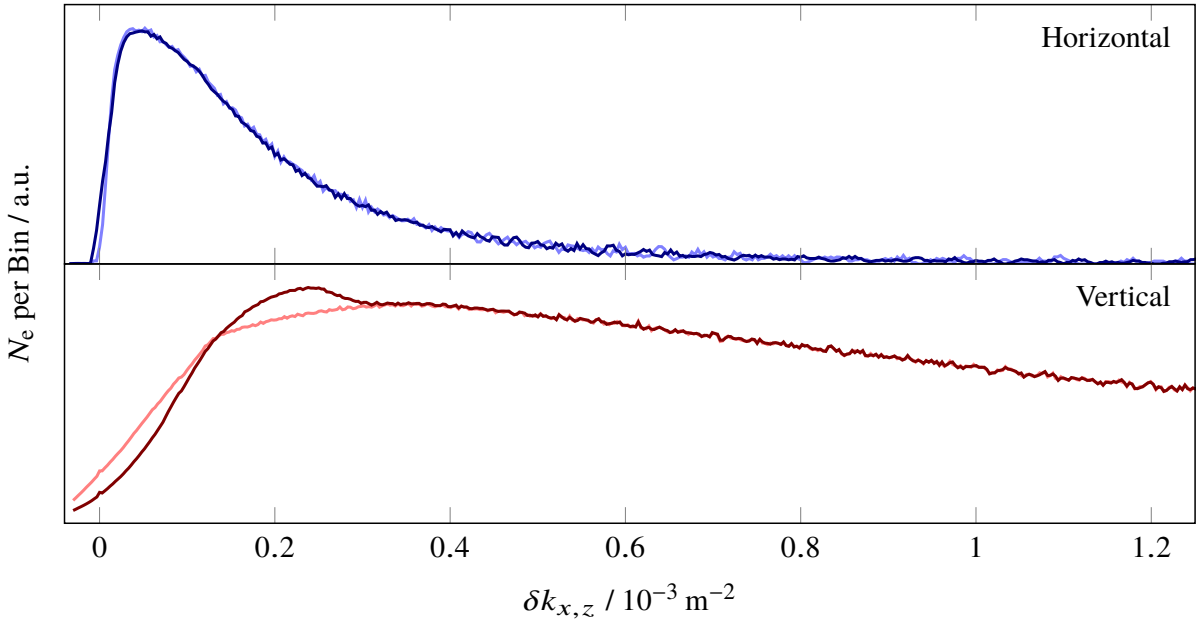

Figure 5.14: Influence of the perturbed transversal ion density distribution due to photo ionization within dipole magnets on the horizontal (top) and vertical $\delta k_{x,z}$ distribution (bottom). The light colored distributions result from the space charge of ions with a regular density distribution. The perturbed ion density distribution causes the dark colored $\delta k_{x,z}$ distributions. In this scenario, the beam energy is equal to 1.2 GeV and the stored current is 35 mA with a neutralization of 50 %.

regular ion distribution, whereas dark colored ones result from the perturbed distribution. The space charge force of the ion cloud does not influence the $\delta k_{x,z}$ distributions' tails at large quadrupole kick strengths. This is expected as the ion cloud is located far away from the electron distribution and the beam's center at $x > \sigma_x$. Consequently, the cloud only contributes to small $\delta k_{x,z}$. Indeed, near the peak of the distributions, a significant effect is visible. The ion cloud shifts the peak of the $\delta k_{x,z}$ distributions towards lower kick strength.

In the horizontal plane, the peak is shifted from $(5.2 \pm 0.3) \cdot 10^{-5}$ to $(3.4 \pm 0.3) \cdot 10^{-5}$ m^{-2}, equivalent to a reduction by a factor of 0.66 ± 0.08. In the vertical plane from $(4.1 \pm 0.5) \cdot 10^{-4}$ to $(2.2 \pm 0.5) \cdot 10^{-4}$ m^{-2}, which is a reduction by a factor of 0.53 ± 0.14. In contrast, the shift of the distributions' centroid is negligible. The shift of the peak $\delta k_{x,z,\mathrm{max}}$ in dipole magnets due to the ion cloud, consequently reduces the ion induced coherent tune shift in both planes.

Perturbed Tune Distribution Downstream of Dipole Magnets

Synchrotron radiation photons which are emitted by the beam close to the end of dipole magnets can exit them and ionize residual gas downstream of the magnet. Thus, this magnet field-free region also shows an asymmetric ion production map. TransversIon can be utilized to determine the perturbed equilibrium ion density distribution in this region.

Simulated Ion Density Distribution In the following, the horizontal ion density distribution is simulated 5 cm after dipole M26 in the storage ring, exemplarily. The ion density distribution is simulated at a beam energy of 1.2 GeV. As the optical functions in the dipole magnet are assumed to be constant in a PhotoIonProd simulation, the same optical functions are used here. To analyze the difference

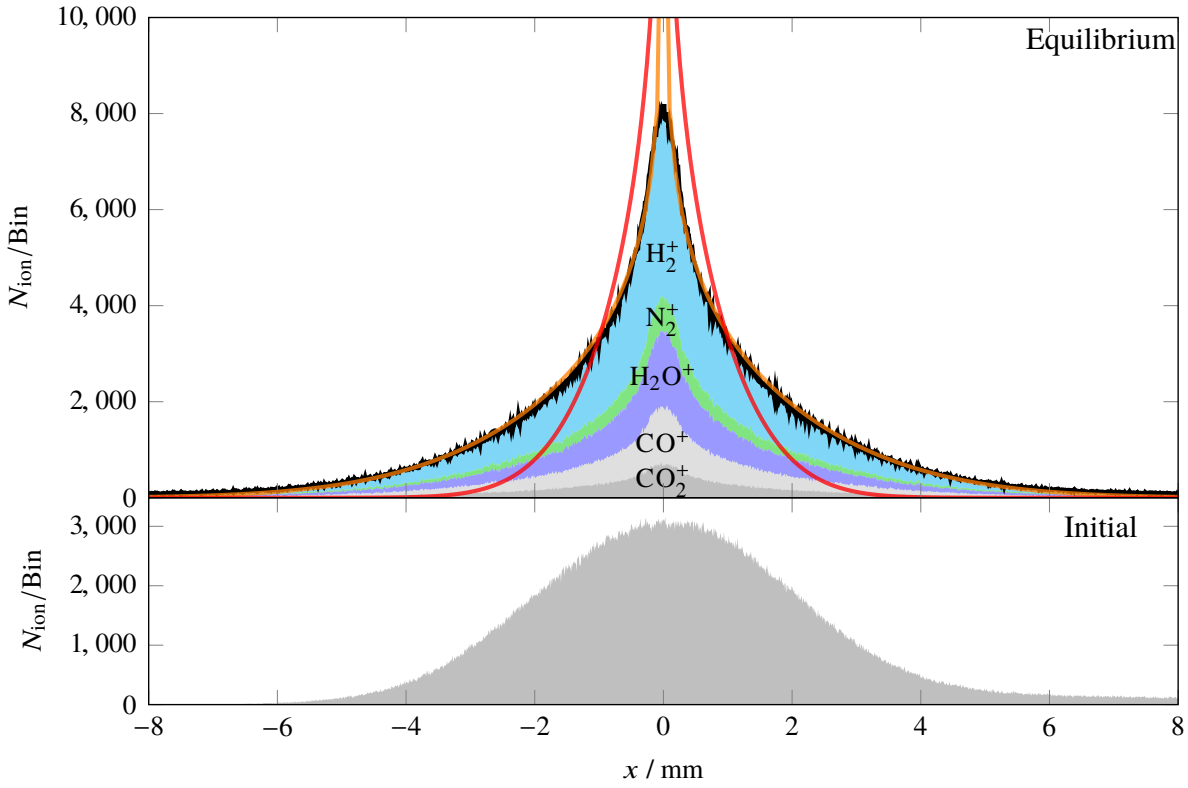

Figure 5.15: Simulated ion distribution in the horizontal plane 5 cm downstream of dipole magnet M26 at $s = 132.2$ m. The top graph shows the equilibrium ion distribution at 1.2 GeV beam energy. The black curve shows the distribution of the local ion population. It is composed of contributions of different ion species which are depicted as colored surfaces. The ion production map of impact and photo ionization is shown in the bottom graph. Due to photo ionization contributions, the distribution differs from the regular one which is shown in red. The orange curve is the modified theoretical distribution with included photo ionization contributions.

between regular and perturbed ion density distribution, first the regular distribution is simulated via TransversIon at this position (see appendix A.19.1). Onto the regular distribution, equation (5.4) is approximated to enable a comparison of the distributions' shapes.

For the same location, the ion density distribution is simulated by TransversIon using an asymmetric ion production map in which impact and photo ionization are considered jointly. The local ion production map for photo ionization has been simulated by PhotoIonProd (compare section 3.4.3).

The simulation result is shown in figure 5.15. In the bottom graph, the initial ion density distribution due to the production process of impact and photo ionization is shown. The distribution is asymmetric and non-zero for positive horizontal positions up to the edge of the beam pipe.

The shape of the simulated distribution (black) resembles the unperturbed distribution of figure 5.7. Yet, significant deviations are visible in comparison to the approximated theoretical ion density distribution (red). Both distributions are symmetric around $x = 0$ mm but the simulated distribution shows a broader width with decreased density. From $\approx \pm 1$ mm outwards, the simulated ion density is overall higher than expected from the theoretical prediction in red.

The photo ionization process generates a significant amount of ions at $x \gg \sigma_x$. Yet, the beam potential is still attractive for these ions and they start to oscillate in the potential horizontally. In equilibrium, the ion density distribution broadens up as these high-amplitude ions oscillate incoherently.

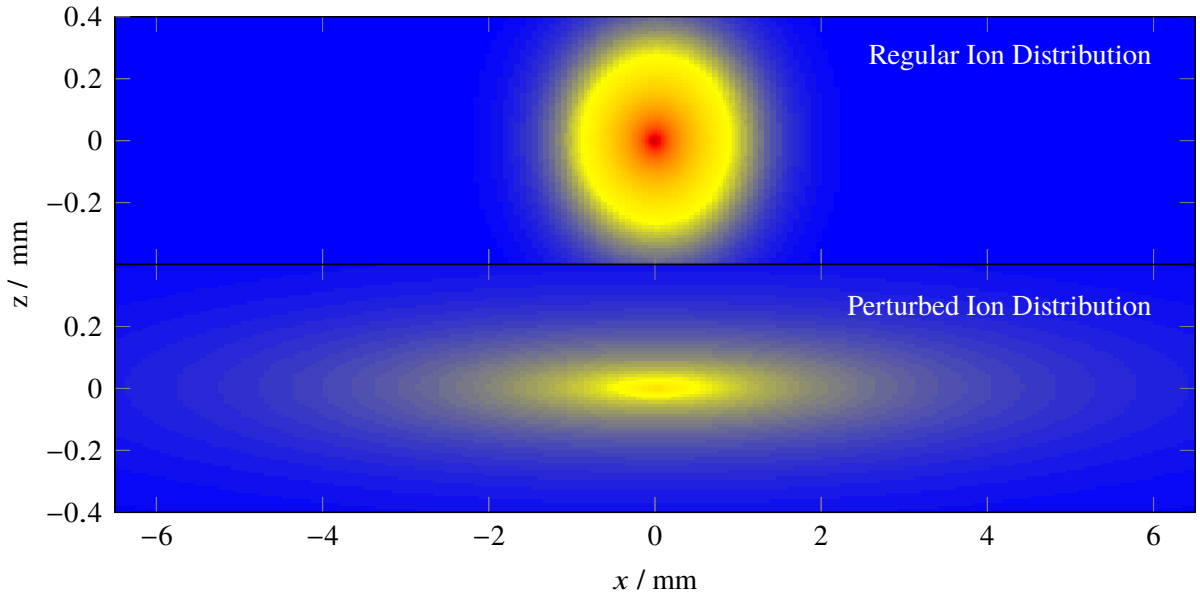

Figure 5.16: Regular (top) and perturbed transversal ion density distribution (bottom) downstream of dipole magnet M10. The ion density increases from blue to red. The perturbation results from the ion production due to photo ionization which shifts the horizontal barycenter of ion production to $x_{\mathrm{cm}} = 1\,\mathrm{cm}$. The beam energy is equal to 1.2 GeV.

To include the broadening of the ion density distribution into the theoretical distribution, equation (5.4) can be modified slightly. This modification is discussed in appendix A.19.2. Here, the horizontal shift of the barycenter of the ion production which is characterized by the parameter x_{cm} from section 3.4.3, is used to determine an effective "width" of the transversal ion production. The approximated orange curve results from a density distribution to which this modification is applied. It follows the course of the simulated distribution adequately.

In figure 5.16, the regular (top) and perturbed transversal ion density distributions (bottom) are shown downstream of dipole magnet M10. The perturbed distribution is obtained by using the modification of appendix A.19.2 with an effective "width" resulting from $x_{\mathrm{cm}} = 1\,\mathrm{cm}$[17]. The neutralization is equal in both cases, resulting in a reduced peak ion density in the perturbed distribution in comparison to the regular one.

$\delta k_{x,z}$ Distribution Downstream of Dipole Magnets Using `dQTool`, the $\delta k_{x,z}$ distribution is simulated for both density distributions to identify the perturbation's influence.

In figure 5.17, the horizontal (top) and vertical quadrupole kick distributions (bottom) are shown for the regular (light colors) and perturbed ion density distributions (dark colors). In the vertical plane, the perturbation leads to a reduction of δk_z of the distribution. The centroid of the distribution is shifted from $(3.99 \pm 0.05) \cdot 10^{-3}$ to $(1.98 \pm 0.02) \cdot 10^{-3}\,\mathrm{m}^{-2}$ and consequently halfes the tune spread (factor 0.497 ± 0.008). The distribution's peak is reduced from $(6.3 \pm 0.9) \cdot 10^{-4}$ to $(4.4 \pm 0.3) \cdot 10^{-4}\,\mathrm{m}^{-2}$ by a factor of 0.7 ± 0.1. In the horizontal plane, a significant alteration of the δk_x distribution is visible. The peak quadrupole kick is reduced from $(2.10 \pm 0.07) \cdot 10^{-4}$ to $(0.21 \pm 0.07) \cdot 10^{-4}\,\mathrm{m}^{-2}$ by a factor of

[17] Note that the value of x_{cm} is understated to map relevant parts of the resulting ion density distribution onto a region with a horizontal width of $\pm 8\sigma_x$. In reality, x_{cm} is in the order of several centimeters (compare figure 3.21) resulting in an even flatter distribution.

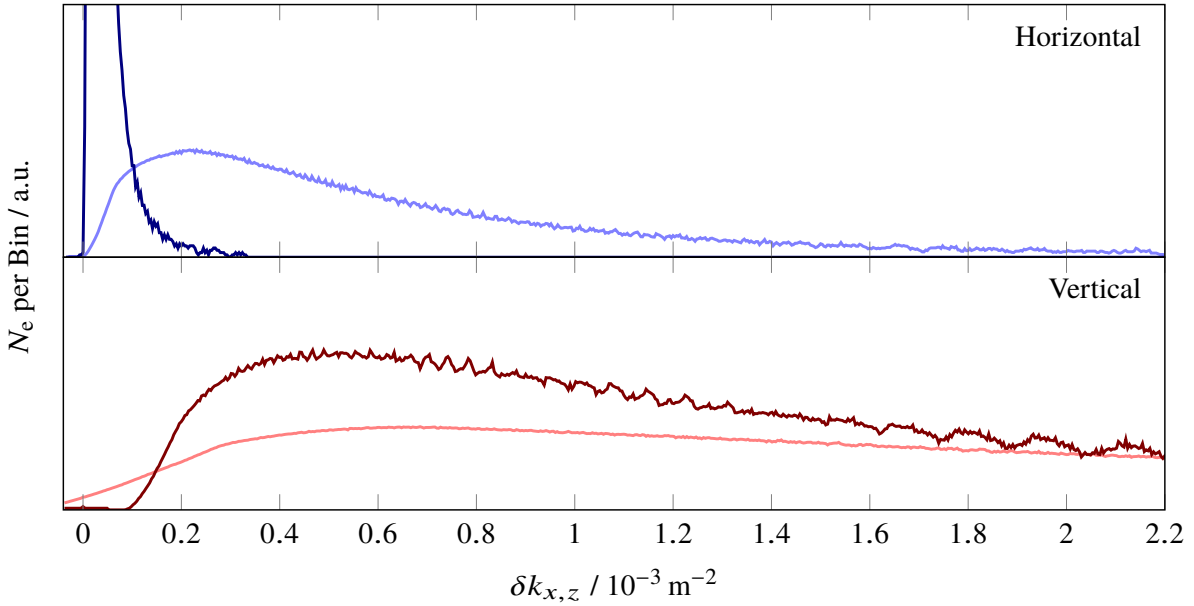

Figure 5.17: Influence of the perturbed transversal ion density distribution due to photo ionization downstream of a dipole magnet on the horizontal (top) and vertical $\delta k_{x,z}$ distribution (bottom). The light colored distributions result from the space charge of ions with a regular density distribution whereas the perturbed ion density distribution generates the dark colored $\delta k_{x,z}$ distributions. In this scenario, the beam energy is equal to 1.2 GeV and the stored current is 35 mA with a neutralization of 65 %.

Correction Factor for:	Centroid		Peak	
	$\langle \delta k_x \rangle$	$\langle \delta k_z \rangle$	$\delta k_{x,\max}$	$\delta k_{z,\max}$
Within Dipole Magnets:	≈ 1	≈ 1	0.66 ± 0.08	0.53 ± 0.14
Downstream of Dipole Magnets:	0.047 ± 0.003	0.497 ± 0.008	0.10 ± 0.03	0.7 ± 0.1

Table 5.1: Compilation of the simulated correction factors for the quadrupole kick distributions. These factors are only valid for the simulated scenario with corresponding beam energy, current and neutralization.

0.10 ± 0.03. Its centroid shifts from $(8.29 \pm 0.06) \cdot 10^{-4}$ to $(0.39 \pm 0.03) \cdot 10^{-4}$ m^{-2} and is reduced by a factor of approximately 0.047 ± 0.003.

In the horizontal plane, the perturbed ion density distribution shows a larger dimension than the electron beam. The ion induced space charge force on individual electrons is therefore more isotropic in the horizontal plane and the sum of forces is lower or almost cancels out for many electrons in the bunch.

Summary: Evaluation of the Photo Ionization's Influence on the Coherent Tune Shift

The different factors, with which the reduction of the horizontal and vertical quadrupole kick distributions within and downstream of dipole magnets are characterized, are shown in table 5.1.

In dipole magnets, the space charge of the peripheral ion cloud reduces $\delta k_{x,z,\max}$ significantly. Downstream of the dipole magnets, especially the horizontal δk_x distribution is altered severely and $\delta k_{x,\max}$ is reduced by a factor of 10. Consequently, a significant reduction of the horizontal ion induced coherent tune shift is expected.

Although these studies are more of qualitative nature, it has become evident that photo ionization

and the associated alteration of the ions' transversal density distribution leads to a modification of the ion induced coherent tune shift. Especially in the horizontal plane, a significant reduction of $\Delta Q_{x,\mathrm{coh}}$ is expected due to contributions to δk_x from regions downstream of dipole magnets.

The low ΔQ_x during tune measurements shown in figure 5.12, for example, can be attributed to this effective reduction of the coherent tune shift in the horizontal plane.

5.2 Beam-Ion Instabilities

The beam electrons and ions oscillate incoherently in the transversal plane: Electrons due to the focusing by the accelerator's magnet optics and ions due to the reversing force of the electron beam. The space charge forces of the electron beam and the ion population reciprocally influence their trajectories. Thus, the beam and ions form a coupled system, which can oscillate at certain frequencies. If the oscillating ions can amplify existing beam oscillations, the coupled beam-ion system escalates and beam instabilities result in which the beam's amplitude increases with time. In dependence of the amplitude's growth rate, a reduction of the beam life time up to a virtually instantaneous beam loss may occur.

One type of these ion induced instabilities is the *conventional*[18] *beam-ion instability* where ions are *trapped* inside the beam potential and cause beam instabilities after they have accumulated to a certain level. These instabilities are also denoted as BII.

5.2.1 Theory on Ion Induced Beam Instabilities

The electrons of the relativistic beam interact electromagnetically with their surroundings: On one hand, they induce charges on the surface of the beam pipe. Due to the finite conductance of the pipe, these charges trail behind the electrons and generate localized oscillating *wake fields* at positions in the accelerator where the pipe's geometry changes. These wake fields act back on the beam as an electromagnetic force. On the other hand, the electrons experience the attractive space charge force of trapped ions, which oscillate around the beam's center of charge. In return, the ions' motion is also influenced by the beam's force. Both react on their mutual motions and are therefore coupled. The ions' space charge force behaves similar to a wake field.

A pilot particle with charge q_1, which propagates with a velocity $\beta c \approx c$ and shows a transversal offset of r_1 from the beam center, generates a Lorentz force of [Kha06, section 2.3]

$$\vec{F}_{\mathrm{wake}}(r_1, r_2, \tau, t) = q_2 \cdot \left(\vec{E}(r_1, r_2, \tau, t) + c \cdot \vec{e}_s \times \vec{B}(r_1, r_2, \tau, t)\right)$$

for a witness particle with charge q_2 and transversal offset r_2 which trails behind the pilot particle on a parallel trajectory with a longitudinal spatial distance of $c\tau$. Here, $\vec{e}_s$ is the unit vector in direction of the particles' propagation. $\vec{E}$ is the electric and $\vec{B}$ is the magnetic field strength of the wake field.

[18] Even when effective ion clearing measures are applied, which prevent a trapping of all ions in the accelerator due to a sufficiently long filling gap (compare section 6.2), ion induced beam instabilities can emerge in case of poor vacuum conditions. When these so called *fast beam-ion instabilities* (FII) occur, the ion density increases linear along the bunch train to neutralization levels in which the ions' space charge force excite beam instabilities. Since FII can occur within a single revolution of the bunch train, a mitigation of its effect cannot be achieved by conventional clearing methods, presented in this work. E.g. [RZ95; Byr+97] provide more information regarding FIIs.

The so called *wake function* is obtained by integrating $\vec{F}_{\text{wake}}$, decomposed into its longitudinal ($\shortparallel$) and transversal components ($\perp$), along the longitudinal beam axis with $s = ct$ ($\mathrm{d}s = c\,\mathrm{d}t$) and normalizing it on the charges q_1 and q_2. The longitudinal wake function is given by [Kha06, section 2.3.1, conversion of equation (2.33)]

$$\mathcal{W}_{\shortparallel}(r_1, r_2, \tau) = -\frac{1}{q_1 q_2} \int F_{\text{wake},\shortparallel}(r_1, r_2, \tau, s)\,\mathrm{d}s$$

and the transversal by [Kha06, section 2.3.1, conversion of equation (2.35)]

$$\mathcal{W}_{\perp}(r_1, r_2, \tau) = -\frac{1}{q_1 q_2\,|r_1|} \int F_{\text{wake},\perp}(r_1, r_2, \tau, s)\,\mathrm{d}s$$

where r_2 is defined to be equal to zero and $\mathcal{W}_{\perp}(r_1, r_2, \tau)$ is additionally normalized to r_1. For ultrarelativistic particles, $F_{\text{wake},\shortparallel}$ is independent from the displacements r_1 and r_2. If $F_{\text{wake},\perp}$ increases linear with the pilot particle's displacement r_1, $\mathcal{W}_{\perp}(r_1, r_2, \tau)$ is also independent from r_1.

The strength of the wake fields is characterized by its *coupling impedance* $Z(\nu) \in \mathbb{C}$ in frequency space. Here, the longitudinal and transversal wake functions are Fourier-transformed into the longitudinal [Ng06, section 1.2]

$$Z_{\shortparallel}(\nu) = \int_{-\infty}^{\infty} \mathcal{W}_{\shortparallel}(\tau) \cdot e^{-\mathrm{i}2\pi\nu\tau}\,\mathrm{d}\tau$$

and transversal

$$Z_{\perp}(\nu) = \mathrm{i} \int_{-\infty}^{\infty} \mathcal{W}_{\perp}(\tau) \cdot e^{-\mathrm{i}2\pi\nu\tau}\,\mathrm{d}\tau \tag{5.7}$$

coupling impedance.

The beam-generated wake fields act back on the beam at a later time. Therefore, the beam experiences electromagnetic perturbations, generally characterized by a disturbance voltage $U(\nu)$, resulting in an energy variation due to the longitudinal and deflections due to the transversal components of the wake fields. An electron beam showing a frequency spectrum of $I(\nu)$ which is called *beam spectrum*, experiences a transversal and/or longitudinal disturbance voltage $U(\nu)$ due to these fields which can be expressed similar to the Ohmic law as

$$U(\nu) = -Z(\nu) \cdot I(\nu)\,. \tag{5.8}$$

The product of the beam spectrum with the coupling impedance determines the disturbance voltage, induced by the wake fields. In e.g. the horizontal plane - the electrons oscillate with a frequency $Q_x \nu_0$ in accordance with their tune Q_x - the equation of motion of the beam's center of charge under the influence of wake fields can be written as [Kos04, section 2.4]

$$\frac{\mathrm{d}^2 x}{\mathrm{d}t^2} + (2\pi\, Q_x \nu_0)^2 \cdot x = \frac{F_{\text{wake},x}}{\gamma m_{\text{e}}}\,. \tag{5.9}$$

Here, $F_{\text{wake},x}$ is the horizontal excitation force due to the wake fields which is proportional to $U(\nu)$ as

$$F_{\text{wake},x} \sim -\mathrm{i}\, Z(\nu) \cdot I(\nu)\,.$$

Since $I(\nu)$ is dependent on the beam's horizontal oscillation frequency $Q_x \nu_0$, resulting in a tune dependent $F_{\text{wake},x}$, the trajectory of the beam's center of charge $x(t)$ is so, too.

If $F_{\text{wake},x}$ increases linear with x, equation (5.9) can be rewritten as

$$\frac{\mathrm{d}^2 x}{\mathrm{d}t^2} + (2\pi\nu_0)^2 (Q_x + \Delta Q)^2 \cdot x = 0$$

where $F_{\text{wake},x}$ is proportional to a quantity $\Delta Q \in \mathbb{C}$ with $|\Delta Q| \ll 1$. Under this assumption, the resulting beam trajectory $x(t)$ can be rewritten as [Kos04, section 2.4, equation 2.4.1]

$$x(t) = \mathrm{Re}\left\{ A \cdot e^{\mathrm{i}2\pi\nu_0 \left(Q_x + \mathrm{Re}(\Delta Q)\right) t} \cdot e^{2\pi\nu_0 \,\mathrm{Im}(\Delta Q) t} \right\}$$

where A is the amplitude of the beam's center of charge.

Thus, $Z(\nu) \sim \mathrm{i}\Delta Q$ determines whether a coherent tune shift is experienced by the beam due to a *reactive impedance* ($|\mathrm{Im}(Z(\nu))| > 0$ and $|\mathrm{Re}(Z(\nu))| = 0$) or beam instabilities emerge due to a *resistive impedance* ($|\mathrm{Re}(Z(\nu))| > 0$ and $|\mathrm{Im}(Z(\nu))| = 0$).

Thus, the impedance of accumulated ions and the beam spectrum $I(\nu)$ influence the occurrence of beam-ion instabilities fundamentally.

Ion Oscillations and Wake Function

As already mentioned in section 2.4.1, the trapped ions oscillate around the center of charge of the beam in the horizontal and vertical plane. Their oscillation frequency is dependent on the strength and spatial form of the beam's attractive reversing Coulomb force, and thus on the shape and depth of the beam potential. Additionally, the different mass-to-charge ratios of the individual ions result in a split-up of the population's frequency spectrum.

The wake function of an ion species i with a local partial neutralization $\hat{\eta}_i(s')$, oscillating with a frequency $\nu^{\text{ion}}_{x,z,i}(s')$, is given as [Wan+13, section III A, conversion of equation (8)]

$$\mathcal{W}^{\text{ion}}_{x,z,i}(s) = \int_0^C \frac{4}{3h \cdot c} \cdot \frac{2\pi\nu^{\text{ion}}_{x,z,i}(s') \cdot \hat{\eta}_i(s')}{\sigma_{x,z}(s') \left(\sigma_x(s') + \sigma_z(s')\right)} \cdot \exp\left(-\frac{2\pi\nu^{\text{ion}}_{x,z,i}(s') s}{2Q_{\text{nl}} c} \right) \sin\left(\frac{2\pi\nu^{\text{ion}}_{x,z,i}(s') s}{c} \right) \mathrm{d}s' \quad (5.10)$$

at a position s. h is the harmonic number of the accelerator with a circumference C. Here, it is assumed that the transversal density distributions of the electron beam and the ions are identical. Additionally, the reversing force of the beam is presumed to increase linear with the ions' displacement from the beam center, resulting in an ion bounce frequency $\nu^{\text{ion}}_{x,z,i}(s')$ which is independent from the displacement (compare equation (2.46)). To compensate for these simplifications, an empirical quality factor Q_{nl} for the ion oscillation is introduced. For a Gaussian density distribution of the electron beam, Q_{nl} is approximately 9 [Wan+11].

The wake function of the whole ion population can be written as

$$\mathcal{W}^{\text{ion}}_{x,z}(s) = \sum_i \mathcal{W}^{\text{ion}}_{x,z,i}(s) \,. \quad (5.11)$$

By using equation (5.7), the transversal impedance $Z^{\text{ion}}_{x,z}(\nu)$ of the ions can be determined. The shape $Z^{\text{ion}}_{x,z}(\nu)$ is basically determined by $\nu^{\text{ion}}_{x,z}(s)$, weighted by $\hat{\eta}(s)$, and its variation along the accelerator. The strength of $Z^{\text{ion}}_{x,z}(\nu)$ scales with the neutralization, of course. The real part of $Z^{\text{ion}}_{x,z}(\nu)$ is proportional to the growth rate of the BII and for $Z^{\text{ion}}_{x,z}(\nu) \cdot I(\nu) \neq 0$, oscillation modes of the beam can be excited.

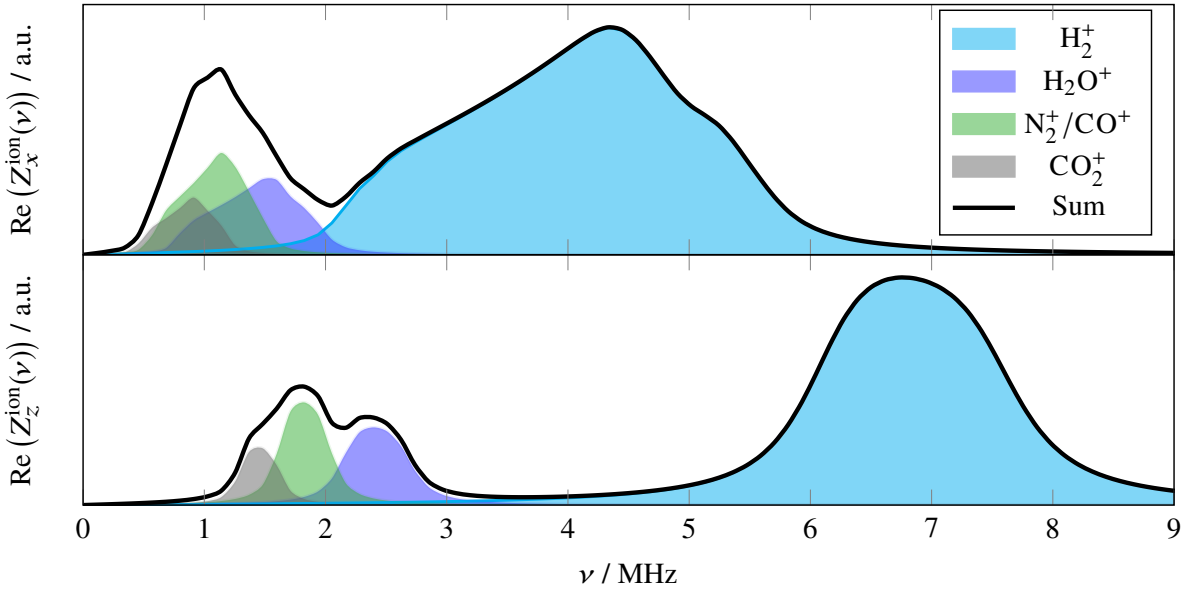

Figure 5.18: Real part of the horizontal (top) and vertical wake impedance (bottom) of ions in the storage ring at a beam energy of 1.2 GeV and a stored current of 200 mA. The neutralization is assumed to be 40 % all along the accelerator. The individual ion species' contributions sum up to the total impedance (black).

In figure 5.18, the calculated $\mathrm{Re}(Z_{x,z}^{\mathrm{ion}}(\nu))$ in the storage ring at a beam energy of 1.2 GeV and a stored current of 200 mA is shown exemplarily. Here, the horizontal and vertical impedance spectrum splits up into a low and a high frequency part. The high frequency part results from H_2^+ ions which contribute on average to approximately half of the ion population and oscillate with a significantly higher oscillation frequency than the heavier ion species. The second part, at lower frequencies, is caused by the heavier ion species of H_2O^+, N_2^+, CO^+ and CO_2^+.

Due to the non-linear dependence of $\nu_{x,z}^{\mathrm{ion}}$ on the ions' mass-to-charge ratio ($\sim \sqrt{Z_i/A_i}$), the impedance contributions of heavier ions tend to overlap in frequency, even though the ions show a significant difference in mass.

In the storage ring, ν_x^{ion} on average is a factor of approximately 2 lower than ν_z^{ion} due to the different horizontal and vertical beam sizes. Therefore, $\mathrm{Re}(Z_x^{\mathrm{ion}}(\nu))$ shows its maximum at a lower frequency when compared to the maximum of $\mathrm{Re}(Z_z^{\mathrm{ion}}(\nu))$. The impedance of H_2^+ ions shows a relative bandwidth[19] of approximately 0.54 in the horizontal plane. The relative bandwidth is equal to 0.25 in the vertical plane. When comparing the other ion species' relative bandwidth, the differences are similar and the ions' impedance is overall broader in the horizontal than in the vertical plane.

Multi Bunch Modes and Beam Spectrum

Due to the mutual space charge interaction of the electron beam with the trapped ions and other electromagnetic wake fields, the motion of the individual bunches are coupled and certain oscillation modes of the beam emerge, if excited by $Z(\nu)$.

These so called *multi bunch modes* express in coherent transversal betatron or longitudinal synchrotron oscillations of each bunch in the accelerator. Here, the modes differ in the phase difference between

[19] The relative bandwidth in this case denotes the ratio of the width of the impedance peak to its center frequency. Here, the width is the distance between the two frequencies where the impedance is half of its peak value.

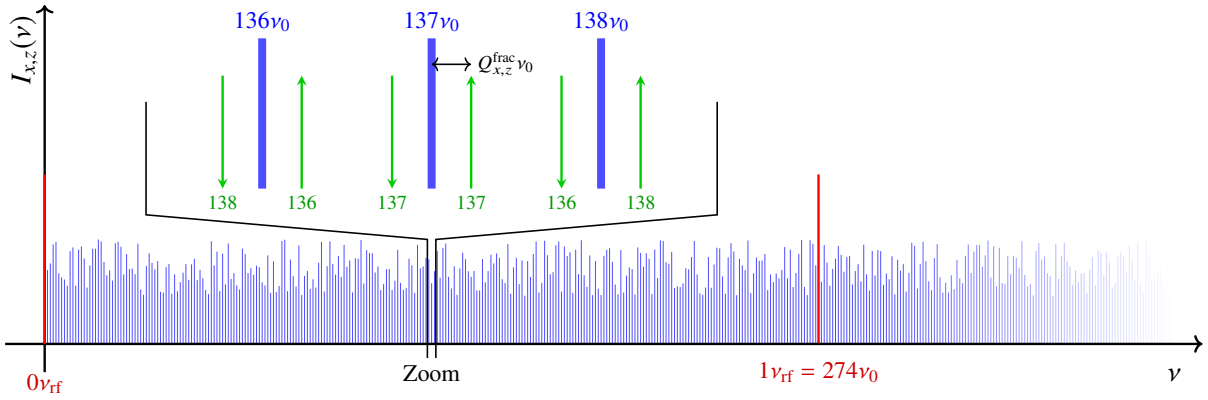

Figure 5.19: Exemplaric beam spectrum of the storage ring with 274 bunches. The rf harmonics $p\nu_{\text{rf}}$ are shown in red whereas the revolution harmonics $\mu\nu_0$ are colored in blue. The zoom to three revolution harmonics shows the upper (arrow up) and lower (arrow down) betatron sidebands at $\nu^{\text{MBM}}_{x,z}$ for $Q^{\text{frac}}_{x,z} < 0.5$ in green.

neighboring bunches which is equal to [Ng06, chapter 10]

$$\Delta\varphi_\mu = \frac{2\pi\mu}{h} \qquad \text{with} \qquad \mu = 0, 1, \ldots, h-1 \,.$$

Every possible oscillation mode in each plane is assigned a multi bunch mode number μ. In an accelerator with h individual bunches, the same number of multi bunch modes can be excited in each plane.

Each multi bunch mode only contributes to distinct frequency domains in the spectrum of the beam. In the transversal plane, these domains are equal to [Kha06, section 2.2]

$$\nu^{\text{MBM}}_{x,z} = p\nu_{\text{rf}} + \mu\nu_0 + Q^{\text{frac}}_{x,z}\nu_0 \qquad \text{with } p \in \mathbb{Z} \,. \tag{5.12}$$

$Q^{\text{frac}}_{x,z}$ is the fractional[20] tune of the beam. For more information regarding the beam spectrum, consult [Kha06, section 2.2] or [Ng06, section 9.2].

A schematic beam spectrum $I(\nu)$ of the storage ring with $h = 274$ bunches is shown in figure 5.19. Here, the *rf harmonics*[21] are shown in red. In between them $h-1$ *revolution harmonics* at $\mu\nu_0$ are visible in blue. Emerging coherent transversal oscillations of a certain multi bunch mode manifest in specific upper or lower betatron sidebands in accordance to the multi bunch mode number μ, which are shown in green in the magnified section.

If, for example, the beam oscillates coherently with mode number μ, an upper betatron sideband at $(\mu + Q^{\text{frac}}_{x,z})\nu_0$ appears, if only the frequency domain from 0 to ν_{rf} is considered. Additionally, a lower sideband emerges at $(h - \mu - Q^{\text{frac}}_{x,z})\nu_0 = \nu_{\text{rf}} - (\mu + Q^{\text{frac}}_{x,z})\nu_0$, mirrored from the negative frequency domain. All modes with $\mu < h/2$ are represented by upper sidebands within a frequency domain reaching from 0 to $\nu_{\text{rf}}/2$. Modes with $\mu \geq h/2$ are also visible in this domain as lower sidebands.

[20] Because the beam spectrum is measured at a fixed position in the accelerator, a determination of the full tune value is not possible. However, the field strength of the accelerator's beam optics is typically known precise enough to determine the integer of the tune.

[21] Rf harmonics correspond to the term $p\nu_{\text{rf}}$ in equation (5.12). They appear in the beam spectrum at multiples of ν_{rf} due to the bunched structure of the electron beam.

Characteristics of Beam-Ion Instabilities

The overlap of the individual multi bunch mode's contributions to the beam spectrum with the impedance spectrum $\mathrm{Re}(Z_{x,z}(\nu))$ determines the growth rates $\Gamma_{x,z,\mu}$ of these modes. The contributions of $I_{x,z}(\nu)$ is proportional to the beam current in the accelerator, resulting in an identical current dependency of $\Gamma_{x,z,\mu}$ under the assumption that $Z_{x,z}(\nu)$ does not alter with the current. However, only if the total growth rate $\Gamma_{x,z}$ exceeds the natural damping rate $\Gamma_{\mathrm{sr}} = 1/\tau_{x,z}$ of beam oscillations by synchrotron radiation (compare equations (2.25) and (2.26) in section 2.3.2), multi bunch instabilities occur if a certain current threshold is exceeded[22].

Energy, Current and Neutralization Dependency of $\mathrm{Re}(Z^{\mathrm{ion}}_{x,z}(\nu))$ In figure 5.20, the change in $\mathrm{Re}(Z^{\mathrm{ion}}_{x,z}(\nu))$ with beam energy and current is shown. The observed shifting of the impedance in frequency domain results from the variation of $\nu^{\mathrm{ion}}_{x,z,i}$ with energy and current (compare equation (2.46)). With increasing current, the impedance shifts towards higher frequencies (compare (top) and (middle)) due to a higher oscillation frequency of the ions. If the beam energy is increased, $\mathrm{Re}(Z^{\mathrm{ion}}_{x,z}(\nu))$ is shifted down in frequency due to lower $\nu^{\mathrm{ion}}_{x,z,i}$ (compare (middle) and (bottom)).

Due to these variations, the overlap between the impedance and the beam spectrum is constantly changing resulting in beam energy and current dependent growth rates of the individual modes. ν^{MBM}_{x} of the corresponding multi bunch modes is denoted as green lines. At 2.2 GeV and 100 mA for example in figure 5.20 (bottom), modes 2 and 271 cannot be excited by the wake impedance of ions. If the energy is decreased to 1.2 GeV (middle) an excitation is possible.

The amplitude of $\mathrm{Re}(Z^{\mathrm{ion}}_{x,z}(\nu))$ also scales with neutralization which increases $\Gamma_{x,z,\mu}$ of excited multi bunch modes accordingly. Also a rising neutralization η is expected to result in a variation of the ions' oscillation frequencies $\nu^{\mathrm{ion}}_{x,z,i}$ (compare equation (2.46)) and thus also changes the shape of $\mathrm{Re}(Z^{\mathrm{ion}}_{x,z}(\nu))$. One might think that $\nu^{\mathrm{ion}}_{x,z,i}$ decreases with increasing η because more ions shield the attractive force of the electron beam and $\mathrm{Re}(Z^{\mathrm{ion}}_{x,z}(\nu))$ shifts to lower frequencies, as visualized in figure 5.21. In a *linear space charge model*, $\nu^{\mathrm{ion}}_{x,z,i}$ therefore is expected to reduce linearly with η. However, simulations[23] of [Mar+14] have shown, that a linear space charge model does not describe the influence of η on $\nu^{\mathrm{ion}}_{x,z,i}$ suitably. The peak of the ion oscillation distribution does *not* shift significantly in frequency in case the space charge interaction between the ions is activated in the simulation. Instead, the distribution broadens towards lower *and* higher frequencies. Therefore, $\nu^{\mathrm{ion}}_{x,z,i}$ is assumed to be independent from the neutralization when calculating the storage ring's wake impedance for accumulated ions in the following section.

Theoretical Wake Impedance of Ions in the Storage Ring Using the theoretical wake impedance of the ion population of equation (5.10), $\mathrm{Re}(Z^{\mathrm{ion}}_{x}(\nu))$ in the storage ring can be obtained for different beam energies, currents and average neutralization[24].

[22] By utilizing a bunch-by-bunch feedback system to damp emerging beam instabilities, the current threshold for a beam instability can be extended to higher currents. This extension depends on the applicable additional damping rate of the system to the beam.

[23] The simulations have been conducted with MOEVE PIC TRACKING, a three-dimensional tracking simulation which models the space charge interaction of an ensemble of ions with the beam electrons and among themselves. For more information, see e.g. [Mar13].

[24] In this model, ν^{ion}_{x} is not shifted with increasing neutralization towards lower frequencies. Additionally, the neutralization is assumed to be constant along the accelerator.

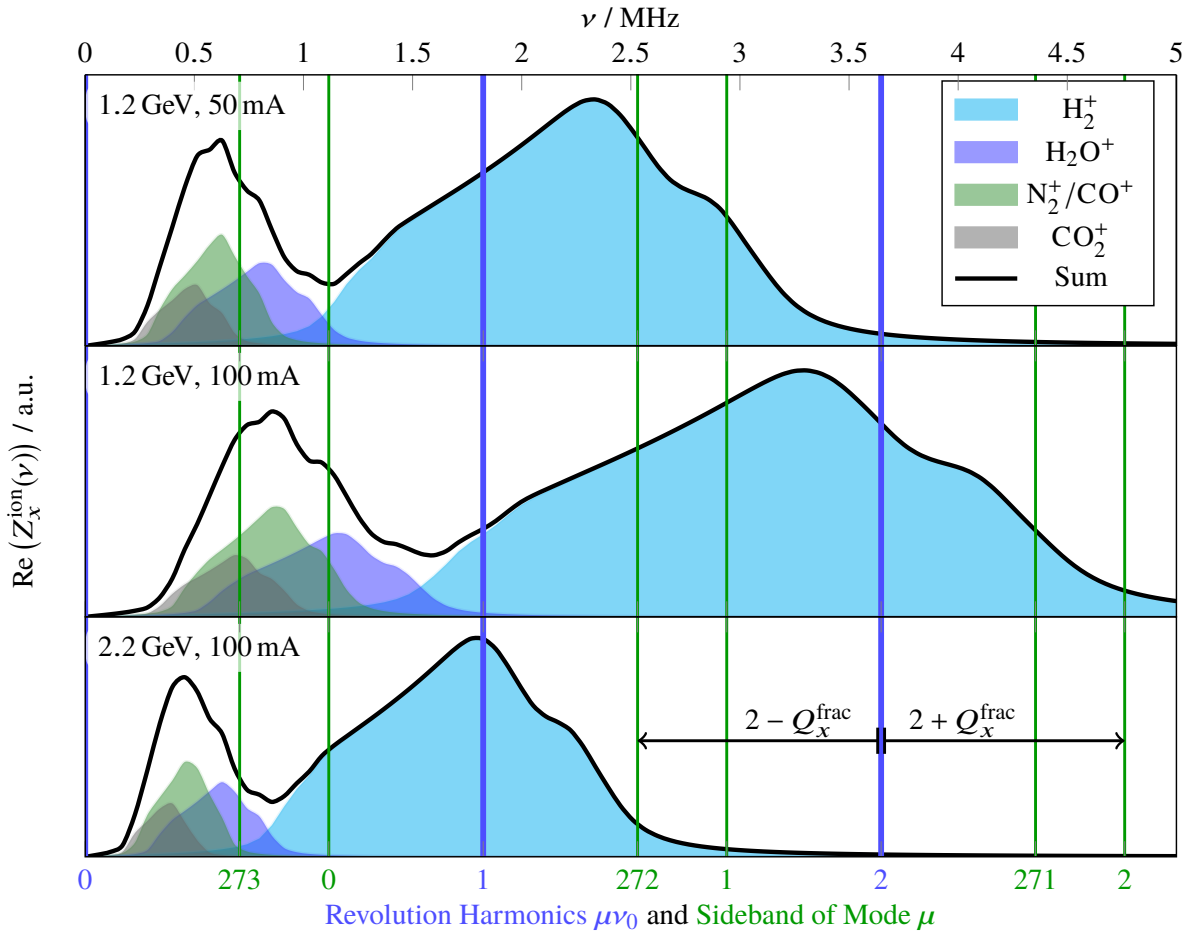

Figure 5.20: Exemplaric spectrum of the horizontal wake impedance of ions at different beam energies and currents for the storage ring with a horizontal tune of 4.612 ($Q_x^{frac} = 0.612$). The spectrum is shown in dimension of MHz. Additionally, the revolution harmonics of the corresponding beam spectrum are shown as blue lines. The upper and lower betatron sidebands are denoted as green lines with their corresponding multi bunch mode numbers.

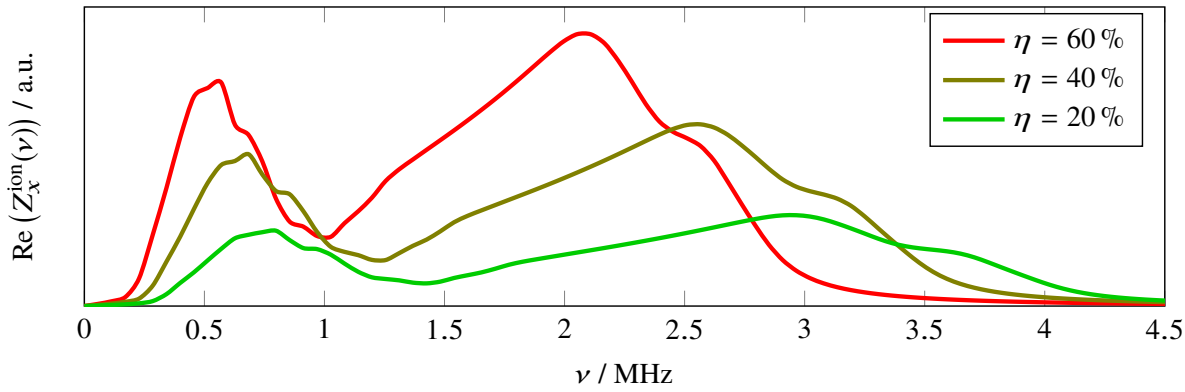

Figure 5.21: Theoretical variation of $\mathrm{Re}(Z_{x,z}^{ion}(\nu))$ with the neutralization level in the storage ring at a beam energy of 1.2 GeV and a current of 100 mA using a linear space charge model.

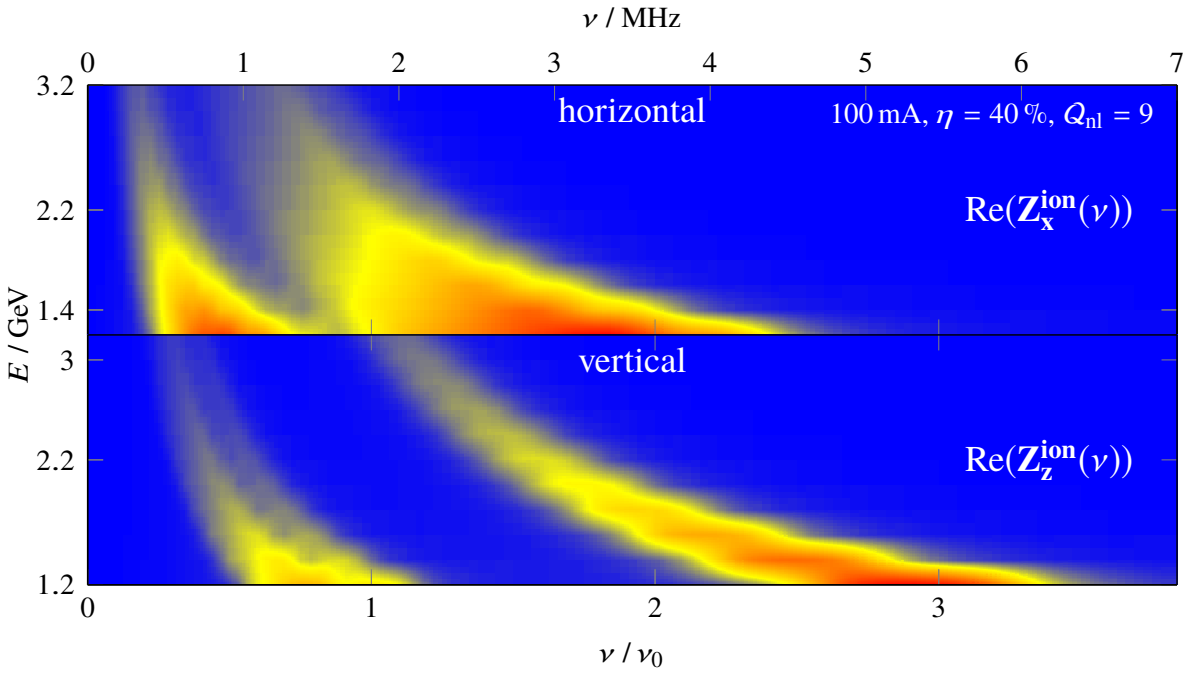

Figure 5.22: Theoretical horizontal (top) and vertical (bottom) impedance of the ion population in the storage ring at a stored beam current of 100 mA at different beam energies. The impedance is shown in arbitrary units and increases from blue (0 Ω) to red.

While figure 5.20 only shows an excerpt of the impedance at different bean energies and currents, in figure 5.22 the relative variation of the ions' impedance with increasing energy for a beam current of 100 mA is shown. In figure 5.23 the impedance's relativ variation with the beam current is shown at 1.2 GeV.

However, it is still unknown how the space charge of a mixture of ion species affects $\mathrm{Re}(Z_x^{\mathrm{ion}}(\nu))$ and is subject of ongoing research. Comparisons between measured and calculated multi bunch mode spectra on page 177 will indeed show that significant differences exist.

5.2.2 Horizontal Beam-Ion Instabilities in the Storage Ring

In case the storage ring is operated at a beam energy of 1.2 GeV with a tune of $Q_x = 4.619$ and $Q_z = 4.431$, horizontal beam instabilities emerge for beam currents higher than approximately 40 to 60 mA[25]. In these instances, the bunch-by-bunch feedback system[26] has been disabled.

The instabilities have been observed using the streak camera which is installed at the diagnostic photon beam line. The streak camera monitors the optical image of the beam, generated by its emitted synchrotron radiation, with a time resolution of down to ps. For more information regarding the streak camera, see [Swi19, section 3.2]. In figure 5.24, 6 streak camera images are shown, each visualizing the evolution of the horizontal beam profile within a time period of 4 µs. As the intensity of synchrotron radiation is proportional to the number of electrons in the accelerator, a periodic intensity modulation is visible in each

[25] The exact threshold currents of these beam instabilities depends on the pressure in the vacuum sytstem of the storage ring.

[26] The bunch-by-bunch feedback system damps emerging coherent transversal and longitudinal beam instabilities by applying counter-phase correction kicks to the oscillation of each individual bunch via broadband kickers. For more detailed information regarding the feedback system, see section 6.2.3 or consult e.g. [Sch15, chapter 6].

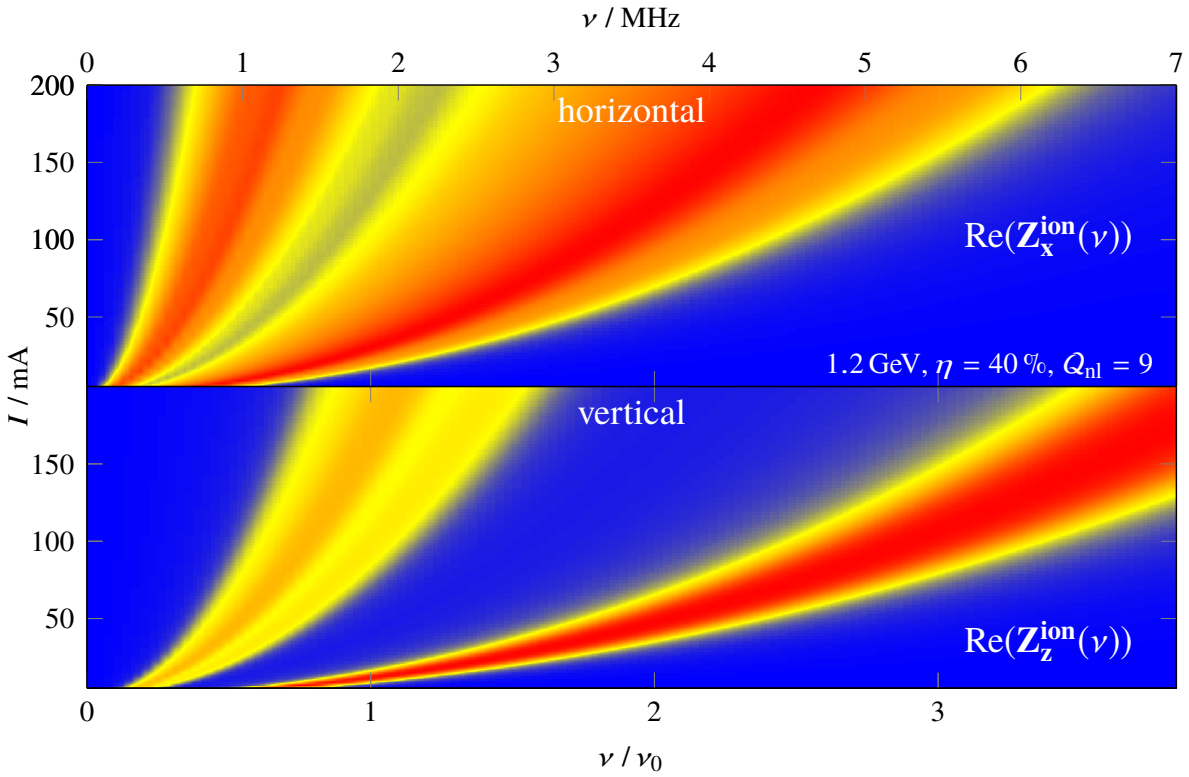

Figure 5.23: Theoretical horizontal (top) and vertical (bottom) impedance of the ion population in the storage ring at a beam energy of 1.2 GeV at different beam currents. The impedance is shown in arbitrary units and increases from blue (0 Ω) to red.

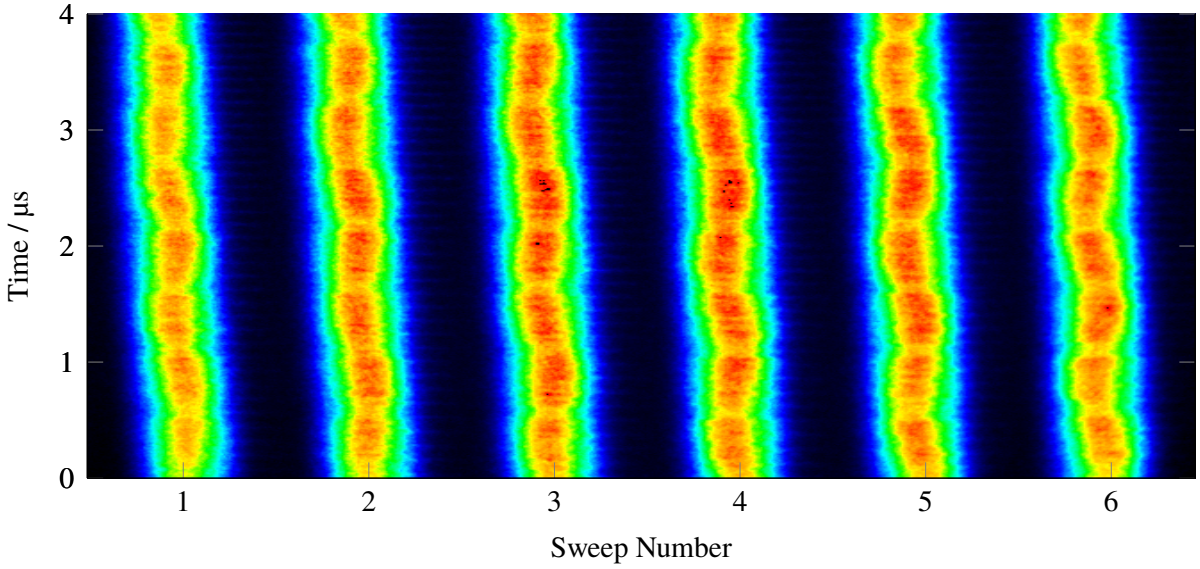

Figure 5.24: Streak camera measurements of the horizontal beam-ion instabilities in the storage ring at a beam energy of 1.2 GeV and a beam current of approximately 75 mA.

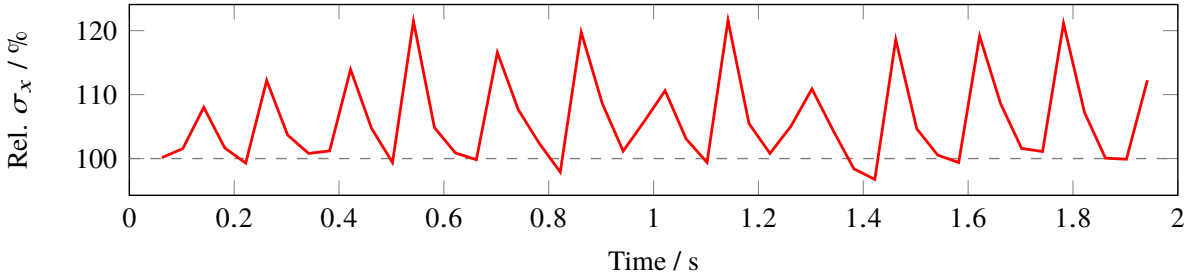

Figure 5.25: Time evolution of the horizontal beam width at a beam energy of 1.2 GeV and a current of approximately 70 mA. The beam width has been measured by a synchrotron radiation light CCD monitor with a time resolution of $1/19\,\mathrm{Hz} \approx 53\,\mathrm{ms}$. The relative error of the measured beam width is estimated by [Swi19, section 3.1.2] as below 5 %.

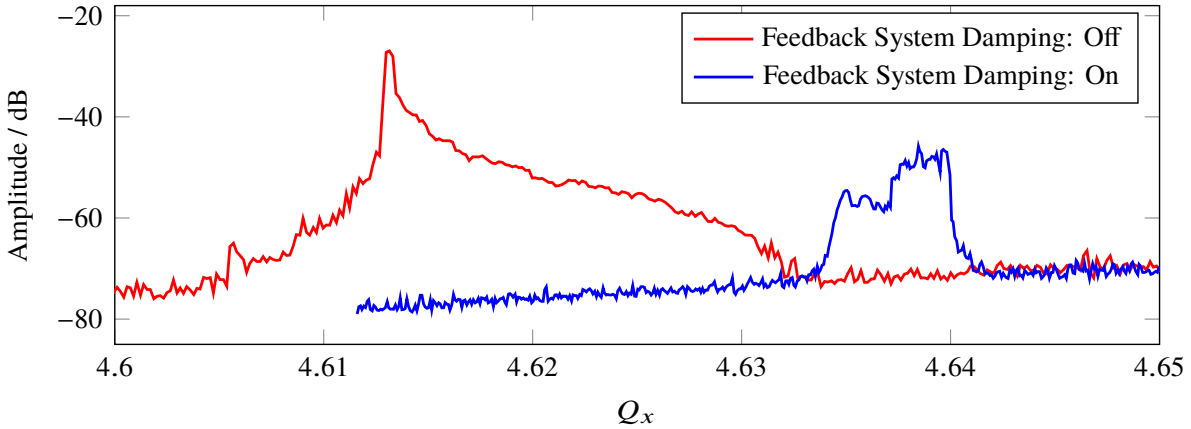

Figure 5.26: Horizontal beam spectrum at a beam energy of 1.2 GeV and a stored current of 100 mA for activated and deactivated horizontal beam damping by the bunch-by-bunch feedback system.

image which results from the storage ring's filling pattern (periodicity $1/\nu_0 = 548\,\mathrm{ns}$). In the observed time period, approximately 2.5 ± 0.2 oscillation periods of the beam are visible in each image, which corresponds to an oscillation frequency of approximately $(0.625 \pm 0.050)\,\mathrm{MHz}$. This frequency indicates an oscillation of the beam with multi bunch mode $\mu = 273$ because this mode shows a contribution at $0.630\,\mathrm{MHz}$[27] in the beam spectrum. Thus, the observed instabilities are identical to coherent multi bunch instabilities of the beam in the horizontal plane.

Note that these instabilities are also noticeable as periodic fluctuations of the horizontal beam width when they are detected by a synchrotron radiation light monitor with a time resolution $\ll 1/(Q_{x,z}^{\mathrm{frac}}\nu_0)$. In figure 5.25, these variations are shown for a time frame of approximately 2 s. A relative increment of up to 22 % of the regular horizontal beam width becomes visible. These coherent beam oscillations can easily be misinterpreted as emittance blow-ups[28].

[27] The contribution of this mode to the beam spectrum emerges as a lower betatron sideband around the first revolution harmonic at $(1 - Q_x^{\mathrm{frac}})\nu_0 = 0.630\,\mathrm{MHz}$ (compare figure 5.20).

[28] A periodic emittance blow-up of the beam has been contributed to trapped ions in certain other accelerators. See for example [WPZ93; Boc+94].

Measurements of the Beam Spectrum

In subsequent measurements, the horizontal beam spectrum has been measured at a beam position monitor in the storage ring using a spectrum analyzer. Figure 5.26 shows the beam spectrum in vicinity of the lower horizontal betatron sideband of the first revolution harmonic at a beam energy of 1.2 GeV and a current of approximately 100 mA during these instabilities. The occurrence of this sideband corresponds to a beam oscillation with multi bunch mode $\mu = 273$. The beam spectrum has been recorded for several minutes while only the maximum contributions to each frequency components in the observed domain are shown. Thus, the shown spectrum does not contain any time information. The frequency of the beam spectrum has already been converted into the corresponding horizontal tunes. When the horizontal bunch-by-bunch feedback system is deactivated (red), a broad sideband is visible in a tune range between 4.61 to 4.63 in close vicinity to the set tune of 4.619 with a relative amplitude of up to −27 dB.

When beam oscillations are damped by the horizontal bunch-by-bunch feedback system, the relative amplitude of the beam instabilities is reduced to approximately −42 dB, as shown in figure 5.26 (blue). Additionally, the center of the sideband is shifted from approximately 4.62 to 4.637 towards higher tunes. In contrast to the broad sideband during instabilities, the damped beam shows a sideband which is approximately a factor of 5 narrower.

Tune Drift During Horizontal Beam Instabilities By using the diagnostic capabilities of the bunch-by-bunch feedback system, the time evolution of these instabilities has been studied. In these measurements, the feedback system has been configured to record the horizontal positions of the center of charge of each bunch within a time period of 25.2 ms. During this period, the beam is not damped horizontally by the feedback system for 20 ms, allowing the beam instabilities to evolve. Thus, these instabilities have been recorded for approximately $46 \cdot 10^3$ revolutions of the electron beam with a time resolution of 2 ns (the bunch spacing, $1/\nu_{\mathrm{rf}}$). The obtained position data is seperated into several (overlapping) time frames and for each frame a frequency analysis has been carried out. The beam spectra resulting from these analyses are sorted chronologically.

This so obtained time evolution of the betatron sideband corresponding to the horizontal tune during a beam instability is shown in figure 5.27. Instead of a broad sideband, as expected from the spectrum in figure 5.26, a narrow sideband is visible which changes in frequency with time. At the beginning of the instability, the beam shows a tune of approximately 4.63. This tune is close to the tune in case the beam is damped and it is expected that this value resemble the beam's initial tune. While its oscillation amplitude increases, the tune shifts to approximately 4.615 reaching its maximal amplitude after 3.5 ms. Then the amplitude of the beam and its tune stays constant for a time period of approximately 1 ms. Eventually, the instability declines and the sidebands shifts towards higher tunes again.

The tune's variation during beam instabilities and while beam instabilities are suppressed by the feedback system can be attributed to the presence of accumulated ions.

Influence of Accumulated Ions Although the optics of the storage ring have been configured for a horizontal tune of 4.619, the beam's coherent tune seems to be equal to approximately 4.63. As these measurements have been conduced with an uncorrected orbit[29] of the beam, a difference between designated and measured tune in the order of ±0.006 is possible according to [Pro18, section 7.2, figure 7.9]. Accumulated ions additionally increase the coherent tune, as has been elaborated in section 5.1.

[29] The closed orbit of the beam is called corrected orbit in case the beam passes through the center of each quadrupole magnet as close as possible.

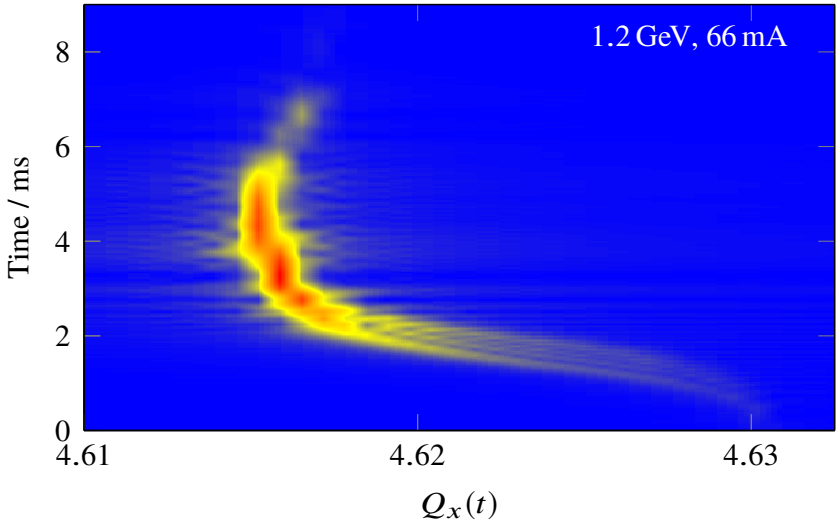

Figure 5.27: Time evolution of the horizontal tune during beam instabilities at 1.2 GeV and 66 mA when biased clearing electrodes are in operation. $Q_x(t)$ has been extracted by a timeframe-wise frequency analysis of the horizontal beam position signal which has been recorded by the bunch-by-bunch feedback system during a timeframe of 20 ms. The amplitude is color-coded and rises from blue to red.

While ions accumulate and the neutralization increases, the beam experiences an increasing positive tune shift. While the beam is stable, no betatron sideband is visible in the beam spectrum. If a certain neutralization level is exceeded, the ions excite a coherent beam oscillation. In this case, both, the beam and the ion cloud, oscillate around each other and their amplitudes increase. Since the spacial distance between the center of charge of the ion cloud and the beam increases during these oscillations, the ions' space charge influence on the beam alters its characteristic: In case both centers of charge are in congruence, the ions induce a coherent tune shift of the beam. This coherent tune shift is reduced and instead a tune spread occurs if both centers are spatially separated from each other[30]. Thus, a reduction of the tune[31] becomes visible with increasing oscillation amplitude in figure 5.27 from 0 to 3.5 ms.

While the coherent amplitude of the beam increases further, ions are partially shaken off the beam. This hypothesis is substantiated by numerical simulations with TransverIon. It is used to determine the fraction of stable ions for different amplitudes of a beam which oscillates horizontally with its fractional tune. The trajectories of 200 000 ions of different[32] species are simulated in the time dependent beam potential for a time frame of 20 µs. If the amplitude of an ion exceeds $10\sigma_x$, it is counted as an instable ion, whereas an ion which stays within this boundary is denoted as stable.

The result of this simulation is shown in figure 5.28 for a beam energy of 1.2 GeV and current of 100 mA. For all relevant ion species, the fraction of stable ions decreases with the oscillation amplitude

[30] In case of separated centers of charge of the ion cloud and the beam, all electrons are drawn into *one* direction towards the cloud. Electrons on one side of the beam center are drawn towards the cloud, which implies that they are focused towards the beam center. Electrons on the other side are defocussed as they are drawn away from the beam center. Thus, the tune distribution of the beam shows a larger width which corresponds to a tune spread. Due to the increased distance between the beam and the ion cloud, also the ion induced coherent tune shift decreases.

[31] The electric and magnetic interaction of the electron beam with the conductive beam pipe and ferromagnetic materials - like iron yokes - also result in a negative coherent tune shift. For more information, see [Ng06, chapter 3, esp. section 3.3.3]. However, this tune shift is mainly dependent on the dimension and transversal shape of the beam pipe geometry along with the iron-yokes' geometry. None of these altered during the occurring instabilities.

[32] The production probability is chosen according to their individual production rate.

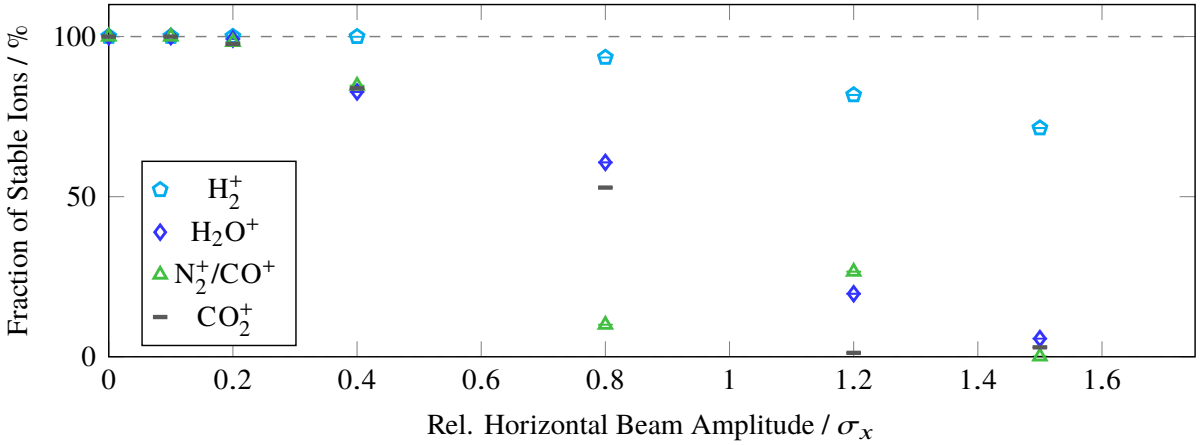

Figure 5.28: Simulated stability of different ion species with the amplitude of coherent beam oscillations in the horizontal plane. In this TRANSVERSION simulation the average beam dimension of the storage ring is used at a beam energy of 1.2 GeV and a current of 100 mA.

of the beam. Yet, H_2^+ ions with low inertia show a higher stability than heavier H_2O^+, N_2^+, CO^+ and CO_2^+ ions. Thus, the ion population indeed is reduced while the oscillation amplitude of the beam increases during the instabilities.

As the number of ions is reduced, the coherent amplitude of the beam begins to decrease as the growth rate of the instability falls below the damping rate of synchrotron radiation. As a consequence, the distance between the beam and the remaining ion cloud reduces and the ion induced positive coherent tune shift increases again (compare figure 5.27 from 4 to 8 ms). The reduced beam amplitude enables the accumulation of new ions which also contribute to the tune shift. Consequently, the observed variation of the tune repeats[33] when enough ions have accumulated to initiate another beam instability.

The bunch-by-bunch feedback system is not able to alter the tune of the accelerator. The positive tune shift in case of suppressed beam instabilities (compare figure 5.26 (blue)) can also be attributed to the influence of accumulated ions on the beam: In case the beam is actively damped, beam instabilities can not occur while the excitation rate does not exceed the damping rate, which is imposed on the beam by synchrotron radiation and the feedback system. Thus, ions accumulate to a higher neutralization because they are not shaken off the beam. This results in a larger tune shift compared to shift of an undamped beam, as visible in figure 5.26 (blue) where the sideband shows a frequency of approximately 4.637. With increasing neutralization also Γ_x increases and at a certain neutralization it exceeds the damping rate and instabilities emerges. Subsequently, ions are shaken off the beam and Γ_x decreases. As a consequence, the feedback system damps down the beam oscillations again before larger amplitudes are reached. Therefore, the sideband in figure 5.26 is significantly lower than in case of an instable beam.

Measured and Simulated Multi Bunch Mode Spectrum

An overlap of $\mathrm{Re}(Z^{\mathrm{ion}}_{x,z}(\nu))$ with the frequency domain of the betatron sidebands $\nu^{\mathrm{MBM}}_{x,z}$ of modes μ leads to their excitation. Here, the shape of $\mathrm{Re}(Z^{\mathrm{ion}}_{x,z}(\nu))$ determines which mode is excited. The growth rate $\Gamma_{x,z,\mu}$ of the oscillation amplitude G'_μ of mode μ depends on the magnitude of $\mathrm{Re}(Z^{\mathrm{ion}}_{x,z}(\nu^{\mathrm{MBM}}_{x,z}))$ in the frequency domain of the corresponding sideband and the beam current in form of $I(\nu^{\mathrm{MBM}}_{x,z})$. G'_μ is

[33] The observed periodicity of this instability cycle is in the order of 10 ms or below. This timescale is similar to the neutralization time T_{n} of approximately 4 ms (compare figure 3.23, $T_{\mathrm{n}} = 1/R_{\mathrm{p}}$).

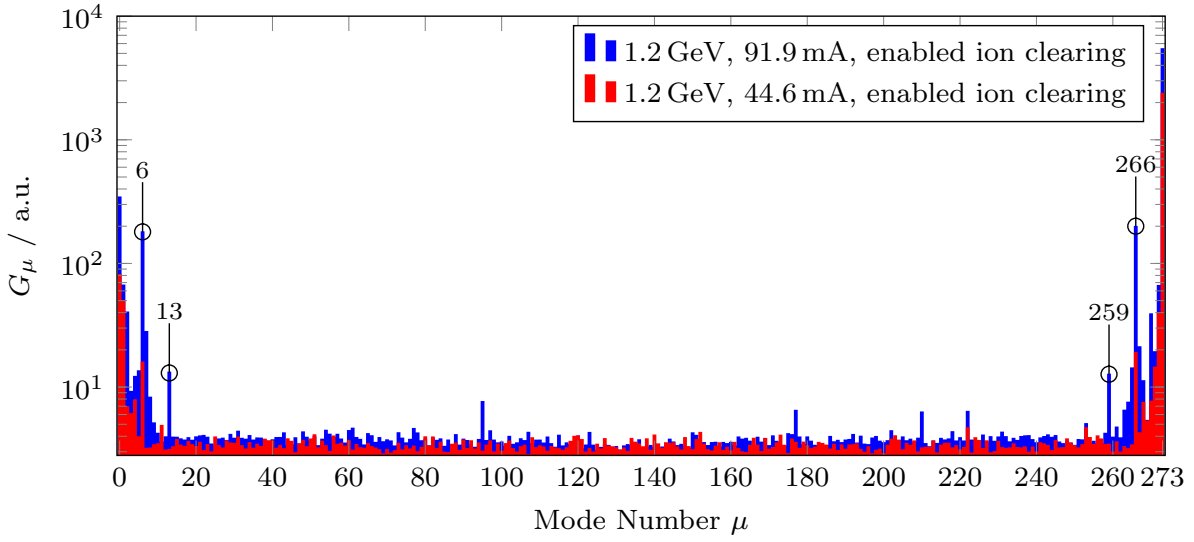

Figure 5.29: Measured horizontal multi bunch mode spectrum for two beam currents at a beam energy of 1.2 GeV with activated ion clearing.

assumed to increase approximately exponentially[34] with time and is proportional to the magnitude G_μ of its corresponding sideband in the beam spectrum. By logarithmizing G_μ, information about $\Gamma_{x,z,\mu}$, and thus $\mathrm{Re}(Z^{\mathrm{ion}}_{x,z}(\nu))$ in the frequency domain of the sidebands, can be obtained.

Using the measured time evolution of the horizontal beam instabilities, recorded by the bunch-by-bunch feedback system, also the multi bunch mode spectrum can be determined. Here, the beam's oscillation in the recorded time period is transferred into the frequency domain by a FOURIER transformation. In the resulting beam spectrum, the individual multi bunch modes can be identified as contributions to the beam spectrum in form of betatron sidebands around the corresponding revolution harmonics. For a known horizontal fractional tune, the magnitude G_μ of each multi bunch mode's sideband can be extracted out of the spectrum.

As the shape of $\mathrm{Re}(Z^{\mathrm{ion}}_{x,z}(\nu))$ reflects in the multi bunch mode spectrum, the spectrum visualizes the significant difference between the measured and calculated wake impedance of ions.

Current Dependency In figure 5.29, the horizontal multi bunch mode spectrum of the storage ring is shown at a beam energy of 1.2 GeV for two beam currents with activated ion clearing measures (biased clearing electrodes). At 44.6 mA, the mode 273, having the lowest frequency component ($(1 - Q_x^{\mathrm{frac}})\nu_0 \approx 0.7$ MHz), is dominant. Additionally, modes 0, 1 and 272 show significant contributions. However, the instability seems to be caused by a low-frequency impedance which expands up towards modes 6 and down to 266. When the beam current is increased to 91.6 mA, the amplitude of these modes increases. The impedance seems to expand towards higher frequencies since new modes with higher frequencies, e.g. mode 13 and 259, are also excited. An expansion of the impedance towards higher frequencies is expected for trapped ions (compare figure 5.23 (top)). Yet, contributions of ions to the wake impedance at these high frequencies (≈ 24 MHz) have not been predicted, as will be discussed below.

[34] In reality, the rise of G'_μ is only exponential at the onset of the instability and then decreases. This behaviour results from $\mathrm{Re}(Z^{\mathrm{ion}}_{x,z}(\nu))$ which is not independent from the beam's oscillation amplitude. Here, ions may be shaken off the beam or show a beam amplitude dependent $\nu^{\mathrm{ion}}_{x,z}$ and change the magnitude and shape of $\mathrm{Re}(Z^{\mathrm{ion}}_{x,z}(\nu))$. Also, the ion oscillation around the

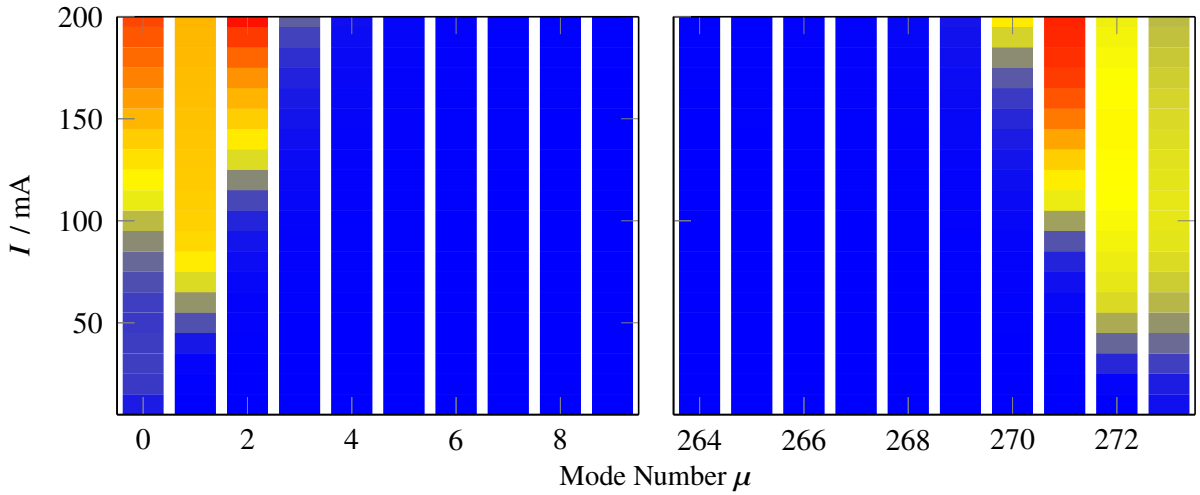

Figure 5.30: Theoretical multi bunch mode spectrum of the horizontal plane at a beam energy of 1.2 GeV for different beam currents. The amplitude of the spectrum $\Gamma_{x,\mu} \sim \log G_\mu$ increases from blue ($0\,\mathrm{ms}^{-1}$) to red.

In figure 5.30, an excerpt of the storage ring's theoretical multi bunch mode spectrum by trapped ions is shown for a beam energy of 1.2 GeV for different beam currents. The modes which are not visualized have a growth rate of $0\,\mathrm{ms}^{-1}$ because the ions' impedance is zero in these frequency domains. The relative growth rate $\Gamma_{x,\mu}$ of the different modes, being negligible small for currents below 50 mA, overall increases with beam current. Additionally, the number of modes, which can be excited by ions, increases from lower to higher frequency with rising beam current. Thus, theory qualitatively predicts an expansion of the instability-driving impedance towards higher frequencies. At 91.9 mA, however, it only predicts an excitation of modes 0 to 1 and 271 to 273 by $\mathrm{Re}(Z^{\mathrm{ion}}_{x,z}(\nu))$. The observed deviations imply that the shape of the impedance also has contributions at significantly higher frequencies than expected.

However, a *resistive wall impedance*[35] resulting from the finite conductance of the beam pipe also causes a transversal impedance which decreases in frequency as $1/\sqrt{\nu}$. Since the ions' and resistive wall impedance are present in the same frequency domain, their impedance adds up and both contribute to $\Gamma_{x,\mu}$, which increases with the beam current. The peaks in the mode spectrum at $\mu = 6$, 13, 259 and 266, however, cannot result from the resistive wall impedance due to its $1/\sqrt{\nu}$ shape and suggests that the observed horizontal beam instability is driven by ions but may also be backed by a resistive wall impedance.

A clear distinction between the ions' impedance and the resistive wall impedance is only possible in this context when changing the neutralization in the accelerator. The growth rate caused by the resistive wall impedance stays constant whereas the ion induced growth rate increases.

Dependence on the Neutralization According to simulations in section 4.3.5, the storage ring shows a neutralization of approximately up to 40 % at a beam energy of 1.2 GeV when the biased clearing electrodes are used to remove ions from the beam. Consequently, a significant decrease of the electrodes' bias voltage or even their deactivation will result in an elevated neutralization. When switching off the

beam increasingly becomes incoherent with time due to their different oscillation frequencies.

[35] Due to the finite conductance of the beam pipe, the charges on the surface of the beam pipe, which are induced by the beam, trail behind the electron beam resulting in long-ranging wakefields which can cause beam instabilities. For more information, see e.g. [Ng06, section 10.1].

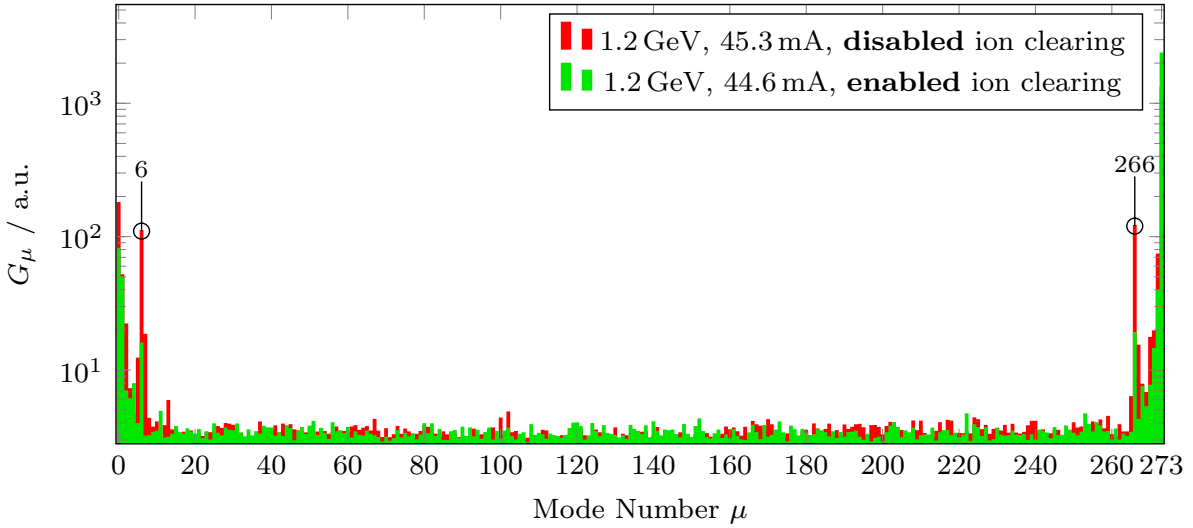

Figure 5.31: Measured multi bunch mode spectrum at a beam energy of 1.2 GeV and a current of approximately 45 mA with activated (top) and deactivated (bottom) ion clearing.

clearing voltage, the neutralization increases by a factor of 2.5 from approximately 40 % to 100 %. This rise also reflects in the multi bunch mode spectrum, as shown in figure 5.31 exemplarily. When the neutralization increases, the amplitude of the low-frequency multi bunch modes between 0 and 7 along with modes between 265 and 273 increases. Thus, ions contribute to the impedance in the frequency range from 0 to 13.9 MHz ($(7 + Q_x^{\text{frac}})\nu_0$) at a beam energy of 1.2 GeV. Here, especially the amplitudes of modes 6 and 266 increase with the neutralization, implying a dominant ion contribution to the excitation of these modes.

According to the calculated multi bunch mode spectrum in figure 5.30, only modes up to $\mu = 1$ could be excited by ions at a comparable beam current. This mode, oscillating with a frequency of 2.9 MHz ($(1 + Q_x^{\text{frac}})\nu_0$), would be excited by H_2^+ ions as they show the highest oscillation frequencies of the ion population. Even if also H_1^+ ions which oscillate with an even higher frequency would hypothetically be present in the storage ring's vacuum system to a significant amount, only a oscillation mode with a frequency at 4.2 MHz could be excited by them. This would still be a factor of 3.3 lower than the oscillation frequency of the observed mode 7.

Thus, in case of neutralization levels between 40 and 100 %, the measured spectrum of $\text{Re}(Z_{x,z}^{\text{ion}}(\nu))$ seems to show higher frequencies than expected. This observation also contrasts with expectations of the linear space charge model in which $\text{Re}(Z_{x,z}^{\text{ion}}(\nu))$ should shift towards lower frequencies as $\nu_{x,z}^{\text{ion}}$ decreases with increasing neutralization.

The observed significant frequency mismatch between measured and expected multi bunch mode spectra along with the findings of [Mar+14] substantiates the fact that the wake impedance of ions, based on the spectrum of $\nu_{x,z}^{\text{ion}}$, is not described suitably in theory in case of a high neutralization > 40 %.

Growth Rate of the Horizontal Instabilities

Under the assumption, that $Z_x^{\text{ion}}(\nu)$ is a broadband impedance which only shifts in the frequency domain insignificantly with the beam current, the growth rate of the instabilities is directly proportional to the number of accumulated ions in the accelerator.

In these measurements, the feedback system has been configured to record the horizontal position of

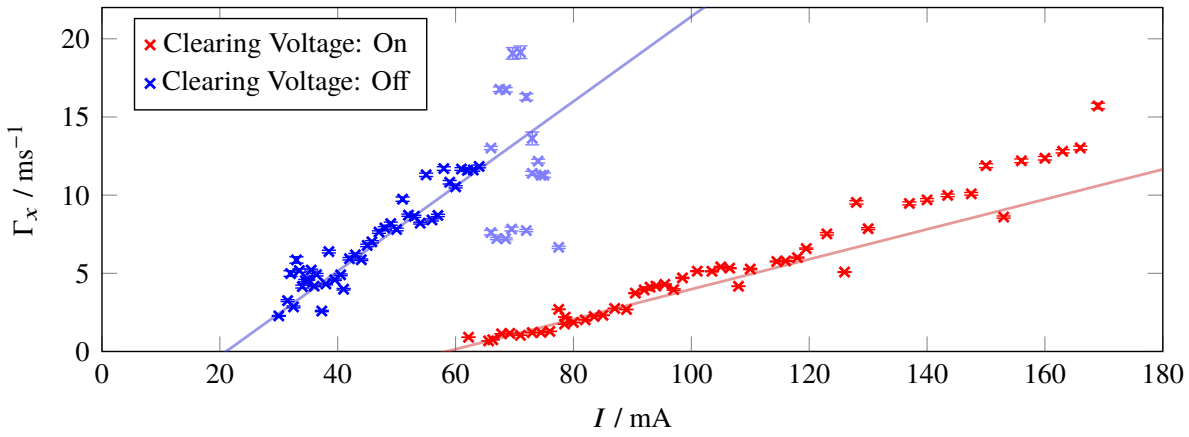

Figure 5.32: Current dependency of horizontal multi bunch instability's growth rates at a beam energy of 1.2 GeV with and without biased ion clearing electrodes. The colored solid lines are linear approximations to the corresponding measurements. The dashed lines indicate the threshold current for the beam instabilities.

each bunch's center of charge within a time frame of 20 ms. During this time frame, the beam has not been damped and horizontal instabilities emerged. Using the absolute value of each bunch's position signal and an appropriate running average filter, the envelope of the beam instability can be generated. The instability initially[36] grows exponentially, enabling a determination of its initial growth rate by approximating an exponential function onto the envelope.

For the measurements, the storage ring has been operated in storage mode at 1.2 GeV with a beam current of up to 170 mA. For a clearing voltage of −3 kV and 0 kV, thus with enabled and disabled ion clearing, the growth rate of the instabilities has been determined for different beam currents.

The growth rates are shown in figure 5.32 for enabled (red) and disable ion clearing (blue). With enabled clearing, the instabilities appear at a threshold beam current of > 60 mA. Their growth rate increases linear with the beam current. By approximating a linear function to the data, the slope of the growth rate with beam current has been obtained as $(0.096 \pm 0.004)\,\mathrm{mA}^{-1}\,\mathrm{ms}^{-1}$. Using this function, a threshold current of (58.5 ± 4.3) mA can also be determined. Without ion clearing, the growth rates increases faster with the current when compared to the case with enabled clearing. This indicates that trapped ions indeed are the main driving mechanism behind the horizontal instabilities. The current threshold for the instabilities' appearance is shifted to lower beam currents and the slope of the current dependent growth rate increases linear in a certain domain.

For beam currents > 65 mA, marked in light blue, fluctuations in Γ_x increase. Here, the made assumptions don't hold true anymore and $Z_x^{\mathrm{ion}}(\nu) \cdot I(\nu)$ varies due to dynamic processes during an instability: On one hand, this fluctuations may results from a volatility in the neutralization due to a shake off of increasing numbers of ions during more severe instabilities. Afterwards new ions cannot accumulate to the same level as have been present at a previous instability before new beam oscillations arise. This results in a lower Γ_x. On the other hand, an increased beam loss due to the instabilities may result in an elevated pressure in the beam pipe due to ESD. Subsequently, ions accumulate to a higher level before beam instability occurs anew and an increased Γ_x is expected. Additionally the coherent tune shifts with the neutralization and adds to the fluctuations in $Z_x^{\mathrm{ion}}(\nu) \cdot I(\nu)$. As these processes are hard to estimate, this domain is excluded from further analyses.

[36] During the course of an instability, its growth rate changes due to e.g. the shaking off ions, increasing decoherence of the beam's and the ion cloud's oscillation as well as a different wake impedance with increasing oscillation amplitudes of the ions.

By linear regression of the growth rates for currents $\leq 65\,\mathrm{mA}$, the slope has been determined as $(0.271 \pm 0.014)\,\mathrm{mA}^{-1}\,\mathrm{ms}^{-1}$ and the threshold current is equal to $(21.1 \pm 2.4)\,\mathrm{mA}$.

The linear increment of the growth rate with the beam current is expected: Assuming a constant neutralization η at different currents, the total number of trapped ions increases linear with the number of electrons. Consequently, Γ_x, proportional to $Z_x^{\mathrm{ion}}(\nu) \cdot I(\nu)$ and thus $\eta \cdot I$, increases linear with the beam current.

When the neutralization increases due to a disabled ion clearing, the slope of Γ_x increases and instabilities emerge at lower beam currents, when the instability's growth rate exceeds the natural damping rate of the beam. Assuming $\eta = 100\,\%$ in case of disabled ion clearing and $\eta \approx 40\,\%$ from the simulation for an enabled clearing (compare section 4.3.5), an increase of the slope of Γ_x by a factor of $100/40 = 2.5$ is expected. The threshold current is expected to drop by an equal factor.

The ratio of the obtained threshold currents is equal to 2.8 ± 0.4 and thus is congruent with the expected value. The slope of Γ_x increases by a factor of 2.8 ± 0.2 when the ion clearing is switched off. It is therefore compliant with the expected value. Since both ratios obtained are above the expected value, this may indicate that neutralization with enabled ion clearing is assumed to be too high. This is possible as the stated simulated neutralization of 40 % only denotes an upper neutralization limit (compare section 4.3.5).

Summary: Evaluation of the Horizontal Beam Instabilities

In the course of this investigation, the horizontal multi bunch instabilities, occurring in the storage ring especially at a beam energy of 1.2 GeV and a stored beam current of approximately > 40 to 60 mA, have been attributed to trapped ions.

The subsequent analysis of the instabilities' multi bunch mode spectrum shows that the majority of the excited oscillation modes of the beam are situated in the low-frequency domain of the spectrum and are caused by the broad-band impedance of the trapped ions. Due to the impedance's contribution in the low frequency domain, an amplification of the instability's growth rate by the storage ring's resistive wall impedance, also present in this frequency domain, can be assumed. Although the frequencies of the prominent oscillation modes of the beam instability are expected from theory, the occurrence of ion induced oscillation modes at significantly higher frequencies cannot be explained. Here, the used model in which $\nu_{x,z}^{\mathrm{ion}}$ stays constant with increasing neutralization as well as a linear space charge model, where $\nu_{x,z}^{\mathrm{ion}}$ decreases with η, can be discarded as basis for a calculation of the wake impedance of ions. Sophisticated numerical simulations like MOEVE PIC TRACKING, in which the ions' mutual space charge interaction is considered, may allow for a development of a suitable impedance model in future.

Additional growth rate measurements of these instabilities show a significant dependence on the neutralization of the accelerator. Here, measured and expected threshold currents for the instabilities's emergence as well as the growth rates' beam current dependency are in agreement.

However, these horizontal beam-ion instabilities only emerge for high beam currents at a beam energy of 1.2 GeV. For higher beam energies, these instabilities have not been observed which is expected due to a reduction of $Z_x^{\mathrm{ion}}(\nu)$, leading to a reduced Γ_x, and an increase of Γ_{sr} with beam energy. Occurring instabilities can be successfully mitigated by the bunch-by-bunch feedback system in combination with operation of ion clearing electrodes, which reduce the average neutralization in the storage ring by a factor of approximately 2.8 when biased with a sufficient high voltage.

CHAPTER 6

Ion Clearing Methods in Electron Accelerators

To avoid the emergence of the undesired ion effects of tune shifts and beam-ion instabilities, discussed in the previous chapter, ion clearing measures have to be applied.

Due to frequent large distance COULOMB interactions of the electron beam with the accumulated ion population, the electron beam continuously transfers energy to the ions. This *beam heating* enables the escape of individual ions out of the beam potential and thus represents a natural clearing process. However, its clearing rate is a factor of approximately 550 to 4 000 lower than the total production rate in the storage ring, as briefly discussed in appendix A.13. Thus, natural clearing does not hinder a growth of the ion population below full neutralization ($\eta = 1$).

Consequently, additional clearing measures have to be applied. In section 6.1, the application of high-voltage clearing electrodes for the local reduction of the ion population will be discussed. Additionally, the operation of the storage ring with an inhomogeneous filling pattern will be outlined in section 6.2. Here, filling gaps are used to specifically destabilize trajectories of individual ion species and prevent their accumulation in the storage ring.

Another ion clearing measure is the beam shaking technique where the beam is excited to coherent transversal oscillation in order to shake off ions and consequently reduce the neutralization. It is presented briefly in appendix A.20.

6.1 Ion Clearing Electrodes

One way to reduce the equilibrium ion population significantly is the use of high voltage biased clearing electrodes. In the following section, the principle of this clearing mechanism will be outlined before discussing its implementation in the storage ring in section 6.1.2. In section 6.1.3, the concept of static neutralization will be utilized to predict how the electrodes' high voltage affects the neutralization in the storage ring. The stated predictions will be reviewed by comparing them to assertions drawn from measurements of the clearing electrodes' ion current in section 6.1.4.

6.1.1 Ion Clearing by High Voltage Electrodes

The dominant fraction of ions which are produced by impact ionization have a low initial transversal oscillation amplitude below σ_x or σ_z. Consequently, they are located close to the beam center where the beam potential shows its transversal minimum. To neutralize these ions, electrically isolated electrodes are installed into the vacuum system. The electrodes are supplied with negative voltages in the order of a few kV.

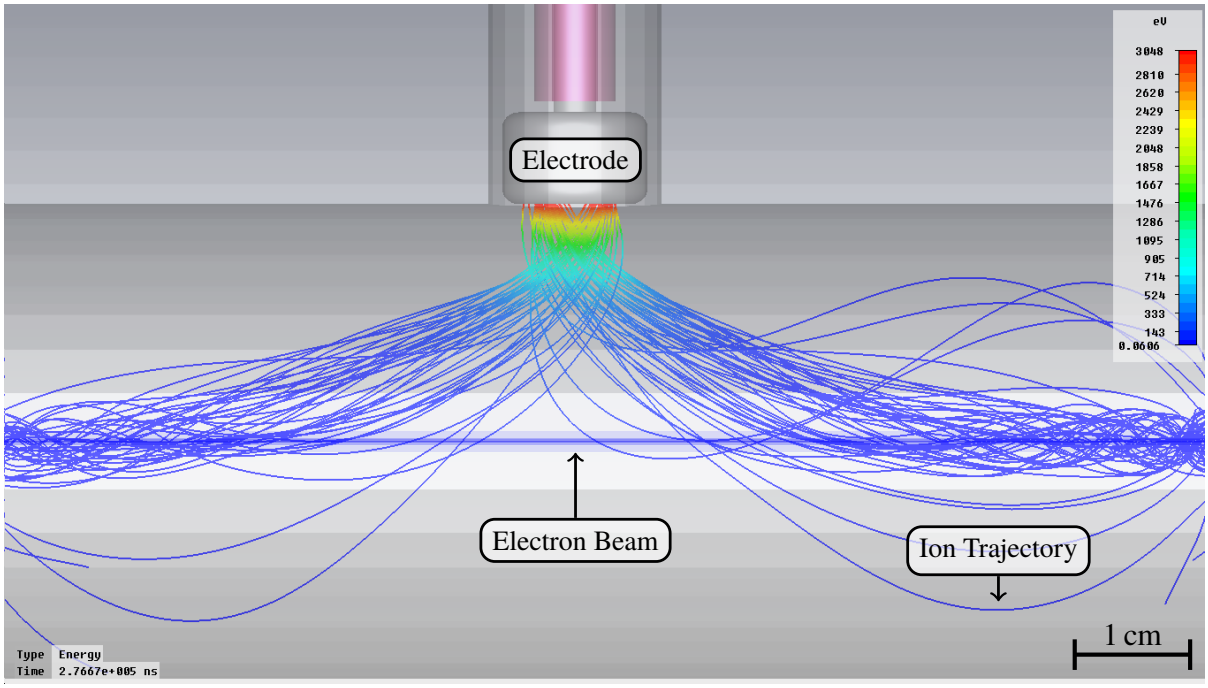

Figure 6.1: Exemplaric trajectories of ions, which drift towards a clearing electrode biased with −3 kV, simulated by CST PARTICLE STUDIO. The color map of the ion trajectories denotes the ions' kinetic energy. Note that the beam dimension and the ions' oscillation amplitudes are not to scale.

If the electrodes' electric field strength at the beam exceeds its field strength, the beam potential is deformed by the electrodes' potential the way that no local minimum is present at the beam center. Consequently, ions which follow the potential to its minimum are accelerated towards the electrode, impinge on it and are neutralized.

This ion clearing method is applied at various accelerators worldwide (compare e.g. [Kas86; Cas+89; BW89]) and subdivides into the use of two different types of clearing electrodes:

- **Local Clearing Electrodes:** This clearing method utilizes electrodes of the button type which are incorporated into the vacuum system. The electrodes' influence on the ion motion is confined to a small area around them which is in the order of a few cm, depending on the their design, bias voltage and the beam potential's depth. They are installed in regions of an accelerator where the local neutralization is expected to be elevated: the local minima of the beam potential, the entrance of dipole magnets (compare section 4.3.5) and potential hollows. Since their fields only affect ions in close proximity, they rely on the longitudinal transport of ions towards them for clearing (see figure 6.1).
- **Continuous Clearing Electrodes:** Instead of the installation of multiple single electrodes in short distances to each other, this electrode is designed[1] as a thin conducting strip, electrically isolated from its attachment, which longitudinally extends on the inner surface of the beam pipe [Hin12, section 10.3 et seq.]. In presence of these electrodes, the ions experience a transversal acceleration towards the electrodes, caused by the electrodes' fields, right after their generation. For more information regarding continuous clearing electrodes, see [Cas+07].

[1] For more information, see [Wan07].

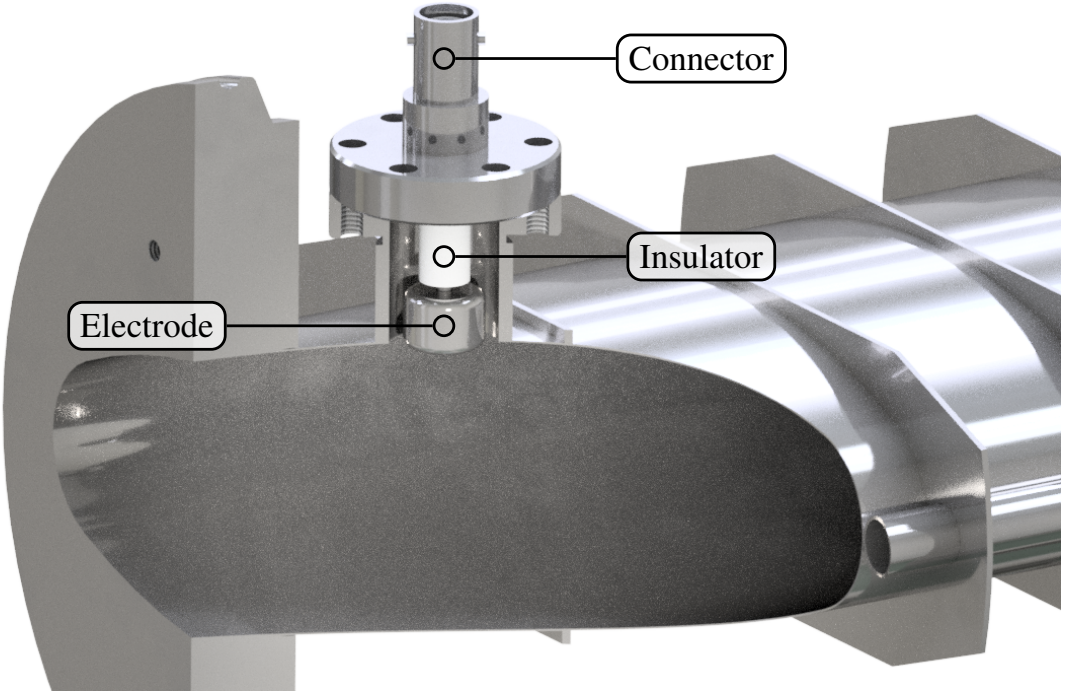

Figure 6.2: Illustration of a clearing electrode integrated into the beam pipe of a quadrupole chamber. A cut through the beam pipe shows the electrode. Visible is the cylindrical button electrode and the ceramic insulator. The electrode is connected to the inner conductor of a coaxial SHV-connector. Courtesy of P. Hänisch, ELSA.

6.1.2 Clearing Electrode Infrastructure of the Storage Ring

In the storage ring, *local* clearing electrodes with negative supply voltage are used to reduce the neutralization. The utilized electrode is visualized in figure 6.2.

Clearing Electrode Distribution

The electrodes are installed near extrema of the beam potential in close proximity[2] to every[3] quadrupole. Consequently, 31 clearing electrodes are installed, accompanied by additional two electrodes at extraction septa MSE6 and MSE22.

The high voltage is generated by a single power supply. It is distributed to the electrodes by a supply line in the storage ring tunnel. Individual stub cables are used to connect the electrodes to the supply line. The current of the power supply is monitored for diagnostic purposes: In principle, conclusions about the ion production rate, the ion accumulation, their longitudinal transport and their stability can be drawn, as will be discussed in the course of this work. To increase the significance of this kind of measurements, a precise current measurement is of importance.

High Voltage Power Supply

Before this work, a power supply, capable of providing a maximum high voltage of $U^{\text{old}}_{\text{CE,limit}} = -3\,\text{kV}$[4] for the electrodes, has been installed. It could supply a peak current of 1.3 mA. The current monitor of this supply provided a DC voltage signal from 0 to 5 V, which has been digitized by a 16-bit ADC digitizer

[2] The distance between the end of the quadrupoles' iron yoke and the electrode is approximately 6 cm.

[3] An exception is quadrupole QD9 in which a quadrupole chamber of an older design without an electrode is installed.

[4] Long term stable at 1.5 V peak-peak, premised a stabilized primary low-voltage power supply is provided [ise].

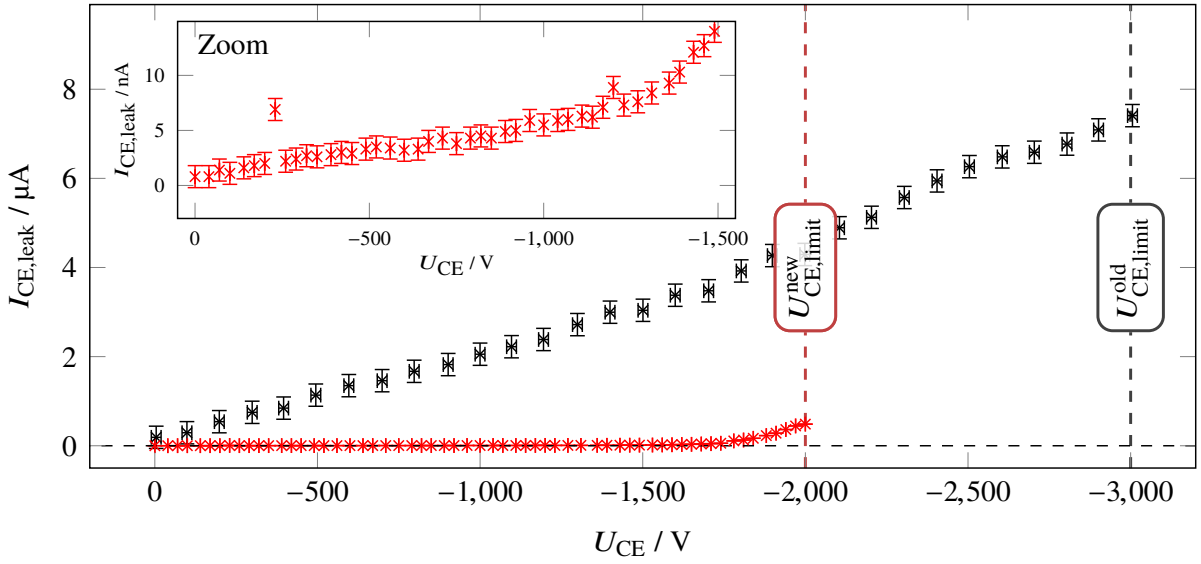

Figure 6.3: Measured characteristic curve of the old and new high voltage power supply of the clearing electrodes. The curve of the old power supply is shown in black. Its maximal high voltage is limited to −3 kV. The characteristic curve for the new power supply, reaching −2 kV maximum voltage, is shown in red. The zoom shows an excerpt of the characteristic curve of the new power supply.

module at a VME[5] crate. The device could be controlled from the ELSA control system. Despite the high resolution of the digitizer, the power supply only had a measured current resolution of approximately 0.25 µA.

Figure 6.3 shows the characteristic curve of this power supply when connected to the electrodes (black): While no beam has been stored in the storage ring, the power supply's current has been measured in dependence of the clearing voltage . Visible is an almost linear increment of the measured current $I_{CE,leak}$ with U_{CE}. This leak current results from a resistance of approximately 500 MΩ inside the power supply[6].

At a beam energy of 1.2 GeV and current of 35 mA with an average pressure of approximately $20 \cdot 10^{-8}$ mbar, ion currents in the order of 4 µA are expected according to simulations with TRACTION (compare section 4.3.4). Thus, a current resolution of below 20 nA is required, if it is desired that 1/200th of the expected current is still distinguishable for ion related diagnostic purposes (see section 6.1.4). The current resolution of the old power supply is a factor of 12.5 too low. When subtracted, the leak current of the power supply poses an additional error on the measured current. Consequently, the old power supply has been replaced by a new one in the course of this work.

The new device provides a stabilized high voltage of maximal $U^{new}_{CE,limit} = -2$ kV with a residual ripple of below 2 mV peak-peak. It is capable of measuring a current in the regime < 100 µA with a resolution of 1 nA [ise12]. The actual values of voltage and current are digitized within the power supply by ADCs with suitable resolution. For control of the voltage set point, a 16-bit DAC within the device is used. Using an RS232[7] interface, the device can be controlled remotely. In the course of this work, full communication of this device with the ELSA control system has been established. All relevant parameters, amongst others the measured voltage and current along with the voltage set point, can be monitored and controlled

[5] A VME is a VMEbus single-board computer.

[6] As this resistance is still measurable in the characteristic curve of the power supply when it is disconnected from the clearing electrode network, it mainly results from the power supply alone.

[7] RS232 is a standard for serial transmission of data.

from a separate menu within the ELSA control system.

The characteristic curve of the new power supply without beam as it is connected to the clearing electrodes is shown in figure 6.3 in red. The linear rise in $I_{\mathrm{CE,leak}}$ results from the electrodes and the connected cables because it is not present if the power supply is disconnected from them. The electrode-cable network has a resistance of approximately 200 GΩ between 0 and −1 kV. Additional averaging of the measured current, cumulated over several seconds, improves the actual resolution to approximately 0.2 nA. This value has been extracted from the average deviation of the measured currents to a fitted function, increasing linearly with U_{CE}. Consequently, the current resolution of the conducted measurement using the new power supply is a factor of approximately 1 250 more precise than measurements with the old device. When an absolute clearing voltage of 1.4 kV is exceeded, field (pre) emission between electrode and beam pipe starts to arise, which can be identified as a non-linear increment of $I_{\mathrm{CE,leak}}$ in this voltage region.

Design and Fields of the Electrodes

A beam pipe of the storage ring with integrated clearing electrode is shown in figure 6.2. The button electrode has the form of a cylinder with a diameter of 12 mm and a height of 8.5 mm made from stainless steel. To locally reduce the electric field strength, thus prevent field emission and arcs for high voltages, the cylinder's edges are rounded with a radius of 1.5 mm. The electrode is mounted on a feed-through, electrically connecting the electrode in vacuum with a coaxial SHV-connector outside. The clearing electrode set-up is flush-mounted to the beam pipe's surface which is designed with a special recess for the electrode. In reference to the electron beam, the electrode is positioned either above or below it with a distance of 22 mm.

For evaluation of the influence of the electrode's field on the ions and the electron beam, the beam pipe with an integrated clearing electrode has been modeled in CST. For an electrode which is biased with a clearing voltage of −3 kV, the electrostatic field solver of CST EM STUDIO has been used to simulate the occurring electric potential within the beam pipe.

Figure 6.4 shows the electrode's potential $U_{\mathrm{CE}}(z, s)$ in the vertical and longitudinal plane. The beam axis at ($x = 0\,\mathrm{mm}$, $z = 0\,\mathrm{mm}$) is shown as blue dashed line. Since the distance between the electrode and the surrounding grounded beam pipe is only 2 mm, the gradient of the potential and thus the electric field strength is at its maximum there. The strength of the part of the electric field which extends towards the beam is comparatively low, although this part is important for the ion clearing process.

For a clearing electrode which is positioned at $s = s_{\mathrm{CE}}$ and $z = z_{\mathrm{CE}}$, figure 6.5 shows vertical and longitudinal cuts through the electrode's potential. The top graph visualizes how the electrode's potential decrease with increasing distance from the electrode. The potential drops from −3 kV at $z_{\mathrm{CE}} = 22\,\mathrm{mm}$ to −118 V at the beam center. Nonetheless, a vertical electric field strength of approximately $E_{z,\mathrm{beam}} \approx 12\,\mathrm{kV\,m^{-1}}$ is present there.

Along the beam axis the electrode's potential also decreases with increasing distance Δs from the electrode, as it can be seen in the bottom graph. The longitudinal region of influence extends ±10 cm around the electrode for an ion with an average thermal kinetic energy (approx. 39 meV, section 2.1.1). For 33 clearing electrodes, the total region of influence amounts to approximately 3.5 m, which is 2 % of the storage ring's circumference. Thus, ion clearing using electrodes in the storage ring relies on the longitudinal transport of ions into the electrodes' region of influence. If an ion is trapped within the potential of the beam, this region decreases with increasing beam potential depth.

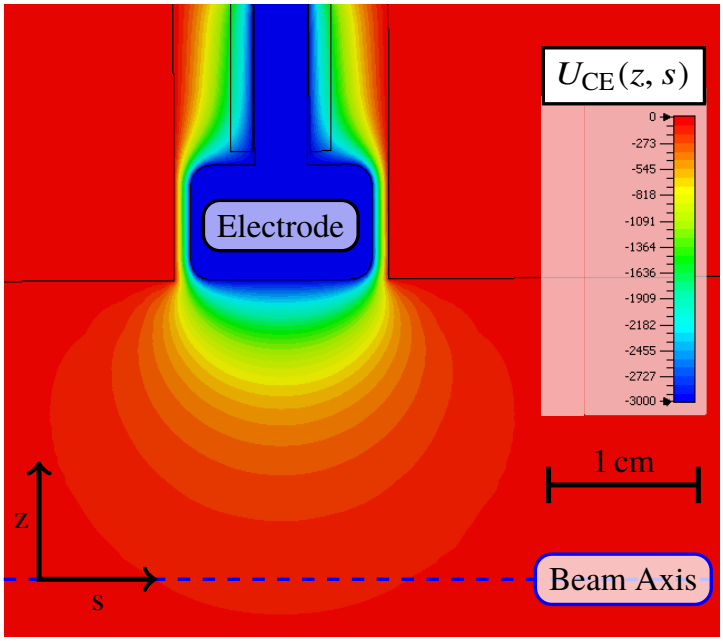

Figure 6.4: Vertical and longitudinal electric potential of the clearing electrode which is used in the storage ring. The electrode is biased with −3 kV. The blue dashed line indicates the position of the beam. The potential is obtained from the electrostatic field solver of CST EM STUDIO.

6.1.3 Estimating the Voltage Dependent Neutralization

The electric potential of the electrode superimposes the beam potential. The depth of the electrode's potential scales linearly with the applied clearing voltage. Thus, the clearing voltage influences the shape of the electric potential in vicinity of the electrode. Consequently, it depends on the clearing voltage whether ions, propagating in this potential, will be drawn towards the electrode or accumulate in vicinity of the beam to a certain neutralization level.

Consider a clearing electrode positioned near a minimum of the beam potential. For a low clearing voltage, the potential is deformed only slightly by the field of the electrode. Consequently, ions are able to accumulate in the potential in front of the electrode. While the ion population increases, the beam potential is deformed by their space charge. After reaching a certain accumulation level, surplus ions will be drawn towards the electrode, because the distance between the beam center and individual ions increases due to the repulsive space charge of the ion population. Eventually, a continuous flow of ions towards the electrode establishes itself, maintaining a constant accumulation level in vicinity of the beam. The established accumulation level is dependent on the shape of the electric potential. Thus, the local and the resulting average neutralization in the storage ring is dependent on the clearing voltage.

Static Neutralization at Clearing Electrodes

The threshold clearing voltage with which the local static neutralization is kept below a certain level can be evaluated using the concept of static neutralization, introduced in section 4.2.2.

Figure 6.6 shows the vertical beam potential of an electron beam with an energy of 1.7 GeV and a current of 50 mA in front of a clearing electrode at $s = s_{CE}$. The black curve shows the initial beam potential without a biased electrode. In this case ions accumulate in the beam potential until $\eta = \eta_{stat} = 1$. The red curve shows a superposition of the same beam potential with the electrode's potential for a low

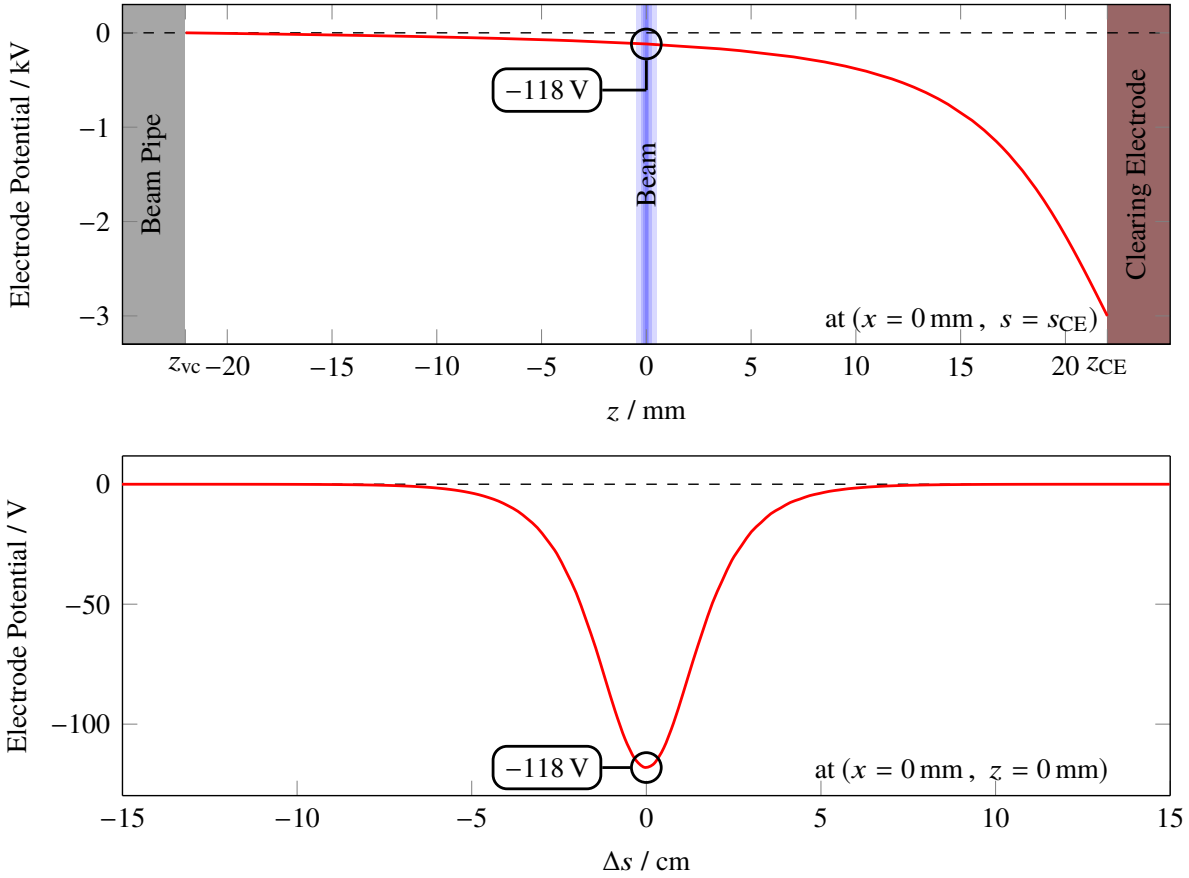

Figure 6.5: Electric potential in vertical and longitudinal direction of a clearing electrode which is positioned at $(x = 0\,\text{mm}, z = z_{\text{CE}}, s = s_{\text{CE}})$ and biased with −3 kV. The top graph shows the electrode's potential in vertical direction. The blue region indicates where the electron beam traverses the potential. Here, the potential is equal to approximately −118 V. The bottom graph shows how the potential curve at the beam center evolves with increasing distance from the electrode. The potential is obtained from the electrostatic field solver of CST EM STUDIO.

clearing voltage of −10 V. The electrode's potential has been obtained from simulations with CST EM STUDIO. The resulting potential has a local maximum U_{max} at z_{b} at a distance of approximately 9.5 mm from the clearing electrode. Ions which are produced near the beam center at $z \approx 0$ mm are not able to reach the electrode due to the potential barrier. The same is true for longitudinally in-drifting ions which are also propagating in vicinity of the beam center as their oscillation amplitude is small compared to z_{b}. With increasing longitudinal distance from s_{CE}, the potential barrier at z_{b} approaches the level of the unperturbed beam potential[8] as the electrode's potential decreases (compare figure 6.5 (bottom)). Consequently, the potential barrier closest to the electrode is the region where ions are able to reach the electrode most likely, provided that their kinetic energy is high enough and/or the beam potential is deformed enough by the ions' space charge to overcome the barrier.

[8] Although the beam potential gets more shallow with increasing longitudinal distance from its local minimum at s_{CE}, it alters more gradual than the electrode's potential.

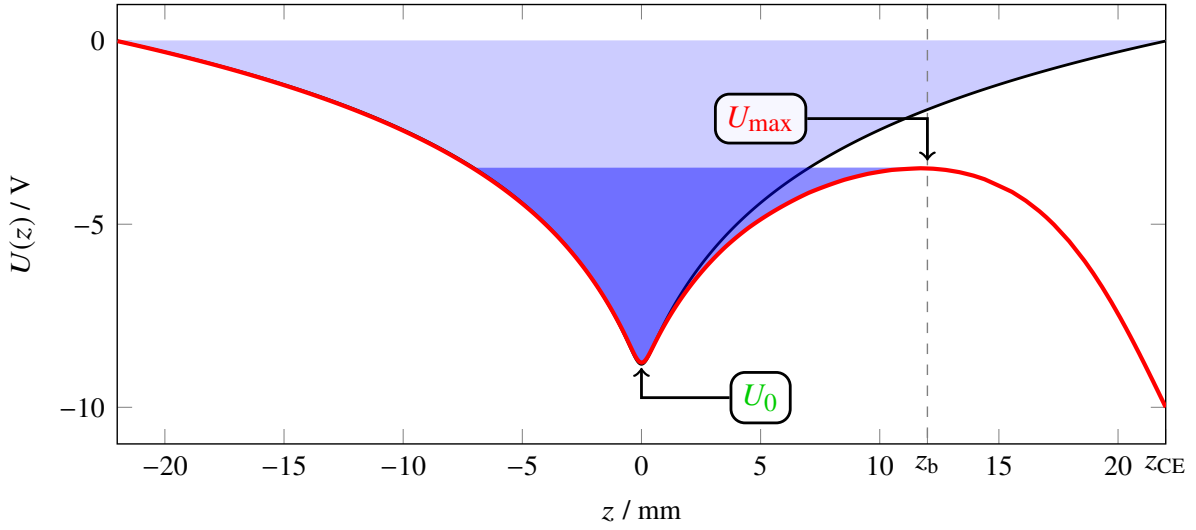

Figure 6.6: Vertical deformation of the beam potential by a clearing electrode (CE) at $z = z_{\mathrm{CE}}$. The unperturbed beam potential is shown as the black curve for a clearing voltage of 0 V. Here, ions accumulate to $U_{\max} = 0\,\mathrm{V}$, visualized as light blue area, resulting in $\hat{\eta}_{\mathrm{stat}} = 1$. For a clearing voltage of −10 V, $\hat{\eta}_{\mathrm{stat}}$ in front of the electrodes is smaller than one, as visualized by the dark blue area. Note that the beam energy is 1.7 GeV and the stored current is 50 mA in the shown scenario.

Estimating the Static Neutralization

Since the described scenario is identical to a potential barrier in the longitudinal plane, equation (4.3) of section 4.2.2 can be used to estimate the local static neutralization $\hat{\eta}_{\mathrm{stat}}(s)$ in vicinity of the clearing electrodes in dependence of their bias voltage.

A MATLAB script has been developed which determines the occurring local neutralization $\hat{\eta}_{\mathrm{stat}}(s)$ in dependence of the clearing voltage for different beam energies and currents. On basis of the precomputed beam potential $\langle U(s)\rangle$ it works as follows:

For a certain beam energy, current and clearing voltage the local beam potential, as it is deformed by the electrode's field, is calculated at positon s_{CE}. The potential barrier $U_{\max}(s_{\mathrm{CE}})$ hinders all proximal ions which have a lower energy (potential plus kinetic energy) than $eU_{\max}(s_{\mathrm{CE}})$ from reaching the electrode.

$\hat{\eta}_{\mathrm{stat}}$ in front of each clearing electrode and its vicinity is calculated via

$$\hat{\eta}_{\mathrm{stat}}(s) = 1 - \frac{U_{\max}(s_{\mathrm{CE}})}{\langle U(s)\rangle}\,.$$

Here, the local static neutralization is calculated only for all neighboring positions s around a single electrode where the time averaged beam potential $\langle U(s)\rangle < U_{\max}(s_{\mathrm{CE}})$ and ions cannot pass the potential barrier. For positions where $\langle U(s)\rangle > U_{\max}(s_{\mathrm{CE}})$, ions are not trapped because they have enough energy to reach the electrode.

The total static neutralization has been obtained for different beam energies and currents along with clearing voltages reaching from 0 to −3 kV. Figure 6.7 shows exemplaric results of this study for beam energies of 1.7 and 2.3 GeV with a beam current of 35 mA. Here, a clearing voltage of −3 kV reduces the *additional* static neutralization in front of the electrodes to zero. At this clearing voltage, the electrodes' electric fields draw all produced or in-drifting ions away from the beam and neutralize them. Obviously, the static neutralization due to potential hollows remains unaffected by the clearing voltage on a level of

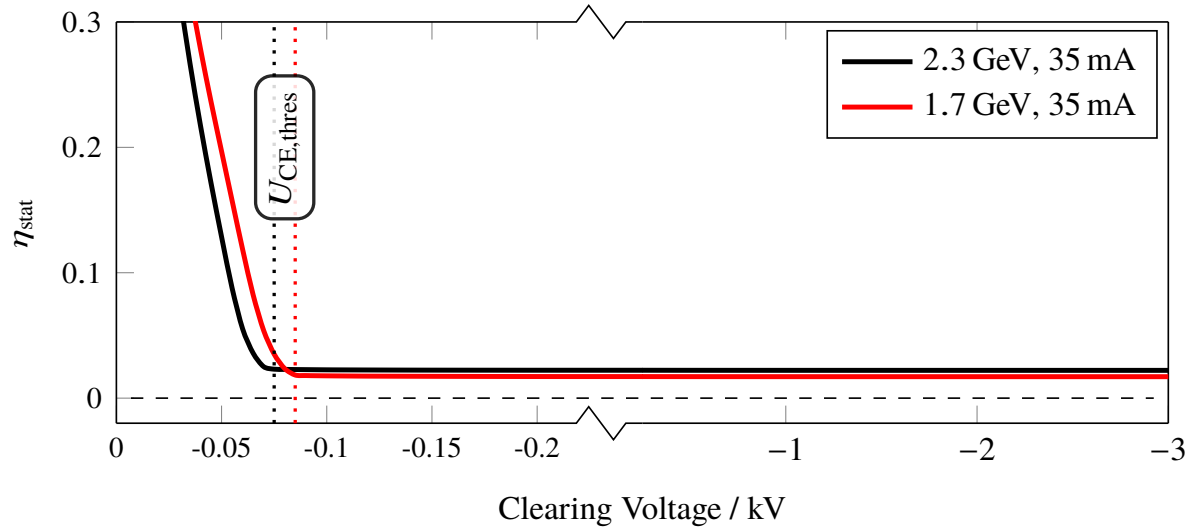

Figure 6.7: Static neutralization in the storage ring for different clearing electrode voltages. At −3 kV the static neutralization is equal to 1.71 % for a beam energy of 1.7 GeV and 1.85 % for 2.3 GeV. As no additional clearing mechanism is in place, η_{stat} is equal to one for a voltage of 0 V. The dotted lines denote the corresponding threshold voltages $U_{\text{CE,thres}}$.

1.71 and 1.85 % for 1.7 and 2.3 GeV, respectively (compare section 4.2.2). Here, an absolute clearing voltage of 100 V is still sufficient to reduce the static neutralization to a minimum. Since this is still the case for −2 kV, the new high voltage power supply is also capable of reducing the static neutralization to a minimum.

Due to the energy dependence of the depth and shape of the beam potential, the minimal voltage $U_{\text{CE,thres}}$ for no additional static neutralization also is energy dependent and shifts towards lower absolute clearing voltages with higher beam energies.

Figure 6.8 shows the calculated $U_{\text{CE,thres}}$ with a tolerable local static neutralization of 1 % for the storage ring. Following these estimations, a clearing voltage of $|U_{\text{CE}}| > 250$ V is necessary for the operation of the storage ring at a beam energy of 1.2 GeV and a current of 25 mA, for example. For the same clearing voltage, a beam current of up to 61 mA can be stored at 3.2 GeV. For a beam current of 200 mA at 1.2 GeV beam energy, $U_{\text{CE,thres}}$ is equal to −2 040 V. This voltage is only required at electrodes positioned near QD quadrupoles where the beam potential is deepest. Here, a clearing voltage of −2 kV will result in a local static neutralization of 1.2 % in QD1 and QD17 (compare figure C.17 in the appendix), which leads to a negligibly small average static neutralization. As mentioned beam parameters are only used seldom and represent extreme operating conditions for the storage ring, the new high voltage power supply is appropriate for this application according to this estimation.

Typically, the clearing voltage in the storage ring is set to −1.4 kV. This voltage is sufficiently large to prevent additional static neutralization and low enough to avoid (pre) field emissions at the electrodes.

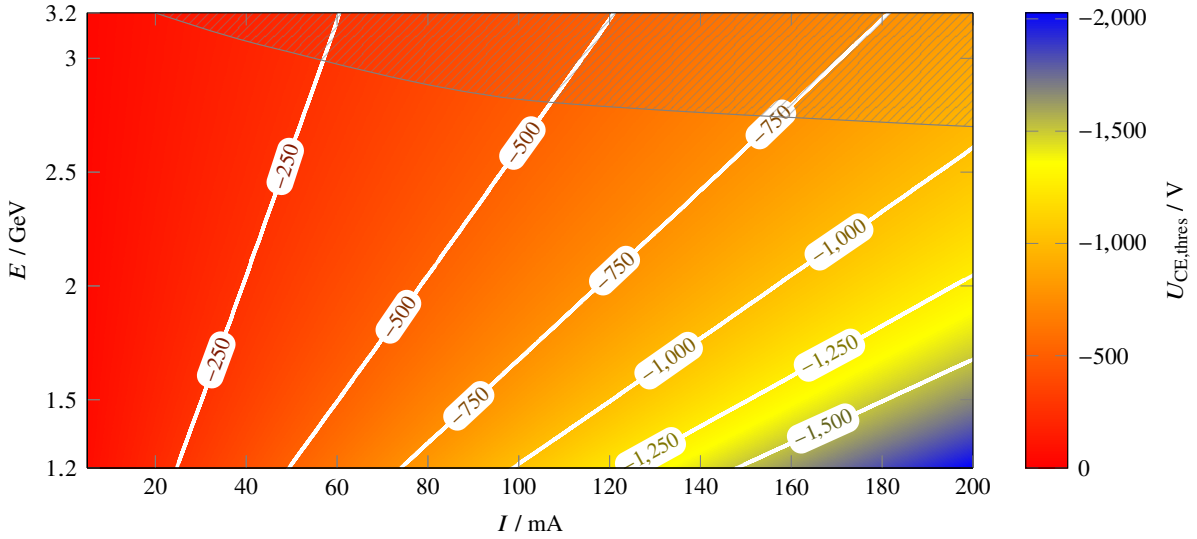

Figure 6.8: Predicted threshold clearing voltages for a local static neutralization of below 1 % at different beam energies and currents for the storage ring. The white lines indicate the contour-lines. The hatched area indicates combinations of beam energy and current, where an operation of the storage ring is only possible to a limited extend due to a beam lifetime below 60 s [Sch15, section 13.1, figure 13.2]. Note that corrections to these threshold voltages are in effect (see page 202).

6.1.4 Ion Current Measurements

The estimates on $U_{\mathrm{CE,thres}}$, made in the previous section, are based on a linear space charge model and under negligence of any ion dynamics[9]. To validate these estimates experimentally and consequently be able to configure the clearing voltage in the storage ring the correct way, the characteristic curve of the clearing electrode system in presence of the electron beam has been measured. These ion current measurements are discussed on page 198 and following. However, first an analytical model of the ion accumulation in front of clearing electrodes is discussed and a theoretical prediction for the measured characteristic curve is elaborated.

Theoretical Model of the Measured Ion Current

The measured current of the clearing electrode system I_{CE} is parameterized as

$$I_{\mathrm{CE}} = \mathrm{e}\, \mathscr{L} \cdot \mathscr{F} \cdot R_{\mathrm{p}} \cdot N_{\mathrm{e}} + I_{\mathrm{CE,leak}} \tag{6.1}$$

in this work, assuming that the average ionization status of the ions is approximately one. $I_{\mathrm{CE,leak}}$ is the leak current of the power supply and the clearing electrode system due to their finite electric resistance and the (pre) field emission current at $|U_{\mathrm{CE}}| > 1\,000\,\mathrm{V}$ (compare figure 6.3, red).

In this model, the produced ions form a constant stream towards the clearing electrodes, which experiences losses to the beam pipe. These losses in longitudinal and transversal direction mainly emerge from to the ions' mutual space charge interaction: Consider an ensemble of ions which is confined in the beam potential in transversal and longitudinal direction. In this configuration, the ions oscillate in

[9] E.g. the alteration of ion propagation trajectories and velocities due to the electric field of the clearing electrodes and the mutual space charge interaction within the ion population as well as magnetic fields.

the beam potential and experience the space charge force of the beam and other ions. Due to beam heating, the beam continuously transfers energy to the ensemble, which is partially cooled away by the gas cooling process (compare appendix A.13). Additionally, each space charge interaction leads to an energy transfer between the ions. Although the average kinetic energy of the confined ion ensemble may be constant in time, certain individual ions gain enough energy to overcome the transversal and longitudinal confinement of the beam potential, impinge on the beam pipe and are neutralized. The higher the neutralization, the weaker is the effective beam potential for ions due to their mutual space charge repulsion, leading to a higher probability for each ion to escape their confinement. These losses - or reduction in the ion stream's transmission - are characterized by the functions $\mathscr{L}$ and $\mathscr{F}$.

The dimensionless parameter $\mathscr{L} \in [0, 1]$, which may be called the longitudinal transmission function, characterizes the longitudinal transmission of ions from their production locations to the clearing electrodes. In this model, $\mathscr{L}$ is assumed to be a function of

- beam energy and current, as the longitudinal ion transport is dependent on the transmission through the dipole magnets' fringe fields (compare figure 4.15 in section 4.3.3).
- the stability of the ions' trajectories. If additional ion clearing mechanisms are applied, like beam shaking or the use of filling gaps, the ions' trajectories may be rendered instable. Instable ions eventually impinging on the beam pipe and are neutralized there. Consequently, the measured current at clearing electrodes is reduced by the fraction of instable ions.
- the clearing voltage, because the extent of the electrodes' longitudinal region of influence is dependent on it: The longer the ions' trajectories from their production position to an electrode, the more likely is a loss of ions as they may pass regions with high local neutralization. Thus, ions which may not have reached an electrode under certain circumstances can be collected with an increased clearing voltage. It is assumed that $\mathscr{L}$ only varies linearly and slightly with the clearing voltage.

If all produced ions are transmitted longitudinally and detected by the clearing electrode system, $\mathscr{L}$ is equal to one. If a fraction of ions is lost, $\mathscr{L}$ is reduced to below one. For a fixed clearing voltage, the measurement of I_{CE} also can be used to indirectly verify the efficiency of clearing measures via the determination of $\mathscr{L}$[10].

$\mathscr{F} \in [0, 1]$ is a dimensionless function which describes the fraction of the detected ions to the total number of potentially detectable ions for different clearing voltages. Potentially detectable ions could have been detected, if the clearing voltage would have been set high enough to prevent a local static neutralization in front of the clearing electrodes. If the voltage is insufficient to draw ions towards the electrodes and all of them are neutralized at the beam pipe, $\mathscr{F}$ is equal to zero. In case the electrode collects all ions within its region of influence, $\mathscr{F}$ is one. Thus, the clearing voltage dependent $\mathscr{F}$ characterizes the interplay between the beam's and clearing electrode's electric potential. Since the measured clearing electrode current mainly depends on this interplay, $\mathscr{F}$ is the important parameter which indicates how the static neutralization varies with the applied clearing voltage. It enables a comparison between prediction and measurements. $\mathscr{F}$ may be called the transversal transmission function. A theoretical model for it is discussed in the following section.

Using the fact that $R_{\mathrm{p}}/\mathcal{P}(E, I)$ is constant for one beam energy (compare equation (2.8) and equation (2.1)), equation (6.1) can be separated into terms which are constant and non-constant for a specific

[10] In the storage ring, the first measurements of this kind, although not analyzed quantitatively with this concept, have been conducted in [Ste95, section 6.2].

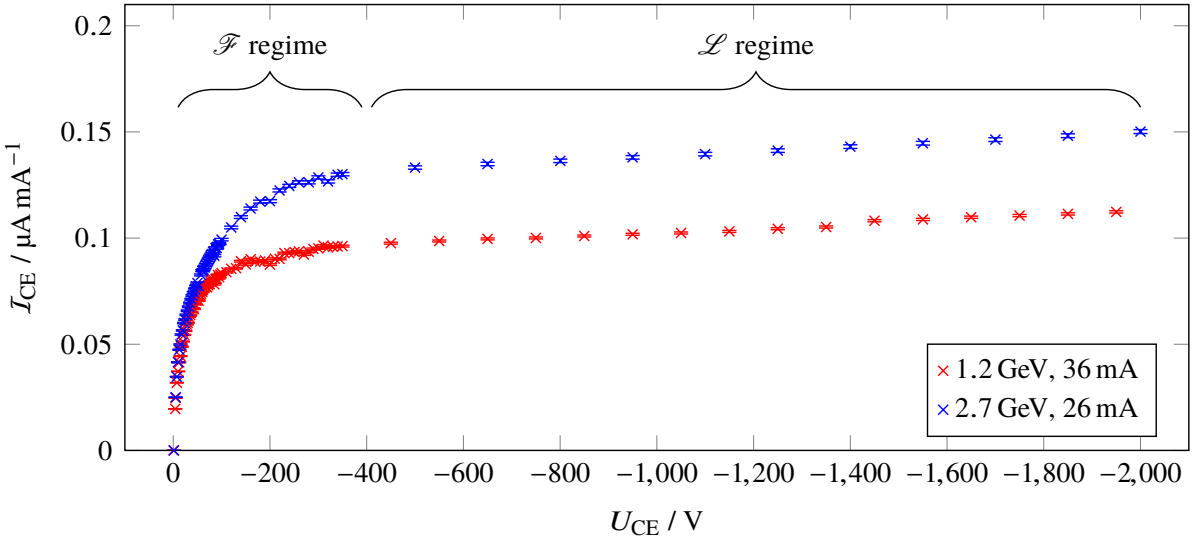

Figure 6.9: Typical characteristic curves of the clearing electrode network, when measured during operation of the storage ring with a stored electron beam.

beam energy as

$$I_{CE} = \underbrace{\frac{C}{\beta c}\frac{R_p}{\mathcal{P}(E,I)}}_{:=\tilde{K}=\text{const.}} \cdot \underbrace{\mathscr{L}\cdot\mathscr{F}\cdot I\cdot\mathcal{P}(E,I) + I_{CE,leak}}_{\text{varying with } I \text{ and } U_{CE}} \cdot$$

Here, $\mathcal{P}(E,I)$ is the average pressure for a certain beam energy and current. The measured current is rescaled as

$$\mathcal{I}_{CE} := \frac{I_{CE} - I_{CE,leak}}{I} = \tilde{K}\cdot\mathscr{L}\cdot\mathscr{F}\cdot\mathcal{P}(E,I) \tag{6.2}$$

to enable an extraction of $\mathscr{F}$ from the measurements in the end. The voltage dependent leak current $I_{CE,leak}$ is subtracted from I_{CE} and the so corrected current is normalized to the beam current I. The resulting quantity $\mathcal{I}_{CE}$ may be denoted as the ion transmission coefficient.

During a measurement of the characteristic curve, the clearing voltage is increased steadily and $\mathcal{I}_{CE}$ is determined. Two typical characteristic curves are shown in figure 6.9 for beam energies of 1.2 and 2.7 GeV at approximately 36 and 26 mA beam current, respectively. For both measurements, $\mathcal{I}_{CE}$ increases linear in the region $|U_{CE}| > 400\,\text{V}$. If the absolute clearing voltage is reduced further, $\mathcal{I}_{CE}$ decreases non-linearly, eventually reaching $0\,\mu\text{A}\,\text{mA}^{-1}$ at a clearing voltage of 0 V.

The linear increment in $\mathcal{I}_{CE}$ for $|U_{CE}| > 400\,\text{V}$ results from the reduced longitudinal losses of the ion stream due to expansion of the clearing electrodes region of influence with increasing clearing voltage. In this region of U_{CE}, $\mathscr{F}$ is equal to one because the electrodes' electric field has already deformed the beam potential in a way that η_{stat} is equal to zero in front of the electrode. The number of collected ions increases with $|U_{CE}|$, resulting in detection of a larger ion current. As this process is parameterized with $\mathscr{L}$, this domain of the characteristic curve may be called $\mathscr{L}$ regime. In the non-linear domain where $|U_{CE}| < 400\,\text{V}$, an ion accumulation in front of clearing electrodes is possible as the electrodes' field strength cannot attract all ions. Here, $\mathscr{F}$ is smaller than one. This domain may be called $\mathscr{F}$ regime.

Note that the measured characteristic curve in shape resembles the measured tune shift of the beam with the electrodes' clearing voltage, shown in figure 5.12. This indicates that the measured ion current is correlated to the neutralization of the beam which will be used in the following model to parameterize $\mathscr{F}$

with η_{stat}.

If $\mathcal{I}_{\mathrm{CE}}$ is normalized to one pressure by using the known $\mathcal{P}(E, I)$[11] and the linear increment in the $\mathscr{L}$ regime is corrected, the characteristic curve enables the extraction of $\mathscr{F}$. Thus, information about how the static neutralization varies with the clearing voltage can be obtained.

Lossy Flow Model To verify the used concept of static neutralization and determine $U_{\mathrm{CE,thres}}$ experimentally with it, a theoretical model of $\mathscr{F}$ - it may be called *lossy flow model* - has been developed in the course of this work.

Assume a clearing electrode which is biased with insufficient clearing voltage to reduce $\hat{\eta}_{\mathrm{stat}}$ to zero in the local beam potential. Consequently, ions will accumulate within the potential hollow up to a neutralization of $\hat{\eta}_{\mathrm{stat}}$, deforming the beam potential with their space charge and eventually enable the escape of additional ions out of the potential hollow. In principle, all ions which are previously trapped within the potential hollow eventually reach the electrode, if the described loss mechanism is ignored. These ions form a flow of initially[12] trapped ions towards the clearing electrode ($\dot{N}_{\mathrm{ion,hollow}}$ with losses $\Delta\dot{N}_{\mathrm{ion,hollow}}$). If the initial velocity or the potential energy of certain ions is high enough, they may be drawn towards the electrode without being trapped within the potential hollow first. They form a "leak" flow of untrapped ions $\dot{N}_{\mathrm{ion,free}}$. On their way towards the clearing electrodes, a part of this flow may cross the beam center where the trapped ion population is located which is accompanied by losses $\Delta\dot{N}_{\mathrm{ion,free}}$.

Consequently, the two flows of trapped and untrapped ions experience losses on their way to the electrode which scales with the number of ions within the potential hollow and thus the static neutralization. Following this train of thought, $\mathscr{F}$ is parameterized as

$$\mathscr{F} = \frac{\dot{N}_{\mathrm{ion,free}} - \Delta\dot{N}_{\mathrm{ion,free}} + \dot{N}_{\mathrm{ion,hollow}} - \Delta\dot{N}_{\mathrm{ion,hollow}}}{\dot{N}_{\mathrm{ion}}} \,. \tag{6.3}$$

$\dot{N}_{\mathrm{ion}}$ is the sum of both flows without losses.

In the following, the abbreviations and relations

$$\mathcal{F} = \frac{\dot{N}_{\mathrm{ion,free}}}{\dot{N}_{\mathrm{ion}}} \,, \qquad \mathcal{H} = \frac{\dot{N}_{\mathrm{ion,hollow}}}{\dot{N}_{\mathrm{ion}}} \qquad \text{and} \quad \mathcal{F} + \mathcal{H} = 1 \tag{6.4}$$

are used. The fraction of untrapped $\mathcal{F}$ and initially trapped ions $\mathcal{H}$ is dependent on the clearing voltage.

The different flows are illustrated in figure 6.10. A part of $\mathcal{F}$ may be produced close to the electrode at (a) and thus reach it without experiencing many space charge interactions with other ions and related losses. Another part of $\mathcal{F}$ is produced on the opposite side of the potential at (b), energetically able to reach the electrode after passing the trapped ion cloud in the vicinity of the beam center. Here, the ions' mutual space charge interaction may lead to losses $\Delta\mathcal{F}$. In the potential hollow a static neutralization of $\hat{\eta}_{\mathrm{stat}}$ is present and enables an escape of the ions as the flow $\mathcal{H}$. This flow, coming from the depth of the potential hollow at (c) to the electrode, also experience losses $\Delta\mathcal{H}$.

The loss flows $\Delta\mathcal{F}$ and $\Delta\mathcal{H}$ are assumed to increase linearly with the static neutralization. They can be expressed as

$$\Delta\mathcal{F} = l_{\mathrm{free}}\hat{\eta}_{\mathrm{stat}}\mathcal{F} \qquad \text{and} \qquad \Delta\mathcal{H} = l_{\mathrm{hollow}}\hat{\eta}_{\mathrm{stat}}\mathcal{H} \,. \tag{6.5}$$

[11] $\mathcal{P}(E, I)$ is estimated by the pressure model of the storage ring, which has been developed in the course of this work (compare section 3.2).

[12] The term "initially" is used because these ions are trapped when they have been generated. Due to beam heating or energy transfers from other ions, they eventually escape their confinement in direction of the clearing electrodes or the beam pipe.

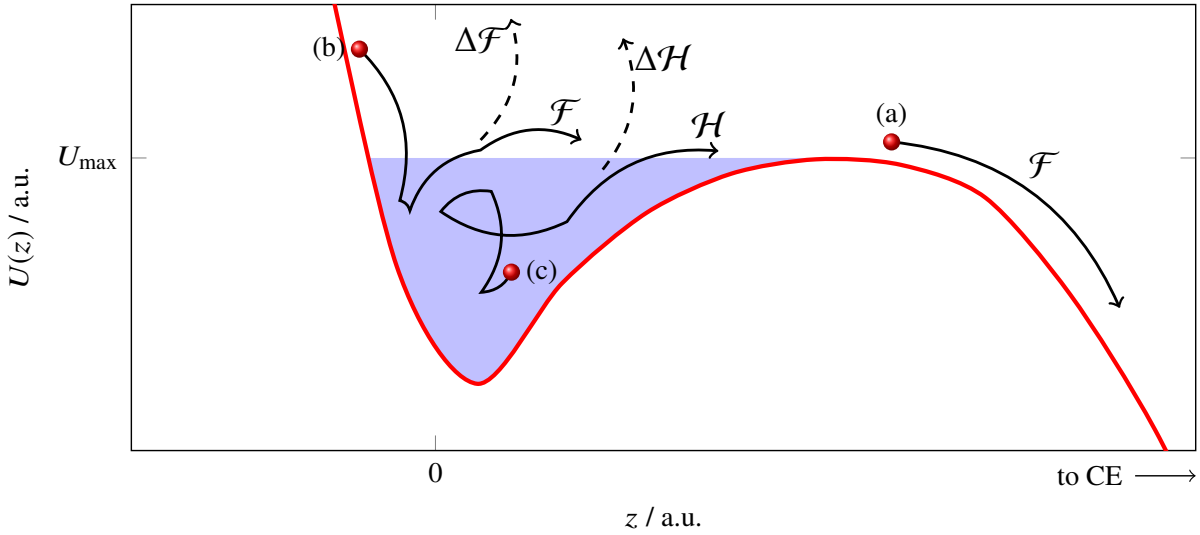

Figure 6.10: Illustration of the different ion flows of the lossy flow model in the vicinity of a clearing electrode (CE). Shown in red is the beam potential superimposed by the potential of the electrode forming a local potential hollow. Ions, produced in vicinity of the beam center at $z = 0\,\mathrm{mm}$, accumulate to a local static neutralization level and thus enable an escape of additional ions out of the potential hollow. Ions, which are produced at (a), are drawn towards the electrode and are neutralized. They form a part of the flow $\mathcal{F}$. An additional contribution comes from ions, produced at (b), which pass the ion cloud in the beam center on their way to the electrode. Here, ion-ion space charge interactions with statistical energy transfers between the ions lead to losses $\Delta\mathcal{F}$ of the flow. Ions which are produced close to the beam center at (c), also experience ion-ion space charge interactions, but may be able to escape the potential hollow, forming the other part of $\mathcal{H}$. Here, also ion-ion space charge interaction lead to losses $\Delta\mathcal{H}$.

Here, $l_{\mathrm{free}} \geq 0$ is the fraction of untrapped ions which experience losses on their way to the clearing electrode. $l_{\mathrm{hollow}} \geq 0$ is the fraction of initially trapped ions which experience losses. In general, l_{free} should be smaller than l_{hollow}, as $\mathcal{F}$ experiences few interactions with other ions than $\mathcal{H}$.

By inserting equations (6.4) and (6.5) into equation (6.3) and expressing every flow with $\mathcal{F}$, an expression for $\mathscr{F}$ is derived with

$$\mathscr{F} = 1 - l_{\mathrm{hollow}}\hat{\eta}_{\mathrm{stat}} + \mathcal{F}\hat{\eta}_{\mathrm{stat}}\left(l_{\mathrm{hollow}} - l_{\mathrm{free}}\right) . \tag{6.6}$$

Here, $\hat{\eta}_{\mathrm{stat}}$ and $\mathcal{F}$ are dependent on the clearing voltage.

In the following, l_{hollow} is set to one because all ions, being produced within the hollow (flow $\mathcal{H}$) will experience space charge interactions with other ions. l_{free} is set to 50 %, as half of the flow $\mathcal{F}$ is produced opposite of the clearing electrode and consequently also experiences space charge interactions with the ions, close to the beam, whereas the other half, directly facing the electrode, is assumed to experience no losses. However, for a more detailed discussion about the properties of $\mathscr{F}$, see appendix A.21.1.

Thus, the transversal transmission function equation (6.6) can be approximated by

$$\mathscr{F} = 1 - \hat{\eta}_{\mathrm{stat}} + \frac{1}{2}\mathcal{F}\hat{\eta}_{\mathrm{stat}} . \tag{6.7}$$

If $\mathscr{F}$ can be extracted out of the measured characteristic curve, a validation of the static neutralization approach is in principle possible. Here, the measured transversal transmission function is compared with the predicted one. To obtain a prediction of $\mathscr{F}_{\mathrm{theo}}$, $\hat{\eta}_{\mathrm{stat}}$ and $\mathcal{F}$ have to be determined numerically for a

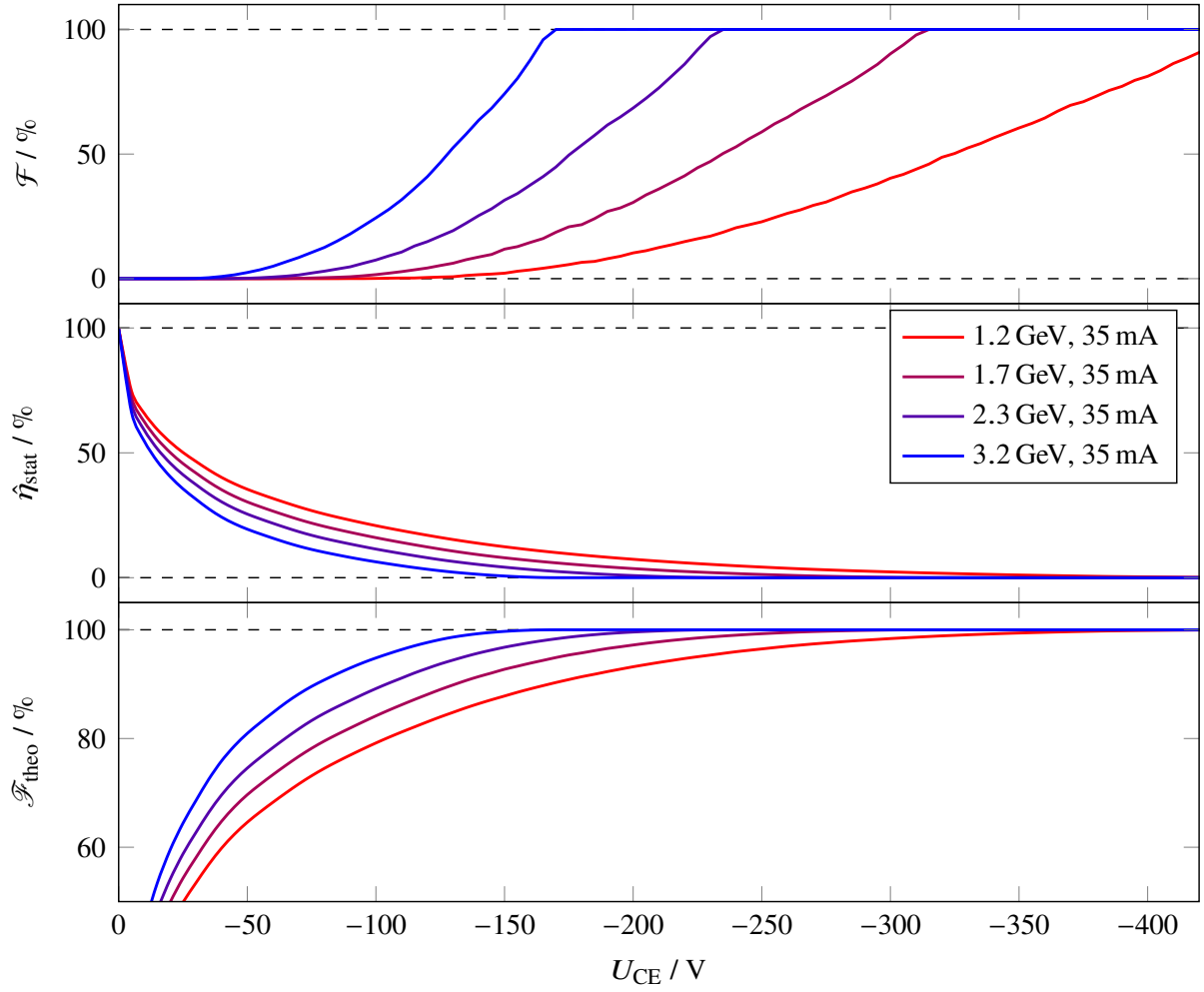

Figure 6.11: Calculated variation of $\mathcal{F}$, $\hat{\eta}_{\mathrm{stat}}$ and the resulting $\mathscr{F}_{\mathrm{theo}}$ for different clearing voltages and beam energies. $\mathscr{F}_{\mathrm{theo}}$ is calculated using equation (6.7) and is equal to 0 % at 0 V.

given potential. The tool TRANSVERSION (compare section 5.1.3) has been utilized to determine their evolution with U_{CE} in the storage ring for a certain beam energy and current. For more information, see appendix A.21.2.

Figure 6.11 exemplarily shows the results of these simulations. Here, $\mathscr{F}_{\mathrm{theo}}$ is determined using equation (6.7) on basis of a simulation of $\mathcal{F}$ and $\hat{\eta}_{\mathrm{stat}}$ for the storage ring at a beam current 35 mA and at different beam energies. The beam potential is deeper for lower beam energies than for higher ones as the beam size increases with energy. Consequently, higher clearing voltages are required at 1.2 GeV to reduce the static neutralization to zero than at 3.2 GeV. The potential depth also influences the flow $\mathcal{F}$. For 3.2 GeV, $\mathcal{F}$ is already approximately 5 % at −50 V whereas a clearing voltage of −150 V is required to rise $\mathcal{F}$ to the same level at 1.2 GeV. Consequently, the predicted transversal transmission function $\mathscr{F}_{\mathrm{theo}}$ is closer to one at a given clearing voltage for higher beam energies than for lower ones. For 3.2 GeV, it reaches a value of one at approximately −150 V whereas a clearing voltage of −350 V is required to do so for 1.2 GeV.

Measurement Procedure and Analysis

To verify the static neutralization approach from which the theoretical minimal threshold voltage $U_{\mathrm{CE,thres}}$ for the clearing electrodes is derived (compare figure 6.8), a comparison between the measured and predicted transversal transmission function $\mathscr{F}$ is necessary. Experimentally, the threshold voltage is the minimal absolute clearing voltage for which the measured $\mathscr{F}$ shows a constant value of one.

To determine the transversal transmission function $\mathcal{F}$, the clearing electrode current I_{CE} of all electrodes is measured at different clearing voltages U_{CE} when the accelerator is operated at a certain beam energy and current in the storage mode. In advance, the leakage current $I_{\mathrm{CE,leak}}$ of the clearing electrode network is determined for the considered clearing voltage range.

The relevant part of the measurements is the low voltage regime with clearing voltages of 0 to −500 V. The measurement has been conducted as fast as possible to minimize the change in beam current due to occurring beam losses. Here, beam current variations during the measurement alter the depth of the beam potential and consequently $\mathscr{F}$. To minimize the variation of $\mathscr{F}$ and also sample the characteristic curve in suitable detail, an adaptive step size of the clearing voltage has been chosen. Within 0 to −100 V, a small step size of 2.5 or 5 V is used. From −100 to −350 V, the step size has been adjusted to 17.5 V and finally a step size of 150 V has been used.

The absolute clearing voltage is increased stepwise from 0 V to 1 500 V. After a step in the clearing voltage, it is waited for a certain time, typically 5 s, before reading out the current. Within this time, balancing currents due to the voltage increment have subsided and do not distort the measured current. In single cases where the balancing currents did alter the measured current I_{CE}, identifiable by sporadic peaks in the measured current I_{CE} which are a factor of 10 to 100 higher than normal, the measured current is discarded.

In the subsequent analysis of the measured characteristic curve, the measured I_{CE} is corrected by the clearing electrode network's leak current and is normalized to the measured beam current to obtain the ion transmission coefficient $\mathcal{I}_{\mathrm{CE}}$. Using the pressure model $\mathcal{P}(E, I)$ (compare section 3.2), $\mathcal{I}_{\mathrm{CE}}$ is further normalized to a pressure of 10^{-8} mbar. The no-load pressure is set to $0.5 \cdot 10^{-8}$ mbar. Since the relative beam current loss during one measurement of the characteristic curve has been 17 %[13] the pressure is almost constant within one measurement and only offsets the pressure-normalized $\mathcal{I}_{\mathrm{CE}}$.

In the $\mathscr{L}$ regime of the characteristic curve, typically at $|U_{\mathrm{CE}}| \geq 500\,\mathrm{V}$ where $\mathcal{I}_{\mathrm{CE}}$ solely increases linearly, a function with constant slope and offset is approximated which represents $\tilde{K} \cdot \mathscr{L}$ in equation (6.2). By dividing the pressure-normalized $\mathcal{I}_{\mathrm{CE}}$ by this function, $\mathscr{F}$ can be extracted from the measurements. It then ranges from 0 to 1.

Beam Current Dependency

To verify the beam current dependency of the predicted transversal transmission function $\mathscr{F}_{\mathrm{theo}}$, the characteristic curve of the clearing electrode network is measured for different beam currents at a fixed beam energy.

Figure 6.12 shows the predicted and measured transmission function at a beam energy of 1.2 GeV for three different beam currents in the relevant clearing voltage region $|U_{\mathrm{CE}}| \leq 500\,\mathrm{V}$. At 0 V, the current for all measurements is zero, also resulting in $\mathscr{F} = 0$. For an increased clearing voltage, the measured $\mathscr{F}$ approaches one. At different beam currents, $\mathscr{F}$ reaches the value of one at different clearing voltages. Thus, the threshold voltage is a function of the beam current. For an average beam current of 14.9 mA,

[13] Note, that this value represents an extreme value during a measurement at 1.2 GeV and initially 46.4 mA where the beam lifetime was low due to a high pressure in the vacuum system. Additionally, the relative beam loss in the relevant low voltage region ≤ −500 V has been half of the stated value.

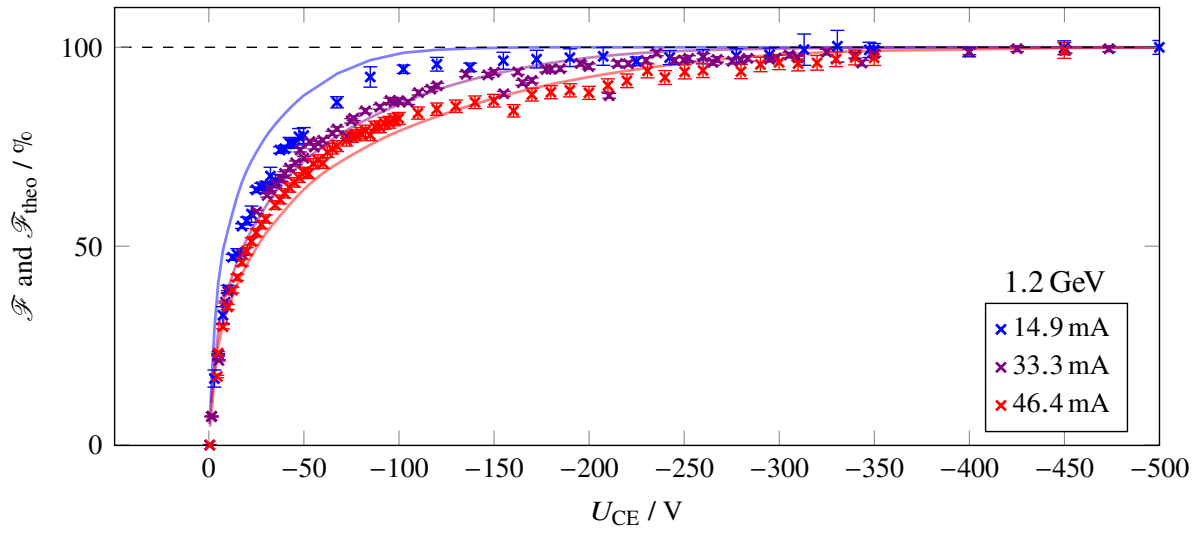

Figure 6.12: Transversal transmission function $\mathscr{F}$ for different beam currents at a beam energy of 1.2 GeV. The measured transmission function is shown for three different beam currents.

	$U_{\text{CE,thres}}$ / V	
I / mA	theoretical	measured
14.9	−155	≈ −200
33.3	−345	≈ −320
46.4	−450	≈ −350 to −450

Table 6.1: Theoretical and measured threshold voltages $U_{\text{CE,thres}}$ for the ion clearing electrodes at a beam energy of 1.2 GeV.

$\mathscr{F}$ is overall higher in comparison to the measurements at beam currents of 33.3 and 46.4 mA. When $\mathscr{F}$ reaches a value comparably to one within its 1σ error region, the corresponding voltage is equal to the measured threshold voltage. The predicted $\mathscr{F}_{\text{theo}}$ for the three measurements are shown in figure 6.12 as lines in colors, corresponding to the measurements. In table 6.1, the theoretical and measured threshold voltages are compared. Qualitatively, the form of the measured $\mathscr{F}$ and predicted $\mathscr{F}_{\text{theo}}$ are in congruence. For the measurement at 46.4 mA, $\mathscr{F}$ first consistently lies above the prediction for voltages up to −150 V and then below it. Here, the beam loss due to the beam's finite life time amounts to 8 mA (≈ 17 % of the initial current, 2.5 mA for the measurements at 14.9 mA and 0.4 mA at 33.3 mA) in the shown voltage region, resulting in a distortion of $\mathscr{F}$. The reduced χ^2 [14] is equal to 5.34, implying that the prediction is a suitable approximation to the measurements with underrated measurement errors. At 14.9 mA, $\mathscr{F}$ lies below the prediction, resulting in a difference between predicted to measured threshold voltage of approximately 45 V (25 V for 33.3 mA and congruent for 46.4 mA). However, the reduced χ^2 of prediction and measurement is equal to 41.25. At 33.3 mA, the reduced χ^2 is equal to 1.6, indicating that $\mathscr{F}_{\text{theo}}$ closely follows $\mathscr{F}$.

[14] The reduced χ^2 is used to characterize the goodness of a hypothetical function to underlying measurement data. It is the χ^2 test, a statistical hypothesis test, divided by the degrees of freedom, i.e. the number of data points. If the reduced χ^2 is (much) greater than one, the function does not describe the measured data suitably. A reduced χ^2 below one indicates an overestimated measurement error. If the reduced χ^2 is equal to one, the matching of the hypothesis and the data is in accordance with respect to the data's measurement error.

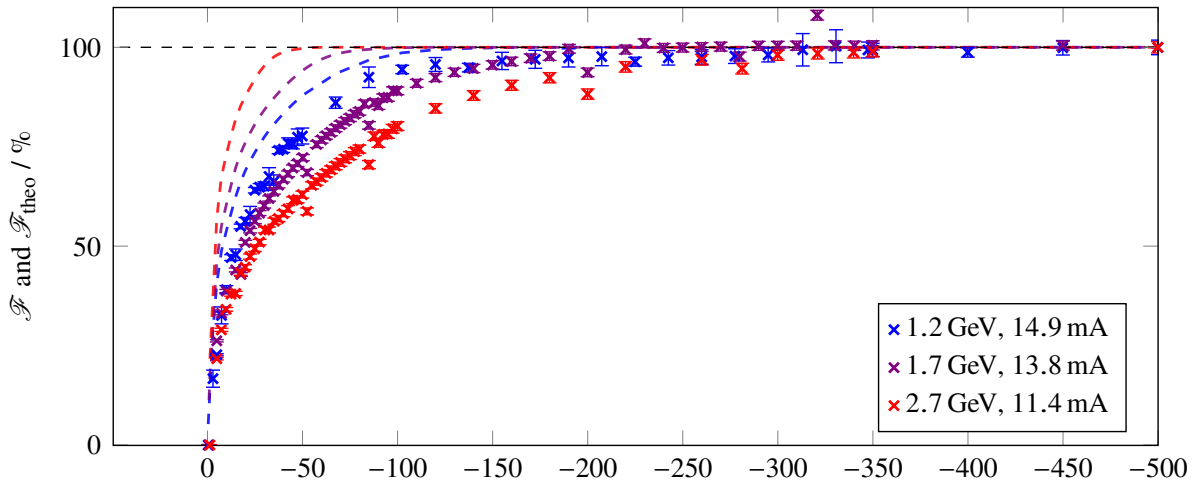

Figure 6.13: Transversal transmission function $\mathscr{F}$ for different beam energies. The graph shows the measured transmission function at three different beam energies at similar beam currents. The predicted transmission functions $\mathscr{F}_{\text{theo}}$ for corresponding beam energies and currents are shown as dashed lines in associated colors.

In general, the current dependency of the predicted transversal transmission function could be verified at a beam energy of 1.2 GeV, although the measurement error seems to be underrated. While the systematical error due to beam loss during the measurement prevents a closer investigations of $\mathcal{F}$ (with the yet unknown parameter l_{free}, compare equation (6.7)), the measurement is precise enough to verify the static neutralization approach and the lossy flow model at 1.2 GeV. Consequently, the predicted threshold voltages, shown in figure 6.8, which are derived from this approach could be verified experimentally at 1.2 GeV.

The same current dependency of the measured transversal transmission function is also visible at beam energies of 2.3 and 2.7 GeV, which are shown in figures C.18 and C.19 in the appendix. Here, $\mathscr{F}$ is consistently shifted closer to one for lower beam currents.

Energy Dependency

The static neutralization approach, on which the lossy flow model is based, is a simplification of the ion dynamic, as has already been discussed in section 4.2.2. If the motion of ions is influenced significantly by other fields than the beam's field, e.g. by magnetic fields, the static approach is not valid anymore. In the following, a case is discussed where the approach breaks down.

Figure 6.13 shows the theoretical and measured transversal transmission function at different beam energies and similar beam currents. All measurements show a similar behavior with U_{CE}, where $\mathscr{F}$ is equal to zero at $U_{\text{CE}} = 0\,\text{V}$ and comparable to one at $U_{\text{CE}} \leq -350\,\text{V}$. The predicted $\mathscr{F}_{\text{theo}}$ are shown as dashed lines with colors which correspond to their measured counterparts.

At 1.2 GeV, the predicted $\mathscr{F}_{\text{theo}}$ is overall higher than the measured $\mathscr{F}$, although it could be argued that the prediction is in the measurement's 2σ error region. For beam energies of 1.7 and 2.7 GeV, a deviation between prediction and measurement becomes clearer: The shape of $\mathscr{F}$, concerning its height, is reversed with beam energy in reference to the predicted $\mathscr{F}_{\text{theo}}$. On one hand, $\mathscr{F}_{\text{theo}}$ shows a threshold voltage of −155, −100 and −60 V for beam energies of 1.2, 1.7 and 2.7 GeV, respectively. On the other hand, the measured $\mathscr{F}$ show threshold voltages of −200, −190 to −220 and −320 V, which again shows the opposite energy dependence than predicted. Consequently, the reduced χ^2 test results in 41.25, 508.9 and 1 529 for 1.2, 1.7 and 2.7 GeV, respectively.

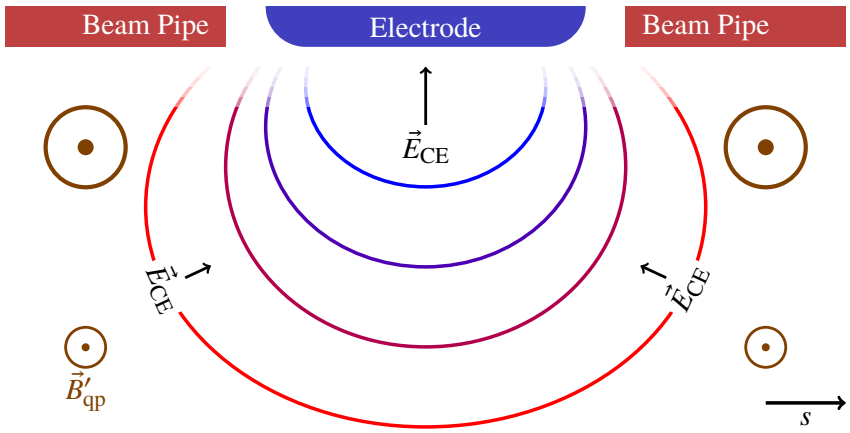

Figure 6.14: Configuration of the electric ($\vec{E}_{CE}$) and magnetic field ($\vec{B}'_{qp}$) at the clearing electrodes in longitudinal direction. The lines indicate equipotential lines of the electric potential between grounded beam pipe and high voltage biased electrode.

In consequence, $\mathscr{F}$ shows an inverse energy dependence in comparison to $\mathscr{F}_{theo}$. Following the interpretation of $\mathscr{F}$, the measurements would indicate that ions are more bound to the electron beam at higher beam energies than at lower energies. Therefore, a higher voltage would be required to draw all trapped ions within the beam potential towards the electrodes. However, the beam potential is less deep at higher beam energies which indicates that there exist circumstances, not considered by the theoretical approach.

Additional investigations of possible error sources, such as the measurements' reproducibility and beam loss, are discussed in appendix A.21.3. However, by including all these error sources, the predicted threshold voltage for e.g. 2.7 GeV is only shifted from −60 to −97.5 V, which is still far away from the measured threshold of −320 V. Also the inverse energy dependence of $\mathscr{F}$ cannot be explained by these error sources.

Effect of the Quadrupole's Fringe Field on the Measured Ion Current

Yet, the observation can be explained qualitatively: In the theoretical approach of $\mathscr{F}_{theo}$, any perturbations of the ion trajectories by magnetic fields are not included. In the storage ring, the clearing electrodes are positioned at a distance of approximately 6 cm from the end of the iron yokes of the quadrupole magnets. Assuming a magnetic fringe field whose field strength decays with the shape of a Gaussian bell curve for an increasing distance from the yokes, the field strength of the main field (54.78 mT for $Q_z = 4.431$ with $k_{QD} = 0.579\,\mathrm{m}^{-2}$) would decrease, leading to a vanishing field ($\approx 0.55 \cdot 10^{-12}$ mT for $k_{QD} = 0.579\,\mathrm{m}^{-2}$) at the electrodes. Using a Hall probe[15], the magnetic fringe field of the quadrupole at the position of an electrode has been measured. The measurements show a magnetic field of (10 ± 4) mT at the position of the electrode. This indicates that the quadrupoles' fringe fields decrease slower with distance than expected and are only reduced to a factor of approximately 1/5th. Thus, the fringe field shows a field strength which is high enough to still influence the ions' motion at the electrodes.

Figure 6.14 shows the configuration of electric and magnetic fields at the clearing electrodes. The fringe field $\vec{B}'_{qp}$ of the quadrupole magnet is orientated transversely whereas the electric field $\vec{E}_{CE}$ points

[15] A Hall probe is a device for the determination of the field strength of a static magnetic field by measuring the emerging voltage from the Hall effect.

towards the electrode, which is mounted on top of the beam pipe. Due to the quadrupole's magnetic field, the ions do not follow $\vec{E}_{\mathrm{CE}}$ directly towards the electrode. Instead they experience a cross-field drift (compare section 2.4.2), inflicted by the transversal magnetic field, along the equipotential lines of the electric potential. During this drift, the ions gyrate in the longitudinal plane, periodically changing the distance to the electrode. The gyro radius and the drift velocity decreases for higher magnetic field strength and increases with the clearing voltage (compare equations (2.49) and (2.51)). Following the equipotential lines, ions may impinge on the beam pipe instead of being neutralized at the electrode. The trajectories of the ions in this field configuration are complex as both electric and magnetic field along with the resulting cross-drift velocity and gyro radii are position dependent. However, if their gyro radius close to the electrode-beampipe gap is much smaller than the gap, the ions may not reach the electrode. In this case no ion current can be measured.

For higher beam energies, the field strength of the quadrupoles is increased to keep a constant tune. This leads to a reduction of the ions' gyro radii and can only be compensated by an increased clearing voltage, if the ions should reach the electrode. Thus, to measure the same ion current, a higher clearing voltage is needed to draw all ions towards the electrode, when the beam energy is increased, which explains the observed behavior in figure 6.13.

Corrections to $U_{\mathrm{CE,thres}}$

Although the transversal transmission function $\mathscr{F}$, extracted from the measured characteristic curves of the clearing electrode network during operation of the storage ring, are in good agreement with the theoretical prediction $\mathscr{F}_{\mathrm{theo}}$ for a beam energy of 1.2 GeV, significant distinctions to the prediction occur for higher beam energies. These distinctions results from the fringe fields of quadrupoles, whose influence of the measured ion current is not included into theory.

The estimated threshold voltages $U_{\mathrm{CE,thres}}$ (compare figure 6.8) for a beam energy of 1.2 GeV could be verified by the measurements. For larger beam energies, it is advised to increase the minimal clearing voltage in reference to the estimated $U_{\mathrm{CE,thres}}$ by a certain factor, which has been obtained by comparing the theoretical with the measured threshold voltages. The factor should be at least 2.2 for a beam energy of 1.7 GeV and a factor of 5.3 for 2.7 GeV to overcome the perturbations by the quadrupoles' magnetic field.

In practice, the stored beam current in the storage ring rarely exceeds 60 mA at beam energies above 2 GeV. Increasing the estimated threshold voltage at 3.2 GeV by a factor of 6, yields a minimal clearing voltage of −1 500 V for prevention of additional local static neutralization in front of the clearing electrodes. The high voltage power supply is capable of providing a maximal clearing voltage of −2 000 V. Thus, an accumulation of ions in front of the electrodes and the resulting additional static neutralization is preventable for almost every practicable combination of beam energy and current in the storage ring, if the clearing voltage is set to approximately −1 500 V. An exception is the operation at a low beam energy of 1.2 GeV and a stored beam current of more than 150 mA. Here, the application of a clearing voltage of −2 000 V is advised.

6.2 Filling Gaps

In this section, ion clearing by using filling gaps will be discussed. Here, the homogeneous filling pattern of the beam is partly interrupted by a series of bunches which show no or nearly no bunch current. In these so called *filling gaps*, the accumulated ion population does not experience the COULOMB force of the electron beam, focusing them towards the beam center, and starts to disperse. If the filling gap is long enough, the amplitude of individual ions may increase with every passage of the filling gap, eventually removing them from the beam.

6.2.1 Principle of Ion Clearing by Application of a Filling Gap

The critical mass A_{crit}, indicating the lowest mass-to-charge ratio with which stable trajectories of ions are occurring, is always well below 1 u in the storage ring. Thus, when operated with a homogeneous filling pattern and within its typical beam energy and current regime, all relevant ion species show stable trajectories and are not cleared intrinsically (see section 4.1). With a homogeneous filling pattern, the time between two bunches in which the focusing COULOMB force of the bunches does not act on the ions is too short to enable the drift of ions outwards. When the following bunch's space charge draws the ions back to the beam center, their small drift distance is reversed. Thus, no amplitude increment of the ions occurs on larger time scales.

An inhomogeneous filling pattern is used to artificially destabilize the trajectories of individual ion species. Here, not every electron bunch shows the same or similar bunch current. A series of bunches shows reduced or negligible bunch current and forms a filling gap, which is mainly characterized by its length. For example, a filling gap of length 13 shows a series of 13 of empty buckets. In one revolution, ions may drift far enough away from the beam center, to experience a reduced reversing force of the beam when the filling gap has passed. In the course of several beam revolutions, the amplitude of these under-focused ions increases further and they are eventually neutralized when hitting the surface of the beam pipe.

The process of the amplitude growth is non-trivial and depends on several factors. One key parameter is the mass-to-charge ratio A/Z of the particular ion species. It determines the bounce frequency $\nu_{x,z}^{\mathrm{ion}}$ (compare equation (2.46) in section 2.4.1) with which an ion oscillates transversely within the beam potential. A/Z also determines how significantly the ion's trajectory is altered when encountering a bunch gap. Of course, also the shape of the transversal beam potential and how it changes in time is of importance. Hence, also dependencies on the beam energy and current along with the filling pattern of the accelerator exist. The first two determine the form and depth of the beam potential, the latter its temporal shape.

In the following, a numerical approach will be discussed which allows for an estimation of the clearing rate of an ion population when exposed to a certain filling pattern.

6.2.2 Determination of the Clearing Rate due to a Filling Gap using FILLINGGAPSIM

In [Ste95, section 5.1], the stability of individual ion species in the storage ring has already been studied using the *stability matrix formalism* of [BB80]. Here, the time structure of the electron beam and thus its time dependent, attractive space charge force, which acts on an ion, is expressed by transfer matrices (see e.g. [Wil00, section 3.4]). The passage of a bunch is represented by the transfer matrix of a focusing lens whereas in-between two consecutive bunches or the passage of an empty bunch, a drift transfer matrix is used. By multiplication of these matrices, the time structure of the bunch train can be expressed in a single matrix. The stability of the individual ion species, when exposed to a certain filling pattern,

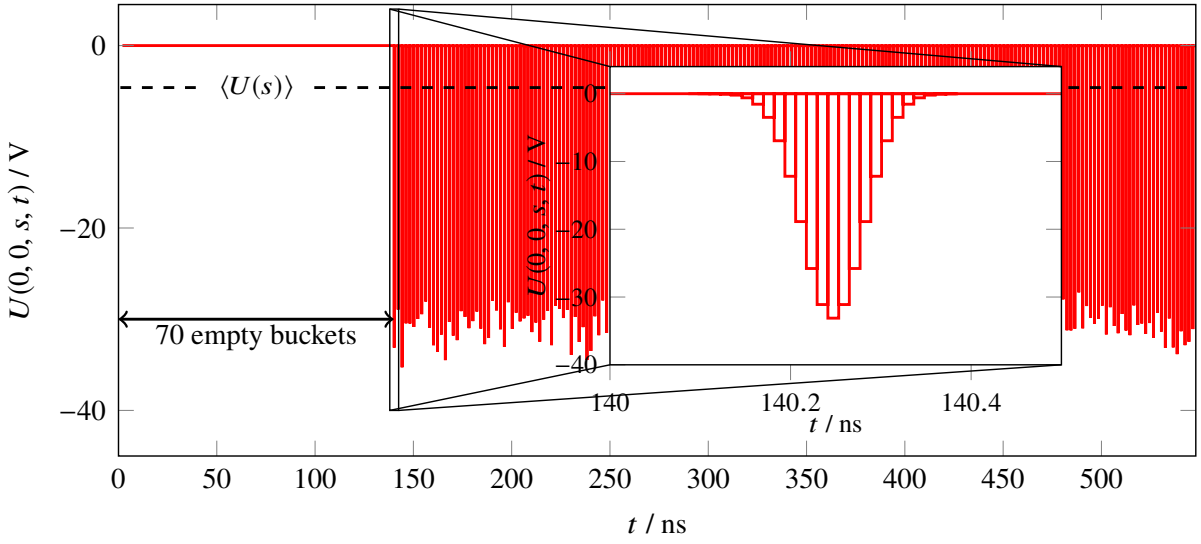

Figure 6.15: Time dependent beam potential in the beam center at $x, z = 0$ mm for a filling gap with a length of 70 buckets. The filled bunches are set to have a bunch current, which varies around 5 % for each bunch. To visualize the Gaussian bunch shape, it is zoomed in to the beginning of the bunch train. The beam energy is 1.7 GeV and the current 25.5 mA. The average beam potential $\langle U(s)\rangle$ is equal to approximately −4.6 V.

can be determined by analyzing the property of the bunch train's transfer matrix using the Floquet theory. Congruent stability analyses have been conducted in the course of this work and can be found in appendix A.12 along with a detailed explanation of the stability matrix formalism.

However, the stability of a particular ion species is not a sufficient criterion for evaluation of the clearing efficiency of a filling pattern: Although a particular ion species may show instable trajectories at a certain bunch current and filling pattern, its production obviously does not stop. If the amplitude of an instable ion species only grows slowly in reference to the timescale of its production rate, the ion's space charge may still have influence on the electron beam and may significantly contribute to the neutralization. Thus, the ion's stability only gives indications about whether or not the filling pattern affects the particular ion species. Instead, the species' clearing rate determines its individual contribution to the neutralization and therefore is a more suitable criterion for a filling pattern's clearing efficiency.

With FillingGapSim developed in the course of this work, a numerical determination of the local clearing rate of individual ion species when exposed to a certain filling pattern is made possible[16]. Both, the stability matrix formalism and FillingGapSim, predict a similar stability of individual ion species, as discussed in appendix A.12.3.

FillingGapSim

The tool is implemented in Matlab. Here, only a short description of the tools functionality is given. For more information, see appendix B.2.7.

In this tool, the horizontal or vertical motion of a certain number of individual ions at a fixed longitudinal position in the accelerator is tracked, when exposed to a repetitive time dependent beam potential.

[16] Additionally, the equilibrium density distribution of an ion population, which is exposed to a filling pattern, can be obtained.

Time Dependent Beam Potential The beam potential is explicitly time dependent and is dependent on the time structure of the filling pattern in the accelerator: The bunch train repetitively passes the ion while the tracking proceeds. In the transversal plane, the bunches show a GAUSSian charge distribution and the beam potential $\langle U(x, z, s)\rangle$ is calculated for a confined region in the horizontal or vertical plane via equation (2.42). Along the bunch train, the beam potential depth is modulated, as shown in figure 6.15. It is zero, if no bunch is present at the ion's position and maximal in the center of the bunch. Since the individual bunches have a GAUSSian charge distribution in the longitudinal plane, the beam potential, which is experienced by an ion, has a shape as

$$U(x, z, s, t) = U_0(x, z, s) \exp\left(-\frac{t^2}{2t_{\text{bunch}}^2}\right)$$

in the course of time t with $t_{\text{bunch}} = \sigma_s/(\beta c)$. Between the bunches and in empty buckets $U(x, z, s, t)$ is zero. $U_0(x, z, s)$ is the beam potential in the center of the bunch at $t = 0\,\text{s}$. It can be determined from the time average beam potential $\langle U(x, z, s)\rangle$ using the *bunching factor*

$$\mathcal{B} = \frac{U_0(x, z, s)}{\langle U(x, z, s)\rangle} = \frac{\beta c}{\sqrt{2\pi}} \cdot \frac{t_{\text{rf}}}{\sigma_s} > 1\,.$$

For the deviation of the bunching factor, see appendix A.18.

The simulated filling pattern can be chosen arbitrary with individual bunch currents for each bunch. The beam potential is precomputed for one revolution with a time resolution of down to $t_{\text{bunch}}/4$. Here, the bunches' longitudinal GAUSSian shape is considered within $\pm 3\sigma_s$ around the bunch center. For the rest, the potential is assumed to be zero.

Tracking The tool consecutively tracks the horizontal or vertical trajectories of typically 5 000 individual ions of different species for a certain time frame as they are exposed to $U(x, z, s, t)$ using the EULER-NEWTON method with a non-equidistant[17] time incrementation. Each ion is produced on basis of probability functions within the bunch train. Which species the ion belongs to is assigned by the production probability of each species. It has a random horizontal or vertical start position and an initial velocity, both based on corresponding probability distributions[18].

Each ion's trajectory is simulated separately for a time frame of typically 110 µs, which corresponds to approximately 200 passages of the bunch train.

Post-Tracking Analysis The time dependent beam potential is precomputed within a domain of typically $\pm 10\sigma_{x,z}$. If the ion trajectory is confined within this domain, its movement is considered as stable. Figure 6.16 shows four exemplaric trajectories of different ion species, when exposed to approximately 100 passages of a bunch train which shows a filling gap of 100 buckets at a beam energy of 1.2 GeV and a current of 35 mA. Within the observed time frame, the oscillation amplitude of N_2^+ and CO_2^+ ions do not increase, indicating the stability of these ions. The amplitude of H_2^+ and H_2O^+ ions in contrast increases with time. When the domain is transcended, the tracking of each ion's motion is stopped and the crossing time is recorded. This time is used for the determination of the clearing rate.

[17] In time frames where $U(x, z, s, t)$ does not change, the time increment Δt is chosen as coarse as possible to calculate the ion's drift within a single step. For example, Δt is equal to t_{rf} in an empty bucket. In bunches, where the beam potential changes frequently, Δt is reduced significantly.

[18] Here, only the ion production map of impact ionization by the electron beam is included.

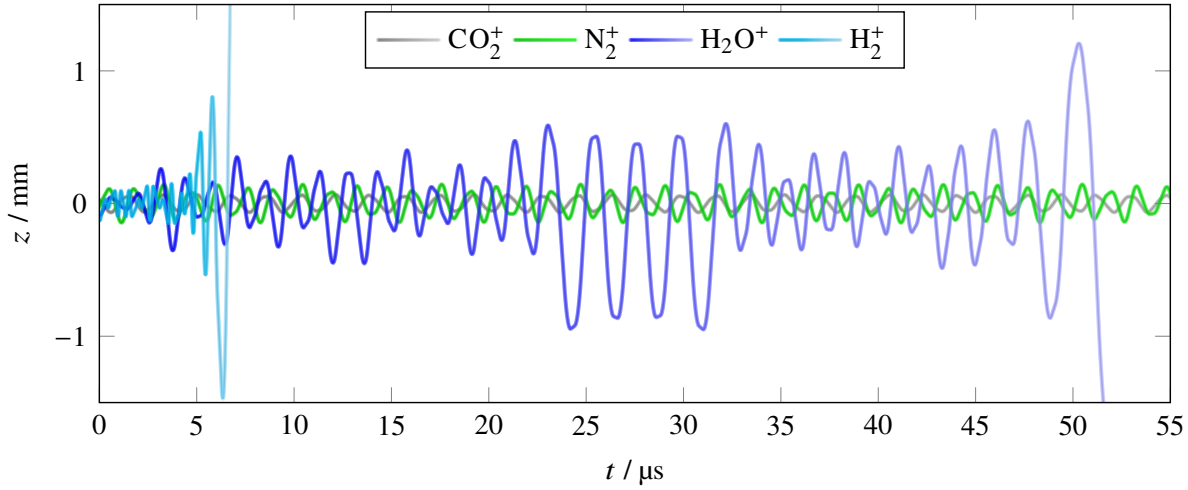

Figure 6.16: Vertical trajectories of four different ion species when exposed to a filling gap with a length of 100 buckets, simulated by FillingGapSim. In this scenario, the beam energy and current are set to 1.2 GeV and 35 mA (200 µA per bunch).

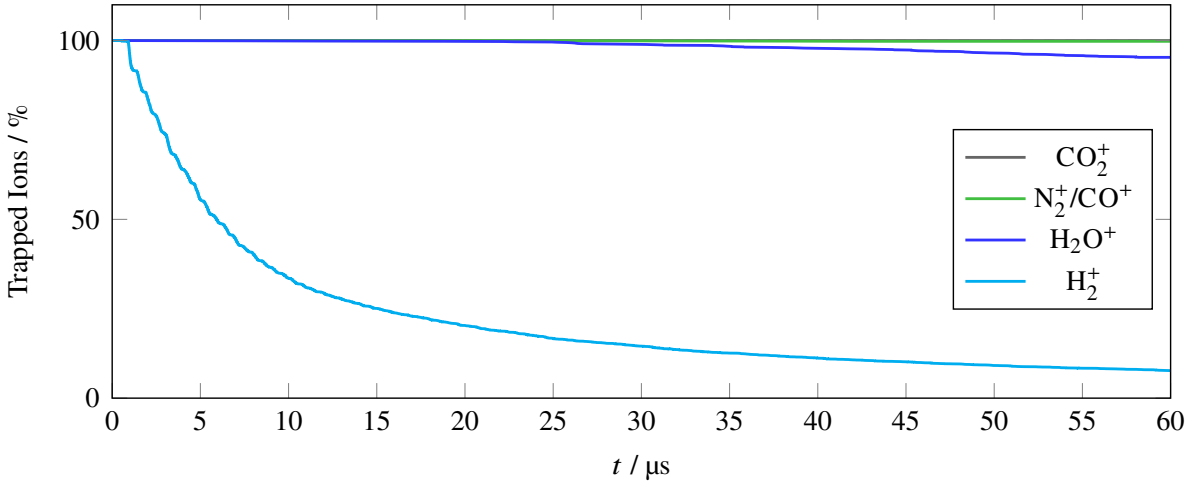

Figure 6.17: Simulated reduction of the trapped ion population with time in the vertical plane. Here, the population is exposed to a filling gap of a length of 110 buckets at a beam energy of 1.2 GeV and a current of 20.5 mA (125 µA per bunch).

Extracting the Clearing Rate In case no ions are produced, the clearing rate of a certain ion species, when exposed to a particular filling pattern, can be extracted from the exponential decay of the number of its trapped individuals (compare equation (2.9) with $R_p = 0\,s^{-1}$).

The time evolution of each species' population within the domain is determined in a post-processing step. An exemplaric evolution of the ion population is shown in figure 6.17. Here, a population of 10 000 ions is exposed to a filling gap of 110 buckets at a beam energy of 1.2 GeV and a beam current of 20.5 mA. The population of N_2^+/CO^+ and CO_2^+ show stable trajectories within the beam potential. The population of N_2^+/CO^+ is only reduced by 2 ‰ within the simulated time frame. H_2O^+ ions are slightly unstable. Its population is reduced by approximately 5 %. In contrast, 50 % of the trapped H_2^+ population is removed from the beam within 5 µs. After a time t_d of approximately 1.5 µs, the fraction of trapped H_2^+ decays

"exponentially"[19]. Here, t_d is the propagation time which the fastest ions need to reach the edge of the domain in the simulation.

By adapting the function

$$N_{\mathrm{ion},i}(t) = N_{0,\mathrm{ion},i} \exp\left(-r_{\mathrm{c},i}\left(t - t_\mathrm{d}\right)\right) + N_{\mathrm{stab},i} \tag{6.8}$$

to the population, the clearing rate[20] $r_{\mathrm{c},i}$ of an ion species i can be extracted. The function also features a constant term $N_{\mathrm{stab},i}$ because in some cases not necessarily *all* ions of a species are either stable or unstable. There exist stable regions within the initial phase space of the ions for certain filling patterns. Thus, the population of trapped ions decays "exponentially" to a certain level $N_{\mathrm{stab},i}$ and than stays constant[21].

Additional Post-Processing Steps Using the determined individual clearing and production rate, FillingGapSim estimates the local partial neutralization of the simulated ion species.

In additional post-processing steps, FillingGapSim generates the initial and final ion distribution in the corresponding simulated horizontal or vertical plane. This allows for an investigation of a possible alteration of the ion density distribution due to a partially unstable phase space at a certain filling pattern (e.g. for $N_{\mathrm{stab},i} > 0$).

Clearing Rate and Neutralization for a Single Filling Gap

Efficiency of a Single Filling Gap To evaluate the efficiency of a single filling gap in the storage ring, FillingGapSim is used to determine the clearing rate of the five relevant ion species at a beam energy of 1.2 GeV and a bunch current of 125 µA (I_0[22]= 34.25 mA). The average dimension of the electron beam in the storage ring is used as beam width. Only the ion dynamic in the vertical plane is considered as the horizontal clearing rates are more than one order of magnitude lower than the vertical ones. For comparison, see figure C.43 in the appendix.

The top graph of figure 6.18 shows the individual clearing rates of four relevant ion species. Note that for a clearing rate below $10^3\ \mathrm{s}^{-1}$, only a small fraction of ions is removed from the beam within the simulated time frame. Consequently, the approximation routine for $N_{\mathrm{ion},i}(t)$ has to extrapolate the exponential reduction of the ions which leads to increased errors. In the bottom graph of figure 6.18, the fraction of stable ions in the beam are shown for the corresponding filling patterns. Values whose absolute error exceeds 100 % are omitted.

The trajectories of CO_2^+ ions are stable at this energy and bunch current. Without filling gap, all other ions are also stable due to the low critical mass of the storage ring (compare section 4.1.2). H_2O^+, N_2^+ and CO^+ ions show a similar behavior in their clearing rates as H_2^+. For a longer filling gap, first the clearing rate increases to a maximum and than reduces again. In comparison to H_2^+, H_2O^+ shows a clearing rate which overall is at least one order of magnitude lower. N_2^+ and CO^+ is reduced by approximately two

[19] The decay is not purely exponentially. An oscillatory substructure is visible, which results from the ions' transversal oscillation. This oscillation resembles a beating between the time structure of the filling pattern and the ions' bounce frequency $\nu_{x,z}^{\mathrm{ion}}$.

[20] Because the clearing rate is subject to variations along the storage ring, $r_{\mathrm{c},i}$ can be converted into a local clearing rate by multiplying with $\Delta s/C$, similar to equation (2.21). Δs is the longitudinal section of the storage ring in which the ions' lifetime is equal to $1/r_{\mathrm{c},i}$ and can assumed to be constant. The sections can in principle than be combined to obtain an average clearing rate.

[21] A case where approximately 75 % of a H_2^+ population stays stable when exposed to two filling gaps of a length of 95 buckets each is shown in figure C.37 in the appendix.

[22] The hypothetical beam current I_0 represents the total beam current if it is assumed that no filling gap is present in an accelerator with a specific bunch current. When a filling gap is applied by reducing the current of specific bunches, the beam current decreases but I_0 is defined as a constant.

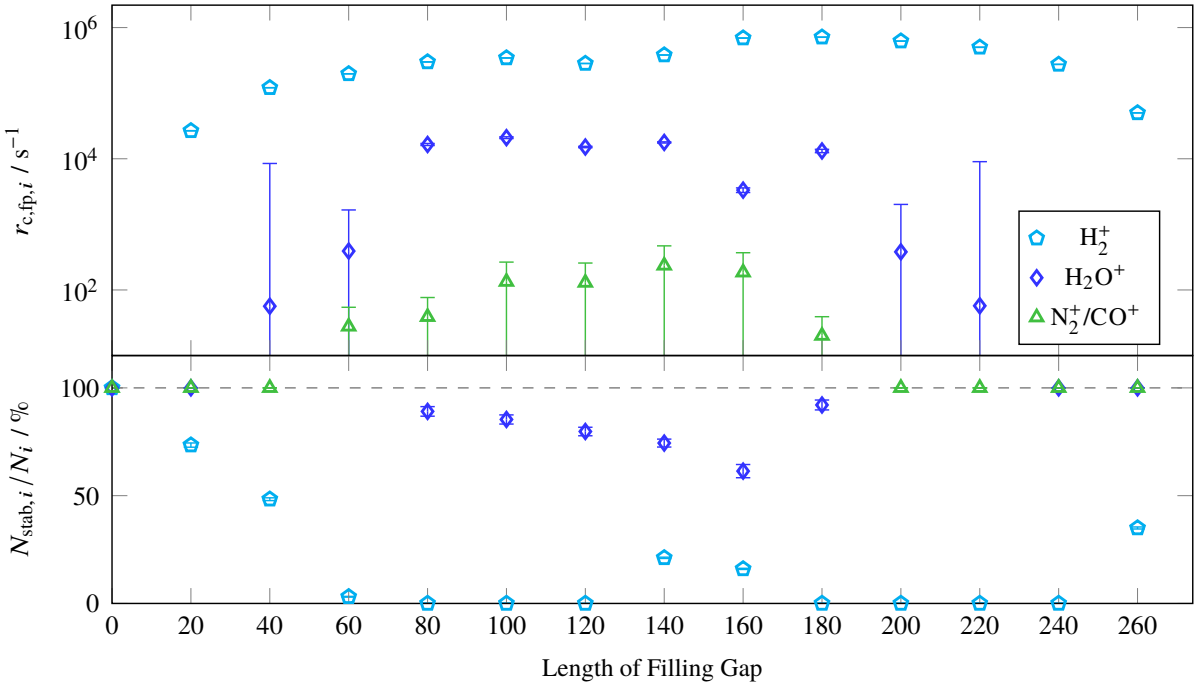

Figure 6.18: Simulated clearing rates in the vertical plane for different ion species when exposed to a filling gap with different length at a beam energy of 1.2 GeV and a bunch current of 125 µA (I_0 = 34.25 mA). In the bottom graph, the fraction of stable ions at these filling patterns is shown. $N_{stab,i}/N_i$ values whose absolute error exceeds 100 % are omitted.

orders of magnitude in comparison to H_2O^+. Here, the clearing rate is in the order of hundreds s^{-1} and thus is similar to the production rate. For H_2O^+, N_2^+ and CO^+ ions, the fraction of stable ions is higher than for H_2^+. For a filling gap of 160 bucket lengths, only a maximal fraction of approximately 40 % of H_2O^+ ions show instable trajectories. Due to the low clearing rate of N_2^+ and CO^+ ions, N_{stab} cannot be determined with reasonable accuracy. The non-zero clearing rate only indicates, that a certain percentage of N_2^+ and CO^+ can be destabilized by a filling gap.

The clearing rates at a beam energy of 1.2 GeV with a bunch current of 250 µA is shown in figure C.44 in the appendix. In comparison to the discussed case with 125 µA, the clearing rates for H_2^+ and H_2O^+ ions are in the same order of magnitude. However, in the following, dedicated studies on the beam energy and current dependency of the ion species' clearing rates using FillingGapSim are discussed.

Beam Energy and Current Dependencies In the top graph of figure 6.19, the clearing rates of the relevant ion species are shown at different beam energies. Here, the ions are exposed to a filling gap of 100 empty buckets. Each filled bucket shows a bunch current of 300 µA (I = 52.2 mA, I_0 = 82.2 mA). For H_2^+ ions, r_{c,fp,H_2^+} decreases from $(649 \pm 5) \cdot 10^3$ s^{-1} at 1.2 GeV to $(168.6 \pm 0.3) \cdot 10^3$ s^{-1} at 3.2 GeV by a factor of approximately four. However, the accumulation of this species is still reduced significantly because the clearing rate exceeds the production rate by several orders of magnitude. Yet, the clearing of H_2^+ ions is less effective for beam energies from 2.2 to 2.8 GeV as up to 50 % of the H_2^+ population cannot be destabilized by this filling gap. H_2O^+ ions show a clearing rate which exceeds their production rate for beam energies of up to 2 GeV. For higher beam energies, the clearing rate is in the same order of the production rate or below. Also the fraction of stable H_2O^+ ions continuously increases for high beam energies, rendering the clearing virtually ineffective for beam energies above 1.4 GeV. At a beam energy of 1.2 GeV, the N_2^+, CO^+ and CO_2^+ ions all show a similar clearing rate of approximately $2 \cdot 10^4$ s^{-1}.

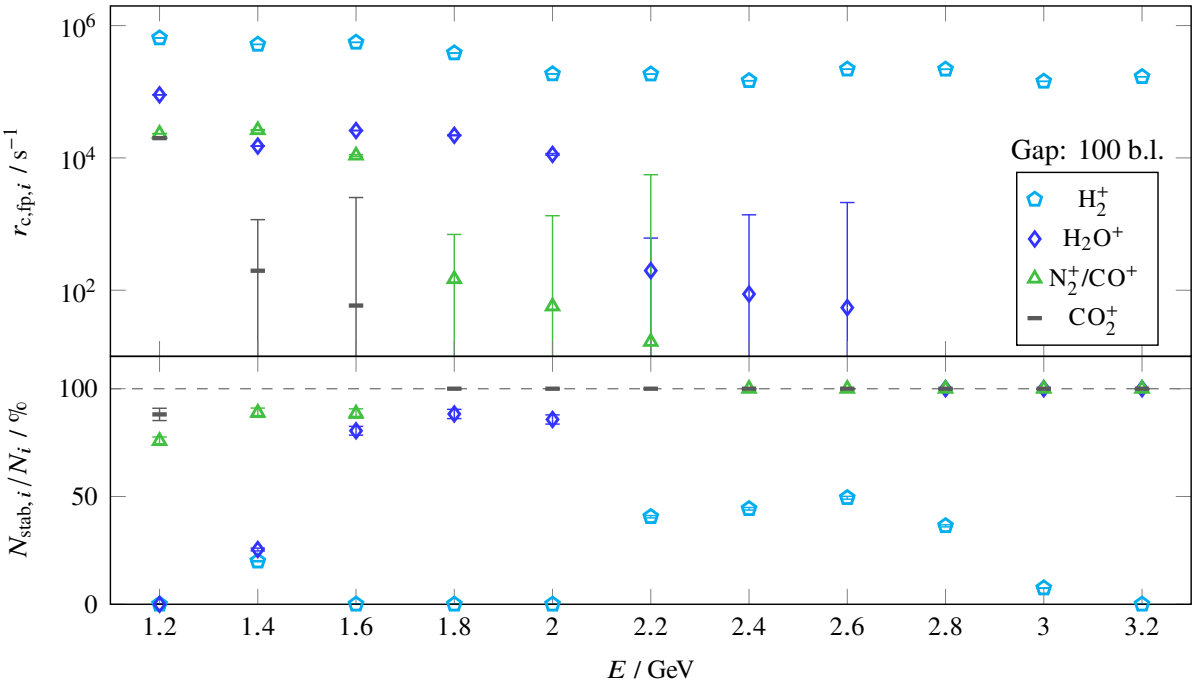

Figure 6.19: Simulated clearing rates in the vertical plane for different ion species when exposed to a single filling gap of 100 bucket lengths at different beam energies for a bunch current of 300 µA (I = 52.2 mA). In the bottom graph, the fraction of stable ions for these beam energies is shown. $N_{\mathrm{stab},i}/N_i$ values whose absolute error exceeds 100 % are omitted.

However, only approximately 25 % of the N_2^+/CO^+ ions and 10 % of CO_2^+ can be destabilized by the filling gap. For higher beam energies than 1.4 GeV, this fraction decreases further. Thus, the gap only reduces the accumulation of this species moderately for low beam energies < 1.4 GeV.

In summary, the clearing rates along with the fraction of unstable ions decreases with increasing beam energy for each ion species. For this bunch current and filling gap length, only H_2^+ ions can effectively be cleared within the whole energy range of the storage ring.

Figure 6.20 shows the ions' clearing rates at a beam energy of 1.2 GeV for a filling gap of 100 bucket lengths. For this study, the bunch current is increased from 100 to 700 µA to determine the clearing rate's dependence on the current. In general, the clearing rates increase with the bunch current and saturate after a certain current. H_2^+ ions reach a clearing rate of approximately $7 \cdot 10^5$ s^{-1} for bunch currents above 300 µA. Their stable fraction is always below 20 % for all bunch currents, enabling a significant reduction of H_2^+ ions. H_2O^+ ions' clearing rate saturate at a bunch current of approximately 500 µA at approximately $2.5 \cdot 10^5$ s^{-1}. The stable fraction of this species varies from approximately 75 % at 100 µA per bunch to zero and back to 50 % for bunch currents larger than 550 µA. With higher mass-to-charge ratio of the ion, the saturation clearing rate decreases to approximately $2.5 \cdot 10^5$ s^{-1} for N_2^+ and CO^+ ions and $0.6 \cdot 10^5$ s^{-1} for CO_2^+ ions. In comparison to H_2^+ and H_2O^+ ions, the fraction of stable N_2^+, CO^+ and CO_2^+ ions only decreases significantly for higher bunch currents. The stable fraction of N_2^+ and CO^+ ions is reduced below 50 % for bunch currents > 300 µA and > 500 µA for CO_2^+ ions, only enabling a significant reduction of these species for high bunch currents.

Thus, heavier ion species seem to be destabilized by filling gaps only for high bunch currents. For low bunch currents, only a small fraction of the population is effectively cleared. The majority of their population show stable trajectories close to the beam center and form a stable heavy ion core in the beam.

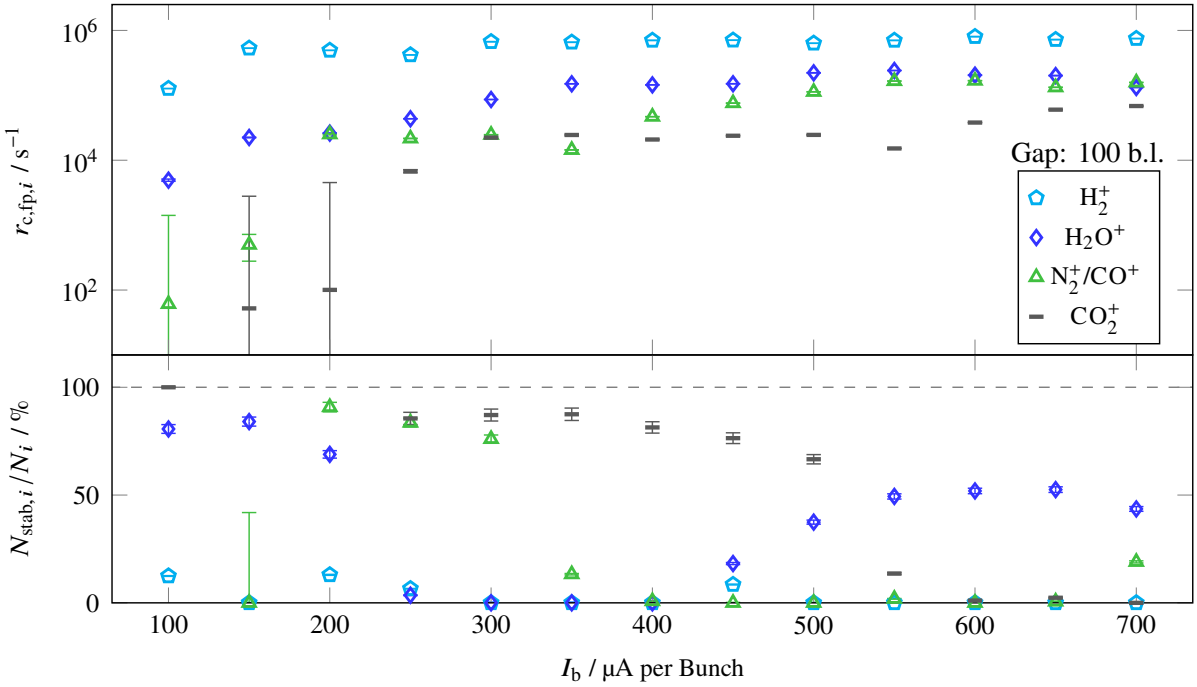

Figure 6.20: Simulated clearing rates in the vertical plane for different ion species when exposed to a single filling gap of 100 bucket lengths at different bunch currents for a beam energy of 1.2 GeV. In the bottom graph, the fraction of stable ions for these bunch currents is shown.

Partial Neutralization The clearing efficiency of a filling pattern can best be evaluated when determining the partial neutralization of the individual ion species.

The population of a single ion species splits up into stable and unstable fractions when exposed to certain filling patterns. The stable fraction is not affected by the clearing rate $r_{c,fp,i}$ induced by the filling pattern and is cleared by e.g. clearing electrodes only. Thus, only a reduced clearing rate $r_{c,ce,i}$ is in effect. The unstable fraction instead shows a total clearing rate $r_{c,fp,i} + r_{c,ce,i}$. Thus, equation (2.20) for $t \to \infty$ cannot be used to determine the equilibrium partial neutralization η_i. Instead, the partial neutralization can be determined via

$$\eta_i = \underbrace{\left(1 - \frac{N_{stab,i}}{N_i}\right) \cdot \frac{r_{p,i}}{r_{c,fp,i} + r_{c,ce,i}}}_{\text{Instable Fraction}} + \underbrace{\frac{N_{stab,i}}{N_i} \cdot \frac{r_{p,i}}{r_{c,ce,i}}}_{\text{Stable Fraction}} \tag{6.9}$$

using the individual ion species' production rate $r_{p,i}$. Here, it is assumed that no mixing between the stable and instable fractions takes place. In reality, the fraction's phase space indeed mix due to the ions' space charge interaction with each other.

However, to determine η_i, $r_{p,i}$ and $r_{c,ce,i}$ have to be estimated for the different simulated filling patterns. For filling gaps of different lengths at a constant bunch current, the total beam current in the accelerator decreases with the gaps' lengths. Consequently, the current dependent average pressure is also different for every filling pattern and results in a different $r_{p,i}$. Using the knowledge and relations obtained in chapter 3, $r_{p,i}$ can be determined for the different patterns. For a beam energy of 1.2 GeV and for beam currents corresponding to the used filling patterns, the production rate for e.g. H_2^+ ions varies from approximately 48 s^{-1} at a filling gap length of 260 bucket lengths to approximately 100 s^{-1} without filling gap. The production rate has to be reduced to approximately 35 % as most of the ions are produced far

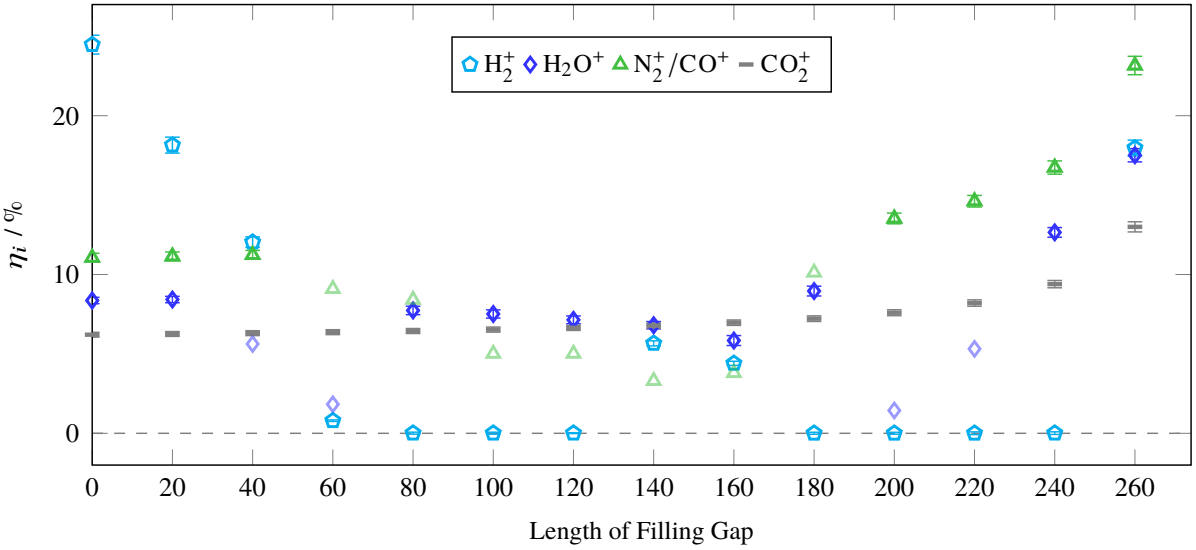

Figure 6.21: Estimated partial neutralization for different ion species, when exposed to a single filling gap at a beam energy of 1.2 GeV and a bunch current of 125 µA (I_0 = 34.25 mA). The semi transparent data points indicate an absolute error which exceeds 100 %. The corresponding error bars are omitted to ensure visibility.

away from the beam by the process of photo ionization[23].

The individual clearing rates $r_{\mathrm{c,ce},i}$ of the ion species have been determined by a simulation with TRACTION for a beam energy of 1.2 GeV and a beam current of 35 mA in section 4.3.4, table 4.3. These clearing rates are scaled with the beam current. The scaling laws are discussed in appendix A.14 and state $r_{\mathrm{c,ce},i}$ being proportional to $\sqrt{I}$ for a magnetic field-free region of the storage ring.

With known production rates, clearing rates and $N_{\mathrm{stab},i}/N_i$ of the individual ion species, their partial neutralization η_i[24] can be determined via equation (6.9). They are shown in figure 6.21. If no filling gap is used in the storage ring, the total neutralization at this energy and current amounts to approximately 50 %, with H_2^+ ions contributing half of it. With increasing length of the filling gap, $r_{\mathrm{c,fp},H_2^+}$ rises and reduces the contribution of H_2^+ ions to zero. For a filling gap between 140 and 160 bucket lengths, H_2^+ rises to approximately 5 % due to formation of a stable fraction of the species' population in the beam. For H_2O^+, the partial neutralization only reduces from (8.4 ± 0.2) % without gap to (5.8 ± 0.3) % at a filling gap with 160 empty buckets. Here, the fraction of unstable H_2O^+ ions is approximately 40 %. Other values obtained for a gap length of e.g. 60 and 200, are lower but also show a significantly higher error due to large errors in the determined clearing rates. For N_2^+ and CO^+ ions, a single filling gap also does not significantly decrease the partial neutralization as the clearing rates are in the order of the production rate. CO_2^+ ions are not affected by a filling gap at all. This species' partial neutralization increases with a longer filling gap because the simultaneously decreasing beam current also results in a reduction of $r_{\mathrm{c,ce},i}$. The same is true for all other considered ion species, which results in an overall higher total neutralization for an even longer filling gap of ≥ 220 bucket lengths.

[23] The space charge interaction of these ions with the beam is negligible due their large distance to the beam. They therefore are assumed to not contribute to the neutralization. This issue has already been discussed in section 4.3.5.

[24] η_i can assumed to be representative for the storage ring as an average. $\hat{\eta}_i$ is subject to variations along the storage ring. For example, the production rate changes due to pressure variations and different contributions of impact and photo ionization along the accelerator. The different clearing rates and $N_{\mathrm{stab},i}/N_i$ are also not constant along the accelerator because ion dynamics change with the beam size and the present configuration of magnetic fields.

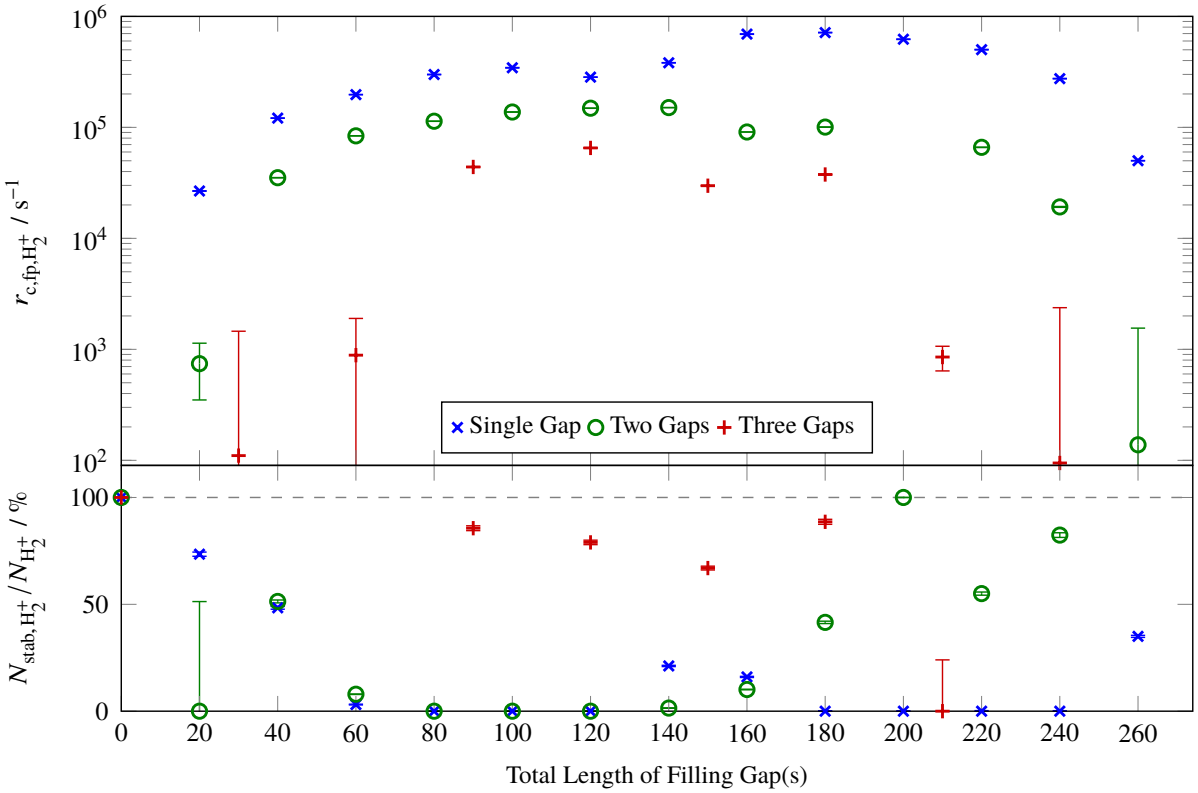

Figure 6.22: Simulated clearing rates in the vertical plane of H_2^+ ions when exposed to one, two or three filling gaps at a beam energy of 1.2 GeV and a bunch current of 125 µA (I_0 = 34.25 mA). In the bottom graph, the fraction of stable H_2^+ ions at these filling patterns is shown. $N_{stab,i}/N_i$ values whose absolute error exceeds 100 % are omitted.

Summarily, the use of a single filling gap is effective for H_2^+ ions only. The obtained clearing rates for the other heavier ions is in the order of their production rates or only destabilize a small fraction of them. However, using a filling gap with a length of 60 buckets removes all H_2^+ ions and thus halves the total neutralization in the storage ring.

Clearing Efficiency of Multiple Filling Gaps

The previous FillingGapSim simulations showed, that even a single filling gap is only able to reduce the partial neutralization of H_2^+ significantly. However, if r_{c,fp,H_2^+} is larger for multiple filling gaps in comparison with a single gap of a certain length, the clearing of H_2^+ ions may be more effective using multiple gaps. To review whether the stability conditions of the individual ion species are congruent and to determine the species' clearing rate, FillingGapSim simulations are conducted at a beam energy of 1.2 GeV and a bunch current of 125 µA with multiple filling gaps.

In the top graph of figure 6.22, the clearing rate of H_2^+ is shown when exposed to one (blue), two (green) and three (red) equidistant filling gaps of equal length. For comparison of these different patterns, the totalized gap length is used. The other ion species are stable for two and three gaps. For a single gap, the stability of these ions has already been discussed in the previous section. The clearing rate for H_2^+ ions ranges from approximately $2 \cdot 10^4$ to 10^6 s^{-1} for a single gap. The stable fraction of this species, shown in the bottom graph of figure 6.22, decreases to zero after a filling gap of 60 bucket lengths and does not exceed 25 % until ≥ 260 bucket lengths. A single filling gap is therefore effective in decreasing

the partial neutralization of H_2^+ ions to zero.

For two filling gaps, which are positioned opposite each other in the storage ring, r_{c,fp,H_2^+} is at least a factor of two lower than for a single filling gap with twice their individual length. For a gap length of 80 bucket lengths each - the total gap length equals 160 bucket lengths - the difference increases to a factor of ten. However, r_{c,fp,H_2^+} is still two orders of magnitude higher than the species' production rate. Thus, the fraction of stable H_2^+ ions decreases congruently to the single gap scenario for a total gap length of < 140 bucket lengths. For longer gap lengths, the stability of the H_2^+ population increases again.

The use of three equidistant filling gaps results in a clearing rate which is approximately ten to one hundred times lower than for a single gap. Additionally, the fraction of stable ions does not deceed 60 % for all possible gap lengths.

Summarily, regarding clearing rates and $N_{stab,H_2^+}/N_{H_2^+}$, a single filling gap is more efficient in reducing the partial neutralization of H_2^+ ions than multiple filling gaps. Whereas three gaps will only reduce the partial neutralization insignificantly due to a high fraction of stable ions and a low clearing rate, two short gaps show a similar effect as a single gap of twice the length. Especially up to a total length of 140 bucket lengths, a similar reduction of the partial neutralization can be expected.

6.2.3 Creation of Filling Gaps in the Storage Ring

The studies with FillingGapSim have shown that the filling pattern indeed has an influence on the ion composition and neutralization in the storage ring.

To clear ions by the application of filling gaps, a manipulation of the filling pattern is mandatory. Here, in principle the beam-manipulation capability of the bunch-by-bunch feedback system can be used. The result of this manipulation is verified by measurements with a streak camera.

Bunch-by-Bunch Feedback System

For the mitigation of transversal and longitudinal multi-bunch instabilities (including the beam-ion instabilities discussed in section 5.2), a digital bunch-by-bunch feedback system is operated at the storage ring. The system damps these instabilities in all three planes, which express in coherent dipole oscillations of the beam, by applying counter-phase correction kicks to the oscillation via broadband kickers. The feedback system for one plane consists of three components. One component is the beam position monitor, which enables the determination of the transversal and longitudinal center of charge of every electron bunch in the accelerator by the beam-induced voltage variations at the monitor's pick-up electrodes. This signal is digitized and separated into the position data of each bunch. Each bunch's position for up to 32 revolutions are provided as an input signal for the second component, the digital control loop. Here, a digital FIR[25] filter determines a correction signal for every bunch assuming a constant tune. The signal is amplified and transmitted to the third component, the broadband transversal and longitudinal kickers. The transversal correction signals are applied onto the beam via a stripline kicker whereas two kicker cavities dampen instabilities in the longitudinal plane [Sch11; Zim10; Heu11]. For more information, consult e.g. [Sch15, section 6].

The bunch-by-bunch feedback system can also be used for diagnostic and beam-manipulation purposes[26] [Sch15, section 6.3]. The system is able to store the position information of every bunch for up to 45 928

[25] A FIR (Finite Impulse Response) filter is used in digital signal processing and generates an impulse response with finite duration.

[26] This diagnostic and beam manipulation abilities can also be used in the ion density beam transfer function measurement technique, which has been developed in the course of this work but whose description exceeds the scope of this thesis. The technique is described in [SMH15; SH16].

revolutions of the electron beam, implying a recorded time frame of approximately 25.2 ms. This data can be used to determine the oscillation frequency of the individual bunches and the frequency spectrum of the beam. For more information regarding the beam spectrum, see section 5.2.1. Independently from the damping effect on the beam, the feedback system can be used to manipulate individual bunches. To do so, the system provides a programmable digital signal generator which generates signals for a generic ensemble of bunches with a fixed frequency or with a frequency sweep. The excitation signals are injected into the signal path, thus are amplified and applied to the beam via the kickers. Here, the relative amplitude of the signal, its central frequency and, in case of a sweep, the frequency range and the duration of the sweep have to be specified.

Filling Pattern Manipulation

Every 20 ms a bunch train from the booster synchrotron, consisting of 116 electron bunches, is injected into the storage ring. Several booster fillings are injected until the desired beam current in the storage ring is reached. Since the harmonic number of the booster is smaller than that of the storage ring, the precise injection time is altered after every injection to obtain a filling pattern which is as homogeneous as possible. For more information regarding the timing system of the storage ring, see [Pro18, chapter 6].

To generate a specific filling pattern, the bunch-by-bunch feedback system is configured to excite certain bunches in the vertical plane prior to any injection from the booster. If e.g. a filling gap of 40 bucket lengths has to be generated, a series of 40 bunches is excited. These bunches are continuously excited vertically with a frequency which corresponds to the beam's vertical tune. The excitation frequency is configured to sweep repeatedly in a range of ±12.5 kHz around the assumed vertical tune with a sweeping speed of 25 kHz ms^{-1}. When a bunch train from the booster synchrotron is injected into the storage ring, the selected bunches are excited to coherent oscillations which result in increased beam loss. Eventually, these bunches show a bunch current, which is not detectable by the bunch-by-bunch feedback system anymore. When the injection is completed, a filling pattern is present in the storage ring which has either filled or "empty" buckets.

Verification of the Filling Pattern

To verify the effect of the applied bunch cleaning, the generated filling pattern can be verified by two ways.

Using the longitudinal bunch-by-bunch feedback system, the charge of each bunch can be monitored. This monitoring feature is not calibrated and does not allow for a determination of the bunch current of individual bunches. However, it allows for a distinction between filled buckets and buckets, whose charge is below the feedback system's sensitivity.

The intensity of synchrotron light, emitted by the electrons in each bunch, is proportional to the bunch current. Therefore, a streak camera can be used to determine the bunch current of each bunch and thus the filling pattern in the storage ring. For more information on the streak camera, see e.g. [Swi19, section 3.2].

The obtained longitudinal intensity profile of the bunch train, which is proportional to the filling pattern, is shown in figure 6.23. Here, approximately two revolutions of the bunch train are visible with one revolution being equal to $1/\nu_0 = 548$ ns. Since the intensity of the bunch train in a single-turn measurement with the streak camera is too low to obtain information about the filling pattern, the shown images are composed of phase-locked superpositions of multiple revolutions of the bunch train. From left to right, a filling gap length of 20, 90, 120 and 200 bucket lengths is desired. For a gap with a length of

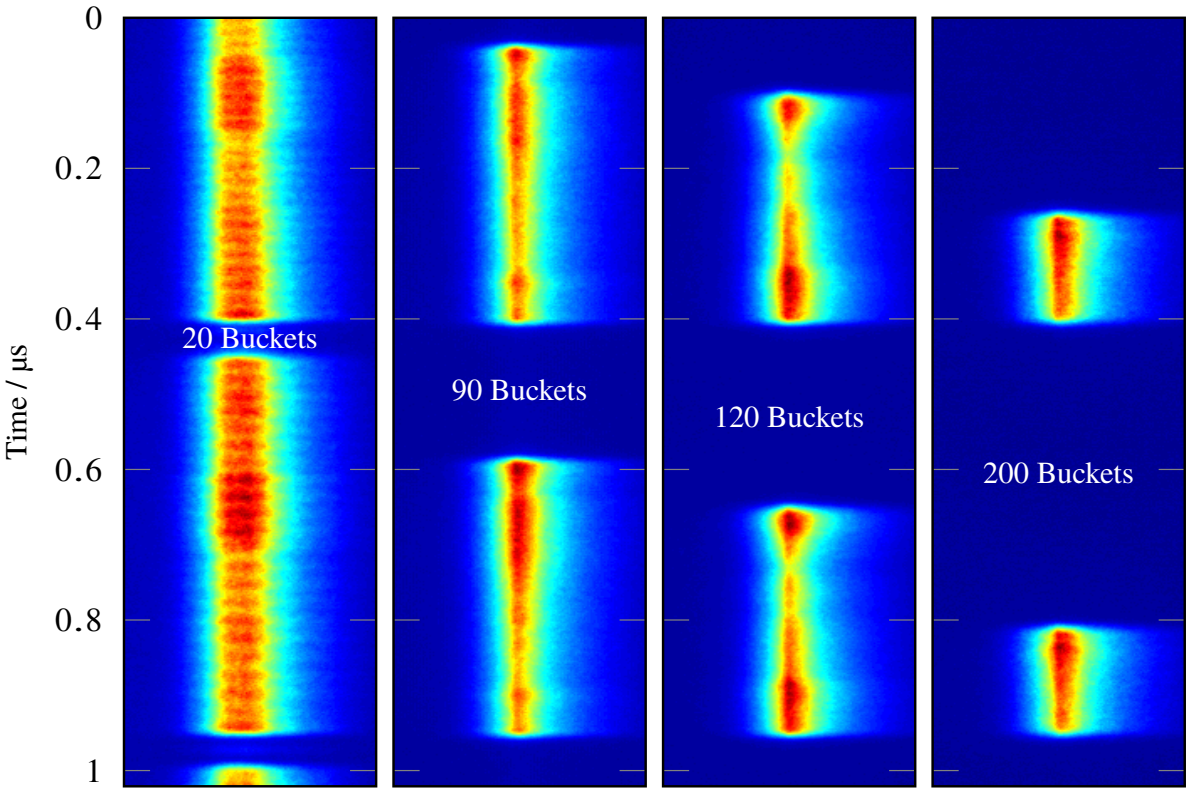

Figure 6.23: Time structure of the filling pattern in the storage ring for approximately two revolutions of the bunch train, measured by the streak camera at a beam energy of 1.2 GeV. The different measurements show filling patterns with a single filling gap of 20, 90, 120 and 200 bucket lengths.

20 buckets, the intensity profile appears broader because ion induced horizontal instabilities of the beam have distorted the measurement (compare section 5.2).

In figure 6.24, the actual longitudinal intensity profile, the isochrone-integrated intensity of the streak camera measurements of figure 6.23, is compared to the desired bunch pattern for different filling gap lengths. Here, all bunch patterns show a continuous transition from filled to empty buckets within a range of approximately 10 buckets. Therefore, the number of bunches per gap with reduced bunch current is approximately 10 buckets (5 buckets at each edge) longer than required. In contrast, the number of bunches within a gap, where the bunch current is negligibly small, is reduced by approximately 10 buckets due to this transitional region (5 buckets at each edge). This transitional behavior originates from the finite bandwidth of the feedback system's amplifier where an excitation signal, applied to a specific bunch, also affects neighboring bunches [Sch15, section 10.4]. Thus, the generation of short filling gaps below the transitional region length of approximately 10 is problematic. Here, at least additional 10 buckets around the desired gap will also show a reduced bunch current.

Summarily, the bunch-by-bunch feedback system can be used to manipulate the filling pattern of the storage ring and successfully generates filling gaps for ion clearing. However, due the feedback system's finite bandwidth, the manipulative capabilities are limited and perfectly homogeneous bunch trains with discrete transitions towards filling gaps cannot be generated.

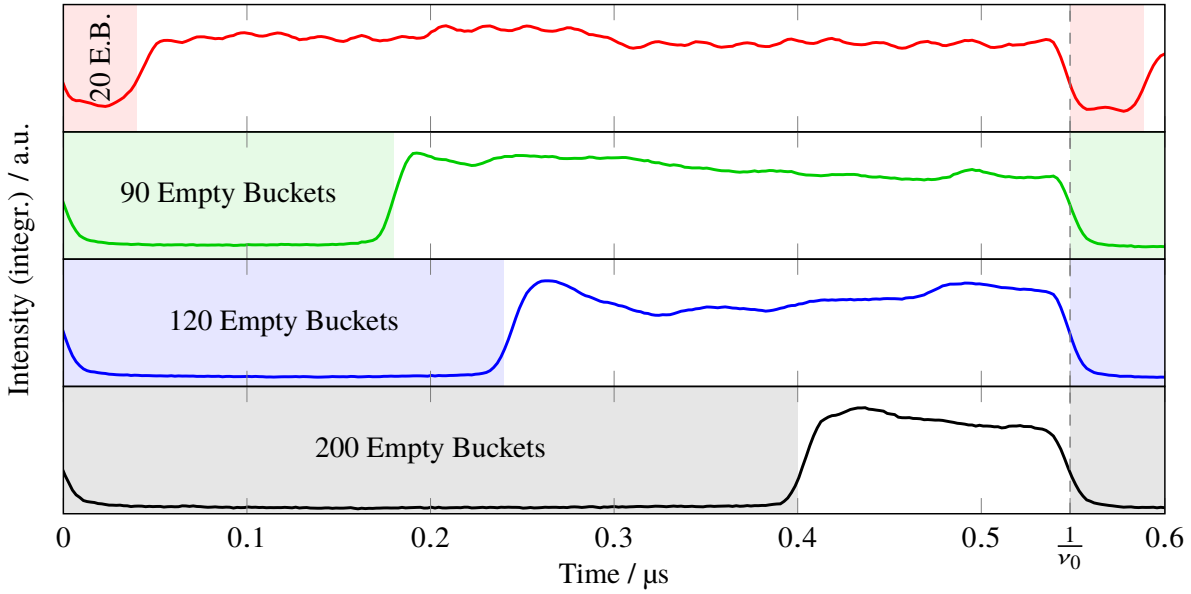

Figure 6.24: Longitudinal intensity profile of manipulated filling patterns with gaps of different lengths. The highlighted area denotes the requested filling gap length. The dashed line indicates the end of one revolution of the bunch train.

6.2.4 Useful Filling Gaps for the Storage Ring

Criterion for Effective Ion Clearing Using Filling Gaps To efficiently clear a particular ion species, in general the clearing rate $r_{\mathrm{c,fp},i}$, induced by the filling pattern, should exceed the species' production rate by a factor of 20 or more. Additionally, the stable fraction $N_{\mathrm{stab},i}/N_i$ of this species should be as low as possible to ensure that the induced clearing rate acts on the majority of the population. Consequently for $N_{\mathrm{stab},i}/N_i = 0$, the partial neutralization of this species would be reduced by 95 % (relative) or more.

Beam Energy, Current and Ion Mass Dependence With increasing beam energy $r_{\mathrm{c,fp},i}$ in general decreases for all ion species and the fraction of stable ions increases. For a higher bunch current, where the depth of the beam potential increases, $r_{\mathrm{c,fp},i}$ rises to a certain level and then approximately stays constant. Also the fraction of unstable ions increases. Thus, the clearing of ions when applying a certain filling pattern is more effective for a lower beam energy and higher bunch current.

$r_{\mathrm{c,fp},i}$ and $N_{\mathrm{stab},i}/N_i$ are also strongly dependent on the mass-to-charge ratio of the different ion species. Heavier ions, like CO_2^+, show a lower clearing rate than light ones (e.g. H_2^+ ions). Also the destabilization of heavier ion species by a certain filling pattern is less probable for a certain beam energy and current than for lighter ions.

Thus, a significant reduction of the partial neutralization is achievable with a shorter filling gap for light ions (e.g. H_2^+ ions). Heavier ions can only be cleared by long filling gaps, if the beam energy is low and the bunch current is high. However, even H_2^+ ions cannot be removed from the beam, if the beam energy is too high. Here, only a partial removal is possible for higher bunch currents.

Proposed Filling Pattern Because approximately 50 % of the produced ions are H_2^+ ions (compare figure 3.24 in section 3.5) which are destabilized easier than heavier ion species for shorter filling gaps, the ion clearing attempt should focus on this species. The experiments also demand that the applied

filling gap should be as short as possible in order to avoid an extension of the measurement times[27].

In comparison with a single filling gap, two filling gaps, each showing half of its length, generate approximately a tens of the clearing rate of the single gap for H_2^+ ions (compare figure 6.22). However, for two filling gaps with 30 empty buckets each and a bunch current of 125 µA at a beam energy of 1.2 GeV, r_{c,fp,H_2^+} is still a factor of approximately 1 500 larger than the production rate. Additionally, $N_{stab,H_2^+}/N_{H_2^+}$ is equal to zero. Thus, the resulting partial neutralization is equal to approximately $1/1500$, effectively clearing H_2^+ ions from the beam and reducing the total neutralization by 50 %. For lower bunch currents and higher beam energies, an extension of the two filling gaps' length to 40 buckets each is advised to still remove fractions of H_2^+ ions. However, for higher beam energies, the ion induced effects on the electron beam in general diminish due to its increased rigidity. Here, ion clearing with clearing electrodes is sufficient to keep the neutralization on a level where no impact of ion accumulation is detectable in the storage ring.

However, for all combinations of bunch current and beam energy, the tool FillingGapSim can now be consulted to substantiate further assertions regarding the effect of filling patterns on the ion population.

6.3 Summary: Ion Clearing Strategies for the Storage Ring

Using the concept of static neutralization, the minimal threshold voltage for the ion clearing electrodes has been determined for the storage ring to avoid an accumulation of ions in front of the electrodes. For a beam energy of 1.2 GeV, these threshold voltages have been validated by measurements of the voltage dependent ion current. For higher beam energies, the fringe fields of the quadrupole magnets in vicinity of the electrodes, whose influence on the ion motion has not been included into the developed formalism for the ion current measurements, shift the threshold towards higher absolute voltages. However, as typical beam currents in the storage ring rarely exceed 60 mA, a clearing voltage of −1 500 V is sufficient to avoid additional static neutralization within the storage ring's typical beam energy range.

It has been shown that almost arbitrary filling gaps can be generated within the storage ring by utilizing the manipulative capabilities of the bunch-by-bunch feedback system. Numerical simulations with FillingGapSim, a developed tool for the determination of the ions' clearing rate when exposed to a particular filling pattern, show that especially heavy ions like CO_2^+ ions cannot be removed from the beam by a filling gap in the storage ring. Therefore, ion clearing measures for the storage ring should concentrate on H_2^+ ions which amount to approximately 50 % of the produced ions. By application of two equidistant filling gaps with a length of 30 buckets, H_2^+ ions can be removed almost entirely from the storage ring at 1.2 GeV, thereby halving the neutralization. For higher beam energies, these gaps have to be extended to achieve a similar reduction of the neutralization.

However, for the storage ring, the application of filling gaps is not necessary as the emerging beam-ion instabilities at low beam energies are successfully mitigated by the transversal bunch-by-bunch feedback system. For higher beam energies, the ions' space charge effects and the related tune shifts diminish and the increased natural damping by synchrotron radiation prevents a build-up of beam-ion instabilities.

[27] A long filling gap and thus a short bunchtrain with high bunch current is not desired by the experiments. The high bunch current results in a high rate of simultaneously extracted electrons within a short timeframe. This leads to saturation effects in the particle detectors because the different generated particle reactions cannot be distinguished in time anymore due to the detectors' finite dead time. A necessary reduction of the extraction rate to prevent saturation would infer a longer total measurement time and consequently higher financial expenses.

CHAPTER 7

Conclusion

In the course of this thesis, several new insights into the phenomena of trapped ions in electron circular accelerators have been gained. Since the developed tools and models as well as the measurements performed are closely contextualized with the storage ring, ELSA-specific findings are reviewed in the following section. In section 7.2, general conclusions and the perspectives of developed models as well as potential points of contact for further simulations and measurements are discussed.

7.1 Ion Phenomena in the ELSA Storage Ring

In the storage ring of the ELSA facility, the electron beam continuously converts neutral residual gas into positive ions due to the production processes of impact and photo ionization. Mass spectrometric analyses have shown that approximately 86 % of residual gas in the accelerator's vacuum system is molecular hydrogen. Water vapor, molecular nitrogen along with carbon mono and dioxide are additional constituents which in total contribute to approximately 13 %. Due to individual ionization cross sections of the constituents, the final composition of produced ions differs from the residual gas species' abundance. Thus, half of the produced ions are H_2^+. The other half comprises H_2O^+, CO^+, CO_2^+ and N_2^+ ions, in descending order of abundance. The share of the individual ion species only varies insignificantly with beam energy.

The ion production rate is linearly dependent on the average pressure. As the pressure varies by more than a factor of five within the typical parameter space of beam energy and current of the storage ring, a customized pressure model has been developed to give a comprehensive overview of the accelerator's ion production capabilities. The model has been derived analytically and comprises the energy dependent processes of electron and photo stimulated desorption. On the basis of pressure data, stored over a period of one year during operation of the accelerator, the model has been suitably parameterized for the accelerator's average pressure. The determined total ion production rate varies from approximately $100\,\mathrm{s}^{-1}$ at a beam energy of 1.2 GeV and a stored beam current of 5 mA to up to $480\,\mathrm{s}^{-1}$ at 3.2 GeV and 200 mA, which has been confirmed by selective measurements of the clearing electrode's ion current, directly proportional to the production rate.

Approximately 40 % of the ions are produced by impact ionization whereas a majority of 60 % of the ion production results from photo ionization by synchrotron radiation photons. However, most of the photo-produced ions show a larger distance from the beam center than ions, produced by impact ionization.

All produced ion species show stable trajectories despite the bunched structure of the electron beam because the storage ring's critical mass-threshold lies well below 1 u within the relevant beam energy and

current parameter space. Therefore, ions accumulate all along the accelerator in potential hollows resulting from volatile variations of the beam potential depth when using different beam pipe geometries. However, this inevitable static neutralization η_{stat} is estimated to be in the order of 2 % but is small compared to the present dynamic neutralization η_{dyn} in the storage ring. Here, a simulation with TracTIon indicates a dynamic neutralization of approximately 40 % at 1.2 GeV and 35 mA, although this value may be overestimated due to systematical errors. This high dynamic neutralization, on one hand, results from an average pressure of approximately $2 \cdot 10^{-7}$ mbar, resulting in an ion production rate of approximately $180\,\mathrm{s}^{-1}$. On the other hand, fringe fields of dipole magnets represent magnetic mirrors especially for light ions, which prevents their propagation through dipoles towards ion clearing electrodes. Consequently, the local neutralization is elevated in vicinity of these fields, even fully neutralizing the beam locally. Additionally, numerical simulations and investigations on the electromagnetic field configuration within rf cavities indicate that ions are not transported through cavities. Consequently, an elevated static neutralization is expected in the rf section of the storage ring, although still η_{stat} is much larger than η_{dyn}.

Due to decreased transmission of light ions through dipole magnets' fringe fields, the clearing rate of especially H_2^+ ions is disproportionately reduced compared to heavier ion species. Therefore, the reduced transmission of light ions compensates their normally higher velocity, and thus shorter lifetime, and results in similar clearing rates for all ion species. As a consequence, the equilibrium ion composition on average resembles the ions' production distribution although large variations are visible on the local scale, especially in vicinity of the dipoles' fringe fields.

Even with enabled ion clearing by biased electrodes, the influence of the ions' space charge on the beam is measurable due to the high neutralization in the storage ring. Especially in the horizontal plane coherent beam instabilities emerge at low beam energies of approximately 1.2 GeV and currents in the order of > 40 mA. These instabilities have been identified to be driven by trapped ions by measuring their growth rates for different clearing voltages using the bunch-by-bunch feedback system. However, provided that the feedback system is configured to damp emerging coherent horizontal beam oscillations and electrodes are biased with an adequate clearing voltage, the amplitude of these beam instabilities is reduced significantly and enables a stable extraction of the beam to the experiments within the relevant current region < 80 mA (at 1.2 GeV). Yet, these instabilities only occur at low beam energies where the natural damping rate of beam oscillations by synchrotron radiation is low. Since most experiments require a beam energy of 2 GeV or higher, these ion induced beam instabilities do not affect productive operation of the storage ring. An adequate clearing voltage is $-1\,500$ V as measurements of the clearing voltage dependent ion current have shown. The application of this clearing voltage to the electrodes prevents an additional static neutralization in front of the electrodes during most operation scenarios of the storage ring.

Although transversal beam-ion instabilities can be suppressed successfully, the ion induced tune shift is still evident, shifting the tune with beam current. As this tune shift complicates the setup of the acclerator's optics, necessary for stable extraction of the electron beam to the experiments, a further reduction of the neutralization is desirable. The installation of additional clearing electrodes at specific positions is therefore proposed in case of a renewal of the vacuum system in future upgrades. For example, the installation of ion clearing electrodes in vicinity of the dipoles' fringe fields would reduce the dynamic neutralization by approximately 1/4th. Additionally, the bunch-by-bunch feedback system can be used to manipulate the filling pattern in the storage ring. If necessary and applicable, it enables the generation of filling gaps to explicitly destabilize certain ion species. For two equidistant filling gaps with a length of 20 to 30 buckets each, almost all H_2^+ ions can be removed from the beam at a beam energy of 1.2 GeV, resulting in a reduction of the dynamic neutralization by approximately 50 %. For higher beam energies, the gaps have to be extended to achieve similar results although in practice they are redundant due to contraction of the tune shift with increasing beam energy.

7.2 Perspectives

In the course of this work, a formalism for the determination of the production rate due to photo ionization by synchrotron radiation photos has been developed. This formalism yields an expression for the total photo ionization production rate which is congruent to the one derived by [Miy87]. Accordingly, the proportion of photo-produced ions to the total ion production is significantly higher than assumed in literature. In the considered storage ring, the average ratio of photo-produced ions to ions produced directly by the beam via impact ionization is approximately 60 % to 40 %. As photo ionization only occurs within dipole magnets and adjacent downstream sections, the local photo ionization production rate is even higher there.

Consequently, consideration of this production process is essential when analyzing the ion dynamics in these regions. Sophisticated numerical tracking simulations such as MOEVE PIC TRACKING, enabling the study of these dynamics in due consideration of mutual space charge interactions of beam electrons and ions, are in need for the transversal and longitudinal ion production maps of these regions. Therefore, PHOTOIONPROD has been developed in the course of this work which provides the ion production map due to impact and photo ionization at arbitrary positions within dipole magnets. The computed total ion production maps, comprising both production processes, show a significant asymmetry in the horizontal plane as the majority of photo-produced ions show a large distance from the beam center. Subsequent ion tracking simulations with TRACTION and TRANSVERSION show that this asymmetry persists within dipole magnets whereas the transversal ion density distribution is widened horizontally in adjacent magnet field-free regions.

As the determined transversal ion distributions show significant distinctions from the theoretical equilibrium ion distribution of [Tav92b], the ions' space charge influence on the electron beam have been investigated using DQTOOL. This tool calculates the tune shift distribution, and thus the coherent and incoherent tune shift, of a bunched electron beam when exposed to an ion population with a specific transversal density distribution. According to results of DQTOOL, the horizontally asymmetric or widened ion distributions within or downstream of dipole magnets reduce the horizontal coherent ion induced tune shift significantly, yet to varying extents.

However, the equilibrium ion density distribution from TRACTION and TRANSVERSION results from tracking of the individual ions' trajectories within the electric potential of the beam where the ions' mutual space charge interaction is not included. These interactions may lead to dispersal of ion accumulations, produced by photo ionization with large distances from the beam center, due to their mutual repulsion. Here, investigations using more advanced numerical tracking simulations, where these space charge interactions are included, may provide more precise equilibrium ion distributions which can be investigated regarding their influence on the beam.

For straightforward estimation of the inevitable neutralization due to accumulated ions in potential hollows, the concept of static neutralization has been elaborated. A first application of this concept could be found for the interpretation of the measured characteristic curve of ion clearing electrodes. Here, the loss of the measured ion current due to the mutual space charge interaction of the trapped ion population in front of the electrodes linearly scales with the static neutralization as long as the influence of magnetic fields on the ions' trajectories is negligible. A further simulative investigation of this loss mechanism, presumably resulting from beam heating and momentum transfers between trapped ions, is desirable to substantiate and extend this concept further.

Furthermore, with the development of the tools FILLINGGAPSIM and TRANSVERSION, the capability has been created to determine individual clearing rates of accumulated ions when using filling gaps and beam shaking. This enables the optimization of these ion clearing measures for a corresponding specific application scenario and determination of the resulting neutralization, if the production rate within the

accelerator is known.

Tracking simulations with TracIon of different ion species within the vertical magnetic guiding field of dipole magnets have shown that ion propagation is more complex in these regions of the accelerator as predicted by theory. While it is assumed that the longitudinal cross-field drift velocity is identical for each ion species, it has become evident that the ions' non-zero gyro radius strongly affects the drift velocity close to the beam center. Since light ions have a smaller gyro radius than heavy ions, a mass dependence for the cross-drift velocity arises. Here, the cross-field drift velocity of light ions approximately follows the theoretical trend, whereas for heavier ions a clear reduction of the drift velocity is observed. Therefore, the removal of heavy ions within dipole magnets could prove difficult and a higher neutralization is expected than could be deduced from theory.

Additionally, fringe fields of dipole magnets act as magnetic mirrors for ions, which are accelerated towards them by the longitudinal gradient field of the beam potential. Here, especially the transport of light ions towards clearing electrodes is hindered which results in an increased local neutralization at the entrance of dipole magnets. The installation of clearing electrodes is recommended there.

A further region, in which ion transport to clearing electrodes is prevented and thus a high neutralization is to be expected, is created by rf cavities. Here, tracking simulations and investigations on the configuration of present electric and magnetic rf fields within the cavities indicate that an ion transport through them is prevented due to emerging longitudinal ponderomotive forces driving ions towards field-free regions. If the hypothesis is confirmed that ions are also trapped in the transverse plane by the axial magnetic rf field, ions may accumulate between the cells of the cavity. Additionally, cavities represent barriers for ion propagation preventing their transport towards clearing electrodes. Consequently, additional potential hollows emerge in the rf section of accelerators. To keep the local neutralization on an acceptable level, this would require the installation of clearing electrodes in between the cavities' cells and at their entrances. In confirmation of these findings, further investigations with sophisticated simulation programs are essential to formulate an adequate ion clearing strategy within rf cavities and their close vicinity.

APPENDIX A

Additional Analyses, Calculations and Informations

A.1 Outgasing Characteristics of a Vacuum System

When pumping a vacuum chamber, the reachable minimal pressure is dependent on the pumping speed of the engaged vacuum pumps and the inflow rate of new residual gas molecules and atoms into the vacuum chamber. The inflow occurs through leaks, a back flow through the pump and due to the mechanisms of diffusion, desorption and permeation [OHa03, chapter 4]:

- In an evacuated vacuum chamber, residual gas molecules and atoms bound to the surface of the chamber desorb into the vacuum. Also vapors, like water vapor, previously adsorbed by the surface, desorb. The rate in which this desorption takes place is dependent on the binding energy of residual gas to the surface. This rate decreases linearly in timescales of approximately hours after the volume has been evacuated.
- Out of the depth of utilized metals and plastics dissolved gases diffuse to the surface and then desorb into the vacuum. As this diffusion rate decreases slower than the desorption rate, this process is the main contributor to the residual gas. Because both degassing processes are energy and thus temperature dependent, a bake-out of the vacuum system can speed up diffusion and desorption processes and therefore reduces the pumping time, which is needed to reach a desired vacuum pressure.
- Light residual gases can permeate through the vacuum chamber. Here, residual gases like H_2 molecules or He can be adsorbed on the outer surface of the vacuum chamber. In this process the H_2 molecule dissociates, the generated H_1 atoms diffuses through the material and then recombine before the molecule is desorbed into the vacuum chamber. The inflow rate of this permeation process is constant over time and thus limits the minimal pressure reachable in the vacuum system, when other degassing rates have already declined with time.

A.2 Total Clearing Rate of an Ensemble of Multiple Ion Species

To express the total clearing rate R_c in terms of the individual clearing rates $r_{\mathrm{c},i}$, it holds that

$$\eta(t) = \sum_{i=1}^{k} \eta_i(t) \,,$$

which can be written as

$$\frac{R_\mathrm{p}}{R_\mathrm{c}}\left(1-\exp\left(-R_\mathrm{c}\cdot t\right)\right) \stackrel{!}{=} \sum_{i=1}^{k}\frac{r_{\mathrm{p},i}}{r_{\mathrm{c},i}}\left(1-\exp\left(-r_{\mathrm{c},i}\cdot t\right)\right) \ .$$

$R_\mathrm{p}/R_\mathrm{c}$ or the equivalent term on the right hand side can be identified as the neutralization in the equilibrium state at $t \rightarrow \infty$. Thus, it follows

$$\eta(t\rightarrow\infty)\left(1-\exp\left(-R_\mathrm{c}\cdot t\right)\right) = \sum_{i=1}^{k}\eta_i(t\rightarrow\infty)\left(1-\exp\left(-r_{\mathrm{c},i}\cdot t\right)\right) \ .$$

Using the definition of the (partial) neutralization of equation (2.11) and equation (2.19), one obtains

$$\frac{N_\mathrm{ion}}{N_\mathrm{e}}\left(1-\exp\left(-R_\mathrm{c}\cdot t\right)\right) = \sum_{i=1}^{k}\frac{N_{\mathrm{ion},i}}{N_\mathrm{e}}\left(1-\exp\left(-r_{\mathrm{c},i}\cdot t\right)\right) \ .$$

Note that the inserted ion numbers are the one extracted from the equilibrium state ion population. The terms $(1-\exp(-a\cdot t))$ can be deducted by the first order Taylor expansion. Thus, after rearranging N_ion and canceling out the time t, one obtains

$$R_\mathrm{c} = \frac{1}{N_\mathrm{ion}}\sum_{i=1}^{k}N_{\mathrm{ion},i}\cdot r_{\mathrm{c},i} \ .$$

A.3 Derivation of the Beam Potential for a Round Electron Beam with Homogeneous Charge Density

The beam is guided through a round beam pipe with radius r_{vc}. To derive the beam potential for a beam with radius a and a constant homogeneous charge density along its radius, one starts with the Gaussian law of electro statics. The electron beam has a charge $\mathrm{d}q$ within a volume with an infinitesimal length $\mathrm{d}s$ along the longitudinal axis. The charge can be expressed in terms of a linear charge density $\lambda = \mathrm{d}q/\mathrm{d}s$ and one obtains

$$\int_A \vec{E}_r\cdot\mathrm{d}\vec{A} = \frac{\mathrm{d}q}{\varepsilon_0} = \frac{\lambda\cdot\mathrm{d}s}{\varepsilon_0} \ . \tag{A.1}$$

$\mathrm{d}\vec{A}$ is an infinitesimal area of the surface of the beam which equals the surface of a cylinder with radius r and height $\mathrm{d}s$. In this derivation, the electron beam has a sharp round form and can be treated as a cylinder with charge q. Therefore, equation (A.1) can be rewritten as

$$\int_A \vec{E}_r\cdot\mathrm{d}\vec{A} = \int_0^{2\pi}\mathrm{d}\varphi\int_0^r \mathrm{d}r\ E_r\,\mathrm{d}s = 2\pi r E_r\,\mathrm{d}s$$

for the infinitesimal segment of length $\mathrm{d}s$. Rearranging the equation to E_r and with the right hand side of equation (A.1), the electric field outside the beam is obtained as

$$E_r(r) = \frac{\lambda}{2\pi\varepsilon_0}\frac{1}{r} \quad \text{for } r \geq a \ .$$

Integration along r yields the electric potential as

$$U_{\mathrm{I}}(r) = \frac{\lambda}{2\pi\varepsilon_0} \ln(r) + H \,. \tag{A.2}$$

The vacuum chamber is grounded. Thus, the relation $U(r_{\mathrm{vc}}) \stackrel{!}{=} 0$ applies. Consequently,

$$H = -\frac{\lambda}{2\pi\varepsilon_0} \ln(r_{\mathrm{vc}}) \,,$$

which can be used to rewrite equation (A.2) to

$$U_{\mathrm{I}}(r) = \frac{\lambda}{2\pi\varepsilon_0} \ln\left(\frac{r}{r_{\mathrm{vc}}}\right) \quad \text{for } r \geq a \,.$$

Inside the beam, λ is not constant anymore but scales as

$$\lambda(r) = \lambda \frac{r^2}{a^2}$$

with the radius. Therefore, the right hand side of equation (A.1) is modified by this expression and one obtains

$$E_r(r) = \frac{\lambda}{2\pi\varepsilon_0} \frac{r}{a^2}$$

for the electric field inside the beam. Integration of this term gives the potential

$$U_{\mathrm{II}}(r) = \frac{\lambda}{2\pi\varepsilon_0} \frac{r^2}{2a^2} + D \,. \tag{A.3}$$

The potential is a physical one and must be continuous with $U_{\mathrm{II}}(a) \stackrel{!}{=} U_{\mathrm{I}}(a)$ at the boundary a of the beam. The constant can thus be expressed as

$$D = \frac{\lambda}{2\pi\varepsilon_0} \left(\ln\left(\frac{a}{r_{\mathrm{vc}}}\right) - \frac{1}{2} \right)$$

and can be integrated into equation (A.3). Finally, the inner beam potential is obtained as

$$U_{\mathrm{II}}(r) = \frac{\lambda}{2\pi\varepsilon_0} \left(\frac{r^2}{2a^2} + \ln\left(\frac{a}{r_{\mathrm{vc}}}\right) - \frac{1}{2} \right) \quad \text{for } r \leq a \,.$$

A.4 A Short Introduction to the Utilized Vacuum Technologies

To generate an average pressure of below $2 \cdot 10^{-8}$ mbar, starting at an atmospheric pressure, several types of pumps, each only operating in a specific pressure range, are used consecutively or parallel. This section will give a short overview of the vacuum technologies utilized at the ELSA storage ring. See for example [OHa03] for more information.

Auxiliary and Backing Pumps

To evacuate the beam pipe, starting from atmospheric pressures, first auxiliary pumps with high pumping speeds are used. These flange-mounted pumps are in operation to generate a first vacuum of 10^{-2} mbar until the other pumps can be used to reduce the pressure even further. In the storage ring rotary lobe pumps are used for this purpose.

Turbo Molecular Pumps (TMP)

A turbo molecular pump, in short TMP, is a vacuum pump which is used in pressures regions of typically 10^{-2} to 10^{-9} mbar. It cannot be operated at atmosphere and is in need of a prevacuum to which it pumps the residual gas of the vacuum system. A backing pump[1] is positioned in between the prevacuum and atmosphere and transports the residual gas out. Here, only a certain ratio of the vacuum system's to the prevacuum's pressure, the so called *compression ratio*, is achievable due to back streaming of the gas. The compression ratio depends on the species of the pumped residual gas. The TMP is a turbine-like structure, in which pairs of stators and rotors are stacked consecutively on top of each other in multiple stages. The stators are stationary rotor blades, whereas the rotor's blades rotate with a frequency of around 1 000 Hz. With this rotational frequency, the blades reach similar velocities as the residual gas. Incoming residual gas gain additional kinetic energy in direction of the prevacuum when getting hit by the rotor blades. On the way they get redirected by collisions with the stator, whose blades have a mirrored orientation to the rotors, and reach another stage of rotors. After several stages, the residual gas reaches the prevacuum.

The TMP's pumping efficiency is correlated to the velocity of the rotors and the velocity of the residual gas. The thermal velocity is dependent on the individual mass of its constituents (compare equation (2.3)). Thus, residual gas constituents with a low mass have a higher velocity than ones with higher mass. It follows, that the TMP's pumping efficiency for light residual gas like H_2 is reduced compared to the efficiency for heavier gas like CH_4 or CO_2. Therefore, one expects a higher contribution of light residual gas in areas affected by TMPs [OHa03, section 11.3].

Ion Getter Pumps (IGP)

With the use of a TMP only pressures of approximately 10^{-7} mbar can be achieved. Therefore, ion getter pumps, in short IGPs, are used additionally. With them pressures of down to 10^{-11} mbar can be realized in a suitable vacuum system [OHa03, section 14.2]. As is shown in figure A.1, an IGP consists of an anode between two cathodes. The anode consists of numerous cylindrically shaped short metal tubes, which are aligned like a honeycomb. Anode and cathodes are electrically isolated from each other by a gap sufficiently large enough to allow residual gas to drift into the setup. This array is framed by a permanent magnet behind the two cathodes, providing a homogeneous magnetic field in the setup.

When a high voltage is applied between cathodes and anode, electrons are emitted due to field emission and spiral towards the anode. On their way, they ionize the residual gas and secondarily enforce the electron cloud with newly produced electrons. The ionized residual gas is accelerated towards the cathode plates and impinge on them with high kinetic energy. Here, the residual gas chemically reacts with the getter material, typically highly reactive titan or tantalum, or is implanted into the material. During the impact of the residual gas, getter material is also detached from one side of the cathode, which deposits on it at another point.. Consequently, this produces new layers of fresh getter material on the cathode, enabling a continuous chemical binding of incoming residual gas molecules and atoms. With

[1] In the storage ring, *diaphragm pumps* are in use which can operate in a pressure region of 10^3 mbar to $5 \cdot 10^{-1}$ mbar [Pfea]. For more information regarding diaphragm pumps, see e.g. [OHa03, section 10.7].

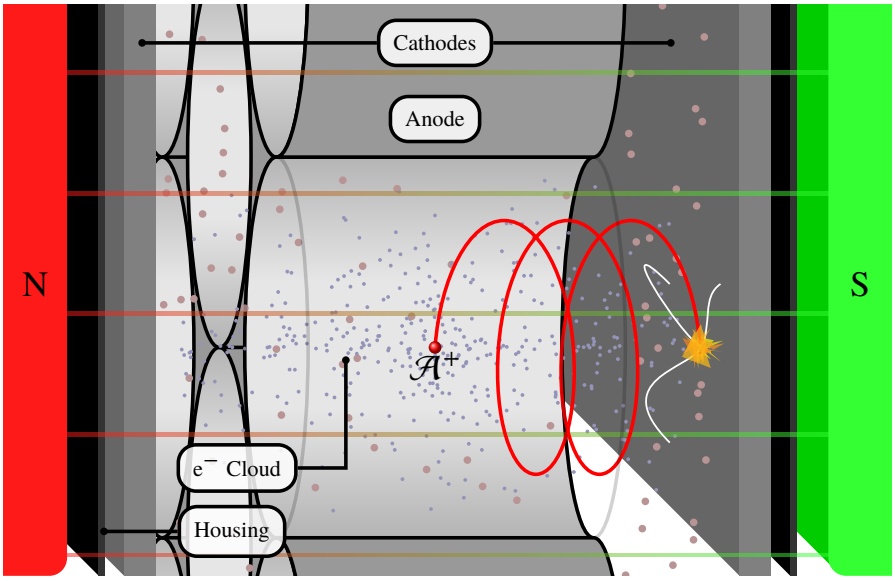

Figure A.1: An ion getter pump consists of an anode between two grounded cathodes. When a high voltage is applied between anode and the cathodes, field-emitted electrons drift towards the anode ionizing incoming neutral residual gas molecules on their way. To extend the electrons' path a permanent magnet is mounted outside the vacuum housing, permeating the setup with a magnetic field and thus forcing the electrons onto spiral orbits. The ionized residual gas $\mathcal{A}^+$ is accelerated towards the cathodes and is chemically or physically bound into the cathode material, where it may redistribute the surface getter material.

this mechanism a reduction of the residual gas density and thus the vacuum pressure occurs. But as the residual gas is only deposited in the getter material an IGP operation is only reasonable under already good vacuum conditions with pressures of $< 10^{-3}$ mbar[2].

Since the residual gas is primarily chemically bounded to the getter material, the gases reactivity determine the IGP's pumping efficiency for it. Consequently, reactive gases, such as O_2, are pumped more efficiently than noble gases which can only be physically bound by implantation into the getter material. Therefore, the IGP's pumping speed for reactive gas is higher than for noble gases [OHa03, section 14.2]. If hydrogen is continuously pumped by IGPs, the pumping speed also decreases significantly: Initially, it is pumped, while it is buried in the getter material, where it adsorbs, diffuses and forms a hydride. If the surface of the getter material is covered with compounds (e.g. nitrogen) which prevent the burying and diffusion process, the hydrogen pumping speed declines [OHa03, section 14.2].

The number of involved electrons and ionized residual gas is proportional to the pressure in the vicinity of the IGP. When measuring the current flowing between anode and cathodes, it consequently can be used to monitor the pressure in the vicinity of the pump.

Vacuum Gauge

Another possibility to monitor the vacuum condition, are the Pirani- and cold cathode gauge [OHa03, section 5.3]. They are used in the storage ring, too. In combination, they can measure pressures from

[2] Because the getter material only has a finite capacity for the deposited residual gas, the pressure region in which the IGP operates defines how long it is able to pump. If the getter material is saturated, the IGP can be heated out. Here, the bound gases desorb back into separated parts of vacuum system where additional pumps, e.g. a TMP removes the gas permanently from the system.

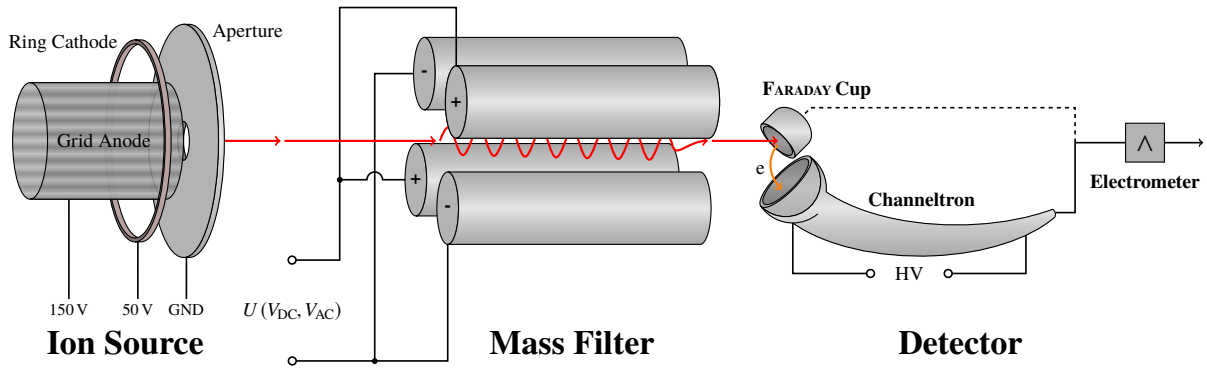

Figure A.2: Schematic setup of a quadrupole mass spectrometer. It consists of three main sections, the ion source, the mass filter and the detector. Residual gas molecules and atoms are ionized by electron bombardment from the ring cathode, punching through the grid anode. The ionized particles are accelerated towards the aperture. A voltage of $U(V_{DC}, V_{AC}) = V_{DC} + V_{AC} \cos(\omega_m t)$ is applied to the quadrupole mass filter . For a voltage sweep with fixed ratio of V_{DC}/V_{AC}, only suitable ionized particles with a specific mass-to-charge ratio A/Z can pass the filter and reach the detector. The filtered particle stream is detected either by a Faraday cup or is amplified by a channeltron to which a high voltage is applied. The signal is detected by an electrometer and is given to adjoining read out hard- and software.

10^3 to $5 \cdot 10^{-9}$ mbar[3] [Pfeb]. In the relevant pressure range of the storage ring, the device is used as a cold cathode ionization gauge. It consists of a grounded cathode and an anode, biased with a high voltage. Due to field emission, electrons leave the cathode and propagate towards the anode. The field of a permanent magnet forces them onto spiral trajectories extending their way towards the anode. On their way, they ionize the residual gas and stimulate gas discharges. These discharges are used to measure the vacuum pressure as the measured current between anode and cathode scales with the pressure in the beam pipe which is connected to the gauge. The probability of the electron ionizing a specific residual gas species varies, as will be discussed in section 3.3. Therefore, the measured pressure is dependent on the composition of the vacuum.

A.5 Functional Principle of a Quadrupole Mass Spectrometer

As it can be seen in figure A.2, the residual gas analyzer consists of a grid ion source and a quadrupole mass filter. Subsequently, either a Faraday cup or a channeltron detects the ion current signal. Here, an amplification of the ion current signal is possible when using the channeltron.

In the grid ion source, the residual gas molecules and atoms are ionized and accelerated towards the mass filter. The source consists of an anode grid in the shape of an open cylinder and an electrically isolated wolfram ring cathode. The cathode is circularly arranged around the grid cylinder and is also called filament. A voltage of 100 V is applied between anode and cathode. When the filament is heated up by an electric current, free electrons are emitted thermionically and are accelerated towards the anode. When reaching the cathode, they penetrate through the thin grid and drift inside the cylinder, ionizing residual gas. Additionally to ionization, dissociation of molecules is also possible. The ring cathode (50 V) and the cylinder anode (150 V) are placed in close proximity to a circular aperture (GND). This

[3] To achieve this large measurement range, the gauge has two measurement modes. For high pressures it uses the pressure dependent thermoconductivity of the residual gas in the vacuum, the Pirani effect, to determine the pressure. Due to the similar setup it can also be used as a cold cathode gauge for low pressures.

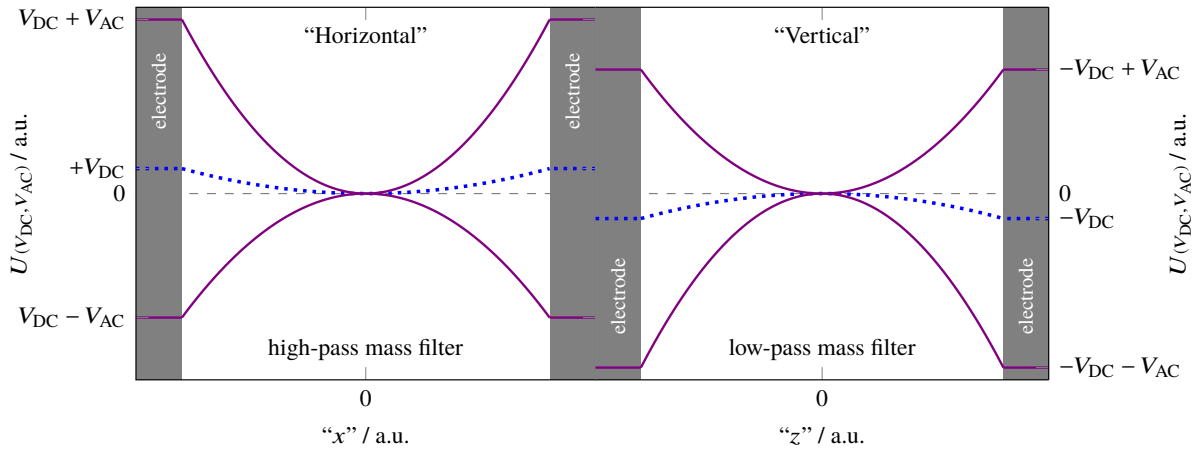

Figure A.3: Time dependent "horizontal" (left) and "vertical" electric potential $U(V_{DC}, V_{AC})$ (right) in between the pencil electrodes of the quadrupole mass filter according to [OHa03, section 8.1.2, figure 8.11]. The time average potential equal to V_{DC} is shown as dotted blue line. The extremal values of $U(V_{DC}, V_{AC}) = V_{DC} + V_{AC}\cos(\omega_m t)$ are shown in violet.

setup allows for an acceleration of the ionized residual gas within the cylinder towards the aperture. The ionized gas which passes through this aperture enters the mass filter.

A quadrupole mass filter allows the passage of ionized gas species with a specific mass-to-charge ratio. Other species show unstable trajectories and collide with the apertures. The filter consists of four cylindrical pencil electrodes, arranged in the form of a square, which are supplied by an AC[4] voltage of $V_{AC}\cos(\omega_m t)$ with a DC[5] voltage offset V_{DC} (see figure A.2). The opposing electrodes have the same polarity. In general, the trajectories of particles exposed to this field configuration can be described by the MATHIEU's differential equation (see e.g. [MD86, section The Equation of Motions]). The solutions to this equation show either stable or unstable trajectories for a particle with a certain mass in dependence of the chosen combination of V_{DC} and V_{AC}.

To describe the ionized particles' motion in the mass filter qualitatively, their motion can be decomposed into two planes. The planes' coordinate axis go through the centers of each opposing electrode pairs.

Thus, in the "horizontal" plane, positioned on the far "left" and "right", are the electrodes on which V_{DC} is positive and thus forces the ionized particles towards the center of the filter (see figure A.3 (left)). This electric field increases towards the electrodes and is zero in the center of the quadrupole. The additional AC part of the voltage V_{AC} forces the incoming ionized particles to "horizontal" oscillations. As "light" particles, with low mass-to-charge ratio, have lower inertia as "heavier" particles, with a higher mass-to-charge ratio, they will be able to follow the alternating field and stay in phase with it. Consequently, they gain energy from the field and oscillate with increasing amplitudes until they recombine on the electrodes and are filtered out. Since "heavy" particles are less affected, this "horizontal" plane acts as a high-pass mass filter.

In the "vertical" plane, the "up" and "down" electrodes show a negative V_{DC}, thus drawing the particles towards them. Similar to the "horizontal" plane, the field decreases with rising distance to the electrode and is zero in the center of the filter as can be seen in figure A.3 (right). When ionized particles enter the filter, they are drawn towards the electrode "vertically". "Heavy" particles which oscillate only with small amplitudes, induced by $V_{AC}\cos(\omega_m t)$, leave the center of the quadrupole and hit one of the "vertical"

[4] An alternating current (AC) is an electrical current which periodically reverses its direction.

[5] An electric current is a direct current (DC), if it flows unidirectional.

electrodes. ”Light“ particles, on the other hand, show larger oscillation amplitudes and swing ”up“ and ”down“ across the field free quadrupole center. Since they are drawn alternatingly to the ”up“ and ”down“ electrode, their trajectory is stable around the center. This ”vertical“ plane acts as a low-pass mass filter to the incoming ionized particle stream.

When a measurement is conducted, the AC along with the DC voltage is increased with a fixed ratio V_{DC}/V_{AC}. With increasing AC and DC voltage this suitable mass-to-charge ratio is scanned from A/Z of 1 to 100 and only suitable ionized particles reach the detector.

The selected ionized residual gas molecules or atoms reach the amplification and detection unit. A FARADAY cup electrometer[6] can be utilized to directly measure the current of the incoming ionized particle beam. If the partial pressure of a residual gas species is below $3 \cdot 10^{-11}$ mbar, the sensitivity of the FARADAY cup electrometer is not sufficient to measure the incoming particle current in a suitable length of integration time. Therefore, a channeltron[7] can be operated in addition to the FARADAY cup to amplify the incoming current by factors of up to 10^8 in dependence of the applied high voltage. Here, the FARADAY cup is biased with a negative voltage in reference to the channeltron and acts as a conversion dynode. The incoming ions impact with the cup and the secondary electrons, emitted from these impacts, reach the channeltron entrance eventually triggering an electron avalanche. The amplified signal is then detected by the electrometer and is processed by adjoining hard- and software readouts. The measured current is proportional to the partial pressure of the particular residual gas species, when the amplification factors are taken into account.

A.6 Detailed MSAUGA Analysis

The main contribution to the peak at $A/Z = 28$, measured by the quadrupole mass spectrometer, results from the residual gases nitrogen and carbon monoxide. To determine a fraction with which these gases contribute to that peak, only their contribution to additional peaks via their fragmentation patterns can be utilized. Of course, these secondary peaks can also be comprised of contributions of different other residual gas species. Therefore, the already non-trivial task of the determination of the most suitable residual gas composition to the particular spectrum is complicated by this circumstance.

Separate analysis processes via MSAUGA are carried out. In one process, the composed default library of fragmentation patterns consisting of the patterns of 65 different possible residual gas species are used for the analysis. In the other analysis process, the complexity of the problem is reduced by lowering the number of species in the library to 11. Here, only species are selected which are expected due to the characteristics of the vacuum system as stated above. The reduced library consists of H_2, CO, CO_2, CH_4, H_2O, O_2 and N_2 along with ammonia NH_3, as its fragmentation pattern contribute mostly to a $A/Z = 17$ peak, which is also dominant in all measurements. Additionally, the noble gases He, Ar and Ne are included. One may call these two processes the ”default“ and the ”complexity-reduced“ analyses. In both analysis processes, MSAUGA is executed various times with different simulation settings. On one hand, a number of simulated generations is chosen being either $0.5 \cdot 10^6$, $1 \cdot 10^6$ or $2 \cdot 10^6$. On the other hand,

[6] A FARADAY cup electrometer detects charged particles within vacuum conditions. It is often designed as a hollow cylinder which is open at one end. This cup shape gives it its name. Charged particles recombine to neutral particles when hitting the cup’s surface, inducing a measurable current.

[7] A channeltron is a curved tube, whose inner surface is coated with a high-resistance material. A high voltage is applied between the ends of the tube and thus a uniform voltage gradient along the channeltron tube is generated. An incoming ionized particle produces multiple secondary electrons when it hits the tube. These electrons are accelerated inside the tube and produce further electrons when impacting on the tube surface. Through this cascading effect, a single incoming charge can be amplified by a factor of up to 10^8.

the seed key[8] is incremented for each generation number from one to 50. At the end of each MSAUGA simulation, its score and results are noted. With this, the stability of the used genetic algorithm can be monitored. For example, an unstable algorithm does not converge to similar solutions when executed with different settings and seed keys.

To visualize the stability of MSAUGA in the two simulation processes, the resulting percentage of the five dominant residual gas species are shown in figure A.4 as a function of the individual simulation's score. The mass spectrum, measured at 2.2 GeV, has been used here as simulation input. In the MSAUGA simulations on the right, the "default" process is shown and on the left side, the "complexity-reduced" case. The performance analysis of the other measurements are shown in figures C.2, C.4, C.6, C.8 and C.10 in the appendix. Note that the measured and reproduced mass spectra via MSAUGA with the best score for the "complexity-reduced" case are shown in the middle graph of figures 3.2 and 3.3 in section 3.1.3 and figures C.3, C.5, C.7 and C.9 in the appendix.

In general, the simulation's score of the "default" process is higher. This is a consequence of the used fragmentation pattern libraries. Since each species in this library has various different A/Z to which it can contribute, even insignificant small peaks in the mass spectrum can be reproduced by MSAUGA if a larger library is used. Therefore, the score is higher for larger libraries. As the interest lies mainly on reproducing the dominant peaks in the mass spectrum, thus obtaining the dominant constituents of the vacuum system, the score's absolute value is not of importance.

The percentages of all residual gas species except nitrogen and carbon monoxide are approximately equal in both analysis processes for the simulations with the highest scores. Only deviations in the order of maximal 0.5 % occur. For N_2 and CO, the deviation is larger. Since both contribute mainly to a dominant peak at $A/Z = 28$, MSAUGA is not able to determine with certainty which of them contribute most to this peak. This may be caused by an incomplete fragmentation pattern library. Here, a complete set of patterns of unconsidered species may be missing or minor mass contributions of already included species are absent. Mass contributions then may not be mapped adequately by the program and defective residual gas compositions result.

In general, the simulations of the "default" process shows larger fluctuations of the resulting percentage in the order of 1 to 3 % (up to 6 % for N_2 and CO) than the "complexity-reduced" process on the left. Here, the maximum fluctuations are 0.3 % (0.6 % for N_2 and CO) and nearly all simulations are within a range of 0.1 % to the result with the highest score. This implies that the algorithm's results are reproducible for the "complexity-reduced" case within a small error range. For the "default" analysis process, this error range is approximately a factor of ten larger.

Both analysis processes reproduce the mass spectrum with approximately the same composition of the main constituents of the vacuum system. Additionally, less simulations are needed to achieve an adequate solution if the complexity of the problem is reduced. For future residual gas analysis with MSAUGA, this legitimizes the possibility to reduce the complexity of the problem by preselecting the most probable residual gas species, if one is only interested in obtaining the composition of the main species.

To obtain the final results of the residual gas analysis via MSAUGA, the simulation's error is evaluated by determining the standard deviation of all analyses of all six mass spectroscopic measurements. For both analysis processes, the "default" and the "complexity-reduced" case, the simulated residual gas value is chosen which shows the highest score, because this particular MSAUGA simulation reproduced the measured spectrum most congruently.

[8] MSAUGA relies on a sequence of randomly generated numbers for its algorithms. This sequence is identical and reproducible for equal seed keys with which the algorithm is initialized.

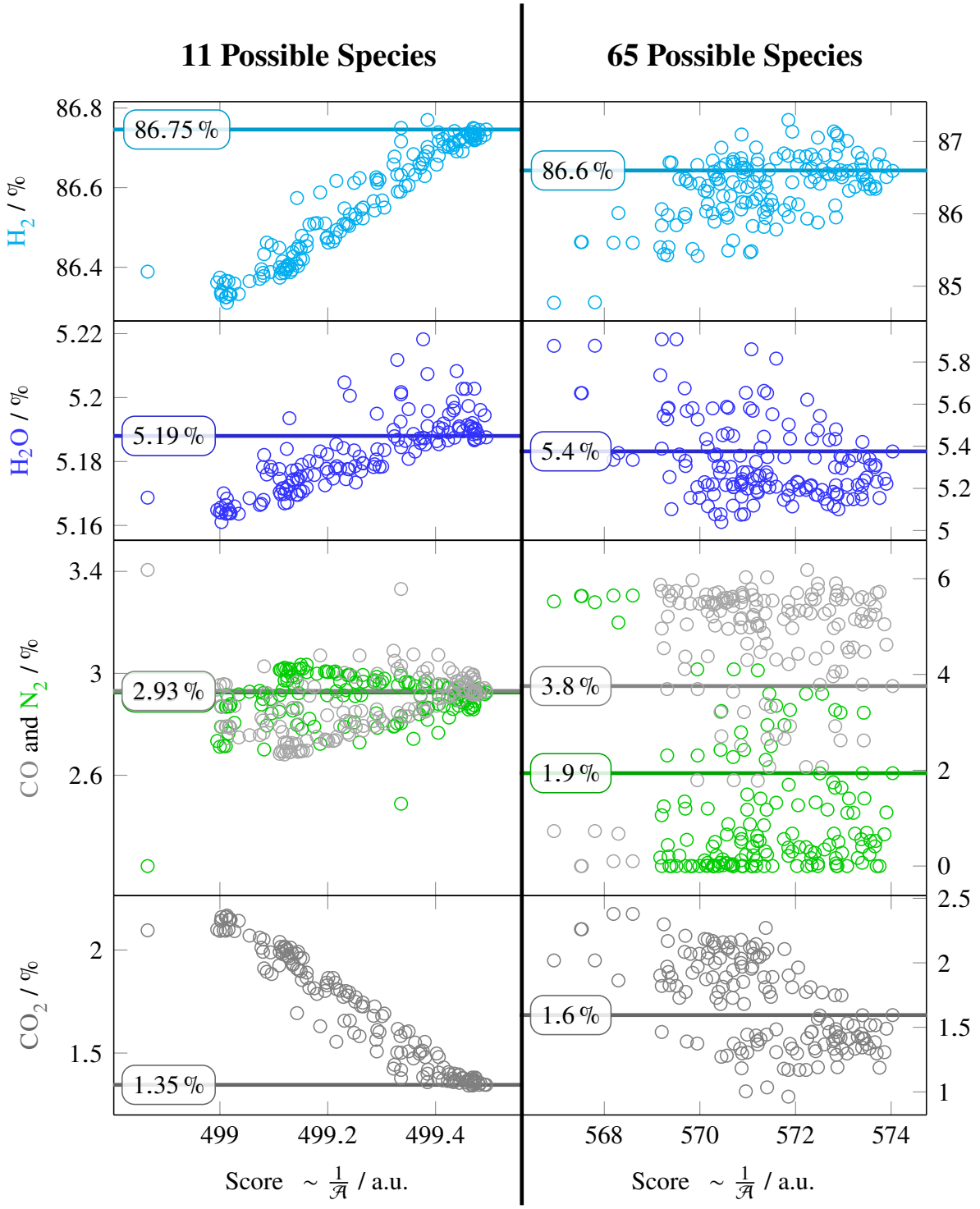

Figure A.4: Percentage of the five dominant residual gas species versus the final score of the MSAUGA simulations on basis of the measured mass spectrum at 2.2 GeV. The graphs on the left side of the central line show the results and scores of MSAUGA simulations which use a fragmentation pattern library of 11 possible residual gas constituents. On the right side, the complete library, consisting of 65 species, is used in the simulations. The horizontal lines in the individual graphs denote the percentage of the particular residual gas species for the highest achieved score in the simulations.

A.7 Evolution of the Pressure with Beam Energy and Current

To obtain an analytical formula for the evolution of the average pressure $\mathcal{P}(E, I)$ in an electron accelerator with beam energy E and current I, one starts with the rate equation for the number of residual gas N in the beam pipe. The differential equation in time t can be written as

$$\frac{\mathrm{d}N}{\mathrm{d}t} = \frac{\mathrm{d}N_{\mathrm{prod}}}{\mathrm{d}t} - \frac{\mathrm{d}N_{\mathrm{pump}}}{\mathrm{d}t} \,, \tag{A.4}$$

where N_{prod} is the number of desorbed gas from the surface of the beam pipe and N_{pump} is the number of gas which is pumped by the vacuum pumps.

In the following, the differential equation's two terms will be discussed in more detail.

A.7.1 Desorption Mechanisms

In this simple ansatz, only desorption from the surface by the process of photon stimulated desorption (PSD) by synchrotron radiation, thermal out-gassing and electron stimulated desorption (ESD) by impinging beam electrons onto the beam pipe's surface is considered.

The production term can be written as

$$\frac{\mathrm{d}N_{\mathrm{prod}}}{\mathrm{d}t} = q_{\mathrm{therm}} + q_{\mathrm{ESD}} + q_{\mathrm{PSD}} \,.$$

Here, q_{therm} is the out-gassing rate, comprising the beam pipe material's out-gassing characteristics. q_{ESD} is the out-gassing rate due to ESD whereas q_{PSD} is the rate by PSD. q_{therm} can assumed to be constant for the relevant beam current and energy range of the storage ring as the accelerators environmental temperature varies only slowly during operation.

q_{ESD} can be expressed as

$$q_{\mathrm{ESD}} = \eta_{\mathrm{e}} \frac{\mathrm{d}N_{\mathrm{e}}}{\mathrm{d}t} = \eta_{\mathrm{e}} \frac{N_{\mathrm{e}}}{\tau}$$

where η_{e} is the molecular desorption yield of electron bombardment on a beam pipe surface, N_{e} is the number of beam electrons in the accelerator and τ is the lifetime of the beam in the accelerator.

The lifetime is a composition of four components and can be expressed as

$$\frac{1}{\tau} = \frac{1}{\tau_{\mathrm{coll}}} + \underbrace{\frac{1}{\tau_x} + \frac{1}{\tau_z} + \frac{1}{\tau_s}}_{\approx 0}$$

where $\tau_{x,z}$ are the lifetimes due to horizontal and vertical collisions of individual beam electrons, situated in the tail of the beam's Gaussian spatial distribution, with the vacuum chamber. Since the dimension of the beam pipe used in the storage ring is chosen ($> 7.5\sigma_x$) to ensure a lifetime of more than 103 d, these contributions can be omitted. τ_s is the lifetime due longitudinal beam losses. As the energy distribution of the beam is also Gaussian, occasionally individual electrons experience large energy losses due to synchrotron radiation in which they leave the rf bucket and the accelerator's energy acceptance and are lost. This contribution is also omitted because the energy acceptance of the accelerator is chosen high enough to ensure a lifetime of at least 1 000 s at a beam energy of 3.2 GeV [Sch15, figure 13.3]. The remaining τ_{coll} is the lifetime due to collisions with the residual gas in which, on one hand, ions are generated and, on the other hand, beam electrons suffer a mainly longitudinal but also transversal momentum loss. If this loss exceeds the accelerators longitudinal and/or transversal acceptance, the

electron is lost. It consequently impinge on the surface of the beam pipe somewhere in the accelerator and cause ESD. The lifetime can be expressed as [Møl99, section 2]

$$\frac{1}{\tau_{\text{coll}}} = \beta c \cdot \sigma_{\text{ii}} \cdot \frac{N}{V} \,. \qquad \text{resulting in} \qquad q_{\text{ESD}} = \eta_{\text{e}} \frac{\sigma_{\text{ii}} \cdot I \cdot C}{\text{e}\, V} \cdot N$$

for the ESD out-gassing rate by using equation (2.1). Here, σ_{ii} is the impact ionization cross section, V is the volume of the vacuum system. In short, q_{ESD} can be written as

$$q_{\text{ESD}} = \eta_{\text{e}} \chi_{\text{e}} \cdot I \cdot N \tag{A.5}$$

The out-gassing rate due to PSD can be written as [Grö99, section 1.1, equation (5)]

$$q_{\text{PSD}} = \eta_{\gamma} \cdot \Phi_{\gamma} \tag{A.6}$$

where η_{γ} is the molecular desorption yield. It defines the number of desorbed molecules per impinging synchrotron radiation photon. It is dependent of the critical energy $\hbar\omega_{\text{c}}$ of the synchrotron radiation and thus changes with the beam energy as will be discussed later in this section. Φ_{γ} is the total synchrotron radiation photon flux. It can be expressed as [Grö99, section 1.1, equation (3)]

$$\Phi_{\gamma} = \underbrace{8.08 \cdot 10^{17}\,\text{GeV}^{-1}\,\text{mA}^{-1}}_{:=\delta} \cdot E \cdot I \,. \tag{A.7}$$

The constant is denoted as δ for the course of this deviation. Consequently, q_{psd} is dependent on the beam energy *and* current.

Additionally, both desorption yields are energy dependent.

PSD Yield From e.g. [Grö99, section 1.4] it is known that η_{γ} is dependent of the critical energy $\hbar\omega_{\text{c}}$ of the synchrotron radiation photons. With increasing energy photons penetrate deeper into the surface of the vacuum chamber. Additionally, for synchrotron radiation photons with energies of hundreds of keV or more, the Compton scattering dominates over the photo effect - the driving effect for PSD and ESD for lower energies. The Compton scattering process produces a shower of recoil electrons and scattered secondary photons. This increases the molecular desorption yield with increasing photon energy.

ESD Yield For the ESD molecular yield η_{e}, also some kind of dependence on the energy of the beam electrons can be assumed. When electrons impinge on the beam pipe's surface, the desorption process can, amongst other processes, be stimulated by an electromagnetic shower due to bremsstrahlung of the electron in the material. The shower heats up the material, dissociates residual gas molecule bindings to the surface and ejects secondary electrons, which in turn produce ESD in the vicinity of the initial impact.

A.7.2 Pumping Rate

The number of pumped residual gas per time scales with the number of residual gas molecules in the beam pipe, thus

$$\frac{\text{d}N_{\text{pump}}}{\text{d}t} = \upsilon \cdot N \,. \tag{A.8}$$

Here, υ is the pumping rate of the vacuum pumps. But this is just a first order approximation assuming a constant pumping rate with pressure.

In the storage ring, the main vacuum pumps are IGPs. Their pumping speed S, given in units of $1\,\mathrm{s}^{-1}$, is not constant with the pressure of the vacuum system. For high pressures $> 10^{-5}$ mbar, the density of the electron and ionized gas clouds in the IGPs is high enough to start glow discharges between anode and cathodes. Consequently, the pumping speed is reduced. For low pressures $< 10^{-7}$ mbar, the pumping speed, being maximum at around 10^{-6} mbar, also decreases. Here, the pumping speed results from an equilibrium between pumped and desorbed gas [Sch99, section 4]. Since the considered pressure values are in the region of 10^{-9} to $5 \cdot 10^{-8}$ mbar, the increasing pumping speed for increasing vacuum pressures is approximated by a linear function as

$$S(\mathcal{P}) = \varrho \cdot \mathcal{P} \ .$$

With this approach, an additional pumping rate by the IGPs is obtained which is added to equation (A.8) as

$$\frac{\mathrm{d}N_{\mathrm{pump}}}{\mathrm{d}t} = \upsilon N + \frac{\mathcal{P} \cdot S(\mathcal{P})}{k_{\mathrm{B}} T} = \upsilon N + \frac{\varrho k_{\mathrm{B}} T}{V^2} \cdot N^2 = \upsilon N + \rho N^2 \ .$$

Here, the ideal gas equation has been used. For convenience, also the pump rate-variation constants are wrapped up in ρ.

A.7.3 Pressure Evolution

Equation (A.4) can be written as

$$\frac{\mathrm{d}N}{\mathrm{d}t} = q_{\mathrm{therm}} + q_{\mathrm{PSD}} + q_{\mathrm{ESD}} - \upsilon \cdot N - \rho N^2 \ .$$

Because q_{ESD} is pressure dependent (compare equation (A.5)), it reduces the pumping rate and the differential equation has the form of

$$\frac{\mathrm{d}N}{\mathrm{d}t} = q_{\mathrm{therm}} + q_{\mathrm{PSD}} + \left(\eta_{\mathrm{e}} \chi_{\mathrm{e}} \cdot I - \upsilon\right) \cdot N - \rho N^2 \ .$$

This Riccatiian differential equation is solved by

$$\begin{aligned} N(t) = &-\frac{1}{2\rho} \sqrt{4 q_{\mathrm{PSD}} \rho + 4 q_{\mathrm{therm}} \rho + \upsilon^2 - 2\upsilon \eta_{\mathrm{e}} \chi_{\mathrm{e}} \cdot I + \eta_{\mathrm{e}}^2 \chi_{\mathrm{e}}^2 \cdot I^2} \ldots \\ &\ldots \tanh\left(\frac{C_1}{2} \sqrt{4 q_{\mathrm{PSD}} \rho + 4 q_{\mathrm{therm}} \rho + \upsilon^2 - 2\upsilon \eta_{\mathrm{e}} \chi_{\mathrm{e}} \cdot I + \eta_{\mathrm{e}}^2 \chi_{\mathrm{e}}^2 \cdot I^2} \ldots \right. \\ &\left. \ldots - \sqrt{4 q_{\mathrm{PSD}} \rho + 4 q_{\mathrm{therm}} \rho + \upsilon^2 - 2\upsilon \eta_{\mathrm{e}} \chi_{\mathrm{e}} \cdot I + \eta_{\mathrm{e}}^2 \chi_{\mathrm{e}}^2 \cdot I^2} \cdot t \right) \ldots \\ &\ldots + \frac{1}{2\rho} \left(\eta_{\mathrm{e}} \chi_{\mathrm{e}} I - \upsilon \right) \end{aligned}$$

C_1 is a constant which could be determined from the initial conditions of $N(t)$. In the equilibrium state at $t \to \infty$ where $\tanh(-t) \to -1$, the number of residual gas stabilizes to

$$N = \sqrt{\frac{q_{\mathrm{PSD}} + q_{\mathrm{therm}}}{\rho} + \frac{\upsilon^2 - 2\upsilon \eta_{\mathrm{e}} \chi_{\mathrm{e}} \cdot I + \eta_{\mathrm{e}}^2 \chi_{\mathrm{e}}^2 \cdot I^2}{4\rho^2}} + \frac{\eta_{\mathrm{e}} \chi_{\mathrm{e}} I - \upsilon}{2\rho} \ .$$

Using the second binomial formula reverse after squaring of the whole equation, the term outside the

square can be integrated into it. One obtains

$$N = \sqrt{\frac{q_{\mathrm{PSD}} + q_{\mathrm{therm}}}{\rho} + \frac{\upsilon^2 - 2\upsilon\eta_{\mathrm{e}}\chi_{\mathrm{e}} \cdot I + \eta_{\mathrm{e}}^2\chi_{\mathrm{e}}^2 \cdot I^2}{2\rho^2}}$$

Including equations (A.6) and (A.7) into this equation yields

$$N = \sqrt{\frac{\eta_\gamma \delta \cdot E \cdot I + q_{\mathrm{therm}}}{\rho} + \frac{\left(\eta_{\mathrm{e}}\chi_{\mathrm{e}} \cdot I - \upsilon\right)^2}{2\rho^2}} \,. \tag{A.9}$$

Parameterizing the Pressure Evolution Since the desorption yield for PSD and ESD changes for different irradiated materials and desorbed gas species, the creation of an exact model is not in the scope of this work. Instead, equation (A.9) is transferred into a pressure and the resulting equation is parameterized suitably. By using the parameters

$$\begin{aligned}
\mathcal{P}_0 &= \frac{k_{\mathrm{B}}T}{V}\sqrt{\frac{q_{\mathrm{therm}} + \frac{1}{2}\rho^{-1}\upsilon^2}{\rho}} \,, \\
\Lambda(E) &= \frac{k_{\mathrm{B}}^2T^2}{V^2}\left(\frac{\eta_\gamma(E)\,\delta E - \rho^{-1}\upsilon\eta_{\mathrm{e}}(E)\,\chi_{\mathrm{e}}}{\rho}\right) \text{ and} \\
\Xi(E) &= \frac{k_{\mathrm{B}}^2T^2}{V^2}\frac{\eta_{\mathrm{e}}^2(E)\,\chi_{\mathrm{e}}^2}{2\rho^2} \,,
\end{aligned}$$

the average pressure of the vacuum system be expressed as

$$\mathcal{P}(E, I) = \frac{k_{\mathrm{B}}T}{V} \cdot N(E, I) = \sqrt{\mathcal{P}_0^2 + \Lambda(E) \cdot I + \Xi(E) \cdot I^2} \,.$$

The parameters $\mathcal{P}_0$, $\Lambda(E)$ and $\Xi(E)$ along with their energy dependence can be obtained by fitting $\mathcal{P}(E, I)$ on the measured datasets for different beam energies.

A.8 Functional Principle of MolFlow+

MolFlow+ determines the local pressure in the modeled vacuum system (see e.g. figure A.5) by emitting test particles with random thermal initial velocity and position from the desorbing surfaces and tracking their movement in the vacuum system. Each collision of the test particle with the inner surface is set as a start point for another random emission of it, as long as it is not removed by one of the pumps.

Since the modeled section of the vacuum system in reality is connected to the adjoining vacuum system of the storage ring, it cannot be considered as an isolated system. To emulate this continuity, every particle impinging at the modeled longitudinal end fitting of the beam pipe, is transmitted to the opposite end fitting where it continues its propagation. The tracking process is repeated for typically 10^6 to 10^9 test particles to reduce the statistical error. Exemplaric trajectories of test particles entering the antechamber of one of the pump sections are shown in figure A.6.

The number of impingements of the particles with each surface segment is recorded. The pressure on one surface is proportional to the fraction of the number of impingements to the total number of tracked

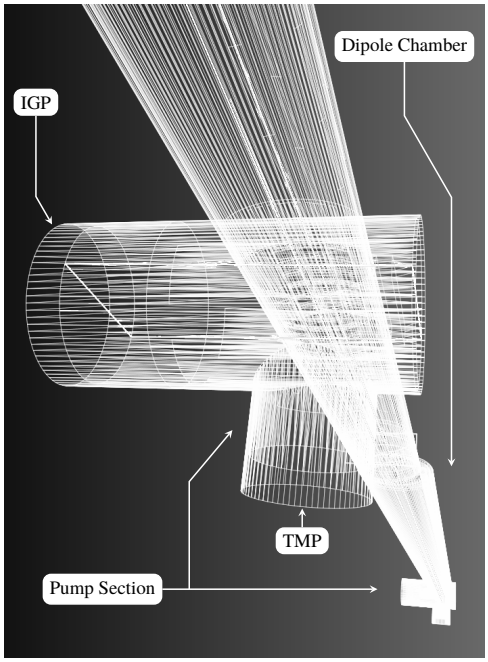

Figure A.5: A section of the storage ring's vacuum system as it has been modeled in MolFlow+. It comprises two pump sections, each equipped with a TMP and IGP, between which a dipole chamber is connected.

test particles. With the known total desorption rate of the vacuum system, the pressure can be determined. An exemplaric simulated pressure profile is shown in figure A.7. See [KA14, section 4] for more details.

A.9 Realistic Impact Ionization Production Rate

Derivation of the Production Rate

In the definition of the production rate (see equation (2.8) and equation (3.5)) the number density of the residual gas inside the beam is assumed to be equal to the density surrounding the beam n_{rgm}. In general, this is an approximation as the local number density of the electrically neutral residual gas is decreased due to the process of ionization. The ionized molecules are replaced by a constant inflow of new neutral residual gas from outside the beam. For the number of residual gas molecules within the beam N_{in}, the differential equation can be formulated as

$$\frac{\mathrm{d}N_{\mathrm{in}}}{\mathrm{d}t} = \frac{\mathrm{d}N_{\mathrm{out}}^{\mathrm{o}\to\mathrm{i}}}{\mathrm{d}t} - \frac{\mathrm{d}N_{\mathrm{in}}^{\mathrm{i}\to\mathrm{o}}}{\mathrm{d}t} - \frac{\mathrm{d}N_{\mathrm{in}}^{\mathrm{ion}}}{\mathrm{d}t} \,. \tag{A.10}$$

Here, $\mathrm{d}N_{\mathrm{out}}^{\mathrm{o}\to\mathrm{i}}/\mathrm{d}t$ is the inflow rate of neutral residual gas molecules into the beam volume V_{beam} and $\mathrm{d}N_{\mathrm{in}}^{\mathrm{i}\to\mathrm{o}}/\mathrm{d}t$ the rate with which neutral residual gas propagates out of it. $\mathrm{d}N_{\mathrm{in}}^{\mathrm{ion}}/\mathrm{d}t$ is the reduction of the number of the neutral residual gas molecules due to ionization. The complete vacuum system has a volume V_{vac} in which the residual gas molecules are present with a number density n_{rgm}. In total, N_{rgm} residual gas molecules are in the system. The complete vacuum system without the beam volume has a number density n_{out}. n_{in} represents the number density of ionization targets for the beam within V_{beam}. The different volumes and densities of the discussed scenario are visualized in figure A.8.

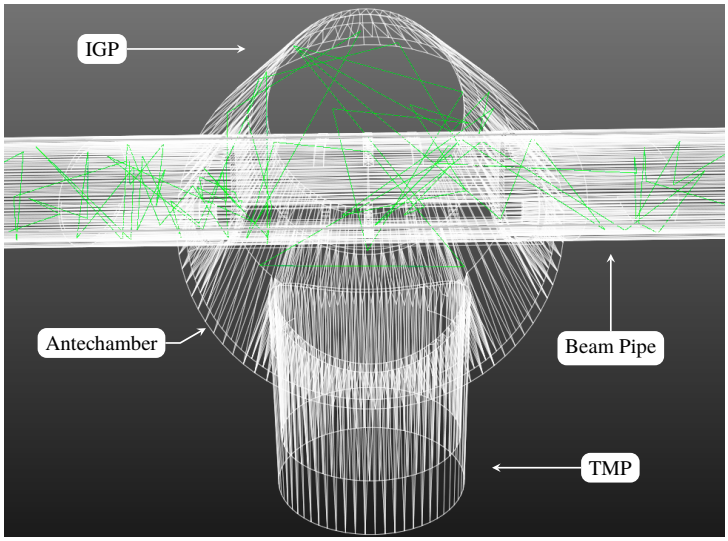

Figure A.6: Trajectories of the residual gas molecules at one of the pumping sections, simulated by MolFlow+. The trajectories are shown as green lines.

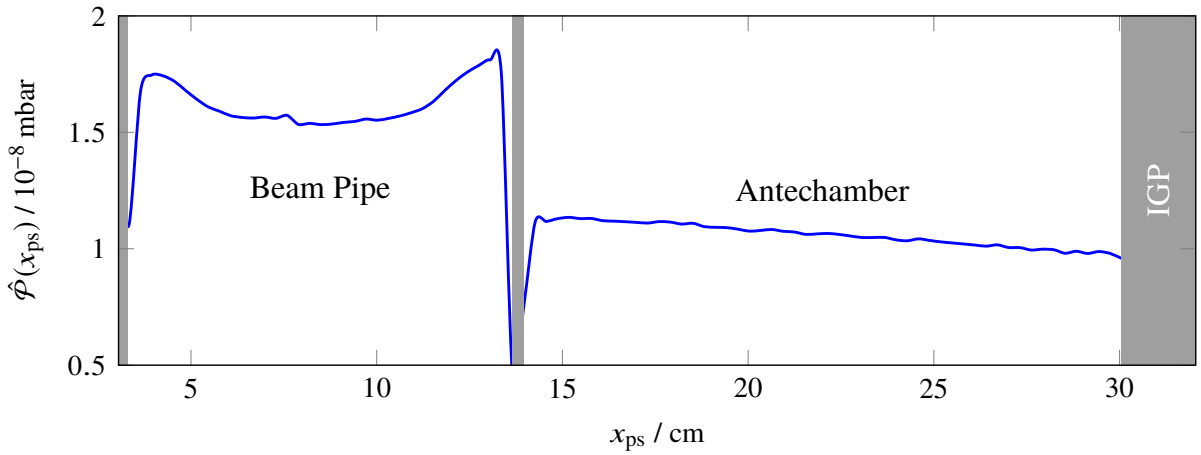

Figure A.7: Simulated pressure profile in the pump section along in the horizontal plane. Here, the beam pipe is connected to the antechamber. The inflowing residual gas is either pumped by the TMP below the perforated beam pipe or the IGP at the front side of the antechamber.

In terms of number density, equation (A.10) can be rewritten as

$$\frac{\mathrm{d}N_{\mathrm{in}}}{\mathrm{d}t} = (V_{\mathrm{vac}} - V_{\mathrm{beam}})\frac{\mathrm{d}n_{\mathrm{out}}^{\mathrm{o}\to\mathrm{i}}}{\mathrm{d}t} - V_{\mathrm{beam}}\frac{\mathrm{d}n_{\mathrm{in}}^{\mathrm{i}\to\mathrm{o}}}{\mathrm{d}t} - \frac{\mathrm{d}N_{\mathrm{in}}^{\mathrm{ion}}}{\mathrm{d}t} \,. \tag{A.11}$$

Here, $n_{\mathrm{out}}^{\mathrm{o}\to\mathrm{i}}$ is the number density of residual gas which is drifting into V_{beam} and $n_{\mathrm{in}}^{\mathrm{i}\to\mathrm{o}}$ is the number density of residual gas which drifts out. $\mathrm{d}N_{\mathrm{in}}^{\mathrm{ion}}$ is the number of residual gas molecules which is singly ionized by the electron beam. The production rate of twofold ionized residual gas is lower than single-ionization as has already been outlined in the introduction of chapter 3. Additionally, this production rate is reduced by a factor of η which is assumed to be smaller than one. Thus, its contribution is omitted.

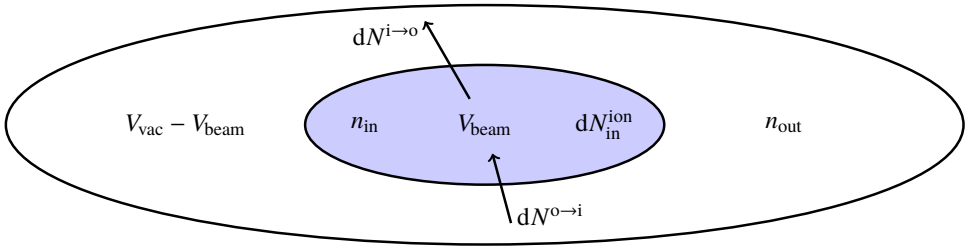

Figure A.8: Different volumes, number densities and particles flows in the scenario.

For the number density reduction due to out-drifting residual gas, one obtains

$$\frac{\mathrm{d}n_{\mathrm{in}}^{\mathrm{i}\to\mathrm{o}}}{\mathrm{d}t} = \frac{1}{V_{\mathrm{beam}}}\frac{\mathrm{d}N_{\mathrm{in}}^{\mathrm{i}\to\mathrm{o}}}{\mathrm{d}t} = \frac{A_{\mathrm{beam}}\,\langle v\rangle}{V_{\mathrm{beam}}} n_{\mathrm{in}}\ . \tag{A.12}$$

This expression is derived from the definition of the particle flow, which can be expressed in terms of a particle current density. This density is the product of particle density and velocity of these particles. A_{beam} is the surface of the beam, being the delimitation to the rest of the vacuum system. $\langle v\rangle$ is the mean velocity of the residual gas molecules and atoms, given by the average thermal drift velocity of equation (2.3).

For the ion production rate, equation (2.8) can be used to obtain

$$\frac{\mathrm{d}N_{\mathrm{in}}^{\mathrm{ion}}}{\mathrm{d}t} = R_{\mathrm{p}} \cdot N_{\mathrm{e}} = \sigma_{\mathrm{ion}}\beta c N_{\mathrm{e}} n_{\mathrm{in}}\ , \tag{A.13}$$

where N_{e} is the number of electrons in the beam.

For simplification, one defines

$$\hat{A} = A_{\mathrm{beam}}\,\langle v\rangle \qquad \text{and} \qquad \hat{G} = \sigma_{\mathrm{ion}}\beta c N_{\mathrm{e}}\ .$$

The inflow density rate can be expressed similarly to equation (A.12) as

$$\frac{\mathrm{d}n_{\mathrm{out}}^{\mathrm{o}\to\mathrm{i}}}{\mathrm{d}t} = \frac{1}{V_{\mathrm{vac}} - V_{\mathrm{beam}}}\frac{\mathrm{d}N_{\mathrm{out}}^{\mathrm{o}\to\mathrm{i}}}{\mathrm{d}t} = \frac{\hat{A}}{V_{\mathrm{vac}} - V_{\mathrm{beam}}} \cdot n_{\mathrm{out}}\ . \tag{A.14}$$

n_{out} can be expressed via the vacuum system's number density n_{rgm} and n_{in} by

$$n_{\mathrm{out}} = \frac{V_{\mathrm{vac}} n_{\mathrm{rgm}} - V_{\mathrm{beam}} n_{\mathrm{in}}}{V_{\mathrm{vac}} - V_{\mathrm{beam}}}\ ,$$

using

$$n_{\mathrm{rgm}} = \frac{N_{\mathrm{in}} + N_{\mathrm{out}}}{V_{\mathrm{vac}}} = \frac{V_{\mathrm{beam}} n_{\mathrm{in}} + \left(V_{\mathrm{vac}} - V_{\mathrm{beam}}\right) n_{\mathrm{out}}}{V_{\mathrm{vac}}}\ .$$

Here, N_{out} is the number of neutral residual gas molecules confined in a volume $V_{\mathrm{vac}} - V_{\mathrm{beam}}$ which are not interacting with the beam. It is implicitly assumed that the number density n_{rgm} in the whole vacuum system remains constant in time. This is a valid assumption since V_{beam} is much smaller than V_{vac} and because the vacuum systems number density is kept constant by incoming new residual gas molecules from the mechanisms of diffusion, permeation and desorption.

The differential equation for the time dependent n_{in} is obtained on basis of equation (A.11) as

$$\frac{\mathrm{d}n_{\mathrm{in}}}{\mathrm{d}t} = \frac{\hat{A}}{V_{\mathrm{beam}}}\left(\frac{V_{\mathrm{vac}}n_{\mathrm{rgm}} - V_{\mathrm{beam}}n_{\mathrm{in}}}{V_{\mathrm{vac}} - V_{\mathrm{beam}}} - \left(1 + \frac{\hat{G}}{\hat{A}}\right)n_{\mathrm{in}}\right) ,$$

using equations (A.12) to (A.14) along with the relation $N_{\mathrm{in}} = V_{\mathrm{beam}}n_{\mathrm{in}}$.

The solution of this differential equation reads

$$n_{\mathrm{in}}(t) = \underbrace{C_1 \cdot e^{-\left(\frac{\hat{A}+\hat{G}}{V_{\mathrm{beam}}} + \frac{\hat{A}}{V_{\mathrm{vac}}-V_{\mathrm{beam}}}\right)t}}_{:=\tilde{P}} + \underbrace{\frac{\hat{A}n_{\mathrm{rgm}}V_{\mathrm{vac}}}{\hat{A}V_{\mathrm{vac}} + \left(V_{\mathrm{vac}} - V_{\mathrm{beam}}\right)\hat{G}}}_{:=n_{\mathrm{rgm}}\cdot\tilde{Q}} . \tag{A.15}$$

The solution consists of a time depended and a time independent part, which are denoted as $\tilde{P}$ and $n_{\mathrm{rgm}} \cdot \tilde{Q}$. C_1 is a constant which corresponds to the initial number density before the beam ionizes the residual gas molecules and atoms. It must be chosen the way that the sum of $\tilde{P}$ and $n_{\mathrm{rgm}} \cdot \tilde{Q}$ equals n_{rgm} for $t = 0\,\mathrm{s}$:

$$C_1 = n_{\mathrm{rgm}}\left(1 - \tilde{Q}\right) = n_{\mathrm{rgm}}\left(1 - \frac{\hat{A}n_{\mathrm{rgm}}V_{\mathrm{vac}}}{\hat{A}V_{\mathrm{vac}} + \left(V_{\mathrm{vac}} - V_{\mathrm{beam}}\right)\hat{G}}\right) .$$

Consequently, equation (A.15) can be rewritten as

$$n_{\mathrm{in}}(t) = n_{\mathrm{rgm}}\left(1 - \tilde{Q}\right) \cdot e^{-\tilde{C}(t-t_0)} + n_{\mathrm{rgm}} \cdot \tilde{Q} .$$

$\tilde{C}$ is the decay constant. This equation describes an exponential decrease of n_{in} to an equilibrium density, which is represented by the $n_{\mathrm{rgm}} \cdot \tilde{Q}$ term. In equilibrium, the rate of which new residual gas drifts into V_{beam} is equal to the rate of out-drifting and ionized residual gas.

Figure A.9 shows how n_{in} changes in time, when the electron beam is injected into the storage ring. Without beam, at $t < t_0$ the number density within the beam is equal to the one outside. When the beam begins to ionize the neutral residual gas at $t \geq t_0$, $n_{\mathrm{in}}(t)$ decreases exponentially with the decay constant $\tilde{C}$. For $t \to \infty$, an equilibrium of inflow- and ionization rate emerges and an equilibrium number density establishes at $n_{\mathrm{rgm}} \cdot \tilde{Q}$.

The equilibrium residual gas density $n_{\mathrm{in}}(t \to \infty)$ reads

$$n_{\mathrm{in}}(t \to \infty) = \frac{\hat{A}n_{\mathrm{rgm}}V_{\mathrm{vac}}}{\hat{A}V_{\mathrm{vac}} + \left(V_{\mathrm{vac}} - V_{\mathrm{beam}}\right)\hat{G}} ,$$

which allows to determine the realistic production rate by its definition in equation (2.6). Because the relation

$$R_{\mathrm{p,real}} = \underbrace{\sigma_{\mathrm{ion}}\beta c}_{=\hat{G}/N_{\mathrm{e}}} \cdot n_{\mathrm{in}}(t \to \infty) \qquad \text{and} \qquad R_{\mathrm{p}} = \sigma_{\mathrm{ion}}\beta c n_{\mathrm{rgm}} ,$$

applies for the realistic and the idealized production rate (compare equation (2.8)), $R_{\mathrm{p,real}}$ can be rewritten in in terms of R_{p}:

$$R_{\mathrm{p}}(t \to \infty) = R_{\mathrm{p,real}} = R_{\mathrm{p}} \cdot \tilde{Q} = R_{\mathrm{p}} \cdot \frac{A_{\mathrm{beam}}\left\langle v\right\rangle V_{\mathrm{vac}}}{A_{\mathrm{beam}}\left\langle v\right\rangle V_{\mathrm{vac}} + \left(V_{\mathrm{vac}} - V_{\mathrm{beam}}\right)\sigma_{\mathrm{ion}}N_{\mathrm{e}}\beta c} ,$$

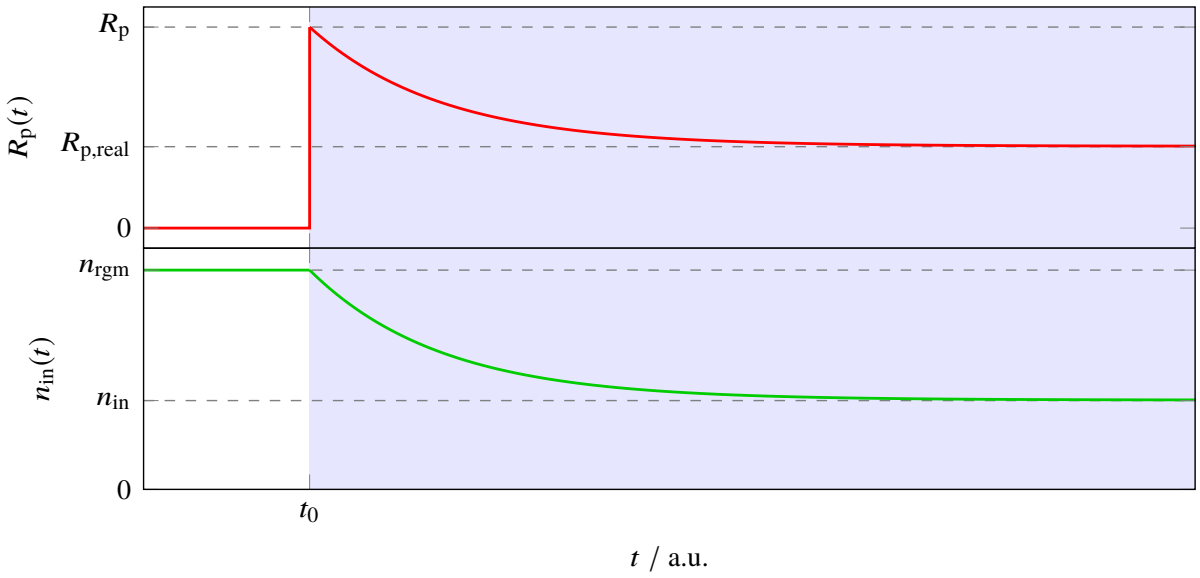

Figure A.9: Schematic progress of $R_p(t)$ and $n_{in}(t)$ with time t. Without electron beam, the production rate is zero and the number density in the region of the beam path is equal to the number density in the vacuum system. When the beam is injected at t_0, denoted as the light blue background, the electron start to ionize residual gas molecules with a production rate R_p which is equal to the idealized one. Because less neutral residual gas molecules drift into the beam volume than the one being ionized, the number density $n_{in}(t)$ drops below the initial density of n_{rgm}. After a specific time an equilibrium between in-drifting and ionization establishes and the number density of neutral gas stabilizes at $n_{in}(t \to \infty)$. So does the production rate at $R_{p,real}$. Note that the effect of the number density reduction is exaggerated to visualize the principle.

which is the realistic production rate of the ionization of residual gas molecules or atoms, assuming a constant pressure and only considering one-fold ionization of the gases. The formula can be rewritten by using equation (2.1) to be more technically applicable as

$$R_{p,real} = R_p \cdot \frac{A_{beam} \langle v \rangle V_{vac}}{A_{beam} \langle v \rangle V_{vac} + \left(V_{vac} - V_{beam}\right) \cdot \frac{\sigma_{ion} I C}{e}} ,$$

where I is the electron current, βc the beam's velocity and C is the circumference of the accelerator.

Estimation for the ELSA Storage Ring

To estimate the deviation of the realistic production rate to the idealized production rate for the ELSA storage ring, namely the parameter $\tilde{Q}$, the beam is approximated as a homogeneous elliptical beam with constant dimensions along the accelerator. For the ellipse's semi-major and minor axis, the average horizontal and vertical beam size have been chosen[9]. In similar approximation, the volume of the vacuum system has been estimated. In accordance with the geometry of the majority of installed elliptical beam pipes, the semi-major and minor axis correspond to 60.6 mm and 20.7 mm, respectively (compare with section 3.1.1). These assumptions allows for an estimation for A_{beam}, V_{vac} and V_{beam}. As the beam

[9] From the optics simulation program ELEGANT, one obtains for the average beta functions $\langle \beta_x \rangle = 8.6\,\text{m}$ and $\langle \beta_x \rangle = 8.8\,\text{m}$ and for the average horizontal dispersion $\langle D_x \rangle = 2.7\,\text{m}$.

emittance, and thus the average beam size, is energy dependent (see section 2.3.3) one obtains values of

$$A_{\text{beam}} = 0.84 \text{ to } 2.25\,\text{m}^2 \qquad \text{and} \qquad V_{\text{beam}} = 0.76 \text{ to } 2.02\,\text{m}^3$$

for beam energies ranging from 1.2 to 3.2 GeV. The complete vacuum system amounts to $V_{\text{vac}} \approx 45\,\text{m}^3$, but it can be seen as a lower estimate, as the vacuum chambers in other integrated components such as septa and kicker are more voluminous than the assumed dimensions.

For an upper-limit estimation of $R_{\text{p,real}}$, it is assumed that the residual gas in the vacuum system is completely consisting of CO_2. Due to its mass of 44 u, this gas species has the lowest mean thermal velocity of all relevant residual gas species. According to equation (2.3), its velocity $\langle v \rangle$ is equal to $189\,\text{m}\,\text{s}^{-1}$. This implies a low inflow rate of new CO_2 into the beam volume. Additionally, CO_2 has the highest impact ionization cross section $\sigma_{\text{ii},i}$ of all relevant species reaching from 2.61 Mb at 1.2 GeV to 2.82 Mb at 3.2 GeV (compare table 3.5). One may assume that this process is the dominant ionization mechanism and $\sigma_{\text{ion}} = \sigma_{\text{ii},i}$.

For an assumed beam current of 200 mA, the realistic production rate can be obtained to be a fraction of

$$\frac{R_{\text{p,real}}}{R_{\text{p}}} = 0.99967 \text{ to } 0.99987$$

of the idealized production rate R_{p} between 1.2 and 3.2 GeV, respectively. Since the nominal current in the storage ring seldomly reaches these beam currents and the vacuum composition is not comprised totally of CO_2 but rather consists of H_2, this effect can be neglected and the realistic impact ionization production rate is equal to the idealized rate.

This effect may has to be taken into account for other accelerators, if

- the beam current exceeds 200 mA in accelerators similar to the storage ring.
- the cross section of the ionization process increases. This may be the case for a future accelerator, in which field ionization is the dominant ion production process.
- the thermal velocity of the residual gas molecules is reduced significantly. This may be the case in accelerators where super conducting magnets or rf cavities are operated. Of course, the pressure in these regions may be already low in comparison with other cryo-less sections due to the condensation of the residual gas on the cold surface of the beam pipes.

A.10 Photo Ionization and the Tool PhotoIonProd

A.10.1 Photo Ionization Interaction Length

For the storage ring, the average interaction length l_{int}, the path length an emitted synchrotron radiation photon propagates until it hits the vacuum chamber, is estimated from geometric considerations. Figure A.10 shows the geometric model for this problem.

When considering a photon being emitted at the beginning of the dipole magnet, an initial interaction length of

$$l_{\text{start}} = \sqrt{\frac{d^2}{4} + Rd}$$

is obtained by simple geometric calculations. Here, the synchrotron radiation spot exactly hits the vacuum chamber edge's which is still positioned within the dipole magnet. d is the horizontal diameter of the beam pipe and R is the bending radius of the electron beam in the dipole magnets. With a radius of approximately 11 m and a beam pipe diameter of approximately 10.5 cm, an interaction length of

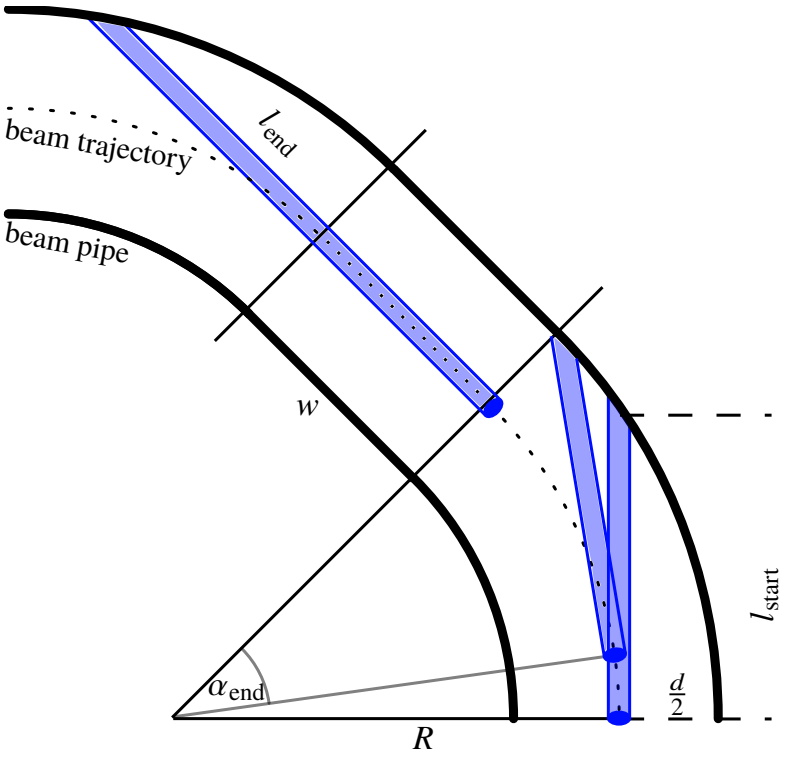

Figure A.10: Schematic drawing for the visualization of the geometric modeling of the interaction length.

1.06 m can be determined. However, this interaction length is not representative for every position in the accelerator. At the end of dipole magnets, this interaction length can be much longer. It depends strongly on the length w of the following drift section. Here, the interaction length increases to

$$l_{\text{end}} = \sqrt{\frac{d^2}{4} + Rd} + w \; .$$

In a worst-case estimation, a mean interaction length is defined for one dipole with an adjoined drift. Out of simple geometric considerations, the angle of beam deflection α_{max} is obtained within which the interaction length is still equal to l_{start} with

$$\alpha_{\text{max}} = \alpha_{\text{dipole}} - \alpha_{\text{end}} = \alpha_{\text{dipole}} - \arcsin\left(\frac{l_{\text{start}}}{R + \frac{d}{2}}\right) \; .$$

For the storage ring, this angle is 9.55° because the 24 dipoles deflect the electron with an angle of $\alpha_{\text{dipole}} = 15°$ each. For the angles $> \alpha_{\text{end}}$, the assumed condition does not hold true anymore. Therefore, the worst-case assumption is made that the interaction length for $\alpha > \alpha_{\text{max}}$ is equal to l_{end}.

For a single dipole, the mean interaction length can be estimated as

$$\langle l_{\text{int}} \rangle = \frac{\alpha_{\text{max}} \cdot l_{\text{start}} + \alpha_{\text{end}} \cdot l_{\text{end}}}{\alpha_{\text{dipole}}} \; .$$

In the storage ring, there basically are three adjoining drift lengths w, 2 dipoles with $w = 1.1$ m, 16

dipoles with $w = 2.3\,\mathrm{m}$ and 6 dipoles with approximately 7.4 m. For the shorter drift, an interaction length of 1.5 m is obtained, for the medium length 1.9 m and for the longer one 3.7 m. Using the number of appearances in the accelerator as a weight, the mean interaction length for synchrotron radiation at the storage ring is estimated as

$$\langle l_{\mathrm{int}} \rangle \leq 2.3\,\mathrm{m}\,. \tag{A.16}$$

α_{break} indicates the angle of beam deflection α in a dipole magnet until which no synchrotron radiation photon, being produced at $\alpha < \alpha_{\mathrm{break}}$, is absorbed at the dipole chamber's walls. From simple geometric considerations, it can be shown that α_{break} is equal to α_{end}. Additionally, this angle can be expressed as

$$\alpha_{\mathrm{break}} = \arccos\left(\frac{R}{R + \frac{d}{2}}\right)\,.$$

A.10.2 Mathematical Background for PhotoIonProd

In the following, the basic mathematical background of PhotoIonProd is briefly sketched. The documentation for this Matlab script can be found in appendix B.2.1.

The script is initialized with the synchrotron radiation source been farest away from the longitudinal position of the photo production map. The distance between source and map is given as the difference in their local angle of beam deflection α. Per definition the map is positioned at $\alpha = 0°$. The initial position of the source is $\alpha = \alpha_0$. If the map is positioned in the midst of a dipole which deflects the electron beam to a total of 15°, α_0 is equal to 7.5°.

The initial distance between the souce and the map is given by

$$l_0 = R \cdot \tan\left(\alpha_0\right)\,.$$

At this distance from the source, an equidistant grid of transversal cartesian $\tilde{x}$ and $\tilde{z}$ coordinates is defined onto which the synchrotron radiation is emitted. These coordinates are transferred into the spherical coordinates φ and Θ prior to the actual simulation and are stored in a look-up table.

The energy dependent angular synchrotron radiation flux is given by [Lee04, chapter 4, section I.3, E, equation 4.71]

$$\breve{\Phi}_\gamma(E_\gamma, \Theta(\tilde{x}, \tilde{z})) = \frac{\mathcal{E}_\gamma\,\mathrm{d}E_\gamma}{\mathrm{d}\Theta\,\mathrm{d}\omega} = \frac{3\mathrm{e}^2}{16\pi^3\varepsilon_0\hbar c}\frac{\delta\omega}{\omega}\left(\frac{\omega}{\omega_\mathrm{c}}\right)^2(1+X^2)^2\left[K_{\frac{2}{3}}^2(\xi) + \frac{X^2}{1+X^2}K_{\frac{1}{3}}^2(\xi)\right] \tag{A.17}$$

with $K_{\frac{2}{3}}$ and $K_{\frac{1}{3}}$ being the modified Bessel functions of the second kind. X and ξ are defined as

$$X = \gamma\Theta \qquad \text{and} \qquad \xi = \frac{\omega}{2\omega_\mathrm{c}}(1+X^2)^{\frac{3}{2}}\,.$$

ω_c is the critical frequency.

For every $\tilde{x}$ and $\tilde{z}$ coordinate of the equidistant grid, transferred to spherical coordinates via the look-up table, the quantity

$$\langle\sigma_{\mathrm{pi},i}(E_\gamma)\rangle \cdot \breve{\Phi}_\gamma(E_\gamma, \Theta(\tilde{x}, \tilde{z})) = \int_0^\infty \breve{\Phi}_\gamma(E_\gamma, \Theta(\tilde{x}, \tilde{z})) \cdot \sigma_{\mathrm{pi},i}(E_\gamma)\,\mathrm{d}E_\gamma \sim \tilde{\Lambda}(\Theta(\tilde{x}, \tilde{z}))$$

is calculated. This term will be in short denoted by the abbreviation $\tilde{\Lambda}$. This $\tilde{\Lambda}$-value is proportional to the photo ionization production rate (compare equation (3.16)).

In the following, trigonometric calculations are performed to project the individual $\tilde{\Lambda}$ values in a correct manner onto the ion production map. Because both planes, the source's and the production map's plane, are purely transversal they are horizontally tilted to each other by an angle, which is given by the difference between their angles α. The expressions of the trigonometric calculations, projecting $\tilde{\Lambda}$ onto the map, are omitted in this work. The results of it can be viewed in the source code of PhotoIonProd. Contact the author of this work to obtain more detailed information.

A.10.3 Local Photo Ionization Production Rate

The total photo ionization production rate $R_{\mathrm{p,pi}}$ can be transferred into a local quantity $\hat{R}_{\mathrm{p,pi}}(s)$. Here, $\hat{R}_{\mathrm{p,pi}}(s)$ is zero in the straight sections and

$$\left\langle \hat{R}_{\mathrm{p,pi}}(s) \right\rangle = R_{\mathrm{p,pi}} \cdot \frac{\Delta s}{2\pi R}$$

for a longitudinal slice of length Δs in the dipole sections (compare section 2.2.5). This quantity is the average production rate along the dipole magnet. Since the integrated number of emitted synchrotron radiation photons by the electron beam increases linear with s in the dipole, or the covered distance in the dipole, the local production rate $\hat{R}_{\mathrm{p,pi}}(s)$ increases accordingly. This linear increment can be expressed by $f(s)$ which is given by

$$f(s) = 2\frac{s}{l_{\mathrm{dipole}}} ,$$

where l_{dipole} is the total length of one dipole. s is the longitudinal position in reference to the beginning of the magnet. Hence, the local production rate is given as

$$\hat{R}_{\mathrm{p,pi}}(s) = R_{\mathrm{p,pi}} \cdot \frac{\Delta s}{2\pi R} \cdot f(s) = R_{\mathrm{p,pi}} \cdot \frac{\Delta s}{\pi R} \frac{s}{l_{\mathrm{dipole}}} . \tag{A.18}$$

Note that the photo ionization production is assumed to be confined to the dimension of the dipole magnets. But synchrotron radiation photons, which are emitted at the end of dipole magnet, are able to leave this confinement and ionize residual gas molecules outside. These outer contributions are omitted as they are difficult to assess and depend on the beam pipe geometry and dimensions at the individual dipole and its surroundings.

Also note that the assumed linear increment of the number of synchrotron radiation photons, which lead to a linear rise in $\hat{R}_{\mathrm{p,pi}}(s)$, only applies if the horizontal dimension of the vacuum chamber in the dipole magnets is very large. Otherwise, synchrotron radiation photons are absorbed when hitting the chamber and a linear increment of the photon number can only be maintained up to a specific angle of beam deflection α_{break} in the dipole magnet. For angles $> \alpha_{\mathrm{break}}$, the number of synchrotron radiation photons is constant. Here, the number of absorbed and emitted synchrotron radiation photons is equal, resulting in a constant local production rate.

A.11 Critical Mass Concept

Transfer Matrix Formalism

To evaluate the stability of different ion species in an accelerator with a bunched beam, the *transfer matrix formalism* (see e.g. [Wil00, section 3.4]) of accelerator physics is utilized. For an ion with fixed longitudinal position in the accelerator, the passage of one bunch to the next can be expressed as the 2×2

matrix

$$\mathcal{M}_{\text{passage},x,z} = \mathcal{M}_{\text{drift}} \cdot \mathcal{M}_{\text{bunch},x,z}$$

for each transversal plane (see figure 4.1 in section 4.1.1). In the gap between the two bunches, no force applies and the ions propagate with a constant velocity[10]. Using a similar coordinate system for the ions' transversal coordinates as for the electron beam (compare section 2.3.1), namely $\mathbf{X}_i = (x_i, x_i')^T$ and $\mathbf{Z}_i = (z_i, z_i')^T$, this drift can be expressed as the matrix [BB80, section 4]

$$\mathcal{M}_{\text{drift}} = \begin{pmatrix} 1 & l_{\text{drift}} \\ 0 & 1 \end{pmatrix}$$

which is equal for the horizontal and vertical plane. Here,

$$l_{\text{drift}} = \beta c \cdot (t_{\text{rf}} - t_{\text{bunch}}) \qquad \text{and} \qquad t_{\text{bunch}} = \frac{l_{\text{bunch}}}{\beta c} .$$

l_{bunch} is the bunch length[11]. In this calculation the longitudinal density distribution of the bunch is assumed to be a discrete one. It is zero for the time between the bunches ($t_{\text{bunch}} \leq t \leq t_{\text{rf}}$) and constant during the bunch passage ($0 \leq t \leq t_{\text{bunch}}$).

Under the assumption that the magnitude of the reversing force of the bunch rises linearly with the ions' displacement from the beam center x_i or z_i, the attractive force of the electron beam resembles a focusing quadrupole magnet in both transversal planes. Thus, $\mathcal{M}_{\text{bunch},x,z}$ can be expressed as [Wil00, section 3.4, equation 3.72]

$$\mathcal{M}_{\text{bunch},x,z} = \begin{pmatrix} \cos\left(\sqrt{k_{x,z}} \cdot \beta c t_{\text{bunch}}\right) & \frac{1}{\sqrt{k_{x,z}}} \sin\left(\sqrt{k_{x,z}} \cdot \beta c t_{\text{bunch}}\right) \\ -\sqrt{k_{x,z}} \sin\left(\sqrt{k_{x,z}} \cdot \beta c t_{\text{bunch}}\right) & \cos\left(\sqrt{k_{x,z}} \cdot \beta c t_{\text{bunch}}\right) \end{pmatrix} . \tag{A.19}$$

where $k_{x,z}$ is the focusing strength of the electron beam for the horizontal or vertical plane.

Focusing Strength of the Beam

The expression of the beam's focusing strength for the ions is derived by comparing the differential equation for the ions' transversal motion in equation (2.44) with the general differential equation of a harmonic oscillator.

The differential equation of an ion i in the beam, generating an assumed harmonic oscillator-like electrical potential, with amplitude x_i is given as

$$\frac{\mathrm{d}^2 x_i}{\mathrm{d}t^2} = \ddot{x}_i = -\left\langle \tilde{D}_x \right\rangle \cdot x_i .$$

Here, $\left\langle \tilde{D}_x \right\rangle$ is the time averaged "spring constant", characterizing the reversing force of the beam. The differential equation for the ion's transversal motion $x_i(t)$ can also be expressed as (compare

[10] The motion can only be assumed to be an unaccelerated motion, when the repelling space-charge force of the other ions is omitted. Otherwise, this period of the ion trajectory can be expressed in terms of the transfer matrix formalism as the matrix of a defocussing quadrupole.

[11] If a bunch with a Gaussian longitudinal charge density is approximated by a discrete charge density, l_{bunch} is equal to σ_s.

equation (2.44))

$$\ddot{x}_i = -\frac{eZ_i}{m_i} E_x(x_i) = -\underbrace{\frac{eZ_i}{m_i}\frac{E_x(x_i)}{x_i}}_{=\langle \tilde{D}_x \rangle} \cdot x_i \ .$$

m_i is the mass and Z_i the ionization state of the ion i. By comparing this expression with the previous formula, an association of terms with $\langle \tilde{D}_x \rangle$ is possible.

In the considered case, the time averaged "spring constant" of the beam is not of importance. Instead, $\tilde{D}_x$ has to be known during the time when the ion directly encounters a bunch. In-between the bunches, $\tilde{D}_x$ is zero and during the passage of a bunch it is equal to $\tilde{D}_{0,x}$. The definition of the time averaged "spring constant" $\langle \tilde{D}_x \rangle$ can be used to obtain $\tilde{D}_{0,x}$ by using the relation

$$\langle \tilde{D}_x \rangle = \frac{1}{t_{\mathrm{rf}}} \int_0^{t_{\mathrm{rf}}} \tilde{D}_x \, \mathrm{d}t = \frac{1}{t_{\mathrm{rf}}} \left(\underbrace{\int_0^{t_{\mathrm{rf}} - t_{\mathrm{bunch}}} \tilde{D}_x \, \mathrm{d}t}_{=0} + \underbrace{\int_{t_{\mathrm{rf}} - t_{\mathrm{bunch}}}^{t_{\mathrm{rf}}} \tilde{D}_x \, \mathrm{d}t}_{= \tilde{D}_{0,x} \cdot t_{\mathrm{bunch}}} \right) .$$

Consequently, $\tilde{D}_{0,x}$ can be expressed in terms of $\langle \tilde{D}_x \rangle$ as

$$\tilde{D}_{0,x} = \frac{C}{h \, l_{\mathrm{bunch}}} \cdot \langle \tilde{D}_x \rangle$$

by using the relations $h \cdot \lambda_{\mathrm{rf}} = C$, $t_{\mathrm{rf}} = C/(h\beta c)$ and $t_{\mathrm{bunch}} = l_{\mathrm{bunch}}/(\beta c)$. h is the harmonic number, the number of bunches in the accelerator. Thus, $\tilde{D}_x$ is longitudinally compressed into h consecutive bunches.

When transferring the differential equations for $x(t)$ to $x(s)$ ($\ddot{x}$ to x''), the relation

$$k_x = \frac{1}{(\beta c)^2} \cdot \tilde{D}_{0,x}$$

applies. Here, k_x is the horizontal quadrupole strength.

By combining all three relations, the quadrupole strength can be obtained as

$$\vec{k}_i = \begin{pmatrix} k_x \\ k_z \end{pmatrix}_i = \frac{1}{(\beta c)^2} \frac{C}{h \, l_{\mathrm{bunch}}} \frac{eZ_i}{m_i} \begin{pmatrix} \frac{E_x(x_i)}{x_i} \\ \frac{E_z(z_i)}{z_i} \end{pmatrix} . \tag{A.20}$$

for the horizontal plane and vertical plane. $k_{x,z}$ is an individual quantity for each ion species.

Ion Stability and Critical Mass

$\mathcal{M}_{\mathrm{bunch},x,z}$ of equation (A.19) can be expressed as

$$\mathcal{M}_{\mathrm{bunch},x,z} = \begin{pmatrix} 1 & 0 \\ -\frac{1}{f_{x,z}} & 1 \end{pmatrix} ,$$

utilizing the thin lens approximation (see [Wie93, section 5.2.3, equation 5.18]) with $1/f_{x,z} = k_{x,z} \cdot l_{\mathrm{bunch}}$ because $l_{\mathrm{bunch}} \ll \lambda_{\mathrm{rf}}$. Consequently, the transfer matrix for the passage of one bunch to the other can be

expressed as

$$\mathcal{M}_{\text{passage},x,z} = \begin{pmatrix} 1 - \frac{l_{\text{drift}}}{f_{x,z}} & l_{\text{drift}} \\ -\frac{1}{f_{x,z}} & 1 \end{pmatrix} ,$$

where l_{drift} is approximately λ_{rf}.

To calculate the transversal coordinates of an ion for n revolutions of the bunch train consisting of h consecutive bunches, thus after a time of $n \cdot h \cdot t_{\text{rf}}$, the transfer matrix $(\mathcal{M}_{\text{passage},x,z})^{h \cdot n}$ can be obtained by multiplying the individual $\mathcal{M}_{\text{passage},x,z}$ matrices.

Because $\mathcal{M}_{\text{passage},x,z}$ is a periodic linear transformation, the Floquet theory can be applied, which states that for a stable trajectory the relation (compare [Pon94, section 5.2, equation (34)])

$$\left| \text{Tr}\left(\mathcal{M}_{\text{passage},x,z} \right) \right| < 2$$

must hold. Thus, only ions can accumulate whose $\mathcal{M}_{\text{passage},x,z}$ shows a trace smaller than ±2. For $\mathcal{M}_{\text{passage},x,z}$,

$$\left| 2 - \frac{l_{\text{drift}}}{f_{x,z}} \right| < 2 \qquad \text{is obtained which can be rephrased to} \qquad \frac{l_{\text{drift}}}{f_{x,z}} < 4$$

because l_{drift} and $f_{x,z} > 0$.

With $l_{\text{drift}} \approx \lambda_{\text{rf}} = \frac{C}{h}$ and the relation for the focal length, the inequation is given as

$$\frac{C}{h} \cdot k_{x,z} \cdot l_{\text{bunch}} < 4 \, .$$

Utilizing the definition of $k_{x,z}$ from equation (A.20), the inequation provides a boundary for the mass-to-charge ratio of a stable ion species. This boundary is called *critical mass*. All ion species which have a mass-to-charge ratio above

$$\left(\frac{A_i}{Z_i} \right)_{\text{crit},x,z} = \frac{\text{e}}{8\pi\varepsilon_0 (\beta c)^3 m_{\text{p}}} \cdot \frac{I}{h^2} \cdot \frac{C^2}{\sigma_{x,z}(s) \left(\sigma_x(s) + \sigma_z(s) \right)}$$

are in principle able to accumulate in the accelerator in the considered plane.

A.12 Stability Matrix Formalism

In appendix A.11, the formalism of transfer matrices and the Floquet stability criterion has been used to evaluate the critical mass for the storage ring. For ions, the passage of one bunch can be expressed by one drift and one focusing matrix, $\mathcal{M}_{\text{drift}}$ and $\mathcal{M}_{\text{bunch},x,z}$ respectively. Here, the index x denotes the matrix for the horizontal plane and z the matrix for the vertical plane. If the trace of the resulting matrix $\mathcal{M}_{\text{passage},x,z}$ exceeds values of ±2, the considered ion species i with mass m_i and ionization status Z_i shows instable trajectories and cannot not be trapped within the beam potential.

This formalism can also be utilized to estimate the stability of a certain ion species when exposed to a particular filling pattern. It may be called *Stability Matrix Formalism*. Here, the transfer matrix for the passage of one complete bunch train $\mathcal{M}_{\text{bt},x,z}$ is arranged by multiplying h individual bunch passage

matrices $\mathcal{M}^{j}_{\text{passage},x,z}$ as

$$\mathcal{M}_{\text{bt},x,z} = \prod_{j=1}^{h} \mathcal{M}^{j}_{\text{passage},x,z} \,. \tag{A.21}$$

Each matrix is modified according to the bunch current of the particular bunch. For a filling gap, a bucket with zero bunch current, $\mathcal{M}^{j}_{\text{passage},x,z}$ morphs into a drift matrix $\mathcal{M}'_{\text{drift}}$ with a length l_{drift} which is equal to the rf wavelength λ_{rf} because the focusing strength $k_{x,z}$ is zero.

Because the so generated transfer matrix $\mathcal{M}_{\text{bt},x,z}$ is periodic with the accelerator's circumference, the Floquet theory applies. Thus, the stability of different ion species in this inhomogeneous filling pattern can be estimated by the trace of $\mathcal{M}_{\text{bt},x,z}$. If the trace of $\mathcal{M}_{\text{bt},x,z}$ exceeds ±2, the ion trajectory can assumed to be instable, preventing an accumulation of these species.

Ion-Ion Space Charge

For now the ion-ion space charge acting with its repulsive force on every individual ion has been ignored. For $\hat{\eta} > 0$, the formalism has to be modified twofold:

First, the focusing strength of the electron bunch on the ions is reduced by the ions' defocusing space charge, which can be expressed as a negative focusing strength $k_{\text{ion},x,z}(\hat{\eta})$ as

$$k_{x,z} = k_{0,x,z} - k_{\text{ion},x,z}(\hat{\eta}) \,. \tag{A.22}$$

Here, $k_{0,x,z}$ is the focusing strength of the electron bunch for $\hat{\eta} = 0$. For a number of $h' \leq h$ equally filled bunches in the accelerator, the horizontal and vertical components of the focusing strength are given by (compare equation (A.20))

$$\begin{pmatrix} k_{0,x} \\ k_{0,z} \end{pmatrix} = \frac{1}{(\beta c)^2} \frac{C}{h'\, l_{\text{bunch}}} \frac{\mathrm{e}Z_i}{m_i} \begin{pmatrix} \frac{E_x(x_i)}{x_i} \\ \frac{E_z(z_i)}{z_i} \end{pmatrix} \,.$$

The other buckets in the accelerator are assumed to be empty with a bunch current of zero. For an unequal filling of the individual bunches, the focusing strength of the jth bunch can be multiplied by a factor $a_{\text{fill},j} > 0$, which scales the bunch current in reference to the average bunch current. For a bunch with the average bunch current, $a_{\text{fill},j}$ is equal to one. For this factor the relation $\sum_j^h a_{\text{fill},j} = h'$ must hold, to ensure that the sum of all bunch currents is equal to the total beam current in the accelerator. The horizontal and vertical components of $k_{\text{ion},x,z}(\hat{\eta})$ can be expressed as

$$\begin{pmatrix} k_{\text{ion},x}(\hat{\eta}) \\ k_{\text{ion},z}(\hat{\eta}) \end{pmatrix} = \frac{\hat{\eta}}{(\beta c)^2} \frac{\mathrm{e}Z_i}{m_i} \begin{pmatrix} \frac{E_x(x_i)}{x_i} \\ \frac{E_z(z_i)}{z_i} \end{pmatrix} \,.$$

The focusing strength of the ions is assumed to scale linearly with the neutralization. In contrast to the electron beam, the ion population is not bunched but shows a constant line charge density along the accelerator when neglecting potential hollows and assuming a constant local neutralization. Thus, $k_{\text{ion},x,z}$ is reduced by a factor of $\hat{\eta} h' l_{\text{bunch}}/C$ in comparison to $k_{0,x,z}$ of the electron beam. Note that this approach implicitly assumes that the transversal electric field $E_{x,z}$ of the ions has the same shape of the electron beam's field. This in general is not true because the transversal density distribution of the electrons and ions are not alike (compare section 5.1.3).

Secondly, for $\hat{\eta} > 0$, the space in-between the bunches is filled with ions. The ion-ion space charge, with its negative focusing strength, disperse or defocus the individual ions. Thus, the drift matrices $\mathcal{M}_{\text{drift}}$

and $\mathcal{M}'_{\text{drift}}$ transform into the matrices of defocusing quadrupoles [BB80, section 7]

$$O^{(\prime)}_{\text{drift},x,z}(\hat{\eta}) = \begin{pmatrix} \cosh\left(\sqrt{k_{\text{ion},x,z}(\hat{\eta})} \cdot l^{(\prime)}_{\text{drift}}\right) & \frac{1}{\sqrt{k_{\text{ion},x,z}(\hat{\eta})}} \sinh\left(\sqrt{k_{\text{ion},x,z}(\hat{\eta})} \cdot l^{(\prime)}_{\text{drift}}\right) \\ \sqrt{k_{\text{ion},x,z}(\hat{\eta})} \sinh\left(\sqrt{k_{\text{ion},x,z}(\hat{\eta})} \cdot l^{(\prime)}_{\text{drift}}\right) & \cosh\left(\sqrt{k_{\text{ion},x,z}(\hat{\eta})} \cdot l^{(\prime)}_{\text{drift}}\right) \end{pmatrix}.$$

Since l_{drift} and l'_{drift} are typically larger than l_{bunch}, $O^{(\prime)}_{\text{drift}}$ has the form of a thick, defocusing quadrupole. The length $l^{(\prime)}_{\text{drift}}$ is equal to either $l'_{\text{drift}} = \lambda_{\text{rf}}$ for an empty bucket or $l_{\text{drift}} = \lambda_{\text{rf}} - l_{\text{bunch}}$ for the bunch-free part of the rf period.

Adaptation of the Formalism to the Storage Ring

Using O_{drift}, O'_{drift} and the modified $k_{x,z}$ from equation (A.22) in $\mathcal{M}_{\text{bunch},x,z}$[12], the individual matrix $\mathcal{M}_{\text{passage},x,z}$ can be evaluated and the bunch train matrix $\mathcal{M}_{\text{bt},x,z}$ is determined via equation (A.21).

Consider the case where one filling gap of a specific length is used. In figure A.11, the traces of the horizontal (top) and vertical (bottom) bunch train matrices of H_2^+ (cyan) and CO_2^+ (black) for different filling gap lengths are shown. The solid line shows the trace of the bunch train matrix where the beam width is set to the transversal average beam width of the storage ring. The dashed line shows the trace at a position in the storage ring, where the vertical beam width is maximal. The dotted line corresponds to the trace, calculated at a position where the horizontal beam width is maximal. In this scenario, the beam energy is equal to 1.2 GeV and the bunch current is 128 µA. For the average beam width, a filling gap length of 80 buckets is necessary to destabilize H_2^+ in the horizontal plane. If the filling gap length is extended to 210 buckets, this ion species is stable again. Here, the total current in the storage ring is reduced from 35 mA to 8.2 mA due to the increased filling gap. Consequently, the average kick, the ion has experienced during the passage of the bunch train, has been reduced significantly resulting in a lower velocity change after the interaction with the bunch train. consequently, the ion does not move too far from the beam center during the bunch gap. The ion is captured again, when the bunch train passes once more. In the vertical plane, the H_2^+ ion is instable for a filling gap length reaching from 85 to 158 and 180 to 260. For CO_2^+ ions, the trace of the bunch matrices is always in the region ±2. Consequently, CO_2^+ cannot be cleared by the use of filling gaps here.

For a beam energy of 1.2 GeV and a bunch current of 183 µA, figure C.20 in the appendix gives an overview how $\text{Tr}(\mathcal{M}_{\text{bt},x,z})$ evolves for different filling gap lengths in dependence of the mass-to-charge ratio of different ion species.

A.12.1 Stability Analysis for the Storage Ring

As becomes visible in figure A.11, the dotted (horizontally maximal beam width) and the dashed (vertically maximal beam width) lines show significant differencies to the solid line (average beam width). Thus, the ion stability depends on the *local* beam width and changes along the accelerator. Ions which may be instable at some position in the storage ring may be stable in another region. Hence, if this analysis approach should be valid for the complete storage ring, it has to be expanded.

[12] To be also capable of providing a valid formalism for longer bunches, which show a Gaussian longitudinal charge density distribution, $\mathcal{M}_{\text{bunch},x,z}$ can also be expressed as a thick focusing quadrupole. Additionally, it can be subdivided into several parts with reduced $k_{x,z}$ and l_{bunch}. For example, a subdivision into six matrices, each with a length of σ_s. Each matrix represents one 1σ slice of the Gaussian bunch with adjusted $k_{x,z}$ according to the charge density in the corresponding bunch slice.

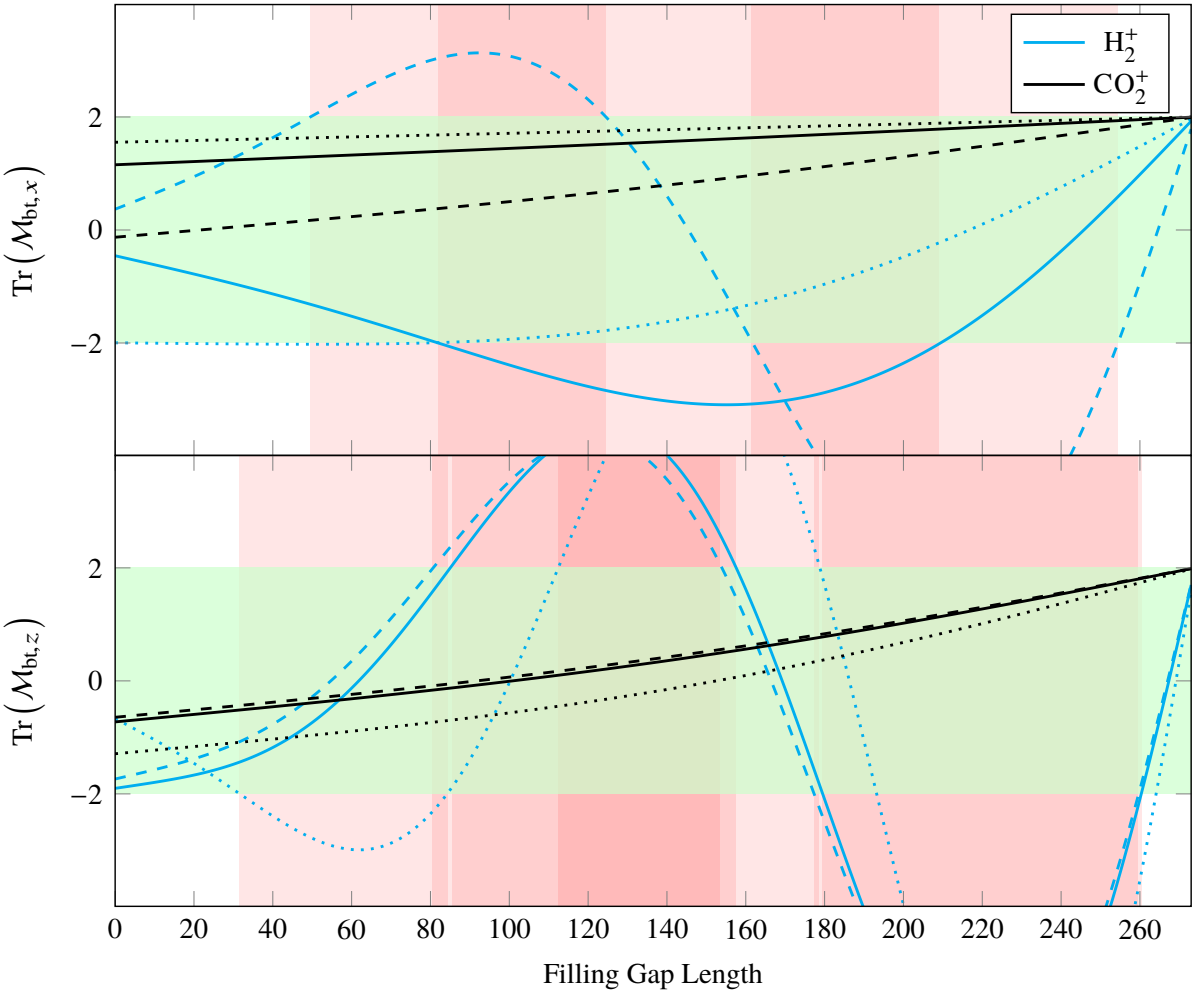

Figure A.11: Simulated trace of the horizontal (top) and vertical (bottom) bunch train matrix for H_2^+ and CO_2^+ ions for different filling gap lengths. Here, the beam energy is equal to 1.2 GeV and the bunch current is 128 µA. For a filling gap length of zero buckets, 35 mA are stored in the accelerator. The neutralization is assumed to be 0 %. The green area indicates the region of stability. The filling gap length intervals in which a species is unstable are highlighted in red. The solid line shows the stability criterion for the average beam width in the storage ring, the dotted line the criterion in a position of the storage ring where the horizontal beam size is maximal. For a maximal vertical beam width, the curve is dashed.

For that purpose with the tool TRACEANALYSIS, implemented in MATLAB, the amount of stable ions in the storage ring for arbitrary filling patterns can be calculated. For a given beam energy, bunch current I_b (or initial current I_0 for filling gap length of zero buckets) and neutralization, the tool subsequently determines which of the relevant ion species is stable at certain longitudinal positions in the storage ring. Here, the ion species are marked as either stable ($|\mathrm{Tr}(\mathcal{M}_{\mathrm{bt},x,z})| \leq 2$) or instable ($|\mathrm{Tr}(\mathcal{M}_{\mathrm{bt},x,z})| > 2$). If an ion species is either horizontally or vertically instable, it is considered to be unstable. The s-axis is sampled with a suitable[13] resolution along the storage ring, allowing for the determination of the fraction of stable ions Υ_stab in the accelerator when exposed to a certain filling pattern. For a successful

[13] Here, the stability analysis is done along one half of the storage ring with a resolution of approximately 50 cm. The second half is ignored because the analysis would give the same results due to mirrored identical optical functions.

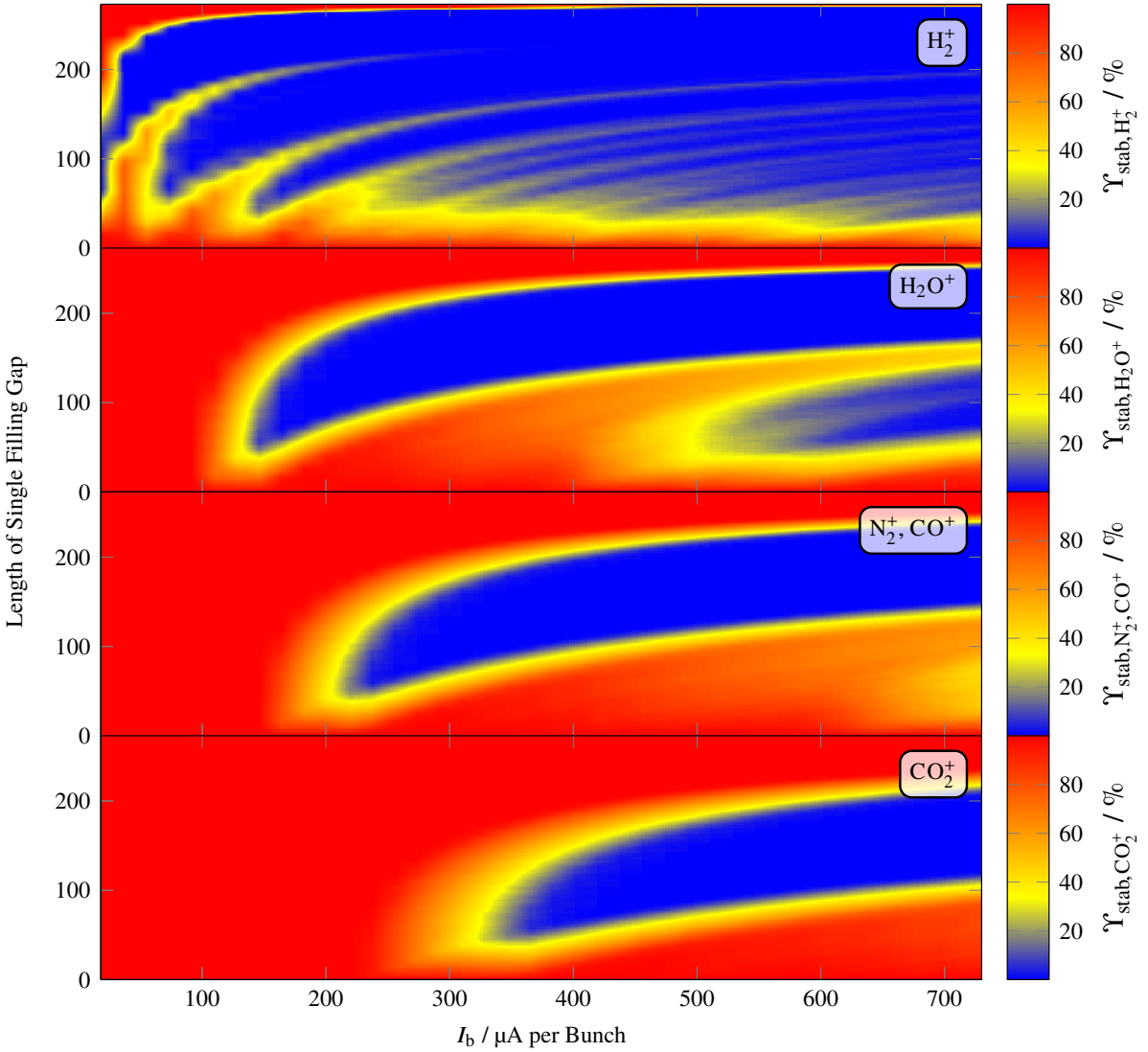

Figure A.12: Percentage of stable ions in the storage ring at a beam energy of 1.2 GeV for different bunch currents when applying one single filling gap of certain length. The neutralization is zero. The bunch current corresponds to an initial current I_0 ranging from 5 to 200 mA.

ion clearing using filling gaps, Υ_{stab} should approach zero for all relevant ion species at a certain filling pattern in the storage ring.

In the following investigation, the effect of one and two filling gaps of different length on the stability of the relevant ion species H_2^+, H_2O^+, N_2^+, CO^+ and CO_2^+ is studied. The stability is analyzed at different beam energies (1.2, 1.7, 2.2, 2.7 and 3.2 GeV) and bunch currents, reaching from 18 to 730 µA (corresponds to I_0 ranging from 5 to 200 mA). The neutralization has not been taken into account.

Single Filling Gap

For different beam energies, bunch currents and mass-to-charge ratios of the relevant ion species, the length of a single filling gap is varied from 0 to 273 buckets. Figure A.12 shows the fraction of stable ions Υ_{stab} in the storage ring for the five relevant species at a beam energy of 1.2 GeV.

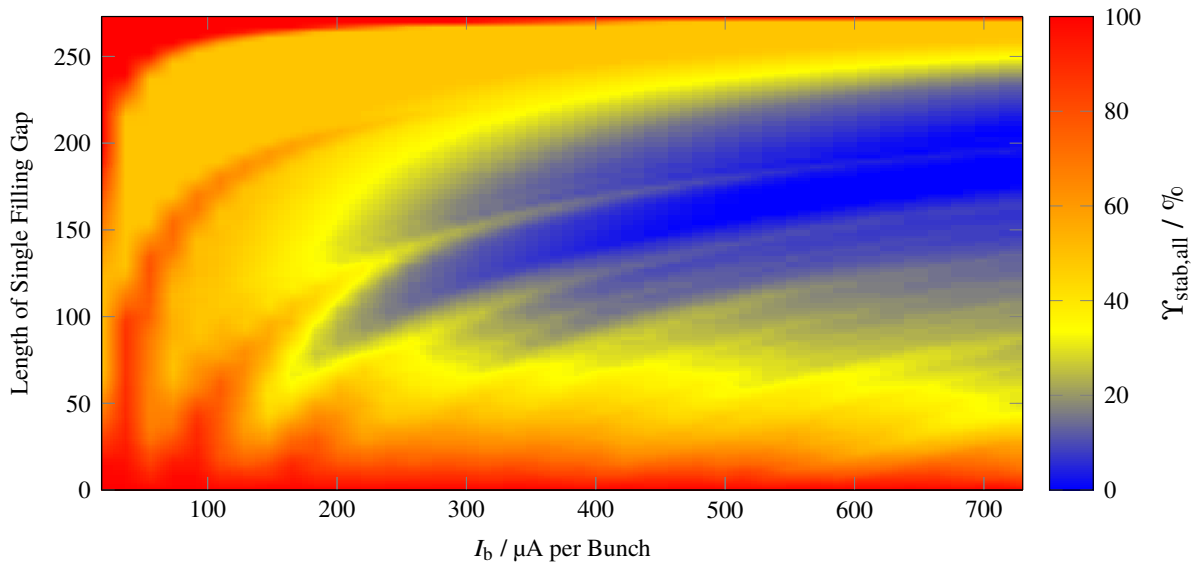

Figure A.13: Stability analysis for the application of a single filling gap at a beam energy of 1.2 GeV and a neutralization of zero. $\Upsilon_{stab,all}$ is the percentage of stable ions in the storage ring. The bunch current corresponds to an initial current I_0 ranging from 5 to 200 mA.

As already discussed in section 4.1.2, all considered ion species are stable for a homogeneous filling pattern with no filling gap. For a filling gap which is longer than 30 bucket lengths, H_2^+ ions with a mass-to-charge ratio of $A/Z = 2$ are horizontally or vertically instable in the complete storage ring. This results in Υ_{stab,H_2^+} being equal to zero for almost every bunch current. However, there are some isles of stability at a bunch current of 35, 100 and 200 µA, where the gap length is increased to 50 to 100 buckets. For large filling gaps of 260 buckets and more, H_2^+ ions are stable again.

For ion species with higher mass-to-charge ratios, the isles of stability expand. Actually, the regions where instability occurs shrink to one or two bands of instability with increasing mass for the considered parameter space. H_2O^+ ions with $A/Z = 18$ cannot be destabilized by any filling gap for bunch currents below 100 µA ($I_0 = 27.4$ mA). For N_2^+ and CO^+ ions with $A/Z = 28$, a minimal bunch current of 150 µA ($I_0 = 41.1$ mA) must be stored to affect the stability of these ion species by a filling gap. For CO_2^+ ($A/Z = 44$), this minimal bunch current increases to 250 µA ($I_0 = 68.5$ mA).

For an effective application of a single filling gap, a large fraction of all produced ions should be rendered instable in the storage ring. To identify combinations of filling gap lengths and bunch currents where an ion clearing with this method is possible, the individual ion species contributions shown in figure A.12 are merged into $\Upsilon_{stab,all}$. Here, the individual $\Upsilon_{stab,i}$ are weighted by their production probability at the considered beam energy (compare figure 3.24) and are averaged. The results of this composition are shown in figure A.13. The percentage of stably produced ions can be reduced below 40 % for filling gaps of a length of 50 to 250 buckets for bunch currents above 150 µA ($I_0 = 41.1$ mA). Here, all relevant ion species except CO_2^+ are instable in the storage ring. Thus, the partial neutralization of CO_2^+ is expected to dominate the total neutralization.

For a bunch current of 400 µA or higher and a filling gap length between 170 and 225 buckets, $\Upsilon_{stab,all}$ is comparable to zero. Here, 62 to 82 % of the buckets in the storage ring are kept empty. Yet, a short bunch train with high bunch current is not desired by the experiments, which rely on the extracted electron beam.

However, it may be more practical to destabilize mainly H_2^+ ions since this species amounts to 52.3 %

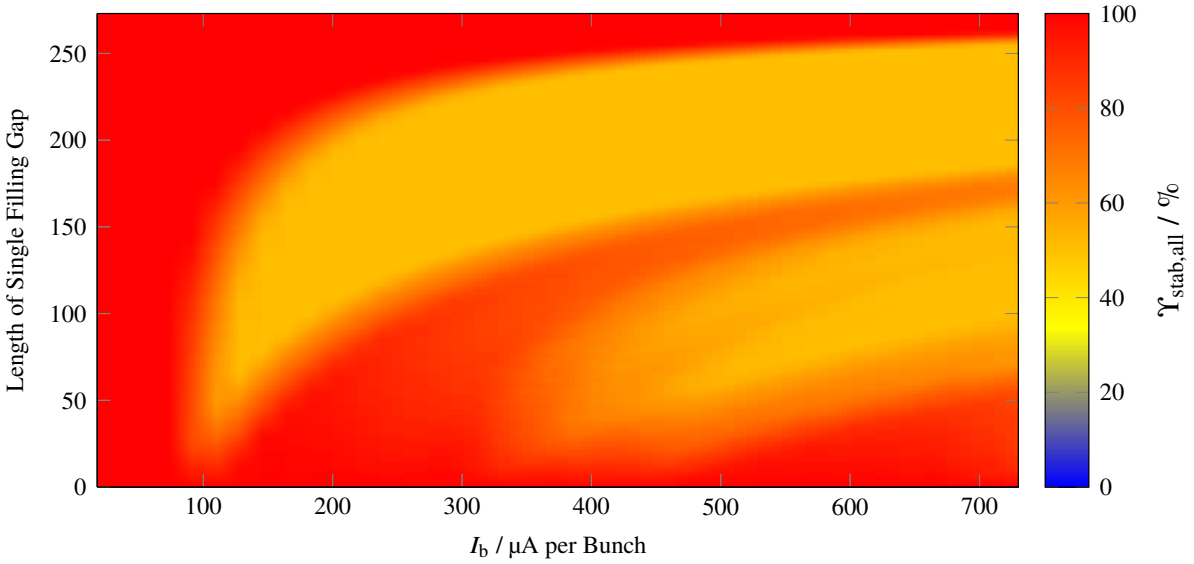

Figure A.14: Stability analysis for the application of a single filling gap at a beam energy of 3.2 GeV and a neutralization of zero. $\Upsilon_{stab,all}$ is the percentage of stable ions in the storage ring. The bunch current corresponds to an initial current I_0 ranging from 5 to 200 mA. The graph is a composition of the individual ion species contributions to $\Upsilon_{stab,all}$ from C.27.

of the produced ions in the storage ring (compare section 3.5). For almost all of the considered bunch currents, a filling gap length of 75 buckets is sufficiently long to destabilize H_2^+ and partially H_2O^+, N_2^+ and CO^+.

For higher beam energies, the beam potential gets shallower due to an increased beam size with reduced charge density. Obviously, the decreased attractive space charge of the electron beam also changes the stability of the individual ion species when exposed to a filling gap. In figures C.21, C.23 and C.25, the results of these stability analyses are shown for beam energies of 1.7, 2.2 and 2.7 GeV. In general, the instability bands shift towards higher bunch currents for an increasing beam energy. Consequently, the minimal bunch current at which a filling gap destabilizes a majority of the ion population in the storage ring increases. For the storage ring's maximum beam energy of 3.2 GeV, figure A.14 shows $\Upsilon_{stab,all}$ for different filling gap lengths and bunch currents. In contrast to $\Upsilon_{stab,all}$ at 1.2 GeV (compare figure A.13), only approximately 50 % of the produced ions can be destabilized by the application of a single filling gap in the considered bunch current range. Here, only the lightest ion species H_2^+ can be removed by filling gaps. For bunch currents below 100 µA (I_0 = 27.4 mA), even this is not possible.

In summary, the application of a single filling gap for ion clearing in the storage ring is only efficient for light ion species like H_2^+ and for low beam energies between 1.2 and 1.7 GeV. Here, a filling gap length of 30 (1.2 GeV) to 70 (1.7 GeV) is sufficient for almost all bunch currents to remove this species. Heavier ion species like H_2O^+, N_2^+, CO^+ and CO_2^+ are only rendered instable for higher bunch currents and/or a longer filling gap. From 2.2 GeV upwards, N_2^+, CO^+ and CO_2^+ cannot be destabilized completely within the considered bunch current region anymore. For 3.2 GeV, all ion species except H_2^+ cannot be destabilized by any filling gap in the storage ring.

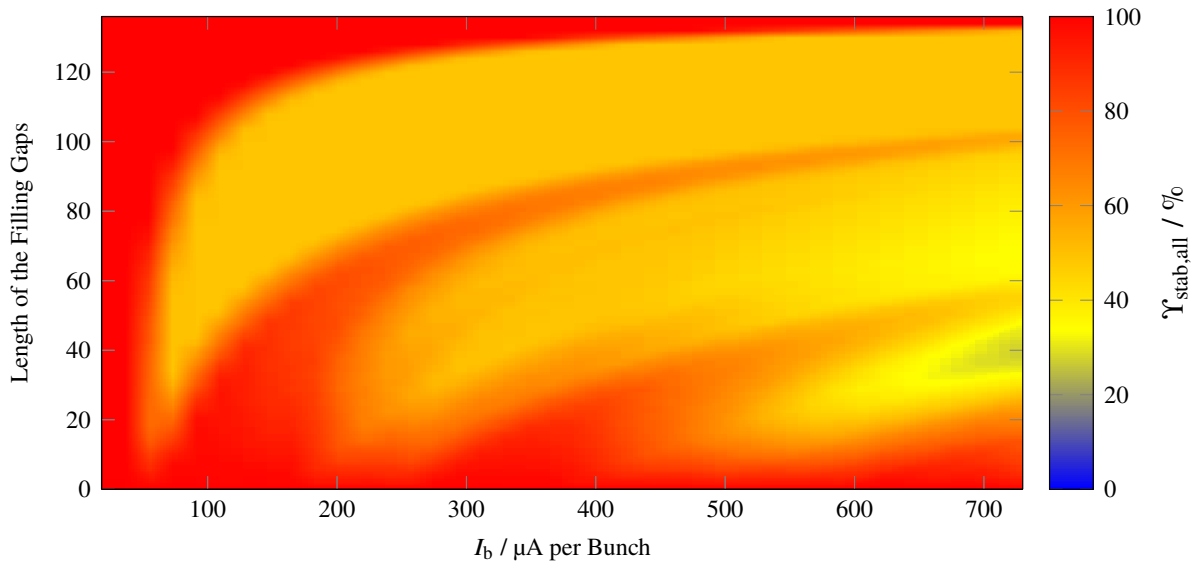

Figure A.15: Stability analysis for the application of two filling gaps at a beam energy of 1.2 GeV and a neutralization of zero. $\Upsilon_{stab,all}$ is the percentage of stable ions in the storage ring. The bunch current corresponds to an initial current I_0 ranging from 5 to 200 mA. The graph is a composition of the individual ion species contributions to $\Upsilon_{stab,all}$ from C.28.

Two Filling Gaps

The application of two filling gaps of equal length, positioned opposite of each other in the storage ring's filling pattern, has been studied, too. Figure A.15 shows the fraction of stable ions for a beam energy of 1.2 GeV. Here, $\Upsilon_{stab,all}$ can only be reduced to approximately 30 % at a bunch current of 730 µA and two filling gaps with a length of 40 buckets. In this configuration only all H_2^+ and H_2O^+ ions and 30 % of N_2^+ and CO^+ ions are destabilized by the gaps.

For higher beam energies, the two filling gaps destabilize a decreasing fraction of ions. For 3.2 GeV, only H_2^+ ions can be destabilized eventually at a bunch current above 400 µA. The destabilizing effect of two filling gaps in the storage ring at other beam energies are shown in figures C.29, C.31, C.33 and C.35.

Influence of the Neutralization on the Ion Stability

In the previous studies not all ion species are rendered unstable when exposed to a certain filling pattern, at certain beam energies and bunch currents. These species consequently accumulate in the accelerator and a fractional neutralization of the beam occurs in dependence of the species' individual production and clearing rates. Accumulated ions partially shield the attractive space charge force of the beam from additional ions and thus alter the ion's motion within the beam. An ion species, which initially has been unstable at a certain filling pattern, may be stabilized by the neutralization of other stable species and eventually also accumulates. This effect is called *ion ladder* and is described in [BB80, section 10]. However, the topic of ion ladders exceeds the scope of this work.

TRACEANALYSIS can also be used to study the influence of the neutralization on the stability of the different ion species. In the stability matrix formalism, the neutralization is represented by a defocusing quadrupole strength $k_{\mathrm{ion},x,z}(\hat{\eta})$ which reduces the focusing quadrupole strength $k_{0,x,z}$ of the beam (compare equation (A.22)).

Figure A.16 shows the fraction of vertically stable H_2^+ (top) and H_2O^+ (bottom) ions in the storage ring

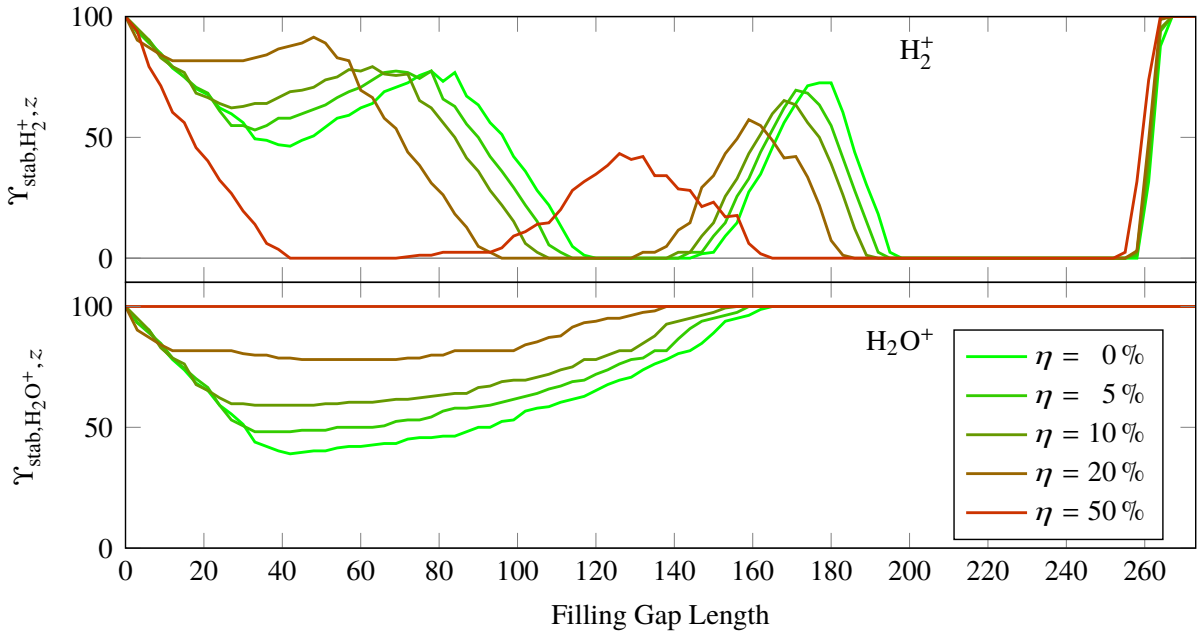

Figure A.16: Stability analysis for the vertical plane at a beam energy of 1.2 GeV and a bunch current of 128 µA (I_0 = 35 mA) for a single filling gap of different lengths. The top graph shows the fraction of vertically stable H_2^+ ions for different neutralizations. The bottom graph shows the stability of H_2O^+ ions for the same neutralizations.

for different neutralizations at a beam energy of 1.2 GeV and a bunch current of 128 µA (I_0 = 35 mA). Here, it is assumed that the local neutralization is constant in the storage ring and thus $\hat{\eta} = \eta$.

At η = 0 %, a fraction of the H_2^+ population in the storage ring is instable for a filling gap length of approximately 2 to 260 bucket lengths. From 120 to 140 bucket lengths and from 200 to 260 bucket lengths, $\Upsilon_{\text{stab},H_2^+,z}$ is equal to zero. Thus, no ion accumulation is possible in the storage ring at these filling patterns. In-between, isles of stability are present where an accumulation is possible in 50 to 80 % of the storage ring. The shown curve is equal to a vertical cut through figure A.12 (top) at a bunch current of 128 µA. For an increasing neutralization, these isles shift towards shorter gap lengths and decrease in height, implying that more H_2^+ ions are destabilized by the accumulation of other ions.

For H_2O^+ ions in this scenario, an increasing neutralization has the opposite effect. At η = 0 %, this species is partially destabilized at filling gap lengths between approximately 2 and 160 bucket lengths. For an increasing neutralization, the fraction of destabilized H_2O^+ ions decreases and the maximal length of destabilizing filling gaps shortens. Eventually at 50 % neutralization, this species is stable throughout the storage ring.

Although increasing neutralization shows an opposite effect on the considered ion species, its influence on the ion stability can be approximated. The neutralization apparently reduces the effective current in the accelerator due to the shielding of the beam's space charge. Thus, for a beam energy of 1.2 GeV, figure A.12 or figure A.13 can be used to estimate the stability of ions for a certain neutralization. For example, η = 50 % reduces the effective bunch current by 50 % to 64 µA per bunch. A vertical cut through figure A.12 at this bunch current will reproduce the stability conditions observed in figure A.16.

A.12.2 Deficiencies of the Stability Matrix Formalism

The stability matrix formalism has some deficiencies:

- The attractive electric field of the electron bunch is only assumed to rise linearly with the transversal displacement of the ion from the beam center. The existing non-linearity of the field with the displacements $> \sigma_{x,z}$ is not included. Thus, the stability of many ions which are produced with displacements higher than $\sigma_{x,z}$ cannot be evaluated with this formalism.
- For large filling gaps, where the beam current in the accelerator trends towards 0 mA, $\mathcal{M}_{\mathrm{bt},x,z}$ converges to a drift matrix with $l_{\mathrm{drift}} = C$. Since the trace of a drift matrix is 2, the formalism implies a stable ion trajectory for large filling gaps. Here, the considered ion species may only drift away from the beam center towards the beam pipe and thus is not trapped in the beam potential anymore. Thus, invalid results occur when using the formalism in these cases.
- It is only determined whether an ion species is instable or not. Although a particular ion species may show instable trajectories at a certain bunch current and filling pattern, the production of this ion species obviously does not stop. If the amplitude of an instable ion only grows slowly in reference to the timescale of the species' production rate, the ion's space charge may still has an influence on the electron beam and may significantly contribute to the neutralization. The species' clearing rate eventually determines its individual contribution to the neutralization. Therefore, the stability criterion only gives indications about whether or not the filling pattern affects the particular ion species.

A.12.3 Comparison between the Stability Matrix Formalism and FillingGapSim

Although FillingGapSim offers ancillary results (individual trajectories, clearing rates, ion density distributions) about an ion population exposed to a certain filling pattern, to TraceAnalysis which utilizes the stability matrix formalism, the simulation of these results in general takes longer computational times. In practice, it may be handy to quickly use TraceAnalysis to estimate the stability of an ion population at a certain filling pattern. As the utilized formalism only takes into account linear fields which are only applicable close to the beam center, a comparison of its results with the more accurate FillingGapSim is reasonable.

Consequently, the stability of the five relevant ion species when exposed to a certain filling pattern is determined by using FillingGapSim within the same parameter space as during studies with TraceAnalysis. The results of TraceAnalysis, broken down to the relevant ion species, for a beam energy of e.g. 1.2 GeV are shown in figure A.12. The resulting stability Υ_{all} of the complete ion population is shown in figure A.13.

The equivalent criterion to the stability of an ion species in FillingGapSim is its transmission probability through a simulation scenario where it is exposed to a certain filling pattern. The fraction of stable ions - their simulated trajectory does not exceed either $\pm 10\sigma_x$ in the horizontal or $\pm 10\sigma_z$ in the vertical plane - to the total number of simulated ions determines the transmission probability T_i. To keep the runtime of the simulation within a suitable timescale, the number of simulated ion trajectories per data point has been reduced to 200, yielding a relative statistical error of 7 %.

Figure A.17 shows the transmission probability of the different ion species when exposed to a single filling gap for various bunch currents at a beam energy of 1.2 GeV. Other beam energies are shown in figures C.39 and C.41. When compared to figure A.12, the stability obtained by FillingGapSim shows similarities to the results of TraceAnalysis. In both, bands of instability form which reach from regions of high bunch currents to certain lower currents. In FillingGapSim, the average beam width is used as the basis for the simulation whereas the TraceAnalysis study comprises all beam widths appearing in

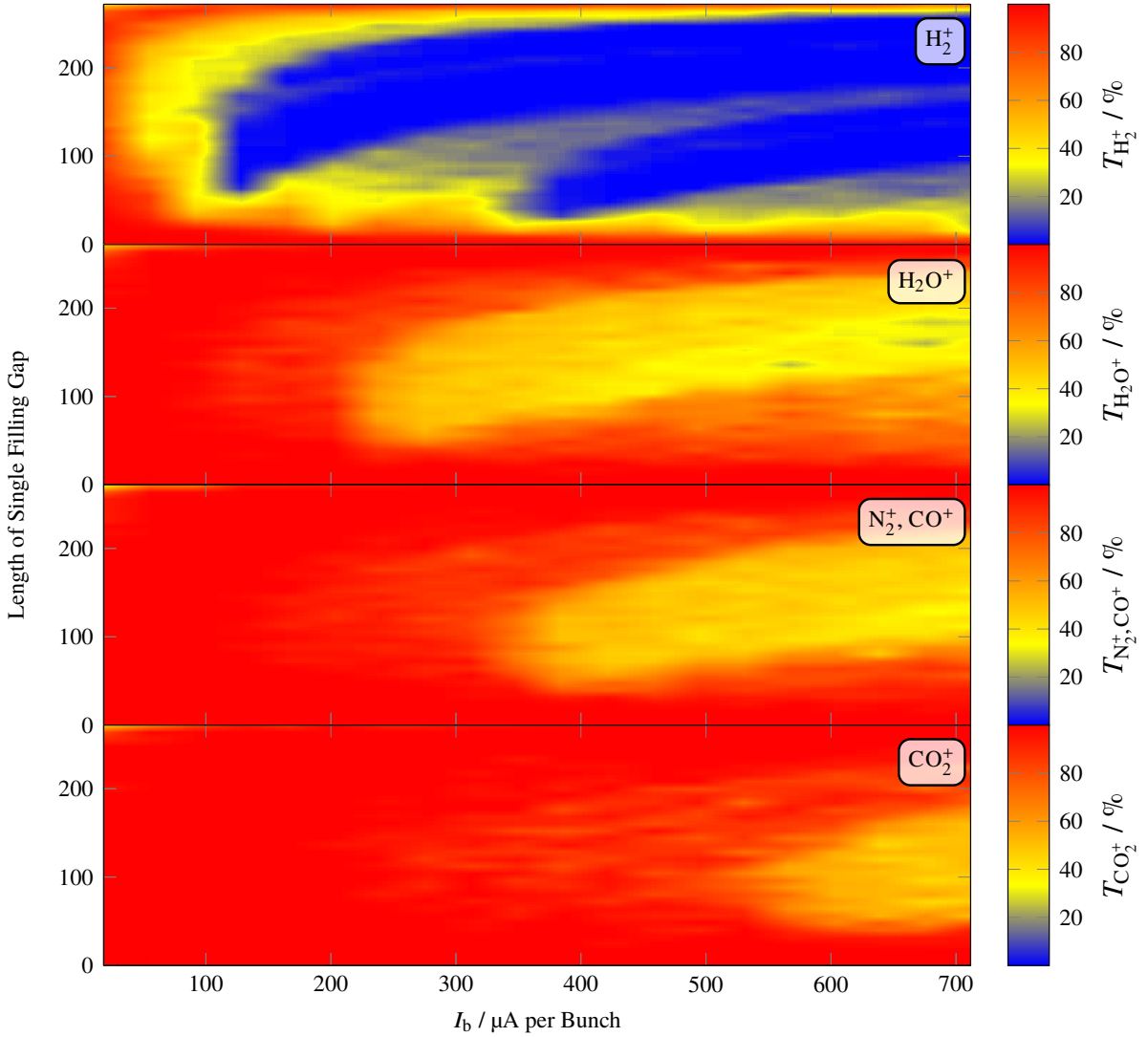

Figure A.17: Stability of different ion species when a single filling gap of a specific length is applied at different bunch currents at a beam energy of 1.2 GeV. The stability criterion is the probability T of a produced ion to stay within a region of $\pm 10\sigma_{x,z}$ for a time frame of 100 µs in a FillingGapSim simulation. Here, the electron beam has a dimension equal to its average size in the storage ring. The bunch current corresponds to an initial current I_0 ranging from 5 to 195 mA. The corresponding compilation of all species can be found in figure C.38.

the storage ring. Therefore, differences in the shape of these bands are expected. However, both methods show that for certain filling patterns and bunch currents, the entire H_2^+ ion population can be cleared. The form and recession of the stability bands with increasing mass is also congruent in both methods.

Nevertheless, it is apparent that the transmission probability does not deceed 30 % for H_2O^+ ions, 35 % for N_2^+ and CO^+ ions and 40 % for CO_2^+ ions. This indicates that the lifetime of the different ion species in the electron beam is in the order of the simulation time and consequently not all ion species' leave the simulation region in time. If the lifetime of the ions is in the order of the neutralization time, the inverse production rate, the resulting neutralization would be in the order of one, rendering the filling pattern without effect.

Considering the stability of the ion population, TraceAnalysis and FillingGapSim produce

congruent results. Yet, FillingGapSim may be substantial in determining the efficiency of the applied filling pattern as the instability is not a sufficient criterion for a successful ion clearing.

A.13 Natural Ion Clearing

Clearing methods are denoted as "natural" ion clearing, if the clearing effect emerges via a physical process which is not fabricated artificially but is inevitably occurring to the ion population. Here, the two antagonistic processes of gas cooling and beam heating are considered.

Beam Heating of Ions in Potential Hollows

Consider an ion being produced from the collision of an electron of the beam with a residual gas molecule. In section 2.1.2, it has been argued, that the average energy transfer to the newly-produced ion during these collisions is negligibly small. Thus, interactions of beam electrons with the particles in the vacuum system with a large impact parameter b, implying distant collisions with low energy transfer, are much more probable to happen (compare equation (2.4)). Although the energy transfer to the ions is negligibly small for one collision, multiple similar collisions heat up the ion population. In case of a long lifetime of individual ions, in which several of these collisions increase their kinetic energy, they may be able to escape the beam potential with depth $\tilde{U}$. Because only ions, which are trapped within potential hollow's show elevated lifetimes, this clearing process may occur there exclusively.

An individual clearing rate for an ion species i of [Pon94, section 2.1, conversion of equation (11)]

$$r_{\mathrm{c,heat},i} = \frac{\mathrm{e}^2}{\left(2\pi\varepsilon_0\beta c\right)^2 \cdot m_\mathrm{p}} \frac{1}{\langle\sigma_x\rangle \langle\sigma_z\rangle} \frac{I}{\tilde{U}} \cdot Z_i' \ln\left(3 \cdot 10^4 {Z_i'}^{-\frac{2}{3}}\right)$$

is obtained. Here, Z_i' is the atomic number of the particular ion species and $\langle\sigma_x\rangle$ along with $\langle\sigma_z\rangle$ are the average horizontal and vertical beam sizes. $\tilde{U}$ can be interpreted in two ways:

1. As the absolute value of the potential depth in the beam center $|U(s)|$. If no other clearing mechanisms are in place, all ions are trapped within the beam potential. When the ions obtain a kinetic energy of $\mathrm{e}U(s)$ by the process of beam heating and momentum transfers, they are able to leave the potential.
2. As the heights of the beam potential barrier $\Delta U = U_{\max}(s_0) - U_0(s_0 + \Delta s)$ (compare figure 4.7 in section 4.2.2) which hinders an ion, which is locally trapped within a potential hollow at $s_0 + \Delta s$, to reach a clearing electrode. Because ΔU is lower than $|U(s)|$, the clearing rate due to heating in general is higher in potential hollows and enables an escape of ions out of a potential hollow before a neutralization of $\hat{\eta}_{\mathrm{stat}}(s)$ is established. Here, the escape of the ion out of a potential hollow is not necessary identical to its removal from the vacuum system and does not necessarily lead to a decreased neutralization.

However, in the following only the first case is considered.

Since the potential depth $|U(s)|$ also scales with the beam current I, the ratio of $I/|U(s)|$ is equal to the "form factor"of the beam potential, which is only defined by the shape of the beam potential. For a compact beam with large beam pipe diameters, which results in a deep beam potential (compare section 2.4.1), $I/|U(s)|$ is small. For a more shallow potential, $I/|U(s)|$ increases.

For the storage ring, $I/|U(s)|$ on average is equal to approximately $4.2\,\mathrm{mA\,V^{-1}}$ at a beam energy of 1.2 GeV. At 3.2 GeV, it is approximately $6.2\,\mathrm{mA\,V^{-1}}$.

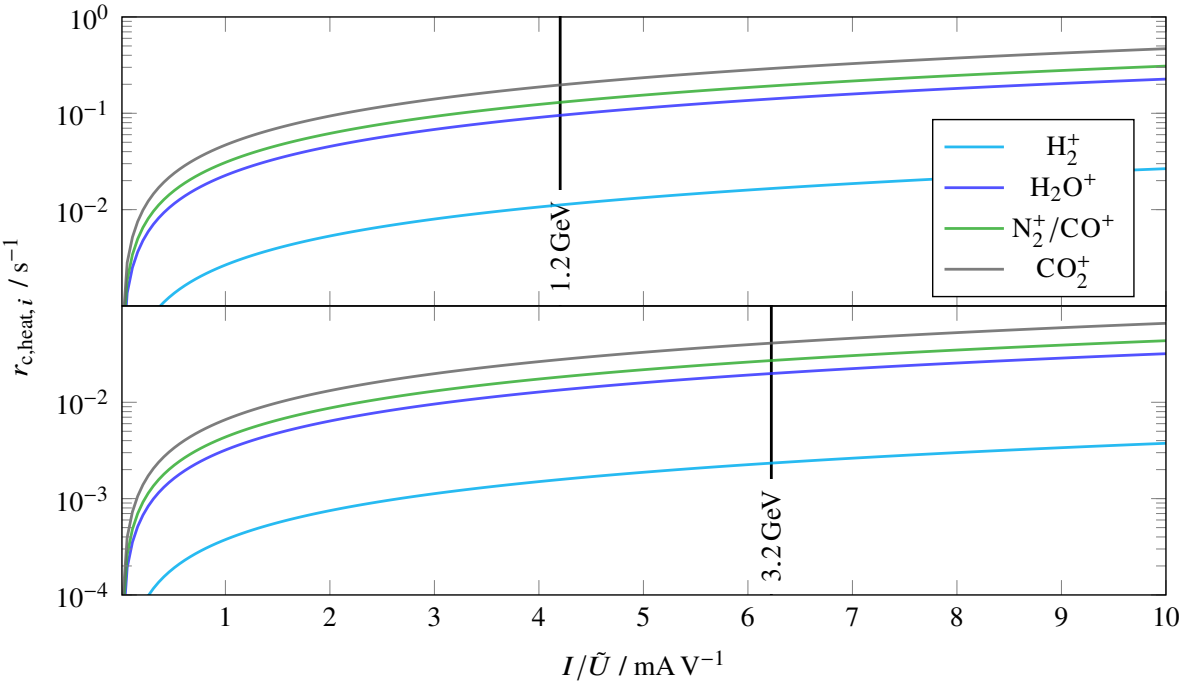

Figure A.18: Clearing rate due to beam heating for different rations of $I/|U(s)|$ at a beam energy of 1.2 GeV (top) and 3.2 GeV (bottom). The intersection of the individual $r_{\mathrm{c,heat},i}$ with the black line indicate the average clearing rate of the particular ion species in the storage ring.

In figure A.18, the individual average clearing rates due beam heating in the storage ring is shown for a beam energy of 1.2 GeV (top) and 3.2 GeV (bottom). With increasing proton number Z_i', the clearing rate increases. Also a more shallow beam potential with larger "form factor" leads to a higher clearing rate.

However, for a beam energy of 1.2 GeV, this clearing rate does not exceed 0.3 s^{-1} in the storage ring. For 3.2 GeV, where the beam size is larger than for 1.2 GeV, it is even lower and does not exceed approximately 0.05 s^{-1} for each ion species.

With a clearing rate lower than 0.3 s^{-1} (0.05 s^{-1}) for 1.2 GeV (3.2 GeV) this natural clearing mechanism is a factor of around 550 (4 000) lower than the total production rate of approximately 165 s^{-1} (200 s^{-1}) at a beam current of 30 mA (compare figure 3.23 in section 3.5). Consequently, $\eta \ll 1$ cannot be achieved by the beam heating process (compare equation (2.13)).

Additionally, the process of gas cooling counteracts the beam heating.

Gas Cooling in Potential Hollows

When ions are trapped within potential hollows for a long period of time, a charge exchange between the positive ion and a neutral residual gas molecule can occur. For a kinetic energy of the ion in the order of a few eV, the positive ion captures the electron from a neutral residual gas molecule:

$$\mathcal{A}_*^+ + \mathcal{A} \quad \Longrightarrow \quad \mathcal{A}_* + \mathcal{A}^+ \,.$$

As the ion $\mathcal{A}_*^+$ in general has a higher kinetic energy (denoted as $*$ in the reaction equation), due to acceleration in the beam's electric fields, than the neutral residual gas molecule $\mathcal{A}$ which propagates with thermal velocities, a reduction of the ion population's kinetic energy occurs.

According to [Pon94, section 2.2], the average time until this charge exchange happens to a He^+ ion is equal to 27 s for a pressure of $1.3 \cdot 10^{-8}$ mbar. Thus, the rate with which this process occurs to an ion is approximately $0.04\,s^{-1}$. Assuming a linear pressure-dependency of the reaction rate, this would imply a gas cooling rate of approximately 0.4 to $1.8\,s^{-1}$ in the pressure regime of the storage ring ($1.3 \cdot 10^{-7}$ to $6.3 \cdot 10^{-7}$ mbar, compare section 3.2).

Thus, the gas cooling reaction rate seems to exceed $r_{c,heat,i}$. Consequently, the already low escape rate of the ions out of potential hollows due to the heating is further diminished by the cooling process. Thus, additional clearing methods are needed in the storage ring to prevent a fully neutralized beam with $\eta = 1$.

A.14 Scaling Laws for the Neutralization with Beam Energy and Current

The neutralization of an ion population in its equilibrium state can be determined by the fraction of production rate to the clearing rate. Both quantities are dependent on the beam energy and current. The following section tries to give a rough estimate on how the neutralization within an accelerator might evolve with beam energy and current.

The clearing rate scales differently with beam energy and current in dependence of the region the ions propagate in.

- In magnet field-free regions, in which an ion is not trapped within potential hollows or magnetic mirrors, the longitudinal acceleration by the gradient field E_s is the dominant factor in the determination of the ion's life time τ_i and thus the clearing rate. For an ion i with mass m_i, the clearing rate scales as

$$\frac{1}{\tau_i} = r_{c,free,i} \sim \sqrt{\frac{\langle E_s \rangle}{m_i}}\,,$$

  assuming a negibly small initial velocity of the ion. The average field $\langle E_s \rangle$, experienced by the ion, scales linearly with the beam current (compare e.g. equation (2.43)). It also decreases quadratically with the beam energy because $E_s \sim \left(\sigma_{x,z}(\sigma_x + \sigma_z)\right)^{-1}$ (compare equation (2.43)) and $\sigma_{x,z}$ increases approximately linearly with the beam energy (compare equations (2.33) and (2.35)). Consequently, the clearing rate increases proportional to

$$r_{c,free,i} \sim \sqrt{\frac{I}{E^2}}$$

  in these regions.
- In dipole magnets, the cross-field drift v_d transports ions if the influence of E_s is omitted. Since this is a linear motion in time, the clearing rate is given as

$$r_{c,dp,i} \sim v_d \overset{\text{equation (2.51)}}{=} \frac{\langle E_x \rangle}{B_z}\,.$$

  As the magnetic field strength B_z is increased linearly with the beam energy (compare equation (B.1)) and $\langle E_x \rangle$ scales similar to $\langle E_s \rangle$ regarding beam energy and current, the clearing rate scales approximately as

$$r_{c,dp,i} \sim \frac{I}{E^3}$$

  in dipoles.

- At the entrance of the dipole magnets, where the magnetic fringe fields form magnetic mirrors which longitudinally trap ions, the average lifetime of the trapped ion population depends on the transmission probability $\tilde{T}_i$ through these fields (compare figure 4.15). The average life time or clearing time of ion species i is equal to

$$\langle \tau_i \rangle = t_0 \cdot \left(\frac{1}{\tilde{T}_i} - \frac{1}{2} \right) = \frac{1}{r_{\mathrm{c,fringe},i}}$$

  where t_0 is the average time scale with which the fringe field region is repeatedly encountered by the ions. t_0 scales as $1/\sqrt{E_s}$. For a transmission of 100 %, the ions pass the fringe fields within a time $t_0/2$ and are neutralized at the clearing electrodes. If the transmission is < 100 %, the lifetime of the ion species on average is prolonged as $1/\tilde{T}_i$. The fraction of $v_s/v_{s,\mathrm{T}}$ has to be > 1 for the transmission of ions through the fringe field (compare equation (4.4)). Thus, it can be assumed that the transmission probability $\tilde{T}_i$ scales like this fraction. v_s is the ion's longitudinal velocity, when encountering the fringe field. It results from the longitudinal acceleration due to E_s and is therefore proportional to $\sqrt{I/E^2}$. $v_{s,\mathrm{T}}$ depends on the cyclotron frequency, which scales with B_z, and therefore increases linear with the beam energy. Thus, the transmission is proportional to $\sqrt{I}/E^2$. In total, the clearing rate in sections with magnetic mirrors is

$$r_{\mathrm{c,fringe},i} \sim \frac{I}{E^3}$$

For a constant $R_\mathrm{p}/\mathcal{P}$, the production rate is only dependent on the pressure. The pressure model of the storage ring scales with beam energy and current as $\sqrt{\mathcal{P}_0^2 + \tilde{A} \cdot E \cdot I + \tilde{B} \cdot E^2 \cdot I + \tilde{C} \cdot E \cdot I^2}$ (compare equation (3.3) in section 3.2). It comprises terms which scale "linear" with beam energy and current as well as terms which saturate and scale as $\sqrt{EI}$. For a worst case estimation on the evolution of the neutralization, only the "linear" terms of the pressure ($\sim E \cdot I$) are considered which hand down the same dependency to the production rate.

Within the magnet field free regions where ions are not trapped by potential hollows and magnetic mirrors, the neutralization scales as

$$\eta_{\mathrm{dyn,free}} \sim \sqrt{I} \cdot E^2 \,.$$

Thus, the neutralization increases with the beam energy.

In the dipole magnets, the neutralization increases as

$$\eta_{\mathrm{dyn,dp}} \sim E^4 \,.$$

For an increasing beam energy, the neutralization increases with E^4. Here, the increased beam size decreases E_x which results in a reduced cross-field drift velocity.

In the region of the dipole's fringe fields, the neutralization scales like

$$\eta_{\mathrm{dyn,fringe}} \sim E^4 \,.$$

For higher beam energies, the dipole's magnetic field strength is increased and the beam width increases, too. This results in a lower ion velocity v_s and a higher $v_{s,\mathrm{T}}$, which significantly reduces $\tilde{T}_i$. As a consequence, the neutralization increases considerably in these regions when the beam energy is increased.

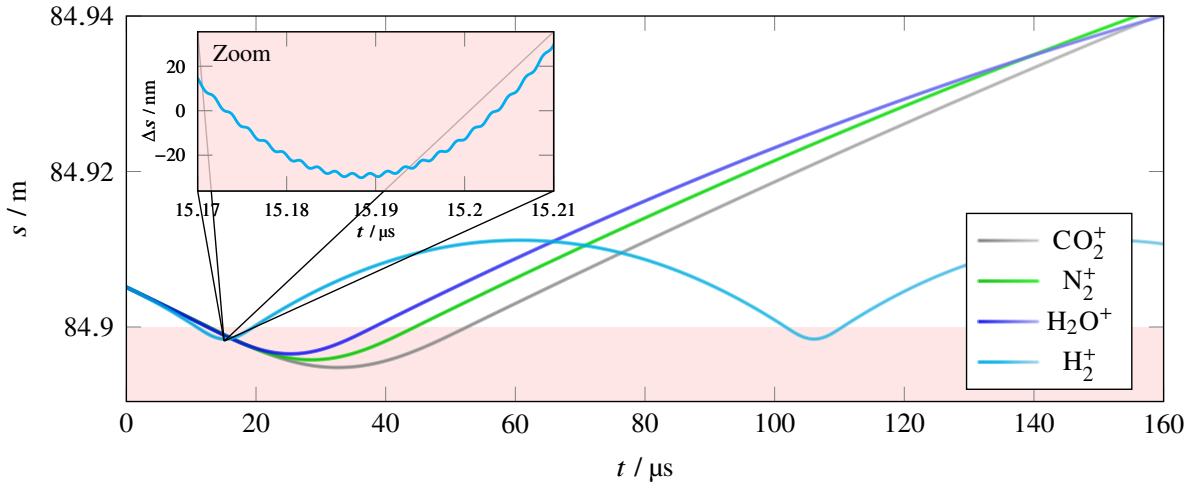

Figure A.19: Trajectories of different ion species with an initial longitudinal velocity of $-400\,\mathrm{m\,s^{-1}}$ when entering cavity 2. The region, where the rf field of cavity 2 is present, is highlighted as light red area.

A.15 Ion Trajectories at the Entrance of RF Cavities

Figure A.19 exemplarily shows H_2^+, H_2O^+, N_2^+ and CO_2^+ ions from the third accumulation region, which propagate with an initial velocity of $-400\,\mathrm{m\,s^{-1}}$ towards the entrance of cavity 2. The regions, where the rf field is present, is highlighted in light red. All ions penetrate the edge of the field, are decelerated and eventually are reflected back. For equal initial velocities of the different ions, their penetration depth only depends on their mass-to-charge ratio. The reflection occurs during multiple rf periods T_{rf}, which causes the undulating trajectory of the H_2^+ ion in the magnification. During the shown time frame, the trapped condition of these ions becomes visible by the exemplaric trajectory of the H_2^+ ion: After being reflected by the rf field, its trajectory again is reversed due to the deceleration by E_s. This ion is trapped in a region with the size of approximately 1 cm at the edge of the rf fields.

A.16 Additional Ion Induced Effects

A.16.1 Pressure Increment

One additional ion effect is the increment of the pressure in vicinity of the beam due to an increased particle density. Here, the particle density is the sum of the residual gas density *and* the density of the trapped ions. However, even for a fully neutralized electron beam, the pressure increment is negligible for a nominal pressure of 10^{-7} to 10^{-8} mbar [BB84, section 8.2].

For a worst case estimation of this effect in the storage ring, an electron beam with a current of 200 mA and an energy of 1.2 GeV is assumed. It has an average number density of approximately $9 \cdot 10^{11}\,\mathrm{m^{-3}}$ assuming a beam volume V_{beam} of $0.76\,\mathrm{m^3}$ (compare appendix A.9). For $\eta = 1$, the ion density is identical. Using the ideal gas law, the ions increase the pressure in the vacuum system by $3.7 \cdot 10^{-11}$ mbar. As the pressure in the storage ring is at least three orders of magnitude higher, the pressure increment can be omitted.

A.16.2 Increased Betatron Coupling

The electric field distribution generated by the ion cloud is not purely horizontally or vertically orientated such as the magnetic field of quadrupole or dipole magnets. Ions being positioned off-axis at $|x| > 0$ and $|z| > 0$ attract each individual beam electron in both planes and the electron's trajectory alters accordingly. Consequently, the ion population also increases the betatron coupling coefficient κ and thus the coupling between the horizontal and vertical plane.

κ can be determined by measuring the transversal synchrotron radiation beam profile using synchrotron light monitors with known optical functions at the radiation's source point similar to [Zan13]. In the storage ring, no significant increment of κ has been detected when switching off all ion clearing electrodes which would increase the neutralization substantially[14].

For more information, see e.g. [Tav92a].

A.17 Derivation of the Space Charge Induced Incoherent Tune Shift

To deduce the incoherent transversal tune shift which is induced by the neutralization of the electron beam by accumulated ions, an unbunched, round electron beam is considered with constant transversal and longitudinal charge density ρ_e. The beam has a radius of a along its radial axis r.

Electric and Magnetic Field of the Electron Beam First, only the electron space charge interaction within the beam is modeled without ions. Using the Gaussian law, the transversal electric field of the beam can be determined via

$$\oint_{\delta V} \vec{E} \cdot \mathrm{d}\vec{A} = \frac{1}{\varepsilon_0} \iiint_V \rho_e \, \mathrm{d}^3 r \, .$$

Here, V is the volume of the cylindrically shaped beam with base A and δV represents the surface of the volume. Since the finite longitudinal dimensions of the beam is equal in the left and right hand side of the equation, it cancels out and one obtains

$$2\pi r E_r(r) = \frac{\pi r^2}{\varepsilon_0} \rho_e \, . \tag{A.23}$$

As the electron beam consists of moving charges, it also generates a circular magnetic field around the beam. Using Ampere's law, the field can be derived via

$$\oint_{\delta A} \vec{B} \cdot \mathrm{d}\vec{s}' = \mu_0 \iint_A \vec{j} \, \mathrm{d}\vec{A} \, ,$$

where μ_0 is the magnetic field constant and $\vec{j}$ is the current density of the beam. A is the area through which the electron current flows whereas δA is the boundary of this area. For a beam which moves along the longitudinal axis s (thus only shows a current density j_s), a circular magnetic field B_φ is obtained which equals

$$2\pi r B_\varphi(r) = \mu_0 \pi r^2 j_s \, . \tag{A.24}$$

Using $\mu_0 = 1/(\varepsilon_0 c^2)$, $j_z = I/A = I/(\pi a^2)$ and the relation of the electric current of this cylindrical beam $I = \pi a^2 \beta c \rho_e$, equations (A.23) and (A.24) can be rewritten and the radial dependency of the radial

[14] At a beam energy of 1.2 GeV this deactivation of the ion clearing would increase the neutralization from approximately 40 % (compare section 4.3.5) to presumably 100 %.

electric field and circular magnetic field can be obtained as

$$E_r(r) = \frac{\rho_\mathrm{e}}{2\varepsilon_0} r = \frac{I}{2\pi\varepsilon_0\beta c}\frac{r}{a^2} \qquad \text{and} \qquad B_\varphi(r) = \frac{\beta\rho_\mathrm{e}}{2\varepsilon_0 c} = \frac{I}{2\pi\varepsilon_0 c^2}\frac{r}{a^2}\,,$$

respectively.

Relativistic Cancellation The force which acts on the electrons due to their space charge is the LORENTZ force. Inserting the previous expressions for the electric and magnetic field of the beam, the radial component of the force

$$F_\mathrm{e}(r) = e\Big(\underbrace{\vec{E}}_{=E_r(r)\vec{e}_r} + \underbrace{\vec{v}\times\vec{B}}_{=-v_s\cdot B_\varphi(r)\vec{e}_r}\Big)\cdot\vec{e}_r = \frac{\mathrm{e}I}{2\pi\varepsilon_0\beta c}\frac{r}{a^2}\left(1-\beta^2\right) = \frac{eI}{2\pi\varepsilon_0\beta c\gamma^2}\frac{r}{a^2} \tag{A.25}$$

can be obtained. $\vec{e}_r$ is the radial unit vector. Here, the velocity $\vec{v}$, being purely longitudinal with component v_s, is expressed as βc and the relation of the LORENTZ factor $1-\beta^2 = 1/\gamma^2$ is used. The electric field leads to a radial dispersal of the electron beam due to its space charge repulsion whereas the circular magnetic field deflects the repulsed electrons back towards the center. For $v = c$ or $\beta = 1$, the defocusing force of the electric field is canceled out by the focusing force of the magnetic field. This state is called *relativistic cancellation*. Thus, the electron-electron defocusing force decreases with $1/\gamma^2$.

Space Charge Field of Accumulated Ions and Bunched Beam Accumulated ions in the beam show only low velocities compared to c ($\beta_\mathrm{ion} \approx 0$). Thus, their magnetic field is equal to zero. Under the assumption, that the ion charge distribution shows a similar shape as the electron beam with an ion charge density of $\rho_\mathrm{ion} = -\hat{\eta}\rho_\mathrm{e}$ which is reduced by the local neutralization $\hat{\eta}$, the attractive COULOMB force acting on the electrons can be expressed as

$$F_\mathrm{ion}(r) = -\frac{\mathrm{e}\hat{\eta}I}{2\pi\varepsilon_0\beta c}\frac{r}{a^2}$$

by recalculating $E_r(r)$ starting from equation (A.23) with ρ_ion.

So far, the electron beam is considered as un-bunched. Due to the bunched structure of the beam, the electrons are compressed into a bunch with GAUSSian longitudinal charge density. The charge density is consequently increased within the bunches and zero in the rest of the rf period. This compression is characterized by the bunching factor $\mathcal{B} > 1$ which is derived in appendix A.18.

Including the superposition of the electron beam's electric field with the field of the ions and the bunched structure of the beam, the total radial force is equal to

$$F(r) = \mathcal{B}\cdot F_\mathrm{e}(r) + F_\mathrm{ion}(r)\,. \tag{A.26}$$

Tune Shift To determine the emerging tune shift of the electron beam the quadrupole kick δk_r due the emerging electromagnetic force $F(r)$ has to be obtained. Therefore, one has to change into the coordinate system of the accelerator. Here, not time derivatives $\ddot{r} = \mathrm{d}^2 r/\,\mathrm{d}t^2$ are used but angular kicks along the longitudinal axis with $r'' = \mathrm{d}^2 r/\,\mathrm{d}s^2$. The angular derivative can be expressed by the time derivative as

$$r'' = \frac{1}{(\beta c)^2}\ddot{r}$$

with which $F(r)$ can generally be expressed as

$$F(r) = \gamma m_e \ddot{r} = \gamma m_e (\beta c)^2 r'' \,. \tag{A.27}$$

The differential equation for radial electron movement along s is given by

$$r'' + \delta k_r \cdot r = 0 \tag{A.28}$$

and resembles the Hillian differential equation without dipole magnets (compare equations (2.28) and (2.29)). Thus, δk_r can be rephrased by using equation (A.27) and including $F(r)$ from equation (A.26) with the corresponding expressions to

$$\delta k_r = -\frac{F(r)}{\gamma m_e (\beta c)^2} \frac{1}{r} \tag{A.29}$$

$$= -\frac{eI}{2\pi\varepsilon_0 m_e (\beta c)^3 \gamma} \frac{1}{a^2} \left(\frac{\mathcal{B}}{\gamma^2} - \hat{\eta} \right) \,. \tag{A.30}$$

However, δk_r is only valid for a bunched, round beam with constant charge density. For an elliptical beam, a^2 is replaced by $\sigma_{x,z}(\sigma_x + \sigma_z)$ [Hin11, section 17.1]. r is decomposed into its horizontal and vertical components.

The horizontal and vertical tune shift due to a small quadrupole kick $\delta k_{x,z}$, which does not significantly alter the optical functions of the accelerator, is given by [Wil00, section 3.15.2, equation 3.274]

$$\Delta Q_{x,z} = \frac{1}{4\pi} \oint \delta k_{x,z}(s) \cdot \beta_{x,z}(s) \, \mathrm{d}s \,.$$

Finally, the tune shift due to the space charge force of the electron beam and the accumulated ions is given by

$$\Delta Q^{\mathrm{sc}}_{x,z} = -\frac{\mathrm{e}I}{8\pi^2 \varepsilon_0 m_e (\beta c)^3 \gamma} \oint_0^C \frac{\beta_{x,z}(s)}{\sigma_{x,z}(s) \left(\sigma_x(s) + \sigma_z(s)\right)} \left(\frac{\mathcal{B}}{\gamma^2} - \hat{\eta}(s) \right) \mathrm{d}s \,.$$

Here, the beam is bunched and has an elliptical shape with constant transversal charge density. The ion density distribution is assumed to resemble the distribution of the electron beam.

Assuming a constant beta function, which is equal to its average $\langle \beta_{x,z} \rangle$ along the accelerator, the tune shift can be expressed as

$$\Delta Q^{\mathrm{sc}}_{x,z} = +\frac{\mathrm{e}IC}{8\pi^2 \varepsilon_0 m_e (\beta c)^3 \gamma} \frac{\eta}{\epsilon_{x,z}} \frac{\sqrt{\langle \beta_{x,z} \rangle}}{\sqrt{\langle \beta_x \rangle} + \sqrt{\langle \beta_z \rangle}} \tag{A.31}$$

for a relativistic electron beam with $\gamma \gg 1$. Here, $\hat{\eta}(s)$ is also assumed to be constant along the accelerator with an average neutralization of η.

A.18 Bunching Factor

The time average beam potential can be expressed by the time dependent beam potential $U(x, z, s, t)$ as

$$\begin{aligned}\langle U(x,z,s)\rangle &= \frac{1}{t_{\mathrm{rf}}}\int_0^{t_{\mathrm{rf}}} U(x,z,s,t)\,\mathrm{d}t \\ &= \frac{1}{t_{\mathrm{rf}}}\int_{-\xi t_{\mathrm{bunch}}}^{\xi t_{\mathrm{bunch}}} U(x,z,s,t)\,\mathrm{d}t + \underbrace{\frac{1}{t_{\mathrm{rf}}}\int_{\xi t_{\mathrm{bunch}}}^{t_{\mathrm{rf}}-\xi t_{\mathrm{bunch}}} U(x,z,s,t)\,\mathrm{d}t}_{=0}\ .\end{aligned}$$

Here, the integral along the entire accelerator is replaced by the integral over one rf period t_{rf} in which one bunch is positioned. The integral is split up into two parts, one part around $\pm\xi t_{\mathrm{bunch}}$ ($\xi > 0$) around the beam center and another part in-between two neighboring bunches, whose contribution is approximately zero.

Observed from a fixed s position in the accelerator, the passing bunch has a Gaussian charge distribution in time. Thus, it holds

$$U(x,z,s,t) = U_0(x,z,s)\exp\left(-\frac{t^2}{2t_{\mathrm{bunch}}^2}\right)$$

with $t_{\mathrm{bunch}} = \frac{\sigma_{\mathrm{bunch}}}{\beta c}$.

The time average beam potential can be expressed as

$$\langle U(x,z,s)\rangle = \frac{1}{t_{\mathrm{rf}}}\int_{-\xi t_{\mathrm{bunch}}}^{\xi t_{\mathrm{bunch}}} U_0(x,z,s)\ \exp\left(-\frac{t^2}{2t_{\mathrm{bunch}}^2}\right)\mathrm{d}t \tag{A.32}$$

$$= \frac{\sqrt{2\pi}\sigma_{\mathrm{bunch}}}{\beta c t_{\mathrm{rf}}}\ U_0(x,z,s)\ \mathrm{erf}\left(\frac{\xi}{\sqrt{2}}\right)\ . \tag{A.33}$$

$\mathrm{erf}\,(y)$ is the error function. Rearranging this equation, the bunching factor $\mathcal{B}$ is determined as

$$\mathcal{B} = \frac{U_0(x,z,s)}{\langle U(x,z,s)\rangle} = \frac{t_{\mathrm{rf}}\beta c}{\sqrt{2\pi}\ \mathrm{erf}\left(\frac{\xi}{\sqrt{2}}\right)\ \sigma_{\mathrm{bunch}}} \overset{\xi\to\infty}{\approx} \frac{t_{\mathrm{rf}}\beta c}{\sqrt{2\pi}\sigma_{\mathrm{bunch}}}\ . \tag{A.34}$$

For the storage ring, $\mathcal{B}$ varies from 23.8 at 1.2 GeV to 8.9 at 3.2 GeV, assuming a constant synchrotron frequency of 89 kHz.

A.19 Transversal Equilibrium Ion Density Distribution

A.19.1 Nominal Ion Density Distribution by TransversIon

To simulate the nominal horizontal ion density distribution in close proximity downstream of dipole magnet M26, TransversIon is configured similarly to simulations where the distribution of section 5.1.3 has been reproduced. 300 000 ions are tracked through the potential of an electron beam with an energy of 1.2 GeV and a current of 35 mA for a duration of 1 ms. The beam potential is precomputed with a horizontal resolution of 9.6 µm. The time increment of the tracking algorithm is equal to 6.4 ns.

For the horizontal ion production map, a Gaussian density distribution with the dimension of the electron beam is used as only the ion production process of impact ionization is considered. The

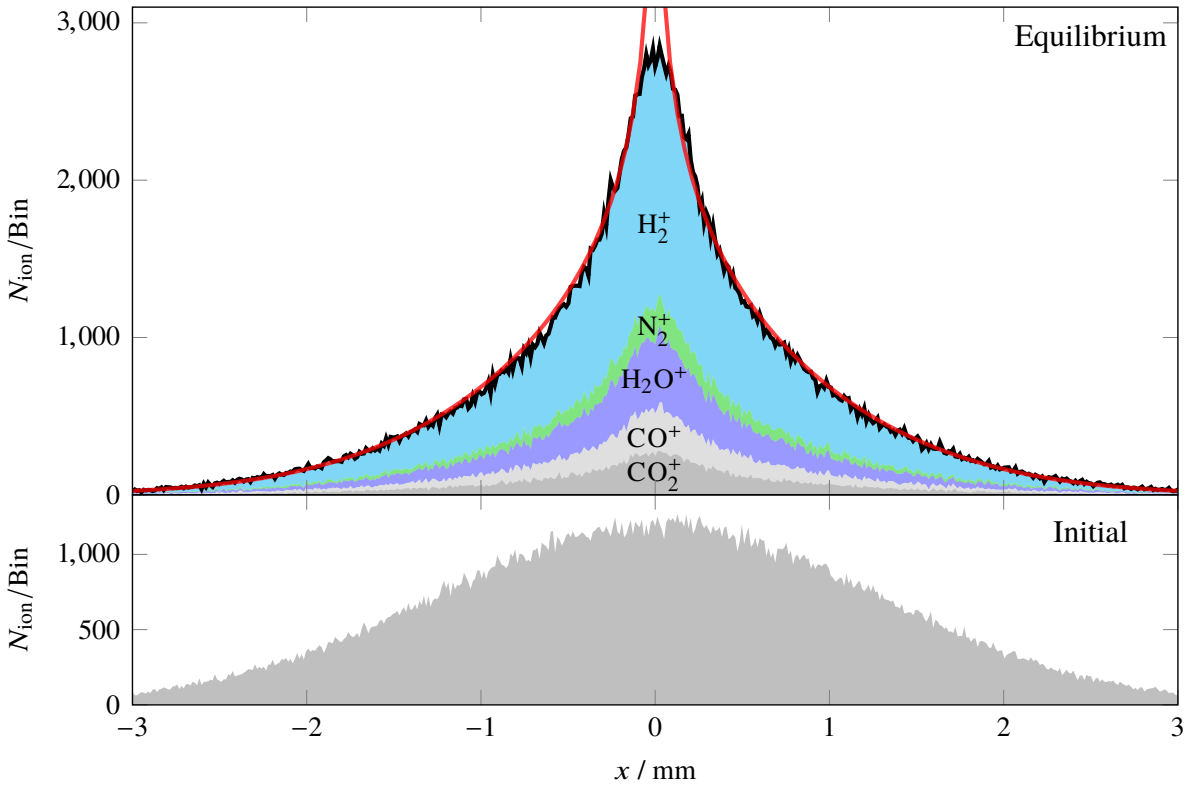

Figure A.20: Nominal ion distribution in the horizontal plane 5 cm after the dipole magnet M26 at s = 132.2 m, simulated by TRANSVERSION. The top graph shows the equilibrium ion distribution for 1.2 GeV beam energy. The black curve shows the ion distribution for the local ion population. It is added up by the contributions of every single ion species which are depicted as colored surfaces. The production map of the ion population is shown in light gray in the bottom graph. Here, a production map for pure impact ionization is used. In red a fit of the idealized theoretical curve from equation (5.4) is shown for this scenario.

production probabilities of the different ion species are chosen accordingly.

Figure A.20 shows the resulting horizontal equilibrium ion density distribution with a binning width of 12.8 µm. If only the process of impact ionization is considered in the ion production map, the distribution (black) follows the theoretical prediction (red). Similar to figure 5.7, the simulated distribution diverges from the theoretical prediction in the beam center as the initial velocity is non-zero and is chosen randomly for each ion. The ion production map which is used in this scenario is shown in the bottom graph.

The approximated theoretical curve can subsequently be compared with the perturbed ion density distribution to visualize deviations.

A.19.2 Modification to the TAVARES Ion Density Distribution

To include the broadening of the ion density distribution due to photo ionization into the theoretical ion density distribution, equation (5.4) has to be changed slightly. In figure 5.15 in section 5.1.4, a modified theoretical equilibrium ion density distribution is shown as the orange curve. The modified density distribution follows the simulated distribution closer than the nominal density distribution. In this empirical modification, the photo ionization contribution is included by using a modified beam width. As already discussed in section 3.4.4, the photo ionization shifts the barycenter of the ion production by x_{cm}

in reference to the beam center. This shift is included into an effective beam width as

$$\sigma_{x,\mathrm{PI}} = \sqrt{\sigma_x^2 + \left(\frac{x_{\mathrm{cm}}}{2}\right)^2} \,.$$

At the end of dipole magnet M26, x_{cm} is equal to $(8.0 \pm 0.1)\,\mathrm{mm}$ at 1.2 GeV. Because σ_x is equal to 0.87 mm, $\sigma_{x,\mathrm{PI}}$ is 4.1 mm. The photo ionization increases the effective beam width by a factor of approximately four. Thus, the horizontal ion density distribution is given as

$$\rho_{\mathrm{ion,PI},x}(x) \sim \exp\left(-\frac{x^2}{4\sigma_{x,\mathrm{PI}}^2}\right) \cdot K_0\left(\frac{x^2}{4\sigma_{x,\mathrm{PI}}^2}\right) \,.$$

This modification is valid in regions downstream of dipole magnets, where synchrotron radiation photons, which escape the magnet, cause a shift of the barycenter of ion production due to photo ionization. In the dipole magnet, where the vertical magnetic field restricts free horizontal ion movement, it cannot be applied.

A.20 Beam Shaking

When this clearing method is applied, a low-amplitude sinusoidal excitation signal is applied onto the beam in the vertical plane via a kicker with a frequency which is slightly different to the tune or the frequency of one of the beam's multi-bunch oscillation modes. In dependence of the excited multi-bunch oscillation mode, corresponding to an upper or lower betatron sideband around a particular revolution harmonic, the excitation frequency should be lower than the sideband's frequency for a lower sideband or higher than an upper sideband's frequency (compare section 5.2.1).

When the ions accumulate in the accelerator and the neutralization increases, the emerging positive tune shift aligns the beam's tune with the excitation frequency, resulting in a short resonant beam oscillation. Consecutively, the neutralization is reduced as ions are shaken off the beam. For more information on beam shaking, see e.g. [Pon94, section 6].

Note that the developed tool TransversIon which has been described in section 5.1.3 and appendix B.2.6, also enables the determination of the clearing rate of individual ion species when the beam is shaken with a certain oscillation frequency and amplitude.

A.21 Supplements to the Ion Current Measurement Technique

A.21.1 Properties of the Transversal Transmission Function $\mathscr{F}$

The transversal transmission function, derived in section 6.1.4, is parameterized as

$$\mathscr{F} = 1 - l_{\mathrm{hollow}}\hat{\eta}_{\mathrm{stat}} + \mathcal{F}\hat{\eta}_{\mathrm{stat}}\left(l_{\mathrm{hollow}} - l_{\mathrm{free}}\right) \,.$$

To evaluate the possible values of l_{hollow} and l_{free}, $\mathscr{F}$ is examined at its extrema. As visible in the top graph of figure A.21 for a clearing voltage of zero, where $\hat{\eta}_{\mathrm{stat}}$ is equal to one and $\mathcal{F} = 0$ (all ions are trapped with $\mathcal{H} = 1$), the measured ion current must be zero (compare equation (6.2)). Thus, $\mathscr{F}\left(U_{\mathrm{CE}} = 0\right) = 0$. For a sufficiently high clearing voltage, where no ion accumulation is possible in front of the electrode and $\hat{\eta}_{\mathrm{stat}}$ is zero, which results in $\mathcal{F}$ being one, it is demanded that $\mathscr{F}(U_{\mathrm{CE}} \to -\infty) = 1$.

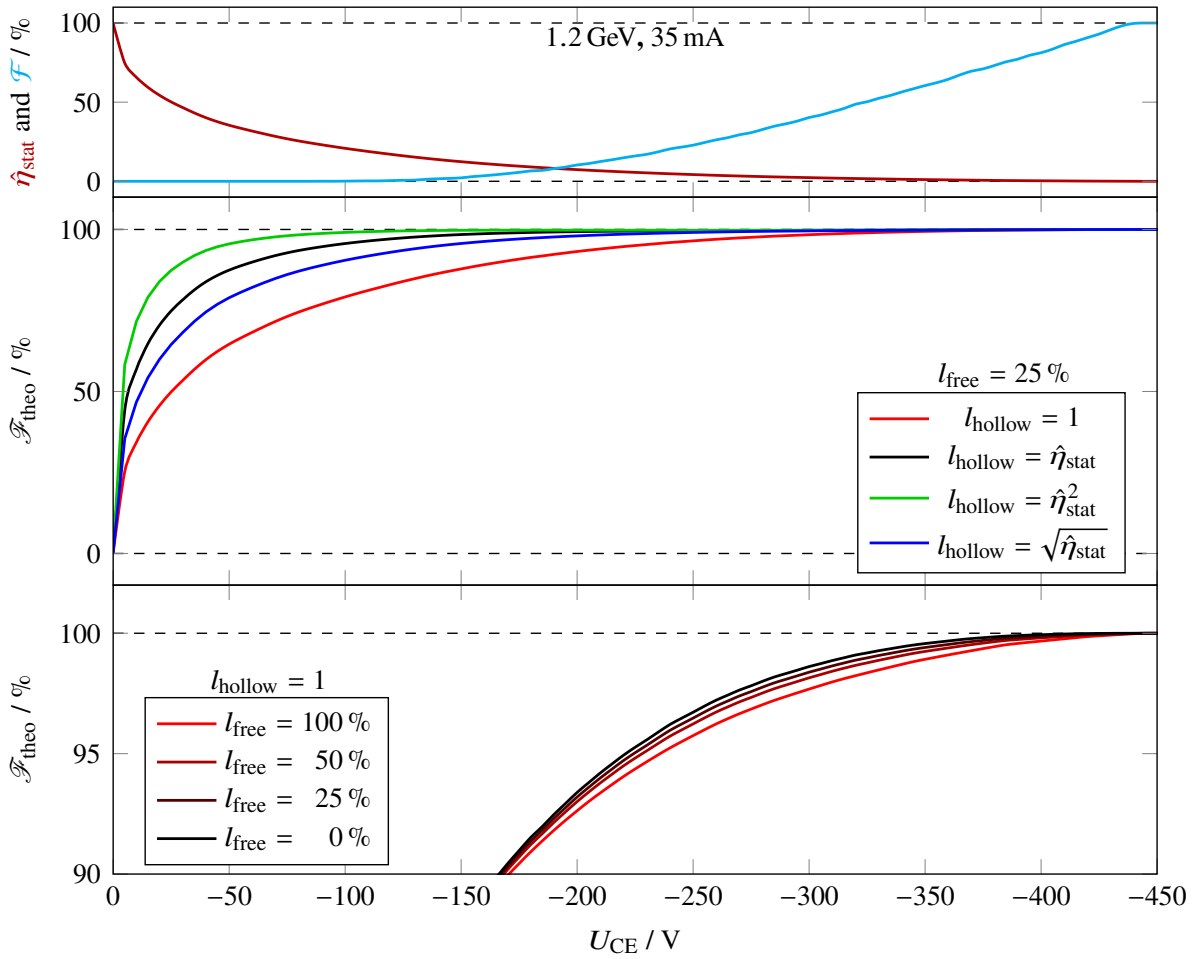

Figure A.21: $\mathscr{F}_{\mathrm{theo}}$ at a beam energy of 1.2 GeV and current of 35 mA for different model parameters. The top graph shows the local static neutralization at the clearing electrode in the vicinity of quadrupole QD1 for different clearing voltages in red. In cyan, $\mathcal{F}$ is visualized for the same clearing voltages. The middle graph exemplarily shows the resulting transversal transmission function $\mathscr{F}_{\mathrm{theo}}$ for $l_{\mathrm{free}} = 25\,\%$ and different approaches of l_{hollow}. The bottom graph shows an excerpt of $\mathscr{F}_{\mathrm{theo}}$ with $l_{\mathrm{hollow}} = 1$ and different values of l_{free}.

If additionally the longitudinal transmission function $\mathscr{L}$ is equal to one, this implies, that all generated ions are collected by the clearing electrodes.

The middle graph of figure A.21 shows the theoretical shape of $\mathscr{F}$ for different mathematically valid approaches of l_{hollow}. For a clearing voltage of zero, $\mathscr{F}$ is also zero. Here, no ion current would be measurable. For voltages below −150 V, where the flow $\mathcal{F}$ is still zero, the term $1 - l_{\mathrm{hollow}}\hat{\eta}_{\mathrm{stat}}$ dominates the shape of the transmission function. Here, the parameterization of l_{hollow} shows its influence on $\mathscr{F}$ most prominently. Where $\mathscr{F}$ reaches 90 % for $l_{\mathrm{hollow}} = 1$ at −170 V, it reaches the same value for lower voltages (−95 V for $l_{\mathrm{hollow}} = \sqrt{\hat{\eta}_{\mathrm{stat}}}$, −60 V for $l_{\mathrm{hollow}} = \hat{\eta}_{\mathrm{stat}}$ and −30 V for $l_{\mathrm{hollow}} = \hat{\eta}^2_{\mathrm{stat}}$). For $l_{\mathrm{hollow}} = 1$, all ions of $\mathcal{H}$ experience losses which scale with $\hat{\eta}_{\mathrm{stat}}$, whereas the fraction of lost ions of $\mathcal{H}$ (losses $\Delta\mathcal{H}$) are reduced for the other chosen approaches. In the following, l_{hollow} is chosen to be one because all ions of $\mathcal{H}$ are expected to suffer losses due to their stay within the potential hollow.

In the bottom graph, the sensitivity of $\mathscr{F}$ to l_{free} is visualized for $l_{\mathrm{hollow}} = 1$. Its influence is only noticeable for clearing voltages, where the static neutralization is not yet zero and where $\mathcal{F} > 0$. Here,

the difference between $l_{\mathrm{free}} = 0\,\%$ and $100\,\%$ is approximately maximal $3\,\%$ of $\mathscr{F}$ at $-270\,\mathrm{V}$.

The second term ($\mathcal{F}\hat{\eta}_{\mathrm{stat}}(l_{\mathrm{hollow}} - l_{\mathrm{free}})$) is a higher order supplement, which corrects the measured current for the "leak" ion current. The conducted measurements of the characteristic curve show only little sensitivity to l_{free}, therefore l_{free} is set to 0.5 in the course of the analysis. This choice is reasonable as it implies that half of the flow $\mathcal{F}$ experience space charge related losses in the potential hollow: Ions which are produced at the side of the beam which is facing the clearing electrode do not cross the ion cloud in the beam center when being drawn towards the electrode. This part of $\mathcal{F}$ consequently does not experience losses. The other half of the ions in the flow $\mathcal{F}$ are produced on the side of the beam which is averted to the electrode and cross the beam center in which losses are inflicted due to ions' mutual space charge interactions.

A.21.2 Numerical Determination of $\hat{\eta}_{\mathrm{stat}}$ and $\mathcal{F}$

The vertical motion of generated ions is tracked for a defined timespan within the electric potential at every clearing electrode in the storage ring, utilizing `TRANSVERSION`. The potential thereby results from the superposition of the local beam potential and the clearing electrode's potential. The local beam potential is calculated for a certain energy and current using the optical functions at the longitudinal position of the electrode. The electrode's potential is scaled with the clearing voltage and is based on the potential which has been simulated using CST (compare section 6.1.2). Into every so-generated potential, $N_{\mathrm{ion}} = 5\,000$ ions of different species are placed with randomized thermal velocities and initial vertical position in accordance with the corresponding probability distributions. Each ion's motion is tracked for a defined timespan and it is determined whether it reaches the clearing electrode or stays trapped within the potential. If a produced ion reaches the clearing electrode the counter $N_{\mathrm{ion,free}}$ is incremented by one. If all ion trajectories have been simulated, $\mathcal{F}$ is determined. Additionally, for each setting, the local static neutralization within the potential is determined using equation (4.3).

Since the beam width variation along the accelerator changes the shape and depth of the beam potential, the process is repeated for every clearing electrode position in the storage ring. The obtained values for $\mathcal{F}$ and $\hat{\eta}_{\mathrm{stat}}$ for the storage ring at one clearing voltage, the individual flows and static neutralizations are averaged. The calculation steps are reiterated for every clearing voltage setting.

A.21.3 Investigations on Additional Error Sources

Reproducibility Some parameters or functions, on which the correct analysis of the measured characteristic curve relies, are not precisely known: On one hand, the longitudinal transmission function $\mathscr{L}$ is *assumed* to simply rise with U_{CE}. Other, non-linear behaviors with U_{CE} are mapped into the transversal transmission function $\mathscr{F}$. $\mathscr{F}$ is *assumed* to be more sensitive on the escape-process of ions out of potential hollows with increasing U_{CE} than $\mathscr{L}$. If the assumed behavior of $\mathscr{L}$ would change from one measurement to another, this would influence the extracted $\mathscr{F}$ gravely. On the other hand, the average pressure $\mathcal{P}(E, I)$ in the vacuum system of the storage ring is only estimated. Here, the developed pressure model (compare section 3.2) can only estimate the expected average pressure in the storage ring for a certain beam energy and current and known no-load pressure $\mathcal{P}_0$. $\mathcal{P}_0$ alters from measurement to measurement and influences the measured I_{CE} from which $\mathscr{F}$ is extracted.

To exclude the influence of the discussed quantities, the characteristic curve is measured at a beam energy of 1.2 GeV and a current of approximately 33 mA at two different dates where the pressure in the storage ring has been different. The extracted $\mathscr{F}$ for this test of the measurements reproducibility is shown in figure A.22. In the context of the individual measurement errors, both measurements are in

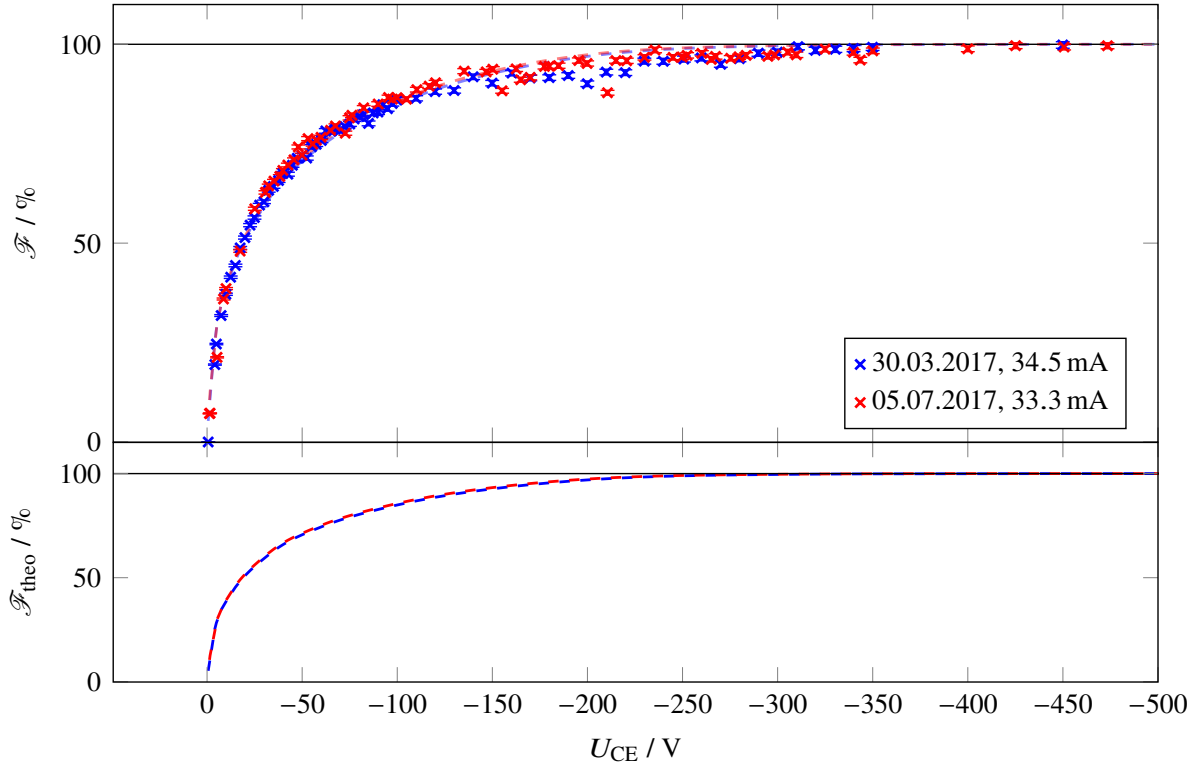

Figure A.22: Comparison of two measurements of the transversal transmission function $\mathscr{F}$ which have been conducted on two different dates at a beam energy of 1.2 GeV. The corresponding theoretical predictions $\mathscr{F}_{\text{theo}}$ for the two measurements are shown in the bottom graph.

agreement with each other. Both also replicate the predicted $\mathscr{F}_{\text{theo}}$. Consequently, these two systematic error sources are not the cause of the difference between measured and predicted $\mathscr{F}$.

Beam Loss If the stored beam current in the storage ring is reduced significantly, the measured $\mathscr{F}$ would deviate from the predicted $\mathscr{F}_{\text{theo}}$, which is calculated for one fixed beam current only. During the measurements, the beam current is reduced by 2.49, 1.1 and 0.74 mA for 1.2, 1.7 and 2.7 GeV, respectively. Thus, the beam loss is equal to 16.7, 8.0 and 6.5 % of the initial current during the corresponding measurements. The relative beam loss has been comparably higher (17 %) for the previous measurement at 1.2 GeV, 46.4 mA (compare figure 6.12). Here, the measurements could reproduce $\mathscr{F}_{\text{theo}}$ with a reduced χ^2 of 5.34. Hence, the experienced beam loss during the measurements is not significant enough to cause the observed deviation.

Beam Potential Depth The depth of the beam potential is dependent on the beam current, the transversal beam size and the geometry of the beam pipe (compare section 2.4.1). The beam current for all measurements shown in figure 6.13 is similar. Also, the beam pipe geometry obviously has not changed with the beam energy. Thus, the only remaining parameter is the transversal beam size.

As already discussed in the theory section of this work, the beam size scales with the emittance of the accelerator, which in turn scales with the beam energy (compare section 2.3.3). For the storage ring, this has been experimentally verified [Zan13, section 6.3]. Thus, the beam potential is less deep for higher beam energies. However, the wrong assumptions about the betatron coupling coefficient κ and the

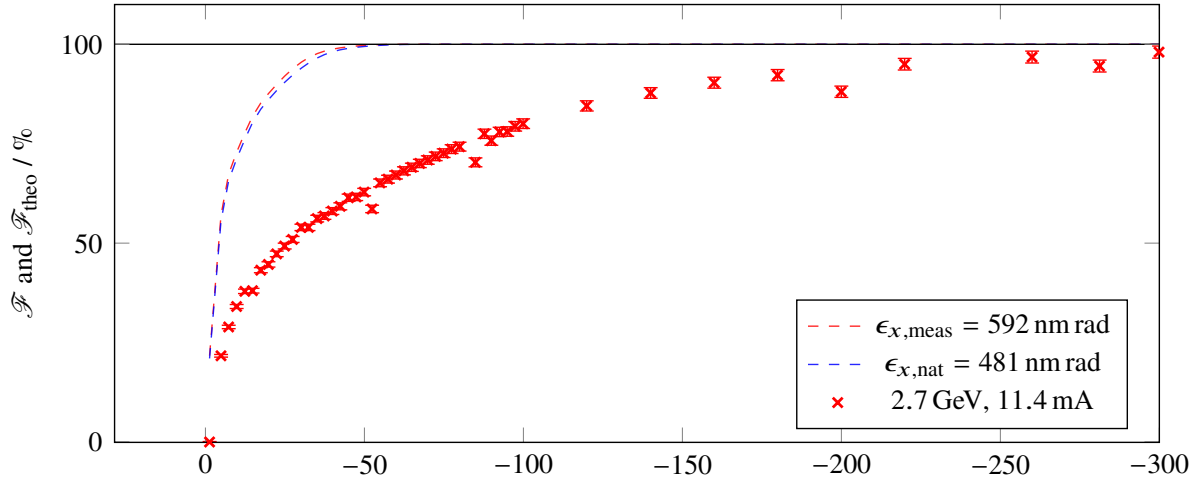

Figure A.23: Transversal loss function $\mathscr{F}$ for a beam current of approximately 11.4 mA at 2.7 GeV in comparison to different $\mathscr{F}_{\text{theo}}$ based on the measured (red, dashed) or natural emittance (blue, dashed).

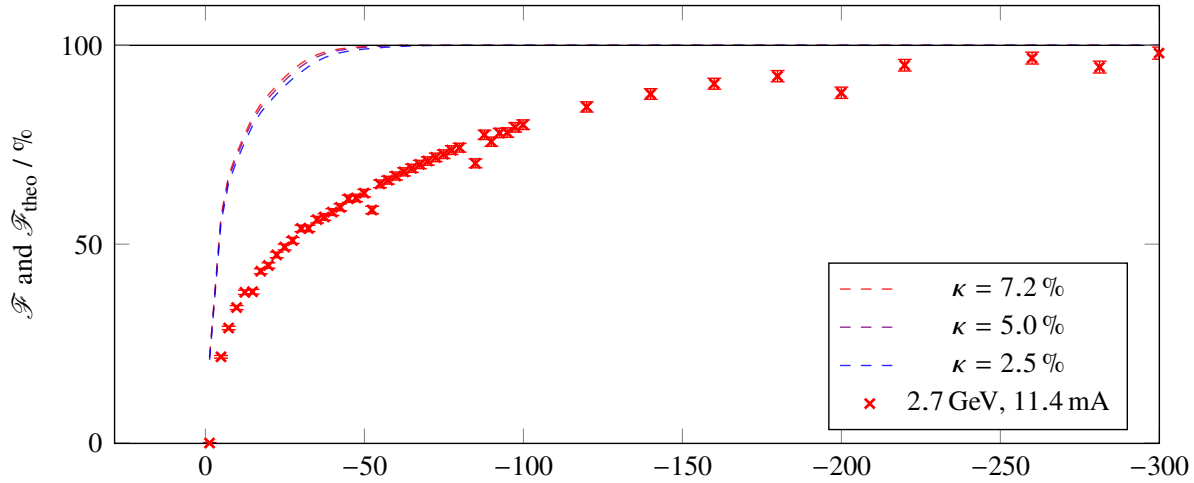

Figure A.24: Transversal loss function $\mathscr{F}$ for a beam current of approximately 11.4 mA at 2.7 GeV in comparison to $\mathscr{F}_{\text{theo}}$ for different couplings between the horizontal and vertical plane.

emittance of the beam may result in an erroneous depth of the beam potential:

The used emittance for the calculation of the beam width and the resulting beam potential is based on the emittance measurements of [Zan13]. To study the emittance's influence on $\mathscr{F}_{\text{theo}}$, instead of the measured emittance, the natural emittance is used. For the measurement at 2.7 GeV and 11.4 mA, a natural emittance $\epsilon_{x,\text{nat}}$ = 481 nm rad is utilized instead of a measured emittance $\epsilon_{x,\text{meas}}$ of 592 nm rad. Figure A.23 shows the comparison between $\mathscr{F}_{\text{theo}}$ for the two emittances and the measurement. When using the natural emittance instead of the measured one, the predicted threshold voltage is shifts from −60 to −67.5 V. But still, the relative deviation between predicted and measured threshold voltage (−320 V) is 374 %.

In this work the betatron coupling coefficient of the storage ring is assumed to be constant at $\kappa = (7.2 \pm 2.7)$ % for all beam energies. Assuming that κ decreases with the beam energy, the vertical beam width would decrease relatively in comparison to the case of a constant κ, resulting in a deeper

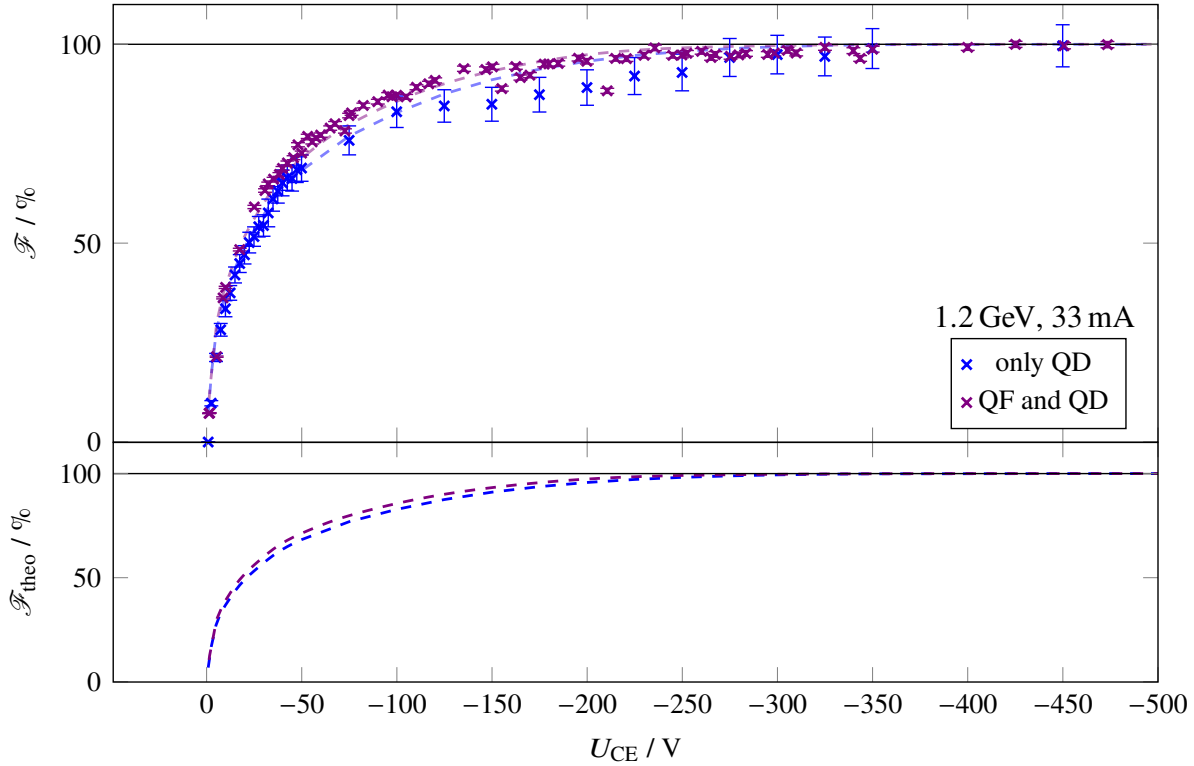

Figure A.25: Transversal loss function $\mathscr{F}$ for a beam current of approximately 33 mA at 1.2 GeV. Here, one characteristic curve (violet) is measured with only the clearing electrodes of the QD quadrupoles connected. In the other measurement (blue), all clearing electrodes are connected.

beam potential. Figure A.24 shows the predicted $\mathscr{F}_{\text{theo}}$ for a coupling of 7.2, 5.0 and 2.5 % in comparison to the measured $\mathscr{F}$ at 2.7 GeV and 11.4 mA. The influence of the altered betatron coupling coefficient on $\mathscr{F}_{\text{theo}}$ is negligibly small: Here, a coupling coefficient of 2.5 % only shifts the theoretical threshold voltage to −65 V, which amounts to an alteration of 5 V in reference to the scenario where κ is equal to 7.2 %. Thus, a change of the coupling coefficient with beam energy can be exclude as a potential error source.

Unequal Participation of QF and QD Clearing Electrodes The measured $\mathscr{F}$ changes if different clearing electrodes are connected to the electrode network. In figure A.25, two measurements of $\mathscr{F}$ where conducted at a beam energy of 1.2 GeV and 33 mA beam current with different settings of connected clearing electrodes. In one measurement, only clearing electrodes in the vicinity of QD quadrupole magnets are connected to the electrode network whereas in the other one all electrode are connected. As predicted by $\mathscr{F}_{\text{theo}}$, a difference in $\mathscr{F}$ for the two settings is visible: At QD quadrupoles, the beam potential has its local minima and thus is deeper than at QF quadrupoles where the beam potential shows its local maxima. Consequently, a higher clearing voltage is required at QD electrodes to draw all ions from the beam than at QF electrodes. Hence, in the measurements using only QD electrodes, $\mathscr{F}$ is consistently lower in the $\mathscr{F}$ regime than in measurements where all electrodes are connected. Here, the additional contributions of the QF electrodes to I_{CE} increases the resulting $\mathscr{F}$.

In $\mathscr{F}_{\text{theo}}$, it is assumed that QD and QF electrodes contribute equally to the measured I_{CE}. Since ions follow the longitudinal gradient of the beam potential to its local minima, clearing electrodes at

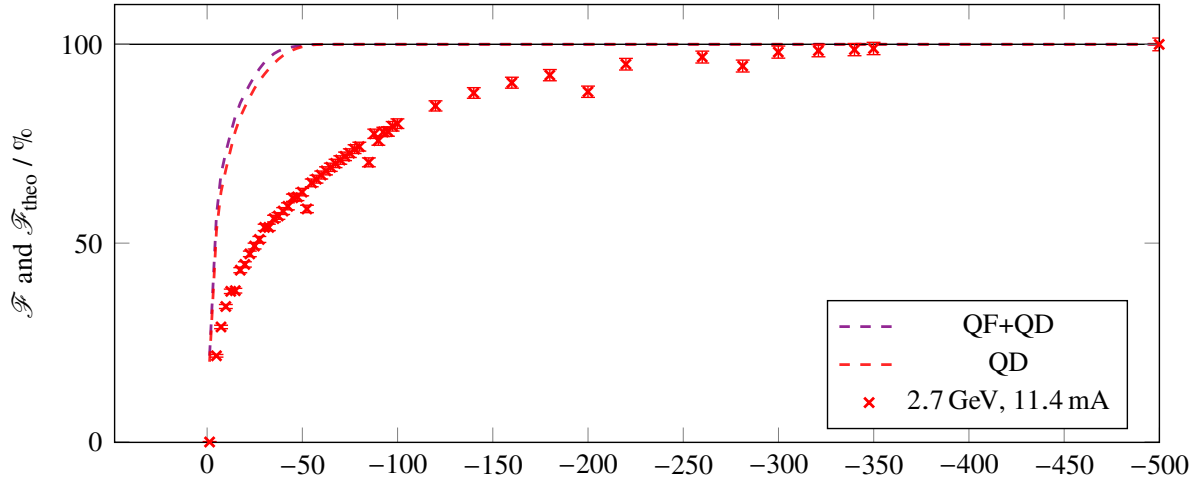

Figure A.26: Transversal loss function $\mathscr{F}$ for a beam current of approximately 11.4 mA at 2.7 GeV in comparison to predicted $\mathscr{F}_{\text{theo}}$ for different settings of connected clearing electrodes. The prediction when utilizing only clearing electrodes at QF quadrupoles are shown as red, dashed line whereas the prediction for all connected clearing electrodes are shown in violet, dashed.

QD quadrupoles, the accumulation point, are assumed to contribute more to I_{CE} than electrodes at QF quadrupoles, which only collect ions in their region of influence. This of course only holds true if the ions' transmission probability, when entering the dipole magnets' fringe fields on their way to the local minima of the potential, is equal to one. If it is smaller than one, as it is the case in the storage ring (compare figure 4.15), a fraction of ions is reflected by the fringe field into the direction of the QF electrodes, eventually being collected there. Thus, the QF electrodes' contribution to I_{CE} increases for a decreasing transmission probability. A small difference of the measured $\mathscr{F}$ for the two electrode settings is visible, indicating that the contribution of the QF electrodes to I_{CE} indeed is not negligible small.

The individual contributions of the QD and QF electrodes poses another source for a potential systematic error which may explain the different between predicted and measured $\mathscr{F}$. Although the transmission probability decreases for an increasing beam energy, it is assumed that the transmission probability is equal to one and thus only QD electrodes contribute to I_{CE} during the measurements. Figure A.26 shows the results of this investigation. Indeed, the predicted threshold voltage shifts from −60 V, when using all electrodes, to −62.5 V, when using only QD electrodes. Nonetheless, the difference between measured and predicted transversal transmission function is still evident.

Combining the Error Sources In figure A.27, the comparison of predicted and measured $\mathscr{F}$ for all the studies are shown. If all discussed effects are combined by using a hypothetical beam, with its vertical beam size resulting from the theoretical natural emittance coupled to the vertical plane with $\kappa = 0.5\,\%$, and involving only QD electrodes, the predicted threshold voltage is shifted to −97.5 V. The prediction for this case is shown as black line in the graph. Yet, the measured threshold voltage is still a factor of 3.28 higher than the prediction. Consequently, the shape and depth of the beam potential can be ruled out as a cause for the deviation between prediction and measurement.

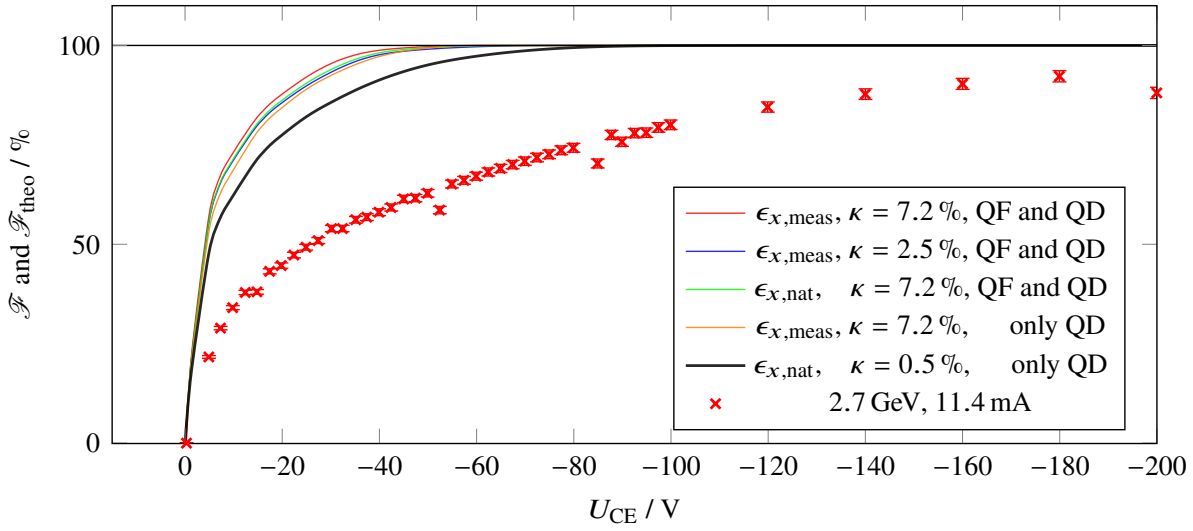

Figure A.27: Comparison of the measured $\mathscr{F}$ for a beam energy of 2.7 GeV and a current of 11.4 mA and the predictions $\mathscr{F}_{\text{theo}}$ for the measurements, if certain systematical errors are assumed. The prediction and measured data for the expected parameters are shown in red. The prediction for a reduced coupling of 2.5 % is shown in blue. In case the natural emittance is used as basis for the prediction, $\mathscr{F}_{\text{theo}}$ is shown as the green line. The prediction for a contribution to the measured current of only the clearing electrodes in the QD quadrupole magnets contribute is denoted as orange line. The prediction for all combined cases is shown in black.

APPENDIX B

Programs and Scripts

In this section of the appendix, a list of useful programs and scripts, related to this thesis, is shown. For each utility, a short description of its purpose and the used approach for its calculations is given. Names of parameters and arrays within the scripts are denoted as *parameter*.

For more information on the usability and transferability of these tools to other accelerators and problems, contact the author of this work (`sauerland@physik.uni-bonn.de`).

B.1 Programs

B.1.1 MSAUGA

The C++ program MSAUGA, developed with major contributions of D. Proft from ELSA, enables the determination of the composition of a residual gas on basis of a measured mass spectrum $p_{\mathrm{meas}}(A/Z)$. To do so, MSAUGA uses a genetic algorithm to map a hypothetical mass spectrum $p_{\mathrm{sim}}(A/Z)$, generated from fragmented and ionized molecules and atoms of a hypothetical residual gas composition, onto the measured spectrum $p_{\mathrm{meas}}(A/Z)$ while minimizing the assessment function $\mathcal{A}$ (compare equation (3.1) in section 3.1.3).

In the genetic algorithm, a population with a constant size of 100 individuals, each being equipped with an individual genome, evolves from one generation to the other. Here, a genome consists of a set of up to 65 genes which each corresponds to the individual share of a species to the analyzed ionized gas current $\gamma_{\mathrm{qma},k}$. The genome can be transferred to a residual gas composition via the individual gas species' relative sensitivity ς and to $p_{\mathrm{sim}}(A/Z)$ via the species' cracking patterns. These transfers can be visualized as follows:

gas composition		"genome"		
$\frac{p_1}{\mathcal{P}}, \ldots, \frac{p_k}{\mathcal{P}}$	$\overset{\varsigma}{\Longleftrightarrow}$	$\gamma_{\mathrm{qma},1}, \ldots, \gamma_{\mathrm{qma},k}$	$\overset{\text{crack. patt.}}{\Longleftrightarrow}$	$p_{\mathrm{sim}}(1), \ldots, p_{\mathrm{sim}}(A/Z)$

The first generation is a population whose individuals are randomly generated with a set of arbitrary genomes. 90 % of the population reproduce pairwise and produce new individuals with a mixed genome. 15 % of all genes of the population mutate in each generation. Here, e.g. one $\gamma_{\mathrm{qma},k}$ of an individual is altered selectively. Subsequently, each individual of the population is rated by translating $\gamma_{\mathrm{qma},k}$ into the hypothetical mass spectrum $p_{\mathrm{sim}}(A/Z)$ and using the expression for $\mathcal{A}$. Only the 100 individuals with

highest rating are used in the follow-up generation. This procedure occurs from generation to generation. Additionally every 5 000 generations, the lower rated half of the population is replaced by 50 individuals with completely randomized new genomes.

In one MSAUGA simulation, typically the evolution of $2 \cdot 10^6$ generations is tracked, each time selecting the fittest individuals. At the end of the simulation, the fittest individual's genome is translated into a residual gas composition. This composition resembles the measured composition $p_{\text{meas}}(A/Z)$ the most.

B.2 MATLAB Scripts

B.2.1 PHOTOIONPROD

A MATLAB script which evaluates the ion production map at a certain position in a dipole magnet (position s or angle of beam deflection within a dipole α) for the process of photo ionization due to synchrotron radiation.

Functional Principle

PHOTOIONPROD calculates the synchrotron radiation photon flux per solid angle, weighted by the photo ionization cross section. This quantity, which is proportional to the production rate at a certain solid angle, is projected onto a transversal ion production map which is positioned somewhere within the dipole magnet. These projected values accumulate on the map while a synchrotron radiation source, an electron beam with GAUSSian intensity profile, approaches the map's position. For more information, see also appendix A.10.2.

Procedure

The functional procedure of this script is the following:

- To start a simulation amongst others the beam energy, the optical functions β_x, β_z, D_x and the accelerator's circumference have to be declared. Also the size, resolution and position of the ion production map has to be configured. Its position within the dipole magnet can be defined via the angle of beam deflection. For an ELSA dipole magnet which deflects the passing beam by a total angle of 15°, a position of 7.5° denotes an ion production map in the midst of the magnet whereas a position of 15° places the ion production map at the end of the magnet.
- First PHOTOIONPROD generates a map of angular coordinates φ and Θ for a specific set of transversal coordinates $\tilde{x}$ and $\tilde{z}$ which are irradiated by the synchrotron radiation source at a distance l_0. This mapping from Cartesian to angular coordinates is necessary as the distribution of the synchrotron radiation is given in angular coordinates (compare equation (A.17) in appendix A.10.2).
- At a position of the synchrotron radiation source furthest away from the ion production map, the simulation is initialized. Here, the irradiation of the map by the source is emulated by calculating $\langle \sigma_{\text{pi},i}(E_\gamma) \rangle \cdot \breve{\Phi}_\gamma(E_\gamma, \Theta(\tilde{x}, \tilde{z}))$, which in short may be called $\tilde{\Lambda}$, for the fixed set of $\tilde{x}$ and $\tilde{z}$.
- If one coordinate set is run through, the synchrotron radiation source is displaced horizontally and vertically and the calculations are carried out again. These displacements are used to emulate a non-point-like source such as the electron beam. The calculated photon flux at these displaced positions is attenuated in accordance of the precomputed two-dimensional bi-GAUSSian intensity profile of the electron bunch. In the center of the beam, the synchrotron radiation source is brightest, whereas its intensity decreases towards the edge of the beam.

- Because the synchrotron radiation photons propagate away from the source like rays towards the ion production map, the $\tilde{\Lambda}$-values can be projected onto the map by using trigonometric relations. The plane of the synchrotron radiation source and ion production map are horizontally tilted to each other as one always considers purely transversal planes. Since the deflection angle at the position of the source and the map are different for most part of the simulations, the so-occurring inclination angle has to be considered in the projection calculations.
- The ion production map has a finite resolution and thus a fixed number of pixels. Each of these pixels correspond to a specific coordinate on the map. When the $\tilde{\Lambda}$-values are projected onto specific positions of the ion production map, the values are stored in the pixel which are closest to the calculated map coordinates. For a far-away source, the projected $\tilde{\Lambda}$-values are accumulated in well separated pixels on the ion production map. If the distance between source and map decreases, the $\tilde{\Lambda}$-values are projected on the map with a spacing smaller than the maps resolution. Thus, they overlap and accumulate in identical pixels. Therefore, with the use of a fixed set of $\tilde{x}$ and $\tilde{z}$ values, the flux density increment of an approaching source has been included.
- If the calculation of the $\tilde{\Lambda}$-values of the Gaussian-shaped synchrotron radiation source and their projection on the ion production map is completed, the synchrotron radiation source is moved closer by one $\Delta\alpha$ to the map and the calculation process starts anew until the source is too close to the map.
- In the post-processing, the ion production map is smoothed by a moving average with a window size of 3 pixels. The map is only proportional to $\breve{R}_{\mathrm{p,pi}}(x, z, s)$ and consequently is normalized by utilizing the declared total production rate $R_{\mathrm{p,pi}}$ (parameter *Rppi*). The total production rate is converted into a local production rate $\hat{R}_{\mathrm{p,pi}}(\alpha)$[1] at the map's position which is given by (compare equation (A.18) in appendix A.10.3)

$$\hat{R}_{\mathrm{p,pi}}(\alpha) = R_{\mathrm{p,pi}} \cdot \frac{\Delta s}{2\pi R} \cdot f(\alpha) \; .$$

  Here, Δs (parameter *deltas*) is the longitudinal width of the map and R (*R*) is the deflection radius. $f(\alpha)$ is the correction factor in dependence of the angle of beam deflection α at the position of the production map. It is given as

$$f(\alpha) = 2 \cdot \frac{\alpha}{\alpha_{\mathrm{dipole}}} \; ,$$

  where α_{dipole} is total deflection angle of one dipole. This correction is necessary as the number of emitted synchrotron radiation photons of the beam increases linear with its propagated pathway within the dipole. Consequently, $\hat{R}_{\mathrm{p,pi}}(\alpha)$ increases linear with α or the propagated pathway in the dipole. Here, one has assumed that the local photo ionization production rate is only present in dipole magnets and not outside. Therefore, the ion production contributions behind the dipole magnet are omitted. Thus, $\hat{R}_{\mathrm{p,pi}}(\alpha)$ is a worst case value. For more information regarding the normalization, see appendix A.10.3.
  Eventually, $\breve{R}_{\mathrm{p,pi}}(x, z, s)$ is generated by normalizing the ion production map IPM by a factor of

$$S = \frac{\hat{R}_{\mathrm{p,pi}}(\alpha)}{\sum_{x,z}(\mathrm{IPM})\,\Delta x\,\Delta z} \qquad \text{like} \qquad \breve{R}_{\mathrm{p,pi}}(x, z, s) = S \cdot IPM \; .$$

[1] $\hat{R}_{\mathrm{p,pi}}(\alpha)$ is identical to $\hat{R}_{\mathrm{p,pi}}(s)$ within dipole magnets. Instead of the distance s, propagated by the beam within the dipole magnet (factor s/l_{dipole}), $\hat{R}_{\mathrm{p,pi}}(\alpha)$ is parameterized by the angle of beam deflection at a certain s position within the magnet (factor $\alpha/\alpha_{\mathrm{dipole}}$).

Δx (*deltayscreen*) and Δz (*deltaxscreen*) are the map's horizontal and transversal resolution.

- The script also calculates the ion production map for the impact ionization process of the electron beam. It resembles the electron beam's density distribution. The prodction map is also normalized to the local impact ionization production rate $\hat{R}_{\mathrm{p,ii}}(s)$. This rate is calculated from the total production rate, which is declared in the *Rpii* parameter.
- In a MATLAB file all relevant parameters is are stored. Additionally, the ion production map and its normalized form is saved as a multi-dimensional array. Also a GNUPLOT-readable file is generated.

B.2.2 1DBEAMPOT

1DBEAMPOT enables the calculation of the time averaged beam potential $\langle U(s) \rangle$ in the beam center at $x = z = 0\,\mathrm{mm}$ along the longitudinal plane in a circular accelerator. 1DSTATNEUT can be utilized on the generated beam potential to identify potential hollows and determine $\hat{\eta}_{\mathrm{stat}}(s)$ within them.

Functional Principle

To determine $\langle U(s) \rangle$, 1DBEAMPOT is in need of the optical functions of the accelerator ($\beta_x(s)$, $\beta_z(s)$, $D_x(s)$) at certain s positions, the horizontal emittance and betatron coupling coefficient along with a list of the beampipe's horizontal and vertical half diameters ($x_{\mathrm{vc}}(s)$, $z_{\mathrm{vc}}(s)$). Also the clearing electrodes' positions along with their longitudinal electric potential at a specific clearing voltage are needed.

Using equation (2.40), the beam potential $\langle U(s) \rangle$ is calculated. The typical resolution of s is approximately 1 cm. To determine $\langle U(s) \rangle$, first the beam potential is calculated with either horizontal or vertical geometrical constrains. Here, the potential value, calculated at horizontal or vertical displacements x_{vc} or z_{vc}, is used to offset the calculated potential at the beam center $x = z = 0\,\mathrm{mm}$ to ensure that the potential at the beam pipe (x_{vc} and z_{vc}) is equal to zero. To estimate the beam potential $\langle U(s) \rangle$, both obtained potentials are averaged to account for different x_{vc} and z_{vc}. Finally, at each clearing electrode's position in the accelerator, the electrodes' electric potential is superimposed with the beam potential.

B.2.3 1DSTATNEUT

This script enables the determination of the local static neutralization $\hat{\eta}_{\mathrm{stat}}(s)$ along an accelerator's beam potential which has been generated by 1DBEAMPOT.

Functional Principle

To identify potential hollows, test ions, being generated at specific positions in the beam potential, are tracked until they reach a clearing electrode or can be categorized as trapped ions. Therefore, a clearing map for the considered region of the accelerator is generated by using the provided list of clearing electrode positions.

Consecutively, test ions are generated at every s position in the beam potential and their one-dimensional trajectories are tracked by using the EULER-NEWTON method. If the test ion is tracked longer than 0.3 ms (a time much longer than the typical lifetime of an ion, if it is cleared at an electrode), the ion's production position is marked as part of a potential hollow. If the test ion is cleared by an electrode, is has obviously not been produced within a potential hollow. Using this method, the beginning and end of all potential hollows can be found along with the individual potential hollow's potential barrier $U_{\mathrm{max}}(s_0)$. By using equation (4.3), the local static neutralization within each potential hollow is obtained.

B.2.4 TracTIon

TracTIon is a Matlab script with which the horizontal and longitudinal motions of a continuously increasing ion population, comprising of different ion species, is simulated in the time average beam potential in presence of the magnetic fields of dipole and quadrupole magnets.

Beam Potential and Magnetic Fields

Beam Potential The beam potential $U(x, s)$ is computed as the time average beam potential generated by an electron beam with two-dimensional Gaussian charge density distribution. The beam width modifies the shape of the beam potential and varies along s. Thus, it is determined beforehand using the storage ring's optical functions. Finally, the beam potential depth is shifted to fulfill the boundary conditions at the beam pipe x_{vc}, where $U(x_{\mathrm{vc}}, s)$ has to be zero.

The potential of the clearing electrodes is also implemented in this scenario. As is discussed in section 6.1, the electrode is positioned at the top of the quadrupole beam pipe and shows a distance of 22 mm to the beam center, which equals to the pipe's vertical half diameter. When the electrode is biased with −3 000 V only an attractive potential of $U_{\mathrm{CE},0} = -118\,\mathrm{V}$ is present for the ions at the beam center, as simulations have shown. For increasing distance from the electrode, the attractive potential is even lower. If the longitudinal distance exceeds 8 cm the electrode's potential is negligibly small. The clearing electrode's potential superimposes the beam potential $U_0(x, s)$. In TracTIon the beam potential ±8 cm around the electrode's longitudinal position is altered as

$$U(x, s) = U_0(x, s) + U_{\mathrm{CE},0} \cdot (1 - \tanh(G(s) \cdot r)) \ .$$

This function smoothly approaches $U_0(x, s)$ for large r, where r is the distance between the position (x, s) and the clearing electrode. $G(s)$ is a decay constant which satisfies the condition that the beam potential is approximately zero at x_{vc} for every s.

Of course, this is not the exact solution for the clearing electrode's potential in the x-s-plane. However, comparisons with the simulated beam potential have shown that it approximates the shape of the electrode's potential for $r > 1$ cm suitably. Additionally, *all* ions which are transported into the region affected by the clearing electrodes potential, are eventually neutralized there. Their time within the electrode's region of influence is also small compared to their prior propagation time within the rest of the ion propagation environment (IPE), resulting only in a negligibly small error.

Magnetic Fields The magnetic fields are precomputed on a map with the same size and resolution as the beam potential map. Since the magnetic field of the dipoles are purely vertical and the horizontal fields of the quadrupoles are zero in the beam center at $z = 0$ mm. Thus, only vertical magnetic fields are calculated. For the field strength $B_{z,\mathrm{dp}}$ of the dipole magnets along their iron yokes holds [Wil00, section 1.3.9, conversion of equation (1.37)]

$$B_{z,\mathrm{dp}} = \frac{E}{\mathrm{e}cR} \tag{B.1}$$

in order to deflect the electron beam with a beam energy E to a trajectory with radius R. Along the x axis $B_{\mathrm{z,dp}}$ is constant. The vertical field of the quadrupole magnets, in contrast, is not. It rises linearly with increasing distance x from the beam center, which is assumed to be also the quadrupoles' center, as

[Wil00, section 3.3.2, equation 3.41]

$$B_{z,\mathrm{QF,QD}} = g_{\mathrm{QF,QD}} \cdot x \qquad \text{with} \qquad g_{\mathrm{QF,QD}} = \frac{E}{ec} \cdot k_{\mathrm{QF,QD}} \,.$$

In manner of the dipole magnets, the field of the quadrupole magnets is longitudinally constant along the iron yoke for a fixed x. If the yoke is exceeded at position s_{yoke}, the magnetic field decreases to zero. These fringe fields are implemented as

$$B_{z,\mathrm{fringe}}(s) = B_{z,0} \cdot \exp\left(-\frac{(s - s_{\mathrm{yoke}})^2}{2\sigma_{\mathrm{fringe}}^2}\right) \qquad \text{for} \qquad s \geq s_{\mathrm{yoke}} > 0 \,,$$

and decrease like a Gaussian bell curve. σ_{fringe} can be determined by demanding that the integrated magnetic field $\int B_z(s)\,\mathrm{d}s \stackrel{!}{=} B_{z,0} \cdot l_{\mathrm{eff}}$. Here, l_{eff} is the effective length of the dipole or quadrupole magnet. Within the iron yokes with a geometrical length of l_{geom}, $B_z(s) = B_{z,0}$. Outside $B_{z,\mathrm{fringe}}(s)$ is present. With these constrains one obtains

$$\sigma_{\mathrm{fringe}} = \frac{l_{\mathrm{eff}} - l_{\mathrm{geom}}}{\sqrt{2\pi}} \,.$$

The fringe fields in TracTion are computed up to $4\sigma_{\mathrm{fringe}}$ away from s_{yoke}. For higher distances, the fringe field is assumed to be negligibly small. Thus, all transitions from magnetic fields to field-free regions are realized with adequate fringe fields.

Tracking Algorithm

To compute the trajectories of individual ions of different masses and ionization status within an ion propagation environment with electric and magnetic fields, TracTion uses a specific tracking algorithm. This algorithm determines the spatial increment in the longitudinal and horizontal plane (Δs and Δx) for a fixed time increment Δt. Here, the previous longitudinal and horizontal velocity of the ion (v_s and v_x) and the longitudinal and horizontal components of the local electric field ($E_s(x, s)$ and $E_x(x, s)$) along with the local vertical magnetic field $B_z(x, s)$ have to be considered.

Runge-Kutta Method TracTion uses the 4th order Runge-Kutta method in combination with a momentum correction scheme based on the individual ion's potential and kinetic energy. The 4th order Runge-Kutta method is an explicit method to approximate the solutions of ordinary differential equations by numerical integration.

Consider an ion at time $t = t_n$ at a position (x_n, s_n) and a velocity $(v_{x,n}, v_{s,n})$ (with $n \in \mathbb{N}$). The Runge-Kutta method is used to approximate the position (x_{n+1}, s_{n+1}) and velocity $(v_{x,n+1}, v_{s,n+1})$ at a time $t_{n+1} = t_n + \Delta t$. Here, the field, the ion propagates into, is "probed" by four interim steps before the actual step is calculated. Therefore, the actual step calculation consists of results from the interim steps as [DF12, section C 1.]

$$x_{n+1} = x_n + \Delta x = x_n + \frac{\Delta t}{6}\left(k_{v1,x} + 2\left(k_{v2,x} + k_{v3,x}\right) + k_{v4,x}\right) \,,$$
$$v_{x,n+1} = v_{x,n} + \Delta v_x = v_{x,n} + \frac{\Delta t}{6}\left(k_{r1,x} + 2\left(k_{r2,x} + k_{r3,x}\right) + k_{r4,x}\right) \,.$$

Here, $k_{v1,x}$ to $k_{v4,x}$ are the accelerations at the position of the four interim steps which are given as

$$k_{v1,x} = \mathfrak{A}_x\left(x_n\,,\ s_n\right)\,, \qquad k_{v2,x} = \mathfrak{A}_x\left(x_n + k_{r1,x}\frac{\Delta t}{2}\,,\ s_n + k_{r1,s}\frac{\Delta t}{2}\right)\,,$$
$$k_{v3,x} = \mathfrak{A}_x\left(x_n + k_{r2,x}\frac{\Delta t}{2}\,,\ s_n + k_{r2,s}\frac{\Delta t}{2}\right)\,, \qquad k_{v4,x} = \mathfrak{A}_x\left(x_n + k_{r3,x}\,\Delta t\,,\ s_n + k_{r3,s}\,\Delta t\right)\,.$$

$k_{r1,x}$ to $k_{r4,x}$ are the changes in velocity occurring due to accelerations at the four interim steps and are given as

$$k_{r1,x} = v_{x,n}\,, \qquad k_{r2,x} = k_{v1,x}\frac{\Delta t}{2}\,,$$
$$k_{r3,x} = k_{v2,x}\frac{\Delta t}{2}\,, \qquad k_{r4,x} = k_{v3,x}\,\Delta t\,.$$

For the longitudinal plane, the expressions are similar. Only the function determining the acceleration $\mathfrak{A}(x, s)$ at position (x, s) is different for the horizontal and longitudinal plane. In this two-dimensional case with only vertical magnetic fields, the acceleration results from the Lorentz force and for the first interim step is implemented as

$$\mathfrak{A}_x\left(x\,,\ s\right) = \frac{\mathrm{e}Z_i}{m_i}\left(E_x(x,s) - k_{r1,s}\cdot B_z(x,s)\right) \tag{B.2}$$
$$\mathfrak{A}_s\left(x\,,\ s\right) = \frac{\mathrm{e}Z_i}{m_i}\left(E_s(x,s) + k_{r1,x}\cdot B_z(x,s)\right)\,. \tag{B.3}$$

Here, m_i is the mass of the individual ion i. Because only singly ionized ions are considered, the ionization status $Z_i = 1$ for all ions. The velocities $k_{r1,x}$ and $k_{r1,s}$ are replaced by the other $k_{r2\ldots4,x}$, $k_{r2\ldots4,s}$ for the follow-up interim steps.

$E_x(x, s)$ and $E_s(x, s)$ are determined as the local gradient of the precomputed beam potential decomposed into its horizontal and longitudinal component, $B_z(x, s)$ by extracting the magnetic field strength from the corresponding precomputed map. The distance of the actual ion position (x_n, s_n) at at time t_n from the nearest maps grid coordinates, encircling the ion position, is used as weights to determine the actual fields at (x_n, s_n). In this process also the gradients and magnetic fields of neighboring grid coordinates are involved to smooth the transition between grid coordinates. More information is provided in the following sections.

Momentum Correction Scheme As can be seen in equations (B.2) and (B.3), the longitudinal and horizontal velocities $k_{r1,s}$ and $k_{r1,x}$ appear in $\mathfrak{A}_x(x, s)$ and $\mathfrak{A}_s(x, s)$ of the horizontal and longitudinal plane. Thus, the velocities of the planes are coupled due to the vertical magnetic field. Consequently, the ion trajectories are not solutions of an ordinary differential equation but a coupled non-linear differential equation. Because the explicit Runge-Kutta method itself is not perfectly suitable for this kind of differential equation and is not symplectic[2], the algorithm is supplemented by a momentum correction scheme based on energy conservation.

When an ion is generated at position (x_0, s_0), the sum E_0 of its potential and kinetic energy is calculated. During the time of its existence in the simulation, E_0 is compared to the actual energy $E(t_n)$ after each

[2] A symplectic tracking algorithm intrinsically reproduce the Hamiltonian mechanics in which the particle's energy is conserved. The accuracy of the energy conservation is dependent on Δt. For more information, see e.g. [GS00].

iteration of the tracking algorithm. A momentum correction factor

$$\mathcal{K}_{n+1} = 1 - \frac{E(t_n) - E_0}{E_0 - \delta_{\mathcal{K}}}$$

is determined with $\mathcal{K}_{n+1}$ being smaller than one, if $E(t_n)$ exceeds E_0, and vice versa. Since $v \sim \sqrt{E}$, the calculated velocities $v_{x,n+1}$ and $v_{s,n+1}$ are both corrected by a factor of $\sqrt{\mathcal{K}_{n+1}}$, so are Δx and Δs, too.

Using this scheme, a determination if either $v_{x,n+1}$ or $v_{s,n+1}$ or both have to be corrected is not possible. The momentum of the individual ion is just scaled to satisfy the conservation of energy. Thus, if $\mathcal{K}_{n+1}$ corrects the momentum too drastically, it may reduce the momentum of one plane too much in favor of the other plane. In practice it turns out, it is suitable to introduce a quantity $\delta_{\mathcal{K}} > 0\,\mathrm{eV}$ which shifts $\mathcal{K}_{n+1}$ closer to one for a given difference between E_0 and $E(t)$. In cases where the ion trajectory is close to the beam pipe, thus the potential energy $eU(x_n, s_n)$ is near zero, $\delta_{\mathcal{K}}$ increases the stability of the algorithm. For a TracTIon simulation with a specific Δt, $\delta_{\mathcal{K}}$ is chosen for each ion species individually by considering the ions' trajectories for high $x \lesssim x_{\mathrm{vc}}$, close to the beam pipe, and low $|x| < \Delta x_{\mathrm{res}}$, close to the beam center in the presence of a magnetic field. On one hand, the ion trajectory should be stable and physically comprehensible during the whole simulation time. On the other hand, $\delta_{\mathcal{K}}$ is chosen the way that the standard deviation of the relative energy difference $(E(t) - E_0)/E_0$ during the simulation is minimized.

Determination of Local Gradients and Magnetic Fields

The potential $U(x, s)$ and $B_z(x, s)$ are computed on discrete positions $(\tilde{\chi}, \tilde{\varsigma})$ on the maps. Since the ion trajectories show continuous positions $(x(t), s(t))$, the gradient ($E_x(x_n, s_n)$ and $E_s(x_n, s_n)$) and the magnetic field $B_z(x_n, s_n)$ at these continuous position (x_n, s_n) a time t_n are computed as follows:

Consider an ion at position (x_n, s_n). In reference to the map's discrete grid, it is positioned horizontally between $\tilde{\chi}_i$ and $\tilde{\chi}_{i+1}$ and longitudinally between $\tilde{\varsigma}_j$ and $\tilde{\varsigma}_{j+1}$. The ion has a normalized distance of

$$\Delta\tilde{\chi}_- = \frac{x_n - \tilde{\chi}_i}{\Delta x_{\mathrm{res}}} \qquad \text{with} \qquad 0 \le \Delta\tilde{\chi}_- \le 1$$

from the lower horizontal grid position and a distance of

$$\Delta\tilde{\chi}_+ = \frac{\tilde{\chi}_{i+1} - x_n}{\Delta x_{\mathrm{res}}}\,,$$

to the upper one which is equal to $\Delta\tilde{\chi}_+ = 1 - \Delta\tilde{\chi}_-$. In the longitudinal plane, the distances are $\Delta\tilde{\varsigma}_- = (s_n - \tilde{\varsigma}_i)/\Delta s_{\mathrm{res}}$ and $\Delta\tilde{\varsigma}_+ = (\tilde{\varsigma}_{i+1} - s_n)/\Delta s_{\mathrm{res}}$. Here, Δx_{res} and Δs_{res} are the horizontal and longitudinal resolution of the map's grid.

To determine $B_z(x_n, s_n)$, the fields at the nearest grid coordinates, the "square" of $(\tilde{\chi}_i, \tilde{\varsigma}_j)$, $(\tilde{\chi}_{i+1}, \tilde{\varsigma}_j)$, $(\tilde{\chi}_i, \tilde{\varsigma}_{j+1})$ and $(\tilde{\chi}_{i+1}, \tilde{\varsigma}_{j+1})$ around (x_n, s_n), are averaged. To obtain a smooth transition to the neighboring grid coordinates when the ion trajectory leaves this "square", the local fields of neighboring coordinates are also averaged and weighted by the normalized distances.

As an example, the determination of $B_z(x_n, s_n)$ is shown as

$$\begin{aligned}
B_{z,i+2} =& \left(\frac{\Delta\tilde{\varsigma}_+}{2} \left(B_z(\tilde{\chi}_{i+2}, \tilde{\varsigma}_{j-1}) + B_z(\tilde{\chi}_{i+2}, \tilde{\varsigma}_j) \right) + \frac{\Delta\tilde{\varsigma}_-}{2} \left(B_z(\tilde{\chi}_{i+2}, \tilde{\varsigma}_{j+1}) + B_z(\tilde{\chi}_{i+2}, \tilde{\varsigma}_{j+2}) \right) \dots \right. \\
& \left. \dots + \frac{\left(B_z(\tilde{\chi}_{i+2}, \tilde{\varsigma}_j) + B_z(\tilde{\chi}_{i+2}, \tilde{\varsigma}_{j+1}) \right)}{2} \right) /2 \,, \\
B_{z,i+1} =& \left(\frac{\Delta\tilde{\varsigma}_+}{2} \left(B_z(\tilde{\chi}_{i+1}, \tilde{\varsigma}_{j-1}) + B_z(\tilde{\chi}_{i+1}, \tilde{\varsigma}_j) \right) + \frac{\Delta\tilde{\varsigma}_-}{2} \left(B_z(\tilde{\chi}_{i+1}, \tilde{\varsigma}_{j+1}) + B_z(\tilde{\chi}_{i+1}, \tilde{\varsigma}_{j+2}) \right) \dots \right. \\
& \left. \dots + \frac{\left(B_z(\tilde{\chi}_{i+1}, \tilde{\varsigma}_j) + B_z(\tilde{\chi}_{i+1}, \tilde{\varsigma}_{j+1}) \right)}{2} \right) /2 \,, \\
B_{z,i} =& \left(\frac{\Delta\tilde{\varsigma}_+}{2} \left(B_z(\tilde{\chi}_i, \tilde{\varsigma}_{j-1}) + B_z(\tilde{\chi}_i, \tilde{\varsigma}_j) \right) + \frac{\Delta\tilde{\varsigma}_-}{2} \left(B_z(\tilde{\chi}_i, \tilde{\varsigma}_{j+1}) + B_z(\tilde{\chi}_i, \tilde{\varsigma}_{j+2}) \right) \dots \right. \\
& \left. \dots + \frac{\left(B_z(\tilde{\chi}_i, \tilde{\varsigma}_j) + B_z(\tilde{\chi}_i, \tilde{\varsigma}_{j+1}) \right)}{2} \right) /2 \text{ and} \\
B_{z,i-1} =& \left(\frac{\Delta\tilde{\varsigma}_+}{2} \left(B_z(\tilde{\chi}_{i-1}, \tilde{\varsigma}_{j-1}) + B_z(\tilde{\chi}_{i-1}, \tilde{\varsigma}_j) \right) + \frac{\Delta\tilde{\varsigma}_-}{2} \left(B_z(\tilde{\chi}_{i-1}, \tilde{\varsigma}_{j+1}) + B_z(\tilde{\chi}_{i-1}, \tilde{\varsigma}_{j+2}) \right) \dots \right. \\
& \left. \dots + \frac{\left(B_z(\tilde{\chi}_{i-1}, \tilde{\varsigma}_j) + B_z(\tilde{\chi}_{i-1}, \tilde{\varsigma}_{j+1}) \right)}{2} \right) /2 \,.
\end{aligned}$$

Finally, the local vertical magnetic field is determined by

$$B_z(x_n, s_n) = \left(\frac{\Delta\tilde{\chi}_+}{2} \left(B_{z,i-1} + B_{z,i} \right) + \frac{\Delta\tilde{\chi}_-}{2} \left(B_{z,i+2} + B_{z,i+1} \right) + \frac{B_{z,i+1} + B_{z,i}}{2} \right) /2 \,.$$

Analogously, the potential $U(x_n, s_n)$ is calculated.

The horizontal and longitudinal electrical fields $E_x(x_n, s_n)$ and $E_s(x_n, s_n)$ are derived from the gradient of the beam potential. In one dimension, the gradient at one point is given as

$$E_x = \frac{U(\tilde{\chi}_m) - U(\tilde{\chi}_{m+1})}{\Delta x_{\text{res}}} \,.$$

TRACTION derives the horizontal and longitudinal gradient similar but also additionally includes the gradient at adjacent grid coordinates, to smoothen the transition when the ion trajectory leaves the local "square" into an adjacent one. As an intermediate step, the calculations

$$\begin{aligned}
\frac{\mathrm{d}U}{\mathrm{d}x}(\tilde{\varsigma}_{j+1}) =& \left[\Delta\tilde{\chi}_- \left(U(\tilde{\chi}_{i+2}, \tilde{\varsigma}_{j+1}) - U(\tilde{\chi}_{i+1}, \tilde{\varsigma}_{j+1}) \right) + \Delta\tilde{\chi}_+ \left(U(\tilde{\chi}_i, \tilde{\varsigma}_{j+1}) - U(\tilde{\chi}_{i-1}, \tilde{\varsigma}_{j+1}) \right) \dots \right. \\
& \left. \dots + \left(U(\tilde{\chi}_{i+1}, \tilde{\varsigma}_{j+1}) - U(\tilde{\chi}_i, \tilde{\varsigma}_{j+1}) \right) \right] /(2\Delta x_{\text{res}}) \,,
\end{aligned}$$

$$\frac{\mathrm{d}U}{\mathrm{d}x}(\tilde{\varsigma}_j) = \Big[\Delta\tilde{\chi}_- \Big(U(\tilde{\chi}_{i+2}, \tilde{\varsigma}_j) - U(\tilde{\chi}_{i+1}, \tilde{\varsigma}_j)\Big) + \Delta\tilde{\chi}_+ \Big(U(\tilde{\chi}_i, \tilde{\varsigma}_j) - U(\tilde{\chi}_{i-1}, \tilde{\varsigma}_j)\Big) \ldots$$
$$\ldots + \Big(U(\tilde{\chi}_{i+1}, \tilde{\varsigma}_j) - U(\tilde{\chi}_i, \tilde{\varsigma}_j)\Big)\Big] / (2\Delta x_{\mathrm{res}})$$

are executed. The horizontal electrical field is then determined by

$$E_x(x_n, s_n) = \Delta\tilde{\varsigma}_- \cdot \frac{\mathrm{d}U}{\mathrm{d}x}(\tilde{\varsigma}_{j+1}) + \Delta\tilde{\varsigma}_+ \cdot \frac{\mathrm{d}U}{\mathrm{d}x}(\tilde{\varsigma}_j) \,.$$

For the longitudinal electrical field $\frac{\mathrm{d}U}{\mathrm{d}s}(\tilde{\chi}_{i+1})$ and $\frac{\mathrm{d}U}{\mathrm{d}s}(\tilde{\chi}_i)$ are computed. $E_s(x_n, s_n)$ is subsequently determined analogously.

As an additional measure, all ions are excluded from the simulation which show a Δx or Δs which exceed the respective resolution of the precomputed maps. Their number is recorded to enable an adjustment of Δt of the tracking algorithm to ensure smooth $B_z(x_n, s_n)$, $U(x_n, s_n)$, $E_x(x_n, s_n)$ and $E_s(x_n, s_n)$.

Macro-Ion Generation Subroutines

Implementation of the Impact Ionization Process Every time index ι which is a multiple of ι_{ii}, the impact ionization subroutine is executed. The routine produces a macro-ion of a specific species at approximately[3] every longitudinal grid point s_{gen} of the precomputed maps. To which species each of the generated macro-ion belongs, is assigned randomly on basis of their production probability (compare section 3.3.2). The horizontal start position is chosen randomly using a Gaussian probability distribution with a standard deviation which resembles $\sigma_x(s_{\mathrm{gen}})$. Consequently, the production map of these ions resembles the dimension of the electron beam. The horizontal and longitudinal initial velocities are also assigned randomly, using the one-dimensional mean thermal velocity (compare equation (2.3)) as the standard deviation of a Gaussian probability distribution.

The time index for impact ionization ι_{ii} is calculated as

$$\iota_{\mathrm{ii}} = \frac{\tau_{\mathrm{ii}}}{\Delta t} = \frac{\mu_{\mathrm{ion}}}{N_{\mathrm{e}} \cdot R_{\mathrm{p,ii}} \frac{\Delta s_{\mathrm{res}}}{C} \cdot \Delta t} \,.$$

Here, τ_{ii} is the average time between the generation of two macro-ions within a defined section of length Δs_{res} when N_{e} electrons are stored in the storage ring and $R_{\mathrm{p,ii}}$ is the total impact ionization production rate.

Implementation of the Photo Ionization Process In the dipole magnets M10 and M11, additionally photo ionization occurs by synchrotron radiation photons which are emitted by the electron beam. The transversal ion production map is asymmetric in the horizontal plane which results from the superposition of the electron beam with the integrated radiation profile of the synchrotron radiation (compare figures 3.18 to 3.20 in section 3.4.4). To implement this process into TracTion, the transversal truncated photo ionization production map $\breve{R}_{\mathrm{p,pi}}(x, z, s_{\mathrm{gen}})$ has been simulated by PhotoIonProd (see section 3.4.4) all along the dipole magnets M10 and M11. Using Matlab's Distribution Fitter[4] functionality, the production map, extracted at $z = 0\,\mathrm{mm}$ from each $\breve{R}_{\mathrm{p,pi}}(x, z, s_{\mathrm{gen}})$, is converted into a probability distribution. These

[3] The exact longitudinal position is blurred by a randomly generated longitudinal offset generated by a superimposed Gaussian probability distribution with a standard deviation of Δs_{res}.

[4] The matlab function fitdist generates probability distribution's, usable in the random function, on basis of a density distribution of arbitrary form.

probability distributions are used to randomly assign the horizontal starting position for each generated macro-ion at a corresponding s_{gen} within the dipole magnets.

Every time index ι which is a multiple of ι_{pi}, the photo ionization subroutine is executed. ι_{pi} is defined similar to ι_{ii} as

$$\iota_{\mathrm{pi}} = \frac{\mu_{\mathrm{ion}} \cdot M_{\mathrm{ramp}}}{N_{\mathrm{e}} \cdot R_{\mathrm{p,pi}} \frac{\Delta s_{\mathrm{res}}}{2\pi R} \cdot \Delta t} \,.$$

Here, the circumference C is replaced by $2\pi R$ as this process only occurs in dipole magnets. In contrast to the impact ionization, the local photo ionization production rate is not constant along s (compare figure 3.22 in section 3.4.4). It first rises linearly with the deflection angle to an angle α_{break} and then stays constant along the rest of the dipole.

This form is mimicked by producing more than one macro-ion per Δs at ι_{pi} with a different longitudinal deployment scheme within the dipoles: The time between two executions of the photo ionization production subroutine is prolonged in time by a factor of $M_{\mathrm{ramp}} \in \mathbb{N}$ in contrast to the impact ionization subroutine. Instead, a total of M_{ramp} times the number of macro-ions are generated when the subroutine is executed. Similar to the implementation of the impact ionization process, ions of random mass and thermal initial velocity are generated on the basis of the known probability distributions at each longitudinal position on the maps within the dipole magnets. In dependence of the local production rate within the dipoles, at some grid positions multiple macro-ions are produced. The number of produced ions per grid position is defined by a function. This function a piecewise constant function for s_{gen} which corresponds to deflection angles lower than α_{break} to approximate the linear rise of the local production rate there. For higher deflection angles, the function is constant. The larger M_{ramp}, on one hand, the shorter is the length of the constant pieces and the better the linear rise is approximated. A large M_{ramp}, on the other hand, reduces the statistical significance because many macro-ions are produced at once followed by a long period where no macro-ions are generated.

Figure 4.12 in section 4.3.2 exemplarily shows the distribution of the horizontal and longitudinal starting positions of approximately six million generated macro-ions in the simulation scenario.

Each generated macro-ion with its s and x-coordinates, Δs and Δx, its velocity v_s and v_x, its mass-to-charge ratio A/Z and its initial energy E_0 and the $\delta_{\mathcal{K}}$ quantity of the particular ion species is stored in a list of active macro-ions. For every new time step, the tracking algorithm runs through this list, determines new coordinates, spatial increments and velocities for each macro-ion.

Ion Clearing

Ions are cleared or removed from the simulation (more precisely the macro-ion list), when they reach specific positions in the ion propagation environment. These positions are defined by another map which shows the same dimension and resolution as the precomputed maps of the beam potential and magnetic fields. Prior to subsequent iteration of the tracking algorithm of a macro-ion, its position is compared with the clearing map.

The macro-ions are cleared when

- they reach[5] the clearing electrodes at the longitudinal edges of the simulation in the center of quadrupoles QF10 and QF12. The charge of the removed macro-ion is transformed into a current detected at each clearing electrode. For one time step, the induced current is accumulated and stored for each clearing electrode separately to obtain a quantity which can be compared to real clearing electrode current measurements.

[5] The ion is cleared, when its longitudinal position is closer than $4\Delta s_{\mathrm{res}}$ from the edge of the IPE. For the horizontal edge, a distance closer than $4\Delta x_{\mathrm{res}}$ is necessary for the ion's removal.

- they show a horizontal amplitude of $\pm x_{\mathrm{vc}}$. Here, the ion impacts on the surface of the beam pipe and is neutralized. The impact position and velocity is recorded[6].
- they are neutralized by the clearing electrode in the vicinity of quadrupole QD11. Here, a defined distance of less than 3.5 mm horizontally or 1 cm longitudinally from the projected electrode position at ($x = 0$ mm, $s = 51.93$ m) results in the removal of the macro-ion and a detected current.

B.2.5 1DNeutalizatIon

This MATLAB script is used to track an accumulating ion population, produced by impact ionization, within an one-dimensional beam potential in the longitudinal plane in sections of an accelerator. Here, the transversal ion oscillations are assumed to show negligibly small amplitudes and thus the ions only experience a longitudinal gradient field which is present in the center of the beam. Also only sections of the accelerator can be simulated with 1DNeutalizatIon in which no magnetic fields are present. These fields may significantly alter the ions' longitudinal motion and lead to different results.

Functional Principle

An increasing number of ions are generated and their individual motion is tracked while propagating in the longitudinal beam potential $U(s)$ until they reach a clearing electrode, positioned somewhere in the considered scenario. After a certain time, the ion population reaches its equilibrium state.

The longitudinal beam potential for the simulated scenario is provided by 1DBeamPot with a spatial resolution of Δs_{res}.

Ion Generation and Clearing Ions are produced only by the process of impact ionization. Similar to TracIon (compare section 4.3.2), several macro-ions are generated at specific time indexes ι which are equal to multiples of ι_{ii}. Then macro-ions are generated within the IPE, each showing a longitudinal distance of Δs_{res} (typically 1 cm) to their neighbors. The individual macro-ions have a mass-to-charge ratio and initial longitudinal velocity on basis of their corresponding probability distributions. All generated macro-ions are managed within a list of the ion population as long as they are not removed by a clearing mechanism.

At both edges of the IPE and additional positions, ion clearing electrodes are positioned. As long as a macro-ion is not within a distance of 1 cm to a clearing electrode, it is not cleared and remains in the population list.

Space Charge Model The ions' mutual space charge interaction is modeled using a basic linear implementation. In a last process before the simulation time is incremented by another Δt, the position of every ion within the population list is recorded with a granularity of 1 cm, matching the resolution of $U_0(s)$ (and $E_{s,\mathrm{cav}}(s,t)$). The macro-ions with a number of $\mathrm{d}N_{\mathrm{ion}}(s)$ per Δs_{res} approximately deform the potential as

$$U(s) = (1 - \hat{\eta}(s)) \cdot U_0(s)$$

[6] This enables the determination of regions within a beam line, where ions increasingly impact onto the beam pipe. In these regions the pressure probably is increased due to emission of secondary residual gas molecules or ions during the impact event. This knowledge can be useful when considering the design of beam pipes with specific coatings which aim for the reduction of the secondary molecular yield of segments of the beam pipe.

when following the linear space charge model expressed in equation (4.2). Here, the local neutralization is given by

$$\hat{\eta}(s) = \frac{\mu_{\text{ion}} \cdot \left(\mathrm{d}N_{\text{ion}}(s) - 1\right)}{N_{\text{e}} \cdot \frac{\Delta s_{\text{res}}}{C}} \,,$$

which is the fraction of ions within a bin of width Δs_{res} to the number of electrons in the same bin. For $\hat{\eta}(s) \to 1$, the deformed beam potential $U(s)$ is less deep which results in a longitudinal gradient field dispersing the ion aggregation with time. The construction $\mathrm{d}N_{\text{ion}}(s) - 1$ is chosen to prevent a deformation of $U_0(s)$ in case of $\mathrm{d}N_{\text{ion}}(s) = 1$. Otherwise, this would lead to a constant acceleration of the macro-ion by its own space charge in this model. The calculated $U(s)$ is used in the tracking algorithm to determine the longitudinal gradient field.

Tracking Algorithm For every time step Δt, the tracking algorithm calculates new spatial increments Δs and velocities for each macro-ion in the population list. Δs is determined using the 4th order Runge-Kutta method similar to TracTIon (compare section 4.3.2). Here, the ion's actual velocity and the longitudinal electric field at its position is considered in the algorithm. The longitudinal electric field is the longitudinal gradient of the beam potential and, in vicinity of rf cavities, its superposition with the rf field of the cavities $E_{s,\text{cav}}$. As the macro-ions' position s_i is computed with higher precision than the resolution Δs_{res} of the potential and fields ($U(s)$ and $E_{s,\text{cav}}(s)$), the ions' distance to the neighboring higher and lower grid points is used as weights to determine $U(s_i)$ and $E_{s,\text{cav}}(s_i)$ by averaging.

Post-Processing In a post-processing step, $N_{\text{ion}}(t)$ and $N_{\text{ion},i}(t)$ are prepared for the user. For the known (individual) production rates of the ion species, the (individual) clearing rates can be determined by using equation (2.10). Also the ion composition at the end of the simulation is determined. 1DNeutalizatIon additionally provides the local longitudinal line density of ions and local neutralization $\hat{\eta}(s)$ within the IPE, to enable the identification of potential hollows and η. A determination of the partial neutralization $\hat{\eta}_i(s)$ is also possible. Also the total and individual ion current of the clearing electrodes within the IPE is determined, to enable a comparison with congruent ion current measurements.

B.2.6 TransversIon

Using TransversIon the oscillation spectrum of an ion population at a particular position in an accelerator can be simulated. Also the clearing rates for the ion clearing measure of beam shaking can be determined.

Functional Principle

In TransversIon, the trajectories of ions within a stationary or time dependent beam potential (average) in the horizontal or vertical plane are simulated by using an Euler-Newton tracking algorithm. Hereby one complete simulation consists of $N_{\mu\text{sim}}$ consecutive micro simulations where a single ion is tracked from its production at $t_0 = 0\,\text{s}$ to t_{end}. $N_{\mu\text{sim}}$ is typically in the order of 200 000 and t_{end} is long compared to the oscillation period of the ions' oscillation and is in the order of tens or hundreds of micro seconds.

The beam potential in which the ions propagate is precomputed for a certain horizontal or vertical range around the beam center. It is calculated according to equation (2.42) given by [Alv87b, section 4]. Consequently, this is not a harmonic potential and $\nu_{x,z}^{\text{ion}}$ depends on the ion's oscillation amplitude. In case the beam oscillates due to beam shaking with a particular amplitude and frequency, one period of this oscillation is precomputed. In this script, the time increment of the tracking algorithm is larger than

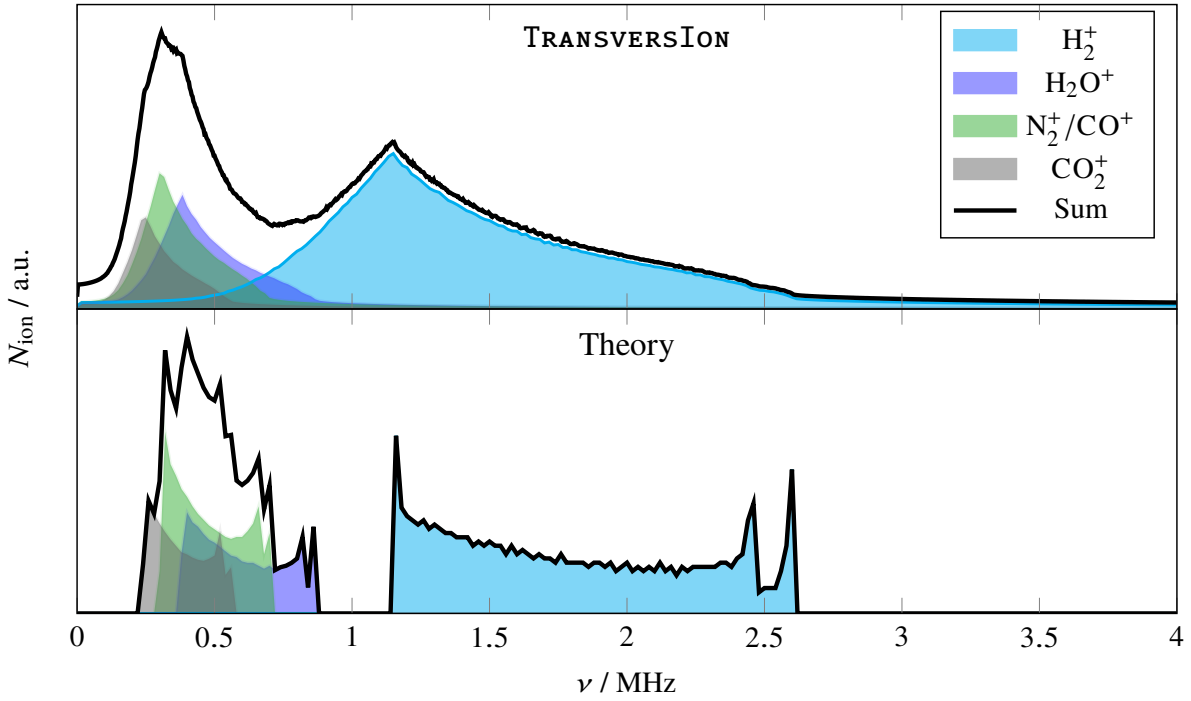

Figure B.1: Horizontal ion frequency spectrum at a beam energy of 1.2 GeV and a current of 35 mA, integrated along one FODO cell of the storage ring. The top graph shows the abundance distribution of the horizontal ion oscillation frequencies, simulated by TRANVERSION. The distribution of the abundance of the theoretical ion frequencies ν_x^{ion} is shown below.

t_{rf}, the time distance of two bunches. Therefore, the bunched structure of the beam is omitted and the time averaged beam potential is used.

The composition of the ion population for the simulation can be configured arbitrarily. Here, probabilities for the production of a particular ion species can be defined. They should be chosen in accordance to the percentage of the individual ion species' production rate to the total production rate. The horizontal or vertical production map of the ion population can be defined as an arbitrary spatial distribution. The velocity distribution of ions at t_0 is GAUSSian with a width equal to the one-dimensional mean thermal velocity $\langle v_{x,z,i} \rangle$ (compare equation (2.3)). Thus, for each micro simulation, the species of the simulated ion, its initial position and velocity are chosen randomly in accordance to the defined distributions.

For the duration of a micro simulation, the horizontal or vertical trajectory $x(t)$ or $z(t)$ of the produced ion in the beam potential is recorded. For each recorded trajectory, a FFT[7] is carried out to analyze the trajectory's frequency components. In the post-processing stage of the simulation, the individual FFT's is added up to obtain the oscillatory behavior of the whole ion ensemble (see e.g. figure B.1). A simulated ion trajectory is only valid if it stays within the horizontal or vertical boundary of the simulation. This boundary is defined by the range on which the beam potential is precomputed, typically the diameter of the beam pipe ($\pm x_{\text{vc}}$ or $\pm z_{\text{vc}}$ around the beam center). If an ion exceeds this boundary, the micro simulations stops and the collision time t_{coll} along with the species of the simulated ion is logged. t_{coll} is used for the determination of the ions' clearing rate due to beam shaking.

[7] FFT is the short form of a fast FOURIER transformation. An efficient algorithm for the calculation of a discrete FOURIER transformation.

In the post-processing stage, on the one hand, the various collision times t_{coll} for each ion species are sorted time-wise. Because at each t_{coll} the ion population is decreased by one ion, $N_{\mathrm{ion}}(t)$ can be calculated. By approximating an exponentially decaying function $N_{\mathrm{ion},0} \exp\left(-\hat{R}_{\mathrm{c}} t\right) + N_{\mathrm{stab},i}$ onto $N_{\mathrm{ion}}(t)$, the total clearing rate is obtained along with the individual rates $\hat{r}_{\mathrm{c},i}$ for instable fraction of each ion species. The procedure is similar to analyses with FillingGapSim (compare section 6.2.2 and appendix B.2.7).

On the other hand, the initial ($x(t_0)$ or $z(t_0)$) and one random horizontal or vertical positions ($x(t_{\mathrm{rand}})$ or $z(t_{\mathrm{rand}})$) of each simulated ion's trajectory is collected. This random-selection ensures that each ion has a different lifetime in the beam potential which emulates the constant generation of new ions. Out of this information the initial ion distribution is generated, which is proportional to the ion production map of the particular plane. Also the equilibrium ion distribution, proportional to $\rho_{\mathrm{ion},x,z}(x \text{ or } z, t)$, is determined. This analysis is also done for each species to obtain species-dependent distributions. For large $N_{\mu\mathrm{sim}}$, the equilibrium ion distribution for a realistically modeled ionization process can be studied, if the beam shaking amplitude is chosen to be equal to zero.

Procedure

The functional procedure of this script is the following:

- After initializing physical constants and the calculation of the horizontal and vertical emittance *emittancex* and *emittancez*, the time increment *deltat* for the tracking algorithm is calculated. One period of the beam oscillation is divided by *tbin* equidistant time slices. *deltat* is the slices' time difference.
- The *AZmap*, which defines what kind of ion species is produced within a certain probability, is generated. This array assigns mass-to-charge ratios to randomly generated numbers between 1 and a number defined by the parameter *produktdistbins*. Also the Gaussian probability distributions *ortsdist* and *vdist* is generated. *vdist* is used to for the determination of each ions initial velocity whereas *ortsdist* determines the initial transversal ion position in accordance to the ion production map.
- The horizontal and vertical beam width (*sigmax* and *sigmaz*) and the theoretical bounce frequencies for certain mass-to-charge ratios are calculated.
- The horizontal and vertical beam potential for the calculated beam width is precomputed. The transversal region around the beam center on which the potential is calculated is defined by *breitex* and *breitez*. This region is equal to $\geq 10\sigma_{x,z}$ and equal to the beam pipe half diameter *randx* and *randz* at maximum. The transversal resolution of the potential is defined via the *binx* and *binz* parameter. For the stationary and oscillating beam, the corresponding potential is calculated for one period. For a simulation scenario which has identical parameters to a previous simulation, a stored beam potential is loaded instead of precomputing it again.
- In the following micro simulation, a number of multiple individual ions (parameter *ionanzahl*) are tracked consecutively through the stationary or oscillating beam potential for a time of *tend*. Since *tend* should be much longer than one period of the beam oscillation, the precomputed potential is used cyclically in the tracking algorithm. The individual ions are produced at a random phase of the beam oscillation. They are generated with random mass-to-charge ratio and a random initial velocity in accordance with the defined probability distributions. Because the ions are produced *by* the beam, their random transversal starting position is shifted in reference to the coordinate origin in accordance with the beam's oscillation phase and amplitude. The trajectory *s*, the spatial increment of the tracking *deltas* and the velocity *v* of the single ion are stored in the *particlemonitor* array. To enable the generation of an initial and equilibrium ion distribution for the horizontal or

vertical plane, the initial and one random position of each ions' trajectory is stored in the *transvdist* array. If the ion exceeds the range of the beam potential during the micro simulation, the tracking stops. The termination time is recorded in the *ioncleartimei* arrays for each ion species. Also lost ions are recorded in the *ionlossmonitor* array.

- If no early termination occurs, the simulated ion trajectory is analyzed after the tracking. The trajectory is freed from DC-offsets and a FFT is carried out on the data. The obtained oscillation spectrum *P1* of a single ion is added to the *frequencyspek* array. In this array, all spectra of the population are summed up. The simple addition of the ions' spectra is possible because the frequency base stays constant as every ion is tracked with the same time increment *deltat* until *tend*.
- After each micro simulation has been performed, the post-processing stage is executed. Here, the transversal ion distributions are extracted from the *transvdist* array. The initial ion distribution for the ion population at $t_0 = 0\,\mathrm{s}$, equal to the transversal ion production map, is generated. Also the transversal equilibrium ion distribution is generated by using the stored arbitrary positions of the ions during the simulation. Since the arbitrary positions are selected randomly from each ion's trajectory, every ion has a different lifetime, emulating the constant production of new ions. Of course, these distributions are also available separately for every ion species. Additionally, the *ioncleartimei* arrays are sorted time-wise. Because the ion number of species i is reduced by one for every recorded time in these arrays, $N_{\mathrm{ion},i}(t)$ can be computed. For each species, a function

$$N_{\mathrm{ion},i}(t) = N_{0,i} \exp\left(-\hat{r}_{\mathrm{c},i} \cdot t\right) + N_{\mathrm{stab},i}$$

with known initial ion number $N_{0,i}$ is fitted onto the data. The decay constant is equal to the species' clearing rates within the simulated scenario and is stored in the *clearingrate* array. For a calculated production rate (parameters *pressure*, *rgm*, *crosssection*), the resulting local neutralization is estimated using equation (2.11). It is stored in the *neutralization* array. The fraction of stable ions to the total ion number gives the ion transfer efficiency of the scenario, stored in the array *iontransfer*.

B.2.7 FillingGapSim

By using FillingGapSim the individual clearing rate for different residual gas species when exposed to different filling patterns can be determined.

Functional Principle

The purpose of this MATLAB script is to study the effect of arbitrary filling patterns on the ion dynamics of different residual gas species. Here, the emphasis is on the extraction of the individual ions' clearing rate when encountering a specific filling pattern. Therefore, the one-dimensional motion (either horizontal or vertical) of ions is tracked when encountering a time varying 2D beam potential (x or z versus time), which corresponds to specific filling pattern.

In the simulation, thousands of single ion tracking simulations are carried out consecutively. Here, numerous ions of different species (according to their production rate) are generated under realistic conditions (randomized thermal velocities and $x(t_0)$ or $z(t_0)$ start positions) and are tracked consecutively via the Euler-Newton algorithm. To increase the tool's performance, the tracking is carried out with a non-equidistant time increment. If the horizontal or vertical ion motion exceeds a distance of $10\sigma_{x,z}$ from the beam's barycenter or hits the vacuum chamber, the single ion tracking simulation stops and the time t_{coll} when the ion has been cleared out is recorded. After every single ion tracking simulation has been carried out, the list of t_{coll} is sorted and a $N_{\mathrm{ion}}(t)$ is generated. As discussed in section 6.2.2 in more detail, an exponentially decaying function equation (6.8) is fitted to $N_{\mathrm{ion}}(t)$ and the clearing rate is extracted.

Additionally, the ion distribution at $t = 0\,\mathrm{s}$ and at $t =$ *tend* is stored. The trace of a transfer matrix corresponding to the simulated bunch pattern $\mathcal{M}_{\mathrm{bt},x,z}$ is also calculated and saved (compare appendix A.12).

Procedure

The functional procedure of this script resembles the one for TRANSVERSION and proceeds as follows:

- The time dependend horizontal beam potential *potentialx* and *potentialz* along with the suitable time increment vector *deltatvector* for the chosen filling pattern is calculated.
- Consecutive trackings of a number of ions (*ionanzahl*) of up to six ion species (production probability configured by *AZmap*) through the horizontal or vertical time dependent potential is carried out until the time *tend* or a boundary ($10\sigma_{x,z}$ or *randx* or *randz*) is exceeded. The horizontal and vertical start position of the ions is chosen randomly along its initial place of production in the bunchtrain (as long as there is a bunch with electrons able to generate an ion).
- In the post processing of the individual ions' simulations, the trajectory is analyzed in frequency and the end time of the ion's simulation is recorded, enable a distinction between cleared and trapped ions.
- When all ions have been simulated, the total and individual clearing rates can be determined as is described in section 6.2.2.

B.2.8 DQTOOL

DQTOOL is a tool to numerically determine the $\delta k_{x,z}$ distribution and the resulting tune spread of an electron bunch with a transversely and longitudinally GAUSSian charge distribution when exposed to the space charge force of an ion charge distribution of arbitrary shape. Its functional principle is discussed in section 5.1.2 in detail.

B.2.9 TRACEANALYSIS

TRACEANALYSIS determines the total and individual fraction of stable ions (Υ_{stab} and $\Upsilon_{\mathrm{stab},i}$) within an entire accelerator or sections of it when exposed to a certain filling pattern. The tool utilizes the stability matrix formalism, presented in appendix A.12.

Functional Principle

For a certain set of ions with corresponding A/Z, the horizontal and vertical transfer matrices $\mathcal{M}_{\mathrm{bt},x,z}$ for the passage of one bunch train with a certain filling pattern is determined at a specific position s with corresponding beam width $\sigma_x(s)$ and $\sigma_z(s)$. If either $|\mathrm{Tr}(\mathcal{M}_{\mathrm{bt},x})|$ or $|\mathrm{Tr}(\mathcal{M}_{\mathrm{bt},z})|$ exceed values of ± 2, the particular ion species is marked as unstable at the considered s position. If both traces are below 2, the ion species is marked as stable.

This calculus is repeated along the accelerator with a suitable longitudinal resolution Δs_{res}. When the stability of the ion species all along the accelerator has been determined, the stable fraction of a particular ion species $\Upsilon_{\mathrm{stab},i}$ is obtained while assuming that the same number of ions are produced at each s position. Using the production probability of the individual ion species, obtained from the species' $r_{\mathrm{p},i}$, as weights, Υ_{stab} for the whole ion population is obtained.

APPENDIX C

Additional Figures, Graphs and Tables

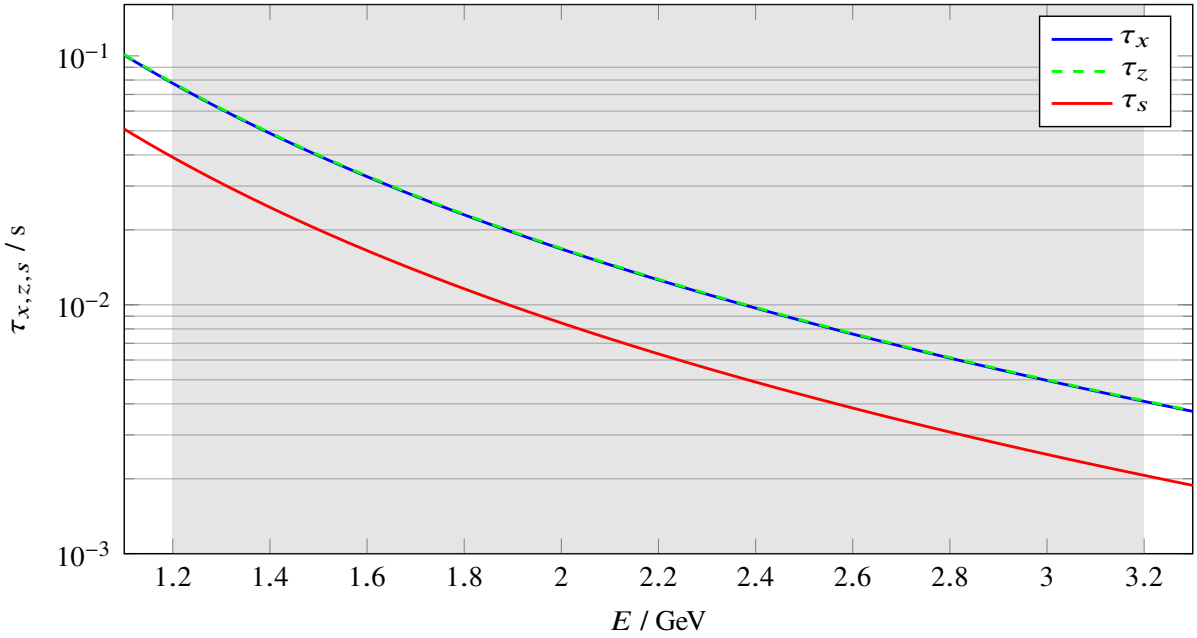

Figure C.1: Damping times of the ELSA storage ring for different beam energies. The gray area denotes the typical energy range of the storage ring.

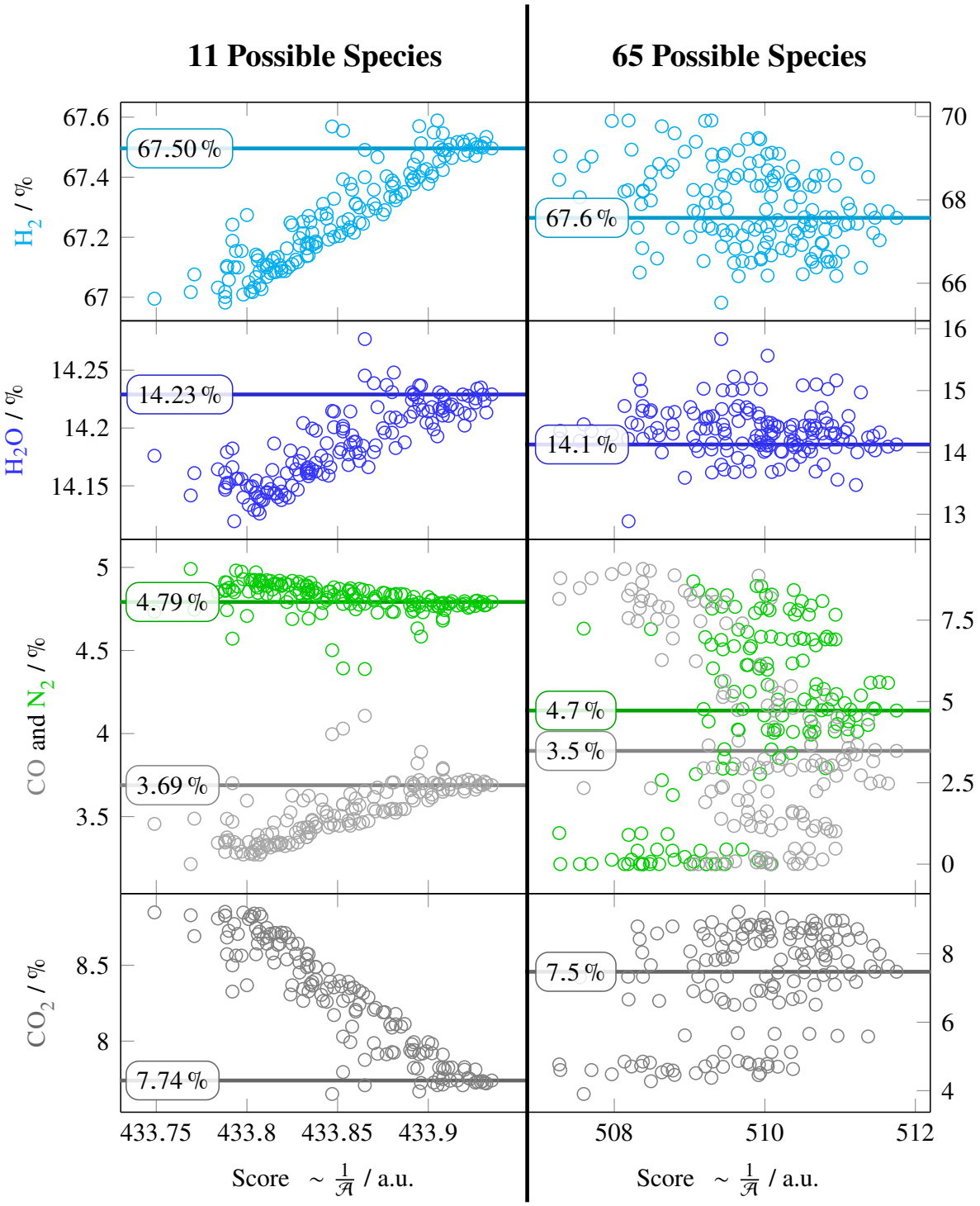

Figure C.2: Percentage of the five dominant residual gas species versus the final score of the MSAUGA simulations on basis of the measured "background" mass spectrum without beam. The graphs on the left side of the central line show the results and scores of MSAUGA simulations which use a fragmentation pattern library of 11 possible residual gas constituents. On the right side the complete library, consisting of 65 species, is used in the simulations. The horizontal lines in the individual graphs denote the percentage of the particular residual gas species for the highest achieved score in the simulations.

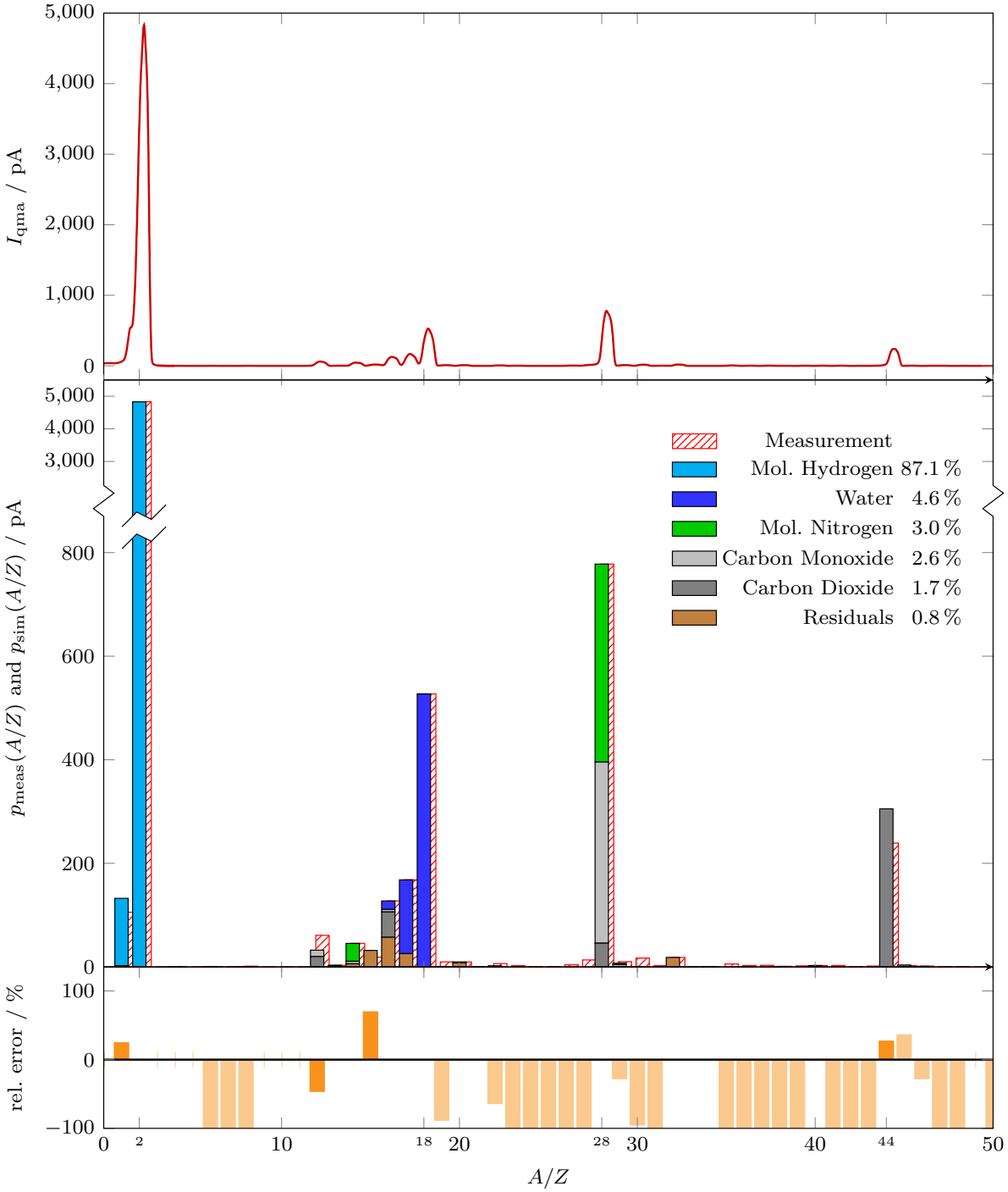

Figure C.3: Residual gas analysis for a measurement at 1.2 GeV beam energy and 35 mA beam current. The upper graph shows the measured current of the quadrupole mass spectrometer I_{qma} for a relevant mass range from $A/Z = 0$ to 50. The red hashed bar plot in the middle graph is the extracted peak height $p_{\mathrm{meas}}(A/Z)$ for each A/Z. The software **MSAUGA** generates a simulated mass spectrum $p_{\mathrm{sim}}(A/Z)$ which consists of contributions of 11 different residual gas species. The spectrum is mapped on $p_{\mathrm{meas}}(A/Z)$ in the middle graph. The gas composition is listed in descending order of relevance. The bottom graph shows the relative deviation between measured and simulated mass spectrum.

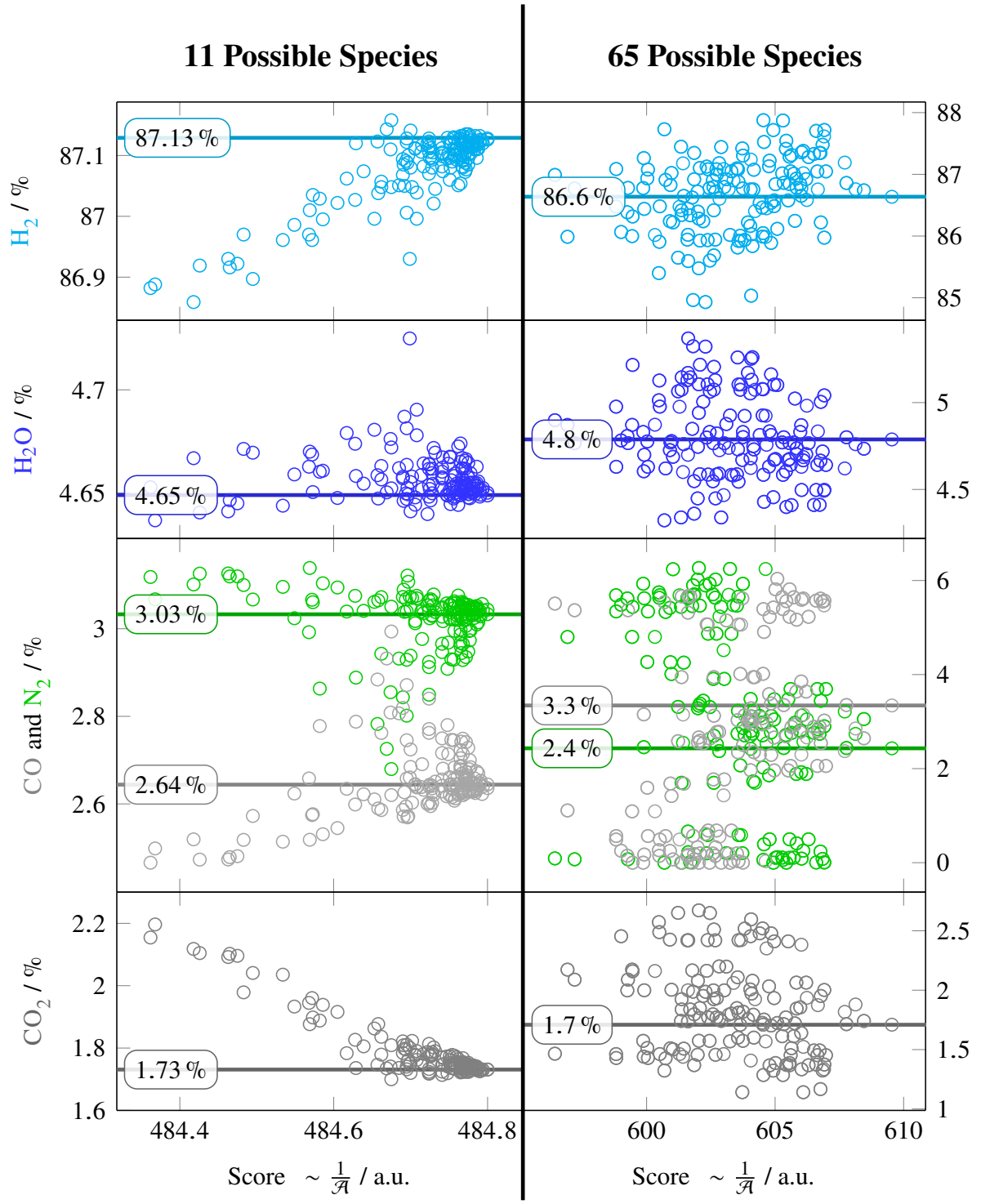

Figure C.4: Percentage of the five dominant residual gas species versus the final score of the MSAUGA simulations on basis of the measured mass spectrum at 1.2 GeV. The graphs on the left side of the central line show the results and scores of MSAUGA simulations which use a fragmentation pattern library of 11 possible residual gas constituents. On the right side the complete library, consisting of 65 species, is used in the simulations. The horizontal lines in the individual graphs denote the percentage of the particular residual gas species for the highest achieved score in the simulations.

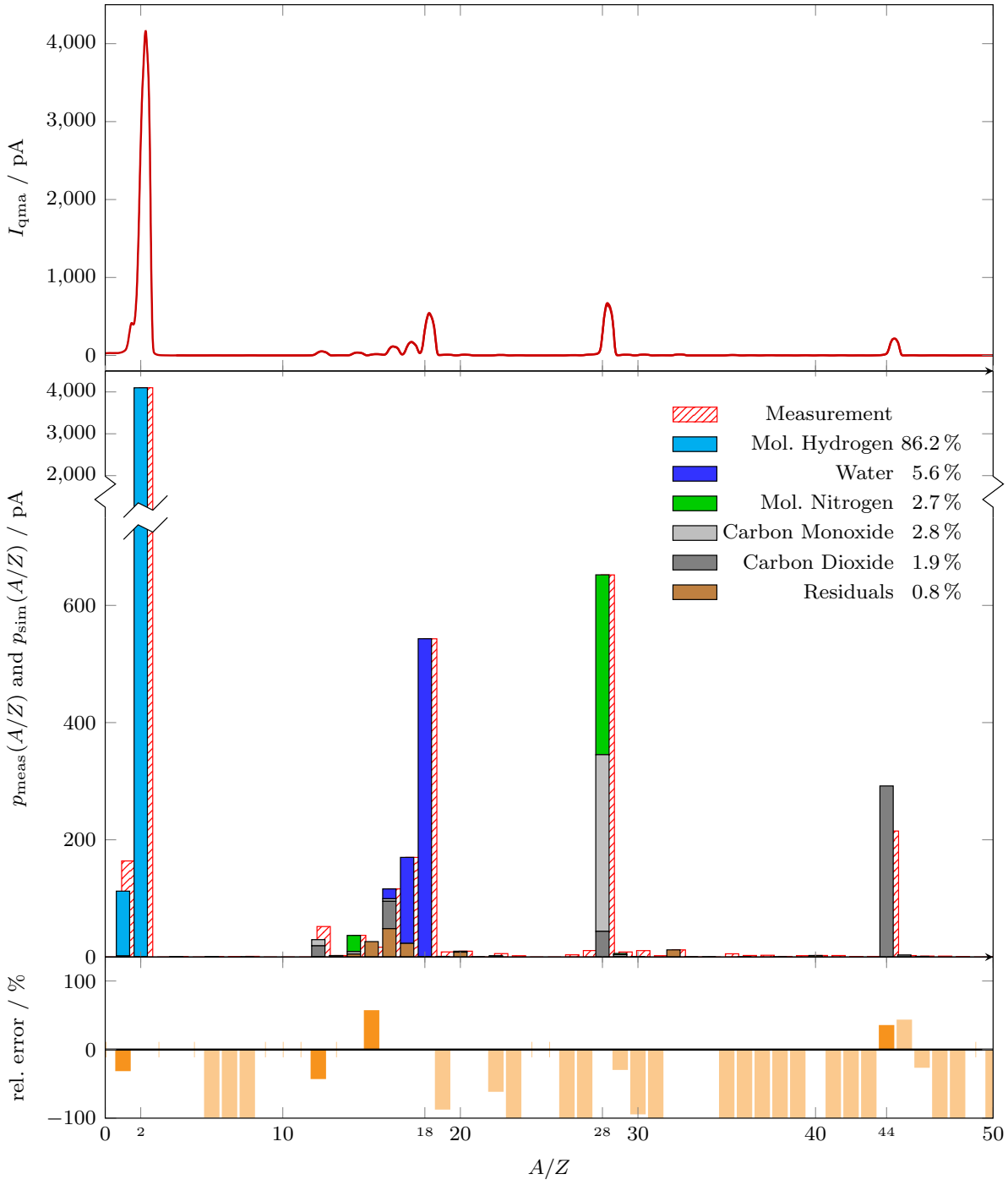

Figure C.5: Residual gas analysis for a measurement at 1.7 GeV beam energy and 35 mA beam current. The upper graph shows the measured current of the quadrupole mass spectrometer I_{qma} for a relevant mass range from $A/Z = 0$ to 50. The red hashed bar plot in the middle graph is the extracted peak height $p_{\mathrm{meas}}(A/Z)$ for each A/Z. The software MSAUGA generates a simulated mass spectrum $p_{\mathrm{sim}}(A/Z)$ which consists of contributions of 11 different residual gas species. The spectrum is mapped on $p_{\mathrm{meas}}(A/Z)$ in the middle graph. The gas composition is listed in descending order of relevance. The bottom graph shows the relative deviation between measured and simulated mass spectrum.

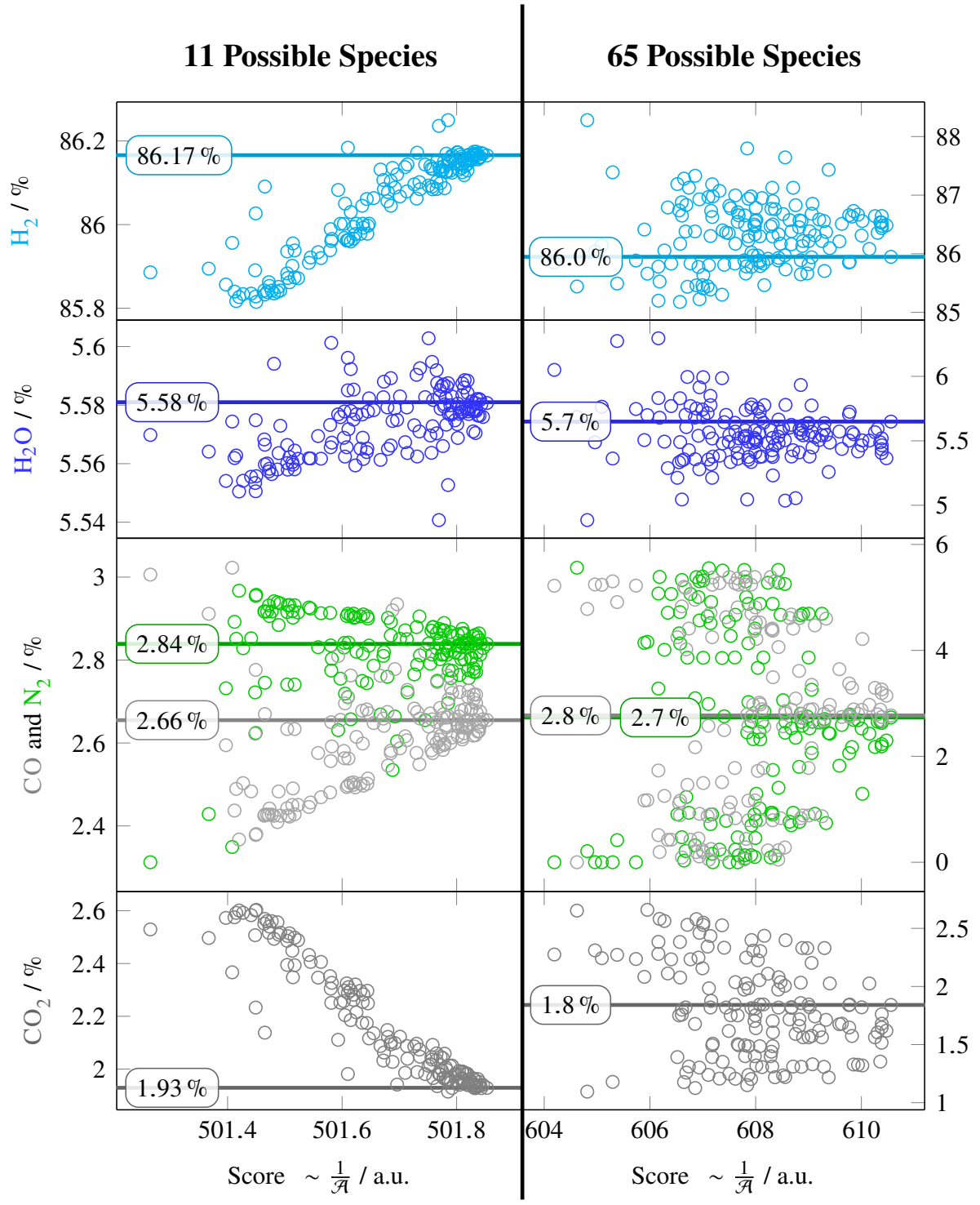

Figure C.6: Percentage of the five dominant residual gas species versus the final score of the MSAUGA simulations on basis of the measured mass spectrum at 1.7 GeV. The graphs on the left side of the central line show the results and scores of MSAUGA simulations which use a fragmentation pattern library of 11 possible residual gas constituents. On the right side the complete library, consisting of 65 species, is used in the simulations. The horizontal lines in the individual graphs denote the percentage of the particular residual gas species for the highest achieved score in the simulations.

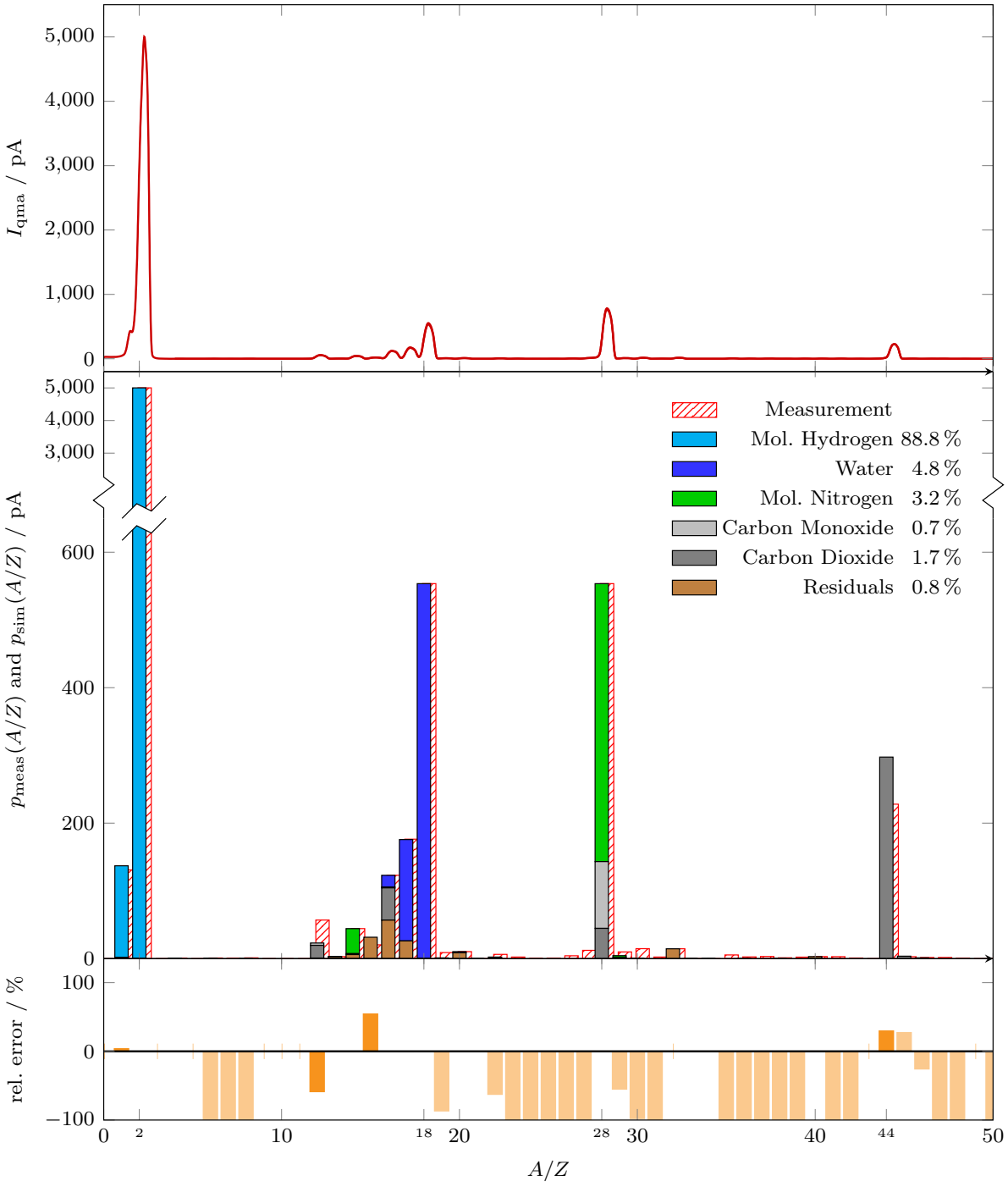

Figure C.7: Residual gas analysis for a measurement at 2.4 GeV beam energy and 35 mA beam current. The upper graph shows the measured current of the quadrupole mass spectrometer I_{qma} for a relevant mass range from $A/Z = 0$ to 50. The red hashed bar plot in the middle graph is the extracted peak height $p_{\mathrm{meas}}(A/Z)$ for each A/Z. The software MSAUGA generates a simulated mass spectrum $p_{\mathrm{sim}}(A/Z)$ which consists of contributions of 11 different residual gas species. The spectrum is mapped on $p_{\mathrm{meas}}(A/Z)$ in the middle graph. The gas composition is listed in descending order of relevance. The bottom graph shows the relative deviation between measured and simulated mass spectrum.

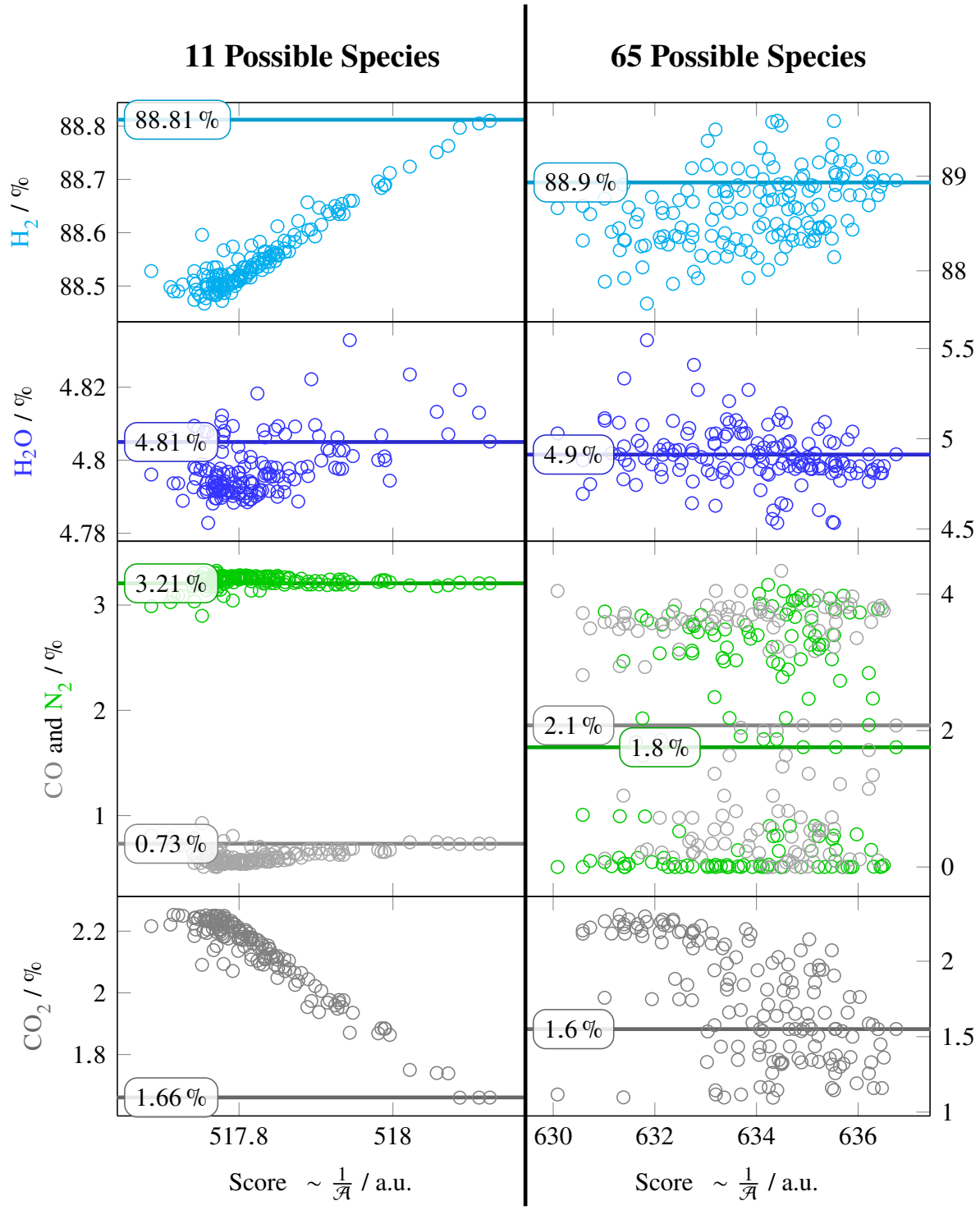

Figure C.8: Percentage of the five dominant residual gas species versus the final score of the MSAUGA simulations on basis of the measured mass spectrum at 2.4 GeV. The graphs on the left side of the central line show the results and scores of MSAUGA simulations which use a fragmentation pattern library of 11 possible residual gas constituents. On the right side the complete library, consisting of 65 species, is used in the simulations. The horizontal lines in the individual graphs denote the percentage of the particular residual gas species for the highest achieved score in the simulations.

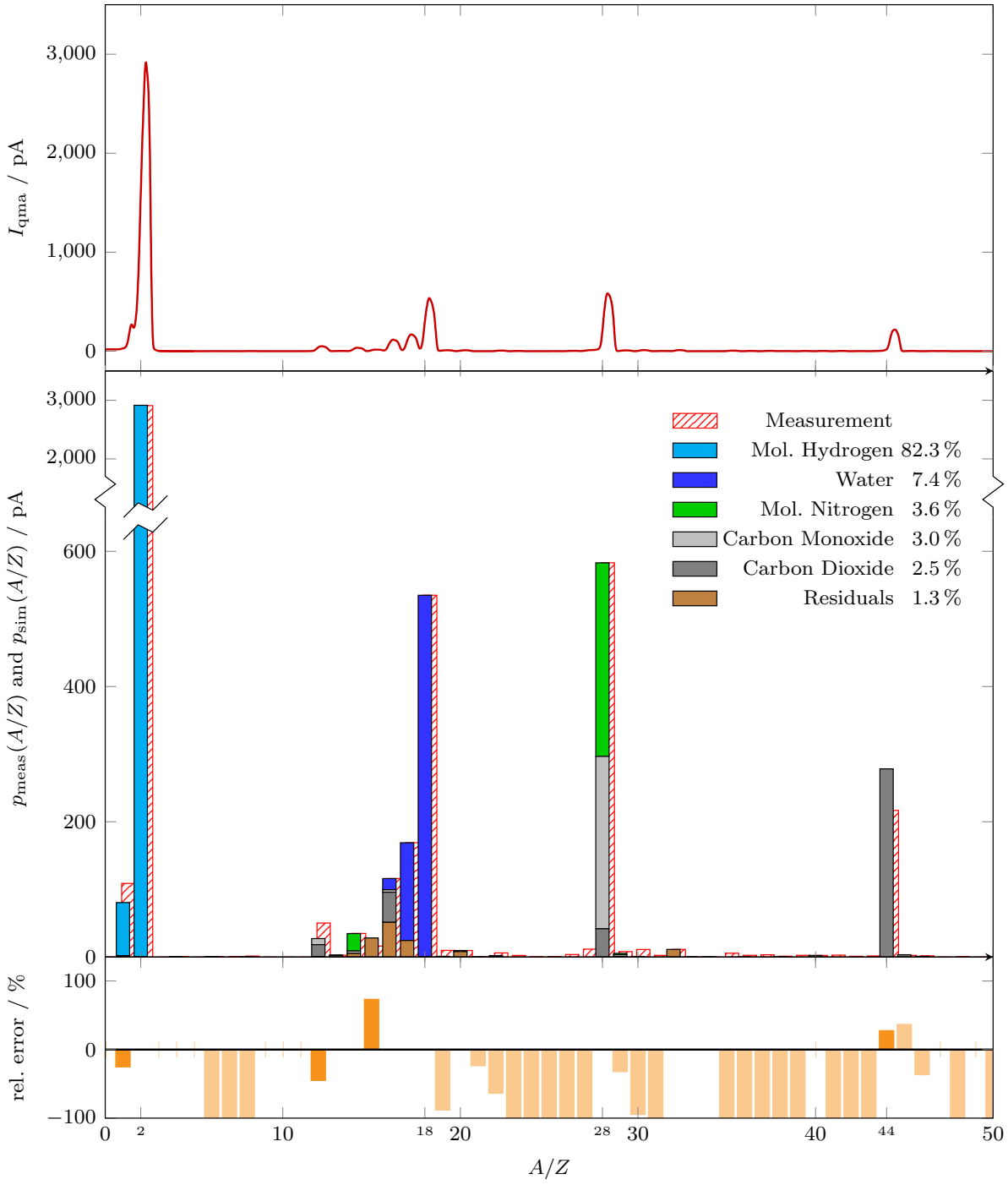

Figure C.9: Residual gas analysis for a measurement at 2.9 GeV beam energy and 35 mA beam current. The upper graph shows the measured current of the quadrupole mass spectrometer I_{qma} for a relevant mass range from $A/Z = 0$ to 50. The red hashed bar plot in the middle graph is the extracted peak height $p_{\mathrm{meas}}(A/Z)$ for each A/Z. The software MSAUGA generates a simulated mass spectrum $p_{\mathrm{sim}}(A/Z)$ which consists of contributions of 11 different residual gas species. The spectrum is mapped on $p_{\mathrm{meas}}(A/Z)$ in the middle graph. The gas composition is listed in descending order of relevance. The bottom graph shows the relative deviation between measured and simulated mass spectrum.

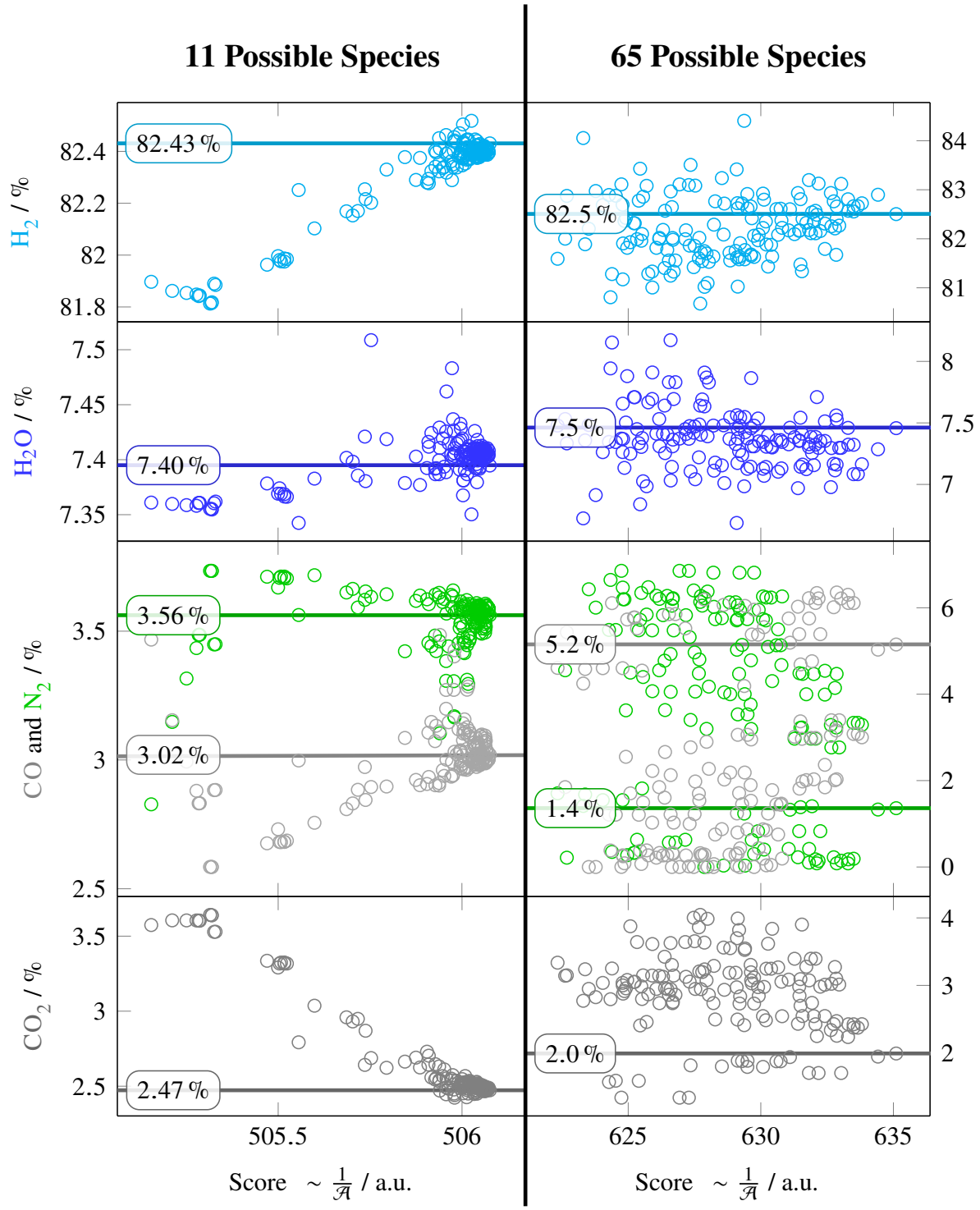

Figure C.10: Percentage of the five dominant residual gas species versus the final score of the MSAUGA simulations on basis of the measured mass spectrum at 2.9 GeV. The graphs on the left side of the central line show the results and scores of MSAUGA simulations which use a fragmentation pattern library of 11 possible residual gas constituents. On the right side the complete library, consisting of 65 species, is used in the simulations. The horizontal lines in the individual graphs denote the percentage of the particular residual gas species for the highest achieved score in the simulations.

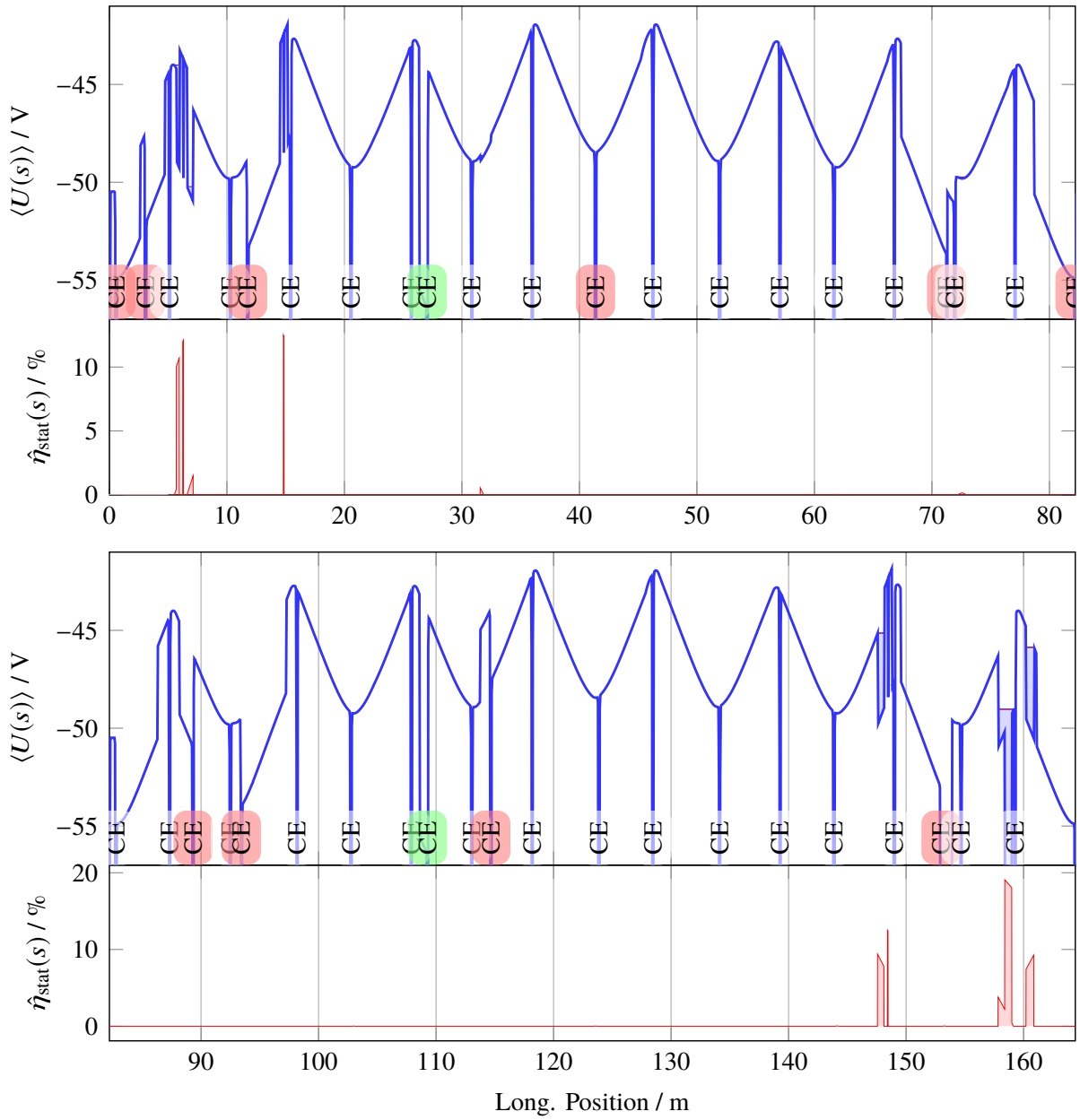

Figure C.11: Average beam potential of the storage ring at the beam center at 1.2 GeV and 200 mA. Shown is the deformation of the beam potential due to local accumulation of ions which form a static neutralization. The upper part of the figure shows the first half of the storage ring's lattice whereas the bottom part shows the second half. For each half, the average beam potential (blue) and its deformed state (violet) due to static neutralization is shown. Potential Hollows can be identified as the light blue plane between native and deformed beam potential. Also the corresponding local static neutralization $\hat{\eta}_{\mathrm{stat}}(s)$ is shown for each half in the lower graph. The beam potential is also deformed by the potential of the clearing electrodes, whose longitudinal position in the lattice is denoted by CE. Red denotes the suggested additional electrodes whereas green shows repositioned electrodes.

1.2 GeV	Frag. Lib.	H_2 / %	H_2O / %	N_2 / %	CO / %	CO_2 / %
	65	86.64 ± 3.71	4.79 ± 0.19	2.43 ± 2.04	3.34 ± 1.96	1.71 ± 0.38
	11	87.13 ± 0.18	4.65 ± 0.10	3.03 ± 0.07	2.64 ± 0.08	1.73 ± 0.10
1.7 GeV	Frag. Lib.	H_2 / %	H_2O / %	N_2 / %	CO / %	CO_2 / %
	65	85.95 ± 2.12	5.65 ± 0.17	2.73 ± 1.81	2.76 ± 1.76	1.84 ± 0.41
	11	86.17 ± 0.11	5.58 ± 0.01	2.84 ± 0.10	2.66 ± 0.23	1.93 ± 0.12
2.2 GeV	Frag. Lib.	H_2 / %	H_2O / %	N_2 / %	CO / %	CO_2 / %
	65	86.60 ± 2.36	5.38 ± 0.15	1.94 ± 1.43	3.76 ± 1.38	1.59 ± 0.35
	11	86.15 ± 0.09	5.19 ± 0.01	2.92 ± 0.10	2.93 ± 0.28	1.35 ± 0.12
2.4 GeV	Frag. Lib.	H_2 / %	H_2O / %	N_2 / %	CO / %	CO_2 / %
	65	88.93 ± 1.80	4.91 ± 0.14	1.76 ± 1.62	2.07 ± 1.57	1.55 ± 0.38
	11	88.81 ± 0.09	4.81 ± 0.01	3.21 ± 0.06	0.73 ± 0.13	1.66 ± 0.07
2.9 GeV	Frag. Lib.	H_2 / %	H_2O / %	N_2 / %	CO / %	CO_2 / %
	65	82.51 ± 2.82	7.46 ± 0.21	1.36 ± 2.30	5.15 ± 2.20	1.99 ± 0.62
	11	82.43 ± 0.14	7.39 ± 0.01	3.56 ± 0.12	3.02 ± 0.35	2.47 ± 0.14
Beam Off	Frag. Lib.	H_2 / %	H_2O / %	N_2 / %	CO / %	CO_2 / %
	65	67.57 ± 1.14	14.13 ± 0.51	4.72 ± 2.79	3.48 ± 2.84	7.48 ± 1.64
	11	67.50 ± 0.07	14.23 ± 0.01	4.79 ± 0.10	3.69 ± 0.10	7.74 ± 0.16

Table C.1: Results of the residual gas analysis.

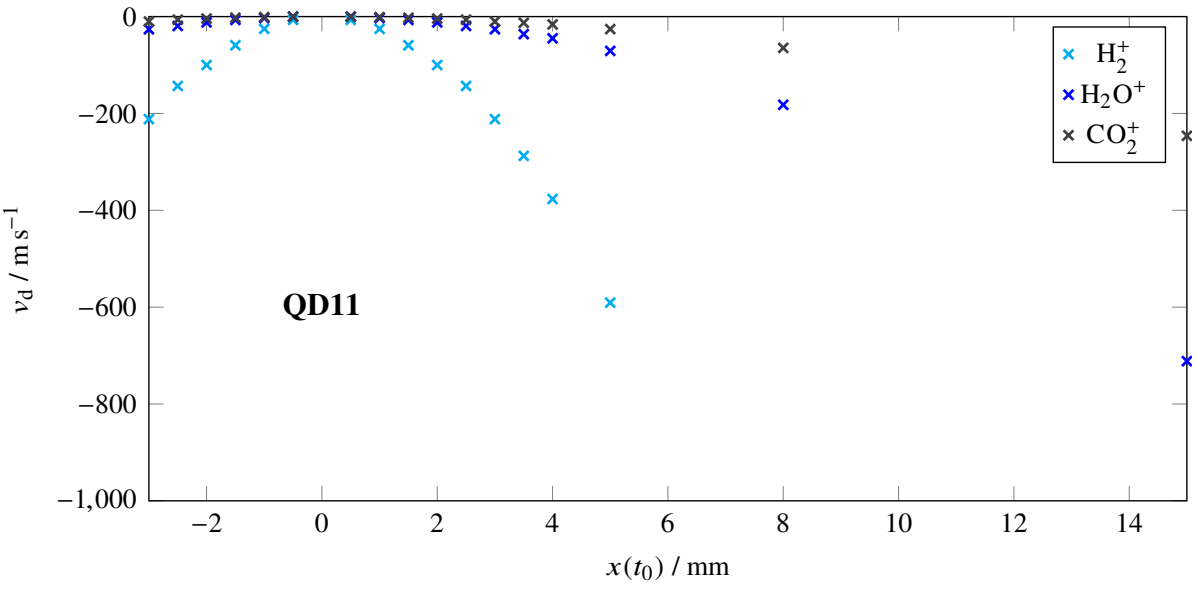

Figure C.12: Longitudinal cross drift velocities v_d for various ion species in quadrupole magnet QD11, which have been simulated with TRACTION. Here, a beam current of 35 mA is stored in the storage ring at an energy of 1.2 GeV. The initial velocity of the ions is set to zero and they are generated at $s = 51.80$ m with different horizontal starting positions $x(t_0)$. Note that v_d is symmetric around $x(t_0)$ and the other half with $x(t_0) < 0$ mm is therefore omitted.

Name			Water	Carbon		Carbon
	Hydrogen	Methane	Vapor	Monoxide	Nitrogen	Dioxide
ς	0.44	1.6	0.9	1.05	1	1.4
str. formula	H_2	CH_4	H_2O	CO	N_2	CO_2
A/Z						
1	2.7	3.8	0.1			
2	100	0.64				
3	0.31	0.009				
⋮						
6		0.0003		0.0008		0.0005
7		0.0013			0.0006	
8				0.0001		0.0005
⋮						
12		2.1		3.5		6.3
13		7.4				0.063
14		15		1.4	9	
15		83			0.026	
16		100	3.07	1.4		16
17		1.3	27.01			
18			100			0.0088
19			0.19			
⋮						
22						0.52
23						0.047
24						0.0012
25						15
26						0.15
27						0.029
28				100	100	
29				1.2	0.71	
30				0.2	0.0014	
⋮						
44						100
45						1.2
46						0.38
47						0.0034
48						0.0005

Table C.2: Collection of cracking patterns of some molecules, probably appearing dominantly in the storage ring's vacuum system [OHa03, appendix E]. ς denotes the relative sensitivity of the gases and vapors.

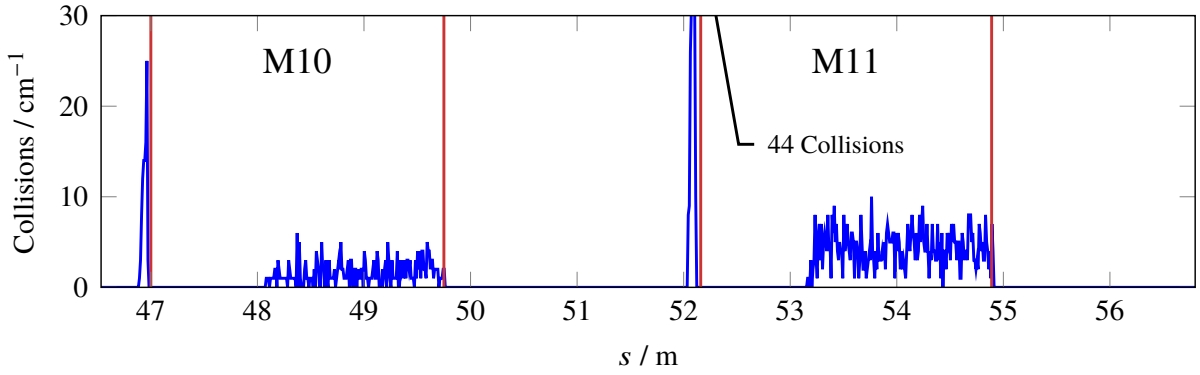

Figure C.13: Collisions of macro-ions with the beam pipe along the simulation scenario. The red lines indicate the beginning and end of the dipole magnets M10 and M11.

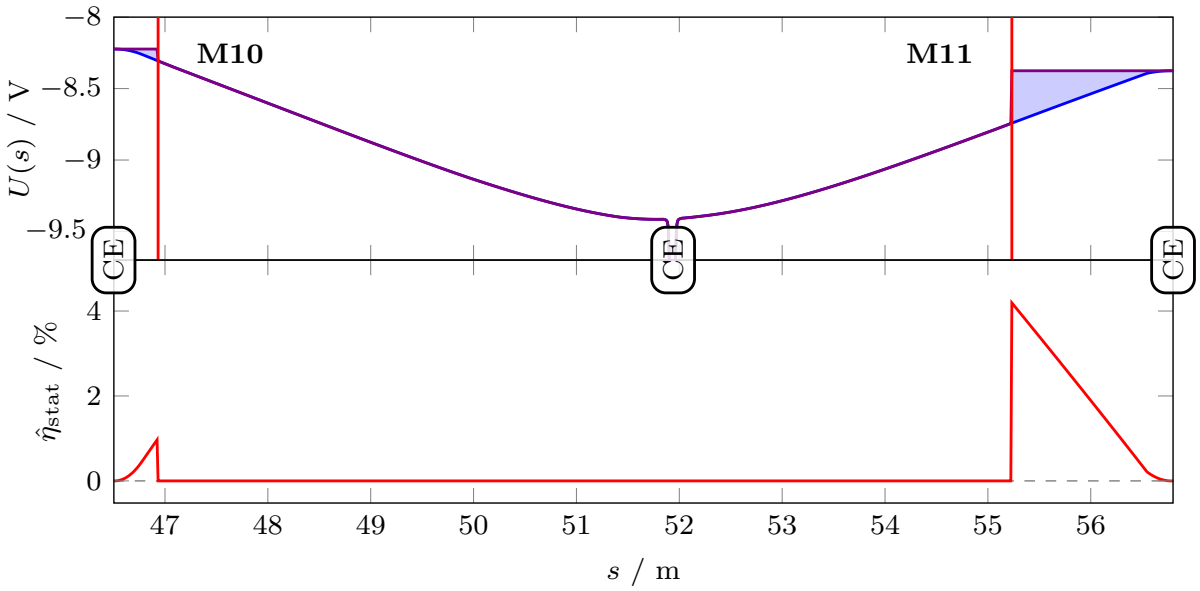

Figure C.14: Local static neutralization assuming that the ions' transmission probability through the fringe fields of dipoles M10 and M11 is zero. The original beam potential is shown in blue whereas the space charge deformed potential is shown in violet.

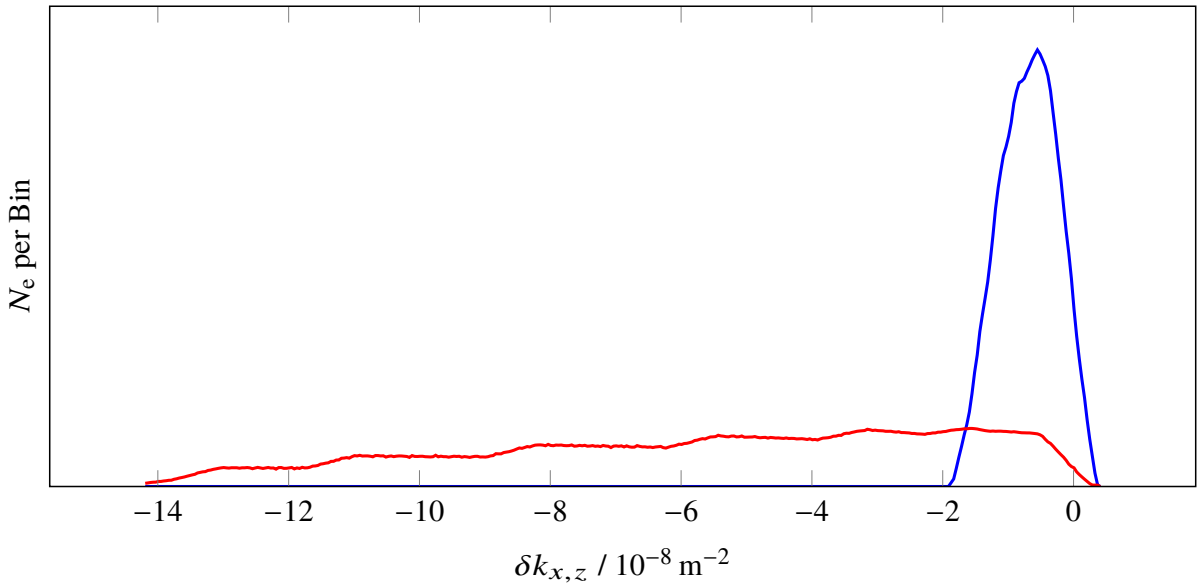

Figure C.15: Distribution of the horizontal (blue) and vertical quadrupole kicks (red) which the beam electron experience for a neutralization of 0 % due to the electrons' mutual space charge interaction. The beam energy is 1.2 GeV and the current is 200 mA.

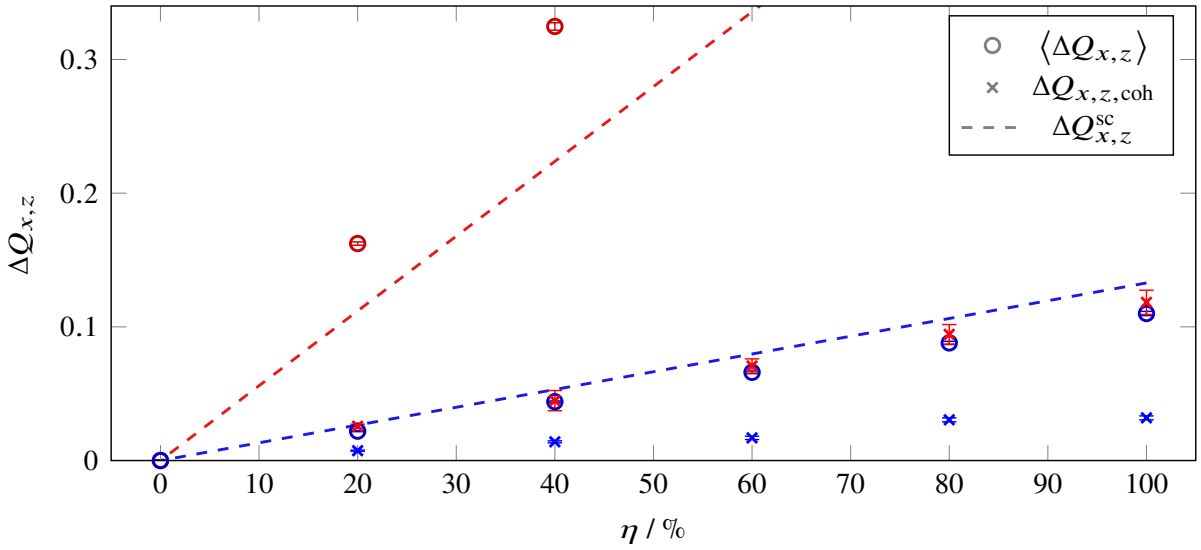

Figure C.16: Characteristics of the ion induced tune shift. The dashed lines indicate the theoretical tune shift $\Delta Q^{\mathrm{sc}}_{x,z}$ in the horizontal (blue) and vertical plane (red) when a simplified space charge model is used. $\langle \Delta Q_{x,z} \rangle$ denotes the shift of the centroid of the tune distribution. $\Delta Q_{x,z,\mathrm{coh}}$ is equal to the coherent tune shift, the peak of the tune distribution. Both, the centroid and coherent shifts are extracted from `pQTool` simulations. In this scenario, the beam energy is 1.2 GeV and a current of 30 mA is stored.

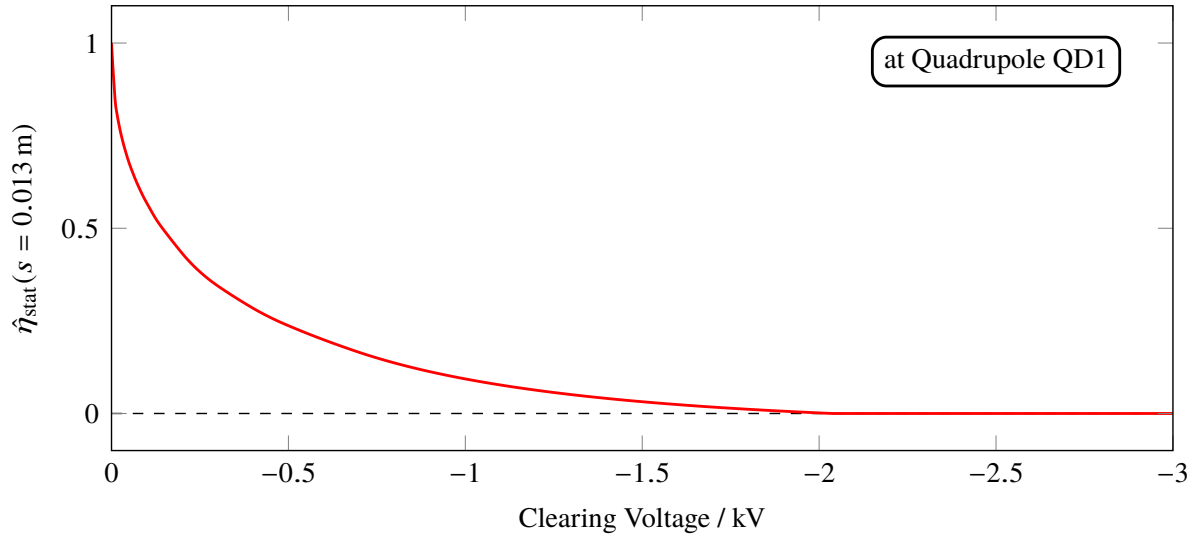

Figure C.17: Local static neutralization at quadrupole QD1 in dependence of the clearing voltage at a beam energy of 1.2 GeV and a beam current of 200 mA.

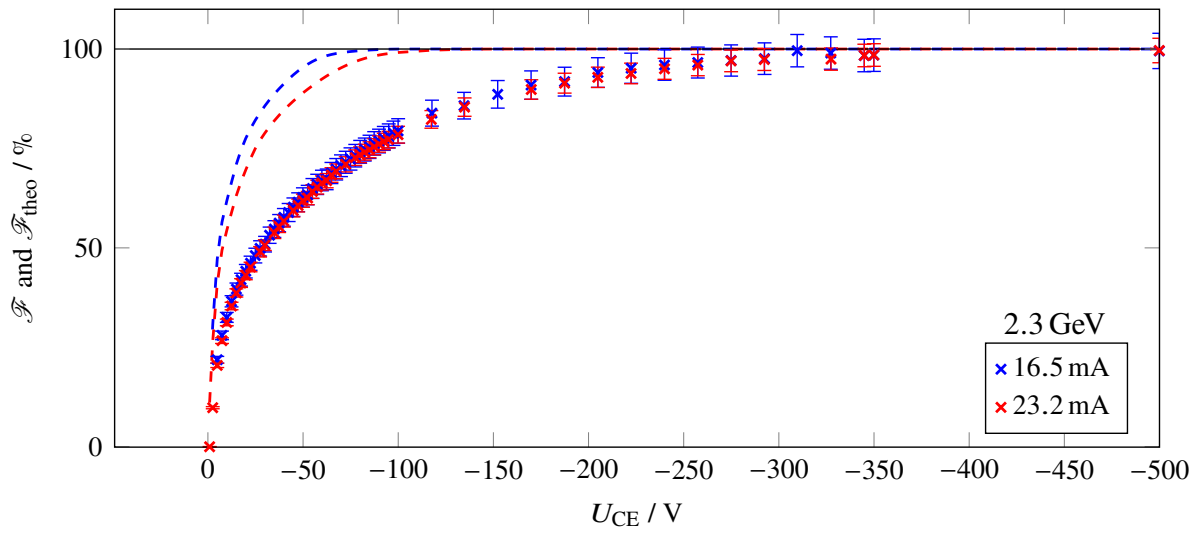

Figure C.18: Transversal loss function $\mathscr{F}$ for different beam currents at a beam energy of 2.3 GeV. The measured loss function is shown for two different beam currents. The predicted loss functions for the corresponding currents are denoted as dashed lines.

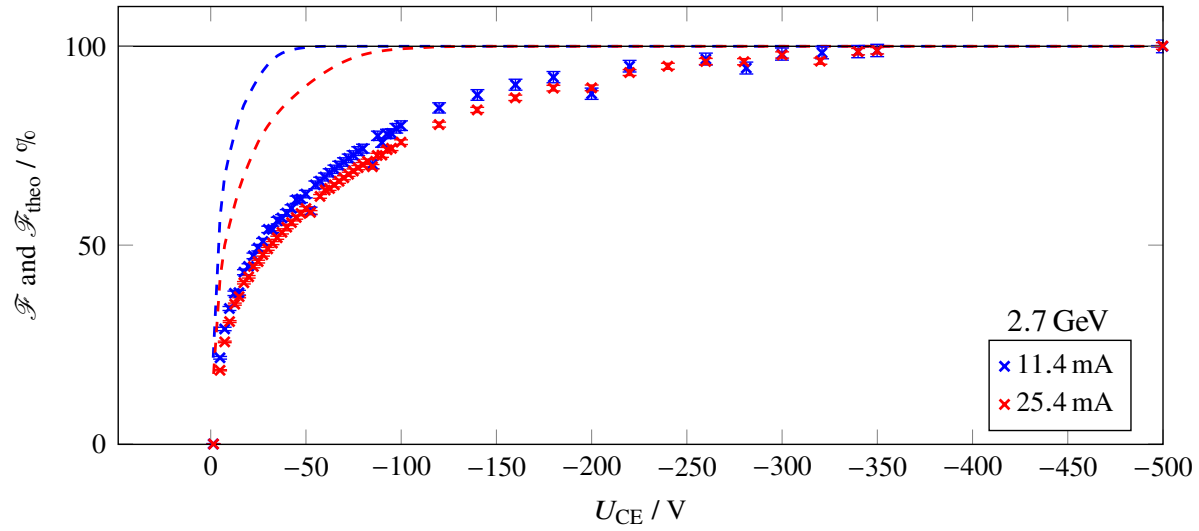

Figure C.19: Transversal loss function $\mathscr{F}$ for different beam currents at a beam energy of 2.7 GeV. The measured loss function is shown for two different beam currents. The predicted loss functions for the corresponding currents are denoted as dashed lines.

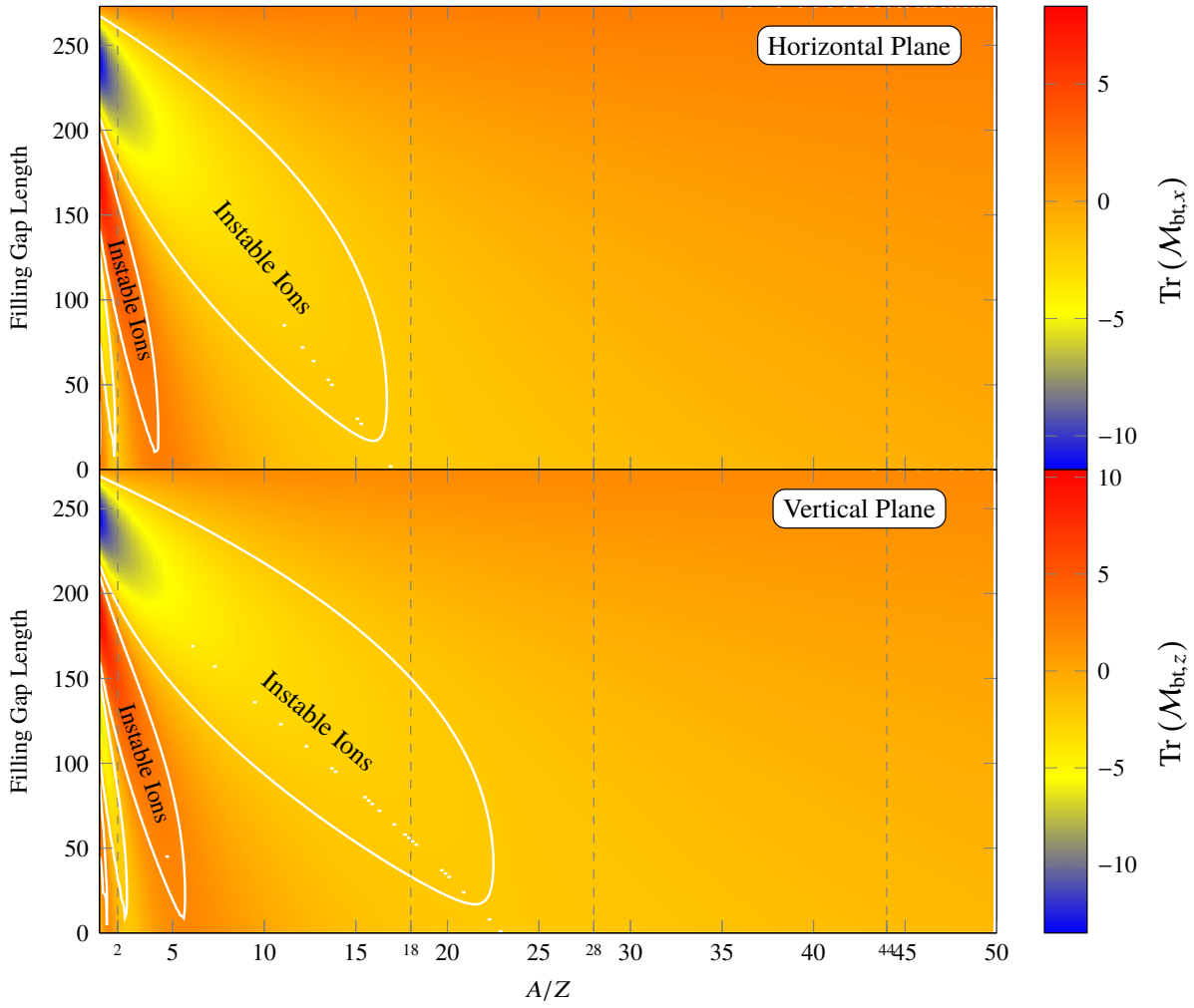

Figure C.20: Trace of the horizontal (top) and vertical (bottom) bunch train matrices for different filling gap lengths and mass-to-charge ratios of the ion species. This stability analysis is valid in regions of the storage ring where the vertical beam width is maximal. The beam is equal to 1.2 GeV and the bunch current is 183 µA. For a filling gap length of zero buckets, a current of 50 mA is stored in the accelerator. The neutralization is assumed to be 0 %. The framed regions indicate domains where $\left|\mathrm{Tr}\left(\mathcal{M}_{\mathrm{bt},x,z}\right)\right| > 2$ and thus the containing ion species are instable at this filling gap length.

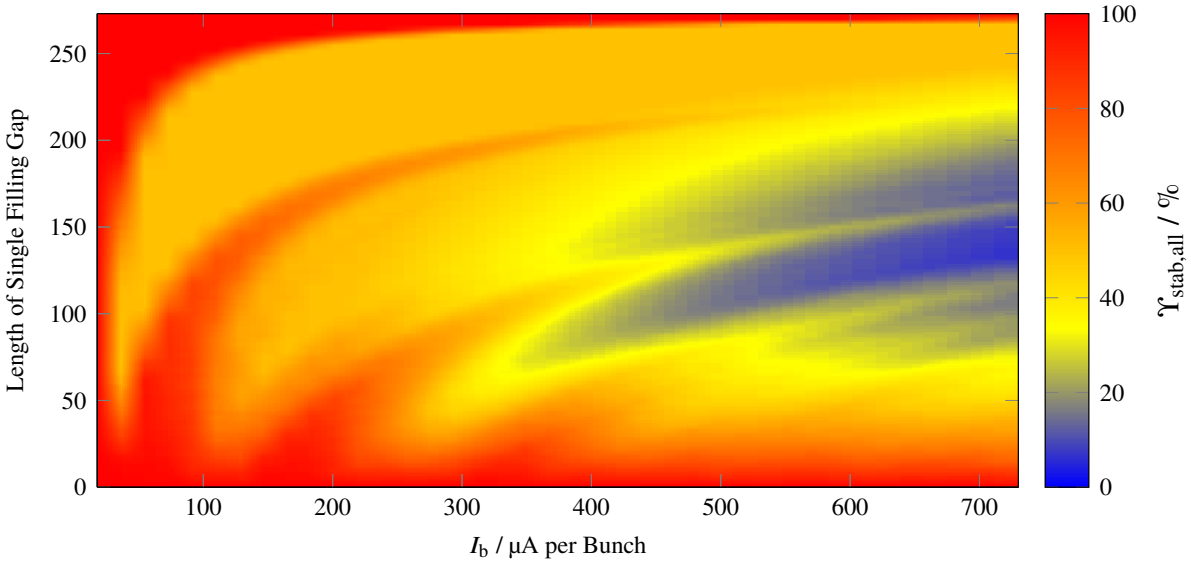

Figure C.21: Stability analysis for the application of a single filling gap at a beam energy of 1.7 GeV and a neutralization of zero. $\Upsilon_{stab,all}$ is the percentage of stable ions in the storage ring. The bunch current corresponds to an initial current I_0 ranging from 5 to 200 mA. The graph is a composition of the individual ion species contributions to $\Upsilon_{stab,all}$ from C.22.

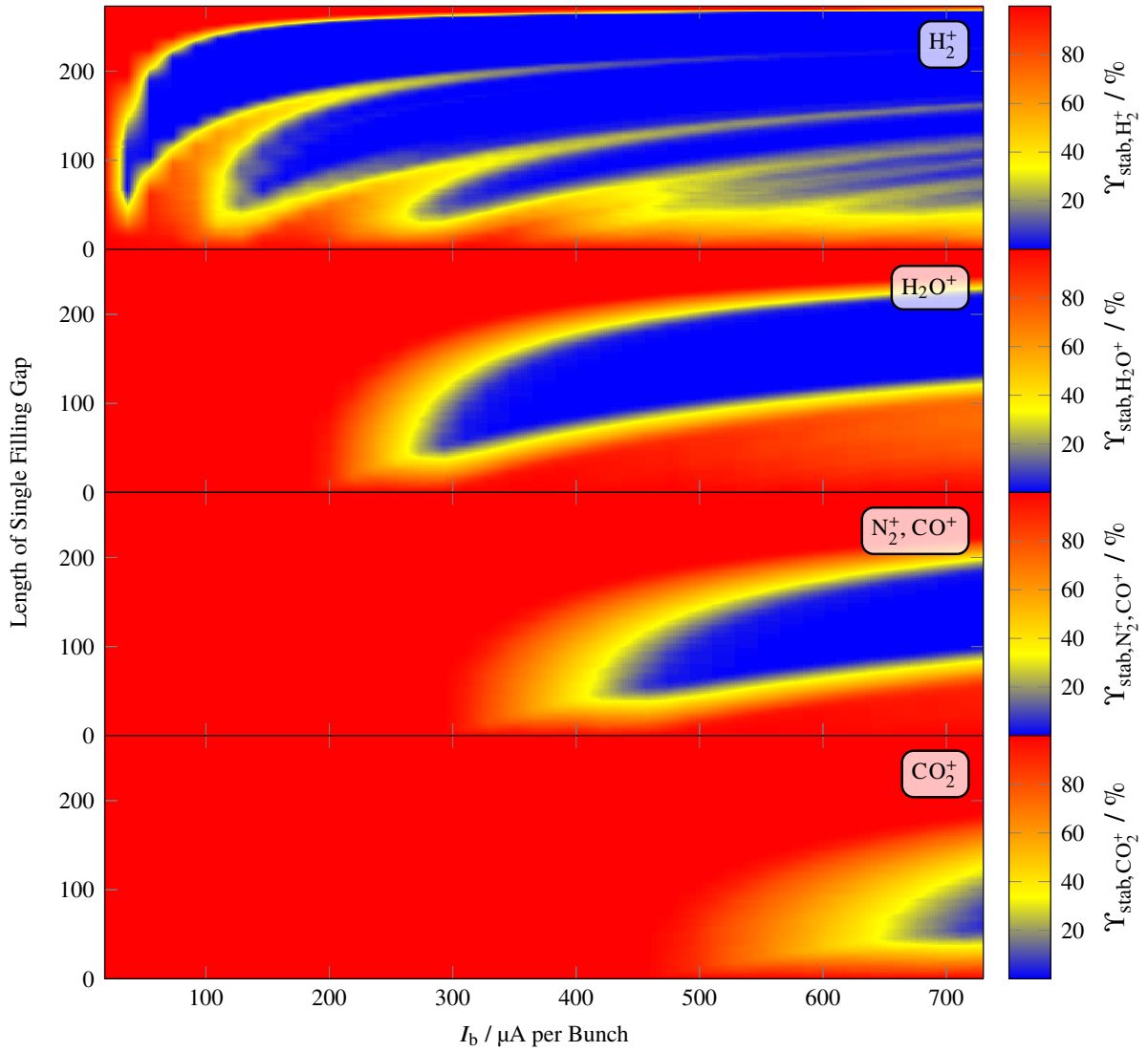

Figure C.22: Percentage of stable ions in the storage ring at a beam energy of 1.7 GeV for different bunch currents when applying one single filling gap of certain length. The neutralization is zero. The bunch current corresponds to an initial current I_0 ranging from 5 to 200 mA.

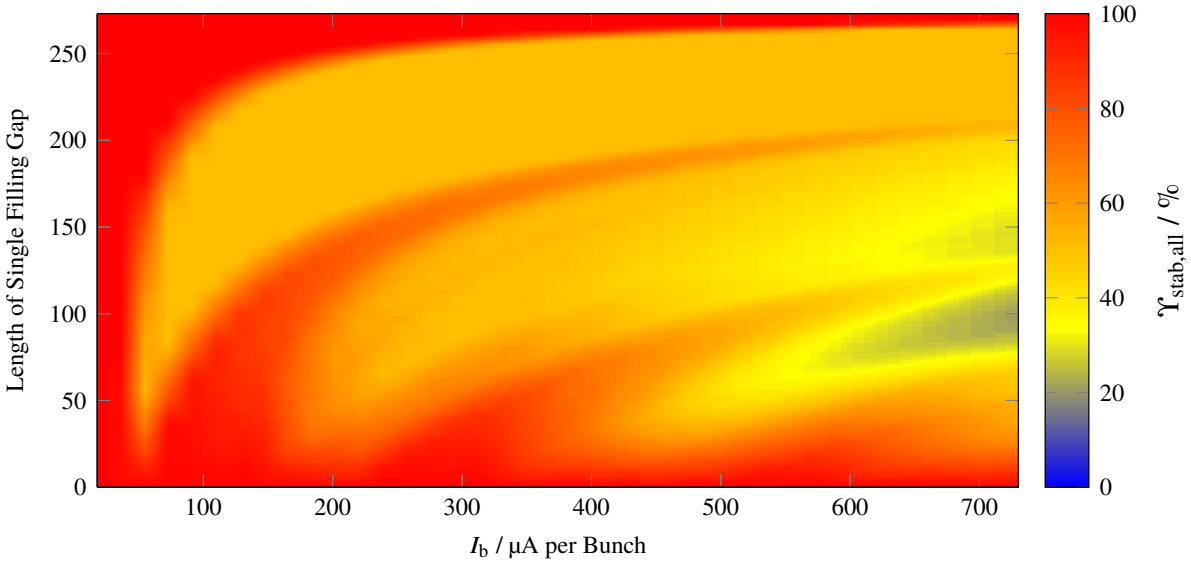

Figure C.23: Stability analysis for the application of a single filling gap at a beam energy of 2.2 GeV and a neutralization of zero. $\Upsilon_{stab,all}$ is the percentage of stable ions in the storage ring. The bunch current corresponds to an initial current I_0 ranging from 5 to 200 mA. The graph is a composition of the individual ion species contributions to $\Upsilon_{stab,all}$ from C.24.

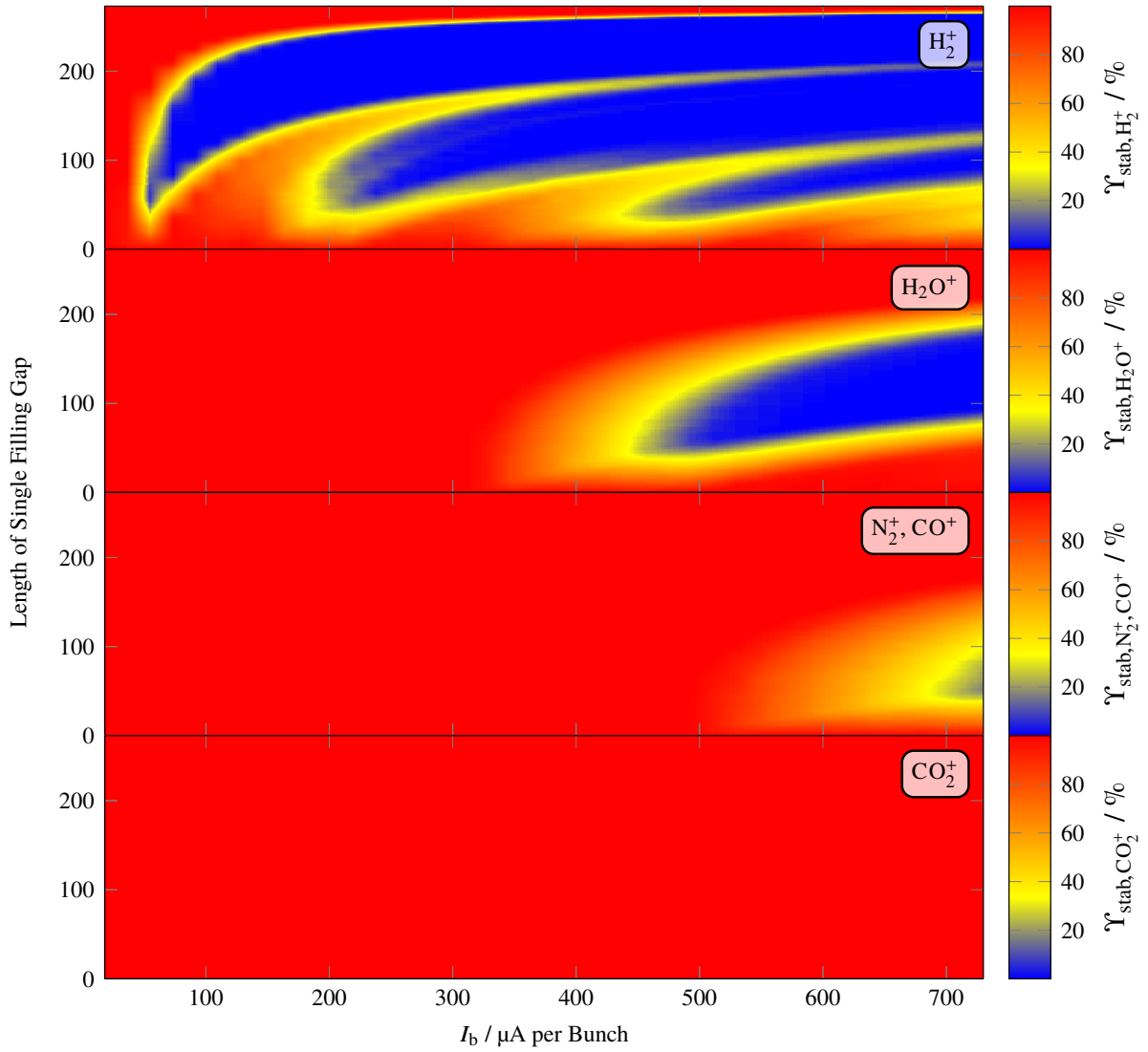

Figure C.24: Percentage of stable ions in the storage ring at a beam energy of 2.2 GeV for different bunch currents when applying one single filling gap of certain length. The neutralization is zero. The bunch current corresponds to an initial current I_0 ranging from 5 to 200 mA.

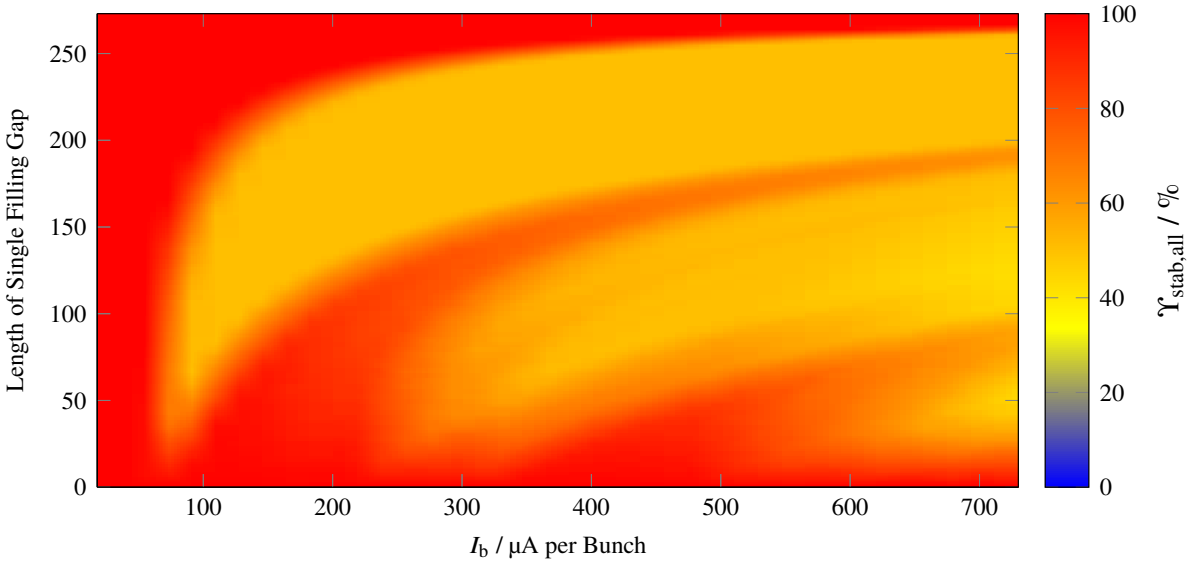

Figure C.25: Stability analysis for the application of a single filling gap at a beam energy of 2.7 GeV and a neutralization of zero. $\Upsilon_{stab,all}$ is the percentage of stable ions in the storage ring. The bunch current corresponds to an initial current I_0 ranging from 5 to 200 mA. The graph is a composition of the individual ion species contributions to $\Upsilon_{stab,all}$ from C.26.

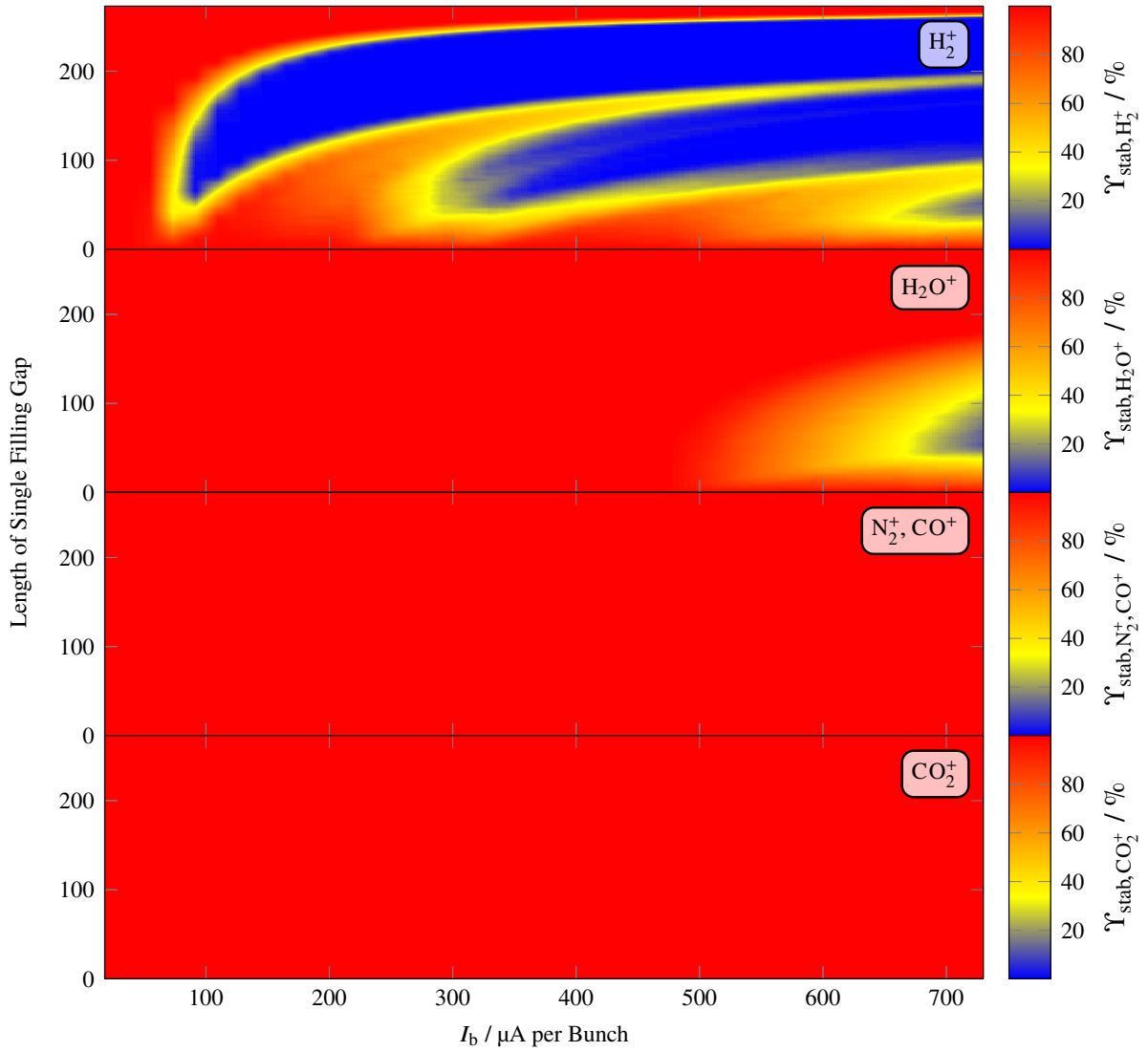

Figure C.26: Percentage of stable ions in the storage ring at a beam energy of 2.7 GeV for different bunch currents when applying one single filling gap of certain length. The neutralization is zero. The bunch current corresponds to an initial current I_0 ranging from 5 to 200 mA.

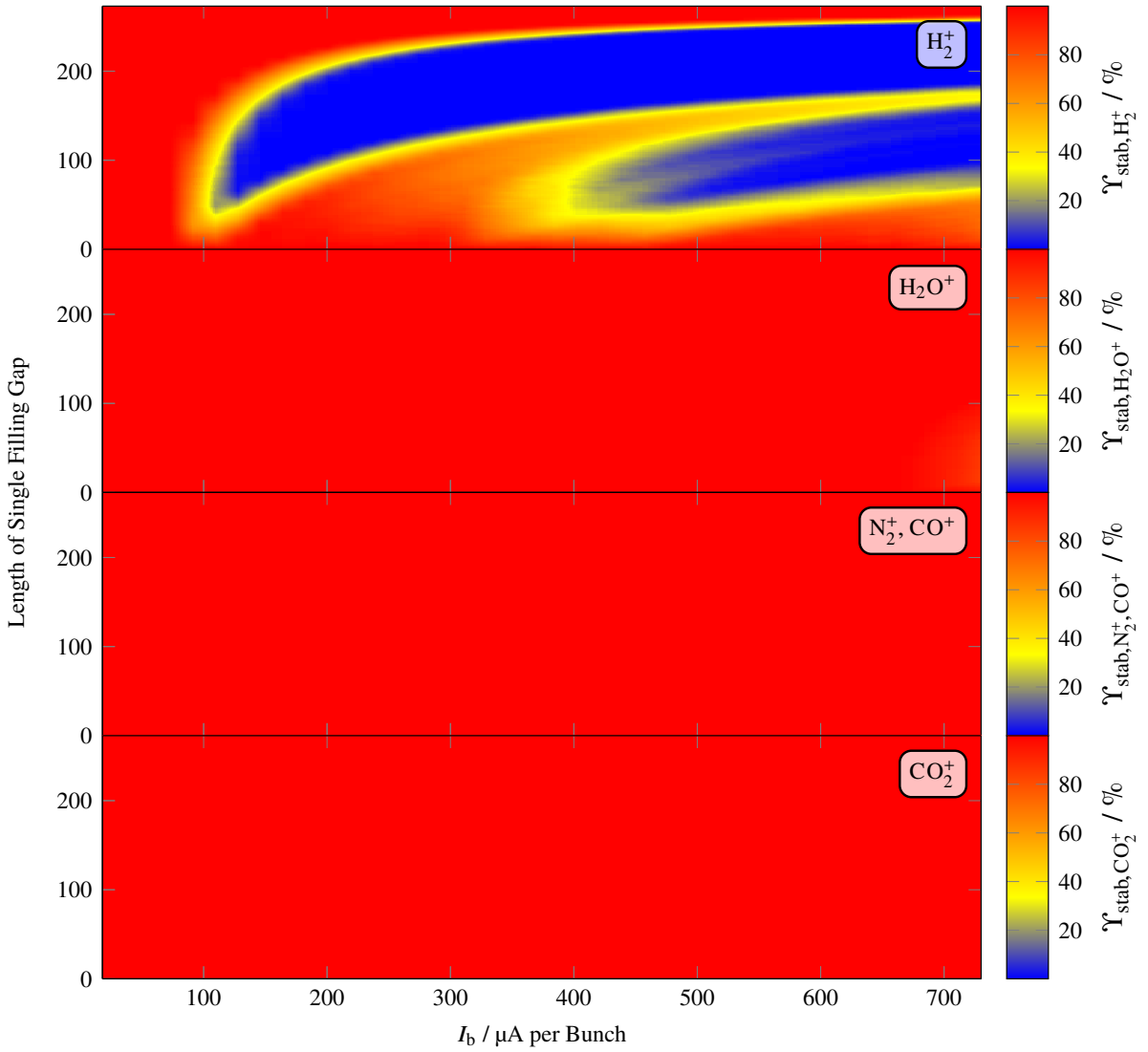

Figure C.27: Percentage of stable ions in the storage ring at a beam energy of 3.2 GeV for different bunch currents when applying one single filling gap of certain length. The neutralization is zero. The bunch current corresponds to an initial current I_0 ranging from 5 to 200 mA.

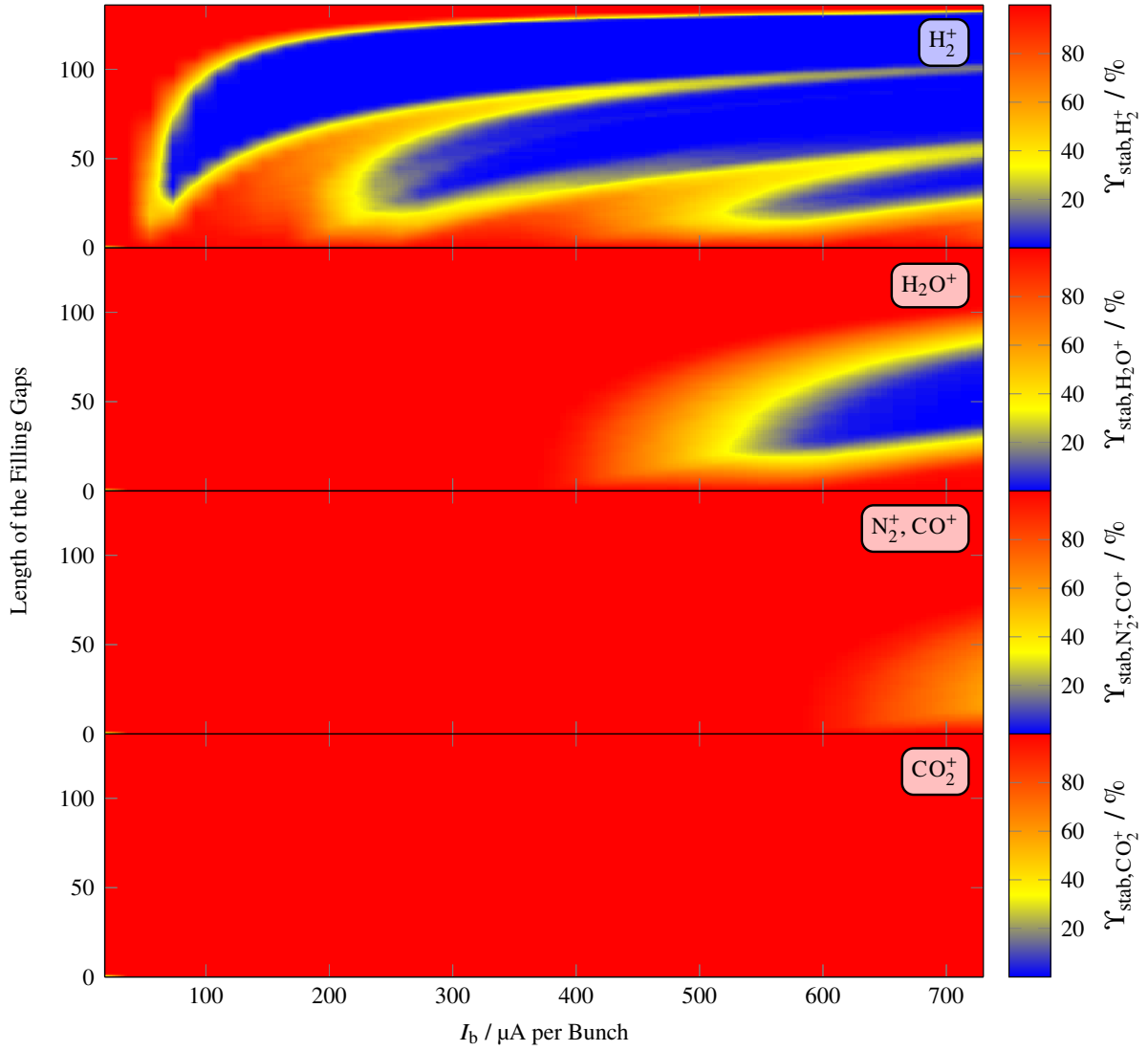

Figure C.28: Percentage of stable ions in the storage ring at a beam energy of 1.2 GeV for different bunch currents when applying two filling gaps of certain length. The neutralization is zero. The bunch current corresponds to an initial current I_0 ranging from 5 to 200 mA.

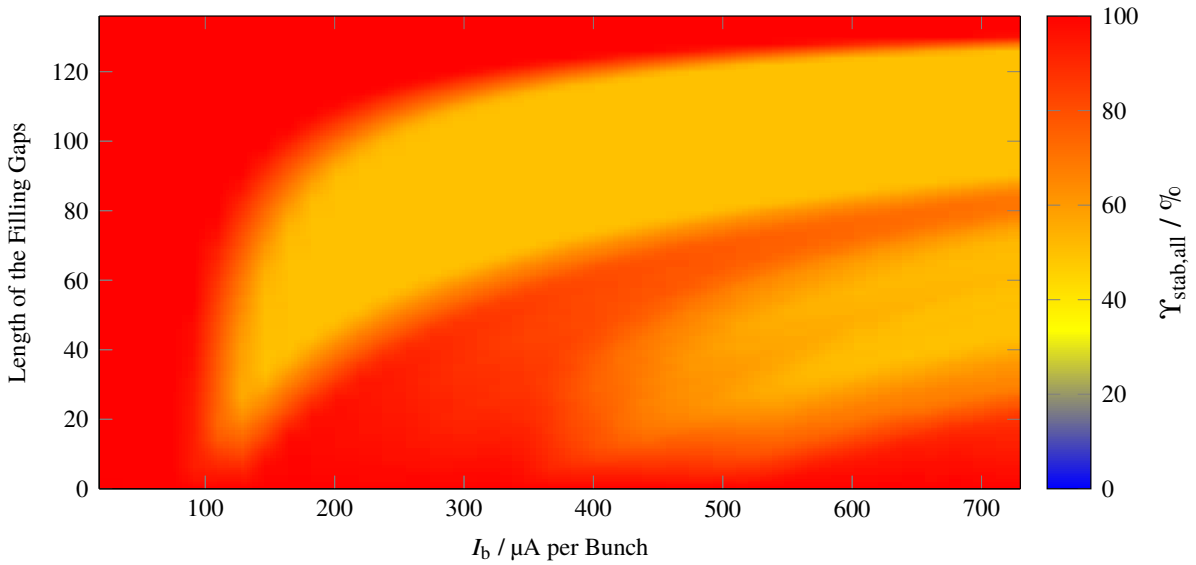

Figure C.29: Stability analysis for the application of two filling gaps at a beam energy of 1.7 GeV and a neutralization of zero. $\Upsilon_{stab,all}$ is the percentage of stable ions in the storage ring. The bunch current corresponds to an initial current I_0 ranging from 5 to 200 mA. The graph is a composition of the individual ion species contributions to $\Upsilon_{stab,all}$ from C.30.

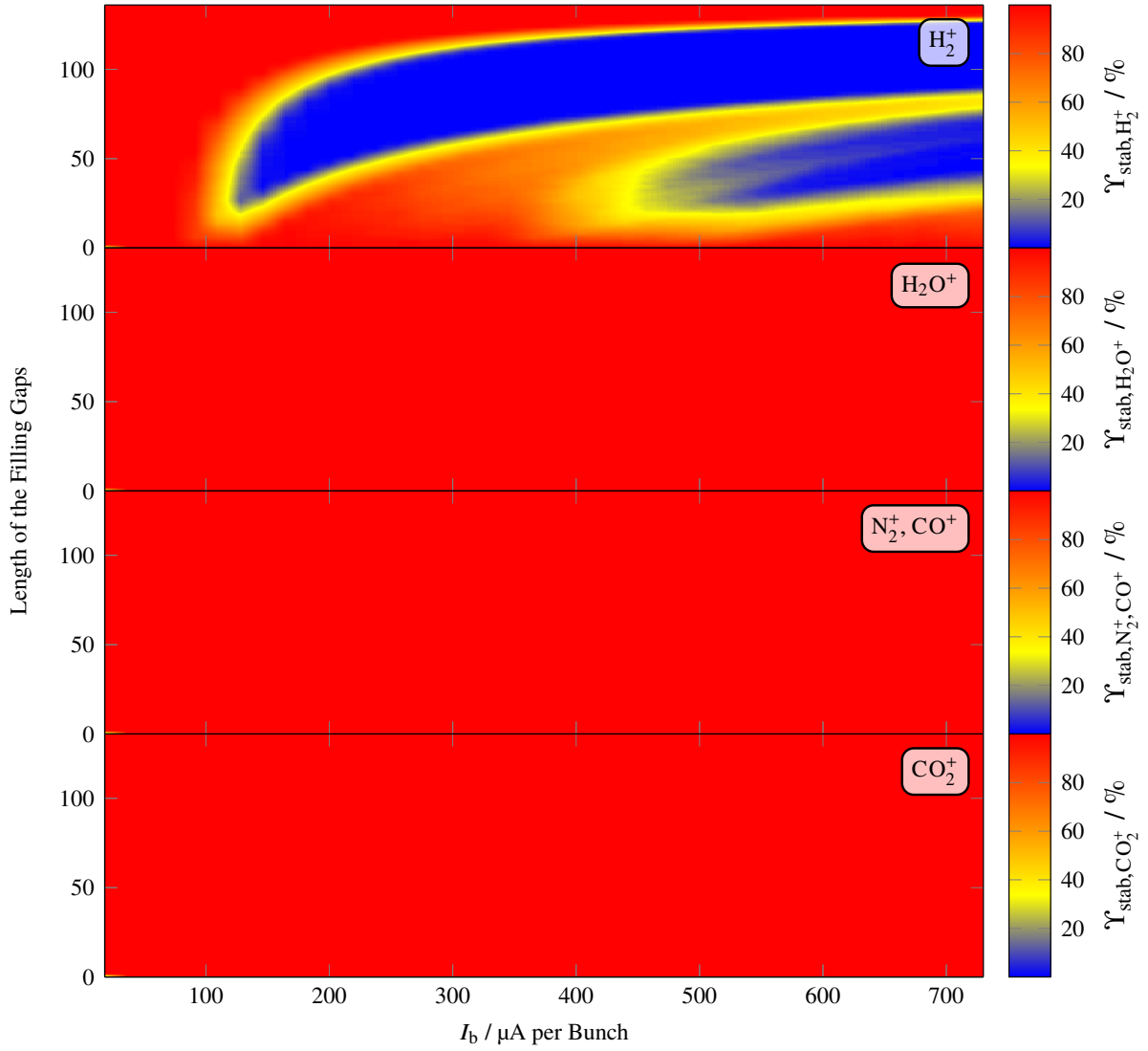

Figure C.30: Percentage of stable ions in the storage ring at a beam energy of 1.7 GeV for different bunch currents when applying two filling gaps of certain length. The neutralization is zero. The bunch current corresponds to an initial current I_0 ranging from 5 to 200 mA.

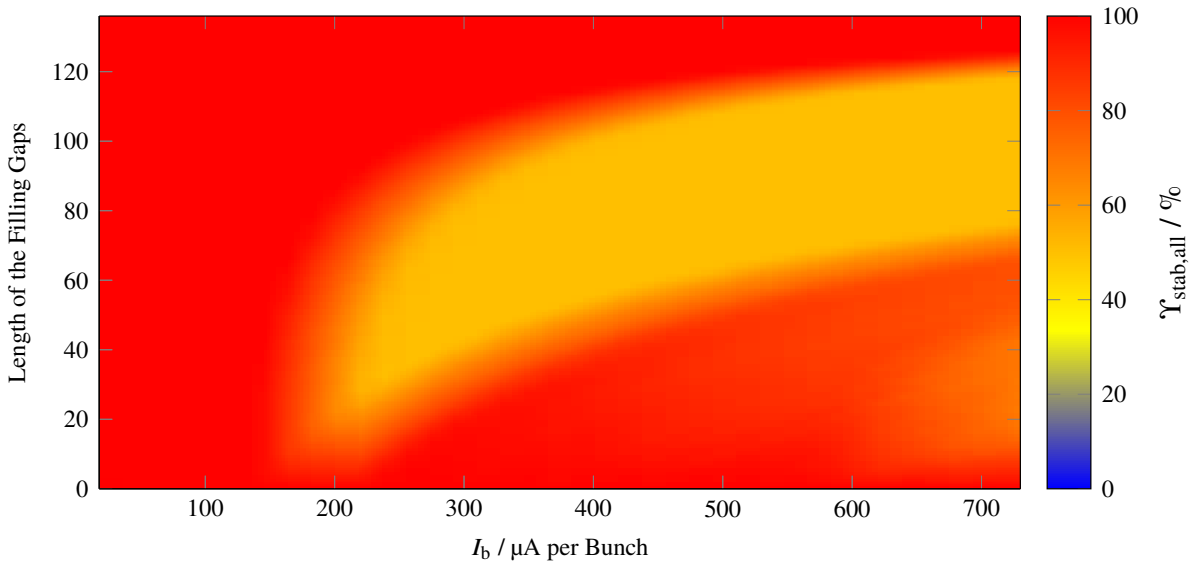

Figure C.31: Stability analysis for the application of two filling gaps at a beam energy of 2.2 GeV and a neutralization of zero. $\Upsilon_{stab,all}$ is the percentage of stable ions in the storage ring. The bunch current corresponds to an initial current I_0 ranging from 5 to 200 mA. The graph is a composition of the individual ion species contributions to $\Upsilon_{stab,all}$ from C.32.

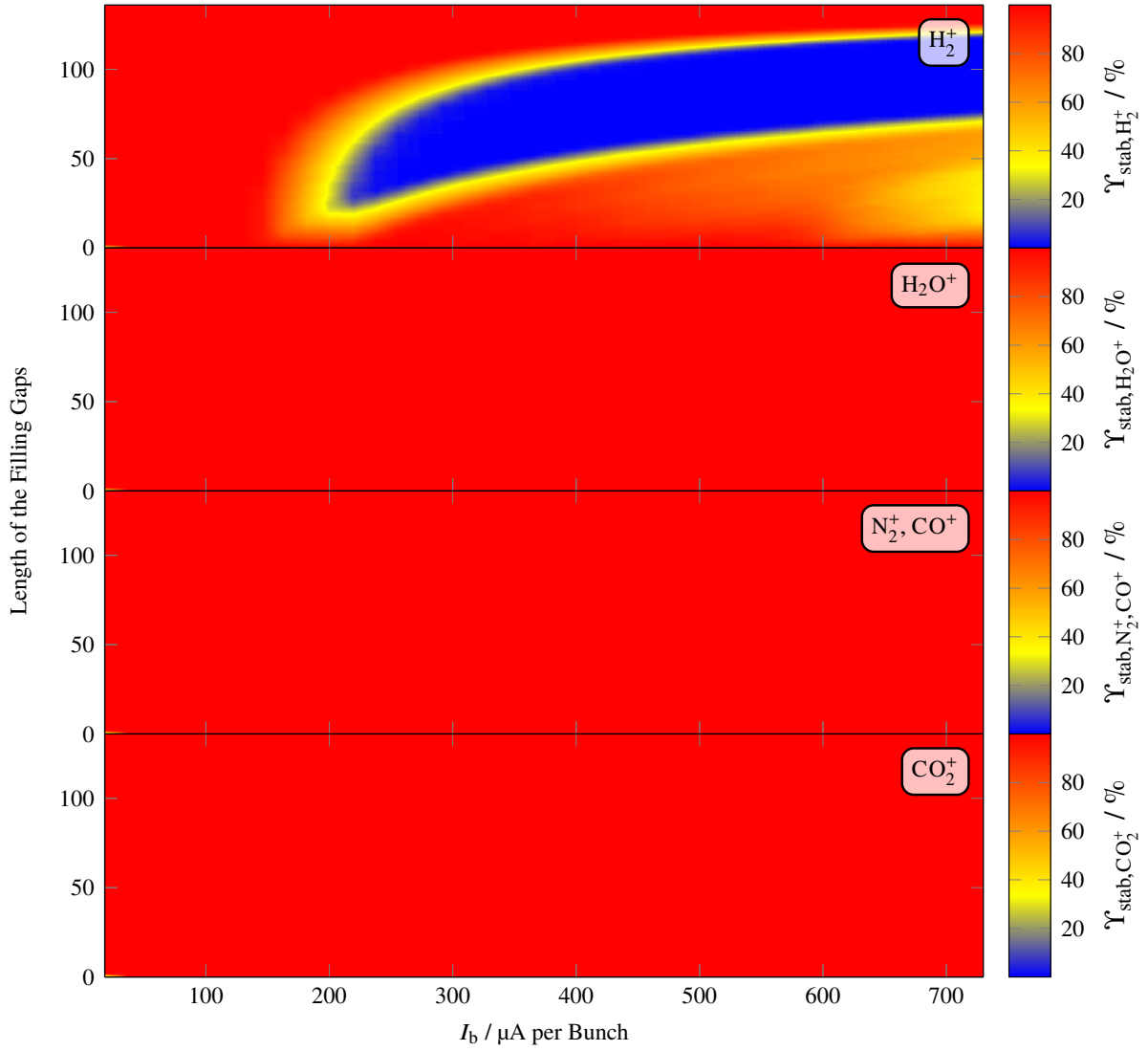

Figure C.32: Percentage of stable ions in the storage ring at a beam energy of 2.2 GeV for different bunch currents when applying two filling gaps of certain length. The neutralization is zero. The bunch current corresponds to an initial current I_0 ranging from 5 to 200 mA.

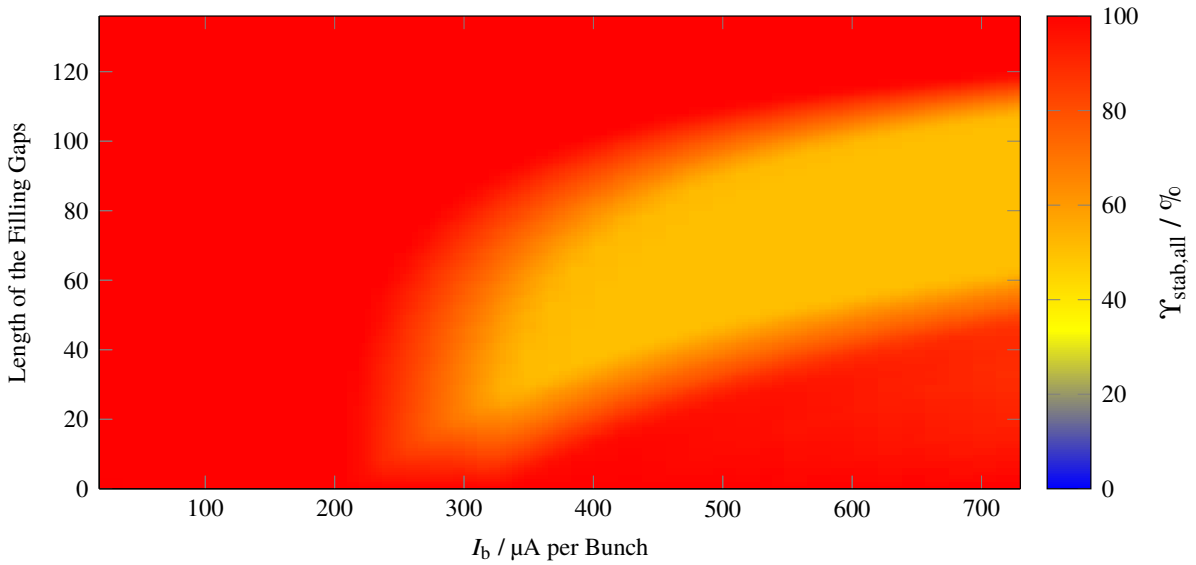

Figure C.33: Stability analysis for the application of two filling gaps at a beam energy of 2.7 GeV and a neutralization of zero. $\Upsilon_{stab,all}$ is the percentage of stable ions in the storage ring. The bunch current corresponds to an initial current I_0 ranging from 5 to 200 mA. The graph is a composition of the individual ion species contributions to $\Upsilon_{stab,all}$ from C.34.

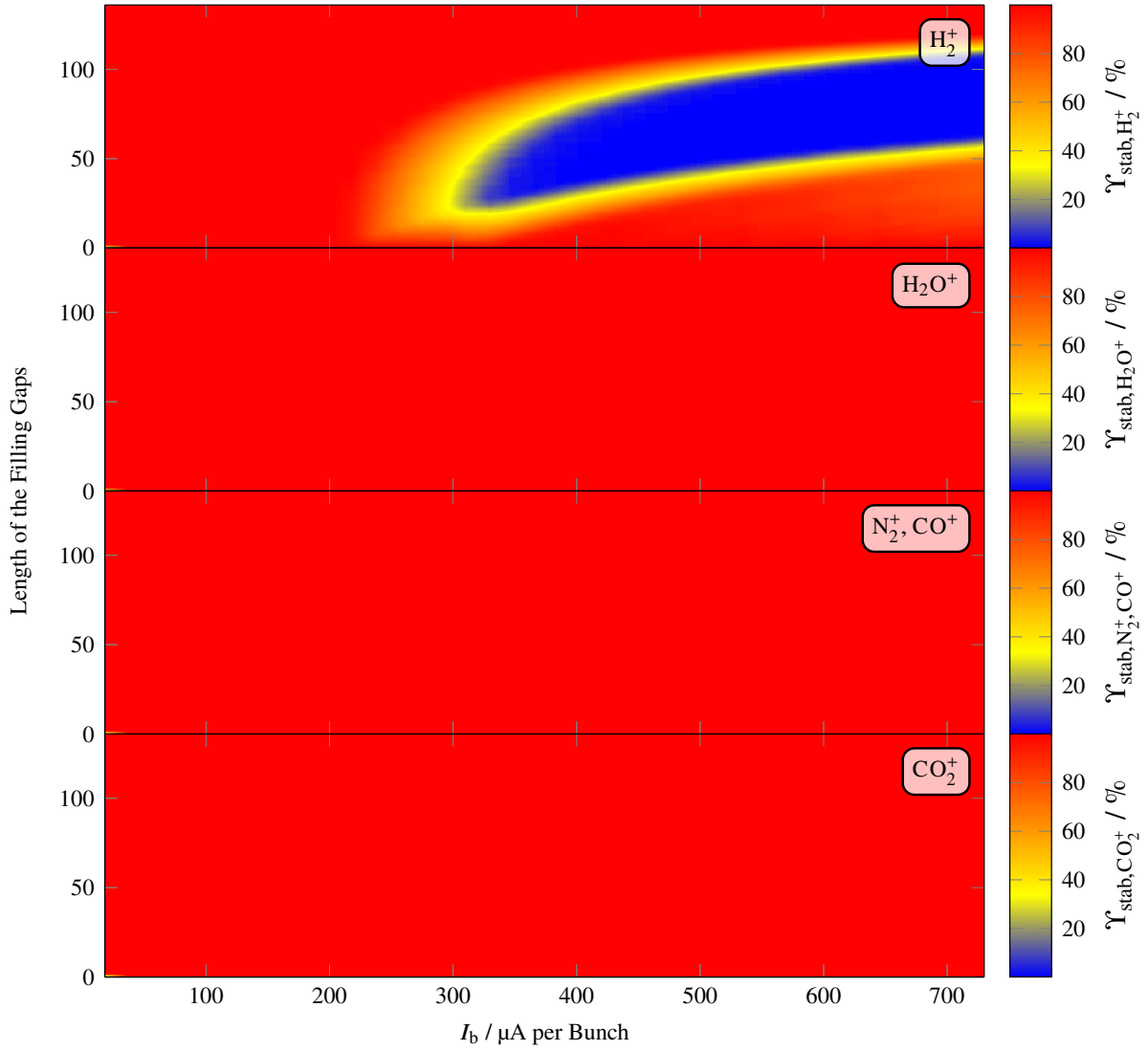

Figure C.34: Percentage of stable ions in the storage ring at a beam energy of 2.7 GeV for different bunch currents when applying two filling gaps of certain length. The neutralization is zero. The bunch current corresponds to an initial current I_0 ranging from 5 to 200 mA.

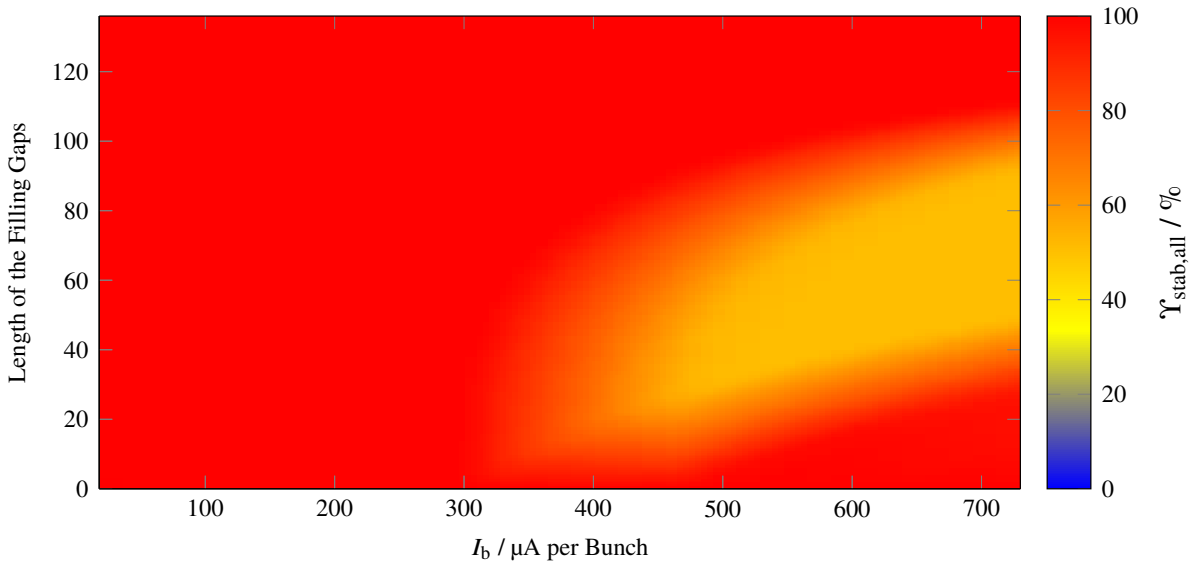

Figure C.35: Stability analysis for the application of two filling gaps at a beam energy of 3.2 GeV and a neutralization of zero. $\Upsilon_{stab,all}$ is the percentage of stable ions in the storage ring. The bunch current corresponds to an initial current I_0 ranging from 5 to 200 mA. The graph is a composition of the individual ion species contributions to $\Upsilon_{stab,all}$ from C.36.

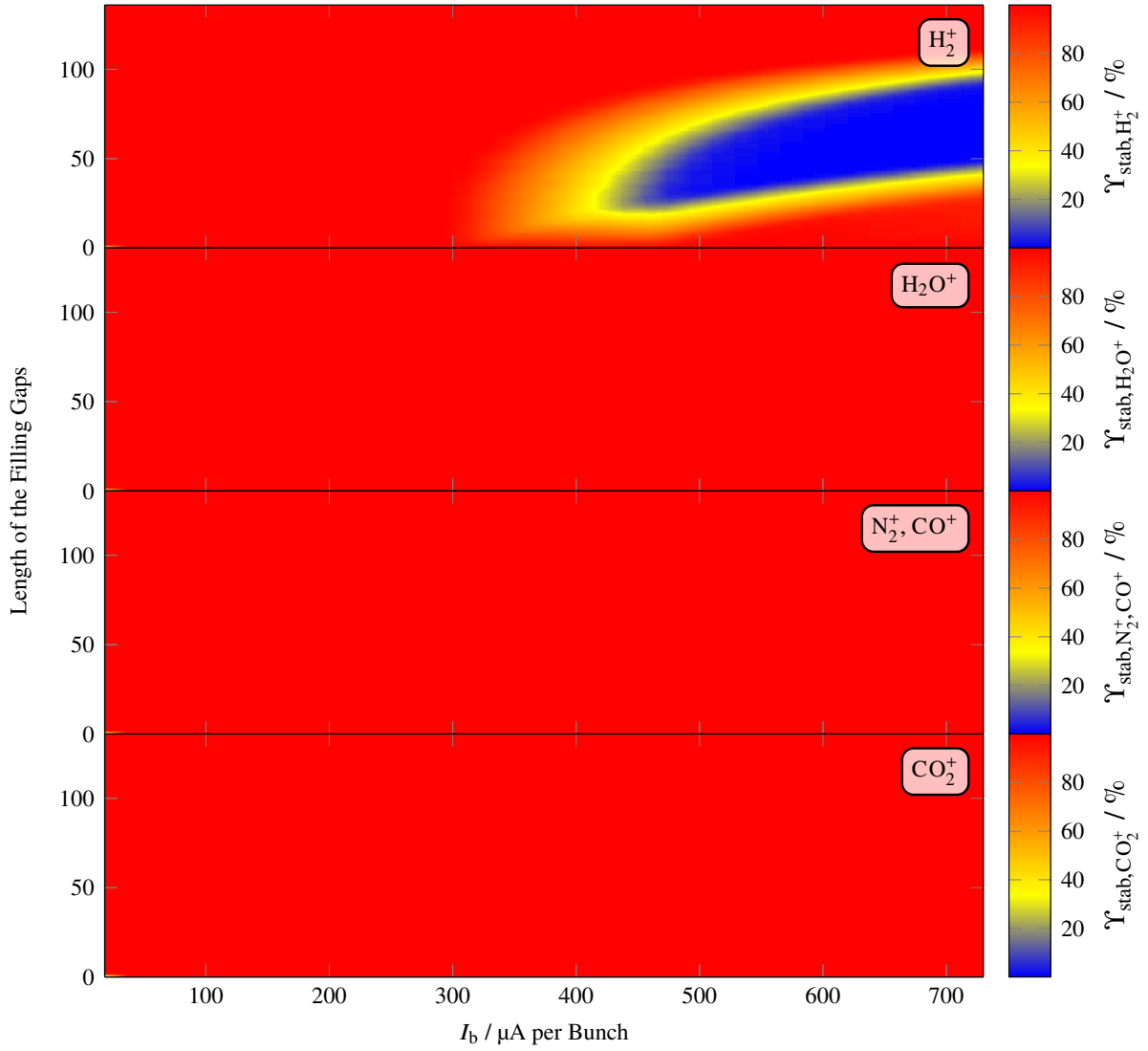

Figure C.36: Percentage of stable ions in the storage ring at a beam energy of 3.2 GeV for different bunch currents when applying two filling gaps of certain length. The neutralization is zero. The bunch current corresponds to an initial current I_0 ranging from 5 to 200 mA.

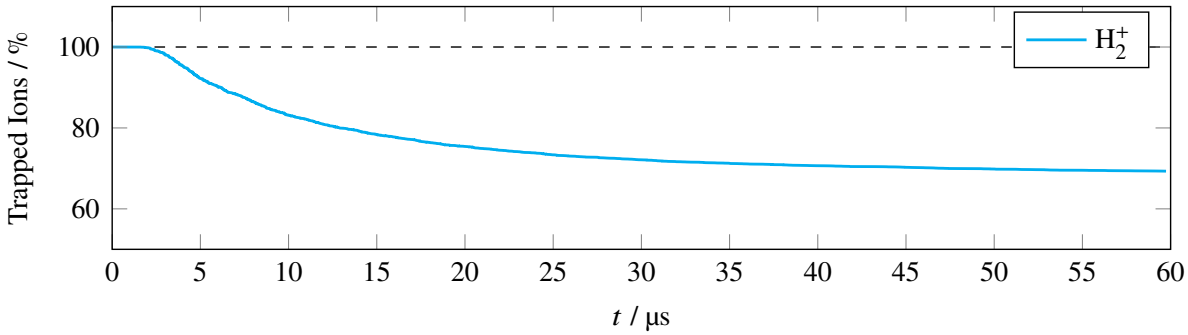

Figure C.37: FillingGapSim simulation of the evolution of the H_2^+ ion population in the vertical plane when exposed to two filling gaps with a length of 95 buckets each. The beam energy is equal to 1.2 GeV and the bunch current is 125 µA.

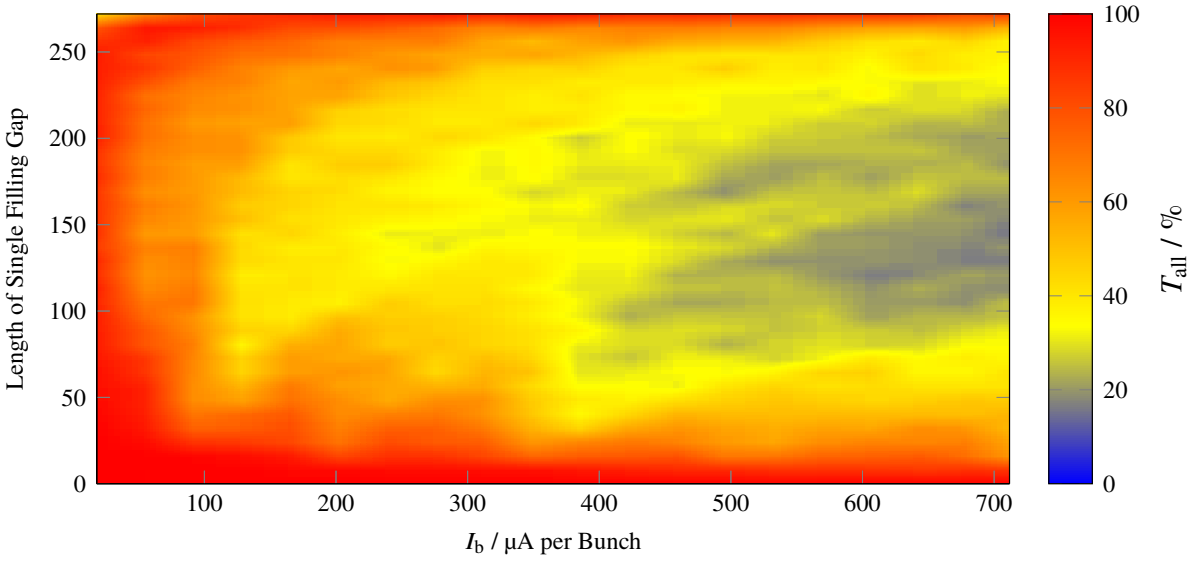

Figure C.38: Stability analysis of the ion population when exposed to a single filling gap of a specific length at different bunch currents at a beam energy of 1.2 GeV. T_{all} is the probability of the produced ions to stay within a region of $\pm 10\sigma_{x,z}$ for a time frame of 100 µs in a FillingGapSim simulation. Here, the electron beam has a dimension equal to its average size in the storage ring. The bunch current corresponds to an initial current I_0 ranging from 5 to 195 mA. The graph is a composition of the individual ion species' contributions T_i of A.17.

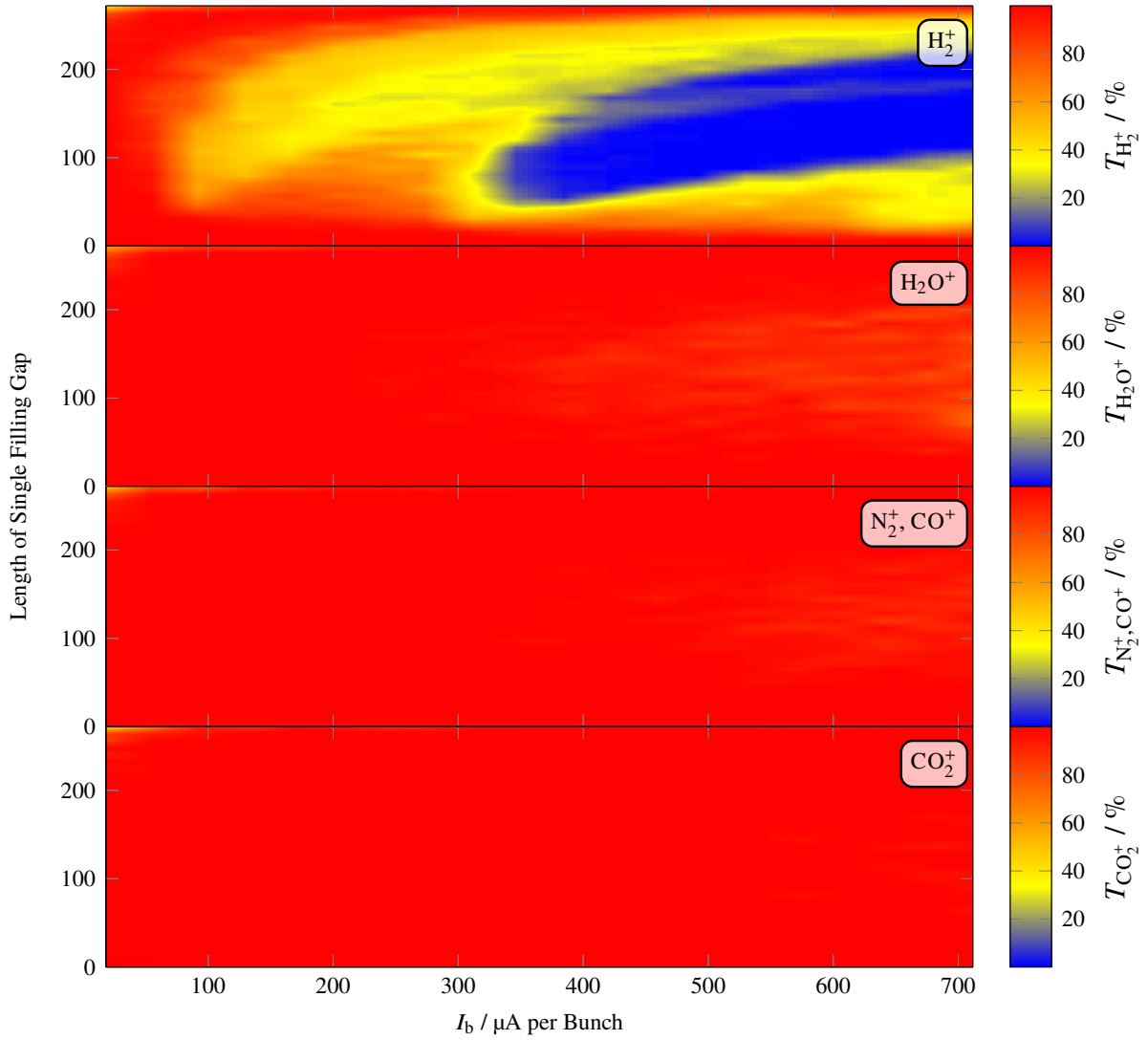

Figure C.39: Stability of different ion species when a single filling gap of a specific length is applied at different bunch currents at a beam energy of 2.2 GeV. The stability criterion is the probability T of a produced ion to stay within a region of $\pm 10\sigma_{x,z}$ for a time frame of 100 µs in a FillingGapSim simulation. Here, the electron beam has a dimension equal to its average size in the storage ring. The bunch current corresponds to an initial current I_0 ranging from 5 to 195 mA. The compilation of all species can be found in figure C.40.

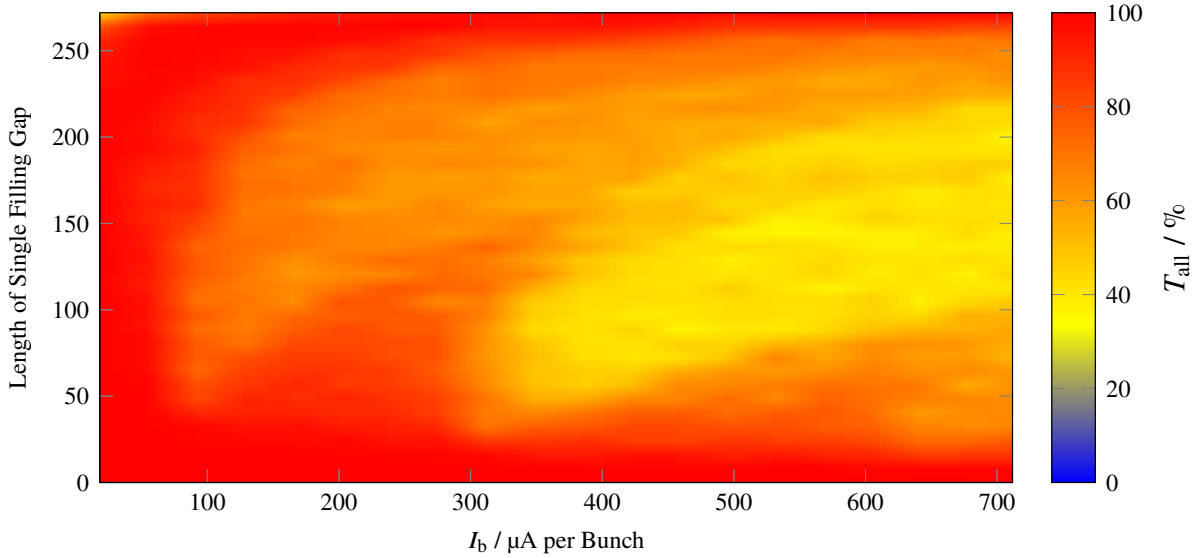

Figure C.40: Stability analysis of the ion population when exposed to a single filling gap of a specific length at different bunch currents at a beam energy of 2.2 GeV. T_{all} is the probability of the produced ions to stay within a region of $\pm 10\sigma_{x,z}$ for a time frame of 100 µs in a FillingGapSim simulation. Here, the electron beam has a dimension equal to its average size in the storage ring. The bunch current corresponds to an initial current I_0 ranging from 5 to 195 mA. The graph is a composition of the individual ion species contributions to $\Upsilon_{stab,all}$ from C.39.

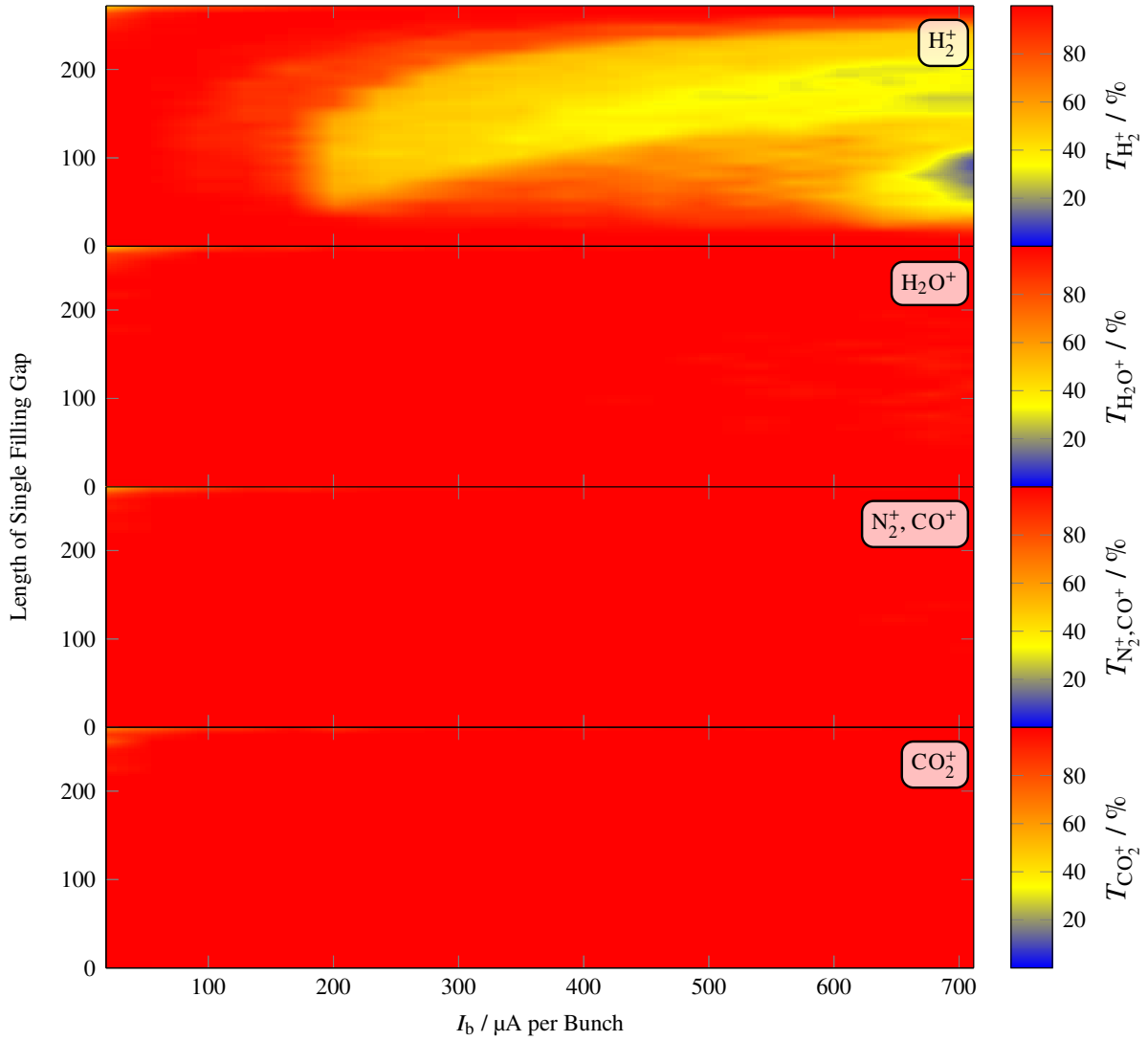

Figure C.41: Stability of different ion species when a single filling gap of a specific length is applied at different bunch currents at a beam energy of 3.2 GeV. The stability criterion is the probability T of a produced ion to stay within a region of $\pm 10\sigma_{x,z}$ for a time frame of 100 µs in a FillingGapSim simulation. Here, the electron beam has a dimension equal to its average size in the storage ring. The bunch current corresponds to an initial current I_0 ranging from 5 to 195 mA. The compilation of all species can be found in figure C.42.

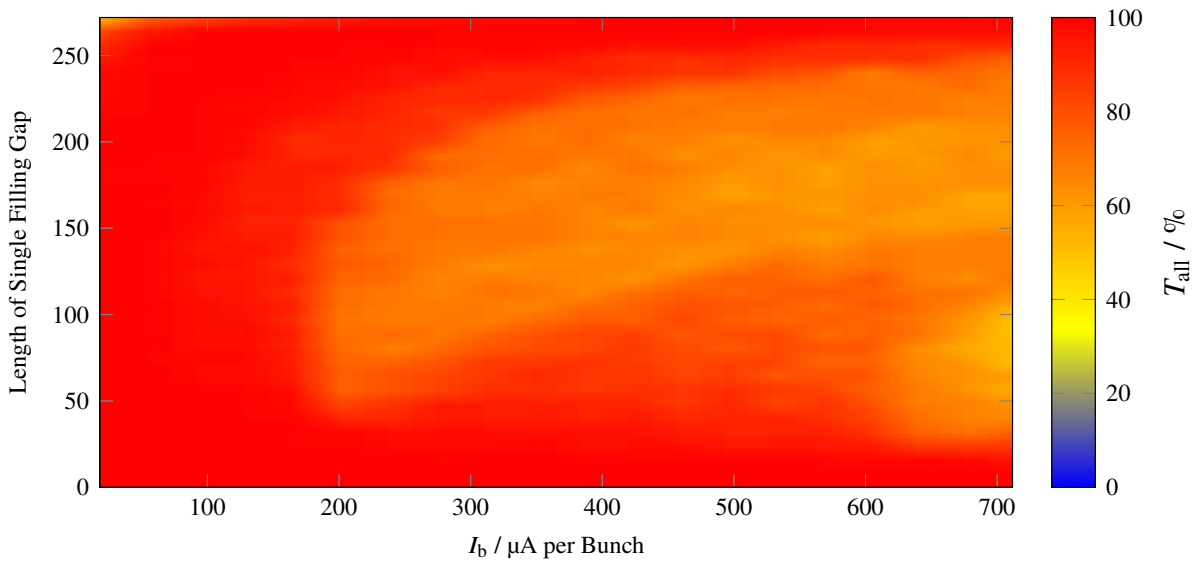

Figure C.42: Stability analysis of the ion population when exposed to a single filling gap of a specific length at different bunch currents at a beam energy of 3.2 GeV. T_{all} is the probability of the produced ions to stay within a region of $\pm 10\sigma_{x,z}$ for a time frame of 100 µs in a FillingGapSim simulation. Here, the electron beam has a dimension equal to its average size in the storage ring. The bunch current corresponds to an initial current I_0 ranging from 5 to 195 mA. The graph is a composition of the individual ion species contributions to $\Upsilon_{stab,all}$ from C.41.

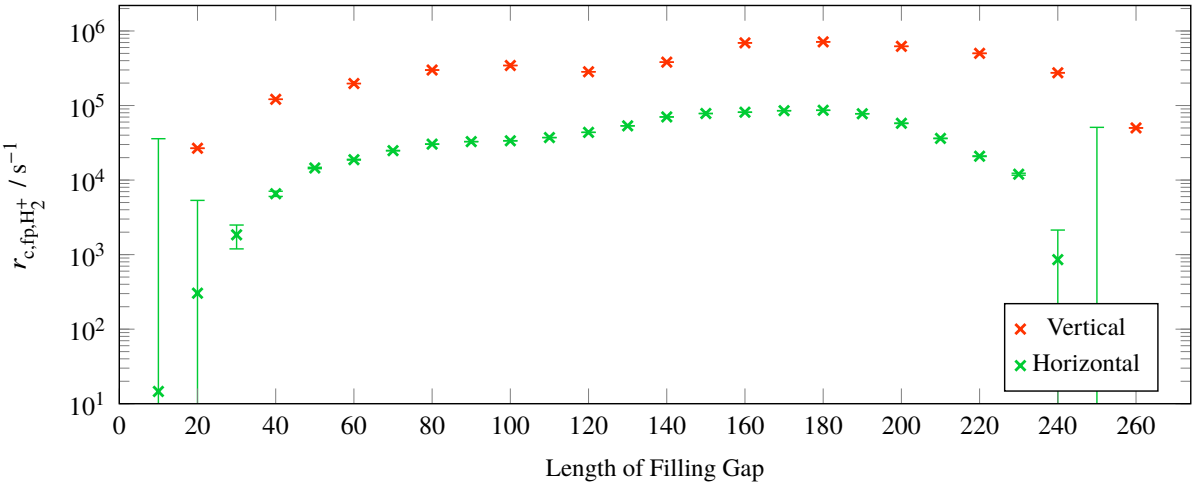

Figure C.43: Comparison of the horizontal and vertical clearing rate of H_2^+ ions for different filling patterns with a single filling gap. The beam energy is equal to 1.2 GeV and the bunch current is 125 µA (I_0 = 34.25 mA).

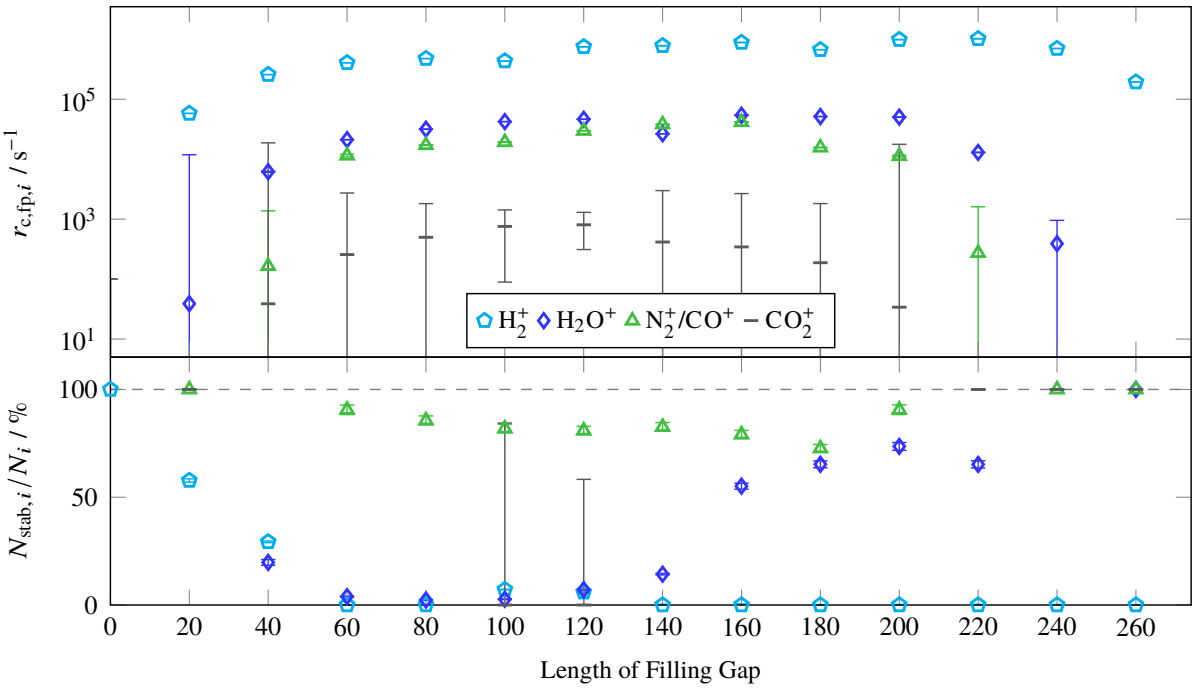

Figure C.44: Simulated clearing rates in the vertical plane of different ion species when exposed to a filling gap with different length at a beam energy of 1.2 GeV and a bunch current of 250 µA (I_0 = 68.5 mA). In the bottom graph, the fraction of stable ions at these filling patterns is shown.

Bibliography

[AM+] S. Agarwal, K. Mierle et al., *Ceres Solver*, URL: https://ceres-solver.org (cit. on p. 61).

[Aic17] I. Aichinger, *Vacuum Simulations in High Energy Accelerators and Distribution Properties of Continuous and Discrete Particle Motions*, CERN-THESIS-2017-252, PhD thesis: Institute of Financial Mathematics and Applied Number Theory, Universität Linz, 2017, URL: https://cds.cern.ch/record/2295265/files/CERN-THESIS-2017-252.pdf (cit. on p. 58).

[Alt+68] K. H. Althoff et al., *The 2.5 GeV Electron Synchrotron of the University of Bonn*, Nuclear Instruments and Methods **61** (1968) 1 (cit. on p. 3).

[Alv87a] R. Alves-Pires, *Beam Dimensions and Beam Potential in the CERN Antiproton Accumulator Complex*, Internal Publication CERN PS/87-70 (AA), 1987 (cit. on p. 95).

[Alv87b] R. Alves-Pires, *Conformal Mapping for Two-Dimensional Electrostatic Beam Potential Calculations*, Internal Publication CERN PS/87-66-(AA), 1987 (cit. on pp. 34, 100, 289).

[Aut79] B. Autin, *Dispersion Suppression with Missing Magnets in a FODO Structure-Application to the CERN Antiproton Accumulator*, IEEE Trans. Nucl. Sci. **26** (1979) 3493 (cit. on p. 30).

[BB80] Y. Baconnier and G. Brianti, *The Stability of Ions in Bunched Beam Machines*, Internal Publication CERN/SPS/80-2, 1980 (cit. on pp. 86, 203, 246, 250, 255).

[BB84] Y. Baconnier and G. Brianti, *Neutralization of Accelerator Beams by Ionization of the Residual Gas*, Internal Publication CERN/PS/PSR 84-24, 1984 (cit. on p. 263).

[Bal91] Balzers AG, *Quadrupole Analysator*, 2nd ed., Balzers Aktiengesellschaft, 1991 (cit. on p. 46).

[BE80] M. Bassetti and G. A. Erskine, *Closed Expression for the Electrical Field of a Two-Dimensional Gaussian Charge*, Internal Publication CERN-ISR-TH/80-06, 1980 (cit. on p. 34).

[Ber+08] M. J. Berger et al., *NIST Standard Reference Database 8 (XGAM)*, XCOM: Photon Cross Sections Database (2008), URL: https://physics.nist.gov/PhysRefData/Xcom/html/xcom1.html (visited on) (cit. on pp. 71, 72).

[Bet30] H. Bethe, *Zur Theorie des Durchgangs schneller Korpuskularstrahlen durch Materie*, Annalen der Physik **397** (1930) 325 (cit. on p. 66).

[Boc+94] C. J. Bocchetta et al., *Ion Trapping Investigations in Elettra*, *Proc. of 4th. European Particle Accelerator Conf., London*, vol. 1153, 1994 (cit. on p. 174).

[BW89] C. J. Bocchetta and A. Wrulich, *The Trapping and Clearing of Ions in ELETTRA*, Nuclear Instruments and Methods in Physics Research Section A: Accelerators, Spectrometers, Detectors and Associated Equipment **278** (1989) 807 (cit. on p. 184).

[Bor00] M. Borland, *ELEGANT: A Flexible SDDS-Compliant Code for Accelerator Simulation*, 2000, URL: https://www.osti.gov/scitech/servlets/purl/761286 (cit. on p. 23).

[Bor+10] M. Borland et al., *The Potential of an Ultimate Storage Ring for Future Light Sources*, Nuclear Instruments and Methods in Physics Research Section A: Accelerators, Spectrometers, Detectors and Associated Equipment **622** (2010) 518 (cit. on p. 1).

[Byr+97] J. Byrd et al., *First Observations of a "Fast Beam-Ion Instability"*, Physical Review Letters **79** (1997) 79 (cit. on p. 165).

[Cas+07] F. Caspers et al., eds., *Joint CARE-ELAN, CARE-HHH-APD, and EUROTEV-WP3 Workshop on Electron Cloud Clearing - Electron Cloud Effects and Technological Consequences "ECL2", CERN, Geneva, Switzerland, 1 - 2 March, 2007*, Workshop on Electron Cloud Effects and Technological Consequences 2, CERN, 2007, URL: https://cds.cern.ch/record/1057138/files/ab-2007-064.pdf (cit. on p. 184).

[Cas+89] F. Caspers et al., *EPA Beam-Vacuum Interaction Ion Clearing System*, tech. rep., CM-P00059146, 1989 (cit. on p. 184).

[Che+06] H. Cherkani-Hassani et al., *Absolute Cross Sections for Electron Impact Ionization and Dissociation of O_2^+*, Journal of Physics B: Atomic, Molecular and Optical Physics **39** (2006) 5105 (cit. on p. 42).

[DF12] J. L. Daniel and J. K. Foster-O'Neal, *The Numerical Open-Source Many-Body Simulator (NOMS)*, Senior Project, Faculty of the Aerospace Engineering Department, California Polytechnic State University, San Luis Obispo, USA, 2012 (cit. on p. 282).

[Ele] Elettra - Sincrotrone Trieste S.C.p.A., *Atomic Calculation of Photoionization Cross-Sections and Asymmetry Parameters*, Online Database, URL: https://vuo.elettra.eu/services/elements/WebElements.html (cit. on pp. 71, 72).

[Fre17] O. Freyermuth, *Studies of ω Photoproduction off Proton at the BGO-OD Experiment*, urn:nbn:de:hbz:5n-48397, PhD thesis: Physikalisches Institut, Universität Bonn, 2017 (cit. on p. 3).

[Gal+88] J. W. Gallagher et al., *Absolute Cross Sections for Molecular Photoabsorption, Partial Photoionization, and Ionic Photofragmentation Processes*, Journal of Physical and Chemical Reference Data **17** (1988) 9, URL: https://doi.org/10.1063/1.555821 (cit. on pp. 42, 71, 72).

[GS00] J. Gans and D. Shalloway, *Shadow Mass and the Relationship between Velocity and Momentum in Symplectic Numerical Integration*, Physical Review E **61** (2000) 4587 (cit. on p. 283).

[Gar10] R. Garoby, *RF Gymnastics in Synchrotrons*, Internal Publication CERN/PS 2000-022 (RF), 2010, URL: https://cds.cern.ch/record/446600/files/ps-2000-022.pdf (cit. on p. 87).

[Gen99] M. Gentner, *Präparation von Teilchenstrahlen für Experimente der Hadronenphysik: Langsame Extraktion an ELFE@DESY und ELSA, sowie Strahlkühlung an HERA*, BONN-IR-99-01, PhD thesis: Physikalisches Institut, Universität Bonn, 1999 (cit. on p. 133).

[Ger+77] H. Gerke et al., *Das PETRA-Cavity*, Internal Report DESY PET-77/08, Deutsches Elektronen Synchrotron, Hamburg, 1977 (cit. on p. 132).

[Grö99] O. Gröbner, *Dynamic Outgassing*, tech. rep., Report Number: CERN 99-05, pp. 127-138: Cern, Geneva, Switzerland, 1999 (cit. on pp. 58, 234).

[Grö+83] O. Gröbner et al., *Studies of Photon Induced Gas Desorption Using Synchrotron Radiation*, Vacuum **33** (1983) 397 (cit. on p. 59).

[Hän19] P. Hänisch, Personal Note, 2019 (cit. on pp. 99, 100, 106).

[HNH15] P. Hänisch, B. Neff and W. Hillert, *Water-Cooled Thin Walled Beam Pipes of the Fast Ramping Storage Ring ELSA*, *Proc. of International Particle Accelerator Conference (IPAC'15), Richmond, USA, May 3-8, 2015*, (Richmond, Virginia, USA), International Particle Accelerator Conference 6, JACoW, 2015 2780, ISBN: 978-3-95450-168-7, URL: https://accelconf.web.cern.ch/AccelConf/IPAC2015/papers/wepma015.pdf (cit. on pp. 44, 89).

[Har17] J. Hartmann, *Measurement of Double Polarization Observables in the Reactions $\gamma p \to p\pi^0$ and $\gamma p \to p\eta$ with the Crystal Barrel/TAPS Experiment at ELSA*, PhD thesis: Helmholtz-Institut für Strahlen- und Kernphysik, Universität Bonn, 2017, URL: https://hss.ulb.uni-bonn.de/2017/4833/4833.htm (cit. on p. 3).

[HS15] I. Hertel and C.-P. Schulz, *Atoms, Molecules and Optical Physics 1*, Springer Verlag Berlin Heidelberg, 2015, ISBN: 978-3-642-54321-0 (cit. on p. 72).

[Heu11] N. Heurich, *Dämpfung von Strahlinstabilitäten im Elektronenbeschleuniger ELSA mithilfe von Breitbandresonatoren*, Master Thesis: Physikalisches Institut, Universität Bonn, 2011 (cit. on p. 213).

[Heu17] N. Heurich, *Die Externe Strahlführung für Detektortests X3ED an der Elektronen-Stretcher-Anlage ELSA*, urn:nbn:de:hbz:5n-49191, PhD thesis: Physikalisches Institut, Universität Bonn, 2017 (cit. on p. 3).

[Hil06] W. Hillert, *The Bonn Electron Stretcher Accelerator ELSA: Past and Future*, The European Physical Journal A - Hadrons and Nuclei **28** (2006) 139, ISSN: 1434-601X, URL: https://doi.org/10.1140/epja/i2006-09-015-4 (cit. on p. 42).

[Hin11] F. Hinterberger, *Ion Trapping in the High-Energy Storage Ring HESR*, Berichte des Forschungszentrums Jülich **4343** (2011) (cit. on pp. 10, 12, 34, 39, 100, 145, 266).

[Hin12] F. Hinterberger, *Counteracting Trapped Ion Effects in the HESR*, Berichte des Forschungszentrums Jülich **4357** (2012) (cit. on pp. 33, 35, 184).

[Ino71] M. Inokuti, *Inelastic Collisions of Fast Charged Particles with Atoms and Molecules — The Bethe Theory Revisited*, Reviews of Modern Physics **43** (1971) 297 (cit. on p. 66).

[ise] iseg Spezialelektronik GmbH, *High Voltage Power Supply BPS-Series (4W)*, URL: https://www.iseg-hv.de (cit. on p. 185).

[ise12] iseg Spezialelektronik GmbH, *Precision NIM High Voltage Supply NHQ HIGH PRECISION series RS232 - Interface*, 2012, URL: https://www.iseg-hv.de (cit. on p. 186).

[Jac62] J. D. Jackson, *Classical Electrodynamics*, John Wiley & Sons, 1962, ISBN: 0-471-43131-1 (cit. on pp. 9, 37).

[Joy07] K. I. Joy, *Numerical Methods for Particle Tracing in Vector Fields*, On-Line Visualization Notes (2007) 1, URL: https://web.cs.ucdavis.edu/~ma/ECS177/papers/particle_tracing.pdf (cit. on p. 93).

[Kas86] T. Kasuga, *Ion Clearing System of UVSOR Storage Ring*, Japanese Journal of Applied Physics **25** (1986) 1711 (cit. on p. 184).

[KP09] R. Kersevan and J.-L. Pons, *Introduction to MOLFLOW+: New Graphical Processing Unit-Based Monte Carlo Code for Simulating Molecular Flows and for Calculating Angular Coefficients in the Compute Unified Device Architecture Environment*, Journal of Vacuum Science & Technology A: Vacuum, Surfaces, and Films **27** (2009) 1017 (cit. on p. 64).

[KA14] R. Kersevan and M. Ady, *MolFlow+ User Guide*, User Guide, 2014, URL: https://molflow.web.cern.ch/sites/molflow.web.cern.ch/files/molflow_user_guide.pdf (cit. on p. 237).

[Kha06] S. Khan, *Collective Phenomena in Synchrotron Radiation Sources*, Springer Berlin Heidelberg New York, 2006, ISBN: 978-3-540-34313-4 (cit. on pp. 165, 166, 169).

[Khe76] S. Kheifets, *Potential of a Three-Dimensional Gaussian Bunch*, Internal Publication Petra Note 119, 1976 (cit. on p. 34).

[Kos04] A. Koschik, *Simulation of Transverse Multi-Bunch Instabilities of Proton Beams in LHC*, PhD thesis: Technischen Universität Graz, 2004 (cit. on pp. 166, 167).

[LP80] F. Lapique and F. Piuz, *Simulation of the Measurement by Primary Cluster Counting of the Energy Lost by a Relativistic Ionizing Particle in Argon*, Nucl. Instrum. Meth. **175** (1980) 297 (cit. on p. 10).

[Lee04] S. Y. Lee, *Accelerator Physics (Second Edition)*, John Wiley & Sons, 2004, ISBN: 978-981-256-182-4 (cit. on pp. 70, 244).

[Mal13] D. W. Maluski, *Magnetfeldvermessung eines Korrektormagneten für ELSA*, Bachelor Thesis: Physikalisches Institut, Universität Bonn, 2013 (cit. on p. 103).

[Mar13] A. Markovik, *Simulation of the Interaction of Positively Charged Beams and Electron Clouds*, PhD thesis: Fakultät für Informatik und Elektrotechnik, Universität Rostock, 2013 (cit. on pp. 75, 93, 106, 170).

[MPR11] A. Markovik, G. Pöplau and U. van Rienen, *Simulation of the Single Bunch Instability due to the Electron Cloud Effect by Tracking with a Pre-Computed 2D Wake Matrix*, *Proc. of International Particle Accelerator Conference (IPAC'11), San Sebastian, Spain, September 4-9, 2011*, (San Sebastian, Spain), International Particle Accelerator Conference 2, JACoW, 2011 2247, ISBN: 978-92-9083-366-6, URL: https://accelconf.web.cern.ch/accelconf/IPAC2011/papers/wepc100.pdf (cit. on p. 75).

[MPR12] A. Markovik, G. Pöplau and U. van Rienen, *Computation of the 2D Transverse Wake Function of an Electron Cloud for Different Parameters*, *Proc. of International Particle Accelerator Conference (IPAC'12), New Orleans, USA, May 20-25, 2012*, (New Orleans, USA), International Particle Accelerator Conference 3, JACoW, 2012 280, ISBN: 978-3-95450-115-1, URL: https://accelconf.web.cern.ch/AccelConf/IPAC2012/papers/moppc063.pdf (cit. on p. 75).

[MR12] A. Markovik and U. van Rienen, *Tracking of a PETRA III Positron Bunch with a Pre-Computed Wake Matrix due to Electron Clouds*, *Proc. of 11th Intl. Computational Accelerator Physics Conf. (ICAP2012), Warnemünde, Germany, August 19-24, 2012*, (Warnemünde, Germany), International Computational Accelerator Conference 11, JACoW, 2012 31, ISBN: 978-3-95450-116-8, URL: https://accelconf.web.cern.ch/accelconf/ICAP2012/papers/moacc3.pdf (cit. on p. 75).

[Mar+14] A. Markovik et al., *Dynamics of Ion Distributions in Beam Guiding Magnets*, *Proc. of International Particle Accelerator Conference (IPAC'14), Dresden, Germany, June 15-20, 2014*, (Dresden, Germany), International Particle Accelerator Conference 5, JACoW, 2014 1668, ISBN: 978-3-95450-132-8, URL: https://accelconf.web.cern.ch/AccelConf/IPAC2014/papers/mopme019.pdf (cit. on pp. 75, 170, 180).

[Mat94] A. G. Mathewson, *Vacuum System Design*, *CAS - CERN Accelerator School : 5th General Accelerator Physics Course*, ed. by S. Turner, vol. 2, Report Number: CERN 94-01, CERN, 0094 717, ISBN: 92-9083-058-1 (cit. on pp. 44, 53).

[MD86] P. E. Miller and M. B. Denton, *The Quadrupole Mass Filter: Basic Operating Concepts*, Journal of chemical education **63** (1986) 617 (cit. on p. 229).

[Min05] S. Minaev, *A Principle of Charged Particle Trapping by RF Electromagnetic Field in the Spherical Cavity*, Nuclear Instruments and Methods in Physics Research Section A: Accelerators, Spectrometers, Detectors and Associated Equipment **553** (2005) 407 (cit. on p. 140).

[Miy87] Y. Miyahara, *Photoionization of Residual Gases in Electron Storage Rings*, Japanese Journal of Applied Physics **26** (1987) 1544 (cit. on pp. 75, 123, 221).

[MTH88] Y. Miyahara, K. Takayama and G. Horikoshi, *Dynamical Analysis on the Longitudinal Motion of Trapped Ions in an Electron Storage Ring*, Nuclear Instruments and Methods in Physics Research Section A: Accelerators,

Spectrometers, Detectors and Associated Equipment **270** (1988) 217 (cit. on pp. 100, 110, 130, 137).

[Møl99] S. P. Møller, *Beam-Residual Gas Interactions*, tech. rep., ISA, Aarhus University, Denmark, 1999 (cit. on p. 234).

[Nat18] National Institute of Standards and Technology, *NIST Computational Chemistry Comparison and Benchmark Database, NIST Standard Reference Database Number 101*, Release: 19th of April 2018, Editor: Russell D. Johnson III, 2018, URL: https://cccbdb.nist.gov/ (cit. on p. 73).

[Ng06] K. Y. Ng, *Physics of Intensity Dependent Beam Instabilities*, World Scientific Publishing Co. Pte. Ltd., 2006, ISBN: 981-256-342-3 (cit. on pp. 147, 148, 166, 169, 176, 179).

[OHa03] J. F. O'Hanlon, *A User's Guide to Vacuum Technology*, 3rd Edition, John Wiley & Sons, 2003, ISBN: 978-0-471-27052-2 (cit. on pp. 41–45, 50, 57, 58, 223, 225–227, 229, 308).

[Ohm00] K. Ohmi, *Simulation of Beam-Beam Effects in a Circular e^+ e^- Collider*, Physical Review E **62** (2000) 7287 (cit. on pp. 101, 148).

[Pau90] W. Paul, *Electromagnetic Traps for Charged and Neutral Particles*, Rev. Mod. Phys. **62** (3 1990) 531, URL: https://link.aps.org/doi/10.1103/RevModPhys.62.531 (cit. on p. 137).

[PS53] W. Paul and H. Steinwedel, *Ein neues Massenspektrometer ohne Magnetfeld*, Zeitschrift für Naturforschung A **8** (1953) 448 (cit. on p. 137).

[Pfea] Pfeiffer Vacuum, *MVP 015-4, Diaphragm Pump, 230 V, 50 Hz - Technical Data*, Pfeiffer Vacuum GmbH, URL: https://www.pfeiffer-vacuum.com/en/products/diaphragm-pumps/mvp-015/?detailPdoId=2644 (cit. on p. 226).

[Pfeb] Pfeiffer Vacuum, *PKR 261, Metal Sealed, DN 25 ISO-KF*, Pfeiffer Vacuum GmbH, URL: https://static.pfeiffer-vacuum.com/productPdfs/PTR26250.en.pdf (cit. on p. 228).

[Pfec] Pfeiffer Vacuum, *Smart Test HLT 550 HLT 560 HLT 570 - Operating Instructions*, Pfeiffer Vacuum GmbH (cit. on p. 46).

[Piw98] A. Piwinski, *The Touschek Effect in Strong Focusing Storage Rings*, Internal Publication DESY 98-179, 1998 (cit. on p. 58).

[Pon94] A. Poncet, *Ion Trapping and Clearing*, Frontiers of Particle Beams: Factories with e+ e- Rings (1994) 202 (cit. on pp. 10, 66, 248, 259, 261, 269).

[Pöp+12] G. Pöplau et al., *Simulations for Ion Clearing in an ERL, Proc. of 11th Intl. Computational Accelerator Physics Conf. (ICAP2012), Warnemünde, Germany, August 19-24, 2012*, (Warnemünde, Germany), International Computational Accelerator Conference 11, JACoW, 2012 143, ISBN: 978-3-95450-116-8, URL: https://epaper.kek.jp/ICAP2012/papers/wep01.pdf (cit. on p. 75).

[PFH14] D. Proft, F. Frommberger and W. Hillert,
Setup of a History Storage Engine Based on a Non-Relational Database at ELSA,
Proc. of Personal Computer and Particle Accelerator Controls Workshop (PCaPAC'14), Karlsruhe, Germany, October 14-17, 2014, (Karlsruhe, Germany),
International Workshop on Personal Computer and Particle Accelerator Controls 10,
JACoW, 2014 34, ISBN: 978-3-95450-146-5, URL:
https://accelconf.web.cern.ch/AccelConf/PCaPAC2014/papers/wpo003.pdf
(cit. on p. 55).

[Pro18] D. Proft, *Optimierung des Beschleunigerbetriebs für Experimente zur Hadron- und Detektorphysik an der Elektronen Stretcher Anlage ELSA*,
PhD thesis: Physikalisches Institut, Universität Bonn, 2018
(cit. on pp. 103, 146, 158, 175, 214).

[RZ95] T. Raubenheimer and F. Zimmermann,
Fast Beam-Ion Instability. I. Linear Theory and Simulations,
Physical Review E **52** (1995) 5487 (cit. on p. 165).

[RP72] F. F. Rieke and W. Prepejchal, *Ionization Cross Sections of Gaseous Atoms and Molecules for High-Energy Electrons and Positrons*, Physical Review A **6** (1972) 1507
(cit. on pp. 66, 67).

[RD] M. S. del Rio and R. J. Dejus, *XOP 2.4*, Collaboration of ESRF and APS,
URL: https://www.esrf.eu/Instrumentation/software/data-analysis/xop2.4
(cit. on p. 70).

[RD11] M. S. del Rio and R. J. Dejus,
XOP v2.4: Recent Developments of the X-Ray Optics Software Toolkit, vol. 8141, 2011 8141 15, URL: https://doi.org/10.1117/12.893911 (cit. on p. 70).

[Rot13] A. Roth, *Breitbandige Feedback-Systeme zur Dämpfung Kohärenter Strahlinstabilitäten am Stretcherring ELSA*, urn:nbn:de:hbz:5n-30908,
PhD thesis: Physikalisches Institut, Universität Bonn, 2013 (cit. on p. 5).

[San70] M. Sands, *The Physics of Electron Storage Rings, An Introduction*, SLAC Report 121,
National Technical Information Service, Springfield, Virginia, 1970 (cit. on pp. 22, 26, 27).

[SH16] D. Sauerland and W. Hillert, *Numerical and Experimental Substantiation of the Ion Density Beam Transfer Function Measurements*, *Proc. of International Particle Accelerator Conference (IPAC'16), Busan, South Korea, May 8-13, 2016*, (Busan, South Korea),
International Particle Accelerator Conference 7, JACoW, 2016 698,
ISBN: 978-3-95450-147-2, URL:
https://accelconf.web.cern.ch/AccelConf/ipac2016/papers/mopor047.pdf
(cit. on p. 213).

[SMH15] D. Sauerland, A. Meseck and W. Hillert,
Estimation of the Ion Density in Accelerators using the Beam Transfer Function Technique, *Proc. of International Particle Accelerator Conference (IPAC'15), Richmond, USA, May 3-8, 2015*, (Richmond, Virginia, USA), International Particle Accelerator Conference 6,
JACoW, 2015 147, ISBN: 978-3-95450-168-7, URL:
https://accelconf.web.cern.ch/AccelConf/IPAC2015/papers/mopwa024.pdf
(cit. on p. 213).

[Sch11] M. Schedler,
Dämpfung Transversaler Multibunchinstabilitäten am Elektronenbeschleuniger ELSA,
Master Thesis: Physikalisches Institut, Universität Bonn, 2011 (cit. on p. 213).

[Sch15] M. Schedler, *Intensitäts- und Energieerhöhung an ELSA*, urn:nbn:de:hbz:5n-42070,
PhD thesis: Physikalisches Institut, Universität Bonn, 2015
(cit. on pp. 5, 21, 83, 84, 131–133, 147, 172, 192, 213, 215, 233).

[Sch17] J. F. Schmidt, *Spindynamik in Elektronensynchrotronen*, urn:nbn:de:hbz:5n-48314,
PhD thesis: Physikalisches Institut, Universität Bonn, 2017 (cit. on p. 133).

[Sch+15] J. F. Schmidt et al.,
Measurement of Momentum Compaction Factor via Depolarizing Resonances at ELSA,
Proc. of International Particle Accelerator Conference (IPAC'15), Richmond, USA, May 3-8, 2015, (Richmond, Virginia, USA), International Particle Accelerator Conference 6,
JACoW, 2015 811, ISBN: 978-3-95450-168-7, URL:
https://accelconf.web.cern.ch/AccelConf/IPAC2015/papers/mopha015.pdf
(cit. on p. 22).

[Sch99] L. Schultz, *Sputter Ion-Pumps*, tech. rep., Paul Scherrer Institut, Villigen, Switzerland, 1999
(cit. on pp. 59, 235).

[Ste95] C. Steier, *Theoretische und Experimentelle Untersuchungen zu Vielteilcheneffekten bei der Elektronen-Stretcher-Anlage ELSA*,
Diploma Thesis: Physikalisches Institut, Universität Bonn, 1995 (cit. on pp. 55, 193, 203).

[Swi19] M. Switka, *Photon Based Electron Beam Analysis at ELSA Utilizing Compton Scattering and Synchrotron Radiation*, PhD thesis in preparation,
PhD thesis: Physikalisches Institut, Universität Bonn, 2019
(cit. on pp. 22, 23, 172, 174, 214).

[Tav92a] P. F. Tavares, *Betatron Coupling in Ion Loaded Electron Beams*,
Internal Publication CERN PS/92-54 (LP), 1992 (cit. on p. 264).

[Tav92b] P. F. Tavares, *Transverse Distribution of Ions Trapped in an Electron Beam*,
Internal Publication CERN PS/92-55 (LP), 1992 (cit. on pp. 153–155, 221).

[Tsa+06] H. J. Tsai et al.,
Correction of the Vertical Dispersion and Betatron Coupling for the TPS Storage Ring,
Proc. of European Particle Accelerator Conferenc (EPAC'06), Edinburgh, Scotland, June 26-30, 2006, (Edinburgh, Scotland), European Particle Accelerator Conferenc 10,
JACoW, 2006 2032, ISBN: 92-9083-278-9,
URL: https://accelconf.web.cern.ch/AccelConf/e06/PAPERS/WEPCH050.PDF
(cit. on p. 27).

[Wan+11] L. Wang et al.,
Suppression of Beam-Ion Instability in Electron Rings with Multibunch Train Beam Fillings,
Physical Review Special Topics-Accelerators and Beams **14** (2011) 08440 (cit. on p. 167).

[Wan+13] L. Wang et al., *Beam Ion Instability: Measurement, Analysis, and Simulation*,
Physical Review Special Topics-Accelerators and Beams **16** (2013) 104402 (cit. on p. 167).

[Wan07] R. Wanzenberg, *Resistive Wall Wakes and Clearing Electrodes*, *Proc. of Electron Cloud Effects and Technological Consequences Workshop (ECL2), CERN, Geneva, Switzerland, March 1-2, 2007*, (CERN, Geneva, Switzerland), ed. by F. Caspers et al., Workshop on Electron Cloud Effects and Technological Consequences 2, 2007 71, URL: https://cds.cern.ch/record/1057138/files/ab-2007-064.pdf (cit. on p. 184).

[Wen94] J. Wenzel, *Entwicklung und Test eines Simulators der Teilchenbewegung in der Bonner 3.5 GeV-Elektronen-Stretcher-Anlage ELSA*, PhD thesis: Physikalisches Institut, Universität Bonn, 1994 (cit. on p. 28).

[WPZ93] S. J. Werkema, D. W. Peterson and P. Zhou, *Transverse Emittance Growth in the Fermilab Antiproton Accumulator with High-Current Antiproton Stacks*, *Particle Accelerator Conference, 1993., Proceedings of the 1993*, IEEE, 1993 3573 (cit. on p. 174).

[Wie93] H. Wiedemann, *Particle Accelerator Physics, Basic Principles and Linear Beam Dynamics*, Springer-Verlag Berlin Heidelberg, 1993, ISBN: 3-540-56550-7 (cit. on pp. 31, 247).

[Wie95] H. Wiedemann, *Particle Accelerator Physics II, Nonlinear and Higher-Order Beam Dynamics*, Springer-Verlag Berlin Heidelberg New York, 1995, ISBN: 3-540-57564-2 (cit. on pp. 27, 147).

[Wil00] K. Wille, *The Physics of Particle Accelerators, An Introduction*, Oxford University Press, 2000, ISBN: 0-19-850549-3 (cit. on pp. 18–21, 23, 25, 30, 31, 57, 58, 100, 130, 131, 137, 145, 203, 245, 246, 266, 281, 282).

[Wil94] E. Wilson, *Non-Linearities and Resonances*, *CAS - CERN Accelerator School : 5th General Accelerator Physics Course*, ed. by S. Turner, vol. 1, Report Number: CERN 94-01, CERN, 0094 239, ISBN: 92-9083-057-3 (cit. on p. 148).

[Yu+13] T. Yu et al., *Petra Cavity Vacuum RF Condition with Field Balance Mechanism for TPS Storage Ring in NSRRC*, *Proc. of International Particle Accelerator Conference (IPAC'13), Shanghai, China, May 12-17, 2013*, (Shanghai, China), International Particle Accelerator Conference 4, JACoW, 2013 2833, ISBN: 978-3-95450-122-9, URL: https://inspirehep.net/record/1339008/files/wepfi061.pdf (cit. on p. 133).

[Zan13] S. Zander, *Optische Strahldiagnose an der Elektronen-Stretcher-Anlage ELSA*, PhD thesis: Physikalisches Institut, Universität Bonn, 2013 (cit. on pp. 5, 27, 28, 30, 92, 264, 272, 273).

[Zhe+14] D. Zheng et al., *Study of a Fast Convolution Method for Solving the Space Charge Fields of Charged Particle Bunches*, *Proc. of International Particle Accelerator Conference (IPAC'14), Dresden, Germany, June 15-20, 2014*, (Dresden, Germany), International Particle Accelerator Conference 5, JACoW, 2014 418, ISBN: 978-3-95450-132-8, URL: https://accelconf.web.cern.ch/AccelConf/IPAC2014/papers/mopme019.pdf (cit. on p. 75).

[Zim86] M. Zimmer, *Messung der Multipolverteilung der ELSA Quadrupol- und Sextupolmagnete*, Diploma Thesis: Physikalisches Institut, Universität Bonn, BONN-IR-86-05, 1986 (cit. on p. 103).

[Zim10] R. Zimmermann, *Ein Kicker-Cavity für ein Longitudinales Feedbacksystem an ELSA*, Diploma Thesis: Physikalisches Institut, Universität Bonn, 2010 (cit. on p. 213).

List of Figures

List of Tables

List of Symbols

$\boldsymbol{A}$, A_i	Mass number of a residual gas species (or ion species i)
$A(E_\gamma)$	Energy dependent part of $r_{\mathrm{p,pi},i}$ in section 3.4
$A(x, s)$	Integration variable in equation (2.42)
A/Z	Mass-to-charge ratio of a particular ion species
A_{beam}	The boundary area of the beam towards the residual vacuum system
$A_{\mathrm{crit},x}$, $A_{\mathrm{crit},z}$	Horizontal and vertical critical mass-to-charge ratio below which an ion accumulation is not possible
A_x	The area of the horizontal phase space ellipse
a	Half diameter of a cylindrical beam
$a_{\mathrm{fill},j}$	Fraction of the current of bunch j to the average bunch current
$\mathcal{A}$	Symbol for a neutral residual gas molecule; In section 3.1.3, the assessment function
$\mathcal{A}_*$	Symbol for a neutral residual gas molecule with increased kinetic energy
$\mathcal{A}^+$	Symbol for an ion
$\mathcal{A}_*^+$	Symbol for an ion with increased kinetic energy
$\mathfrak{A}_x(x, s)$, $\mathfrak{A}_s(x, s)$	Horizontal and longitudinal acceleration functions of TracTIon
$\vec{\boldsymbol{B}}$	Vector of the magnetic field
$B(s)$	Spatial dependent part of $r_{\mathrm{p,pi},i}$ in section 3.4
$B(z, s)$	Integration variable in equation (2.42)
$\vec{B}'_{\mathrm{qp}}$	Magnetic fringe field of a quadrupole
$B_x(s)$, $B_z(s)$	Horizontal and vertical component of a magnetic field
$B_{z,\mathrm{dp}}$	Vertical magnetic field strength within dipole magnets
$B_{x,z,\mathrm{cav}}$	Circular magnetic rf field within cavities
$B_{z,0}$	Vertical magnetic field within the iron yokes of a magnet
$B_\varphi(r)$	Circular magnetic field of the electron beam
b	The impact parameter for an impact process
$\mathcal{B}$	Bunching factor
$\boldsymbol{C}$	Circumference of the accelerator
C_i	Parameter for the determination of the impact ionization cross section of species i
C_{q}	Quantum excitation constant
$\tilde{C}$	Decay constant of the residual gas density in appendix A.9
c	Speed of light
C	Conductance of the vacuum system
$C^\dagger$	Specific conductance

$\boldsymbol{D}$	An integration constant
$D_x(s)$, $D_z(s)$	Horizontal and vertical dispersion within the accelerator
d	Horizontal beam pipe diameter
$\tilde{D}_x$	"Spring constant" of the reversing force of the electron beam
$\mathcal{D}$	Parameter of the magnet lattice of the accelerator
$\boldsymbol{E}$	Energy of the electron beam
$\vec{E}(x, z)$	Electrical field strength vector
E_b	Ionization energy of a certain residual gas molecule
E_I	Ionization parameter, equal to $Z' \cdot 3.5\,\mathrm{eV}$
E_kin	Kinetic energy of the beam electron
$E_r(r)$	Radial electric field of the electron beam
$E_s(s)$	Longitudinal electric field resulting from the longitudinal gradient of the beam potential
$E_{s,\mathrm{cav}}(s, t)$	Longitudinal field strength within rf cavities
E_therm	A kinetic energy which corresponds to the thermal energy
$E_x(x, z)$, $E_z(x, z)$	Horizontal and vertical component of the transversal electrical field strength
$E_{z,\mathrm{beam}}$	Vertical electrical field strength from the clearing electrode at the beam center
E_0	Initial energy of a generated ion in TracTIon
E_γ	Energy of a synchrotron radiation photon
$E_\perp$	Transversal electric field strength of a continuous clearing electrode
e	Elementary charge
$\vec{e}_s$	Unit vector in longitudinal direction
e^-	Symbol for an electron
$\tilde{E}_0$	Average energy for the formation of an ion-electron pair ($\approx 35\,\mathrm{eV}$)
$\mathcal{E}_\gamma(E_\gamma)$	Energy dependent part of $\mathcal{G}_\gamma(E_\gamma, s - w)$
$\boldsymbol{F}_\mathrm{e}(r)$	Radial force acting on the electrons within the beam
F_x	Horizontal excitation force acting on the beam due to wake fields
$\vec{F}_\mathrm{el}(\vec{r})$	Force resulting from mutal Coulomb repulsion of electron within the beam
$\vec{F}_\mathrm{e-e}(\vec{r})$	The balance of force acting on an electron within the beam without ions
$\vec{F}_\mathrm{e-ion}(\vec{r})$	The balance of force acting on an electron due to the ions' space charge
$F_\mathrm{ion}(r, \hat{\eta})$	Radial force due to ions which acts on ions within the beam
$\vec{F}_\mathrm{mag}(\vec{r})$	Force due to the magnetic attraction of two parallel currents within the beam
$\left\langle F_\mathrm{rf} \right\rangle_{t_1}^{t_2}$	Average force within an rf field between time t_1 and t_2
$\vec{F}_\mathrm{wake}(r_1, r_2, \tau, t)$	Lorentz force, acting on the beam, due to wake fields
$f_{x,z}$	Focal length of the electron beam to accumulated ions
$\mathcal{F}$	Normalized untrapped ion flow towards the clearing electrode
$\mathscr{F}$	Transversal transmission function for ion current measurements
$\mathscr{F}_\mathrm{theo}$	Theoretical transversal transmission function of a certain ion current measurement
$\boldsymbol{G}_\mu$	Coherent transversal amplitude of the electron beam oscillating with multi bunch mode μ
$G_i(t)$	Time dependent transversal position of the electron beam in reference to a beam with zero oscillation amplitude
g_QD, g_QF	Magnetic transversal gradient in QD and QF quadrupole magnets
$\mathcal{G}_\gamma(E_\gamma, s - w)$	Synchrotron radiation flux per photon energy expressed as a longitudinal line density

$\boldsymbol{H}$	An integration constant
h	Harmonic number, equal to the number of bunches within the accelerator
h'	Number of equally filled bunches in the accelerator
$\mathcal{H}$	Normalized flow of trapped ions towards the clearing electrode
$\mathcal{H}(s)$	A parameter derived from the lattice of the accelerator
$\hbar$	PLANCK's constant
$\boldsymbol{I}$	Beam current in the accelerator
$I(E_\gamma)$	Energy flux of synchrotron radiation, integrated over all emission angles for a photon energy E_γ
$I(\nu)$	Beam spectrum
I_b	Bunch current
I_CE	Measured current of the clearing electrode system
$I_\mathrm{CE,leak}$	Leakage current of the clearing electrode system
$I_\mathrm{CE,sim}$	Ion current of the clearing electrode system, simulated by TRACTION
I_qma	Ion current measured by the quadrupole mass spectrometer
I_0	Hypothetical beam current if all bunches would show identical I_b
$\mathrm{Im}(y)$	Imaginary part of a complex value y
i	Imaginary unit
$\mathcal{I}_\mathrm{CE}$	Ion transmission coefficient
$\boldsymbol{J}'_\nu(y)$	Derivative of the BESSEL function (1st kind)
$\mathcal{J}_2$, $\mathcal{J}_5$	Second and fifth synchrotron integral
$\boldsymbol{K}(x, z, s)$	Curvilinear coordinate system within an accelerator
$K_\nu(y)$	Modified BESSEL function of the second kind
$k(s)$	Quadrupole strength of the quadrupole magnets
k_B	BOLTZMANN constant
k_QD, k_QF	Quadrupole strength of the QD and QF quadrupole magnets
$k_{r,1\ldots4,x}$	Change in the ion's velocity at the positions of the four interim steps of a RUNGE-KUTTA method
$k_{v,1\ldots4,x}$	Accelerations at the positions of the four interim steps of a RUNGE-KUTTA method
$k_{\mathrm{ion},x,z}(\hat{\eta})$	Negative horizontal or vertical focusing strength for ions within the beam due to the ions' mutual space charge repulsion
k_x, k_z	Focusing strength of the electron beam to accumulated ions
$k_{0,x}$, $k_{0,z}$	Focusing strength of the electron beam without the space charge effect of accumulated ions
$\tilde{K}$	Constant characterizing the ion production probability in ion current measurements
$\mathcal{K}_{n+1}$	Correction factor for the ion's momentum in TRACTION
$\boldsymbol{L}$	Path length of the electron beam in chapter 2 and distance between two electrodes in chapter 6
L_CE	Effective longitudinal dimension of the clearing electrode
l	Distance of a continuous clearing electrode from the beam center
l_bunch	Bunch length
l_dipole	Effective length of a dipole magnet
l_drift	The length within λ_rf where no beam attraction is present
l'_drift	The drift length within one empty rf period, equal to λ_rf

l_{eff}	Effective longitudinal length of a dipole or quadrupole magnet
l_{free}	Fraction of $\mathcal{F}$, which experience ion space charge related losses
l_{geom}	Geometric longitudinal dimension of the iron yokes of a dipole or quadrupole magnet
l_{hollow}	Fraction of $\mathcal{H}$, which experience ion space charge related losses
l_{int}, $l_{\text{int}}(s)$	Interaction length
l_0	Initial distance between a synchrotron radiation source and an ion production map
$\mathscr{L}$	Longitudinal transmission function for ion current measurements
$\boldsymbol{M}_i$	Total dipole matrix element of impact ionization
M_{ramp}	Parameter for the adjustment of the photo ionization subroutine in TRACTION
m_{e}	Mass of an electron
m_i	Mass of an ion species i
m_j	Mass of a residual gas molecule j
m_{p}	Mass of a proton
m_{SD}, m_{SF}	Sextupole strength of the SD and SF sextupole magnets
$m_{x,\text{coh}}$, $m_{z,\text{coh}}$	Simulated slope of the horizontal and vertical coherent tune shift with beam current and neutralization
$\mathcal{M}_{\text{bunch}}$, $\mathcal{M}_{\text{bunch},x,z}$	A matrix describing the beam-ion attraction of a passing bunch
$\mathcal{M}_{\text{bt},x,z}$	Transfer matrix for the passage of one complete bunch train in front of an ion
$\mathcal{M}_{\text{drift}}$	The transfer matrix of a drift
$\mathcal{M}_{\text{passage},x,z}$	A transfer matrix describing a passage of one rf period in front of an ion
$\boldsymbol{N}$	Total number of residual gas molecules in the vacuum system
N_{CE}	Number of clearing electrodes in the accelerator
N_{e}	Total number of electrons within the beam
N_{in}	Number of residual gas within the beam
$N_{\text{in}}^{\text{i}\to\text{o}}$	Number of residual gas drifting out of the beam
$N_{\text{in}}^{\text{ion}}$	Number of residual gas within the beam volume which get ionized
N_{ion}	A total number of ions
$N_{\text{ion},i}$	A total number of an ion species i
$N_{\text{out}}^{\text{o}\to\text{i}}$	Number of residual gas outside of the beam drifting into it
N_{prod}	Number of desorbed residual gas into the vacuum system
N_{pump}	Number of removed residual gas from the vacuum system by pumps
N_{rgm}	A total number of residual gas molecules
$N_{\text{rgm},i}$	Number of residual gas species i
$N_{\text{stat},i}$	Number of stable ions of species i when applying a certain filling pattern
$N_1(x, z)$	Number of electrons within a bunch slice at position x and z
$N_2(x', z')$	Number of electrons within a bunch slice at position x' and z'
$N_{2,\text{ion}}(x', z')$	Number of ions within a bunch slice at position x' and z'
$\dot{N}$	Number rate of produced ions
$\dot{N}_{\text{ion,free}}$	Removal rate of untrapped/free ions
$\dot{N}_{\text{ion,hollow}}$	Removal rate of ions which intialy were trapped within a potential hollow
n	Number of revolutions within a circular accelerator
n_i	Principle quantum number
n_{in}	Number density within the beam volume
n_{rgm}	Number density of the residual gas within the vacuum system
$n_{\text{rgm},i}$	Partial number density of the residual gas species i within the vacuum system

$\dot{n}_\gamma(E_\gamma)$	Synchrotron radiation flux spectrum per bandwidth
$\hat{N}_\mathrm{e}$	The average local number of beam electrons.
$\mathcal{O}^{(\prime)}_{\mathrm{drift},x,z}(\hat{\eta})$	Horizontal or vertical defocusing transfer matrix in between two bunches for non-zero $\hat{\eta}$
$\boldsymbol{P}_\mathrm{rf}$	Rf power provided to the rf cavities
p_i	Partial pressure of residual gas species i
$p_\mathrm{meas}(A/Z)$	Measured peak of the ion current of the mass spectrometer at a certain mass-to-charge ratio A/Z
$p_\mathrm{sim}(A/Z)$	Peak ion current, simulated by `MSAUGA`
p_0, p	Momentum of the (design) particle within the accelerator
$\mathcal{P}(E,I)$, $\mathcal{P}_\mathrm{avg}(E,I)$	Average total pressure within the accelerator's vacuum system (for a certain beam energy and current)
$\mathcal{P}(s)$	Local total pressure along the beam pipe's center in the accelerator
$\mathcal{P}(s_\mathrm{bp})$	Local total pressure along the center of the beam pipe in the `MolFlow+` simulation
$\mathcal{P}_\mathrm{IGP}$	Total pressure in the vicinity of the IGPs
$\mathcal{P}_\mathrm{IGP,model}(E,I)$	Total IGP pressure of the pressure model
$\mathcal{P}_0$	No-load pressure of the vacuum system
$\hat{\mathcal{P}}(s)$	Local total pressure at a position s in the vacuum system
$\boldsymbol{Q}$	The throughput within a vacuum system
$Q^\mathrm{frac}_{x,z}$	Fractional share of horizontal or vertical tune
Q_nl	Effective quality factor due to the non-linearity of the beam potential
Q_x, Q_z, Q_s	Horizontal, vertical and longitudinal tune of the accelerator
$Q_{x,\mathrm{res}}$, $Q_{z,\mathrm{res}}$	Tune of an horizontal and vertical optical resonance
Q_0, $Q_{x,0}$, $Q_{z,0}$	Initial horizontal and vertical tune without tune shifts
$\tilde{Q}$	Factor with which the pressure within the beam is reduced due to ionization in appendix A.9
q	In chapter 2, the total charge within the electron beam; In section 3.2, the desorption rate
q_ESD	Outgassing rate of electron stimulated desorption
q_PSD	Outgassing rate of photo stimulated desorption
q_thermal	Thermal outgassing rate
q_x, q_z	Horizontal and vertical bounce tune of the ions
q_1, q_2	Electric charge of the pilot and witness particle when considering wake fields
$\tilde{q}$	Gas desorption rate per unit surface area
$\boldsymbol{R}$	Deflection radius of the dipole magnets of the accelerator
R_c	The total ion clearing rate within an accelerator
R_p	The total ion production rate within an accelerator
$R_{\mathrm{ppi},i}$	The ion production rate due to photo ionization within an accelerator
$R_{\mathrm{p}i}$	The ion production rate of ion species i within an accelerator
$R_\mathrm{p,real}$	Realistic ion production rate due to impact ionization, discussed in appendix A.9
R_S	The shunt impedance of an rf cavity
R_0	An arbitrary rate
$R^\dagger_\mathrm{c}(s)$	A specific ion clearing rate

$R_{\mathrm{p}}^{\dagger}(s)$	A specific ion production rate
$\vec{r}$	Distance vector between position (x, z) and (x', z')
$r_{\mathrm{c,ce},i}$	Clearing rate of ion species i due to application of clearing electrodes
$r_{\mathrm{c,dp},i}$	Estimated clearing rate of ion species i within dipole magnets
$r_{\mathrm{c,free},i}$	Estimated clearing rate of ion species i within field-free regions
$r_{\mathrm{c,fringe},i}$	Estimated clearing rate of ion species i within the dipoles' fringe field regions
$r_{\mathrm{c,fp},i}$	Clearing rate of ion species i due to application of a certain filling pattern
$r_{\mathrm{c,heat},i}$	Clearing rate due to beam heating of an ion species i
$r_{\mathrm{c},i}$	Clearing rate of an ion species i
$r_{\mathrm{p},i}$	Production rate of an ion species i
$r_{\mathrm{p,pi},i}^{\dagger}(s)$	Specific photo ionization production rate of ion species i
r_{vc}	Position corresponding to the surface of the beam pipe in a radial vacuum chamber
r	A radius
$r(s)$	Start point of the integration in equation (2.42)
$r_{\mathrm{cycl},i}$	Gyro radius of an ion species i within a magnetic field
r_0	An arbitrary rate
$\hat{R}_{\mathrm{c}}(s)$	A local total clearing rate
$\hat{R}_{\mathrm{p}}(s)$	A local total production rate
$\hat{R}_{\mathrm{p,ii}}(s)$	A local ionization production rate
$\hat{R}_{\mathrm{p,pi}}(s)$	A local photo ionization production rate
$\breve{R}_{\mathrm{p,ii}}(x, z, s)$	Impact ionization production map
$\breve{R}_{\mathrm{p,pi}}(x, z, s)$	Photo ionization production map
$\mathrm{Re}(y)$	Real part of a complex quantity y
$\boldsymbol{S}$, S_{eff}	The (effective) pumping speed of a vacuum pump
s	Longitudinal coordinate or distance in reference to an absolute longitudinal position
s_{a}, s_{b}, s_{c}	Markers for the determination of the transmission probability through fringe fields
s_{CE}, $s_{\mathrm{electrode}}$	The position of a clearing electrode in reference to the lattice zero point
s_{prod}	Initial longitudinal position of a produced ion
s_{yoke}	Longitudinal position where a magnet's iron yoke begins or ends
$\mathcal{S}_{\gamma}(s - w)$	Spatial dependent part of $\mathcal{G}_{\gamma}(E_{\gamma}, s - w)$
$\boldsymbol{T}$	Environmental Temperature
T_{c}	Clearing time of an ion
$T_{\mathrm{c,lCE},i}$	Clearing time due to local clearing electrodes for ion species i
$\hat{T}_{\mathrm{c,lCE},i}(s)$	Local clearing time due to local clearing electrodes for ion species i
$\hat{T}_{\mathrm{c,cCE},i}$	Local clearing time due to a continuous clearing electrode for ion species i
T_i	Transmission probability of ion species i in a FillingGapSim computation
T_{n}	Neutralization time of the electron beam
T_0	Revolution time of the electron beam within the accelerator
t	A time
t_{bunch}	The bunch length in time domain
t_{d}	Propagation time within which the fastest ions reach a the edge of the simulated domain
t_{rf}	Time of one period of the rf fields
t_0	An initial time in reference to some process. Typically t_0 is set to zero.
$\tilde{T}_i$	Transmission probability of ion species i through the dipole's fringe field
$\mathrm{Tr}(Y)$	Trace of matrix Y

$\boldsymbol{U}$	A value of an electric potential or a voltage
$\langle U \rangle$, $\langle U(s) \rangle$	Time-average beam potential at position $x = z = 0\,\mathrm{mm}$ also often denoted as U
$U(x, z, s)$	Beam potential at position (x, z, s)
U_{acc}	Acceleration voltage within an rf cavity
$\left\langle U_{\mathrm{bG}}(x, z, s) \right\rangle$	Time-average beam potential of a beam with two-dimensional Gaussian charge distribution
U_{CE}	Voltage applied to the clearing electrode system
$U_{\mathrm{CE}}(z, s)$	Electric potential of a clearing electrode at a certain position
$U_{\mathrm{CE,limit}}^{\mathrm{old}}$, $U_{\mathrm{CE,limit}}^{\mathrm{new}}$	Maximal clearing voltage for the old and the new high voltage power supply
$U_{\mathrm{CE,thres}}$	Minimal clearing voltage to prevent local additional static neutralization
$U_{\mathrm{CE},0}$	Clearing electrode potential on the beam axis in front of the electrode
$U_{\mathrm{I}}(r)$, $U_{\mathrm{II}}(r)$	Radial beam potential in regions I and II
U_{max}, $U_{\mathrm{max}}(s_0)$	Potential barrier's maximal value (at position s_0)
U_{rev}	Circumference voltage
U_0, $U_0(s)$	Beam potential depth at the beam center without a deformation by the ions' space charge
$U(v)$	Deflective voltage induced by wake fields which acts on the beam
$\tilde{U}$	Specific beam potential depth for the process of beam heating
$\boldsymbol{V}$	A volume
V_{AC}, V_{DC}	AC and DC compositions of the quadrupole mass filter's voltage
V_{beam}	Volume of the beam within the vacuum system
V_{int}	Interaction volume through which ionizing particles flow
V_{vac}	Volume of the vacuum system
$\langle v \rangle$	Mean thermal velocity of the residual gas in appendix A.9
$\vec{v}_{\mathrm{d}}$	Cross-field drift velocity vector
v_{dp}	Idealized longitudinal cross-field drift velocity in dipole magnets
$v_{\mathrm{rms},j}$	Average thermal velocity of a residual gas molecule of species j
$v_{s,\mathrm{T}}$	Minimal longitudinal velocity of an ion to pass a dipole's fringe field
$v_{s,0}$	Initial longitudinal velocity
$v_{x,j}$, $v_{z,j}$, $v_{s,j}$	A particle's velocity j in transversal x or z or longitudinal direction s
$v_{\perp,i}$	Velocity component perpendicular to the magnetic field
$\boldsymbol{W}_{\mathrm{I}}$	Hydrogen ionization energy of 13.6 eV
w	Propagation path of an emitted synchrotron radiation photon until it interacts with the beam pipe after $l_{\mathrm{int}}(s)$
$\mathcal{W}_{\shortparallel}(\tau)$, $\mathcal{W}_{\perp}(\tau)$	Longitudinal and transversal wake function
$\mathcal{W}_{x,z,i}^{\mathrm{ion}}(s)$	Horizontal or vertical wake function due to an ion species i
$\mathcal{W}_{x,z}^{\mathrm{ion}}$	Total wake function due to accumulated ions
$\boldsymbol{X}$	Six-dimensional vector of a beam electron trajectory in $K(x, z, s)$
x	Horizontal position in reference to the beam center
x_{C}	Horizontal center of the beam in reference to $K(x, z, s)$
x_{CE}	Horizontal distance of a clearing electrode from the beam center
x_{cm}	Horizontal shift of the ion production barycenter from the beam center
x_i	Horizontal position of an ion i
x_{prod}	Initial horizontal position of a produced ion
x_{vc}	Horizontal position corresponding to the beam pipe's surface
$x_{0,i}$, $x(t_0)$	Initial horizontal amplitude of an ion of species i

$\boldsymbol{Z}$, Z_i	Ionization status of a residual gas molecule (of species i)
Z'	Atomic number
$Z^{\text{ion}}_{x,z}(\nu)$	Horizontal or vertical accelerator impedance due to accumulated ions
$Z_{\shortparallel}(\nu)$, $Z_{\perp}(\nu)$	Longitudinal and transversal coupling impedance
z	Vertical position in reference to the beam center
z_{b}	Vertical distance of the potential barrier maximum to the beam center
z_{C}	Vertical center of the beam in reference to $K(x, z, s)$
z_{CE}	Vertical distance of a clearing electrode from the beam center
z_i	Vertical position of an ion i
z_{prod}	Initial vertical position of a produced ion
z_{vc}	Vertical position corresponding to the beam pipe's surface
$\boldsymbol{\alpha}_{\text{break}}$	Maximal angle of beam deflection within dipole magnets up to which emitted photons propagate a specific path length
α_{c}	The momentum compaction factor
α_{dipole}	Deflection angle of the electron beam after passing through one dipole magnet
α_s	Longitudinal damping constant, equal to $1/\tau_s$
$\alpha_x(s)$	A twiss parameter, an optical function of the accelerator
$\boldsymbol{\beta}$	Fraction of the electron beam's velocity to the speed of light c
$\beta_x(s)$, $\beta_z(s)$	One twiss parameter, the horizontal and vertical beta functions of the accelerator at position s
$\boldsymbol{\Gamma}_x$	Measured growth rate of horizontal beam instabilities
Γ^{theo}_x, Γ^{theo}_z	Theoretical horizontal and vertical growth rate of the beam when adding all $\Gamma_{x,z,\mu}$
Γ_{sr}	Damping rate of the electron beam due to synchrotron radiation
$\Gamma_{x,\mu}$, $\Gamma_{z,\mu}$	Theoretical horizontal and vertical growth rate of a multi bunch mode μ
$\gamma_{\text{qma},i}$	Quantity proportional to the residual gas composition in `MSAUGA`
γ_{sr}	Symbol for a synchrotron radiation photon
$\gamma_x(s)$	A twiss parameter, an optical function of the accelerator
$\boldsymbol{\Delta}B_{z,\text{dp}}$	Vertical magnetic field error within dipole magnets
$\Delta E_{\text{nucleus}}$	Energy transfer to the residual gas molecule during ionization
ΔE_{e}	Energy transfer to the orbital electron of the residual gas molecule
ΔE_{rev}	Synchrotron radiation energy loss of the beam per revolution
$\Delta\mathcal{F}$	Losses of $\mathcal{F}$
$\Delta\mathcal{H}$	Losses of $\mathcal{H}$
ΔL	Deviation of the path length in reference to L
$\Delta\dot{N}_{\text{ion,free}}$	Rate loss of $\dot{N}_{\text{ion,free}}$
$\Delta\dot{N}_{\text{ion,hollow}}$	Rate loss of $\dot{N}_{\text{ion,hollow}}$
Δp	Momentum deviation of an individual electron or statistical deviation of the ensemble of beam electrons
$\Delta p_{\text{meas}}(A/Z)$	Error p_{meas} at a certain A/Z
$\Delta\mathcal{P}_{ij}$	Error of pressure value j at energy i
ΔQ	The complex tune shift ($\in \mathbb{C}$) due to wake fields
ΔQ_{coh}, $\Delta Q_{x,\text{coh}}$, $\Delta Q_{z,\text{coh}}$	Coherent horizontal and vertical tune shift
ΔQ_{incoh}	Incoherent tune shift

$\Delta Q_{x,z}^{\mathrm{sc}}$	Theoretical horizontal or vertical tune shift due to electron-electron and electron-ion space charge
Δs	Longitudinal displacement in reference to some position or longitudinal thickness of something
Δs_{res}	Longitudinal pixel resolution of the IPE in TracTIon
Δt	Time increment within one iteration of a particle tracking
ΔU	Height of the potential barrier within the beam potential
Δx	Horizontal distance to some point
Δx_{res}	Horizontal pixel resolution of the IPE in TracTIon
Δz	Vertical distance to some point of reference
$\Delta\mathcal{K}_{x,z}(x, z, x', z')$	Horizontal and vertical quadrupole kick for electrons at (x, z) due to the space charge of electrons and ions at (x', z')
$\Delta\varphi_{\mathrm{rms}}$	R.m.s. phase displacement in reference to φ_0
$\Delta\varphi_{\mu}$	Phase difference between each bunch for a certain multi bunch mode μ
$\Delta\Psi_{x,z}$	Horizontal or vertical betatron phase difference after one revolution in the accelerator
$\Delta\tilde{\varsigma}_{+}$, $\Delta\tilde{\varsigma}_{-}$	Normalized longitudinal distance between an ion position and $\tilde{\varsigma}$
$\Delta\tilde{\chi}_{+}$, $\Delta\tilde{\chi}_{-}$	Normalized horizontal distance between an ion position and $\tilde{\chi}$
δ	Proportionality constant between synchrotron radiation photon flux and the beam energy and current
δk_r, δk_x, δk_z	Radial, horizontal and vertical quadrupole kick
$\langle k_{x,z} \rangle$	Centroid of the horizontal and transversal tune distribution
$\delta k_{x,\mathrm{max}}$, $\delta k_{z,\mathrm{max}}$	$\delta k_{x,z}$ where the tune distribution shows its maximum
$\delta_{\mathcal{K}}$	Parameter for the adjustment of the momentum correction scheme of TracTIon
$\eth(x, x', z, z')$	Function ensuring the convergence of the sum of forces in dQTool
$\eth_{\mathrm{dipole}}$	A quantity being one within and zero outside dipole magnets
$\boldsymbol{\epsilon}_x$, ϵ_z	Horizontal and vertical emittance of the accelerator
$\epsilon_{x,0}$	Natural horizontal emittance
ε_0	Electric field constant
$\boldsymbol{\mu}$	Multi bunch mode number
μ_{ion}	Number of ions represented by one macro-ion
μ_0	Magnetic field constant
$\boldsymbol{\eta}$	Total neutralization of the electron beam
η_{dyn}	Dynamic neutralization within the accelerator
$\eta_{\mathrm{e}}(E_\gamma)$	Molecular desorption yield for electron stimulated desorption
η_i	Partial neutralization of the electron beam resulting from ion species i
η_{stat}	Static neutralization within the accelerator
$\eta_\gamma(E_\gamma)$	Molecular desorption yield for photo stimulated desorption
$\hat{\eta}(s)$	Local total neutralization
$\hat{\eta}_{\mathrm{dyn}}(s)$	Local dynamic neutralization
$\hat{\eta}_{\mathrm{dyn,sim}}$	Simulated local dynamic neutralization by TracTIon at a pressure of 10^{-8} mbar
$\hat{\eta}_{\mathrm{stat}}(s)$	Local static neutralization
$\boldsymbol{\Theta}$	Vertical deflection angle due to the clearing electrodes' fields
Θ	Polar angle of a spherical coordinate system

$\boldsymbol{\iota}$	A time index in a tracking simulation
ι_{ii}	Time index after which the ion generation subroutine for impact ionization is activated in TracTIon
ι_{pi}	Time index after which the ion generation subroutine for photo ionization is activated in TracTIon
$\boldsymbol{\kappa}$	Betatron coupling coefficient
$\tilde{\boldsymbol{\Lambda}}(\Theta)$	Quantity proportional to the photo ionization production rate at polar angle Θ
$\Lambda(E)$	Polynomical parametrization of $\mathcal{P}_{\mathrm{IGP,model}}$
Λ_1, Λ_2	Parameters of $\Lambda(E)$
λ, $\lambda(t)$	A (time dependent) line charge density of the beam
λ_{rf}	The rf wavelength of the accelerator
$\boldsymbol{\nu}$	The frequency of an oscillation
ν^{ion}, $\nu^{\mathrm{ion}}_{x,i}$, $\nu^{\mathrm{ion}}_{z,i}$	Horizontal and vertical ion oscillation frequency within the beam of an species i
ν_{rf}	Frequency of the rf cavities
ν_s	Synchrotron frequency
ν_0	Revolution frequency of the electron beam within the circular accelerator
$\boldsymbol{\Xi}(E)$	Polynomical parametrization of $\mathcal{P}_{\mathrm{IGP,model}}$
Ξ_1, Ξ_2	Parameters of $\Xi(E)$
$\boldsymbol{\pi}$	The mathematical constant π, defined as the ratio of a circle's circumference to its diameter.
$\boldsymbol{\rho}$	Non-linear pumping constant of an IGP
$\rho_{\mathrm{ion}}(x,t)$	Equilibrium density distribution of the ion population
ϱ	Proportionality between pumping speed and pressure
$\boldsymbol{\sigma}_{\mathrm{fringe}}$	Longitudinal decay constant of magnetic fringe fields
$\sigma_{\mathrm{fringe,QP}}$	Longitudinal decay constant of the fringe field of a quadrupole magnet
σ_{ion}	Total ionization cross section
$\sigma_{\mathrm{ion},i}$	General ionization cross section of species i
$\sigma_{\mathrm{ii},i}$	Impact ionization cross section for the ion species i
$\sigma_{\mathrm{pi},i}$	Photo ionization cross section for the ion species i
$\sigma_{\mathrm{pi},i}$	Photo ionization cross section of a particular shell of a residual gas species i
$\sigma_x(s)$, $\sigma_z(s)$, σ_s	1σ horizontal, vertical and longitudinal beam width
$\sigma_{x'}$	1σ angular deviation of the beam
ς	Relative sensitivity of the residual gas species during an analyzation of a mass spectrum
$\tilde{\varsigma}$	Discrete longitudinal position at a grid point of a map
$\boldsymbol{\tau}$	Life time of an ion within the accelerator
τ_{coll}	Lifetime of the electron beam due to collisions with the residual gas
τ_{e}	Lifetime of the electron beam
τ_x, τ_z, τ_s	Horizontal, vertical and longitudinal damping constants due to synchrotron radiation

$\boldsymbol{\Upsilon}_{\text{stab,all}}$	Stable fraction of all produced ions within the accelerator
$\Upsilon_{\text{stab},i}$	Stable fraction of produced ions of species i within the accelerator
υ	Removal rate of the residual gas by the pumps
$\boldsymbol{\Phi}$	A particle flux, as number of particles per second
Φ_γ	Synchrotron radiation photon flux
φ	Azimuthal angle in a spherical coordinate system
φ_0	Design phase of the beam in reference to the cavity's rf field
χ_e	Characteristic constant for the electron stimulated desorption
$\tilde{\chi}$	Discrete horizontal position at a grid point of a map
$\boldsymbol{\Psi}_x$, Ψ_z	Horizontal and vertical betatron phase
Ψ_x^0, Ψ_z^0	Horizontal and vertical initial betatron phase
$\boldsymbol{\omega}$	A photon frequency
ω_c	Critical frequency of the synchrotron radiation spectrum
$\omega_{\text{cycl},i}$	Angular cyclotron frequency of ion species i
ω_m	Oscillation frequency of the quadrupole mass filter
ω_0	Angular revolution frequency of the electron within the accelerator

Acknowledgements

The accomplishment of this thesis has only been made possible with the support and helpfulness of many great people. My sincere thanks therefore go to all those who have contributed to the success of this work. Especially the ELSA group deserves my thanks, which is why I am switching to German to personally mention and thank some of them explicitly:

Mein besonderer Dank gilt Herrn Professor Dr. Wolfgang Hillert für die Möglichkeit der Promotion und des Studiums dieses interessanten und speziellen Themenbereichs der Beschleunigerphysik. Ich bin zudem dankbar für die Möglichkeit selbstständig und frei arbeiten zu können und war mir gleichzeitig stets seiner wissenschaftlichen Unterstützung gewiss.

Herrn Professor Dr. Klaus Desch danke ich für die Übernahme des Koreferats. Ebenso bedanke ich mich bei Herrn Professor Dr. Carsten Urbach und Herrn Professor Dr. Peter Vöhringer, dass sie sich als Mitglieder der Promotionskomission zur Verfügung gestellt haben.

On behalf of the many collaboration partners at the University of Rostock who work tirelessly to perfect their MOEVE Pic Tracking program, I would like to thank Professor Dr. Ursula van Rienen and Dr. Aleksandar Markovic for the fruitful cooperation. I would also like to thank Professor Dr. Atoosa "Ati" Meseck from Helmholtz Center Berlin for the numerous lively scientific discussions and good ideas regarding ion-related analysis concepts and measurement techniques.

Der gesamten ELSA-Mannschaft danke ich für den herzlichen Umgang und die tolle Arbeitsatmosphäre, die mir eine wundervolle Zeit beschert hat, an welche ich mich sehr gerne zurückerinnern werden. Ein großer Dank geht insbesondere an Philipp Hänisch und Franz Gerhard Engelmann für die technische Planung und Koordinierung von Hardwareinstallationen und allen Technikern für die Unterstützung bei ihrer Umsetzung. Dr. Andreas Dieckmann sei gedankt für Hilfestellungen im Bereich der Elektronik und Dr. Frank Frommberger für Unterstützung bei der Lösung von IT-Problemen aller Art. Herzlichen Dank auch an Dennis Proft, Manuel Schedler und Jens-Peter Thiry für die Hilfe beim Betrieb der *Alten Dame* während der Teststrahlzeiten und die vielen produktiven und lustigen Stunden im Kontrollraum zu allen Tages- und Nachtzeiten.

Ein ganz großer Dank gilt den aktuellen und ehemaligen Mitgliedern der Arbeitsgruppe, welche die Gruppe zu dem gemacht haben was sie ist: Eine bunte, lustige, teils chaotische aber immer gutmütige Truppe, in der man nicht nur als Kollegen nebeneinander arbeitet sondern vielmehr als Freunde miteinander lebt. Der angenehmen Arbeitsatmosphäre die meine Freunde im Büro, Dennis Proft, Jan Schmidt, Jens-Peter Thiry und Michael Switka verbreitet haben ist es zu verdanken, dass ich an jedem Tag gerne zur Arbeit gegangen bin. Auch für unsere lebhaften und teils hitzigen Diskussionen, die neben der Physik auch vor den großen und wichtigen Themen wie Gesellschaft und Politik nicht halt gemacht haben, möchte ich mich ganz herzlich bedanken.

Für das Korrekturlesen dieser Arbeit danke ich Frank Frommberger, Manuel Schedler, Jan Schmidt, Michael Switka und insbesondere Dennis Proft, dem ein Großteil der Korrekturarbeit zufiel.

Ohne die bedingungslose Unterstützung meiner Familie; meines Bruders, meiner Großeltern und vor allem meiner Eltern wäre mein Studium und damit diese Arbeit nicht möglich gewesen. Daher gilt ihnen mein intensivster und immerwährender Dank.